Formation, réparation osseuse mandibulaire et approches thérapeutiques dans les ostéochondrodysplasies liées à des mutations FGFRs

Anne Morice

THESE DE DOCTORAT D'UNIVERSITE PARIS CITE
Spécialité Génétique

Ecole doctorale ED 562 Bio Sorbonne Paris Cité
Institut des maladies génétiques (Imagine), Inserm U1163, Université Paris Cité
UMR_S 1163
Equipe Bases Moléculaires et Physiopathologiques des ostéochondrodysplasies

Formation, réparation osseuse mandibulaire et approches thérapeutiques dans les ostéochondrodysplasies liées à des mutations *FGFRs*

Anne MORICE

Dirigée par Laurence LEGEAI-MALLET et co-dirigée par Roman Hossein KHONSARI

Présentée et soutenue publiquement le 20 Janvier 2023

Composition du jury :

Céline COLNOT *rapporteur*
Directrice de recherche
Inserm U955, Institut Mondor de Recherche Biomédicale, Faculté de Santé de Créteil, Université Paris-Est Créteil

Yann HEUZE *rapporteur*
Chargé de recherche
Pacea UMR S199, Université de Bordeaux

Jeanne AMIEL *examinatrice*
Professeur des Université Praticien Hospitalier
Génétique Médicale, Hôpital Necker Enfants Malades, Inserm U1163, Institut Imagine, Université Paris Cité

Sarah BECK *examinatrice*
Chargée de recherche
Inserm UMR 1087 / CNRS UMR 6291 IRS-UN ; Nantes Université

Boris LAURE *examinateur*
Professeur des Université Praticien Hospitalier
Centre Hospitalier Régional Universitaire de Tours, Université de Tours

Arnaud PICARD *examinateur*
Professeur des Université Praticien Hospitalier
Hôpital Necker Enfants Malades ; Université Paris Cité

Roman Hossein KHONSARI *co-directeur de thèse*
Professeur des Université Praticien Hospitalier
Hôpital Necker Enfants Malades ; Université Paris Cité ; Institut Imagine, Inserm U1163

Laurence LEGEAI-MALLET *directrice de thèse*
Directrice de Recherche
Institut Imagine, Inserm U1163 ; Université Paris Cité

Table des matières

Abréviations

AR : Acide Rétinoïque
Birc2 : Baculoviral IAP Repeat containing 2
BMP : Bone Morphogenetic Protein
CATSHL: camptodactyly, tall stature, and hearing loss
CNP : C-natriuretic peptide
Col : Collagen
Comp : Cartilage Oligomeric Protein
Dmp : Dentin Matrix Acidic Phosphoprotein 1
Dusp : Dual-Specificity Phosphatase 6
Erk : Extracellular signal-regulated kinase
FGF : Fibroblast Growth Factor
FGFR : Fibroblast Growth Factor Receptor
FRS2 : FGF-Regulated Substrate 2
Grb2 : Growth Factor Receptor Bound 2
Hmgb2 : High Mobility Group Box 2
HS : Heparane Sulfate
Ig : boucles pseudo immunoglobuline
Ihh : Indian hedgehog
Kif17 : Kinesin family member 17
MAPK : Mitogen-Activated Protein Kinase
MMP : Matrix Metalloproteinase
Msx : Msh homeobox
NPR2 : Natriuretic Peptide Receptor 2
Osx : Osterix
Phospho1: Phosphatase, orphan 1
PI3K : Phosphoinositide 3-kinase
PIP : phosphatidylinositol-4,5-bisphosphate
PKC : Protein Kinase C
PLCgamma : Phospholipase C gamma
PPARgamma : Peroxisome Proliferator activated Receptor gamma
PTHrP : Parathyroid Hormone-related Protein
Runx2 : Runt-related transcription factor 2
Socs3 : Suppressor of Cytokine Signalling 3
Sox : SRY-Box Transcription Factor
STAT : Signal Transducer and Activator of Transcription

Résumé

Les patients atteints d'ostéochondrodysplasies liées à des mutations activatrices dans les gènes *FGFR2* et *FGFR3* présentent des malformations craniofaciales et mandibulaires. Ce projet de thèse a pour objectif de déchiffrer le rôle précis du gène *FGFR3* chez les patients atteints d'ostéochondrodysplasie et dans un modèle murin d'hypochondroplasie $Fgfr3^{N534K/+}$ au cours de la formation et de la réparation osseuse mandibulaire. A partir d'un modèle de fracture non stabilisée de la mandibule de souris $Fgfr3^{N534K/+}$ et de leurs contrôles, les différentes étapes de la réparation osseuse endochondrale ont été étudiées à l'aide d'approches morphométriques, scanographiques, histologiques et de transcriptomique spatiale.

Nous avons tout d'abord montré des anomalies morphologiques mandibulaires majeures chez les patients porteurs de faciocraniosténoses *FGFR2* et *FGFR3* et dans l'achondroplasie (*FGFR3*), consolidant nos connaissances sur les corrélations génotype / phénotype dans ces syndromes. Notre analyse a montré une corrélation entre la sévérité des anomalies morphologiques craniomaxillofaciales des achondroplases et la sévérité des apnées du sommeil, soulignant l'importance de la prise en charge des anomalies morphologiques maxillomandibulaires, notamment via des gestes chirurgicaux nécessitant une étape de consolidation osseuse.

En parallèle, nous avons étudié l'impact de la mutation $Fgfr3^{N534K/+}$ au niveau des cartilages de formation mandibulaire primaire (Meckel) et secondaires (condylien) en période anté- et post-natale. Des anomalies de formation et de résorption du cartilage de Meckel, et un défaut de différenciation chondrocytaire étaient présents au sein du cartilage condylien chez les souris mutantes. L'ensemble de ces anomalies entraînaient un défaut de croissance et des modifications morphologiques mandibulaires.

Les fractures non stabilisées de la mandibule réalisées chez des souris $Fgfr3^{N534K/+}$ont permis d'analyser les cals de réparation. Nous avons observé des anomalies majeures de réparation, caractérisées par un retard sévère de consolidation osseuse, et la présence de pseudarthrose chez les souris $Fgfr3^{N534K/+}$. Nos études révèlent un défaut majeur de différenciation chondrocytaire au sein du cartilage de réparation, un retard de mise en place et de résorption du cartilage et des défauts microarchitecturaux de l'os nouvellement formé du cal. Nous avons également conduit des études de transcriptomique spatiale à la fois dans la partie cartilagineuse et osseuse à J14 post fracture. Au niveau du cartilage, les résultats obtenus confirment le défaut de différenciation et de maturation chondrocytaire, comme révélé par la diminution significative de l'expression de gènes exprimés par les chondrocytes matures ou en phase de transdifférenciation en ostéoblastes (*Col11, Col1a, Dmp1, Phospho1, Hmgb2*). L'expression de *Kif17*, un gène exprimé au sein du cil primaire était fortement diminuée chez les mutants, soulignant l'impact de la mutation au cours de la formation du cartilage du cal. Au niveau de l'os nouvellement formé du cal, les résultats montrent un défaut d'homéostasie osseuse. Nous avons aussi mis en évidence des différences majeures d'expression de gènes impliqués dans les mécanismes d'autophagie et d'apoptose (*Smad1, Comp, Birc2)* et une diminution de l'expression de *Alkbh2* traduisant un défaut de réparation de l'ADN. Nos analyses montrent la surexpression de gènes impliqués dans la régulation négative de la voie des MAPKinases, suractivée par la mutation $Fgfr3^{N534K/+}$, il s'agit de *Dusp9* (cartilage) de *Socs3* et *Dusp3* (os du cal).

Enfin, nous avons étudié l'impact d'antagonistes de FGFR3 (inhibiteur de tyrosine kinase et analogue du CNP) sur la réparation osseuse. Nos études précliniques ont montré que les souris $Fgfr3^{N534K/+}$ traitées présentent une consolidation normale, un remodelage osseux du cal de réparation accéléré et une absence de pseudarthrose.

L'ensemble de ces résultats ouvre des perspectives thérapeutiques majeures chez les patients porteurs d'ostéochondrodysplasies FGFRs au cours de la réparation osseuse.

Abstract

Patients with osteochondrodysplasia, linked to activating mutations in the FGFR2 and FGFR3 genes, have craniofacial and mandibular malformations. This thesis project aims to decipher the exact role of FGFR3 gene in patients with osteochondrodysplasia and in a mouse model of hypochondroplasia *Fgfr3*$^{N534K/+}$ during mandibular bone formation and repair.

Using a model of non-stabilized mandibular fracture performed in *Fgfr3*$^{N534K/+}$ mice and their controls, the different stages of endochondral bone repair were studied using morphometric, microCT, histological and spatial transcriptomics approaches.

We first showed major mandibular morphological abnormalities in patients with FGFR2 and FGFR3 related craniosynostoses and in achondroplasia (FGFR3), consolidating our knowledge concerning genotype phenotype correlations in this context. In addition, our analysis showed a correlation between the severity of craniomaxillofacial morphological abnormalities and the severity of sleep apnea in achondroplasia patients, highlighting the importance of managing maxillomandibular morphological abnormalities.

In parallel, we studied the impact of the *Fgfr3*$^{N534K/+}$ mutation on mandibular, primary (Meckel) and secondary (condylar) cartilage in the ante- and postnatal period. Abnormalities in the formation and resorption of Meckel cartilage and altered chondrocyte differentiation within condylar cartilage were observed in mutant mice.

All these abnormalities lead to growth defects and mandibular morphological changes.

Following non-stabilized mandibular fractures, we observed major repair abnormalities, characterized by delayed bone consolidation, and the presence of pseudarthrosis in *Fgfr3*$^{N534K/+}$ mice.

Our studies revealed reduction of chondrocyte differentiation, delayed cartilage formation and formation, and microarchitectural defects in the newly formed bone of the callus.

We also conducted spatial transcriptomics studies in both cartilaginous and bone regions at day 14 post fracture. At cartilage level, the results confirm reduction of chondrocyte differentiation and maturation, as revealed by the significant decrease in the expression of genes expressed by mature chondrocytes or in the phase of transdifferentiation into osteoblasts (*Col11, Col1a, Dmp1, Phospho1, Hmgb2*). The expression of *Kif17*, a gene expressed within the primary cilia was found greatly diminished in mutants, highlighting here the impact of the mutation during the formation of callus cartilage. At the level of the newly formed bone of the callus, the results showed a defect of bone homeostasis. We also highlighted major differences in gene expression involved in autophagy and apoptosis mechanisms (*Smad1, Comp, Birc2*) and a decrease in *Alkbh2* expression reflecting altered DNA repair.

Our analyses showed the overexpression of genes involved in the downregulation of the MAPKinase pathway, overactivated by the *Fgfr3*$^{N534K/+}$ mutation, these are *Dusp9* (cartilage), *Socs3* and *Dusp3* (bone callus).

Finally, we investigated the impact of FGFR3 antagonists (tyrosine kinase inhibitor and CNP analog) on bone repair. Our preclinical studies have shown that treated *Fgfr3*$^{N534K/+}$ mice present normal consolidation, accelerated bone callus remodelling, and absence of pseudarthrosis.

All these results are promising and give major therapeutic perspectives in patients with FGFRs osteochondrodysplasias during bone repair.

I. Introduction

A. Fibroblast Growth Factor et leurs récepteurs, les Fibroblast Growth Factor Receptors

1. Les Fibroblast Growth Factors

Les **Fibroblast Growth Factors (FGFs)** font partie d'une grande famille de ligands impliqués dans de nombreux processus biologiques intervenant dans le développement, l'homéostasie et le métabolisme tissulaire et cellulaire (Goetz and Mohammadi, 2013). Il existe chez l'Homme et la souris, 22 FGFs répartis en 3 familles principales sur la base de leur similarité de séquence (Ornitz and Itoh, 2001) : les FGFs canoniques ayant une action paracrine, les FGFs endocrines, et les FGFs intracellulaires. Parmi les FGFs canoniques, il existe 5 sous-familles de ligands : la sous-famille Fgf1 (Fgf1, Fgf2), la sous-famille Fgf4 (Fgf4 à 6), la sous-famille Fgf7 (Fgf3, Fgf7, Fgf10, Fgf22), la sous-famille Fgf8 (Fgf8, Fgf17, Fgf18) et la sous-famille Fgf9 (Fgf9, Fgf16, Fgf20). Parmi les FGFs endocrines, il existe une sous-famille Fgf15/19 (Fgf15/19 (Fgf15 chez la souris, Fgf19 chez l'Homme), Fgf21, Fgf23). La famille des ligands intracellulaires correspond à la sous-famille Fgf11 (Fgf11 à 14) (Figure 1).

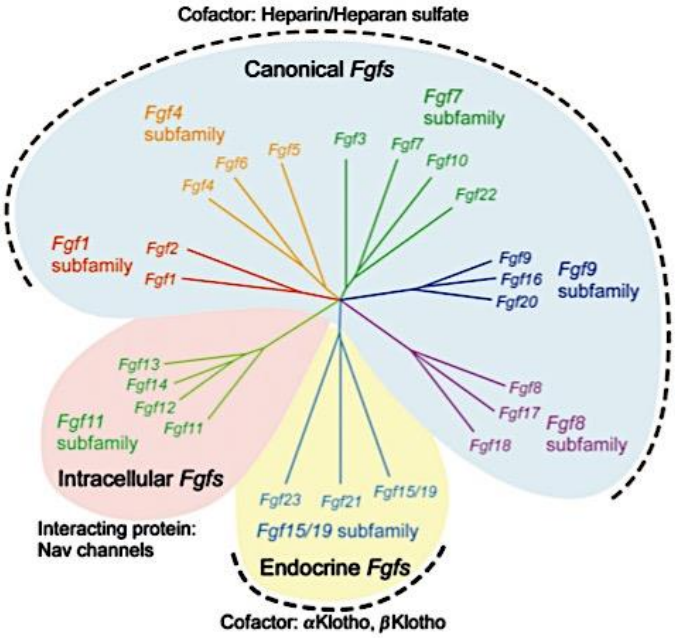

Figure 1. Analyse phylogénétique classant les 22 ligands FGF en 3 familles de Fgfs, dont 7 sous-familles : la famille des Fgfs canoniques, avec les 5 sous-familles Fgf1, 4, 7, 8, 9 ; la famille des Fgfs endocrines, avec les sous-familles Fgf15/19, Fgf21, Fgf23 ; la famille des Fgfs intracellulaires, avec les sous-familles Fgf11 à 14 (Ornitz and Itoh, 2015).

Les FGFs paracrines et endocrines exercent leur action par l'intermédiaire de leurs récepteurs, les Fibroblast Growth Factors Receptors (FGFRs), présents au niveau de la membrane cellulaire, composés de trois domaines : un domaine extracellulaire, au niveau duquel les FGFs interagissent par l'intermédiaire d'un site de fixation, un domaine transmembranaire, et un domaine intracellulaire ayant une activité tyrosine kinase. Les ligands FGFs ont une affinité de liaison avec les chaines héparane sulfate des Glygosaminoglycans des Protéoglycans Heparane Sulfate présents abondamment à la surface cellulaire, et dans la matrice péricellulaire et extracellulaire (Asada et al, 2008). Cette affinité de liaison est variable selon les FGFs. Elle est forte pour les ligands paracrines, ce qui a pour conséquence d'induire une action de ces FGFs uniquement à proximité de leur sécrétion. A l'opposé, les FGFs endocrines ont une faible affinité de liaison pour les chaines héparane sulfate, ainsi, leur diffusion systémique est possible, et ils peuvent atteindre une cible cellulaire distante de leur site de sécrétion (Goetz et al, 2007, Asada et al, 2008). Alors que les ligands paracrines nécessitent l'héparane sulfate comme co-récepteur (Yayon et al, 1991), les ligands endocrines ont une action par l'intermédiaire d'un co-récepteur Klotho (Kurosu et al, 2006, 2007).

Il existe plusieurs types de régulation des FGFs : l'interaction du ligand avec les héparanes sulfates, comme précédemment décrit, mais également la dimérisation des ligands, l'épissage alternatif et le clivage protéolytique. Le mécanisme de dimérisation réversible régule l'activité des ligands de la sous famille Fgf9, leur dimérisation ayant un effet de régulation négative de ces ligands, qui se fixent normalement à leur récepteur sous la forme monomérique (Kalinina et al, 2009, Plotnikov et al, 2001, Harada et al, 2009). L'épissage alternatif est connu dans la régulation de Fgf8 et Fgf17. Il a pour effet de modifier l'extrémité N-terminale de la protéine, et ainsi, de réguler l'affinité de liaison du Fgf au récepteur FGFR, modulant alors son activité biologique (Olsen et al, 2006, Crossley et al, 1995, Xu et al, 1999). Le clivage protéolytique est un mode de régulation confirmé pour Fgf23, ayant pour effet de l'inactiver (Goetz et al, 2010). Ce mécanisme est aussi décrit pour les ligands de la sous famille Fgf7 et pour Fgf8, mais son rôle de régulation n'a pas encore été confirmé in vivo (Hsu et al, 1998, Kim et al, 2012).

Les ligands intracellulaires ne se lient pas aux FGFRs. Ils sont cytosoliques, et interagissent avec des canaux sodiques voltage-dépendant Nav, jouant un rôle dans l'excitabilité neuronale (Goldfarb et al, 2007).

Les FGFs déclenchent des processus biologiques distincts, en fonction de l'organe, de leur liaison et de leur spécificité aux récepteur FGFRs. En effet, l'affinité des ligands aux FGFR varient selon le type de ligand (Tableau 1).

FGF subfamily	FGF	Cofactor	Receptor specificity
FGF1 subfamily	FGF1		All FGFRs
	FGF2		FGFR 1c, 3c > 2c, 1b, 4Δ
FGF4 subfamily	FGF4		FGFR 1c, 2c > 3c, 4Δ
	FGF5		
	FGF6		
FGF7 subfamily	FGF3	+ Heparin or Heparan sulfate	FGFR 2b > 1b
	FGF7		
	FGF10		
	FGF22		
FGF8 subfamily	FGF8		FGFR 3c > 4Δ > 2c > 1c >> 3b
	FGF17		
	FGF18		
FGF9 subfamily	FGF9		FGFR 3c > 2c > 1c, 3b >> 4Δ
	FGF16		
	FGF20		
FGF15/19 subfamily	FGF15/19	+βKlotho	FGFR 1c, 2c, 3c, 4Δ
	FGF21		FGFR 1c, 3c
	FGF23	+αKlotho	FGFR 1c, 3c, 4

Tableau 1. Cofacteurs et récepteurs spécifiques des FGFs canoniques et endocrines (Ornitz and Itoh, 2015).

2. La famille des Fibroblast Growth Factor Receptors

Il existe 2 types de récepteurs aux FGFs : les récepteurs à haute affinité et les récepteurs à faible affinité. Les récepteurs à faible affinité correspondent à des protéoglycanes à héparine ou héparane sulfate (HSPG) (Burgess and Maciag, 1989). Les récepteurs à haute affinité correspondent aux récepteurs FGFR1 à 4, spécifiques des FGFs, le récepteur FGFR5 ou FGFRL1 (Fibroblast Growth Factor Receptor like protein 1) présente une variation importante du domaine extracellulaire, lui conférant une faible affinité de liaison aux ligands FGFs (Sleeman et al, 2001).

a) FGFR 1 à 4

Structure

Ces récepteurs sont composés d'un domaine extracellulaire comprenant 3 domaines immunoglobulin-like (Ig) (D1 à D3), avec site de fixation du ligand FGF au niveau des domaines D2-D3, un domaine transmembranaire, et un domaine intracellulaire avec activité tyrosine kinase (Jaye et al, 1992 ; Johnson and Williams, 1993 ; Mohammadi et al, 2005). Un domaine composé de résidus acides se situe entre les boucles D1 et D2 du domaine extracellulaire (Mohammadi et al, 2005). Le domaine D1 est impliqué dans les mécanismes d'auto-inhibition du récepteur.

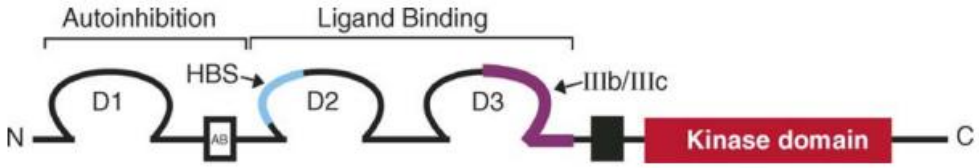

Figure 2. Représentation schématique de la structure des FGFRs : HBS (Heparin Binding Site), AB (Acid Box), D1, D2, D3 correspondent au domaine extracellulaire de la protéine, le domaine tyrosine kinase est localisé en intramembranaire (Mohammadi et al, 2005).

Régulation

Epissage alternatif du domaine D3 des FGFRs

La spécificité de liaison des ligands FGF aux récepteurs FGFR1, FGFR2 et FGFR3 est conditionnée par le mécanisme d'épissage alternatif, à l'origine de la formation d'isoformes b (spécifique des tissus épithéliaux) d'isoformes c (spécifique des tissus mésenchymateux). La portion N-terminale de la protéine du domaine D3 est codée par l'exon 7 (ou exon IIIa), alors que la portion C-terminale est codée soit par l'exon 8 (exon IIIb) ou 9 (exon IIIc). L'isoforme IIIa code pour un site extracellulaire de fixation des FGF, sans capacité connue d'induction de signalisation intracellulaire (Duan et al, 1992). Les isoformes b interagissent spécifiquement avec les ligands FGFs secrétés par les tissus mésenchymateux, alors que les isoformes c, avec les ligands secrétés par les tissus épithéliaux (Miki et al, 1992 ; Zhang et al, 2006). Cette régulation tissulaire crée des boucles de signalisation paracrine spécifiques entre les tissus épithéliaux et mésenchymateux, intervenant dans la régulation des mécanismes s'exerçant lors du développement et dans le cadre du maintien de l'homéostasie tissulaire (Alarid et al, 1994 ; De Moerlooze et al, 2000). Pour exemple, les ligands de la sous-famille FGF7 sont exprimés au niveau mésenchymateux, et induisent la plus forte activité lors de leur fixation à l'isoforme b de FGFR2. A l'inverse, les ligands de la sous-famille FGF8 sont exprimés au sein des tissus épithéliaux et activent préférentiellement les isoformes c des FGFRs (Zhang et al, 2006).

Dimérisation ligand-dépendante des FGFRs

Les FGFs paracrines, pour parvenir à induire une liaison robuste avec le récepteur FGFR et permettre la formation d'un complexe stable FGF-FGFR avec un ratio 2:2 (Figure 3), nécessitent comme cofacteur une chaine d'héparane sulfate qui renforce les contacts ligand-recepteur et recepteur-recepteur.

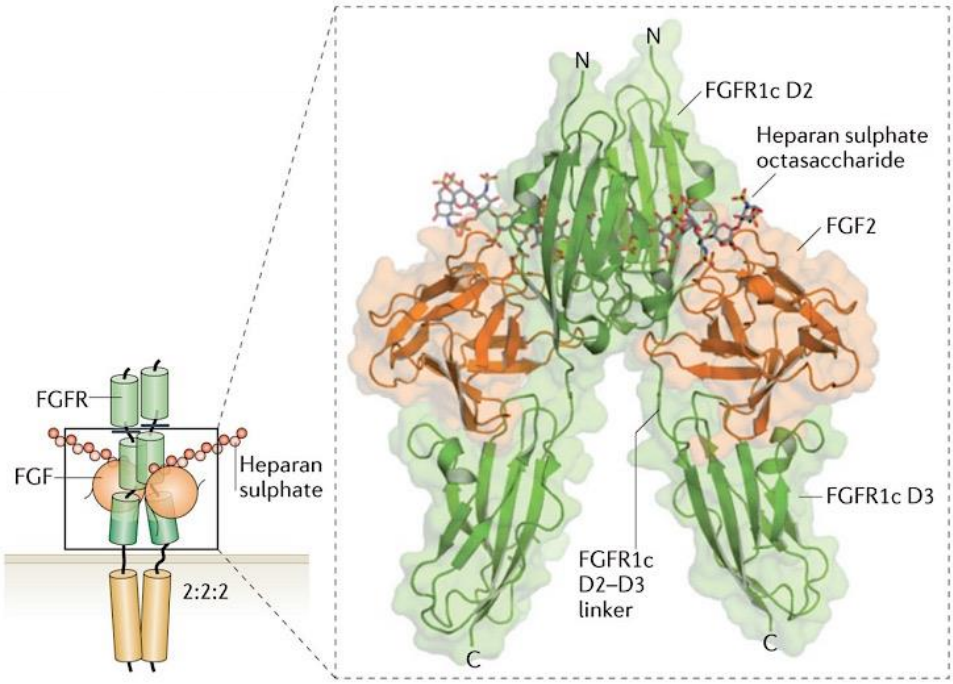

Figure 3. Représentation schématique du complexe de dimérisation FGFR/FGF/chaines d'héparane sulfate (Goetz and Mohammadi, 2013).

Au niveau du site primaire d'interaction entre le ligand et le récepteur se forme un important réseau de ponts hydrogènes entre le ligand, le domaine D3 et le domaine de liaison entre D2 et D3. Ce réseau de ponts hydrogènes confère une rigidité structurale au complexe d'interaction D2-D3/D3/ligand, et sa composition ainsi que sa géométrie déterminent l'orientation du domaine D3 et de la liaison D2/D3 au sein du complexe (Schlessinger et al, 2000, Olsen et al, 2004, 2006, Plotnikov et al, 1999, 2000, 2001 ; Yeh et al, 2003 ; Stauber et al, 2000).
La substitution de résidus clés au sein de ce réseau de ponts d'hydrogène régule la spécificité des interactions ligand/récepteur et pourrait conditionner l'intensité et la durée du signal déclenché en aval. Ce mécanisme de substitution a été décrit pour les ligands de la sous-famille Fgf8, à l'origine de modifications structurelles du complexe Fgf8b/FGFR2c (Schlessinger et al, 2000).

b) FGFR5 ou FGFRL1 (Fibroblast Growth Factor Receptor like protein 1)

Ce récepteur possède un peptide-signal, 3 répétitions Ig-like, un segment transmembranaire et un court fragment intracytoplasmique. Il ne comprend pas de domaine tyrosine kinase. Les domaines extracellulaires et transmembranaires partagent une homologie de séquence à hauteur de 45 % avec les autres FGFRs, et se lient au ligand FGF-2 avec une faible affinité. Ses

fonctions précises sont peu connues, cependant, il semble être impliqué dans la régulation négative des autres récepteurs, notamment de FGFR1 (Wiedermann and Trueb, 2000 ; Kim et al, 2001 ; Sleeman et al, 2001 ; Amann and Trueb, 2013).

c) FGF et FGFRs nucléaires

Certains ligands paracrines peuvent pénétrer dans le noyau cellulaire après leur passage au travers de la membrane plasmique (Coleman et al, 2014 ; Ornitz and Itoh, 2015). Il s'agit de FGF1 et FGF2. Les mécanismes par lesquels ces ligands ont la capacité de pénétrer le noyau cellulaire ne sont pas encore totalement élucidés, mais il semble que l'étape de liaison avec le FGFR, le cofacteur heparine/heparane sulfate et HSP90 soit nécessaire (Wesche et al, 2006 ; Sorensen et al, 2006). FGF1 nucléaire est impliqué dans des mécanismes de régulation du cycle cellulaire, de différenciation, de la survie cellulaire et d'apoptose (Bouleau et al, 2005 ; Rodriguez Enfedaque et al, 2009). Les récepteurs FGFR1 et 2 sont aussi connus pour pouvoir pénétrer le noyau cellulaire, leur action nucléaire est indépendante de leur activité tyrosine kinase (Coleman et al, 2014 ; Ornitz and Itoh, 2015).

d) L'interaction FGF/FGFRs et les voies de signalisation

L'interaction FGF/FGFRs est conditionnée par la disponibilité du ligand pour qu'il puisse se fixer sur le récepteur et initier les cascades de signalisation intracellulaire. Fibroblast Growth Factor Binding Protein (FGF-BP) est une protéine extracellulaire ayant des sites de fixation distincts pour les chaines d'héparane sulfate et pour les FGFs. FGF-BP a la capacité de mobiliser les FGFs de la matrice extracellulaire, et de les présenter aux FGFRs correspondants (Wu et al, 1991 ; Czubayko et al, 1997).

Le ligand FGF se fixe au niveau des domaines D2 et D3 du domaine extracellulaire du récepteur, entraînant la formation d'un réseau de ponts hydrogènes, entre les chaînes β du domaine D3 et du ligand FGF. Cette interaction a pour effet de modifier la conformation des domaines D2 et D3, de permettre la dimérisation du récepteur et par voie de conséquence de modifier la conformation des domaines transmembranaires et intracellulaires, initiant ainsi la transphosphorylation des domaines tyrosine kinase (Yayon et al, 1991 ; Ornitz et al, 1992 ; Mohammadi et al, 1996 ; Schlessinger et al ; 2000 ; Goetz and Mohammadi, 2013).

Le récepteur FGFR phosphorylé ainsi activé induit à son tour la phosphorylation de protéines adaptatrices de quatre voies de signalisation intracellulaires : la voie RAS-MAPK (Mitogen

Activated Protein Kinase, PI3K-AKT (Phosphoinositide 3-kinase), PLCγ (Phospholipase Cγ) et la voie STAT (Signal Transducer and Activator of Transcription).

La voie RAS-MAPK

L'activation de la voie des MAPK est initiée par la phosphorylation du cofacteur FRS2α, lié au récepteur dans la zone juxtamembranaire. La phosphorylation de FRS2α et l'activation de ERK1/2 sont partiellement dépendantes de la phosphorylation du site Y463, et de la présence de CRKL (Moon et al, 2006 ; Seo et al, 2009). FRS2α phosphorylée se lie ensuite à la protéine GRB2 (Growth factor Receptor-bound 2), et à une enzyme à activité tyrosine phosphatase SHP2 (Kouhara et al, 1997 ; Hadari et al, 1998). GRB2 à son tour recrute la protéine SOS (Son of Sevenless) (Kouhara et al, 1997), ce qui enclenche l'activation de la voie de signalisation via RAS, une protéine à activité GTPase (Ornitz and Itoh, 2015) (Figure 4). En aval de l'activation de MEK, plusieurs MAPK distinctes peuvent être phosphorylée : JNK, p38, Erl1 et 2 (Ornitz and Marie, 2015 ; Tsang and Dawid, 2004). Cette voie régule l'expression de différents gènes, via l'interaction dans le noyau de la MAPK activée avec le facteur de transcription ETS (E26 transformation-specific) (Tsang and Dawid, 2004).

La voie PI3K-AKT

L'activation de la voie PI3K-AKT, comme pour la voie RAS-MAPK est initiée par la phosphorylation du cofacteur FRS2α. FRS2α phosphorylé se lie ensuite à GRB2, qui recrute à son tour GAB1, ce qui enclenche l'activation de voie de signalisation PI3K-AKT en aval (Lamothe et al, 2004). Contrairement à la voie RAS-MAPK, l'activation de la voie PI3K-AKT a un effet d'inhibition de FOXO1 (Forkhead box class transcription factor), un effecteur pro-apoptotique inactivé par la phosphorylation de AKT ; et de TSC2 (cytosolic tuberous sclerosis complex 2), ayant pour effet de stimuler la croissance et la prolifération cellulaire (Manning and Cantley, 2007) (Figure 4).

La voie PLCγ

La phosphorylation de PLCγ induite par l'activation du domaine tyrosine kinase entraine l'hydrolyse du phosphatidylinositol 4,5-bisphosphate en inositol triphosphate (IP3) et diacylglycerol (DAG). IP3 augmente le niveau de calcium intracellulaire et DAG active la PKC. PKC activée va phosphoryler plusieurs cibles intracellulaires, dont Raf, à l'origine de l'activation de Erk indépendamment de FRS2 (Brewer et al, 2016).

La protéine adaptatrice GRB14 a un rôle connu de régulation en aval de FGFR1, par sa fixation au niveau du domaine tyrosine kinase au site Y766 (Figure 4). Cette fixation de GRB14 au récepteur a pour effet d'inhiber la phosphorylation des résidus tyrosines et l'activation de PLCγ (Browaeys-Poly et al, 2010).

La voie des STAT

La voie STAT est également activée en aval de l'activation du complexe FGFR, suivant la phosphorylation dans le domaine tyrosine kinase 2 du récepteur, en position Y677. L'activation à ce niveau entraine le recrutement des protéines STAT 1, 3 et 5, et de cofacteurs des familles JAK (Janus Kinase) et SRC. Cette interaction JAK-STAT entraine la phosphorylation et la dimérisation de la protéine STAT, ayant une capacité de pénétration nucléaire sous cette forme. Les protéines STAT sont impliquées dans la régulation de la survie, de la migration et de la prolifération cellulaire (Dudka et al, 2010, Ornitz and Itoh, 2015).

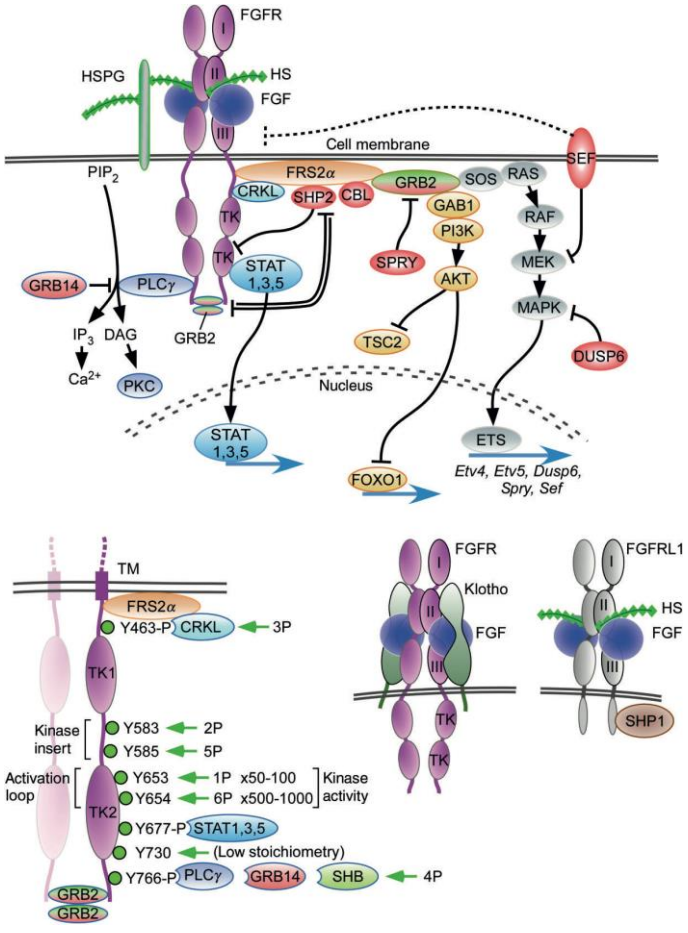

Figure 4. Représentation schématique des voies de signalisation activée en aval de l'interaction FGF/FGFR (Ornitz and Itoh, 2015).

B. Développement du squelette craniofacial et mandibulaire

La formation et le développement de l'extrémité céphalique sont des processus impliquant une diversité d'acteurs tissulaires et cellulaires, d'origines multiples, se mettant en place avec une coordination spatiotemporelle indispensable au bon déroulement du développement. On distingue deux entités anatomiques et fonctionnelles distinctes : le neurocrâne, et le viscérocrâne. Le neurocrâne est divisé en 2 régions : la voûte du crâne correspondant à la région supérieure assurant la protection du cerveau sous-jacent, et la base du crâne correspondant à la région inférieure de la boite crânienne. Le viscérocrâne correspond aux éléments dont dérivent les structures de la face et du cou.

1. Formation de l'extrémité céphalique en période embryonnaire et fœtale chez l'Homme

La mise en place du tube neural est un préliminaire indispensable à la formation du squelette craniofacial. Chez l'Homme, lors de la 3ème semaine du développement, une flexion céphalique apparaît, marquant le niveau du mésencéphale en formation. A partir de la 5ème semaine, le tube neural se compose, en avant de la flexion cervicale, du prosencéphale, du mésencéphale et du rhombencéphale, et se prolonge en arrière par la corde spinale (Rubenstein et al, 1998). Le prosencéphale se subdivise ensuite en télencéphale et en diencéphale, et le rhombencéphale en metencéphale et myelencéphale. Au 70ème jour, les méninges dérivées des cellules de la crête neurale recouvrent le télencéphale, alors que les méninges dérivées du mésoderme recouvrent les structures plus caudales (Figure 5) (Larsen et al, 2001 ; Richtsmeier and Flaherty, 2013).

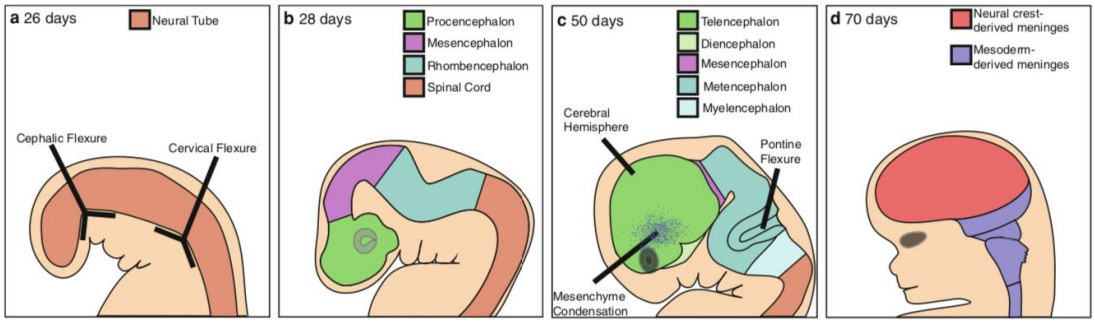

Figure 5. Développement du tube neural chez l'Homme (Larsen et al, 2001 ; Richtsmeier and Flaherty, 2013).

L'ossification de la voûte crânienne débute à partir de la 8ème semaine de gestation. Le premier os à se former est l'os frontal, puis les os interpariétaux, les alisphénoïdes, l'écaille du temporal et les os pariétaux (Figure 6).

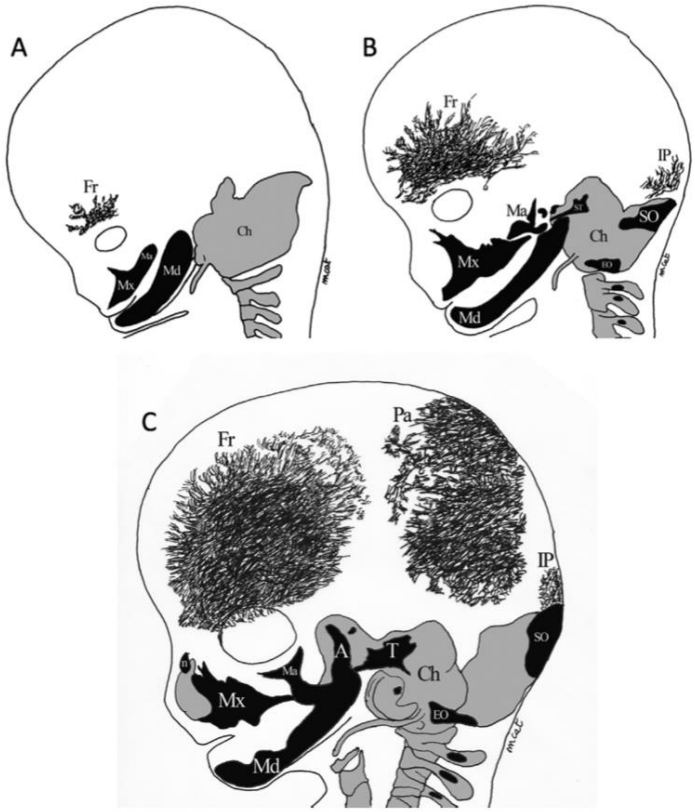

Figure 6. Représentation schématique de l'extrémité céphalique d'un embryon/fœtus humain. A : 8 semaines de gestation, B : 9 semaines de gestation ; C : 10 semaines de gestation) (Catala et al ; 2019). A : Alisphénoïde ; Ch : Chondrocrâne ; EO : Exo-occipital ; Fr : Frontal ; IP : Interpariétal ; Ma : malaire ; Md : Mandibule ; Mx : Maxillaire ; n : Nasal ; SO : Supraoccipital ; ST : partie squameuse du temporal ; T : temporal.

L'origine embryologique des os craniofaciaux est mixte : les os de la face, l'os frontal, et au niveau de la base du crâne, les os présphénoïde et basisphénoïde dérivent des crêtes neurales, alors que les os pariétaux, interpariétaux, occipital, et l'os basioccipital au niveau de la base du crâne dérivent du mésoderme paraxial (Catala et al, 2019 ; Catala, 2019) ; ceci a également été montré chez la souris (Richtsmeier and Flaherty, 2013). Chez l'homme et la souris, les sutures coronales située à la jonction entre les os frontaux et les os pariétaux constituent la frontière entre les 2 territoires d'origine embryologique différente. Au niveau de la base du crâne, cette limite correspond à la synchondrose sphéno-occipitale.

Les étages moyens et inférieurs de la face dérivent des bourgeons faciaux primordiaux naso-frontaux, maxillaires et mandibulaires, qui constituent les parois de la cavité du stomodéum ou

future cavité buccale à partir du début de la 4ème semaine de gestation. Le bourgeon naso-frontal dérive de la migration des cellules des crêtes neurales prosencéphaliques, et les bourgeons dérivés des arcs branchiaux (maxillaires et mandibulaires), des cellules des crêtes neurales mesencéphaliques et rhombencéphaliques.

Les bourgeons maxillaires et mandibulaires dérivent des extrémités dorsales et ventrales du 1èr arc branchial, respectivement. De la partie postérieure de l'ébauche maxillaire dérive l'os malaire, et la partie postérieure de l'ébauche mandibulaire participe à la formation des ébauches de l'oreille moyenne (marteau, enclume).

2. Ossification du squelette craniofacial

La formation des os craniofaciaux repose sur des mécanismes d'ossification membranaire, endochondrale ou mixte. Les os frontaux, pariétaux, temporaux, maxillaires et zygomatiques, et les sutures crâniennes dérivent du processus d'ossification membranaire. Les os de la base du crâne, l'os occipital et les osselets de l'oreille moyenne dérivent du processus d'ossification endochondrale. L'os mandibulaire est formé à la fois par les processus d'ossification membranaire et endochondrale.

a) Mécanisme d'ossification membranaire

Lors de l'ossification membranaire, ou intramembranaire, les progéniteurs mésenchymateux se condensent et se différencient directement en ostéoblastes, passant par les stades successifs d'ostéoprogéniteurs, d'ostéoblastes immatures puis matures, et d'ostéocytes, phase terminale de la différenciation ostéoblastique.
La condensation mésenchymateuse est induite par l'intermédiaire de signaux et protéines locales, stimulant la prolifération cellulaire et leur adhésion (SHH (Sonic Hedgehog), BMP, WNT, N-Cadherin, NCAM (Neural Cell Adhesion Molecule), syndecans, heparanes sulfates). Les voies TWIST, BMP, FGF, et WNT participent au maintien de ce processus initial (Passos-Bueno et al, 2008 ; Rice and Rice, 2008, Long and Ornitz, 2013).
Ces différentes étapes sont régulées par différents facteurs de transcription (Marie, 2008 ; Long, 2012) (Figure 7). Runx2 est un facteur de transcription majeur de la différenciation ostéoblastique, qui régule l'expression de nombreux gènes ostéoblastiques, tels que *Collagen I*, *Bone Sialoprotein* (BSP), *ostéopontine* (OP), *alkaline phosphatase* (ALP), *transforming*

growth factor (TGFβ), et l'*ostéocalcine* (Fujita et al, 2004 ; Marie, 2008). Osterix (Osx) est un facteur de transcription également clé de la différenciation ostéoblastique, intervenant à un stade plus avancé de la différenciation (Figure 7).

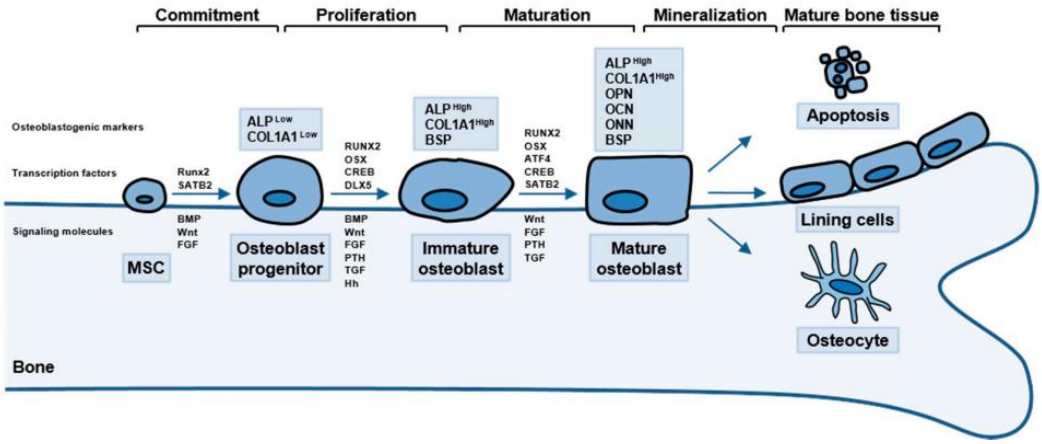

Figure 7. Représentation schématique des différentes étapes de la différenciation ostéoblastique dans le cadre de l'ossification membranaire, et des facteurs de transcription régulant ce processus. MSC, mesenchymal stem cell. BMP, bone morphogenetic protein. FGF, fibroblast growth factor. RUNX2, runt-related transcription factor 2. PTH, parathyroid hormone. TGF, transforming growth factor. Hh, hedgehog. SATB2, special AT-rich sequence-binding protein 2. OSX, osterix. ATF4, activating transcription factor 4. CREB, cAMP-responsive element-binding. ALP, alkaline phosphatase. OPN, osteopontin. OCN, osteocalcin. ONN, osteonectin. BSP, bone sialoprotein. COL1A1, collagen type 1 alpha 1 chain. (Amarasekara et al, 2021).

Les ostéoblastes produisent les éléments constitutifs de la matrice extracellulaire, dont le collagène de type 1, principal composant de la matrice. La matrice extracellulaire, aux stades initiaux de la différenciation ostéoblastique, n'est pas minéralisée : il s'agit d'une matrice dite ostéoïde.

Au stade d'ostéoblaste mature, certains ostéoblastes entrent en apoptose, en quiescence en périphérie de la matrice osseuse (« lining cells »), ou se différencient en ostéocytes. A ce stade d'ostéoblaste mature, puis d'ostéocyte, est produite l'ostéocalcine, ayant un rôle de liaison du calcium au sein de la matrice extracellulaire. L'ALP permet la libération du phosphate au sein de la matrice, indispensable à la formation de cristaux d'hydroxyapatite, permettant alors la minéralisation de la matrice extracellulaire (Blair et al, 2011).

Les ostéocytes produisent également la sclérostine, qui stimule la voie WNT et qui joue un rôle de régulateur négatif de la différenciation ostéoblastique. La sclérostine agit de concert avec

FGF23, également secrété par les ostéocytes, en réponse à des niveaux sériques élevés de phosphates, et a une action de réabsorption du phosphate au niveau rénal (Long, 2012).

b) Mécanisme d'ossification endochondrale

L'ossification endochondrale est un processus d'ossification qui nécessite la mise en place d'un cartilage intermédiaire, son maintien conditionnant la poursuite de la croissance des berges osseuses bordant ce cartilage, ce cartilage étant ensuite remplacé par une matrice osseuse minéralisée.

Ce processus, en période anténatale, comme dans le cadre de l'ossification membranaire, débute par la condensation de cellules mésenchymateuses, provenant soit de la crête neurale dans la région craniofaciale, soit du mésoderme dans les autres régions. Cette condensation mésenchymateuse est un prérequis indispensable à la différenciation chondrocytaire ultérieure. Cette étape de condensation fait intervenir des mécanismes d'adhésion cellulaire, médiés notamment par NCAM et N-Cadherine (DeLise et al, 2000). La voie des BMP, par l'activation de récepteurs SMADs 1, 5 et 8, est également indispensable à la formation des condensations mésenchymateuses chondrogéniques (Feng and Derynck, 2005 ; Massague et al, 2005). La voie FGF/FGFR joue un rôle déterminant également à ce stade de condensation, par la promotion de la survie cellulaire (Yu and Ornitz, 2008).

A la suite de cette étape de condensation mésenchymateuse s'opère l'étape de différenciation chondrocytaire. Ce stade initial de différenciation est dépendant de SOX9 (SRY-Box Transcription Factor), puis de SOX5 et 6 (Han and Lefebvre, 2008, Lefebvre et al, 2021) (Figure 8). SOX9 induit l'expression de FGFR3 au sein de ces cellules mésenchymateuses, ayant pour effet une régulation positive de la prolifération et de la différenciation chondrocytaire. Au centre des zones de condensation, les chondrocytes secrètent une matrice riche en collagène de type II, IX et XI et des protéoglycans (aggrecan). Les chondrocytes situés en périphérie forment le périchondre, caractérisé par l'expression de FGFR1 et FGFR2, et par la sécrétion d'une matrice riche en collagène de type I (Caplan and Pechak, 1987 ; Delezoide et al., 1998 ; Ornitz and Marie, 2015). La voie des BMPs est également indispensable à la poursuite de la différenciation chondrocytaire au sein de ces zones de condensation.

Un point d'ossification primaire est ensuite formé, par remplacement de ces chondrocytes par des ostéoblastes issus du périchondre, mais également par transdifférenciation des chondrocytes en ostéoblastes (Long et al, 2012 ; Ono et al ; 2014).

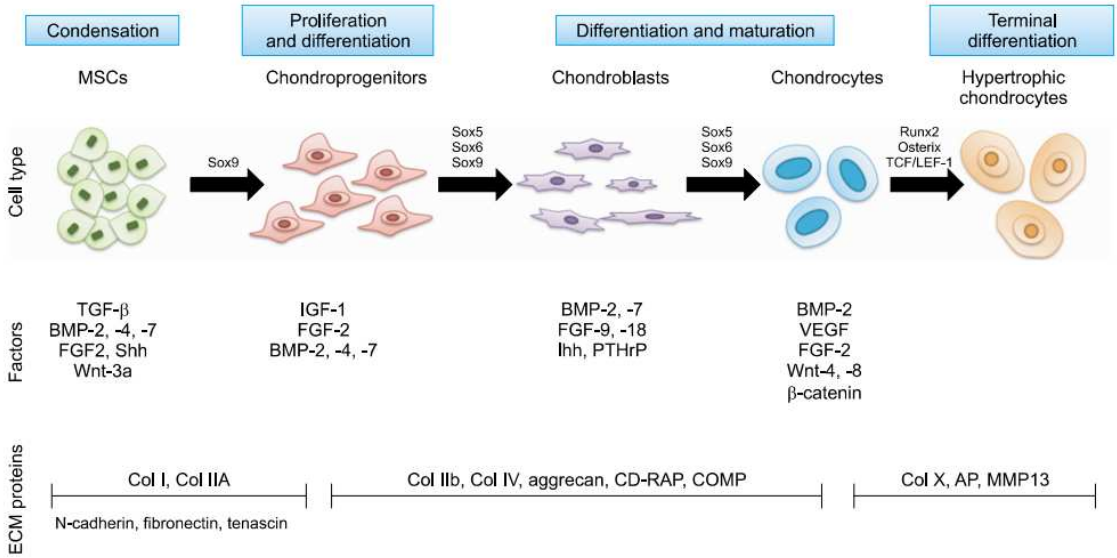

Figure 8. Etapes de différenciation chondrocytaire à partir de la condensation des cellules souches mésenchymateuses (MSCs), facteurs de différenciation, et protéines de la matrice extracellulaire (ECM) secrétés par les chondrocytes selon leur stade de différenciation : AP, alkaline phosphatase ; CD-RAP, cartilage-derived retinoic acid-sensitive protein; Col, collagen; COMP, cartilage oligomeric protein; MMP, matrix metalloproteinase; VEGF, vascular endothelial growth factor (Park and Cho, 2010).

Ossification endochondrale : exemple de la plaque de croissance des os longs

Suivant la phase de formation de l'ébauche cartilagineuse, les chondrocytes prolifèrent rapidement afin de permettre la croissance linéaire des segments osseux. Les chondrocytes centraux subissent une phase de maturation progressive, passant par les stades de chondrocytes préhypertrophiques, puis hypertrophiques, caractérisés par la sécrétion de collagène de type X (Poole et al, 1989). Le collagène de type II est secrété dès les stades initiaux de la différenciation par les chondrocytes immatures, sa sécrétion est maintenue y compris au stade hypertrophique, bien que son taux d'expression par les chondrocytes hypertrophique soit plus faible (Lian et al, 2019). A la phase terminale de différenciation, les chondrocytes hypertrophiques expriment MMP13 (Matrix Metalloproteinase 13), et deviennent généralement apoptotiques ou bien se transdifférencient en osteoblastes (Galea et al, 2020). De façon concomitante se produit une invasion vasculaire au niveau du cartilage hypertrophique, ainsi que la différenciation des cellules du périchondre interne en ostéoblastes, à l'origine de la formation du périoste (Caplan and Pechak, 1987). Cette néovascularisation initie également la différenciation des ostéoprogéniteurs en ostéoblastes, à l'origine de la formation du centre primaire d'ossification nécessaire à la formation de l'os trabéculaire (Maes et al, 2010).

La maturation des chondrocytes au niveau de la plaque de croissance embryonnaire se fait de façon régulée, avec délimitation de couches successives dans le sens épiphyse vers diaphyse : il s'agit des zones prolifératives, préhypertrophiques, hypertrophiques, et au niveau diaphysaire, de la couche d'os trabéculaire en formation. La zone proliférative peut être subdivisée en 2 parties, celle des chondrocytes arrondis, et celle des chondrocytes plus allongés, disposés en pile d'assiette (Figure 9) (Long and Ornitz, 2013).

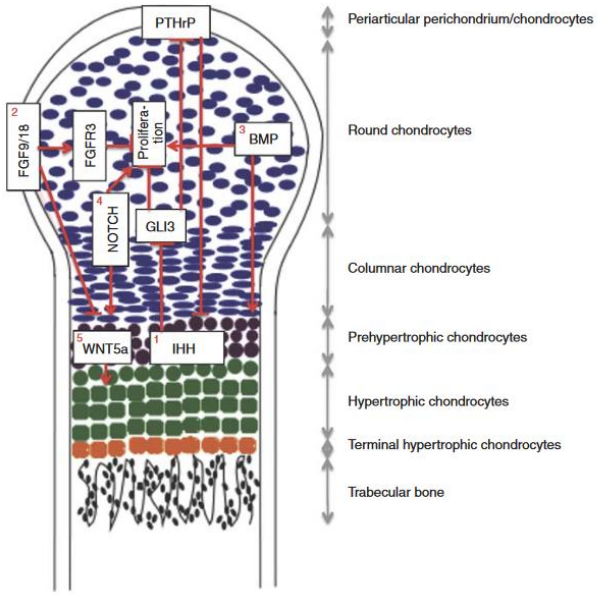

Figure 9. Organisation de la plaque de croissance en couches cellulaires successives : représentation schématique de la plaque de croissance embryonnaire des os longs chez la souris à un stade tardif (E15.5 – E19) ; et facteurs de régulation du développement de la plaque de croissance (Long and Ornitz, 2013).

Cette organisation au sein de la plaque de croissance conditionne la croissance longitudinale du squelette endochondral, et est soumis à une régulation fine, provenant de signaux extracellulaires, et de facteurs nucléaires.

IHH et PTHrP (Parathyroid hormon related protein) coordonnent la prolifération et la maturation chondrocytaire via un mécanisme de feedback négatif. IHH est secrété par les chondrocytes préhypertrophiques et les chondrocytes hypertrophiques précoces, et stimule la prolifération et la maturation chondrocytaire et la transcription de PTHrP via l'inhibition de GLI3. PTHrP est exprimé à des taux élevés par les cellules du périchondre périarticulaire, et à des taux plus faibles, par les chondrocytes prolifératifs situés à proximité de la surface articulaire (Lee et al, 1995). PTHrP a pour effet d'inhiber la maturation chondrocytaire associée à l'expression de IHH. La voie FGF/FGFR a un rôle majeur de régulation au sein de la plaque de croissance. FGF9 et FGF18, secrétés par les cellules du périchondre, activent spécifiquement

FGFR3, au niveau de la couche des chondrocytes prolifératifs et préhypertrophiques. L'activation de FGFR3 à ce niveau a un effet d'inhibition de la prolifération chondrocytaire via les voies de signalisation AKT et STAT, et d'inhibition de la différenciation chondrocytaire via la voie des MAPK, à un stade embryonnaire tardif et en période postnatale (Li et al, 1999 ; Priore et al ; 2006 ; Long and Ornitz ; 2013 ; Ornitz and Legeai-Mallet ; 2017). FGFR1 est exprimé par les chondrocytes préhypertrophiques et hypertrophiques, et FGFR2 au sein de la zone proliférative. Les BMPs, exprimés dans la plaque de croissance par les chondrocytes prolifératifs et les cellules périchondrales, ont un rôle de régulation positive de la prolifération et de la maturation chondrocytaire. Cette voie antagonise les effets de la voie FGF/FGFR (Ornitz and Marie, 2015). La voie WNT, et en particulier WNT5a, exprimé par les chondrocytes préhypertrophiques, stimule la maturation chondrocytaire, en particulier la transition vers le stade hypertrophique (Yang et al, 2003). Cette voie WNT est régulée négativement par l'activation de FGFR3, réprimant ainsi le passage des chondrocytes au stade hypertrophique. FGFR3 exerce également son rôle d'inhibition à ce niveau de la différenciation chondrocytaire par la stimulation du facteur de transcription Sox9, qui a un rôle de régulation de l'entrée des chondrocytes dans la phase de différenciation au stade préhypertrophique (Krejci et al., 2012). L'activation constitutive de FGFR3 est à l'origine d'une désorganisation des plaques de croissance, et de leur fusion prématurée, conduisant à la limitation majeure de la croissance longitudinale du squelette et au phénotype de nanisme, comme observé dans l'achondroplasie et la dysplasie thanatophore (Legeai-Mallet et al, 2004).

Un autre facteur de transcription, Runx2, exprimé par les chondrocytes préhypertrophiques et hypertrophiques dans leur stade précoce, a un rôle de stimulation de la différenciation des chondrocytes en chondrocytes hypertrophiques (Yoshida et al, 2004). La voie NOTCH a également un rôle de stimulation de la prolifération et de la différenciation chondrocytaire au sein de la plaque de croissance (Dong et al, 2010).

3. Formation des sutures crâniennes

Les sutures crâniennes correspondent aux zones de jonction séparant les différents os constituant la voûte crânienne. Ces zones de jonction sont initialement d'origine fibrocellulaire, et leur maintien est un nécessaire indispensable à la croissance de la boîte crânienne, sous l'effet de la poussée de la croissance encéphalique (Khonsari, 2013 ; Nieman et al, 2012). Avec l'âge, les sutures crâniennes deviennent de plus en plus interdigitées, et leur ossification repose sur un mécanisme d'ossification membranaire (Miura et al, 2009). La fusion prématurée d'une ou

plusieurs sutures crâniennes, ou craniosténose, est à l'origine de déformations variables de la voûte crânienne et de l'étage craniofacial, dont les causes sont multifactorielles (génétique, environnementales, toxiques), isolées ou syndromiques (Twigg and Wilkie, 2015).

La suture coronale est la première à se former lors du développement embryonnaire, les autres sutures (métopique située entre les 2 os frontaux, sagittale située entre les os pariétaux, et lambdoïdes situées entre les os pariétaux et l'os occipital), sont formées plus tardivement (Rice and Rice, 2008 ; Morriss-Kay and Wilkie, 2005).

Il est distingué 5 processus dans la formation des sutures : la spécification des cellules souches et leur migration, le lignage, la délimitation de la suture, la prolifération et la différenciation ostéoblastique, et le maintien de l'homéostasie de la suture (Twigg and Wilkie, 2015).

Il existe au sein des sutures, une population de cellules ostéogéniques non différenciées, présentant des propriétés de cellules souches, exprimant Gli1, un marqueur classique de la voie Hedgehog (Wilkie, 1997 ; Lana-Elola et al, 2007 ; Zhao et al, 2015). Chez la souris, il a été montré que dans le cadre de la formation de la suture coronale, ces cellules proviennent du mesoderme céphalique paraxial, dans la région jonctionnelle entre le mésencéphale et le diencéphale, localisé immédiatement de façon adjacente au tube neural, au stade embryonnaire E7.5, en réponse à l'accumulation de SHH dans la notochorde adjacente. Cette population cellulaire migre latéralement durant le stade E8.5 - E9.5 en région supraorbitaire (Deckelbaum, et al, 2012).

Au stade E9.5 à 11.5, cette population cellulaire supraorbitaire constitue un centre d'organisation cellulaire, constitué de groupes cellulaires avec un potentiel ostéogénique, provenant des crêtes neurales (futur os frontal), du mésoderme (future os pariétal), séparés par un groupe de cellules souches non différenciées provenant du mésoderme paraxial (Twigg and Wilkie, 2015). Entre E11.5 et E13.5, ces populations cellulaires migrent et viennent recouvrir l'encéphale en formation (Deckelbaum, et al, 2012 ; Yoshida et al, 2008 ; Ting et al, 2009). Cette organisation cellulaire précoce est régulée par EN1 (engrailed 1), MSX2, et TWIST1, présent au sein du centre de régulation supraorbitaire au stade E11 (Deckelbaum, et al, 2012). D'autres boucles de régulation entrent en jeu dans ce processus, telles que les voies BMP, WNT et FGF (Mishina and Snider, 2014). Au stade E12 – E13.5, l'expression de Runx2 et Osx est initiée (Twigg and Wilkie, 2015).

La frontière entre les dérivés de la crête neurale en avant, et ceux du mésoderme en arrière, devient identifiable à partir du stade E9.5, délimitant alors la suture coronale, uniquement dérivées de cellules du mésoderme (Jiang et al, 2002 ; Yoshida et al, 2008). Le maintien de

cette frontière dépend de plusieurs facteurs de transcription tels que EN1, TWIST 1, MSX2, EPHRIN/EPH et JAGGED/NOTCH (Ting et al, 2009 ; Merrill et al, 2006).

En période postnatale, Gli1 est également exprimé dans les cellules mésenchymateuses indifférenciées des sutures crâniennes. Dans ce contexte, dès E14.5, Indian Hedgehog (IHH), secrété par les cellules différenciées des berges de la suture semble être le facteur clé du maintien du recrutement d'ostéoprogéniteurs indifférenciés à partir du mésenchyme situé au sein de la suture (Zhao et al, 2015). Un autre facteur participant au maintien des sutures, est TWIST1, également exprimé au sein du mésenchyme sutural à E16 (Johnson et al, 2000), est un antagoniste direct de Runx2, ayant pour effet de diminuer les taux de BSP et de l'ostéocalcine, prévenant ainsi la différenciation ostéoblastique au sein de la suture (Connerney et al, 2006).

En plus du maintien de la suture, la croissance de la voûte crânienne est stimulée par des signaux induisant la différenciation ostéoblastique, provenant de la matrice ostéoïde située le long des fronts ostéogéniques en expansion (Morriss-Kay and Wilkie, 2005). La voie FGF/FGFR, et en particulier, FGF2, FGF9, FGF10 et FGF18, FGFR1 et FGFR2 sont des facteurs cruciaux dans ce contexte (Iseki et al, 1999 ; Hajihosseini et al, 2009 ; Ornitz and Marie, 2002 ; Ohbayashi et al, 2002 ; Harada et al ; 2009). Fgfr2 est exprimé dans les ostéoprogéniteurs en prolifération, alors que Fgfr1 est exprimé à un stade de différenciation plus avancé (Figure 10).

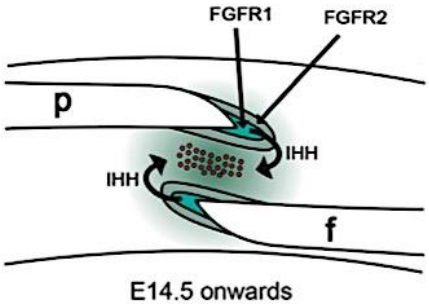

Figure 10. Représentation schématique d'une suture coronale au stade E14.5 (chez la Souris), montrant l'expression de Indian Hedgehog (IHH) par les cellules différenciées des berges de la sutures, stimulant le maintien du recrutement d'ostéoprogéniteurs indifférenciés à partir du mésenchyme sutural, et celle de FGFR1 et FGFR2 stimulant la croissance des os de la voûte crânienne (p : os pariétal ; f : os frontal) (Twigg and Wilkie, 2015).

Chez l'Homme, contrairement à ce qui est observé chez la Souris, FGFR3, exprimé dans les ostéoprogéniteurs en prolifération, est un facteur déterminant dans la formation des sutures (Delezoïde et al, 1998 ; Teven et al, 2014 ; Cornille et al ; 2022) (Figure 11).

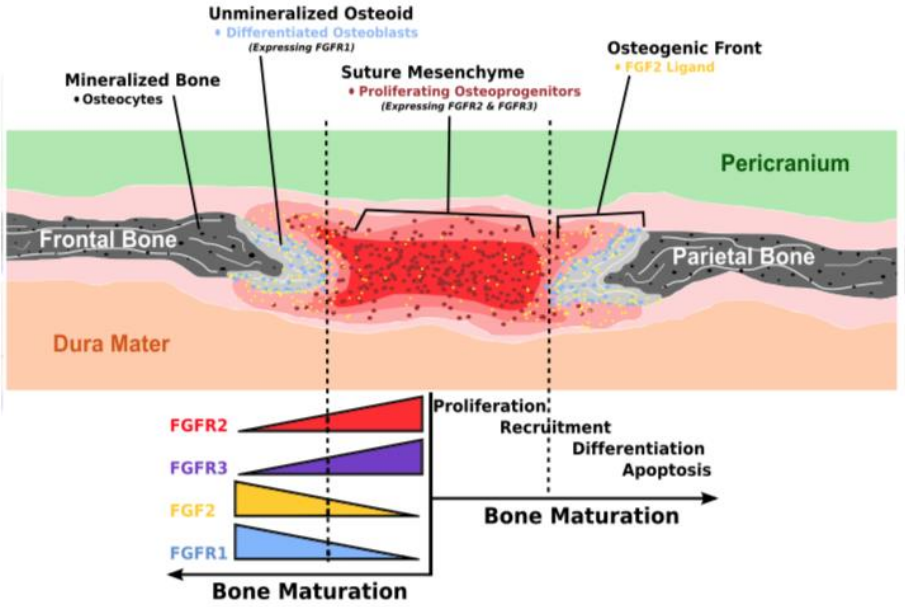

Figure 11. Représentation schématique d'une suture coronale en formation : en présence de faibles concentrations de FGF2, les cellules ostéoprogénitrices indifférenciées exprimant FGFR2 et FGFR3 prolifèrent au sein du mésenchyme de la suture, entre les deux fronts ostéogéniques. A des taux plus élevés de FGF2, les ostéoprogéniteurs se différencient en ostéoblastes. Ceci induit une augmentation de l'expression de FGFR1, et la déposition d'une matrice ostéoïde le long des fronts ostéogéniques (Teven et al, 2014).

La dure-mère sous-jacente à la suture participe également à la régulation de la différenciation ostéoblastique au sein de la suture, par l'expression de FGF2, BMP4 et de TGFβ (Miura et al, 2009).

Au sein des sutures matures, la résorption osseuse par les cellules ostéoclastiques, est indispensable au maintien de l'homéostasie de la suture. Ainsi des défauts de résorption ostéoclastiques, comme observé dans certaines formes d'ostéopétrose, s'accompagnent de craniosténose (Niemjnen et al, 2011).

4. Synchondroses de la base du crâne

Les synchondroses de la base du crâne correspondent aux zones de jonction cartilagineuse situées entre les os de la base du crâne, elles jouent un rôle majeur dans la croissance longitudinale du crâne (McBratney-Owen et al, 2008 ; Wei et al, 2016). Il existe plusieurs synchondroses distinctes, avec un temps de fermeture différent selon le site (Figure 12) :

- la synchondrose sphénoethmoïdale, située entre l'os présphénoïde et l'ethmoïde dans la partie la plus antérieure de la base du crâne, se fermant à partir de l'âge médian de 3-5 mois, la fermeture étant normalement complète à 5 ans (Vu et al, 2021) ;
- la synchondrose intersphénoïdale, située entre les os présphénoïde et basisphénoïde, se fermant entre l'âge de 2 et 3 ans (Madeline and Elster, 1995) ;
- la synchondrose sphéno-occipitale, située entre les os basisphénoïde et basioccipital, se fermant à l'âge médian de 9 ans, la fermeture étant achevée à l'âge de 17 ans (Vu et al ; 2021) ;
- la synchondrose intraoccipitale, entre l'os basisphénoïde et l'os occipital, se fermant à partir de l'âge médian de 4 ans, la fermeture étant complète à l'âge de 10 ans (Vu et al ; 2021).

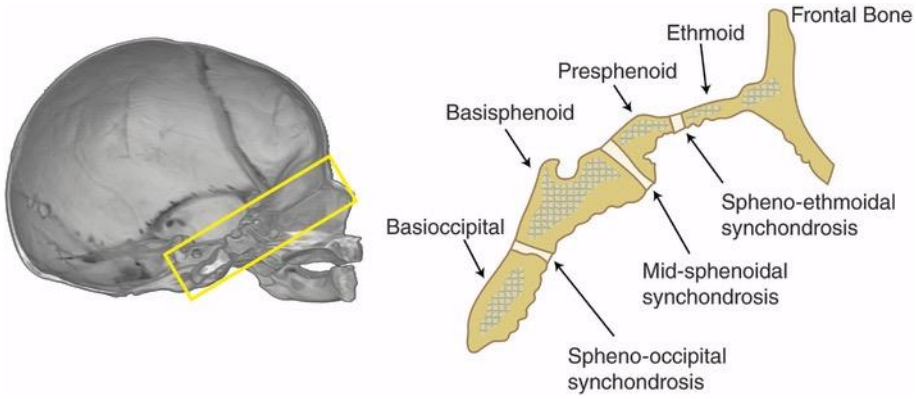

Figure 12. Visualisation de la base du crâne chez un nouveau-né dans le plan sagittal (Lesciotto and Richtsmeier, 2019).

L'ossification précoce des synchondroses entraîne une limitation de la croissance antéropostérieure de la base du crâne, et par voie de conséquence une hypoplasie de l'étage moyen de la face, comme observé dans l'achondroplasie, et dans certaines craniosynostoses (Di Rocco et al ; 2014 ; Goldstein et al ; 2014).

La formation de la base du crâne repose sur un mécanisme d'ossification endochondrale, qui commence avec la formation d'une ébauche cartilagineuse issue de la condensation de cellules mésenchymateuses (McBratney-Owen et al, 2008). La prolifération chondrocytaire permet le maintien des synchondroses, et ainsi, l'élongation de la base du crâne (Matsushita et al, 2009). Les chondrocytes immatures deviennent hypertrophiques, puis apoptotiques. Il existe ensuite

une invasion d'ostéoblastes issus du périchondre, induisant la formation de centre d'ossification (St-Jacques et al, 1999).

Les synchondroses sont composées de plaques de croissance bipolaires, avec successivement une couche de chondrocytes de réserve, une couche proliférative, pré hypertrophique, et hypertrophique, générant une croissance longitudinale dans des directions opposées, alors qu'au niveau des longs, il s'agit d'une plaque de croissance unipolaire (Wei et al, 2016).

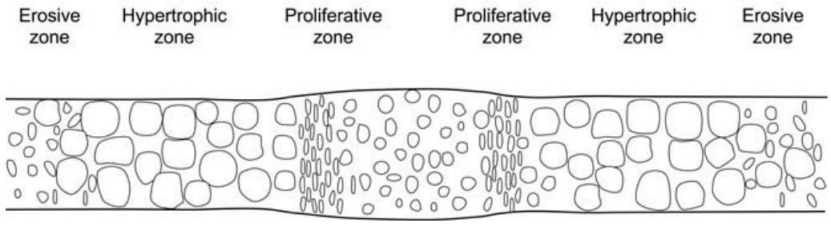

Figure 13. Représentation schématique d'une synchondrose sphénooccipitale. La zone érosive est le site de la dégradation de la matrice extracellulaire produite par les chondrocytes hypertrophiques, et par son remplacement par une matrice osseuse secrétée par les ostéoblastes nouvellement différenciés (Rice et al, 2003).

Comme au sein des plaques de croissance, le développement des synchondroses de la base du crâne est finement régulé par de nombreuses voies de signalisation et facteurs de transcription. Runx2 a été détecté au sein des condensations cartilagineuses au niveau de la base du crâne en période embryonnaire (Funato et al, 2020), son expression étant régulée à la fois par HDAC4 (histone deacetylase 4) et MEF2C (myocyte enhancer factor 2C) (Vega et al, 2004 ; Arnold et al, 2007). Runx2 participe à l'ossification des synchondroses de la base du crâne, sa surexpression entraînant une fusion prématurée des synchondroses (Takeda et al, 2001), alors que son haplo-insuffisance, à l'origine de la dysplasie cléidocrânienne, entraîne un retard de fusion (Al Kaissi et al, 2013). TBX1 (T-box Transcription Factor Family 1) est un régulateur spécifique de la différenciation chondrocytaire et de l'ossification au niveau de la synchondrose sphénooccipitale, il a un rôle de régulation négative de Runx2 (Funato et al, 2020).

La voie FGF/FGFR a un rôle majeur au sein des synchondroses de la base du crâne. FGFR3 stimule la différenciation ostéoblastique via l'activation de la voie des MAPK, et sa suractivation dans un modèle murin d'achondroplasie G380R, entraîne une diminution de la prolifération chondrocytaire, une augmentation de la différenciation ostéoblastique, et par voie de conséquence, une fusion prématurée des synchondroses de la base du crâne (Matsushita et al, 2009). Ce phénomène de fusion prématurée des synchondroses de la base du crâne est également présent dans le modèle murin d'achondroplasie, $Fgfr3^{Y367C/+}$ (Di Rocco et al, 2014).

Ceci est également observé chez l'Homme dans le syndrome de Muenke, craniosynostose syndromique lié à une mutation gain de fonction de FGFR3 (Laurita et al, 2011). FGFR2 est exprimé par les ostéoprogéniteurs situés de part et d'autre des synchondroses, et semble également stimuler le processus d'ossification (Eswarakumar et al, 2002). L'activation constitutive de FGFR2 est à l'origine de fusion prématurée des synchondroses de la base du crâne, comme observé chez les patients porteurs de craniosynostoses syndromiques liées à FGFR2 (syndromes d'Apert, Crouzon, Pfeiffer) (Goldstein et al ; 2014). L'expression de l'isoforme c de Fgfr1 a été détectée au sein des ostéoblastes de la synchondrose sphénooccipitale (dans la zone érosive ; Figure 13), et dans le périoste, mais son rôle précis reste à déterminer à ce niveau (Rice et al, 2003).

PTHrP a un rôle de maintien de la prolifération chondrocytaire, et inhibe la différenciation chondrocytaire via l'inhibition de l'expression de Runx2 (Li et al, 2004). PTHrP entraîne également la translocation nucléaire de HDAC4, et par voie de conséquence entraîne l'inhibition de la transcription de MEF2C (Kozhemyakina et al, 2009). L'inactivation de PTHrP entraîne une minéralisation excessive de la base du crâne (Lanske et al, 1996). Il a également été démontré le rôle de la voie Ihh au sein des synchondroses : Ihh est exprimé au sein des chondrocytes préhypertrophiques sous la dépendance de la régulation de Runx2, et stimule la prolifération et la différenciation chondrocytaire (Young et al, 2006).

Les protéines impliquées dans la formation du cil primaire, telles que KIF3A (Kinesin family member 3A), IFT88 (Intraflagellar transport), jouent un rôle majeur au cours de la formation des synchondroses de la base du crâne. En effet, leur délétion entraîne une ossification précoce de la base du crâne, via l'inhibition de la voie de signalisation Ihh (Huangfu et al, 2003, Koyama et al, 2007 ; Ochiai et al ; 2009).

La voie WNT/β-Catenin, et en particulier LEF1 (Lymphoid enhancer factor 1) joue un rôle de régulation au sein des synchondroses, sa surexpression étant à l'origine d'une accélération de la différenciation des chondrocytes hypertrophiques, et d'augmentation de l'ossification périostée au niveau des synchondroses intersphénoïdale et sphénooccipitale (Nagayama et al, 2008).

La famille des facteurs de transcription SIX (sine oculis homeobox) est également impliquée au cours du développement des synchondroses de la base du crâne. La délétion de Six2 est à l'origine d'ossification prématurée des synchondroses, liée à une diminution de la prolifération chondrocytaire, et à l'accélération de la différenciation terminale des chondrocytes (He et al, 2010).

5. Formation mandibulaire : ossification mixte membranaire et endochondrale

La mandibule dérive du premier arc pharyngé, et est caractérisée par une spécification précoce liée à l'absence d'expression des gènes Hox (Hunt et al, 1991). Le développement osseux de la mandibule repose sur un mécanisme d'ossification membranaire prénatal, dans la région du corpus mandibulaire, sur un processus d'ossification endochondrale post natal, dans les régions symphysaires, angulaires et condyliennes (Rice et al, 2003) (Figure 14).

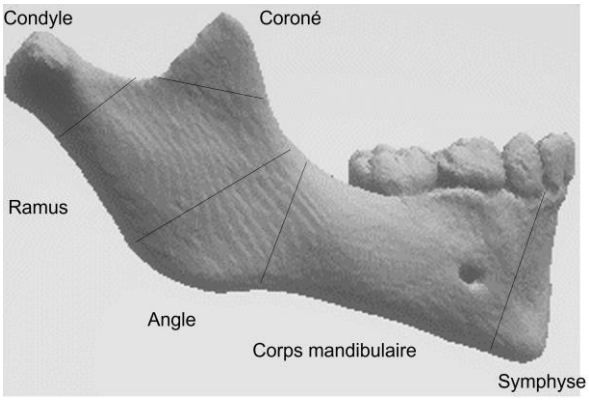

Figure 14. Visualisation de la face latérale d'une mandibule humaine à partir de reconstructions 3D d'un scanner mandibulaire d'un enfant en denture temporaire : dans le sens postéroantérieur, régions anatomiques condylienne, ramique (branche montante), angulaire, du corps mandibulaire (branche horizontale), et symphysaire.

a) Cartilage de Meckel

Mise en place et disparition du cartilage de Meckel

Le **cartilage de Meckel** est présent chez tous les vertébrés à mâchoires (gnathostomes) (Mallat, 2008). Il s'agit d'un cartilage transitoire se mettant en place en anténatal, et disparaissant à la naissance. Le cartilage de Meckel est formé à partir de mésenchyme mandibulaire, dérivé des cellules des crêtes neurales (Le Douarin and Dupin, 1993). Le début de la formation du cartilage de Meckel en anténatal est précoce, à partir du stade embryonnaire E10 chez la souris (Ramaesh and Bard, 2003). A E11, est observée une condensation mésenchymateuse dans la région du germe de la première molaire mandibulaire (Frommer and Margolies, 1971). Il existe ensuite une expansion antérieure et postérieure du cartilage de Meckel à partir du stade E13 (Chai et al, 2000). Au stade E13.5, le cartilage de Meckel est composé de préchondroblastes condensés

commençant à secréter de la matrice extracellulaire riche en collagène de type II (Frommer and Margolies, 1971). L'expansion du cartilage de Meckel se fait transversalement à partir de la périphérie du cartilage, et longitudinalement, via un mécanisme de différenciation du mésenchyme chondrogénique et par la prolifération transverse des chondrocytes (Kaucka et al, 2017). De façon concomitante, la formation des germes dentaires s'initie (Frommer and Margolies, 1971). Chez les rongeurs, la denture mandibulaire est composée à terme d'une paire d'incisives à croissance continue et d'une rangée de 3 molaires par arcade.

A partir du stade E15, le cartilage de Meckel peut être subdivisé en 3 parties : antérieure (distale), intermédiaire ou centrale, et postérieure (proximale) (Figure 15).

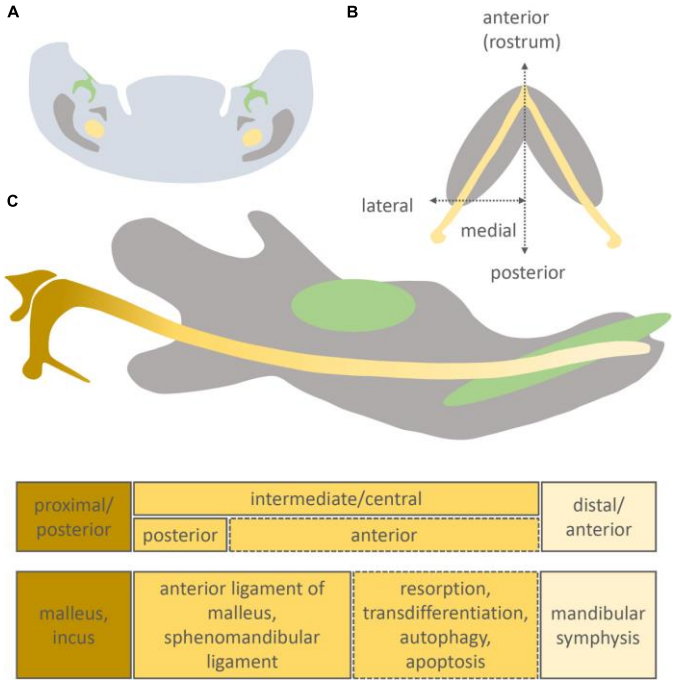

Figure 15. Position du cartilage de Meckel au sein de la mandibule, et devenir des parties postérieure, intermédiaire, et antérieure (Scandova et al, 2020).

A ce stade, les chondrocytes continuent leur maturation au niveau de la zone intermédiaire, caractérisée par la présence d'un périchondre, et d'une matrice extracellulaire, alors que ceux situés rostralement restent moins différenciés. A E16, les chondrocytes sont hypertrophiques au niveau de la partie intermédiaire, et sécrètent une matrice riche en collagène de type X (Ishizeki et al, 1999 ; Shimo et al, 2004). A partir de ce même stade, s'initient la calcification du périchondre et de la matrice des chondrocytes hypertrophiques, et une invasion capillaire de cette matrice calcifiée. A E17, des îlots d'os nouvellement formé sont observés, caractérisés par l'expression de collagènes de type I et II et d'ostéopontine (Ishizeki et al, 1999). La

dégradation de la matrice collagénique débute autour des incisives entre les stades E15 et E16, s'étendant en région molaire, et laissant en place la partie la plus antérieure du cartilage de Meckel. A partir du stade E17, la partie intermédiaire du cartilage de Meckel commence à disparaître, et à E19, la partie la plus postérieure du cartilage est complètement déconnectée de la partie antérieure (Figure 16).

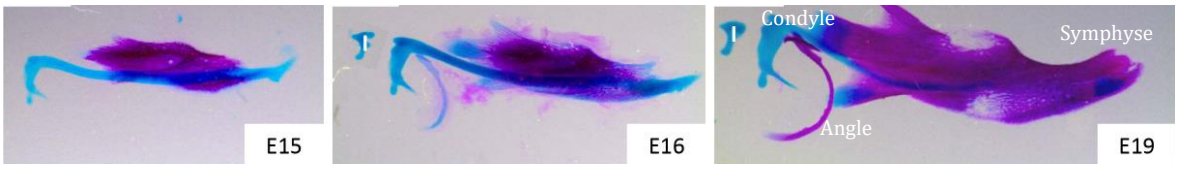

Figure 16. Analyse macroscopique du cartilage de Meckel au cours du développement (coloration alizarin red/bleu alcian), montrant la disparition de la partie intermédiaire du cartilage de Meckel au stade E19, avec individualisation des cartilages symphysaires, de l'angle et du condyle (adapté de Svandova et al, 2020).

Les extrémités antérieures et postérieures du cartilage de Meckel sont à l'origine respectivement de la formation de la symphyse mandibulaire, et des osselets de l'oreille moyenne, l'incus et le malléus (Bhaskar et al, 1953 ; Amin and Tucker, 2006 ; Svandova et al, 2020) via un mécanisme d'ossification endochondrale. Au stade P0-P1, toute la partie intermédiaire du cartilage de Meckel s'est complètement résorbée (Amin and Tucker, 2006 ; Anthwal et al, 2013).

Les mécanismes conduisant à la disparition de la partie intermédiaire du cartilage de Meckel restent incomplètement élucidés (Svandova et al, 2020). Ce phénomène est initié par la résorption de la matrice extracellulaire du cartilage de Meckel, faisant intervenir des précurseurs ostéoclastiques TRAP positifs et des macrophages, observés dès E16 au niveau du périchondre (Tsuzurahara et al, 2011). Trois hypothèses principales sont décrites pour expliquer la poursuite de la disparition de la partie intermédiaire du cartilage de Meckel : 1/ la possibilité d'ossification du cartilage de Meckel par transdifférenciation des chondrocytes en ostéoblastes comme démontré *in vitro* (Ishizeki et al, 1996 , 1999, 2009, 2012 ; Harada and Ishizeki, 1998 ; Eames et al ; 2004), mais les preuves supportant ce phénomène restent limitées *in vivo* (Ishizeki et al, 1999) ; 2/ l'hypothèse apoptotique : l'apoptose est un mécanisme majeur de mort cellulaire programmée, cependant, les cellules apoptotiques sont relativement rares au niveau de cartilage de Meckel et essentiellement situées au niveau du périchondre, ayant à ce niveau un rôle probable de limitation de l'expansion latérale du cartilage de Meckel (Harada and Ishizeki, 1998 ; Amano et al, 2010 ; Yang et al, 2012) ; 3/ l'hypothèse de l'autophagie : ce

mécanisme de mort cellulaire est compatible avec la présence de marqueurs majeurs d'autophagie (Beclin 1 et LC3) colocalisés avec des caspases activées (2 et 8) dans la partie centrale du cartilage de Meckel, dont l'expression prédomine dans les zones préhypertrophiques et hypertrophiques (Yang et al, 2012 ; Bilikova et al, 2019).

Chez l'homme, la condensation mésenchymateuse au niveau mandibulaire devient évidente à partir du 32ème jour (équivalent stade 13 chez la souris), et des attaches musculaires associées au cartilage de Meckel sont observées au 44ème jour du développement (équivalent stade 18 chez la souris) (Wyganowska and Przystanska, 2011). Alors que chez la souris, les 2 extrémités antérieures du cartilage de Meckel fusionnent sur la ligne médiane, elles semblent rester séparées chez l'homme (Rodriguez-Vazquez et al, 1997).

Régulation cellulaire et moléculaire au sein du cartilage de Meckel

L'engagement et la prolifération chondroblastique sont régulés par des facteurs multiples, notamment les BMPs, soumis à une régulation de leur expression par site et temps au cours du développement du cartilage de Meckel ; en particulier Bmp2 et Bmp7 sont exprimés précocement au stade E11,5 – E12,5 (Wang et al, 2013). Noggin, un régulateur négatif de la voie de signalisation des BMPs est exprimé pendant toute la période anténatale au sein du cartilage de Meckel (Zimmerman et al, 1996). Son absence entraîne une augmentation du volume du cartilage de Meckel, et la persistance de sa partie intermédiaire (Wang et al, 2013).

TGFβ est un facteur connu de stimulation de la prolifération des chondrocytes dérivés des crêtes neurales (Chai et al, 1994 ; Ito et al, 2002 ; Oka et al, 2007). Ce facteur induit l'expression de Ctgf, exprimé au sein du cartilage du Meckel entre les stades E12.5 et E15.5, ce facteur est impliqué dans les mécanismes de condensation cellulaire (Shimo et al, 2004).

La différenciation et la maturation des chondroblastes au sein du cartilage de Meckel sont régulées par 3 facteurs de transcription principaux, Sox9, Runx2 et Osx. Sox9 est impliqué aux stades précoces de différenciation chondrocytaire, sa délétion entraîne une agénésie du cartilage de Meckel (Mori-Akiyama et al ; 2003). Runx2 est exprimé au niveau des zones chondrocytaires hypertrophiques du cartilage de Meckel, et a un rôle dans la différenciation chondrocytaire (Amano et al, 2014 ; Zhang et al, 2013). Osx est présent abondamment par les chondrocytes hypertrophiques du cartilage de Meckel, sa délétion est à l'origine d'une absence de développement de l'os mandibulaire, bien que le cartilage de Meckel soit développé (Zhang et al, 2013 ; Nakashima et al, 2002).

La voie des FGF/FGFR est impliquée au cours du développement mandibulaire, dès les stades précoces de formation du cartilage de Meckel. L'expression de *Fgfr3* a été montrée au sein du

cartilage de Meckel, participant à son élongation (Rice et al, 2003 ; Havens et al, 2008 ; Biosse Duplan et al, 2016). Son activation constitutive dans le modèle murin d'achondroplasie *Fgfr3*$^{Y367C/+}$, entraîne une augmentation du volume du cartilage de Meckel, un défaut de différenciation chondrocytaire, un retard de résorption du cartilage de Meckel, et une hypoplasie mandibulaire, soulignant ici le rôle majeur de FGFR3 au cours du développement mandibulaire (Biosse Duplan et al, 2016). *Fgfr1* et *Fgfr2* sont également exprimés au cours du développement mandibulaire mais présentent des patterns et une temporalité d'expression différents (Havens et al, 2008 ; Yu et al ; 2015) : à E13.5, *Fgfr1* est exprimé fortement au sein des cellules mésenchymateuses, et faiblement au sein du cartilage de Meckel, alors que *Fgfr2* est exprimé plus fortement au sein du cartilage de Meckel, et au niveau du périoste de la mandibule en formation. A E14,5, *Fgfr1* n'est plus exprimé au sein du cartilage de Meckel, il reste exprimé fortement au sein des tissus osseux mandibulaires, et son expression est plus faible au sein des tissus mésenchymateux. A ce même stade, l'expression de *Fgfr2* persiste au sein du cartilage de Meckel, et devient plus intense au niveau du périchondre du cartilage de Meckel et du périoste de l'os mandibulaire, alors que son expression est absente au sein des tissus osseux de la mandibule en formation (Yu et al, 2015).

Dans les modèles murins de craniosténoses *Fgfr2* (Apert, Crouzon, Pfeiffer), il a été montré des anomalies de formation mandibulaire en période anténatale, caractérisées par une augmentation du volume du cartilage de Meckel (stade E16.5), un défaut de minéralisation, et une augmentation de l'activité ostéoclastique. Les analyses morphométriques réalisées à P0 ont montré des modifications significatives de la forme et de la taille mandibulaire des souris mutantes *Fgfr2* (Motch Perrine et al, 2019).

b) Cartilage condylien : cartilage permanent

Le condyle mandibulaire constitue l'extrémité supéro-distale de la mandibule, il s'agit d'une surface articulaire convexe recouverte d'un cartilage permanent, le cartilage condylien, s'articulant avec le condyle temporal, lui-même concave vers le bas, permettant les mouvements d'ouverture buccale, de diduction et de propulsion mandibulaire. Le maintien de ce cartilage condylien est indispensable au bon fonctionnement de l'articulation temporomandibulaire. Le cartilage condylien n'est pas dérivé du cartilage de Meckel, il s'agit d'une structure formée à partir d'un manchon cartilagineux individualisé en période anténatale dès le stade E16 chez la souris (Svandova et al, 2020). Le condyle est formé selon le mécanisme d'ossification endochondrale et participe activement à la croissance de la branche montante

mandibulaire (Roberts and Hartsfiel, 2004 ; Parada and Chai, 2015). La microarchitecture du condyle a des points communs avec celle de la plaque de croissance des os longs, avec la présence de couches successives de chondrocytes prolifératifs, de chondrocytes hypertrophiques, d'ostéoblastes et de matrice osseuse. Dans la partie périphérique, les chondrocytes sont allongés et prolifératifs, alors que dans la partie centrale, ils sont plus espacés et arrondis, et deviennent hypertrophiques en direction antéroinférieure (Kantomaa et al, 1992 ; Luder et al, 1988).

L'expression des *Fgfrs* a également été montrée au sein du condyle, avec des patterns d'expression différents selon le récepteur : *Fgfr1c* est exprimé au sein du cartilage condylien et des ostéoblastes de la zone érosive (ou zone d'apposition de matrice osseuse) ; *Fgfr2* est exprimé au sein du périchondre (fortement l'isoforme b et plus faiblement l'isoforme c), et *Fgfr2c* au sein de la zone érosive (Rice et al, 2003). *Fgfr3* est exprimé au sein des chondrocytes condyliens, et au niveau du périchondre (isoformes b et c) (Rice et al, 2003). Dans le modèle murin d'achondroplasie $Fgfr3^{Y367C/+}$, la mutation activatrice de *Fgfr3* entraine un défaut de différenciation chondrocytaire au sein du cartilage condylien, et une hypoplasie condylienne, soulignant ici aussi, le rôle majeur de FGFR3 au cours du développement condylien (Biosse Duplan et al, 2016).

C. Réparation osseuse

1. Réparation osseuse en pathologie humaine

Comme dans le cadre de l'ossification squelettique, la réparation osseuse repose sur les processus d'ossification membranaire et endochondrale. La réparation osseuse membranaire implique une transition directe des cellules mésenchymateuses en cellules ostéoprogénitrices. Ce mode de réparation membranaire s'opère dans le cadre de fractures ou ostéotomies stabilisées. Dans le cadre d'ostéotomies ou de fractures peu ou non stabilisées, ou d'ostéotomies avec translation importante des segments osseux, le processus de réparation osseuse endochondrale est initié avec mise en place d'un cartilage intermédiaire transitoire, qui est résorbé et remplacé par de l'os néoformé, formant le cal de réparation (Thompson et al, 2002 ; Gomez-Barrena and al, 2015 ; Hagiwara et al, 2015 ; Liu Xuanchi et al, 2021 ; Bahney et al, 2019) (Figure 17).

Dans le cadre de la distraction osseuse ostéogénique, les deux mécanismes de réparation osseuse se mettent en place, tout d'abord le processus endochondral puis membranaire. La distraction ostéogénique est un processus permettant d'obtenir une ostéogenèse entre deux segments osseux graduellement séparés par des forces de traction (Ilizarov and Ledyaev, 1992). Ce principe de néoformation osseuse progressive repose sur la création d'un foyer d'ostéogenèse à partir de corticotomies ou d'ostéotomies (Figure 17). Une ossification progressive a lieu sur le site distracté au fur et à mesure de la phase de distraction active, et l'os néoformé subit des phases de maturation puis de remodelage osseux avant de devenir indifférencié par rapport à l'os adjacent. En cours de distraction, le processus de réparation endochondrale se met en place, et est relayé par le mécanisme d'ossification membranaire, après l'arrêt de la phase de distraction (Yasui et al, 1997 ; Osawa et al ; 2017 ; Gambari et al, 2019).

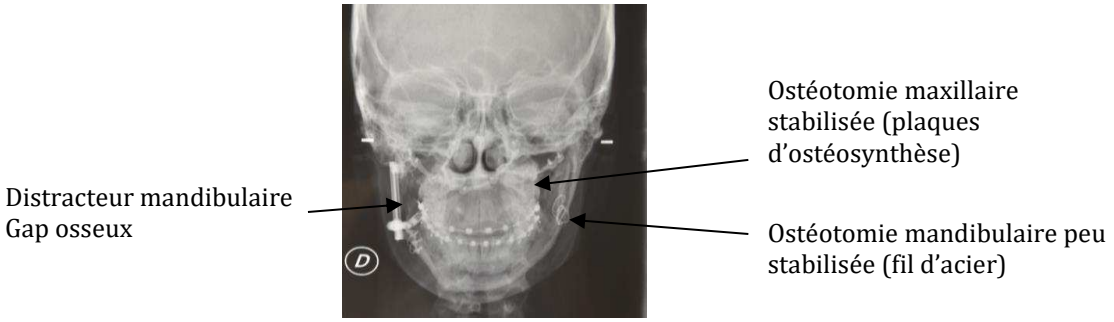

Figure 17. Téléradiographie de crâne de face d'un patient avec distracteur mandibulaire droit, en fin de distraction, ayant créé un gap osseux entre les 2 segments distractés, une ostéotomie maxillaire stabilisée par des plaques d'ostéosynthèse, et une ostéotomie peu stabilisée à l'aide d'un fil d'acier.

2. Mécanismes cellulaires et moléculaires impliqués au cours de la réparation osseuse

Plusieurs phases successives se mettent en place au cours du phénomène de réparation : il s'agit 1/ de la phase inflammatoire, dont l'initiation se fait de façon concomitante à la mise en place de l'hématome fracturaire ; 2/ de la phase fibrovasculaire, avec le recrutement des cellules progénitrices mésenchymateuses qui se différencieront ensuite en chondrocytes et en ostéoblastes ; 3/ de la phase de formation osseuse, soit directement à partir des ostéoprogéniteurs issus des cellules mésenchymateuses (réparation membranaire), soit également à partir des chondrocytes (réparation endochondrale) ; et 4/ de la phase de remodelage du cal de réparation (Bahney et al, 2019) (Figure 18).

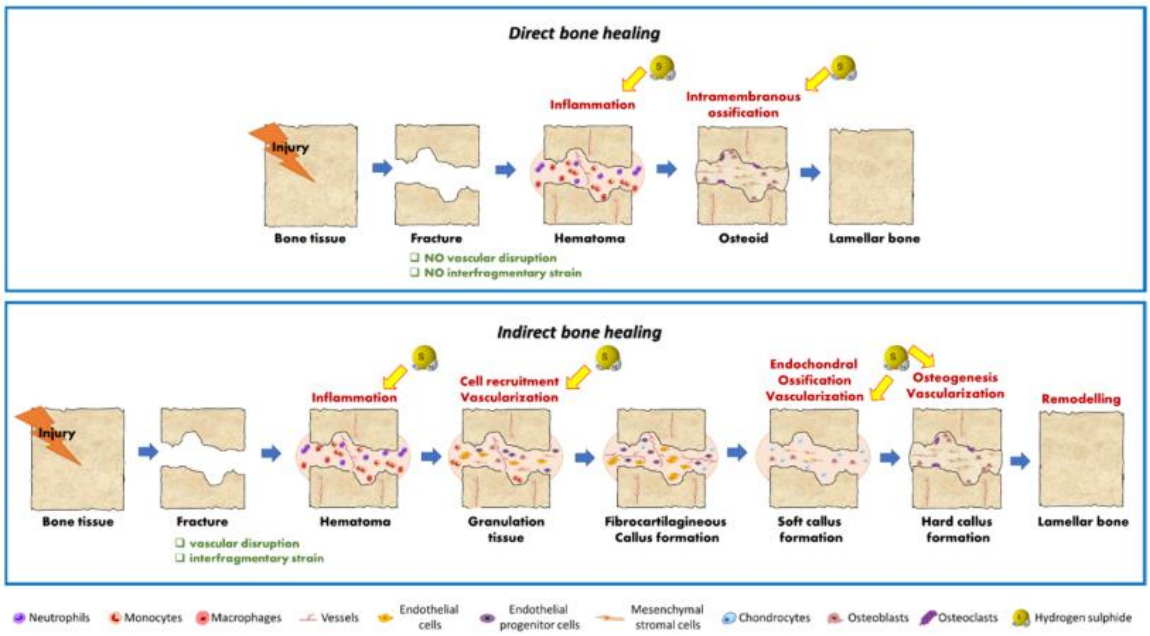

Figure 18. Représentation schématique des processus de réparation membranaire (« direct bone healing »), caractérisé par la différenciation directe des cellules mésenchymateuses en ostéoblastes ; **ou endochondrale (« indirect bone healing »)**, avec mise en place d'un cal fibrocartilagineux intermédiaire (Gambari et al, 2019).

1/ Phase inflammatoire

Dès le stade initial de la fracture, un hématome riche en fibrine se forme, afin de permettre l'hémostase. De cet hématome, sont relarguées des cytokines pro-inflammatoires, ayant un rôle de recrutement des lymphocytes, macrophages, et polynucléaires neutrophiles et éosinophiles (Einhorn, 1995 ; Bahney et al, 2019). Ces acteurs cellulaires jouent à la fois un rôle d'induction et de régulation de la réponse inflammatoire locale au niveau du périoste, de la moelle osseuse

et de l'hématome fracturaire, et un rôle de débridement des tissus dévitalisés en ce qui concerne les macrophages et les polynucléaires neutrophiles (Xing et al, 2010).

Plusieurs cytokines inflammatoires et facteurs de croissance sont relargués par ces cellules pro-inflammatoires, dont l'Interleukin 1 (IL1), l'IL6, TNFα, les FGFs, notamment FGF2, PDGF (Platelet-Derived Growth Factor), et TGFβ, indispensables à la mise en place du processus de réparation osseuse (Bankers-Fulbright et al, 1996 ; Yang et al, 2007 ; Gerstenfeld et al, 2003 ; Barnes et al, 1999 ; Hurley et al ; 2016 ; Wildemann et al ; 2003). La réaction inflammatoire liée à la voie du complément, et notamment C5a, joue également un rôle majeur dans le déroulement de la réponse inflammatoire initiale lors de la réparation osseuse (Ehrnthaller et al, 2013 ; Kovtun et al, 2017).

A la suite de cette phase initiale pro-inflammatoire et de débridement macrophagique, un changement de phénotype macrophagique s'opère, ceux-ci exerçant alors une action anti-inflammatoire, jouant un rôle de promotion du retour à l'homéostasie tissulaire (Gordon and Martinez ; 2010, Bahney et al ; 2019).

2/ Phase fibrovasculaire

A la suite de la phase inflammatoire, une phase de néo-vascularisation s'initie. VEGF (Vascular Endothelial Growth Factor) est un facteur de croissance majeur impliqué dans les phénomènes d'angiogenèse et de vasculogenèse. Au cours de la réparation osseuse, VEGF est secrété par de nombreuses cellules inflammatoires et mésenchymateuses, et par les ostéoblastes et chondrocytes hypertrophiques, sous l'induction de HIF1-alpha (Hypoxia Inducible Factor) exprimé en réponse aux conditions hypoxiques. HIF1-alpha et VEGF présentent un pic d'expression à J10 post fracture, dans le contexte de réparation endochondrale (Otrock et al, 2007 ; Hu and Olsen, 2017 ; Komatsu et al, 2004). La libération de VEGF sur le site de fracture dépend de l'action de la dégradation de la matrice extracellulaire induite par les métalloprotéases, notamment MMP2, 9, et 13 (Behonick et al, 2007 ; Colnot et al ; 2003). D'autres protéines de la matrice, telles que la thrombospondine (TSP) et l'ostéopontine, jouent un rôle modulateur de la revascularisation lors de la réparation osseuse (Taylor et al, 2009 ; Duvall et al ; 2007).

Le recrutement de cellules progénitrices mésenchymateuses se fait de façon concomitante à la néovascularisation, à partir de sources locales : périoste, endoste, moelle osseuse (Colnot, 2009). Il a été montré que l'invasion des cellules mésenchymateuses provenant du périoste sur le site de réparation est initiée dès J2 post-fracture (Matthews et al ; 2014). Plusieurs cytokines et facteurs sont indispensables à la régulation du recrutement des cellules mésenchymateuses,

tels que SDF1 (Stromal cell-derived factor) (via CXCR4), dont la transcription est régulée par HIF1-alpha ; et la voie de signalisation Notch, qui joue un rôle dans la régulation de la prolifération et la migration des cellules progénitrices mésenchymateuses (Kitaori et al, 2009 ; Wang et al ; 2016).

3/ Formation du cal osseux : ostéoblastes et chondrocytes

Les cellules progénitrices mésenchymateuses se différencient au sein du cal de réparation en cellules progénitrices ostéochondrales sous l'effet initial de Sox9, facteur majeur initiant la chondrogenèse, et qui a un effet de répression de Runx2, facteur majeur de différenciation ostéoblastique. Ces deux facteurs jouent ainsi un rôle de modulation du devenir des cellules progénitrices ostéochondrales (Eames et al, 2004). Le déclenchement préférentiel du processus de réparation endochondrale est favorisé par la présence de mouvements s'exerçant sur le cal de réparation, et par la tendance à l'hypoxie (Le et al, 2001 ; Burke et al, 2013).

La voie des BMP joue également un rôle majeur d'orientation de la différenciation des cellules progénitrices chondrogéniques. Les cellules du périoste expriment BMP2 et BMP4, et prolifèrent en réponse à BMP5 et BMP6 (Marsell et al, 2009). L'expression de BMP2 oriente la différenciation des progéniteurs en cellules chondrogéniques, alors que la répression de son expression est nécessaire à la mise en place du mécanisme de réparation membranaire (Tsuji et al, 2006 ; Yu et al, 2010). La voie Wnt joue également un rôle majeur au cours de la réparation osseuse, sa délétion étant à l'origine d'un défaut de réparation, cependant ses mécanismes d'action restent à préciser dans ce cadre (Secreto et al, 2009 ; Chen et al ; 2007).

3.1/ Formation du cal osseux en contexte de réparation membranaire

La différenciation directe des cellules mésenchymateuses en ostéoblastes (ossification membranaire) est le mécanisme de réparation observé dans le cadre des fractures ou ostéotomies stabilisées (cf supra). Ce processus est également observé au niveau du périoste et de l'endoste dans le cadre des fractures moins stabilisées (Bahney et al, 2019). Les cellules du périoste ont un potentiel ostéochondral, avec différenciation ostéoblastique le long du périoste, ou chondrogénique après migration au sein du cal de réparation, alors que les cellules de l'endoste n'ont qu'un seul potentiel de différenciation ostéoblastique (Colnot, 2009, Bahney et al, 2019).

3.2/ Formation du cal osseux en contexte de réparation endochondrale

La différenciation chondrocytaire des cellules progénitrices du cal de réparation est concomitante à la résolution de la réponse pro-inflammatoire, elle s'initie à partir des cellules

progénitrices du périoste (Colnot, 2009). Sox9 joue un rôle essentiel dans le maintien du phénotype chondrocytaire et de la maturation en chondrocyte hypertrophique, et régule avec Sox5 et Sox6, la formation d'une matrice dense en collagène de type II, participant à la stabilisation du défect osseux. Lors de cette phase, la néo-vascularisation est réprimée au sein du cartilage du cal de réparation (Bell et al, 1997 ; Hattori et al, 2010). La phase de maturation chondrocytaire en chondrocyte hypertrophique se met ensuite en place, avec sécrétion de matrice riche en collagène de type X (Bahney et al, 2019). Les chondrocytes hypertrophiques secrètent des facteurs angiogéniques, tels que VEGF, PDGF et PlGF (Placental Growth Factor), et induisent une 2ème phase d'invasion vasculaire (Gerber et al, 1999 ; Andrew et al, 1995 ; Maes et al, 2006). De façon simultanée, les chondrocytes hypertrophiques perdent l'expression de Sox9, permettant ainsi l'expression de promoteurs ostéogéniques, tels que Runx2 et beta-catenine (Hu et al, 2017 ; Dy et al, 2012). A partir de ce stade, les chondrocytes hypertrophiques commencent à exprimer des marqueurs osseux, tels que l'ALP, Osx, l'ostéopontine et l'ostéocalcine, induisant ainsi la calcification de la matrice (Gerstenfeld and Shapiro, 1996 ; Gerstenfeld et al, 2002). A la suite de la calcification de la matrice, la formation osseuse s'initie. Les chondrocytes hypertrophiques situés au niveau de la zone de transition entre cartilage et os néoformé sont enchâssés dans la matrice osseuse adjacente aux vaisseaux néoformés (Hu et al, 2017). Les BMPs, exprimés par les chondrocytes hypertrophiques et les cellules endothéliales, ainsi que les facteurs systémiques acheminés au niveau de la zone de réparation grâce à la néovascularisation, tels que le calcium extracellulaire, PTH, et la vitamine D, participent à la régulation du métabolisme phosphocalcique et à la minéralisation de la matrice osseuse (Yu et al, 2010, Bahney et al, 2019). Le devenir des chondrocytes hypertrophiques est mixte, soit ils deviennent apoptotiques, dans ce contexte de réparation osseuse avec cartilage transitoire, soit ils se transdifférencient en ostéoblastes. Cette transdifférenciation du stade de chondrocyte hypertrophique en ostéoblaste semble s'opérer soit directement, soit après dédifférenciation à partir du stade de chondrocyte hypertrophique, avant de proliférer et de se redifférencier en ostéoblastes (Galéa et al, 2021 ; Zhou et al, 2014 ; Hinton et al, 2017 ; Bahney et al, 2014 ; Song et al, 2004) (Figure 19).

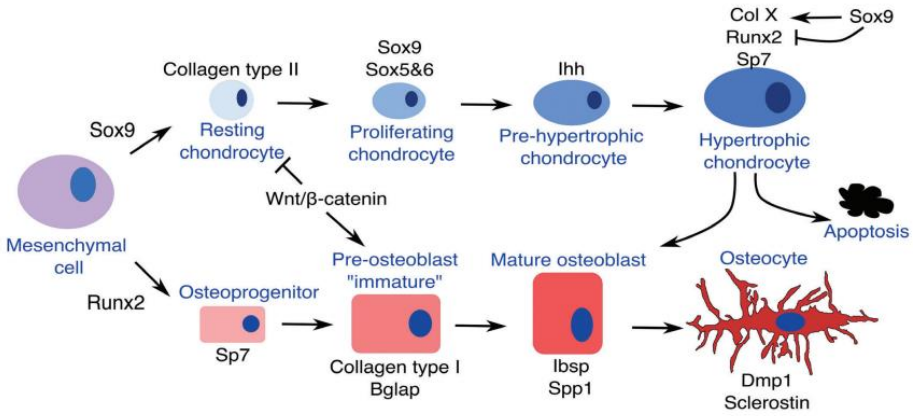

Figure 19. Voies de différenciation chondrocytaire et ostéoblastique, et devenir mixte des chondrocytes hypertrophiques, vers la voie apoptotique ou par transdifférenciation en ostéoblastes (Galea et al, 2021).

4/ Remodelage du cal osseux

Le remodelage du cal correspond à la dernière phase de la réparation osseuse. Cette phase s'initie lorsque que le cal osseux est complètement formé, pontant ainsi entièrement la zone d'interruption osseuse. La phase de remodelage du cal permet la restitution d'un os lamellaire mature, de même nature que la structure osseuse initiale interrompue. Cette phase est permise par l'action des cellules ostéoclastiques, cellules géantes multinuclées, présentant une structure membranaire spécifique (sealing zone), permettant l'adhésion à la surface osseuse à résorber. La résorption de la matrice osseuse se fait grâce aux conditions de pH acide au sein de la lacune de résorption (lacune de Howship), par dissolution des cristaux d'hydroxyapatite. La digestion de la matrice collagénique se fait sous l'action de protéases (Teiltelbaum, 2007 ; Vaananen et al, 2000). Les cellules ostéoclastiques dérivent de la lignée hématopoiétique monocytaire/macrophagique, sous l'action de MCSF, et de RANKL (Receptor Activator of Nuclear Factor kappaB ligand), secrété par la lignée ostéoblastique, et activant le récepteur RANK, exprimé par les précurseurs ostéoclastiques (Feng, 2005). L'activation ostéoclastique est également nécessaire lors des phases précoces, lors du débridement initial, afin de permettre la résorption de fragments osseux présents au niveau des berges osseuses (Bahney et al, 2019). La résorption de la matrice cartilagineuse est dépendante de l'action conjointe de MMPs, en particulier MMP13, secrété par les chondrocytes hypertrophiques et les ostéoblastes, jouant un rôle de dégradation du collagène de type II et de l'aggrecan ; et de MMP9, secrété par les cellules endothéliales et macrophagiques, ayant un rôle de résorption de la matrice collagénique dégradée (Colnot et al, 2003 ; Wu et al, 2013).

3. Expression et rôles de la voie FGF/FGFR au cours de la réparation osseuse

a) En conditions physiologiques

Les FGFs et les FGFRs sont exprimés dès l'initiation de la réparation, lors de toutes les phases de réparation dans de multiples types cellulaires, dont les cellules mésenchymateuses, chondrocytaires, ostéoblastiques, ostéoclastiques, et inflammatoires (Du et al, 2012). Plusieurs études montrent une variation spatiotemporelle de leur expression au cours du processus de réparation osseuse. Cependant, les patterns d'expression des FGFs et des FGFRs varient selon les études, selon le modèle et la technique de mesure utilisés (Du et al, 2012).

Dans un modèle de fracture tibiale non stabilisée chez la souris (réparation endochondrale), Fgf1, 2 et 5 sont exprimés précocement au cours de la réparation osseuse, dès J1 post fracture. A ce stade précoce de la réparation, Cd68, Bmp2 et Vegfa étaient également surexprimés (Schmid et al, 2009). Entre J4 et J9 post fracture, les gènes impliqués dans le processus de chondrogenèse (Sox9) deviennent plus fortement exprimés, et l'expression des gènes ostéoblastiques augmente (Bsp, Runx2, Osx) (Schmid et al, 2009). A J9 post fracture, Fgf16 et 18 sont surexprimés. Il a été montré que l'expression de Fgf18 prédomine au niveau du périchondre et du périoste (Liu et al ; 2002). A ce même moment, Col2a1 et Col10a1 sont également surexprimés, l'expression de Vefga continue d'augmenter, ainsi que celle de Ptch1 (voie hedgehog) (Chen and Struhl, 1996 ; Schmid et al, 2009). A J14, l'expression de Fgf1 et Fgf17 prédomine, alors que les niveaux d'expression de Fgf2, 9, 16 et 18 sont maintenus à un niveau supérieur à celui observé en l'absence de fracture (Schmid et al, 2009). A partir de ce stade, les marqueurs chondrogéniques diminuent, alors que les marqueurs ostéoblastiques augmentent encore (Bsp, Runx2, Osx), ainsi que Cd68, marqueur du remodelage osseux médié par la lignée macrophagique/ostéoclastique (Schmid et al, 2009). A partir de J9, Fgfr1, 2 et 3 sont surexprimés, mais l'initiation de l'augmentation et la survenue du pic d'expression varient selon le récepteur : l'initiation de l'augmentation de l'expression de Fgfr1 et 2 est plus précoce (dès J1) que celle de Fgfr3 (J4) et dont le pic d'expression est observé aux alentours de J9-J10 post fracture (Schmid et al ; 2009) (Figure 20). Fgfr1 et 2 sont exprimés au sein des cellules progénitrices du périoste, des chondrocytes et des ostéoblastes, ainsi qu'au niveau ostéoclastique en ce qui concerne Fgfr1 (Nakajima et al, 2001 ; Rundle et al, 2002). Fgfr3 est exprimé au sein des cellules mésenchymateuses, des chondrocytes préhypertrophiques et hypertrophiques du cal de réparation, des ostéoblastes et du périoste (Rundle et al, 2002 ;

Nakajima et al, 2003 ; Su et al, 2008). Alors que l'expression de Fgfr1 et 2 est maintenue au même niveau entre J9 et J14, celle de Fgfr3 tend à diminuer à partir de J9 (Schmid et al ; 2009).

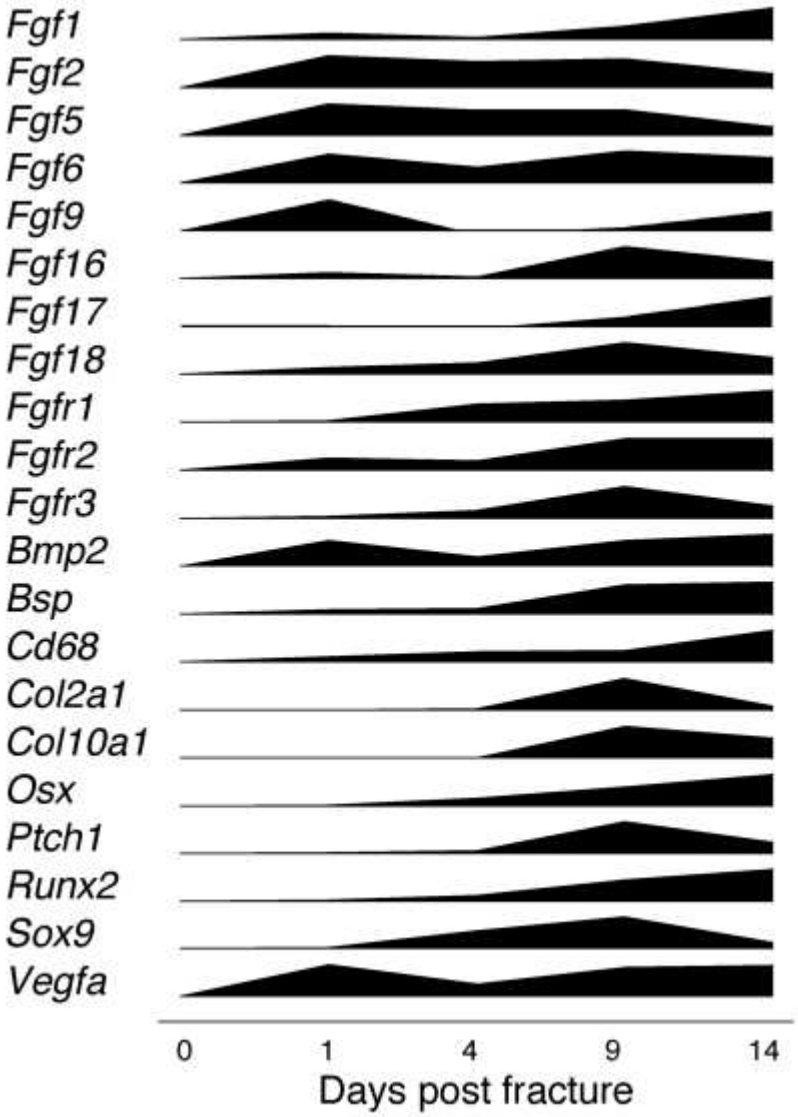

Figure 20. Expression relative des gènes de la voie FGF/FGFR et des gènes associés impliqués dans le processus de réparation osseuse endochondrale dans un modèle murin de fracture non stabilisée du tibia (Schmid et al ; 2009).

L'expression des Fgfs4, 8 et 20 n'a pas été retrouvée au cours de la réparation osseuse dans ce modèle (Schmid et al, 2009). Dans d'autres modèles animaux (rat, lapin), il a été montré que l'expression de Fgf1, 2 et 18 est également augmentée au cours du processus de réparation osseuse dans le cadre de la distraction ostéogénique (Haque et al, 2007 ; Pacicca et al ; 2003). Cependant, les données manquent en ce qui concerne l'expression de la voie FGF/FGFR au cours de la distraction ostéogénique.

b) En conditions pathologiques : apport des modèles murins

L'impact des mutations dans les gènes *FGFRs* reste peu étudié au cours de la réparation osseuse. La génération de modèles murins porteurs de mutations *FGFRs* est une étape indispensable à l'étude de l'implication des gènes *FGFRs* au cours de la réparation osseuse. En effet, l'analyse *in vivo* est un prérequis indispensable dans la compréhension fine de ce processus mettant en jeu de multiples facteurs cellulaires et moléculaires et leurs interactions au sein de l'environnement tissulaire de la fracture.

Quelques études ont rapporté l'impact de mutations dans le gène *FGFR3* dans des modèles murins d'achondroplasie, essentiellement après fracture non stabilisée, stabilisée ou dans le cadre de la distraction ostéogénique, au niveau des os longs. A ce jour, l'impact de ces mutations après fracture du squelette craniofacial et notamment mandibulaire n'a jamais été étudié.

Il a été observé au sein du modèle murin d'achondroplasie, $Fgfr3^{G369C/+}$, des anomalies de réparation osseuse caractérisées par un retard de consolidation avec retard de résorption cartilagineuse au sein du cal de réparation, après fracture tibiale non stabilisée et stabilisée (Su et al, 2008 ; Chen et al ; 2017). Plus récemment, dans le modèle $Prx1^{Cre};Fgfr3^{Y367C/+}$, permettant l'expression d'une mutation mimant l'achondroplasie au niveau des os longs, il a été montré après fracture non stabilisée des tibias, des anomalies sévères de consolidation osseuse avec pseudarthrose et retard de résorption cartilagineuse au sein des cals de réparation et anomalies de différenciation chondrocytaire (Julien et al, 2020). Osawa et al, dans un modèle murin d'achondroplasie $Fgfr3^{G380R/+}$ ont montré la présence d'anomalies de différenciation chondrocytaire au sein des cals de réparation après distraction ostéogénique des tibias, mais le volume du cal osseux ne semble pas impacté à J14 post fracture dans ce cadre (Osawa et al, 2017).

A l'inverse de ce qui est observé dans le cadre de mutations activatrices de *FGFR3* dans les modèles murins d'achondroplasie, l'inactivation constitutive de *Fgfr3* dans le modèle murin $Fgfr3^{-/-}$, a permis d'observer, après fracture stabilisée des tibias, une augmentation de la différenciation chondrocytaire et ostéoblastique au sein des cals de réparation, et une accélération du remodelage osseux, par rapport aux contrôles (Xie et al, 2017).

L'impact des mutations dans le gène *FGFR2* est à ce jour extrêmement peu étudié. En pathologie humaine, il semble que le type de mutation *FGFR2* (syndrome de Crouzon, Apert ou Pfeiffer) influence le délai et la qualité de la réparation osseuse après chirurgies osseuses craniofaciales (Morice et al, 2017 ; Oyama et al ; 2009). Au sein du modèle murin de Crouzon,

Fgfr2$^{C342Y/+}$, bien qu'il soit connu que le gène *FGFR2* joue un rôle de promotion de la différenciation ostéoblastique, l'étude de Alcon et al, à partir de défects de calvaria, n'a pas montré d'amélioration significative dans le processus de comblement osseux, après transplantation de cellules souches dérivées de tissu adipeux issues de souris mutantes Crouzon (Alcon et al, 2018). L'étude de la réparation osseuse au sein des modèles murins de craniosténose FGFR2 doit être cependant poursuivie, pour élucider le rôle de FGFR2 à la fois au cours de la réparation d'origine membranaire et endochondrale, ce qui n'a jamais été étudié.

D. Pathologies squelettiques et FGFRs

Les mutations activatrices gain-de-fonction dans les gènes *FGFR1*, *FGFR2 et FGFR3* sont à l'origine d'ostéchondrodysplasies (chondrodysplasies et craniosténoses). Il s'agit de pathologies liées à des mutations hétérozygotes, avec transmission autosomique dominante, dont la survenue est le plus souvent sporadique.

La majorité des chondrodysplasies sont liées à des mutations *FGFR3*, il s'agit de l'achondroplasie, de l'hypochondroplasie et du nanisme thanatophore. Ces pathologies se caractérisent par un nanisme rhizomélique et des malformations craniofaciales (macrocéphalie, rétrusion maxillaire, dysmorphie mandibulaire).

Les craniosténoses sont caractérisées par des malformations craniofaciales liées à la fusion prématurée d'une ou plusieurs sutures crâniennes. Des mutations dans les gènes *FGFR1*, *FGFR2* et *FGFR3* sont à l'origine du syndrome de Pfeiffer (*FGFR1* et *FGFR2*), des syndromes de Crouzon, Apert, Jackson-Weiss et Baere Stevenson (*FGFR2*) (Wilkie et al, 1995 ; Rutland et al, 1995 ; Sabatino et al, 2004) et des syndromes de Muenke et Crouzon avec *acanthosis nigricans* (*FGFR3*) (Robin et al, 1993 ; Meyers et al, 1995 ; Muenke et al, 1997 ; Cornille et al, 2022). Les craniosténoses liées à *FGFR1*, *FGFR2 et FGFR3* se caractérisent par la présence d'une craniosynostose uni- ou bi-coronale avec fusion d'une ou plusieurs autres sutures crâniennes, à l'origine de déformations crâniennes variables, avec hypertélorisme, exorbitisme, et recul de l'étage supérieur et moyen de la face. Les syndromes d'Apert, de Pfeiffer et de Muenke associent à ce phénotype craniofacial, des anomalies des extrémités (Wilkie et al, 1995 ; Rutland et al, 1995 ; Sabatino et al, 2004, Robin et al, 1993 ; Meyers et al, 1995 ; Muenke et al, 1997), alors que dans le syndrome de Crouzon avec *acanthosis nigricans* (CAN), syndrome extrêmement rare, des anomalies cutanées (*acanthosis nigricans*) sont associées (Cornille et al, 2022).

1. Chondrodysplasies liées à FGFR3

L'ensemble des chondrodysplasies regroupent un grand de nombre de pathologies squelettiques affectant la formation cartilagineuse et osseuse au cours du développement. Il s'agit d'une famille de pathologies hétérogènes, comptant plus de 450 syndromes (Rimoin et al, 2007). Les mutations activatrices gain-de-fonction dans le gène *FGFR3* sont à l'origine de formes variables de nanisme rhizomélique (achondroplasie, hypochondroplasie, nanisme thanatophore, SADDAN), caractérisées par un tronc et des membres courts, la réduction de croissance affectant de façon prédominante la partie proximale des membres. A l'opposé, le syndrome

CATSHL, lié à une haploinsuffisance de *FGFR3*, se caractérise par une hypercroissance squelettique.

a) L'achondroplasie

L'achondroplasie (OMIM 100800) est la forme la plus fréquente de chondrodysplasie liée à *FGFR3*, dont l'incidence est estimée entre 1/30 000 et 1/10 000 (Horton et al, 2007, Baujat et al, 2008).

Phénotype clinique

Le phénotype clinique est caractérisé par la présence d'un nanisme rhizomélique sévère, avec tronc et membres courts, majoritairement dans leur partie proximale. Une incurvation des tibias est retrouvée de façon variable (Horton et al, 2007, Baujat et al, 2008). La taille maximale atteinte chez les patients est comprise entre 120 et 130 cm en moyenne : 129,9 (± 6,25) en moyenne chez les hommes, et 122,4 (5,9) chez les femmes (soit -3 à -4 DS) (Hoover-Fong et al, 2021).

Le diagnostic peut être suspecté en anténatal, lors de l'échographie du 3ème trimestre devant la présence de membres courts (Coi et al, 2019).

A l'étage craniofacial, les patients présentent des anomalies dominées par une macrocéphalie avec front bombé, une rétrusion maxillo-zygomatique de sévérité variable, une ensellure nasale plus ou moins marquée, avec prognathisme mandibulaire relatif, en rapport avec le maxillaire rétrus (Di Rocco et al, 2014) (Figures 21, 22). Des anomalies de taille et de forme mandibulaire ont été également montrées (Biosse Duplan et al, 2016). Une fusion prématurée des synchondroses de la base du crâne et des sutures crâniennes, essentiellement au niveau de la suture squamo-sphénoidale est souvent observée (Di Rocco et al, 2014). Des anomalies cérébrales sont également décrites, en rapport avec un élargissement des espaces subarachnoïdiens, et souvent associées à une compression cervico-médullaire par sténose au niveau du foramen magnum, et à une hypertension intracrânienne (Di Rocco et al, 2014). Au niveau axial, la brièveté du tronc s'accompagne d'anomalies de la statique rachidienne, et du volume de la cage thoracique.

Figure 21. Photographie de profil d'un patient achondroplase (Service d'Orthopédie, Hôpital Necker Enfants Malades).

Figure 22. Photographies de face et de profil de patients porteurs d'achondroplasie confirmée, montrant la présence d'un phénotype craniomaxillofacial de sévérité variable, mineure (à gauche), modérée (centre), à sévère (droite), caractérisé par la présence de front bombé, d'ensellure nasale marquée, d'une macrocrânie, d'une rétromaxillie, et une tendance au prognathisme mandibulaire relatif (Service de Chirurgie Maxillofaciale et Chirurgie Plastique, Hôpital Necker - Enfants Malades).

Conséquences fonctionnelles

Les conséquences fonctionnelles sont multiples dans l'achondroplasie. Des apnées du sommeil sont retrouvées de façon pathologique dans environ 60% des cas (Julliand et al, 2012, Tenconi et al, 2017), essentiellement de type obstructive, liées à la réduction de la filière aérienne de cause multiple (végétations adénoïdes, amygdales, sténose des choanes, macroglossie, rétrusion maxillaire) et d'origine centrale, par compression cervico-medullaire au niveau du foramen magnum (Julliand et al, 2012, Tenconi et al, 207, Holzman et al, 2008, Onodera et al, 2006). La corrélation anatomofonctionnelle, entre la sévérité du phénotype craniofacial et les apnées obstructives du sommeil, n'a pas été à ce jour établie.

Une surdité mixte, de transmission et centrale, est décrite chez les patients achondroplases (Shohat et al, 1993, Gorlin et al, 1976, Collins et al, 2007).

Sur le plan cognitif et comportemental, le développement intellectuel semble normal, cependant, certaines fonctions semblent plus impactées, notamment la mémoire de travail,

l'arithmétique, l'attention et les fonctions exécutives, et une diminution du QI (quotient intellectuel) verbal est parfois observé (Wigg et al, 2016).

Bases génétiques et moléculaires de l'achondroplasie

La transmission génétique est de type autosomique dominante, et est sporadique dans 80 %. L'âge paternel avancé semble être un facteur de risque dans l'achondroplasie (Ornitz and Legeai Mallet, 2017, Wilkin et al, 1998).

Une mutation substitution récurrente hétérozygote de Glycine en Arginine en position 380 (G380R), dans le domaine transmembranaire du récepteur FGFR3, est retrouvée dans plus de 97% des cas (Rousseau et al, 1994, Shiang et al, 1994, Horton et al, 2002). Dans les autres cas, les mutations connues sont : p.Ser217Cys, p.Ser279Cys, p.Ser344Cys, et p.Gly375Cys.

Les mutations gain-de-fonction de *FGFR3* responsables de l'achondroplasie, entrainent une activation constitutive du récepteur FGFR3, ce dernier étant activé en présence ou en absence de ligand FGF, ayant pour conséquence une phosphorylation excessive des résidus tyrosine kinase, une perturbation de son internalisation, avec persistance du récepteur à la membrane cellulaire, et une suractivation des voies de signalisations situées en aval (He et al, 2011, Naski et al, 1996, Monsonego-Ornan et al, 2000).

b) L'hypochondroplasie

L'hypochondroplasie (OMIM 14600) est une forme de nanisme rhizomélique, présentant des caractéristiques communes avec l'achondroplasie, s'exprimant souvent de façon plus modérée (Maroteaux and Falzon, 1988, Walker et al, 1971). Aucune étude ne rapporte le taux d'incidence précis de l'hypochondroplasie, cependant il semble admis qu'elle survienne avec une incidence proche de celle de l'achondroplasie, soit entre 1/40 000 et 1 pour 15 000 naissances. Comme pour l'achondroplasie, l'âge paternel avancé semble être un facteur de risque de survenue de cette pathologie (Bober et al, 2020).

Phénotype clinique

Une grande variabilité de sévérité phénotypique est décrite, des formes mineures, modérées à sévères, dont le diagnostic différentiel avec l'achondroplasie est parfois difficile à établir cliniquement (Rousseau et al, 1996, Flynn and Pauli, 2003). Dans les formes plus modérées, le diagnostic est établi généralement plus tardivement dans l'enfance, aux alentours de l'âge de 3 ans. Cependant, des données récentes de la littérature suggèrent que le diagnostic de certaines

formes d'hypochondroplasie pourrait être posé plus précocement, y compris en période anténatale (Sabir et al, 2020).
La taille maximale atteinte par les patients adultes porteurs d'hypochondroplasie est de 143.6 cm (131-154.5 cm) (hommes) et de 130.8 cm (124-138 cm) (femmes) (Maroteaux and Falzon, 1998, Arenas et al, 2018).

Les anomalies craniofaciales retrouvées sont similaires à celles retrouvées dans l'achondroplasie, s'exprimant avec une sévérité variable, des formes subnormales aux formes plus sévères. Le phénotype craniofacial reste néanmoins peu étudié dans l'hypochondroplasie (Figure 23).

Figure 23. Photographies d'une patiente porteuse d'hypochondroplasie, de face et de profil, montrant un aplatissement modéré maxillo-malaire (Service de Génétique Médicale, Hôpital Necker Enfants Malades, Dr Geneviève Baujat).

Des anomalies cutanées de type *acanthosis nigricans* sont parfois retrouvées, correspondant à des lésions hyperpigmentées et hyperkératosiques, prédominant aux niveaux des plis cutanés (Berk et al, 2010, Blomberg et al, 2010).

Conséquences fonctionnelles

Les conséquences fonctionnelles sont identiques à celles retrouvées dans l'achondroplasie, et s'expriment à un degré de sévérité dépendant le plus souvent de la sévérité phénotypique. Cependant, certains auteurs rapportent une incidence plus importante du déficit intellectuel chez les patients porteurs d'hypochondroplasie que chez les patients achondroplases (Walker

et al, 1971, Hall And Spranger, 1979, Wynne-Davies and Patton, 1991). Ces données sont controversées, et restent à confirmer.

Bases génétiques et moléculaires de l'hypochondroplasie

La transmission génétique est de type autosomique dominante. De multiples mutations hétérozygotes ont été associées à l'hypochondroplasie, la plus fréquente est la mutation substitution p.Asn540Lys, dans environ 60 % des cas (Bellus et al, 1995, Ornitz and Legeai-Mallet, 2017, Bober et al, 2020), affectant le domaine tyrosine kinase 1 du récepteur FGFR3. Cette mutation entraîne la phosphorylation des domaines tyrosine kinase, indépendamment de la présence de ligand FGF (Raffioni et al, 1998). Les autres mutations les plus fréquemment retrouvées, sont p.Tyr278Cys, p.Ser348Cys (dont le phénotype ressemble à une forme modérée d'achondroplasie) (Hasegawa et al 2014, Couser et al 2017, Bengur et al 2020, Heuertz et al, 2006), p.Lys650Asn, p.Lys650Gln, p.Lys650Thr. Les variants p.Lys650Asn et p.Lys650Gln sont associés à un phénotype axial plus modéré (Bellus et al, 2000), et les variants p.Lys650Gln et p.Lys650Thr, à une survenue plus fréquente d'*acanthosis nigricans* (Berk et al 2010, Blomberg et al 2010).

c) La dysplasie thanatophore (ou nanisme thanatophore)

Il s'agit d'une forme sporadique très sévère de nanisme rhizomélique, le plus souvent létale, avant ou à la naissance, liées à une détresse respiratoire majeure, et/ou à une compression médullaire (Maroteaux et al, 1967). L'incidence de la dysplasie thanatophore est estimée entre 1/50 000 et 1/20 000 naissances.

Phénotype clinique

Au phénotype axial et appendiculaire sévère, s'associe souvent la présence de fusion prématurée des sutures crâniennes (le plus souvent des sutures coronales), avec parfois synostoses multiples et crâne en trèfle, ainsi que de malformations cérébrales sévères, prédominant au niveau des lobes temporaux, associées à une hydrocéphalie (Itoh et al, 2013).
Le diagnostic est généralement établi entre les 2èmes et 3èmes trimestres de grossesse, devant la présence d'une longueur des membres inférieure au 5ème percentile, une macrocéphalie. L'étroitesse de la cage thoracique et l'aplatissement des corps vertébraux peut être détectée en période anténatale. Il existe 2 formes cliniques de dysplasie thanatophore (TD), la TD1 (OMIM 187600) et la TD2 (OMIM 187601). A la naissance, la micromélie sévère s'accompagne

fréquemment de plis cutanés redondants et d'une brachydactylie avec une main caractéristique dite en « trident », et une incurvation des fémurs dans la TD1. La TD2, les fémurs sont droits et est plus souvent associée à une craniosynostose multiple avec crâne en trèfle (Figure 24).

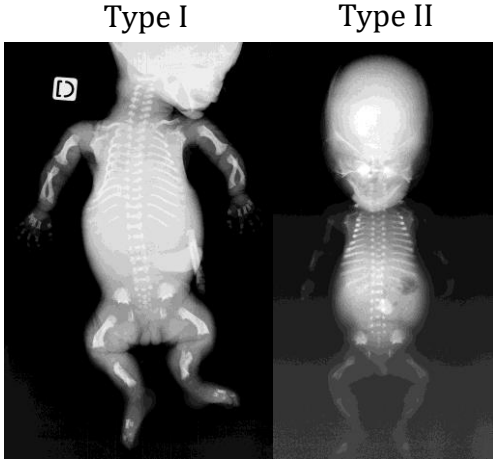

Figure 24. Radiographies de patients porteurs de dysplasie thanatophore (de type I à gauche et de type II à droite), montrant la présence d'hypoplasie majeure des membres, avec incurvation des fémurs (type I) et fémurs très courts et droits (type II), et l'aplatissement des corps vertèbraux (Dr Laurence Legeai-Mallet).

Bases génétiques et moléculaires

La transmission est autosomique dominante, mais la mutation survient le plus souvent *de novo*, avec une récurrence très faible, cette dernière étant possible dans le cadre de mosaïsme parental (Hyland et al 2003). La pénétrance est de 100 %.

La TD1 est liée le plus souvent à une mutation faux-sens, affectant le domaine extracellulaire ou intracellulaire, en position p.Arg248Cys, p.Tyr373Cys dans environ 90 % des cas ou en position p.Lys650Met (Passos-Bueno et al 1999, Xue et al 2014). Dans les autres cas, il s'agit d'une mutation faux-sens en position ou d'une mutation non-sens en position p.Ter807Leu, ou p.Ter807Gly, p.Ter807Arg, p.Ter807Cys, p.Ter807Trp. Ces mutations non-sens entraînent un allongement de la protéine FGFR3 dans son domaine intracellulaire (Tavormina et al, 1995).

La TD2 est liée à une mutation p.Lys650Glu, située dans le domaine tyrosine kinase de FGFR3 (Bellus et al, 2000).

Ces mutations entrainent une suractivation très importante de FGFR3 et des voies MAPK et STAT situées en aval, indépendamment de la présence de ses ligands (Krejci et al, 2008, Legeai-Mallet et al, 2004, Gibbs et Legeai-Mallet, 2007).

d) Syndrome SADDAN

Le SADDAN (OMIM 616482), est une forme très rare d'achondroplasie sévère, associée à un retard de développement et à des lésions cutanées d'*acanthosis nigricans* (Severe Achondroplasia Developemental Delay and *Acanthosis Nigricans*). Cette pathologie est associée à une mutation faux-sens en position p.Lys650Met (Bellus et al, 1999) au sein du domaine tyrosine kinase de FGFR3, responsable d'une activation constitutive du récepteur.
Les patients présentent une incurvation des fémurs, des tibias et des clavicules, et parfois des anomalies neurologiques telles que l'épilepsie (Bellus et al, 1999).

e) Syndrome CATSHL (camptodactylie, tall stature, and hearing loss)

A l'opposé des syndromes précédemment décrits, le syndrome CATSHL (OMIM 610474) est lié à une perte de fonction de la protéine FGFR3. Il s'agit de mutations dominantes faux-sens en position p.Arg621His et p.Thr546Lys, au sein du domaine tyrosine kinase de FGFR3. Il s'agit d'un syndrome associant une camptodactylie, une taille staturale excessive avec troubles induits de la statique rachidienne, et une surdité d'origine centrale. Au niveau céphalique, les patients présentent une microcéphalie et des os wormiens (os surnuméraires au niveau de la calvaria) (Toydemir et al, 2006, Makrythanasis et al, 2014).

2. Faciocraniosténoses liées aux FGFRs

a) Craniosténoses : formes cliniques

Les craniosténoses désignent une vaste famille de pathologies craniofaciales liées à une fusion prématurée d'une ou plusieurs sutures crâniennes à l'origine de déformations variables de la voûte du crâne, selon le site de la suture fusionnées. La prévalence des craniosténoses est estimée entre 1/2000 et 1/3000 naissances, 20 % d'entre elles sont d'origine syndromique (Lajeunie et al, 1995, Johnson and Wilkie, 2011, Wilkie et al, 2017). Les gènes mutés connus pour être responsables de craniosténose sont listés en annexe (Tableau a.1). Des mutations dans les gènes *FGFRs* (1, 2 et 3) sont retrouvées dans plus de 75% des cas (Lattanzi et al, 2017). L'âge paternel semble associé à une survenue plus fréquente de ces pathologies (Glaser et al 2000, Goriely and Wilkie, 2012). Les autres mutations retrouvées le plus fréquemment concernent les gènes TWIST (syndrome de Saethre-Chotzen) (Gallagher, et al, 2003). A ce

jour, plus d'une cinquantaine de gènes ont été associés à des craniosténoses syndromiques (Twigg and Wilkie, 2015).

Le site de la suture fusionnée, son caractère uni ou bilatéral, et le nombre de sutures atteintes, détermine la déformation du crâne, celle-ci étant induite par la poussée cérébrale sous-jacente, s'exerçant perpendiculairement à la suture fusionnée (Virchow et al, 1857, Delashaw et al 1989).

On distingue plusieurs types de craniosténose selon le site de la/les sutures fusionnées (Twigg et Wilkie, 2015) (Figure 25) :

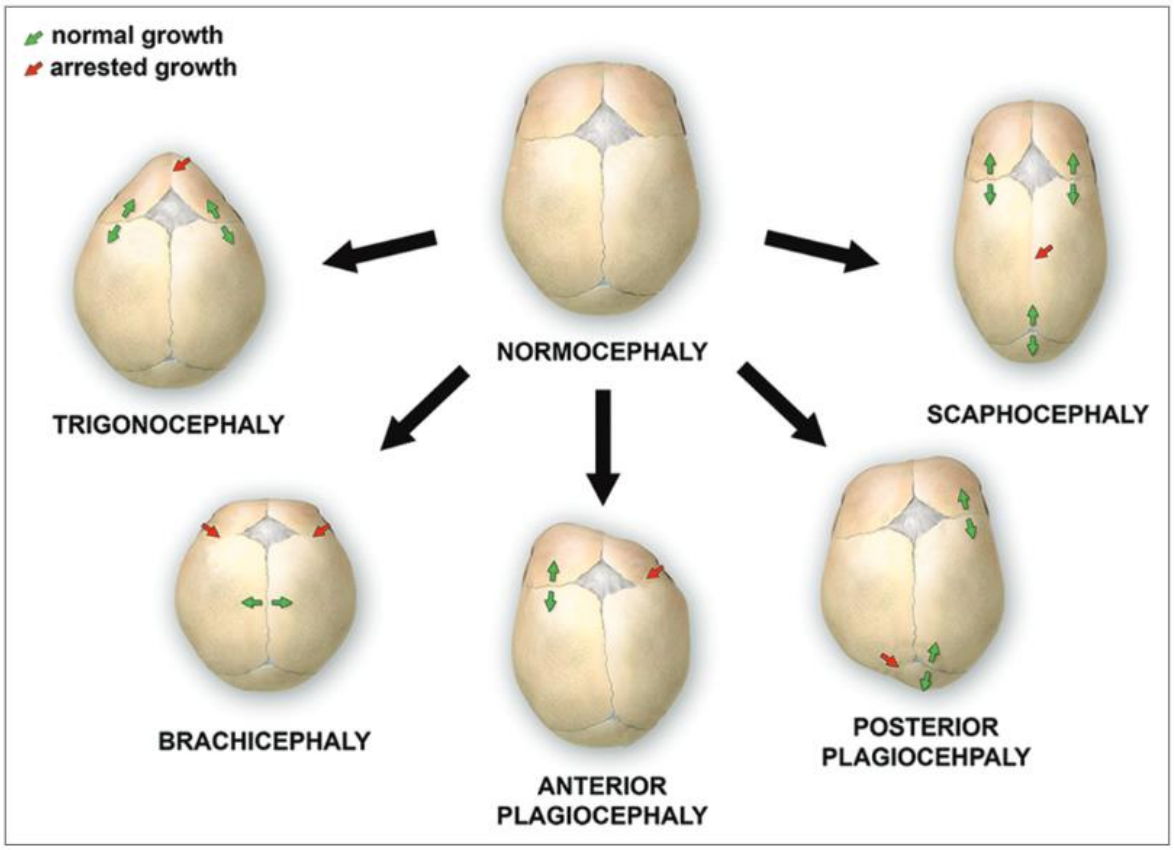

Figure 25. Représentation des déformations typiques du crâne selon le/les types de sutures crâniennes fusionnées précocement (selon Kajdic et al, 2018).

- La brachycéphalie : il s'agit d'une déformation liée à la fusion bilatérale des sutures coronales, avec un élargissement de la distance transversale du crâne, et une réduction de la croissance de l'étage supérieur et moyen de la face, avec pour conséquence un exorbitisme, un hypertélorisme et une rétrusion fronto-zygomatique ; celle-ci est la plus fréquemment observée dans les craniosténoses syndromiques.
- La plagiocéphalie : celle-ci est due à la fusion prématurée d'une suture coronale, de façon unilatérale, il s'agit de la plagiocéphalie antérieure, s'accompagnant d'un

aplatissement de l'hémifront homolatéral, et parfois d'une déviation de la racine nasale ; lorsque la fusion concerne une suture lambdoïde, il s'agit de plagiocéphalie postérieure, à distinguer de la plagiocéphalie positionnelle, dans laquelle il n'existe pas de craniosténose, mais un élargissement de la suture lambdoïde homolatérale, liée à un appui prolongé dans la première année de vie.

- La scaphocéphalie : il s'agit d'une déformation du crâne caractérisée par un allongement de la distance antéropostérieure, avec front et partie postérieure du crâne bombés, liée à une fusion prématurée la suture sagittale.
- La trigonocéphalie : il s'agit d'une déformation triangulaire du front, lié à une fusion prématurée de la suture métopique, s'accompagnant d'un rapprochement des canthi internes (hypotélorisme).
- L'oxycéphalie concerne la déformation conique du crâne, en rapport avec la fusion prématurée des sutures coronales, et d'une autre / d'autres suture(s) crânienne(s).
- La pansynostose est le terme définissant la fusion d'au moins 3 sutures, à l'origine de microcéphalie, parfois d'une forme du crâne en « trèfle », avec un risque d'hypertension intracrânienne sévère.

b) Syndrome de Pfeiffer (FGFR1 et FGFR2)

L'incidence du syndrome de Pfeiffer, ou acrocéphalosyndactylie de type V (OMIM 101600) est estimée à 1/100 000 naissances (Robin et al, 1993). Il s'agit d'une faciocraniosténose liée à la fusion prématurée des sutures coronales, avec déformation du crâne de type brachycéphalie, avec exorbitisme, hypertélorisme et rétrusion de l'étage fronto-facial. A ces anomalies craniofaciales, peuvent s'associer des anomalies des doigts et des orteils, à type d'élargissement et déviation du pouce et de l'hallux, et bradydactylie.

Trois formes distinctes de syndrome de Pfeiffer sont décrites (Cohen, 1993, Vogel and Fryns, 2006, Ko, 2016) :

- Le type I, ou Pfeiffer « classique », définit par une forme modérée de brachycéphalie, s'accompagnant d'anomalies des extrémités. Le développement intellectuel et neurologique est généralement normal.
- Le type II, se caractérise par un crâne en « trèfle », avec exorbitisme sévère, des anomalies des extrémités, et parfois une ankylose ou synostose du coude, et un retard important du développement.
- Le type III, est une forme sévère, comme le type II, mais il n'existe pas de déformation en trèfle du crâne.

Les formes cliniques de type II et III sont des formes sporadiques, et associées à des conséquences fonctionnelles respiratoires et neurologiques souvent sévères.
Le syndrome de Pfeiffer de type I, est lié à des mutations dominantes dans les gènes FGFR1 p.Pro252Arg (FGFR1) et FGFR2. Les formes cliniques de type II et III sont liées uniquement à des mutations affectant FGFR2 (chromosome 10q26 de FGFR2) (Figure 26 A, D).

c) Syndrome ou maladie de Crouzon (FGFR2)

Il s'agit de la faciocraniosténose syndromique liée à *FGFR2* la plus fréquente (OMIM 123500). La prévalence est estimée à 1/50 000. La transmission est de type autosomique dominant, mais les cas sporadiques sont fréquents, estimés entre 30 à 60 % des cas (Al Qattan and Phillips, 1997, Robin et al, 1993). Le phénotype clinique (brachycéphalie, exorbitisme, rétrusion fronto-faciale) est hétérogène (Shiller, 1959) (Figure 26). La fusion prématurée des sutures coronales est présente à la naissance, ou apparaît parfois de façon retardée, aux alentours de l'âge de 2 ans, avec une aggravation progressive du phénotype (Schmetz et al, 2021). Cette variabilité phénotypique s'accompagne d'une grande variabilité génotypique, en effet, à ce jour, plus de 47 mutations distinctes ont été identifiées (Passos Bueno et al, 2008). Les mutations les plus fréquemment rencontrées affectent le domaine extracellulaire de FGFR2, en particulier la boucle IgIII dans 95% des cas, au niveau de l'exon 8 (IIIa), et au niveau de l'exon 10 (IIIc) à l'origine de ponts disulfures aberrants entre des résidus cystéine (Miraoui et Marie, 2010). Ces ponts disulfures stabilisent la boucle III, permettant ainsi l'activation du récepteur indépendamment de la présence d'un ligand FGF (Gorry et al, 1995, Wilkie, 1997). Les mutations les plus fréquemment rencontrées sont p.Cys342Tyr, p.Cys278Phe, puis p.Tyr105Cys, p.Gly338Glu, p.Ser267Pro, p.Ser347Cys, etc (Wilkie et al, 1997). Certaines mutations sont retrouvées à la fois dans le phénotype de syndrome de Crouzon et de Pfeiffer (p.Cys278Phe, p.Cys342Tyr, p.Cys342Arg, p.Cys342Ser, p.Cys342Trp (Wilkie et al, 1997).
De façon sporadique, quelques mutations concernent la boucle IgI (p.Cys62Ala) (Sharma et al, 2012), ou les domaines tyrosine kinase de la protéine (N549H, R678G) (Kan et al, 2022, Ciurea and Toader, 2009).

d) Syndrome d'Apert (FGFR2)

Le syndrome d'Apert ou acrocephalosyndactylie de type II (OMIM 101200), est un syndrome très rare (incidence 1/60 000) de craniosténose sévère syndromique bicoronale (Figure 26), associée à des syndactylies osseuses et membraneuses des extrémités, avec fusion totale ou

partielle des 2, 3 et 4èmes doigts (Blank, 1959). Une fusion prématurée des sutures lambdoïdes et sagittale est souvent associée (Wenger et al, 2019). Un déficit intellectuel mineur à modéré est observé, cependant un développement intellectuel normal a également été rapporté. Le déficit intellectuel est souvent en lien avec des malformations cérébrales associées (corps calleux, système limbique) (Cohen and Kreiborg, 1990, Wenger et al, 2019). Dans plus de 98% des cas, une mutation p.Ser252Trp et p.Pro253Arg est retrouvée. Dans les autres cas, il s'agit d'insertion Alu dans l'exon 9 de FGFR2 ou à sa proximité. La plupart des cas surviennent de façon sporadique, dans les autres cas, une transmission autosomique dominante est retrouvée (Mantilla-Capacho et al, 2005). Des fusions de vertèbres cervicales sont fréquemment retrouvées (68%), typiquement au niveau de C5-C6 (Kreiborg et al, 1992). Une fente palatine peut être associée, le plus souvent dans le cadre de la mutation p.Ser252Trp.

e) Syndrome de Jackson-Weiss (FGFR2)

Le syndrome de Jackson-Weiss (OMIM 123150) est un syndrome plus rare de faciocraniosténose coronale. Le phénotype associe les anomalies craniofaciales typiques d'une craniosténose coronale, et des anomalies des extrémités, avec élargissement des hallux. Le phénoype est proche de celui du syndrome de Pfeiffer, mais il n'existe pas de déformation des pouces dans le syndrome de Jackson-Weiss (Jackson et al, 1976). Les mutations décrites concernent le domaine extracellulaire du récepteur (p.Cys342Ser, p.Cys342Arg, p.Gln289Pro, P.Ala344Gly), à l'origine d'une suractivation de FGFR2 ligand-dépendante (Robin et al, 1993, Tartaglia et al, 1997, Wilkie, 1997). La transmission est autosomique dominante.

f) Syndrome de Beare-Stevenson Cutis Gyrata (FGFR2)

Le syndrome de Beare-Stevenson Cutis Gyrata (OMIM 123790), est un syndrome extrêmement rare, qui associe au phénotype de craniosténose coronale, des anomalies cutanées (cutis gyrata (plis et laxité excessifs de la peau), acanthosis nigricans), des malformations des oreilles, des anomalies ano-génitales, et un cordon proéminent. L'espérance de vie est faible (Przylepa et al., 1996). Dans les quelques cas décrits dans la littérature, les cas sont sporadiques, et une mutation Y375C, S372C, ou une délétion 1506del63 (Przylepa et al, 1996, Slavotinek et al, 2009).

g) Syndrome de Muenke (FGFR3)

Le syndrome de Muenke (OMIM 602849) est l'une des faciocraniosténoses syndromiques la plus fréquente, sa prévalence est estimée à 1/30 000 (Vajo et al, 2000). Elle compte pour environ 25 à 30 % des craniosténoses syndromiques (Kruska et al, 2016, 1993, Moloney et al, 1997, Morriss-Kay and Wilkie, 2005). Le syndrome de Muenke se caractérise par une synostose bi- ou uni-coronale, dans ce cas, la déformation frontofaciale est asymétrique, se caractérisant par une plagiocéphalie antérieure homolatérale (Figure 26). Les sutures lambdoïdes, sagittale voire métopique peuvent également être fusionnées (Kruszka et al, 2016, Renier et al, 2000). Le phénotype clinique craniofacial est relativement hétérogène, des formes mineures à sévères, avec parfois crâne en « trèfle » en cas de pansynostose (Abdel-Salam et al, 2011). Des anomalies des extrémités peuvent être observées, notamment une déformation des phalanges moyennes en « dé à coudre », une brachydactylie, et une fusion carpale ou tarsale (Muenke et al, 1997, Agochukwu et al, 2013). Des cas de surdité centrale ont été rapportés (Hollway et al, 1998).

La mutation hétérozygote p.Pro250Arg est spécifiquement associée à ce syndrome (Bellus et al, 1996, Muenke et al, 1997) ; elle a pour conséquence une augmentation de l'affinité des ligands FGFs pour le récepteur muté (Ibrahimi, et al, 2004). La pénétrance est variable, environ 15% des patients porteurs de cette mutation ne présentent pas de craniosténose (Kruska et al, 1993, 2016, Moko and Blandin de Chalain, 2001).

h) Syndrome de Crouzon avec acanthosis nigricans (FGFR3)

Le syndrome de Crouzon avec acanthosis nigricans (OMIM), est un syndrome extrêmement rare (1 pour 1 000 000) (OMIM 612247), caractérisé par un phénotype de faciocraniosténose bicoronale, avec des lésions d'*acanthosis nigricans*, survenant dans la première décade chez 80 % des patients. Il s'agit d'une forme d'*acanthosis nigricans* atypique et diffuse. D'autres anomalies associées ont été décrites, notamment intraorales, il s'agit de fente palatine, et de cémentomes des mâchoires (Breitbart et al, 1989, Meyers et al, 1995, Arnaud-Lopez et al, 2007, Cohen, 1999). Une unique mutation, pAla391Glu dans le gène *FGFR3* a été associée spécifiquement à ce syndrome (Meyers et al, 1995, Wikes et al, 1996), à l'origine d'une suractivation de FGFR3 ligand-indépendante (Li et al., 2006 ; Chen et al., 2013, 2011).

Figure 26. Photographies de patients porteurs de faciocraniosténoses syndromiques FGFR1 (Pfeiffer : A), FGFR2 (Crouzon : B, Apert : C, Pfeiffer : D), FGFR3 (Muenke : E ; Crouzon avec acanthosis nigricans : F).

3. Prise en charge thérapeutique

a) Chondrodysplasies

Traitements chirurgicaux

L'approche thérapeutique la plus ancienne consiste enl'allongement progressif des membres par distraction osseuse ostéogénique à l'aide de distracteurs externes (procédure d'Ilizarov, Ilizarov et al, 1969). Des distractions ostéogéniques d'un seul segment de membre (des membres supérieurs ou inférieurs), ou de plusieurs segments de façon simultanée sont décrites (Ko et al, 2019, Shabtai et al, 2021). Ces procédures ont été réalisées chez des patients achondroplases et hypochondroplases (Yasui et al, 1997, Hiraki et al, 2006, Kitoh et al, 2007, 2014). Il s'agit de procédures longues et invasives, dont la tolérance difficile peut compromettre l'allongement final, notamment lorsque le dispositif de contention doit être retiré précocement. Plus récemment, le développement de distracteurs internes à activation magnétique, pourrait permettre d'améliorer la tolérance de la procédure, en particulier chez des patients jeunes (Paley, 2015). Au niveau rachidien, une prise en charge chirurgicale est parfois nécessaire chez certains patients présentant une sténose du canal lombaire (Huet et al, 2020).

A l'étage cranio-cervical, les patients nécessitent parfois une décompression de la charnière cervico-occipitale, en cas de conséquences fonctionnelles liées à la compression cervico-médullaire (apnées centrales, troubles neurologiques) (Baujat et al, 2008, Kashanian et al, 2022).

Au niveau craniomaxillofacial, la réalisation d'un traitement orthodontique voire chirurgical visant à corriger la rétrusion maxillaire et le décalage dentosquelettique dans l'achondroplasie a été rarement rapporté dans la littérature. Les apnées obstructives sont d'origine multifactorielle (réduction des voies aériennes supérieures,végétations adénoides,

hypertrophie amygdalienne, hypotonie, macroglossie, rétrusion maxillaire), et il n'a pas été établi à ce jour de corrélation anatomo-fonctionnelle entre la sévérité des anomalies morphologiques maxillofaciales et la sévérité des apnées obstructives. L'expansion maxillaire pourrait avoir un rôle bénéfique dans le cadre de la prise en charge du syndrome d'apnées obstructives du sommeil. Ce traitement orthopédique dento-facial est souvent nécessaire chez les patients achondroplases pour traiter l'insuffisance transversale du maxillaire. Dans certains cas, l'avancement maxillaire peut être stimulé par la mise en place de dispositifs orthopédiques d'avancée maxillaire, de type masque de Delaire (Figure 27).

Figure 27. Masque de Delaire chez une patiente, avec tractions élastiques d'avancée maxillaire (selon Kılıçoğlu et al, 2017).

La réalisation d'ostéotomies et de distraction ostéogénique maxillaire peuvent être indiqués dans le cas de décalage dento-squelettique important. Il s'agit le plus souvent d'ostéotomies maxillaires de type Le Fort I, ou de distraction ostéogénique maxillaire lorsque le décalage à corriger est important, et/ou lorsque l'intervention doit être réalisée de façon interceptive, en cours de croissance, dans le cadre de conséquences morphologiques et fonctionnelles (apnées obstructives du sommeil) importantes (Figure 28).

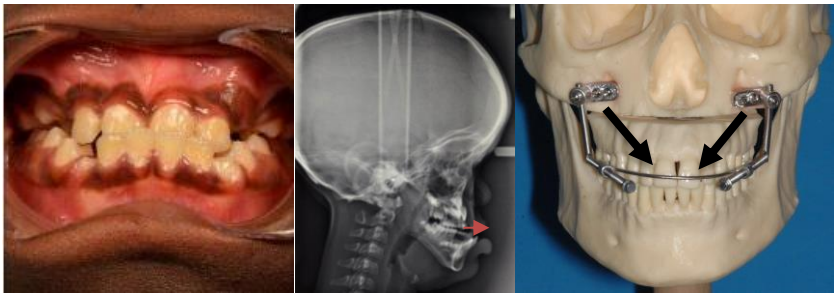

Figure 28. Photographie occlusale de face, et téléradiographie de profil d'un patient porteur d'achondroplasie, montrant le décalage dentosquelettique important lié à la rétrusion maxillaire, et photographie de face d'un modèle 3Dmontrant la réalisation d'une ostéotomie de type Le Fort I, avec distracteur interne, dont le but est de réaliser un avancement progressif du maxillaire.

Différents types d'ostéotomies sont rapportés dans la littérature, le plus souvent couplées à une distraction ostéogénique. Il s'agit d'ostéotomies de Le Fort I ou de Le Fort I modifiée, avec réalisation d'un trait d'ostéotomie plus haut, à hauteur de l'étage zygomatique, d'ostéotomies de type Le Fort II ou III (Elwood et al, 2003, Susarla et al, 2017). Bien que leur étude soit basée sur un faible nombre de patients, les auteurs rapportent une régression des apnées obstructives plus importante après ostéotomies de Le Fort II +/- Le Fort I, qu'après ostéotomies de type Le Fort III (Susarla et al, 2017) (Figure 29).

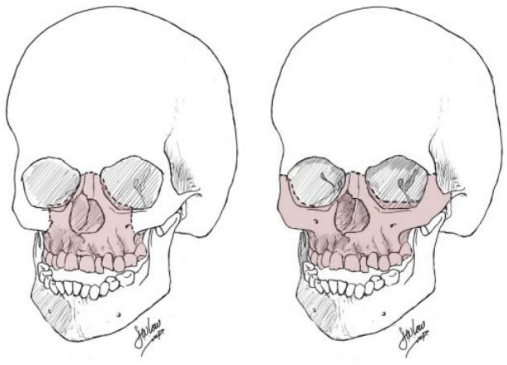

Figure 29. Traits d'ostéotomies de type Le Fort II (gauche) et Le Fort III (droite), réalisant une disjonction craniofaciale (selon Tahiri and Taylor ; 2014).

Approches pharmacologiques

Plusieurs approches pharmocologiques sont développées dans l'achondroplasie, dans le but d'augmenter la croissance osseuse, par une action ciblée sur l'hyperactivation du récepteur FGFR3 et de ses voies de signalisation situées en aval.

Dans l'achondroplasie, grâce à l'apport des modèles murins d'achondroplasie (*Fgfr3*$^{Y367C/+}$, généré au sein de notre équipe (Pannier et al, 2009, Jonquoy et al, 2012, Komla Ebri et al, 2016), ou portant la mutation G380 (Naski et al, 1998), deux types d'approches thérapeutiques se sont développées ces dernières années, soit par action directe spécifique sur le récepteur suractivé, soit par voie indirecte, par l'intermédiaire d'autres voies venant ainsi inhiber la suractivation des voies de signalisation situées en aval de FGFR3 (Figure 30).

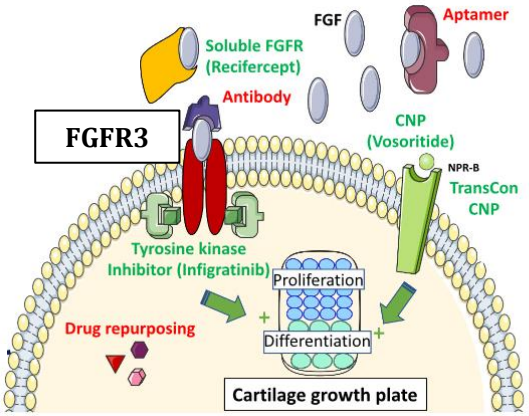

Figure 30. Représentation schématique des différentes options thérapeutiques en cours de phase préclinique, et en cours de phase clinique (infigratinib, vosoritide) chez les patients achondroplases (adapté de Legeai-Mallet and Savariryan, 2020).

Les analogues du CNP

L'utilisation des CNP comme approche thérapeutique est une des premières pistes thérapeutiques envisagées pour l'achondroplasie. Le CNP (C-Natriuretic Peptide), et son récepteur, NPR-B (Natriuretic Peptide Receptor B (NPR-B), sont des régulateurs clés de la croissance osseuse longitudinale (Chusho et al, 2001). La perte de fonction de NPR-B est en cause dans la dysplasie acromésomélique (de type Maroteaux) ; il s'agit d'une forme disproportionnée de nanisme (Bartels et al, 2004). A l'inverse, la suractivation de CNP et/ou de NPR-B ont pour conséquence une croissance excessive chez les patients atteints (Bocciardi et al, 2007, Moncla et al, 2007, Hannema et al, 2013). L'activation de NPR-B par le CNP, entraîne une inhibition de la voie des MAP Kinases, activées en aval de FGFR3. Une amélioration significative de la croissance osseuse a été démontrée dans un modèle murin transgénique d'achondroplasie, soit après surexpression du CNP au sein du cartilage, soit après traitement par CNP, par perfusion continue par voie intraveineuse (Yasoda et al, 2004, 2010). Le CNP ayant une courte demi-vie, un analogue de celui-ci avec demi-vie plus longue, le BMN111 (vosoritide) a été développée par BioMarin. L'effet positif du vosoritide a été montré en phase préclinique *in vitro* à partir de cellules humaines de patients achondroplases, et *in vivo*, dans le modèle murin d'achondroplasie *Fgfr3*$^{Y367C/+}$ (Lorget et al, 2012). Après traitement des animaux mutants en phase de croissance, une amélioration significative de la croissance osseuse et du phénotype, y compris craniofacial ont été observées. Ces effets positifs du vosoritide ont été également montrés dans le modèle murin d'achondroplasie *Fgfr3*$^{G380R/+}$ (Wendt et al, 2015). L'effet du vosoritide a été testé en phase clinique (escalade de doses avec injection sous cutanée

quotidienne) à partir de 2014, chez des enfants âgés de 5 à 14 ans (Clinical-trials.gov, number NCT02055157). Compte tenu des résultats prometteurs obtenus sur la croissance staturale (+1,5 cm/an) (Savarirayan et al, 2019), un essai clinique de phase 3 (ClinicalTrials.gov number, NCT03197766) a été mené chez des patients achondroplases âgés de 5 à 18 ans. Les résultats ont confirmé le gain de croissance chez les patients traités par rapport au groupe placebo (+1,57 cm/an) (Savarirayan et al, 2020). Les patients inclus dans cet essai clinique, sont actuellement suivis jusqu'à la fin de croissance pour déterminer les effets à long terme de ce traitement (ClinicalTrials.gov number, NCT03424018). Actuellement un nouvel essai clinique de phase 2 est conduit chez des patients plus jeunes de 0 à 2 ans, versus âgés de plus de 2 ans, pour tester la tolérance de ce traitement, dans le but de tester l'effet du vosoritide (Voxzogo®) sur la morphologie et la taille du foramen magnum (ClinicalTrials.gov number, NCT04554940). En parallèle, un autre analogue du CNP, le TransCon-CNP, avec une durée de vie plus longue, est testé en phase clinique de phase 2 (ClinicalTrials.gov number, NCT04085523), ce traitement a pour but d'améliorer la tolérance du traitement, en permettant des injections hebdomadaires, plutôt que quotidiennes.

Les inhibiteurs de tyrosine kinase

Ces approches se sont basées initialement sur l'expérience du traitement de certains cancers liés à une signalisation FGF/FGFR aberrante (myélome, cancers génito-urinaires ou pulmonaires) (Legeai Mallet and Savarirayan, 2020, Ferguson et al, 2021).

Les inhibiteurs de tyrosine kinase ont pour effet de bloquer la phosphorylation excessive des résidus tyrosine kinase, et de réduire l'hyperactivation des voies de signalisation situées en aval du récepteur. Plusieurs molécules ont été développées dans le traitement de plusieurs types de cancers, de la vessie et de myélomes, il s'agit de CHIR-258 (Trudel et al, 2005), PD173074, SU5402, ARQ087, et NVP-BGJ398 (Kunova Bosakova et al, 2019, Legeai Mallet and Savariryan, 2020). NVP-BGJ398, plus sélectif pour FGFR3 que pour les autres FGFRs (Kunova Bosakova et al, 2019) a été testé en phase préclinique dans des modèles murins dans le cadre du traitement de tumeurs rhabdoides (Wörle et al, 2013), de carcinome hépatocellulaire (Sheller et al, 2015), et de l'hypophosphatémie FGF23 (Wörle et al, 2013).

Le NVP-BGJ398 a également une action ciblée sur le tissu osseux et cartilagineux, comme démontré dans le modèle murin d'achondroplasie *Fgfr3*$^{Y367C/+}$, dans lequel il a été montré une amélioration significative de la croissance osseuse, au niveau des os longs, avec restauration de la désorganisation de la plaque de croissance après traitement des animaux mutants. Une amélioration significative a également été montrée au niveau de la colonne vertébrale et de la

charnière cervico-occipitale, ainsi que de la morphologie craniofaciale chez les animaux *Fgfr3*$^{Y367C/+}$ traités (Komla Ebri et al, 2016, Di Rocco et al, 2014, Biosse Duplan et al, 2016). Actuellement, le BGJ398 (infigratinib; QED therapeutics), est testé en phase clinique (phase II) avec escalade de doses, avec prise par voie orale, chez des enfants achondroplases âgés de 3 à 11 ans (ClinicalTrials.gov number, NCT04265651; PROPEL-2) (Legeai-Mallet and Savariryan, 2020).

Aptamère des FGFRs

Un aptamère est une molécule d'acide nucléique simple brin, courte, ayant une activité neutralisante spécifique et à faible antigénicité. Un aptamère ciblant spécifiquement FGF2 (APT-F2P/RBM007 ; Ribomic Inc.), empêche la liaison de FGF2 aux récepteurs FGFRs, bloquant ainsi l'activation des voies de signalisation situées en aval. Cette molécule a montré son efficacité dans le traitement de certains cancers FGF2-dépendants (Hamamoto et al, 2018) et dans des modèles murins et de rat, d'arthrite et d'ostéoporose (Jin et al, 2016). Actuellement, cette molécule fait l'objet d'études précliniques visant à tester son effet sur la croissance osseuse dans des modèles murins d'achondroplasie.

Récepteur FGFR3 soluble ou « decoy receptor »

Compte tenu du fait que l'activation du récepteur FGFR3 soit dépendante de l'activation de ligands FGF, il a été développé une forme soluble de FGFR3, le TA-46 ou recifercept, visant à limiter la fixation de ligand FGF au niveau de FGFR3. Les études précliniques visant à tester cette molécule dans un modèle murin d'achondroplasie, a montré des effets prometteurs sur la croissance osseuse (Garcia et al, 2013). Actuellement, une étude de phase clinique est en cours chez des patients achondroplases âgés de 0 à 10 ans afin de tester l'effet du recifercept sur la croissance osseuse) ClinicalTrials.gov number, NCT03794609; Dreambird).

Anticorps anti-FGFR3

Un anticorps spécifique anti-FGFR3 (le B-701/vofatamab) a été développé dans le traitement de certains cancers liés à FGFR3 (vessie, myélomes, poumon) (Rauchenberger et al, 2003, Trudel et al, 2006, Yin et al, 2016). Celui-ci pourrait être un candidat médicament dans l'achondroplasie, et être l'objet de nouveaux essais précliniques.

(-)-Epicatechin

L'(-)-Epicatechin est un dérivé du *Theobroma Cacao*, il s'agit d'une molécule de la famille des polyphénols, qui a un rôle connu dans de nombreux processus biologiques. Cette molécule agit sur la voie des MAP Kinases. Ses effets ont été démontrés dans de nombreux tissus et types cellulaires, tels qu'au sein des neurones, des adipocytes, et du tissu hépatique (Cady et al, 2010, Jang et al ; 2015, Cordero-Herrera et al, 2015).

L'effet de l'(-)-Epicatechin a été plus récemment démontré dans le tissu cartilagineux, dans le modèle murin d'achondroplasie, dans lequel il a été montré une amélioration significative de l'organisation de la plaque de croissance et de la croissance osseuse chez les animaux mutants traités. Ses effets spécifiques au sein du chondrocyte ont été démontrés, avec (1) l'élongation des cils primaires chondrocytaires et son action spécifique sur la voie Ihh (Indian Hedgehog) dans ce processus, et (2), son effet d'inhibition des voies de signalisation en aval de FGFR3 (Martin et al, 2022). Ces résultats ouvrent des perspectives thérapeutiques prometteuses dans l'achondroplasie.

Meclozine

La meclozine est un médicament bien connu de la famille des anti-histaminiques, ayant des effets anti antivertigineux et antiémétiques. De part ces effets de régulateur négatif de la phosphorylation de ERK (voie des MAP Kinases), ce médicament a fait l'objet d'études précliniques dans un modèle murin d'achondroplasie. Les résultats préliminaires ont montré une amélioration du phénotype squelettique chez les souris traitées (Matsushita et al, 2015). Cette molécule a été testée récemment chez des patients achondroplases dans le cadre de la phase clinique de type I, dans le cadre des études de tolérance chez ces patients (Kitoh et al, 2020).

Statines

Les statines sont largement connues pour leur effet hypocholestérolémiant. Cette molécule a également été testée dans un modèle murin d'achondroplasie. Les résultats des études précliniques réalisées sont controversés. En effet, il été rapporté dans une étude, un effet positif chez les animaux traités, avec une amélioration du phénotype squelettique (Yamashita et al, 2014), alors que dans une autre, il a été observé un retard du développement cartilagineux, et une régulation négative de l'expression de régulateurs clés du cartilage des plaques de croissance (Bush et al, 2015). Une étude plus récenten'a pas retrouvé d'effet négatif des statines

in vitro sur la prolifération et la différenciation chondrocytaire (Fafilek et al, 2017). A ce jour, aucune étude clinique n'a débuté pour ces molécules dans l'achondroplasie.

b) Faciocraniosténoses

Traitements chirurgicaux

L'indication et le calendrier de réalisation des interventions neurochirurgicales et craniofaciales dépendent du type et nombre de sutures fusionnées, de la sévérité des conséquences morphologiques qui en découle, et surtout de leurs conséquences fonctionnelles (exorbitisme, apnées du sommeil, hypertension intracrânienne, malformation de Chiari (ptose et compression des amygdales cérebelleuses au niveau du foramen magnum).

Dans le cadre des craniosténoses bicoronales, l'avancement frontofacial monobloc avec distraction est une procédure très utilisée car elle permet de corriger à la fois l'exorbitisme et la rétrusion maxillaire (Mathijssen et al, 2006, Khonsari et al, 2016, 2020, Saxby et al, 2018) (Figure 31). Cette intervention peut être réalisée en cours de croissance (âge moyen 3,9 ± 3 ans) (Khonsari et al, 2020).

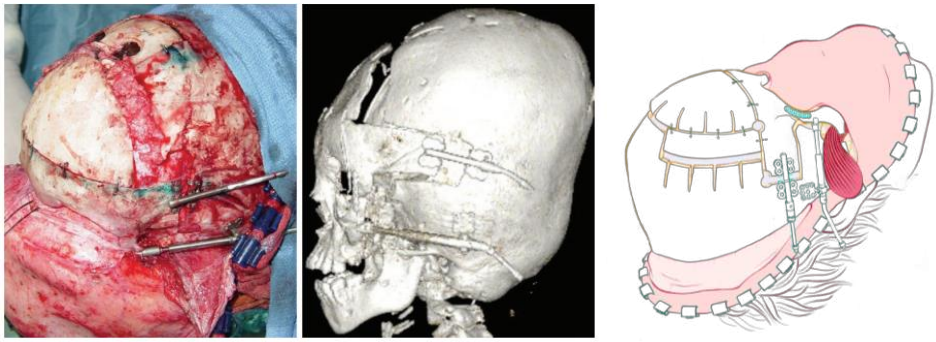

Figure 31. Vue peropératoire (gauche) et reconstruction 3D d'un scanner post opératoire (centre), et schéma peropératoire montrant les traits d'ostéotomies de l'avancement frontofacial monobloc avec distracteurs internes frontocrâniens et temporomalaire, avec renforcement frontozygomatique à l'aide d'une plaque en titane (Morice et al, 2018 ; Khonsari RH).

Une expansion postérieure ou latérale de la voûte crânienne avec distraction à visée de décompression, peut être indiquée de façon précoce dans la première année de vie, visant à traiter l'hypertension intracrânienne et éviter l'évolution turricéphalique de la forme du crâne au cours de la croissance (Lu et al, 2019, Khonsari et al, 2020). L'effet de l'avancement frontofacial monobloc dans le traitement des apnées obstructives est démontré, et cet effet semble d'autant plus important qu'une expansion postérieure précoce de la voûte crânienne a été réalisée au préalable, de façon précoce, ainsi qu'un geste ORL précoce de désobstruction

des voies aériennes (Khonsari et al, 2020). Plusieurs procédures additionnelles peuvent être nécessaires au cours de la croissance de l'enfant ; il peut s'agir d'un 2ème avancement frontofacial, d'ostéotomies de type Le Fort III, ou maxillaires (Le Fort I, disjonction maxillaire). En cas d'hypertension intracrânienne persistante, une dérivation du liquide céphalorachidien peut être indiquée (ventriculostomie, dérivation ventriculaire) mais en raison de l'origine pluri-factorielle de ces hypertensions persistantes (compression, composante veineuse, trouble de résorption), la dérivation est rarement une solution satisfaisante. En cas de malformation associée de type Chiari, une décompression chirurgicale peut être indiquée.
Dans le cadre d'une synostose unicoronale, un avancement fronto-orbitaire est indiqué, permettant à la fois de symétriser la projection frontale, et du bandeau supraorbitaire (Figure 32).

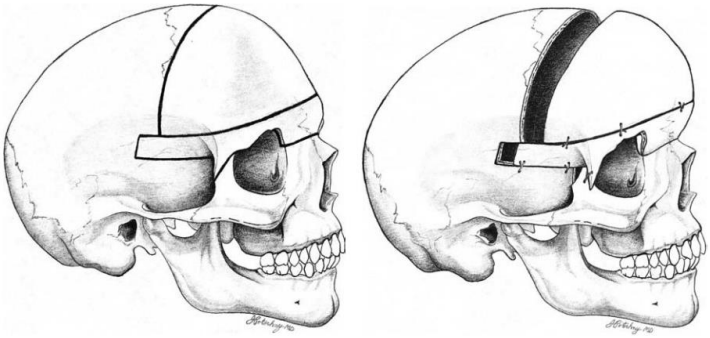

Figure 32. Ostéotomies réalisées dans le cadre de la technique d'avancement fronto orbitaire (de Grabb and Smith's Plastic Surgery, Sixth Edition by Charles H. Thorne).

Approches pharmacologiques

A ce jour, aucune approche pharmacologique ne fait l'objet d'essai clinique chez les patients porteurs de faciocraniosténose FGFR.
Plusieurs études précliniques ont testé des molécules antagonistes de FGFR2 dans des modèles murins de Crouzon, et d'Apert.

Syndrome de Crouzon

Inhibiteur de tyrosine kinase

Un inhibiteur de tyrosine kinase, le PD173074, a été testé dans le modèle murin de Crouzon, *Fgfr2c*$^{C342Y/+}$ (Eswarakumar et al, 2006, Perlyn et al, 2006). Les auteurs rapportent, à partir

d'études *ex vivo*, une absence de fusion des sutures coronales des calvarias issues d'animaux mutants traités pendant 2 semaines avec cet inhibiteur (Perlyn et al, 2006). Cependant, l'affinité de PD173074 serait plus importante pour FGFR1 et FGFR3 que pour FGFR2 (Miyake et al, 2010, Mohammadi et al, 2018) ; ainsi l'action de ce traitement dans le cadre des mutations activatrices de FGFR2 pourrait correspondre à un effet indirect sur les autres récepteurs FGFRs, régulant également l'ostéogénèse.

Analogue du CNP, le BMN111

Une étude préclinique a testé *in vivo* chez des animaux mutants *Fgfr2c*$^{C342Y/+}$, le BMN111 (Holmes et al, 2018). Une modification partielle du phénotype craniofacial a été observée après traitement, sans action sur la fusion prématurée des sutures coronales. Cet effet partiel peut être dû au traitement trop tardif des animaux mutants (stade postnatal P3), alors que la fusion prématurée des sutures coronales s'était déjà initiée.

Syndrome d'Apert

shRNA (small hairpin RNA)

Dans un modèle murin d'Apert, *Fgfr2*$^{S252W/+}$, il a été montré une amélioration significative du phénotype de souris mutantes croisées avec des souris exprimant un shRNA spécifique de l'allèle muté *Fgfr2*$^{S252W/+}$. Les souris issues de ce croisement ne présentent pas de fusion prématurée des sutures crâniennes. Cette construction a pour effet de diminuer la suractivation de la voie Erk en aval de FGFR2. Ce même effet est observé après traitement avec un inhibiteur spécifique de MEK (U0126) (Shukla et al, 2007).

Récepteur FGFR2 soluble

Un récepteur soluble FGFR2 portant la mutation S252W a été testé tout d'abord *in vitro* dans des cultures de cellules humaines (clones stables de MG63 (ostéosarcome)) (Tanimoto et al, 2004). Il a été démontré que ce récepteur soluble avait une action d'inhibition de la différenciation ostéoblastique perturbée par cette mutation activatrice (Tanimoto et al, 2004). Cet effet a ensuite été démontré *ex vivo* à partir de cultures de calvaria issues de souris mutantes *Fgfr2*$^{S252W/+}$, l'absence de fusion des sutures coronales était obtenue lorsque celles-ci étaient au contact de la forme soluble sFGFR2IIIc^{S252W} (Yokota et al, 2014).

II. Objectifs de ma thèse de sciences

Les gènes *FGFR2* et *FGFR3* sont des gènes majeurs impliqués dans les mécanismes d'ossification membranaire et endochondrale, et sont exprimés au sein des lignées chondrocytaires et ostéoblastiques lors du développement du squelette et de la réparation osseuse.

Les mutations gain de fonction activatrices dans les gènes *FGFR2* et *FGFR3*, responsables des phénotypes de craniosténose (*FGFR2*, *FGFR3*) et de chondrodysplasie (*FGFR3*), sont à l'origine de perturbations majeures affectant les processus d'ossification membranaire et endochondrale.

Le développement de modèles murins *Fgfrs* mimant la pathologie humaine et leurs études approfondies sont indispensables à la meilleure compréhension des mécanismes physiopathologiques impactés par ces mutations.

Dans ma thèse, je me suis plus particulièrement intéressée à la formation et à la réparation osseuse mandibulaires. J'ai à la fois étudié des cohortes de patients associés à des mutations FGFRs et un modèle murin *Fgfr3*. La formation mandibulaire repose à la fois sur les mécanismes d'ossification endochondrale et membranaire, et reste peu étudiée dans le cadre des chondrodysplasies et faciocraniosténoses liées à *FGFR2* et *FGFR3*. L'impact de ces mutations activatrices *FGFR2* et *FGFR3* est également très peu étudié au cours de la réparation osseuse, et il n'a jamais été étudié au niveau mandibulaire.

Le 1er volet de mon projet de thèse consistait à étudier l'impact de ces mutations activatrices *FGFR2* et *FGFR3* sur la morphologie mandibulaire et craniofaciale à partir de cohortes de patients porteurs de faciocraniosténoses et de chondrodysplasies.

Dans ce cadre, une première étude avait pour objectif de mieux caractériser le phénotype mandibulaire et d'objectiver d'éventuelles corrélations génotype / phénotype dans une cohorte de patients porteurs de faciocraniosténoses *FGFR2* et *FGFR3*. Cette étude a été réalisée à l'aide d'approches quantitatives par morphométrie géométrique 3D à partir de scanners réalisés à un âge précoce avant chirurgie craniofaciale, afin d'éliminer les facteurs potentiels influençant la morphologie mandibulaire. Ces résultats sont présentés dans l'article publié : Morice A, et al. Early mandibular morphological differences in patients with *FGFR2* and *FGFR3*-related syndromic craniosynostoses: A 3D comparative study. Bone. 2020;141:115600.

J'ai ensuite conduit une 2ème étude, qui consistait à mieux caractériser le phénotype craniomaxillofacial des patients atteints d'achondroplasie, et son évolution avec l'âge, ce qui n'avait jamais été étudié jusqu'ici. Cette étude a été réalisée à partir d'analyses quantitatives multimodales, morphologiques, céphalométriques et par morphométrie géométrique 3D à partir de scanners. De plus, le lien entre la sévérité des anomalies morphologiques craniomaxillofaciales et celle du syndrome d'apnées obstructives du sommeil a été étudiée afin de mettre en évidence d'éventuels facteurs de corrélation anatomo-fonctionnelle dans cette pathologie. Les résultats sont rapportés dans l'article : Morice et al. Craniofacial growth and function in achondroplasia: a multimodal 3D study on 15 patients (Orphanet Journal of Rare Diseases, sous presse).

Le 2ème volet de mon projet consistait à étudier l'impact d'une mutation activatrice dans le gène *FGFR3*, dans un modèle murin mimant l'hypochondroplasie, *Fgfr3*$^{N534K/+}$, à la fois au cours de la formation mandibulaire et au cours des différentes étapes de la réparation osseuse mandibulaire après fracture non stabilisée de la branche montante. Le modèle murin d'hypochondroplasie étudié est le premier modèle pour cette chondrodysplasie, généré au sein de notre laboratoire. J'ai tout d'abord caractérisé les différentes étapes de la formation de la mandibule au cours de la période anté-natale et post-natale en réalisant des analyses histologiques, immunohistologiques et morphométriques. J'ai ensuite réalisé des fractures non stabilisées de la mandibule et étudié les différentes étapes de la réparation osseuse (J7, J10, J14, J21, J28) en conduisant des approches morphométriques (micro-scanners, histologie), des études immuno-histologiques, des analyses transcriptomiques (transcriptomique spatiale) et des études *in vitro* à partir d'ostéoblastes murins.

J'ai complété cette étude réparation osseuse en testant l'effet d'antagonistes de FGFR3 au cours de la réparation osseuse mandibulaire. Il s'agit d'antagonistes utilisés pour activer la croissance osseuse de ces patients de petites tailles. J'ai utilisé l'infigratinib (BGJ398), un inhibiteur des tyrosines kinases, validé en préclinique et aujourd'hui administré en clinique (phase 2) chez des patients achondroplases ; et le vosoritide (BMN111), un analogue du CNP, validé également en phase préclinique. Pour cette molécule (BMN111), les essais de phase II et III ont été achevés et aujourd'hui ce traitement a obtenu son autorisation de mise sur le marché. Ces molécules n'avaient jamais été testées au cours de la réparation osseuse.

III. Résultats

A. Partie 1 : données humaines

1. Article 1 :

Morice *et al*. Early mandibular morphological differences in patients with FGFR2 and FGFR3-related syndromic craniosynostoses: A 3D comparative study. Bone, 141, 115600. https://doi.org/10.1016/j.bone.2020.115600

a) Introduction

La morphologie mandibulaire résulte de facteurs multiples, génétiques, et épigénétiques, expliquant ainsi la grande hétérogénéité phénotypique mandibulaire chez les individus (Atchley and Hall, 1991). La forme mandibulaire est aussi constamment modifiée avec l'âge, en rapport avec les nombreux facteurs anatomiques et fonctionnels, tels que l'éruption dentaire, les pertes dentaires, la mastication et la fonction linguale (Guevara Perez, 2018 ; Coquerelle et al, 2013). Identifier les facteurs intrinsèques influençant la morphologie mandibulaire dans le cadre des craniosténoses syndromiques est de ce fait compliqué, d'autant plus que la morphologie mandibulaire est également influencée par les modifications de la base du crâne.

Dans mon projet de thèse, j'ai analysé le phénotype mandibulaire et ses corrélations éventuelles avec le génotype dans le cadre des craniosténoses FGFRs. A ce jour, aucune analyse de ce type n'avait été réalisé, il était donc nécessaire de mettre en place une étude visant à mieux caractériser le phénotype mandibulaire et d'objectiver d'éventuelles corrélations génotype phénotype. Cette étude a été réalisée à partir d'une cohorte de patients porteurs de craniosténoses FGFR2 et FGFR3, à l'aide d'approches quantitatives par morphométrie géométrique 3D à partir de scanners mandibulaires. Les scanners étudiés étaient réalisés à un âge précoce avant chirurgie craniofaciale, afin d'éliminer les facteurs potentiels influençant la morphologie mandibulaire.

b) Abstract

Les craniosténoses syndromiques sont définies par la présence de fusion prématurée d'une ou plusieurs sutures crâniennes, à l'origine de déformation de la voûte crânienne et de rétrusion de l'étage moyen de la face.

Les faciocraniosténoses syndromiques FGFRs représentent 75% des causes des craniosténoses syndromiques. Des modifications de la morphologie mandibulaire ont été décrites chez des

patients porteurs de faciocraniosténoses FGFRs, cependant le phénotype mandibulaire reste peu étudié dans ce cadre.

Une meilleure caractérisation du phénotype mandibulaire dans le cadre des faciocraniosténoses FGFRs est nécessaire, afin de mieux comprendre l'implication des voies FGFRs au cours du développement craniofacial.

L'objectif de notre étude était d'analyser la morphologie mandibulaire à un âge précoce dans une cohorte de patients porteurs de faciocraniosténoses FGFR2 (syndromes de Crouzon et d'Apert) et FGFR3 (syndromes de Muenke, et Crouzon avec *acanthosis nigricans*).

Pour répondre à cet objectif, nous avons analysé de façon quantitative et comparative, la morphologie mandibulaire des patients, par morphométrie géométrique à partir de reconstructions tridimensionnelles de scanners mandibulaires. Les scanners utilisés étaient réalisés à un âge précoce, avant chirurgie craniofaciale, afin de limiter l'impact des modifications de la base du crâne, sur la morphologie mandibulaire. Trente et un landmarks anatomiques et onze courbes avec semi-landmarks « glissants » (ou « sliding semi-landmarks ») ont été définis et placés sur les reconstructions 3D des scanners mandibulaires des patients et de témoins appariés à l'âge et au sexe.

Au total, 40 patients (12 avec syndrome de Crouzon, 12 avec syndrome d'Apert, 12 avec syndrome de Muenke, et 4 avec syndrome de Crouzon avec *acanthosis nigricans*) et 40 témoins étaient inclus (âge moyen 13,7 mois ± 11.9).

La morphologie mandibulaire était significativement différente entre les différents groupes de patients, et entre patients et témoins. La forme mandibulaire dans le cadre des craniosténoses FGFR2 était caractérisée par la présence d'ouverture de l'angle goniaque, de raccourcissement de la branche montante, et d'une symphyse haute et proéminente. Le raccourcissement de la branche montante était plus marqué chez les patients porteurs de syndrome d'Apert que dans le cadre de syndrome de Crouzon ; et chez les patients porteurs de syndrome de Crouzon, les distances intercondyliennes et intergoniaques étaient réduites. La distance intercondylienne était également réduite chez les patients porteurs de syndrome de Crouzon avec *acanthosis nigricans*. Les analyses statistiques de variance ont montré des différences significatives concernant la morphologie mandibulaire entre les différents groupes de patients, Apert *vs* Crouzon, Crouzon *vs* Muenke et Apert *vs* Muenke ($p<0,05$).

Nos résultats confirment la présence de différences morphologiques mandibulaires significatives à un âge précoce dans cette cohorte de patients porteurs de craniosténose FGFR2 et FGFR3, et renforcent l'hypothèse de corrélation génotype-phénotype en ce qui concerne la morphologie mandibulaire.

c) Article

Bone 141 (2020) 115600

Contents lists available at ScienceDirect

Bone

journal homepage: www.elsevier.com/locate/bone

Full Length Article

Early mandibular morphological differences in patients with *FGFR2* and *FGFR*3-related syndromic craniosynostoses: A 3D comparative study

A. Morice[a,b,*], R. Cornette[c], A. Giudice[d], C. Collet[e,f], G. Paternoster[g], É. Arnaud[g], E. Galliani[a], A. Picard[a], L. Legeai-Mallet[b], R.H. Khonsari[a,b,g]

[a] Service de Chirurgie Maxillo-Faciale et Chirurgie Plastique, Hôpital Universitaire Necker – Enfants Malades, Assistance Publique – Hôpitaux de Paris, Centre de Référence Maladies Rares MAFACE Fentes et Malformations Faciales, Université de Paris, Paris, France
[b] Laboratoire 'Bases Moléculaires et Physiopathologiques des Ostéochondrodysplasies', INSERM UMR 1163, Institut Imagine, Paris, France
[c] Institut de Systématique, Evolution, Biodiversité (ISYEB), Muséum National d'Histoire Naturelle, Sorbonne Université, Ecole Pratique des Hautes Etudes, Université des Antilles, CNRS, CP 50, 57 rue Cuvier, 75005 Paris, France
[d] Università Degli Studi di Catanzaro 'Magna Graecia', Catanzaro, Italy
[e] BIOSCAR, INSERM U1132, Université de Paris, Hôpital Lariboisière, 75010 Paris, France
[f] Service de Biochimie et Biologie Moléculaire, CHU-Paris-GH Saint Louis Lariboisière Widal, Paris, France
[g] Service de Neurochirurgie, Hôpital Universitaire Necker – Enfants Malades, Assistance Publique – Hôpitaux de Paris, Centre de Référence Maladies Rares CRANIOST Cranioténoses et Malformations Craniofaciales, Université de Paris, Paris, France

ARTICLE INFO

Keywords:
Craniosynostosis
FGFR2
FGFR3
Mandibular shape
3D geometric morphometrics

ABSTRACT

Syndromic craniosynostoses are defined by the premature fusion of one or more cranial and facial sutures, leading to skull vault deformation, and midfacial retrusion. More recently, mandibular shape modifications have been described in *FGFR*-related craniosynostoses, which represent almost 75% of the syndromic craniosynostoses. Here, further characterisation of the mandibular phenotype in *FGFR*-related craniosynostoses is provided in order to confirm mandibular shape modifications, as this could contribute to a better understanding of the involvement of the FGFR pathway in craniofacial development.

The aim of our study was to analyse early mandibular morphology in a cohort of patients with *FGFR2*- (Crouzon and Apert) and *FGFR3*- (Muenke and Crouzonodermoskeletal) related syndromic craniosynostoses. We used a comparative geometric morphometric approach based on 3D imaging. Thirty-one anatomical landmarks and eleven curves with sliding semi-landmarks were defined to model the shape of the mandible.

In total, 40 patients (12 with Crouzon, 12 with Apert, 12 with Muenke and 4 with Crouzonodermoskeletal syndromes) and 40 age and sex-matched controls were included (mean age: 13.7 months ± 11.9). Mandibular shape differed significantly between controls and each patient group based on geometric morphometrics. Mandibular shape in *FGFR2*-craniosynostoses was characterized by open gonial angle, short ramus height, and high and prominent symphysis. Short ramus height appeared more pronounced in Apert than in Crouzon syndrome. Additionally, narrow inter-condylar and inter-gonial distances were observed in Crouzon syndrome. Mandibular shape in *FGFR3*-craniosynostoses was characterized by high and prominent symphysis and narrow inter-gonial distance. In addition, narrow condylar processes affected patients with Crouzonodermoskeletal syndrome. Statistical analysis of variance showed significant clustering of Apert and Crouzon, Crouzon and Muenke, and Apert and Muenke patients ($p < 0.05$).

Our results confirm distinct mandibular shapes at early ages in *FGFR2*- (Crouzon and Apert syndromes) and *FGFR3*-related syndromic craniosynostoses (Muenke and Crouzonodermoskeletal syndromes) and reinforce the hypothesis of genotype-phenotype correspondence concerning mandibular morphology.

1. Introduction

Craniosynostoses – reported in 1:2000 to 1:3000 live births, comprising at least 20% of syndromic cases [1] – are defined by the premature fusion of one or more cranial and facial sutures, leading to various craniofacial anomalies, among which: skull vault deformation, potentially causing increased intracranial pressure, shallow orbits leading to exorbitism, and midfacial retrusion that can be associated

* Corresponding author at: Service de Chirurgie Maxillo-Faciale et Chirurgie Plastique, Hôpital Necker - Enfants Malades, 149 rue de Sèvres, 75015 Paris, France.
E-mail address: anne.morice2@aphp.fr (A. Morice).

https://doi.org/10.1016/j.bone.2020.115600
Received 19 May 2020; Received in revised form 10 August 2020; Accepted 14 August 2020
Available online 18 August 2020

with obstructive sleep apnoea syndrome [2–4].

Various mutations have been reported in syndromic craniosynostoses and affect key signalling pathways involved in craniofacial development, such as FGFRs/TWIST pathways, MSX2, EFR, TCF12 and SMAD6 [5]. Mutations in genes from the FGFR (Fibroblast Growth Factor Receptor) pathways are reported in almost 75% of syndromic craniosynostoses [6]. Such *FGFR*-related conditions are due to specific activating heterozygous mutations localized in *FGFR1* (Pfeiffer syndrome type 1) [1], *FGFR2* (Apert, Crouzon, Pfeiffer type 2 and 3 syndromes, Antley-Bixler, Beare-Stevenson cutis gyrata syndromes, Bent Bone Dysplasia and Saethre-Chotzen like syndrome) [5–9] and *FGFR3* genes (Muenke syndrome and Crouzonodermoskeletal syndrome). Muenke syndrome is the most frequent *FGFR*-related syndromic craniosynostosis [10]. Crouzonodermoskeletal syndrome is an exceedingly rare syndrome sharing similarities with Crouzon syndrome and including skin lesions (*acanthosis nigricans*) [11–14]. Most of these FGFR mutations are gain of function, inducing high activity of the receptor in presence and in absence of its FGF ligands, thus disturbing bone formation.

It has been demonstrated that *FGFR* genes are implicated in bone formation and both axial and appendicular skeletal development as illustrated by the phenotype of chondrodysplasia [15–18]. Skull vault, frontal bone and midfacial anomalies have been extensively described in *FGFR*-related syndromic craniosynostoses [3,19–22]. Several studies also report mandibular shape modifications in *FGFR2*- and *FGFR3*-related craniosynostoses [23–27] as well as in achondroplasia (*FGFR3*) [28].

The mandible is a dermal bone derived from neural crest cells migrating into the first pharyngeal arch [29–33]. Mandibular bone ossifies early during the 6th week of pregnancy [34]. In mouse and chick models, *Fgfr2* and *Fgfr3* genes are expressed during mandibular formation at the sites of primary (Meckel cartilage) and secondary cartilages (condyles, symphysis) and have key roles in mandibular intramembranous and endochondral ossification [35–39].

A better characterisation of the human mandibular phenotype is necessary in *FGFR*-related craniosynostoses. This could help to better understand the implication of the FGFR pathway in craniofacial development and highlight homologies between mouse models and human phenotypes.

The aim of our study was to analyse mandibular morphology at early ages in a cohort of patients with *FGFR2*- (Crouzon and Apert) and *FGFR3*- (Muenke and Crouzonodermoskeletal) related syndromic craniosynostoses, using a comparative geometric morphometric approach based on 3D imaging, allowing shape comparisons between each *FGFR*-craniosynostosis subtype and age and sex-matched controls, and between the different *FGFR*-craniosynostosis subtypes.

2. Patients and methods

2.1. Patients

We retrospectively included 40 patients presenting with genetically confirmed *FGFR2*- or *FGFR3*-related syndromic craniosynostoses, and available craniofacial computed tomographic (CT) scan. Only CT-scans performed at early ages before fronto-facial or fronto-orbital advancement, or in the immediate post-operative period after posterior vault expansion (at post-operative days 1 or 2), were included, in order to avoid potential confounding factors related to the effects of surgery on mandibular shape. The following clinical parameters were collected: gender, type of mutation, age at CT-scan and at first surgical procedure and tracheostomy. The database used to select patients covered the birth period 2003–2017. All patients were initially managed in the National Referral Center for craniofacial malformations (Centre de Référence Maladies Rares CRANIOST), located within our hospital. The study was approved by the local Ethical Committee (Comité d'Éthique de Necker – Enfants Malades, approval number: 2018 RK18).

2.2. Controls

Controls were selected among age and gender-matched patients free of any reported craniofacial anomalies who underwent CT-scans for the assessment of benign craniofacial trauma or infections (mandible excluded). All CT-scans were extracted from the same database (clinical database of Necker – Enfants Malades).

2.3. Comparative study of mandibular morphology based on 3D geometric morphometrics

Segmentation and 3D reconstructions were performed based on DICOM raw data using 3D Slicer 4 [40] by isolating the mandible based on its cortical and trabecular bone density thresholds. Visual adjustments of the cortical bone density threshold were done for each CT-scan, without smoothing factors to keep the correct contours and avoid any loss of information concerning anatomical variations. The 3D surface mesh obtained for each patient and control was saved in STL format.

Thirty-one anatomical landmarks and eleven curve with sliding semi-landmarks were defined in order to model the shape of the mandible, based on previous studies [41–43] and were placed using Viewbox 4 (dHal Software, Kifissia, Greece), by the same author (AM). Names and definitions of the landmarks and curves are provided on Fig. 1. Using Morpho J v. 1.06 [44], a Procrustes ANOVA analysis for error measurement of 'factor repetition' showed no significant differences in landmarking positioning, allowing valid comparative analysis of shape variability among individuals (see Supplementary Table 1).

Comparative mandibular morphology was assessed based on 3D geometric morphometrics [45] using R [46] for data processing. Landmarks coordinates were superimposed using a Generalized Procrustes Analysis (GPA) [47]. Sliding semi-landmarks of curves have been allowed to slide minimizing the bending energy [43] using the 'gpagen' function of the 'geomorph' package [48]. Coordinates after GPA were assessed using principal component analysis (PCA) which gives information about raw variability. Both analyses, GPA and PCA were performed using the 'gpagen' and 'plotTangentSpace' functions of the 'geomorph' package [48]. Ten PC axis have been kept for statistical analysis representing 90% of total shape variation [49]. The 3D visualizations along the axes of the PCA have been made using 'Thin Plate Splines' (TPS) [50], from the average shape to the extremes shapes of the axes thanks to the 'tps3d' function of the 'Morpho' package [50]. In a first step, the 3D model of a control specimen (representative of the median age of the studied population) has been warped to the mean shape (corresponding to the mean coordinates of all specimens, defining the area 'zero' of the PCA) to create a 3D model of the mean shape. In a second step, this 3D mean shape has been deformed using TPS interpolation according to the extreme shape of the PC axes.

Then, to assess comparisons between groups, Canonical Variate Analyses (CVA) have been performed using the 'CVA' function of the 'Morpho' package [51]. Eleven datasets were created for mandibular shape comparisons within the total group of patients and controls, between patients and controls for each syndrome independently, as well as between each groups of patients.

Multiple ANalysis Of VAriance (MANOVAs) were performed considering 'type of syndrome' and 'age at CT-scan' as classifiers, considering 90% of total shape variability (corresponding to ten axes of the PCA).

2.4. Statistical analysis

Quantitative data were expressed as mean ± Standard Derivation or median ± Interquartile range and were compared using the Kruskal-Wallis test. $p < 0.05$ was considered as significant.

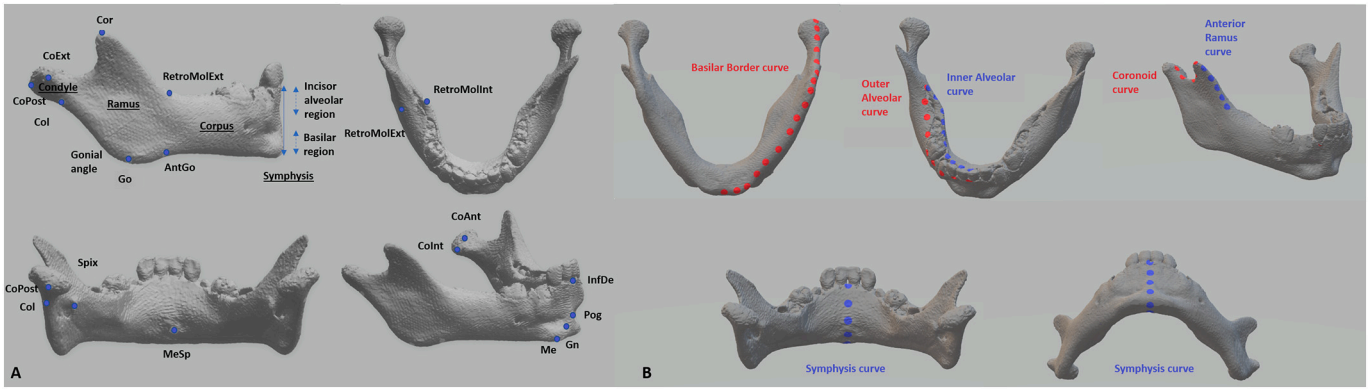

Fig. 1. Landmarks on the buccal and lingual sides digitized on hemi mandibles surface three-dimensional models: a: anatomical landmarks (31); b: curves (11) (based on previous studies [41,42]).

3. Results

3.1. Patients

Forty patients were included into our study: 12 patients with Crouzon syndrome, 12 with Apert syndrome, 12 with Muenke syndrome and 4 with Crouzon syndrome with *acanthosis nigricans*, and 40 age and sex-matched controls. Male/female ratio was 16/24 and mean age at inclusion (date of CT-scan) was 13.7 months ± 11.9, without statistical difference between the four groups ($p = 0.15$). Patients characteristics, types of mutations and of craniosynostosis, and age at CT-scan for each group were summarized in Table 1. Seventeen patients (6/12 in Crouzon, 4/12 in Apert, 4/12 in Muenke, and 3/4 in Crouzon with *acanthosis nigricans* group) had benefited from posterior skull vault expansion prior to the date of CT-scan, at post-operative days 1 or 2. Three patients had severe ventilation disorders requiring temporary tracheostomy (two with Crouzon with *acanthosis nigricans* and one with Crouzon syndrome).

3.2. Comparative geometric morphometric analysis of mandibular shape

GPA and PCA analyses were performed on the total group of patients and controls. PCA of the mandible shapes showed a clear shape separation of patients and controls along PC2 while PC1 comprised age related shape changes, as confirmed by linear regression tests ($r^2 = 0.42$; $p < 10^{-4}$). The plots of PC scores and 3D shape changes associated with PC1 and PC2 by morphing the mean mandibular surface model are shown in Fig. 2. Mean 3D mandibular shape differed significantly between patients and controls ($p < 10^{-3}$). 3D mandibular shape differences obtained after CVA are shown in Fig. 3.

3.2.1. In FGFR2-related craniosynostoses

The plots of PC scores and wire frames of the first two PCs and 3D shape changes associated to PC2 for patients and control groups are shown in Fig. 4. ANOVA analyses showed significant statistical shape differences along PC2 between patients and controls in Crouzon and Apert groups ($p < 10^{-2}$).

Mandibular shape in Crouzon patients was characterized by (1) open gonial angle, (2) short ramus height, (3) narrow inter-gonial and inter-condylar distances and (4) slightly high and prominent symphysis at the level of alveolar bone.

Mandibular shape in Apert patients was characterized by (1) open gonial angle, (2) short ramus height and (3) slightly high and prominent symphysis at both basilar and alveolar levels.

3.2.2. In FGFR3-related craniosynostoses

The plots of PC scores and wire frames of the first two PCs and 3D shape changes associated to PC2 for patients and controls group are shown in Fig. 5. ANOVA analyses showed significant statistical shape differences along PC2 between patients and controls in Muenke group ($p < 10^{-3}$). The low number of patients in Crouzonodermoskeletal subgroup did not allow ANOVA analysis.

Mandibular shape in Muenke patients was characterized by (1) slightly high and prominent symphysis at the level of basilar border only and (2) open sigmoid notch with anteriorly placed coronoid process and (3) narrow inter-gonial distance.

Mandibular shape in Crouzonodermoskeletal patients was characterized by (1) prominent symphysis at both alveolar and basilar levels

Table 1
Patient's characteristics: number per group, sex ratio, type of mutation and of craniosynostosis, and age at CT-scan.

Patient group	Patient's number Sex ratio (F/M)	Mutations	Types of craniosynostosis (n)	Median age (IQR) at CT-scan (months)
Crouzon *FGFR2*	12 (7/5)	Cys342Tyr (n = 4) Tyr105Cys (n = 2) Cys278Phe (n = 2) Gly338Glu (n = 2) Ser267Pro (n = 1) Arg347Cys (n = 1)	BCS + MS + SS + BLS (2), BCS + MS + SS (1), BCS + SS + BLS (1), BCS + SS (1), BCS (1), UCS (1), UCS + partial BLS (1), UCS + MCS (1), SS (1), BLS (1), None (1)	11 (16.9)
Apert *FGFR2*	12 (6/6)	Ser252Trp (n = 11) Pro253Arg (n = 1)	BCS (9), BCS + SS (1), UCS (1), MS + SS (1)	8.9 (9.2)
Muenke *FGFR3*	12 (9/3)	Pro250Arg (n = 12)	BCS (10), UCS (2)	6.8 (4.8)
CAN *FGFR3*	4 (3/1)	Ala391Glu (n = 4)	BCS (2), BCS + SS (1), UCS + BLS (1)	22.7 (12.6)

CAN: Crouzon with acanthosis nigricans; IQR: Inter Quartile Range.
BCS: bilateral coronal synostosis, UCS: unilateral coronal synostosis, SS: sagittal synostosis, MS: metopic synostosis; BLS: bilateral lambdoid synostosis.

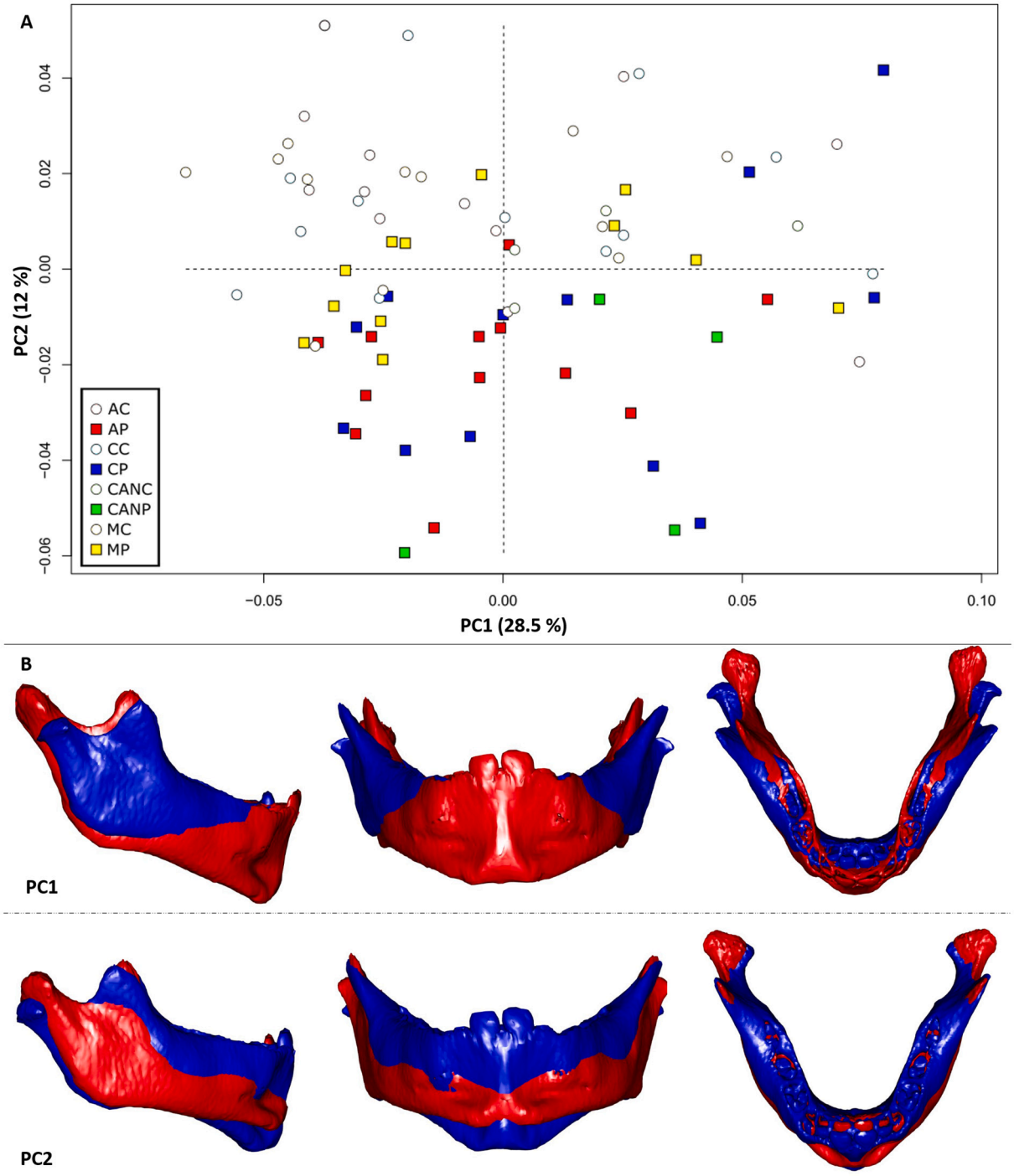

Fig. 2. Plots of Principal Components (PC) scores for PC1 and PC2 with corresponding variances (in %) (A), and (B) 3D shape changes associated with PC1 and PC2 by morphing the extreme mandibular surface model (blue: negative values; red: positive values). A: patients (square box); controls (round box): AP: Apert Patients; AC: Controls for Apert Patients; CP: Crouzon Patients; CC: Controls for Crouzon Patients; CANP: CAN (Crouzonodermoskeletal) patients; CANC: Controls for CAN Patients; MP: Muenke Patients; MC: Controls for Muenke Patients. (For interpretation of the references to colour in this figure legend, the reader is referred to the web version of this article.)

and (2) narrow inter-condylar and inter-gonial distance.

3.2.3. Comparison of mandibular shape between the groups of FGFR2 and FGFR3- craniosynostoses

To analyse shape differences between each patient group, a MANOVA test was performed and showed statistically significant differences between Crouzon and Apert ($p = 0.04$), Crouzon and Muenke ($p < 10^{-3}$) and Apert and Muenke patients ($p < 10^{-3}$). 3D mandibular shape differences between patient groups obtained after CVA are shown in Fig. 6.

Short ramus height appeared more pronounced in Apert than in Crouzon syndrome and did not obviously affect patients with *FGFR3*-syndromes. In Crouzon syndrome, condylar processes appeared narrower when compared to Apert and Muenke syndromes. The angular processes were also narrower in Crouzon and Muenke syndromes, when compared with Apert syndrome. Coronoid processes were anteriorly

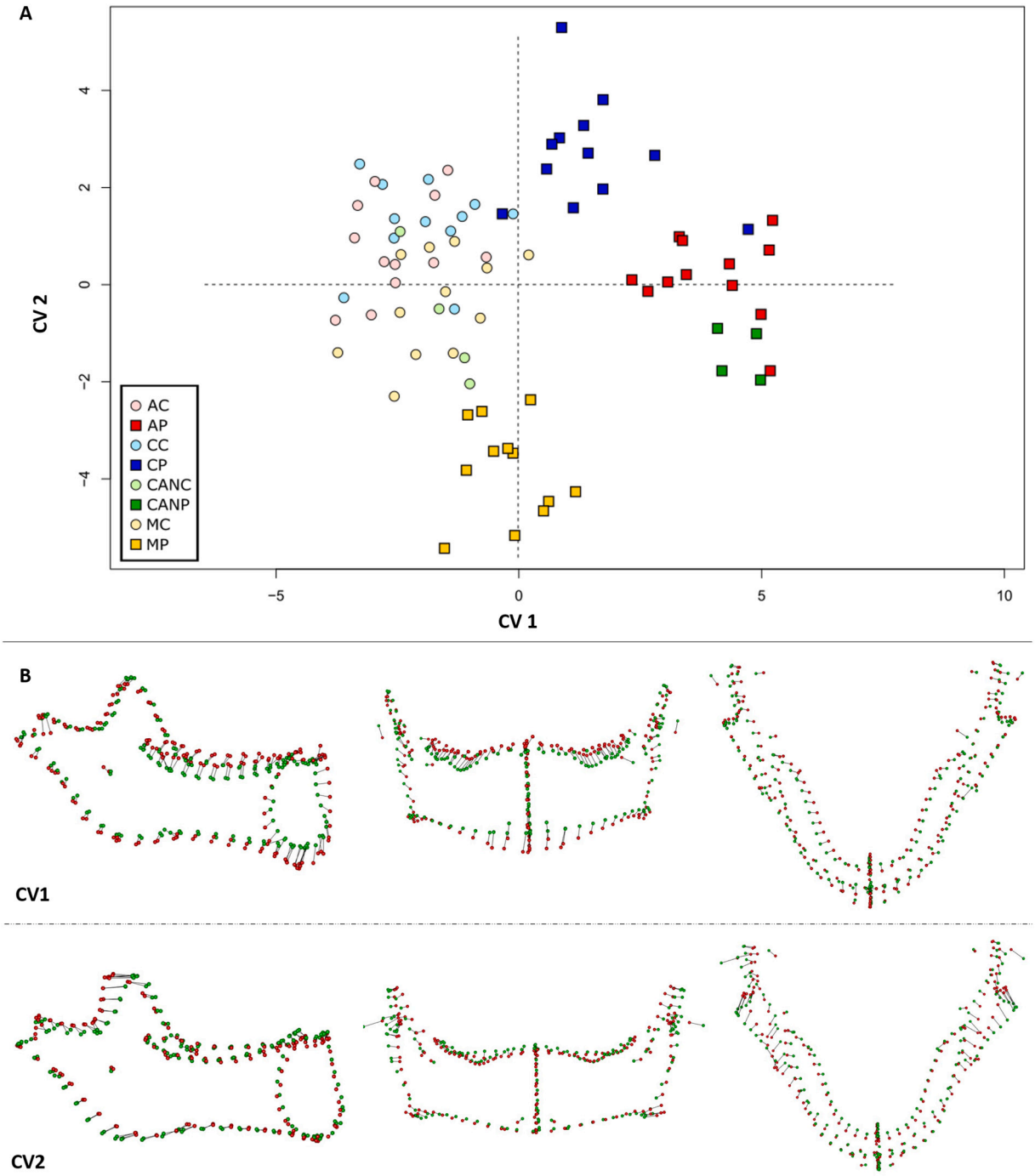

Fig. 3. Plots of Canonical Variate (CV) scores (A) and 3D mandibular shape associated to CV1 and CV2 (B) (n = 40 patients: 12 with Crouzon syndrome, 12 with Apert syndrome, 12 with Muenke syndrome, 4 with Crouzonodermoskeletal syndrome and n = 40 age and sex-matched controls).
A: patients (square box); controls (round box): AP: Apert Patients; AC: Controls for Apert Patients; CP: Crouzon Patients; CC: Controls for Crouzon Patients; CANP: CAN (Crouzonodermoskeletal) patients; CANC: Controls for CAN Patients; MP: Muenke Patients; MC: Controls for Muenke Patients.
B: The dots represent the extreme values (green: negative values; red: positive values) of each anatomical landmark and curves with sliding semi-landmarks.

displaced in Muenke syndrome when compared with the other groups. The position of the symphysis did not differ obviously among groups. No statistically significant shape separation was observed between Crouzonodermoskeletal patients (n = 4) and the other groups (data not shown).

4. Discussion

Mandibular shape results from genetic and epigenetic factors, thus explaining the high phenotypic heterogeneity among individuals [52]. Mandibular shape is also constantly modified along life, related to numerous anatomical and functional factors such as dental eruption, tooth loss, mastication, and lingual function [41,42,53]. Determining intrinsic mandibular anomalies in craniosynostosis syndromes is thus a technical challenge, where mandibular shape is also affected by skull base changes.

High genetic variability characterizes Crouzon syndrome, with at least 47 distinct mutations described to date [54], while Apert syndrome is characterized by a very small set of mutations (*FGFR2*^{S252W}, *FGFR2*^{P253R}, and *FGFR2*^{S252F} in a lesser extent) [55,56] and Muenke and

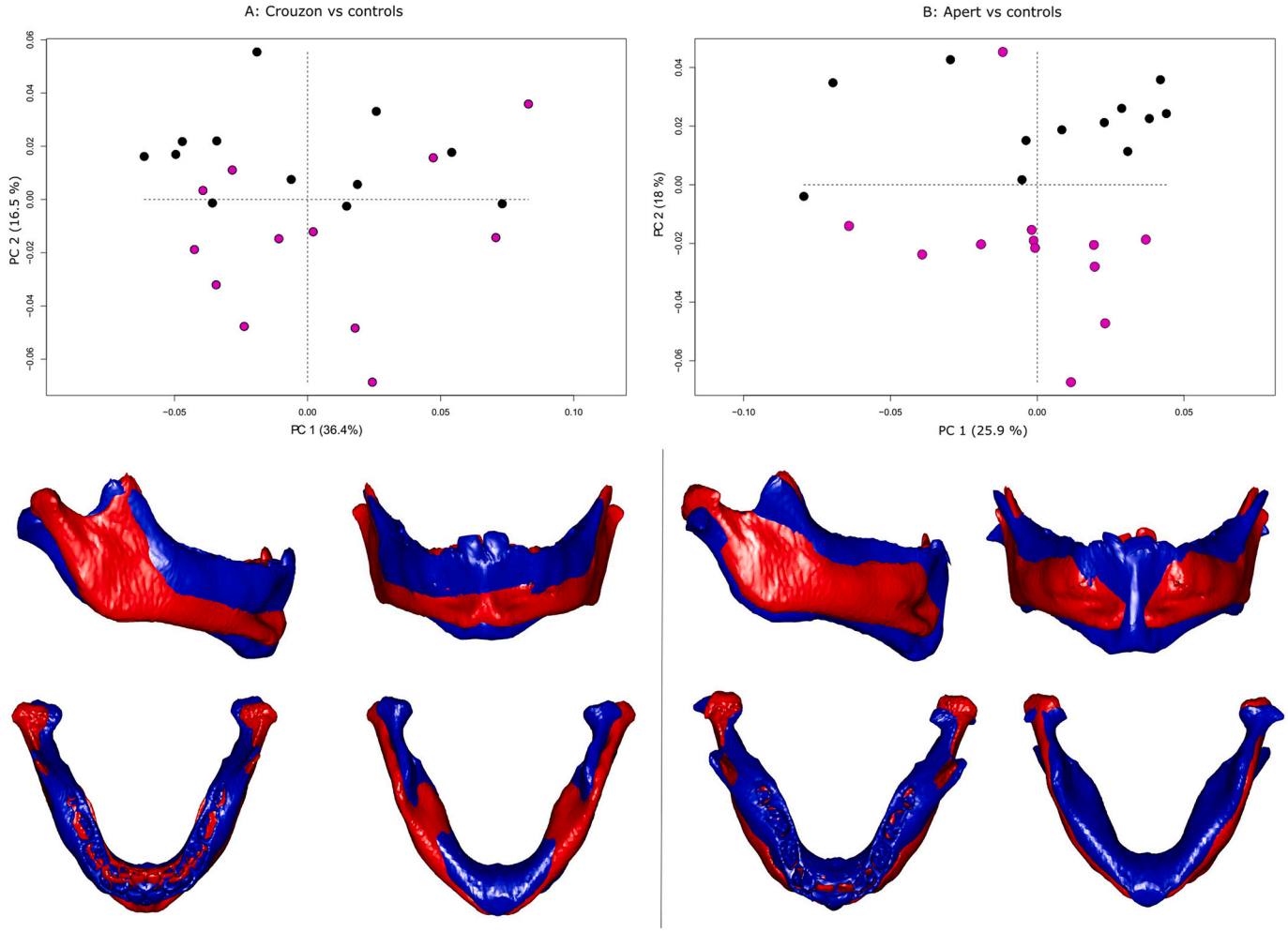

Fig. 4. Comparison of mandibular shape between patients with *FGFR2*-craniosynostoses and controls: plots of Principal Components (PC) scores for PC1 and PC2 with corresponding variances (in %) (patients (magenta), controls (black)), and 3D shape changes associated with PC2 by morphing the extreme mandibular surface model (blue: negative values; red: positive values) for A: Crouzon group (n = 12 patients; n = 12 controls); B: Apert group (n = 12 patients; n = 12 controls). (For interpretation of the references to colour in this figure legend, the reader is referred to the web version of this article.)

Crouzonodermoskeletal syndromes are caused by a unique mutation (*FGFR3*^{P250R} and *FGFR3*^{A391E}, respectively) [10,11]. Although based on a relatively small sample of genotyped patients, our cohort was representative of the main mutations usually reported in these syndromic craniosynostoses. Only four patients diagnosed with the extremely rare Crouzonodermoskeletal syndrome with confirmed A391E mutation could be included in this study.

Our results showed significant distinct mandibular shapes at early ages in Crouzon, Apert, Muenke and Crouzonodermoskeletal syndromes when compared with age and sex-matched controls and highlight genotype-phenotype correspondence in *FGFR2*- and *FGFR3*-related syndromic craniosynostoses. Although Crouzon and Apert patients displayed comparable mandibular shapes (open gonial angle, short ramus height, slightly high and prominent symphysis), anatomical variations were stronger in the Apert than in the Crouzon subgroup, which is consistent with previous findings for the upper third of the face, the midface [3,21,57,58] and the mandible [59,60].

Significant differences in mandibular shapes were observed in Muenke and Crouzonodermoskeletal subgroups relative to controls. However, changes did not obviously affect ramus height and gonial angulation, unlike *FGFR2*-craniosynostoses. These morphological differences between *FGFR2*- and *FGFR3*-craniosynostoses reinforce the hypothesis that activating mutations in *FGFR2* and *FGFR3* genes may affect membranous and endochondral ossification processes within different manners, and hence generate variable craniofacial and mandibular phenotypes. Concerning mandibular formation, *FGFR2* and *FGFR3*-activating mutations may have differential intrinsic effects on the primary (Meckel cartilage) and secondary condylar and symphyseal cartilages, then affecting mandibular development and morphology. In addition, it has been shown that patients affected by achondroplasia (linked to activating mutations in *FGFR3* gene), presented defective size and orientation of the ramus [28]. Overall, this underlines the different effects of the distinct mutations in *FGFR3* gene – responsible for craniosynostosis and chondrodysplasia – on mandibular formation and morphology.

Of note, we observed anteriorly displaced coronoid processes in Muenke subgroup relative to controls and other patient groups. This morphological feature may be induced by the cranial shape modifications, particularly affecting the temporal region, then influencing temporal muscles dynamics at both temporal and coronoid insertions levels.

In all subgroups, tendency for prominent and high symphysis was observed. Symphysis shape is determined by the combined effects of dental eruption and occlusion, and the position of the mandible relative to the maxilla, as well as tongue function and suprahyoid muscles insertion sites [41,61]. We could not control all potential influencing factors of mandibular shape in this retrospective study. In addition, we could not confirm that prominent symphysis reflected true

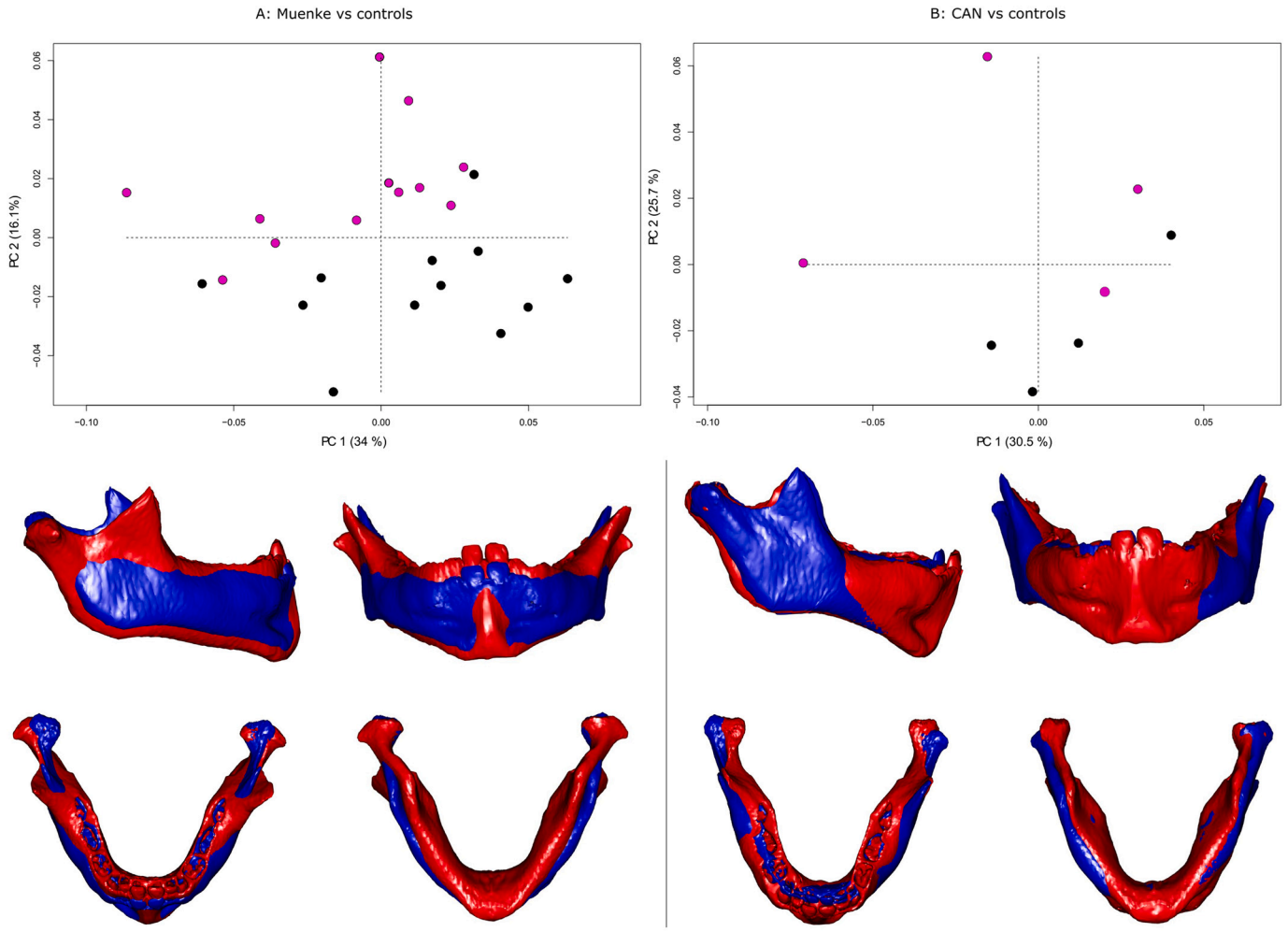

Fig. 5. Comparison of mandibular shape between patients with *FGFR3*-craniosynostoses and controls: plots of Principal Components (PC) scores for PC1 and PC2 with corresponding variances (in %) (patients (magenta), controls (black)), and 3D shape changes associated with PC2 by morphing the extreme mandibular surface model (blue: negative values; red: positive values) for A: Muenke group (n = 12 patients; n = 12 controls); B: CAN (Crouzonodermoskeletal) group (n = 4 patients; n = 4 controls). (For interpretation of the references to colour in this figure legend, the reader is referred to the web version of this article.)

prognathism, as all patients had moderate to extreme midfacial retrusion. The severity of midfacial retrusion varies among individuals with reported genotype-phenotype correlations [3]. In fact, midfacial retrusion appeared more pronounced in Apert than in Crouzon syndrome, more obvious in Apert cases carrying *FGFR2*^{S252W} mutation relative to those carrying *FGFR2*^{P253R} mutation, the latter leading to more severe midfacial retrusion than does *FGFR3*^{P250R}, responsible for Muenke syndrome [3,62].

Crouzon syndrome is characterized by its wide spectrum of craniofacial features, from normal phenotype to severe cloverleaf skull malformations. In our series, we also observed high variability of craniosynostosis, from no synostosis at the time of the study (in one patient) to severe cloverleaf skull shape, and moderate to severe frontomaxillary retrusion. Noticeably, phenotypic features may be absent at birth and evolve gradually during the first years of life [63–65]. However, we observed homogeneous mandibular shapes in the group of Crouzon patients even though six distinct mutations were observed in this group.

Several authors have reported various and sometimes divergent mandibular phenotypic features in *FGFR2*-related syndromic craniosynostoses, in terms of proportions and shapes [23–27,60]. First, these divergent results may be explained by the heterogenous ages at inclusion in the different series. Secondly, mandibular morphology was analysed by various methods, often after craniofacial surgery procedures, thus challenging the comparisons between the studies. Of note, the mandibular shape and particularly intercondylar width, depend on the distance between the condylar fossa on the skull base, as shown in Crouzon and Apert syndromes [27]. Similar results have been found in artificially deformed skulls, where external mechanical constraints had been intentionally exerted on the skull vault with different deforming devices as observed worldwide [66–69]: secondary skull base modifications induced a shift in the position of the glenoid fossa, thus influencing mandibular shape [67,69]. In syndromic craniosynostoses, intrinsic skull base deformations could thus act as potential secondary influencing factors on mandibular shape. We showed a slight narrowing of the condylar processes in Crouzon and Crouzonodermoskeletal syndromes when compared with controls, which was consistent with previous findings [23,27]. This finding thus most probably resulted from the combined effects of (1) repercussions of the vault deformation on the skull base, (2) intrinsic skull base deformations and (3) intrinsic mandibular shape characteristics.

Of note, all included CT-scans were performed at early ages before fronto-facial and fronto-orbital surgery, thus ruling out potential effects of surgery on mandibular shape. In fact, fronto-facial surgery involved maxillary advancement [22,70,71] and could thus influence mandibular morphology.

Concerning mean age at selected CT-scan, no significant differences were observed between groups. We confirmed by metric measurements,

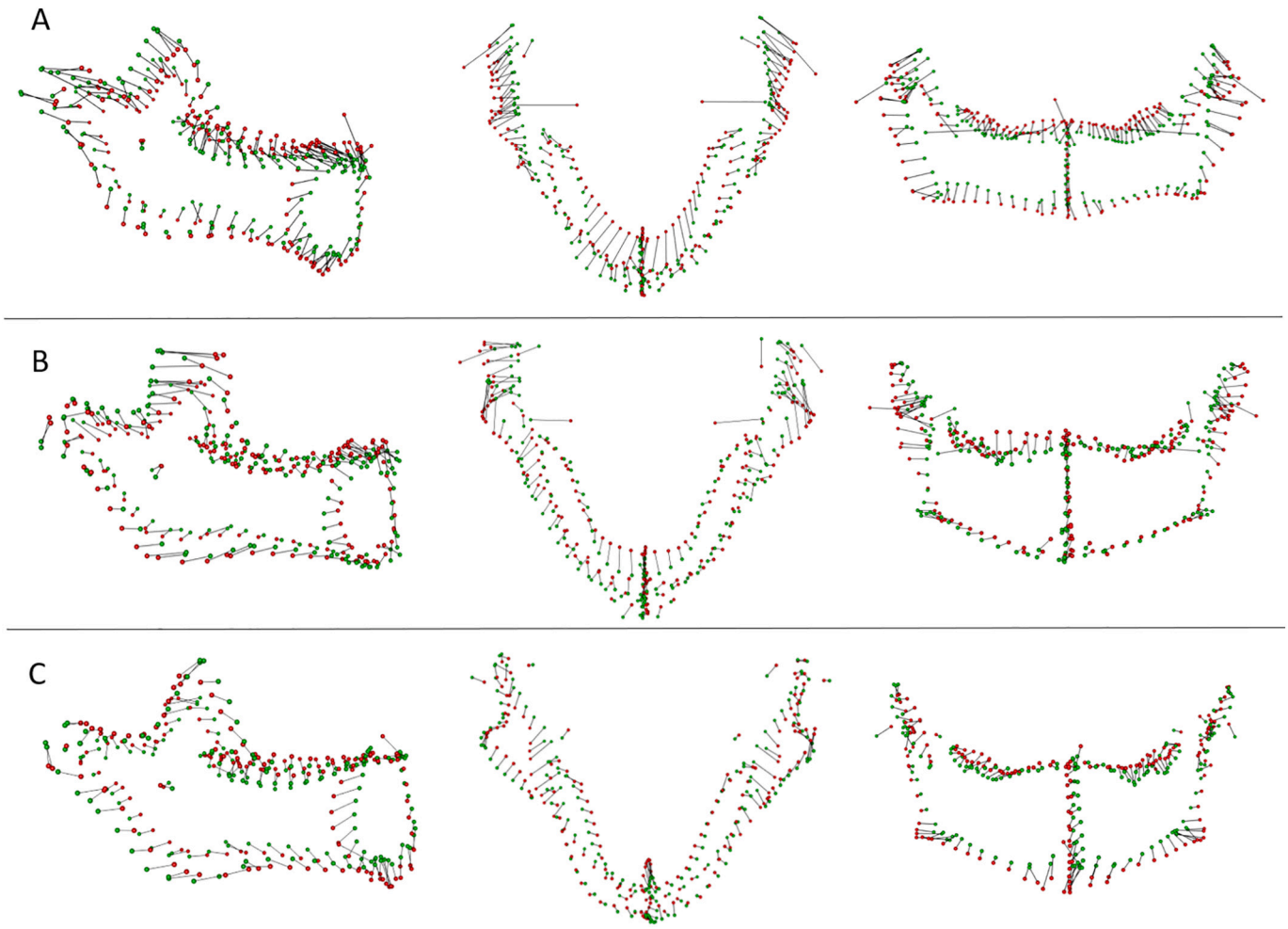

Fig. 6. 3D representations showing mandibular shape variations between patient groups using Canonical Variate Analysis, for A: Crouzon vs Apert group; B: Crouzon vs Muenke group; C: Apert vs Muenke group. The dots represent the extreme values (green: negative values; red: positive values) of each anatomical landmark and sliding curve semi-landmark (n = 12 patients; n = 12 controls for each group). (For interpretation of the references to colour in this figure legend, the reader is referred to the web version of this article.)
All comparisons were statistically significant ($p < 0.05$).

wider angles in Crouzon and Apert patient group when compared with controls ($p = 0.03$ and $p = 0.003$, respectively). Although mean ages were not statistically different between groups, quantifying mandibular size differences with metric values based on linear measurements would require a different study design, with strictly the same ages in each group, which was not fully the case in our population of growing children. We aimed to detect shape differences among groups, independently of mandibular size, which varies among individuals, particularly with age. We thus performed a General Procrustes Analysis, as it allows valid shape comparisons for objects of different sizes and detection of proportional changes of one anatomical region relatively to another.

Concerning results of PCA, while PC1 comprised age-related changes, PC2 clearly separated patients from controls, thus excluding the sole effect of age on mandibular morphological variations. Finally, comparisons between each patients group showed statistically significant morphological differences between Crouzon and Apert, Crouzon and Muenke, and Apert and Muenke patients. Overall, our results strengthen the hypothesis that mandibular shape in *FGFR*-related syndromic craniosynostoses results from the *FGFR* activating mutation disturbing ossification processes and reinforce the hypothesis of genotype-phenotype correspondence. No statistical difference was found for morphological comparisons between Crouzonodermoskeletal patients and the other groups, most probably due to the small sample of this extremely rare syndromic craniosynostosis.

Early tracheostomy was required for two patients with Crouzonodermoskeletal syndrome and one patient with Crouzon syndrome. These patients presented severe midfacial retrusion, and the mandible appeared as 'prognathic' relative to the maxilla. Although this small sample size did not allow statistical comparisons, linear measurements of the mandibles could not reveal significant differences between patients with or without tracheostomy.

FGFR-related syndromic craniosynostoses are due to gain-of-function activating mutations of *FGFR* genes. The impact of a constitutive activation in *FGFR2* and *FGFR3* on endochondral ossification has been first shown for long bones (*FGFR3*) and skull base synchondrosis (*FGFR2* and *FGFR3*) with altered chondrocyte proliferation and differentiation [72–80]. The impact of activating mutations in *FGFR2* and *FGFR3* on mandibular formation has been more recently studied [28,82–84]. Mandibular bone is formed by intramembranous ossification induced before birth at the site of Meckel cartilage, and by endochondral ossification at the site of condylar, angular and symphyseal cartilages, serving as growth centres after birth [38,81]. Mandibular shape differences have been observed in mouse models for Apert (*Fgfr2*$^{+/S252W}$, and *Fgfr2*$^{+/P253R}$) and Crouzon syndromes (*Fgfr2c*$^{C342Y/+}$), with affected ramus morphology in all models. The greatest magnitude of morphological changes was for *Fgfr2*$^{+/S252W}$ mice, while the Crouzon model showed the most limited changes; interestingly,

anterior body shape changes were only seen in this Crouzon model [82]. This study also demonstrated increased Meckel cartilage volume and increased proliferation of osteoblasts and chondrocytes forming this cartilage in *Fgfr2*$^{+/S252W}$ mice [82]. Concerning *FGFR3* activating mutations, in a mouse model for Muenke syndrome, *Fgfr3*^{P244R}, temporomandibular joint developmental processes were disturbed [83,84]. A mouse model for achondroplasia, *Fgfr3*$^{G380R/G380R}$, presented structural anomalies of primary (Meckel) and secondary cartilages of the condylar region, demonstrating the implication of *FGFR3* in both membranous and endochondral ossification [28].

FGFR2 and *FGFR3* code for a tyrosine kinase receptor. FGF receptors have an extracellular ligand-binding portion composed of immunoglobulin-like domains (IgI, IgII, and IgIII), a transmembrane region, and intracellular tyrosine kinase domains (TK1 and TK2) [8,12]. The FGF family, composed of at least 22 known FGF ligands, binds an FGFR, resulting in receptor monomer dimerization, activation of kinase domains and phosphorylation of the receptor [8]. The impact of the mutations within the FGF receptor extracellular ligand binding domain may also be an explanation for the variability of the mandibular phenotype: while mutations within the IgII-IgIII linker region result in altered ligand-binding specificity and/or affinity as in Apert and Muenke syndrome [85–89], mutations within the IgIII linker region result in aberrant intermolecular disulfide bonds between unpaired cysteine residues leading to the constitutive activation of the receptor, as in Crouzon syndrome [89–91]. Crouzonodermoskeletal syndrome is due to a single point mutation (pAla391Glu) localized in transmembrane domain of FGFR3 resulting in an increase of the phosphorylation level of FGFR3 independently of the presence of ligand [11,92]. Further molecular and biological studies are required to better clarify the affected signalling pathways downstream FGF receptors involved in the craniofacial phenotype of *FGFR*-related craniosynostoses.

Mandibular development is affected in various malformation syndromes without craniosynostosis such as in Robin sequence, Treacher Collins or Nager syndromes, due to mutations in distinct genes, in which mandibular hypoplasia and retrognathia are observed within various degrees of severity [93,94]. Comparing mandibular shapes between craniosynostosis and non-craniosynostosis craniofacial syndromes may help in the understanding of the intrinsic effects of the different mutations on mandibular development and morphology. In our series, we aimed to analyse mandibular shapes at early ages to avoid potential confounding factors related to the effects of surgery on mandibular shape. As mandibular shape varies all along growth, especially the condylar region which is a major center of post-natal growth, analysing mandibular shape at the end of the growth when the condyle achieved a complete ossification, would be required to confirm changes in mandibular vertical height, as we observed in *FGFR2*-craniosynostosis. In fact, mandibular vertical height may be underestimated in the youngest patients, before complete ossification of the secondary condylar cartilages occurs [95].

To conclude, our results demonstrated distinct mandibular shapes at early ages in different subtypes of *FGFR2*- (Crouzon and Apert syndromes) and *FGFR3*-related syndromic craniosynostoses (Muenke and Crouzonodermoskeletal syndromes) and reinforce the hypothesis of genotype-phenotype correspondence concerning mandibular morphology. Studies on larger cohorts and integration of skull base and midface morphological data in the analysis of mandibular shape are required to determine whether the mandible is less subjected to inter-individual variations than other craniofacial features. Mandibular shape would therefore be a valid clinical parameter in the characterisation of *FGFR*-related craniosynostoses.

Supplementary data to this article can be found online at https://doi.org/10.1016/j.bone.2020.115600.

CRediT authorship contribution statement

Dr. Anne Morice contributed to the conception, design, acquisition, analysis, and interpretation of the data, writing and revision of the manuscript.

Dr. Raphael Cornette contributed to the acquisition and analyses of the data and critical analysis of the manuscript.

Dr. Amerigo Giudice contributed to the acquisition of the imaging data.

Dr. Corinne Collet contributed to the acquisition of the genetic diagnoses.

Drs Eric Arnaud, Giovanna Paternoster, Eva Galliani and Pr Arnaud Picard contributed to the selection of the cohort and management of the patients.

Drs Laurence Legeai-Mallet and Roman Hossein Khonsari contributed to the conception, design, analysis, and interpretation of the data and the critical analysis of the manuscript.

All of the authors contributed to the revision of the manuscript and approved the final version.

Funding sources statement

This research did not receive any specific grant from funding agencies in the public, commercial, or not-for-profit sectors.

Acknowledgements

We thank Drs PA Diner, C Tomat, S James and Pr M Zerah for their contribution to the management of the patients.

References

[1] D. Johnson, A.O. Wilkie, Craniosynostosis, Eur. J. Hum. Genet. 19 (4) (2011 Apr) 369–376, https://doi.org/10.1038/ejhg.2010.235 (Epub 2011 Jan 19).
[2] Y. Heuzé, G. Holmes, I. Peter, J.T. Richtsmeier, E.W. Jabs, Closing the gap: genetic and genomic continuum from syndromic to nonsyndromic craniosynostoses, Curr. Genet. Med. Rep. 2 (3) (2014 Sep 1) 135–145.
[3] Y. Heuze, N. Martinez-Abadias, J.M. Stella, E. Arnaud, C. Collet, Fructuoso Garcia G., M. Alamar, L.J. Lo, S.A. Boyadjiev, F. Di Rocco, et al., Quantification of facial skeletal shape variation in fibroblast growth factor receptor-related craniosynostosis syndromes, Birth Defects Res. A Clin. Mol. Teratol. 100 (2014) 250–259.
[4] K. Flaherty, N. Singh, J.T. Richtsmeier, Understanding craniosynostosis as a growth disorder, Wiley Interdiscip. Rev. Dev. Biol. 5 (4) (2016 Jul) 429–459, https://doi.org/10.1002/wdev.227.
[5] T. Armand, E. Schaefer, F. Di Rocco, P. Edery, C. Collet, M. Rossi, Genetic bases of craniosynostoses: an update, Neurochirurgie. 65 (5) (2019 Nov) 196–201, https://doi.org/10.1016/j.neuchi.2019.10.003 (Epub 2019 Oct 9).
[6] W. Lattanzi, M. Barba, L. Di Pietro, S.A. Boyadjiev, Genetic advances in craniosynostosis, Am. J. Med. Genet. A 173 (5) (2017) 1406–1429.
[7] A.O. Wilkie, S.F. Slaney, M. Oldridge, M.D. Poole, G.J. Ashworth, A.D. Hockley, R.D. Hayward, D.J. David, L.J. Pulleyn, P. Rutland, et al., Apert syndrome results from localized mutations of FGFR2 and is allelic with Crouzon syndrome, Nat. Genet. 9 (2) (1995 Feb) 165–172.
[8] S.C. Azoury, S. Reddy, V. Shukla, C.X. Deng, Fibroblast growth factor receptor 2 (FGFR2) mutation related syndromic craniosynostosis, Int. J. Biol. Sci. 13 (12) (2017 Nov 2) 1479–1488, https://doi.org/10.7150/ijbs.22373.
[9] P. Rutland, L.J. Pulleyn, W. Reardon, M. Baraitser, R. Hayward, B. Jones, S. Malcolm, R.M. Winter, M. Oldridge, S.F. Slaney, et al., Identical mutations in the FGFR2 gene cause both Pfeiffer and Crouzon syndrome phenotypes, Nat. Genet. 9 (2) (1995 Feb) 173–176.
[10] M. Muenke, K.W. Gripp, D.M. McDonald-McGinn, K. Gaudenz, L.A. Whitaker, S.P. Bartlett, et al., A unique point mutation in the fibroblast growth factor receptor 3 gene (FGFR3) defines a new craniosynostosis syndrome, Am. J. Hum. Genet. 60 (3) (1997 Mar) 555–564.
[11] G.A. Meyers, S.J. Orlow, I.R. Munro, K.A. Przylepa, E.W. Jabs, Fibroblast growth factor receptor 3 (FGFR3) transmembrane mutation in Crouzon syndrome with acanthosis nigricans, Nat. Genet. 11 (4) (1995 Dec) 462–464.
[12] N.H. Robin, M.J. Falk, C.R. Haldeman-Englert, FGFR-related craniosynostosis syndromes, in: M.P. Adam, H.H. Ardinger, R.A. Pagon, S.E. Wallace, Bean LJH, K. Stephens, A. Amemiya (Eds.), GeneReviews® [Internet], University of Washington, Seattle, Seattle (WA), 1993-2020.
[13] D.N. Schweitzer, J.M. Graham, R.S. Lachman, E.W. Jabs, K. Okajima, K.A. Przylepa, W.R. Wilcox, Subtle radiographic findings of achondroplasia in patients with Crouzon syndrome with acanthosis nigricans due to an Ala391Glu substitution in FGFR3, Am. J. Med. Genet. 98 (1) (2001) 75–91.
[14] L. Arnaud-López, R. Fragoso, J. Mantilla-Capacho, P. Barros-Núñez, Crouzon with acanthosis nigricans: further delineation of the syndrome, Clin. Genet. 72 (5) (2007) 405–410.
[15] A. Montero, Y. Okada, M. Tomita, M. Ito, H. Tsurukami, T. Nakamura, T. Doetschman, J.D. Coffin, M.M. Hurley, Disruption of the fibroblast growth factor-

2 gene results in decreased bone mass and bone formation, J. Clin. Invest. 105 (8) (2000 Apr) 1085–1093.
[16] D.M. Ornitz, FGF signaling in the developing endochondral skeleton, Cytokine Growth Factor Rev. 16 (2) (2005 Apr) 205–213.
[17] David M. Ornitz, Pierre J. Marie, Fibroblast growth factor signaling in skeletal development and disease, Genes Dev. 29 (2015) 1463–1486, https://doi.org/10.1101/gad.266551.115.
[18] D.M. Ornitz, P.J. Marie, Fibroblast growth factors in skeletal development, Curr. Top. Dev. Biol. 133 (2019) 195–234, https://doi.org/10.1016/bs.ctdb.2018.11.020.
[19] M.L. Cunningham, M.L. Seto, C. Ratisoontorn, C.L. Heike, A.V. Hing, Syndromic craniosynostosis: from history to hydrogen bonds, Orthod. Craniofac. AtRes. 10 (2007) 67–81.
[20] G. Holmes, C. O'Rourke, S.M. Motch Perrine, N. Lu, H. van Bakel, J.T. Richtsmeier, E.W. Jabs, Midface and upper airway dysgenesis in FGFR2-related craniosynostosis involves multiple tissue-specific and cell cycle effects, Development. 145 (19) (2018 Oct 5), https://doi.org/10.1242/dev.166488 pii: dev166488.
[21] B.L.M. Way, R.H. Khonsari, T. Karunakaran, J. Nysjö, I. Nyström, D.J. Dunaway, R.D. Evans, R.D. Hayward, J.A. Britto, Correcting exorbitism by monobloc fronto-facial advancement in crouzon-pfeiffer syndrome: an age-specific, time-related, controlled study, Plast. Reconstr. Surg. 143 (1) (2019 Jan) 121e–132e, https://doi.org/10.1097/PRS.0000000000005105.
[22] J. Bouaoud, Q. Hennocq, G. Paternoster, S. James, E. Arnaud, R.H. Khonsari, Excessive ossification of the bandeau in Crouzon and Apert syndromes, J. Craniomaxillofac. Surg. 48 (4) (2020 Apr) 376–382.
[23] S. Boutros, P.R. Shetye, S. Ghali, C.R. Carter, J.G. McCarthy, B.H. Grayson, Morphology and growth of the mandible in Crouzon, Apert, and Pfeiffer syndromes, J. Craniofac. Surg. 18 (1) (2007 Jan) 146–150.
[24] J.D. Wink, N. Bastidas, S.P. Bartlett, Analysis of the long-term growth of the mandible in Apert syndrome, J. Craniofac. Surg. 24 (4) (2013 Jul) 1408–1410, https://doi.org/10.1097/SCS.0b013e31828dcf09.
[25] J.C. Kolar, K. Ditthakasem, J.A. Fearon, Long-term evaluation of mandibular growth in children with FGFR2 mutations, J. Craniofac. Surg. 28 (3) (2017 May) 709–712, https://doi.org/10.1097/SCS.0000000000003494.
[26] A. Khominsky, R. Yong, S. Ranjitkar, G. Townsend, P.J. Anderson, Extensive phenotyping of the orofacial and dental complex in Crouzon syndrome, Arch. Oral Biol. 86 (2018 Feb) 123–130, https://doi.org/10.1016/j.archoralbio.2017.10.022.
[27] X. Lu, R. Sawh-Martinez, A.J. Forte, R. Wu, R. Cabrejo, A. Wilson, D.M. Steinbacher, M. Alperovich, N. Alonso, J.A. Persing, Mandibular spatial reorientation and morphological alteration of Crouzon and Apert syndrome, Ann. Plast. Surg. 83 (5) (2019 Nov) 568–582, https://doi.org/10.1097/SAP.0000000000001811.
[28] M. Biosse Duplan, D. Komla-Ebri, Y. Heuzé, V. Estibals, E. Gaudas, N. Kaci, C. Benoist-Lasselin, M. Zerah, I. Kramer, M. Kneissel, D.G. Porta, F. Di Rocco, L. Legeai-Mallet, Meckel's and condylar cartilages anomalies in achondroplasia result in defective development and growth of the mandible, Hum. Mol. Genet. 25 (14) (2016 Jul 15) 2997–3010.
[29] D.M. Noden, The role of the neural crest in patterning of avian cranial skeletal, connective, and muscle tissues, Dev. Biol. 96 (1983) 144–165, https://doi.org/10.1016/0012-1606(83)90318-4.
[30] G. Couly, A. Grapin-Botton, P. Coltey, N.M. Le Douarin, The regeneration of the cephalic neural crest, a problem revisited: the regenerating cells originate from the contralateral or from the anterior and posterior neural fold, Development. 122 (1996) 3393–1407.
[31] Y. Chai, X. Jiang, Y. Ito, P. Bringas Jr., J. Han, D.H. Rowitch, P. Soriano, A.P. McMahon, H.M. Sucov, Fate of the mammalian cranial neural crest during tooth and mandibular morphogenesis, Development. 127 (8) (2000 Apr) 1671–1679.
[32] M.J. Depew, T. Lufkin, J.L.R. Rubenstein, Specification of jaw subdivisions by Dlx genes, Science. 298 (2002) 381–385, https://doi.org/10.1126/science.1075703.
[33] A. Frisdal, P.A. Trainor, Development and evolution of the pharyngeal apparatus, Wiley Interdiscip. Rev. Dev. Biol. 3 (2014) 403–418, https://doi.org/10.1002/wdev.147.
[34] M. Lipski, I.M. Tomaszewska, W. Lipska, G.J. Lis, K.A. Tomaszewski, The mandible and its foramen: anatomy, anthropology, embryology and resulting clinical implications, Folia Morphol. (Warsz) 72 (4) (2013 Nov) 285–292.
[35] D.P. Rice, R. Rice, I. Thesleff, Fgfr mRNA isoforms in craniofacial bone development, Bone. 33 (1) (2003 Jul) 14–27.
[36] B.A. Havens, B. Rodgers, M. Mina, Tissue-specific expression of Fgfr2b and Fgfr2c isoforms, Fgf10 and Fgf9 in the developing chick mandible, Arch. Oral Biol. 51 (2) (2006 Feb) 134–145 (Epub 2005 Aug 18).
[37] B.A. Havens, D. Velonis, M.S. Kronenberg, A.C. Lichtler, B. Oliver, M. Mina, Roles of FGFR3 during morphogenesis of Meckel's cartilage and mandibular bones, Dev. Biol. 316 (2) (2008 Apr 15) 336–349, https://doi.org/10.1016/j.ydbio.2008.01.035.
[38] C. Parada, Y. Chai, Mandible and tongue development, Curr. Top. Dev. Biol. 115 (2015) 31–58, https://doi.org/10.1016/bs.ctdb.2015.07.023.
[39] K. Yu, K. Karuppaiah, D.M. Ornitz, Mesenchymal fibroblast growth factor receptor signaling regulates palatal shelf elevation during secondary palate formation, Dev. Dyn. 244 (11) (2015 Nov) 1427–1438, https://doi.org/10.1002/dvdy.24319.
[40] A. Fedorov, R. Beichel, J. Kalpathy-Cramer, J. Finet, J.-C. Fillion-Robin, S. Pujol, C. Bauer, D. Jennings, F.M. Fennessy, M. Sonka, J. Buatti, S.R. Aylward, J.V. Miller, S. Pieper, R. Kikinis, 3D slicer as an image computing platform for the quantitative imaging network, Magn. Reson. Imaging 30 (9) (2012 Nov) 1323–1341 PMID: 22770690. PMCID: PMC3466397.
[41] Coquerelle M, Prados-Frutos JC, Benazzi S, Bookstein FL, Senck S, Mitteroecker P, Weber GW. Infant growth patterns of the mandible in modern humans: a closer exploration of the developmental interactions between the symphyseal bone, the teeth, and the suprahyoid and tongue muscle insertion sites. J. Anat. 2013 Feb;222(2):178–92. doi: https://doi.org/10.1111/joa.12008.
[42] S.V. Guevara Perez, Castolo G. de la Rosa, L. Thollon, M. Behr, A 3D characterization method of geometric variation in edentulous mandibles, Morphologie. 102 (339) (2018 Dec) 255–262, https://doi.org/10.1016/j.morpho.2018.08.001.
[43] P. Gunz, P. Mitteroecker, Semilandmarks: a method for quantifying curves and surfaces, Hystrix 24 (1) (2013) 103–109, https://doi.org/10.4404/hystrix-24.1-6292.
[44] C.P. Klingenberg, MorphoJ: an integrated software package for geometric morphometrics, Mol. Ecol. Resour. 11 (2) (2011 Mar) 353–357, https://doi.org/10.1111/j.1755-0998.2010.02924.x Epub 2010 Oct 5 21429143.
[45] M.L. Zelditch, D.L. Swiderski, H.D. Sheets, Geometric Morphometrics for Biologists: A Primer, Academic Press, Cambridge, 2012.
[46] R. Core Team, R: A language and environment for statistical computing, R Foundation for Statistical Computing, Austria. URL, Vienna, 2019, https://www.R-project.org/.
[47] F.J. Rohlf, D. Slice, Extensions of the Procrustes method for the optimal superimposition of landmarks, Syst. Zool. 39 (1) (1990) 40–59.
[48] D.C. Adams, M.L. Collyer, A. Kaliontzopoulou, Geomorph: Software for Geometric Morphometric Analyses, R package version 3.0.6, 2018. https://cran.r.
[49] M. Baylac, M. Frieß, Fourier descriptors, Procrustes superimposition, and data dimensionality: an example of cranial shape analysis in modern human populations, Modern Morphometrics in Physical Anthropology, Springer, Boston, MA, 2005, pp. 145–165.
[50] F.L. Bookstein, Principal warps: thin-plate splines and the decomposition of deformations, IEEE Trans. Pattern Anal. Mach. Intell. 11 (6) (1989) 567–585.
[51] S. Schlager, Morpho and Rvcg - shape analysis in R, in: G. Zheng, S. Li, G. Szekely (Eds.), Statistical Shape and Deformation Analysis, Academic Press, 2017, pp. 217–256 ISBN 9780128104934.
[52] W.R. Atchley, B.K. Hall, A model for development and evolution of complex morphological structures, Biol. Rev. Camb. Philos. Soc. 66 (1991) 101–157, https://doi.org/10.1111/j.1469-185X.1991.tb01138.x.
[53] M. Bastir, P. O'Higgins, A. Rosas, Facial ontogeny in Neanderthals and modern humans. Proceedings of the Royal Society, Biol. Sci. 274 (2007) 1125–1132.
[54] M.R. Passos-Bueno, A.L. Sertié, F.S. Jehee, R. Fanganiello, E. Yeh, Genetics of craniosynostosis: genes, syndromes, mutations and genotype-phenotype correlations, Front Oral Biol. 12 (2008) 107–143, https://doi.org/10.1159/000115035.
[55] S.F. Slaney, M. Oldridge, J.A. Hurst, G.M. Moriss-Kay, C.M. Hall, M.D. Poole, et al., Differential effects of FGFR2 mutations on syndactyly and cleft palate in Apert syndrome, Am. J. Hum. Genet. 58 (5) (1996) 923–932.
[56] J.M. Ko, Genetic syndromes associated with craniosynostosis, J. Korean Neurosurg. Soc. 59 (3) (2016) 187–191.
[57] S. Kreiborg, M.M. Cohen Jr., Is craniofacial morphology in Apert and Crouzon syndromes the same? Acta Odontol. Scand. 56 (1998) 339–341.
[58] J. Levasseur, J. Nysjö, R. Sandy, J.A. Britto, N. Garcelon, S. Haber, A. Picard, P. Corre, G.A. Odri, R.H. Khonsari, Orbital volume and shape in Treacher Collins syndrome, J. Craniomaxillofac. Surg. 46 (2) (2018 Feb) 305–311, https://doi.org/10.1016/j.jcms.2017.11.028.
[59] M. Costaras-Volarich, S. Pruzansky, Is the mandible intrinsically different in Apert and Crouzon syndromes? Am. J. Orthod. 85 (1984) 475–487.
[60] P. Elmi, J.H. Reitsma, P.H. Buschang, E.B. Wolvius, E.M. Ongkosuwito, Mandibular asymmetry in patients with the Crouzon or Apert syndrome, Cleft Palate Craniofac J. 52 (3) (2015 May) 327–335, https://doi.org/10.1597/13-143.
[61] M.S. Ahn, S.M. Shin, T. Yamaguchi, et al., Relationship between the maxillofacial skeletal pattern and the morphology of the mandibular symphysis: structural equation modeling, Korean J. Orthod. 49 (3) (2019) 170–180, https://doi.org/10.4041/kjod.2019.49.3.170.
[62] E.B. Ridgway, J.K. Wu, S.R. Sullivan, S. Vasudavan, B.L. Padwa, G.F. Rogers, et al., Craniofacial growth in patients with FGFR3Pro250Arg mutation after fronto-orbital advancement in infancy, J. Craniofac. Surg. 22 (2011) 455–461.
[63] E. Lajeunie, R. Cameron, V. El Ghouzzi, et al., Clinical variability in patients with Apert's syndrome, J. Neurosurg. 90 (1999) 443–447.
[64] J.P. Connolly, J. Gruss, M.L. Seto, et al., Progressive postnatal craniosynostosis and increased intracranial pressure, Plast. Reconstr. Surg. 113 (2004) 1313–1323.
[65] M.F. Hoefkens, C. Vermeij-Keers, J.M. Vaandrager, Crouzon syndrome: phenotypic signs and symptoms of the postnatally expressed subtype, J. Craniofac. Surg. 15 (2004) 233–240 (discussion 241–242).
[66] E.J. Dingwall, Artificial Cranial Deformation—A Contribution to the Study of Ethnic Mutilation, John Bale, Sons & Danielsson, Ltd., London, 1931.
[67] M. Cottin, R.H. Khonsari, M. Friess, Assessing cranial plasticity in humans: the impact of artificial deformation on masticatory and basicranial structures, Comptes Rendus Palevol. 16 (5–6) (August–September 2017) 545–556.
[68] T.A. Püschel, M. Friess, G. Manríquez, Morphological consequences of artificial cranial deformation: modularity and integration, PLoS One 15 (1) (2020 Jan 24) e0227362, , https://doi.org/10.1371/journal.pone.0227362 (eCollection 2020).
[69] I. Ferros, M.J. Mora, I.F. Obeso, P. Jimenez, A. Martinez-Insua, Relationship between the cranial base and the mandible in artificially deformed skulls, Orthod. Craniofacial Res. 19 (4) (2016 Nov) 222–233, https://doi.org/10.1111/ocr.12128 (Epub 2016 Aug 10).
[70] A. Morice, G. Paternoster, A. Ostertag, S. James, M. Cohen-Solal, R.H. Khonsari, E. Arnaud, Anterior skull base and pericranial flap ossification after frontofacial monobloc advancement, Plast. Reconstr. Surg. 141 (2) (2018 Feb) 437–445.
[71] R.H. Khonsari, S. Haber, G. Paternoster, B. Fauroux, M.P. Morisseau-Durand, V. Cormier-Daire, L. Legeai-Mallet, S. James, Q. Hennocq, E. Arnaud, The influence of fronto-facial monobloc advancement on obstructive sleep apnea: an assessment

of 109 syndromic craniosynostoses cases, J. Craniomaxillofac. Surg. (2020 Apr.), https://doi.org/10.1016/j.jcms.2020.04.001.
[72] O. Segev, I. Chumakov, Z. Nevo, D. Givol, L. Madar-Shapiro, Y. Sheinin, M. Weinreb, A. Yayon, Restrained chondrocyte proliferation and maturation with abnormal growth plate vascularization and ossification in human FGFR-3(G380R) transgenic mice, Hum. Mol. Genet. 9 (2) (2000 Jan 22) 249–258.
[73] K. Yu, J. Xu, Z. Liu, D. Sosic, J. Shao, E.N. Olson, D.A. Towler, D.M. Ornitz, Conditional inactivation of FGF receptor 2 reveals an essential role for FGF signaling in the regulation of osteoblast function and bone growth, Development. 130 (13) (2003 Jul) 3063–3074.
[74] Q. Wang, R.P. Green, G. Zhao, D.M. Ornitz, Differential regulation of endochondral bone growth and joint development by FGFR1 and FGFR3 tyrosine kinase domains, Development. 128 (19) (2001 Oct) 3867–3876.
[75] L. Legeai-Mallet, C. Benoist-Lasselin, A. Munnich, J. Bonaventure, Overexpression of FGFR3, Stat1, Stat5 and p21Cip1 correlates with phenotypic severity and defective chondrocyte differentiation in FGFR3-related chondrodysplasias, Bone. 34 (1) (2004 Jan) 26–36.
[76] L. Yin, X. Du, C. Li, X. Xu, Z. Chen, N. Su, L. Zhao, H. Qi, F. Li, J. Xue, J. Yang, M. Jin, C. Deng, L. Chen, A Pro253Arg mutation in fibroblast growth factor receptor 2 (Fgfr2) causes skeleton malformation mimicking human Apert syndrome by affecting both chondrogenesis and osteogenesis, Bone. 42 (4) (2008 Apr) 631–643, https://doi.org/10.1016/j.bone.2007.11.019 (Epub 2008 Jan 31).
[77] T. Matsushita, W.R. Wilcox, Y.Y. Chan, A. Kawanami, H. Bükülmez, G. Balmes, P. Krejci, P.B. Mekikian, K. Otani, I. Yamaura, M.L. Warman, D. Givol, S. Murakami, FGFR3 promotes synchondrosis closure and fusion of ossification centers through the MAPK pathway, Hum. Mol. Genet. 18 (2) (2009 Jan 15) 227–240, https://doi.org/10.1093/hmg/ddn339.
[78] F. Di Rocco, M. Biosse Duplan, Y. Heuzé, N. Kaci, D. Komla-Ebri, A. Munnich, E. Mugniery, C. Benoist-Lasselin, L. Legeai-Mallet, FGFR3 mutation causes abnormal membranous ossification in achondroplasia, Hum. Mol. Genet. 23 (11) (2014 Jun 1) 2914–2925, https://doi.org/10.1093/hmg/ddu004 (Epub 2014 Jan 12).
[79] S. Pannier, E. Mugniery, A. Jonquoy, C. Benoist-Lasselin, T. Odent, J.P. Jais, A. Munnich, L. Legeai-Mallet, Delayed bone age due to a dual effect of FGFR3 mutation in Achondroplasia, Bone. 47 (5) (2010 Nov) 905–915, https://doi.org/10.1016/j.bone.2010.07.020 (Epub 2010 Jul 29).
[80] E. Mugniery, R. Dacquin, C. Marty, C. Benoist-Lasselin, M.C. de Vernejoul, P. Jurdic, A. Munnich, V. Geoffroy, L. Legeai-Mallet, An activating Fgfr3 mutation affects trabecular bone formation via a paracrine mechanism during growth, Hum. Mol. Genet. 21 (11) (2012 Jun 1) 2503–2513, https://doi.org/10.1093/hmg/dds065 (Epub 2012 Feb 24).
[81] W.E. Roberts, J.K. Hartsfield, Bone development and function: genetic and environmental mechanisms, Semin. Orthod. 10 (2004) 100–122.
[82] S.M. Motch Perrine, M. Wu, N.B. Stephens, D. Kriti, H. van Bakel, E.W. Jabs, J.T. Richtsmeier, Mandibular dysmorphology due to abnormal embryonic osteogenesis in FGFR2-related craniosynostosis mice, Dis. Model. Mech. 12 (5) (2019 May 30), https://doi.org/10.1242/dmm.038513 pii: dmm038513.
[83] S.R. Twigg, C. Healy, C. Babbs, J.A. Sharpe, W.G. Wood, P.T. Sharpe, G.M. Morriss-Kay, A.O. Wilkie, Skeletal analysis of the Fgfr3(P244R) mouse, a genetic model for the Muenke craniosynostosis syndrome, Dev. Dyn. 238 (2) (2009 Feb) 331–342, https://doi.org/10.1002/dvdy.21790.
[84] T. Yasuda, H.D. Nah, J. Laurita, T. Kinumatsu, Y. Shibukawa, T. Shibutani, N. Minugh-Purvis, M. Pacifici, E. Koyama, Muenke syndrome mutation, FgfR3P^{244}R, causes TMJ defects, J. Dent. Res. 91 (7) (2012 Jul) 683–689, https://doi.org/10.1177/0022034512449170 (Epub 2012 May 23).
[85] J. Anderson, H.D. Burns, P. Enriquez-Harris, A.O. Wilkie, J.K. Heath, Apert syndrome mutations in fibroblast growth factor receptor 2 exhibit increased affinity for FGF ligand, Hum. Mol. Genet. 7 (9) (1998) 1475–1483.
[86] K. Yu, A.B. Herr, G. Waksman, D.M. Ornitz, Loss of fibroblast growth factor receptor 2 ligand-binding specificity in Apert syndrome, Proc. Natl. Acad. Sci. U. S. A. 97 (2000) 14536–14541.
[87] O.A. Ibrahimi, A.V. Eliseenkova, A.N. Plotnikov, K. Yu, D.M. Ornitz, M. Mohammadi, Structural basis for fibroblast growth factor receptor 2 activation in Apert syndrome, Proc. Natl. Acad. Sci. U. S. A. 98 (2001) 7182–7187.
[88] O.A. Ibrahimi, F. Zhang, A.V. Eliseenkova, et al., Biochemical analysis of pathogenic ligand-dependent FGFR2 mutations suggests distinct pathophysiological mechanisms for craniofacial and limb abnormalities, Hum. Mol. Genet. 13 (2004) 2313–2324.
[89] K.M. Neilson, R. Friesel, Ligand-independent activation of fibroblast growth factor receptors by point mutations in the extracellular, transmembrane, and kinase domains, J. Biol. Chem. 271 (1996) 25049–25057.
[90] K. Mangasarian, Y. Li, A. Mansukhani, C. Basilico, Mutation associated with Crouzon syndrome causes ligand-independent dimerization and activation of FGF receptor-2, J. Cell. Physiol. 172 (1997) 117–125.
[91] S.C. Robertson, A.N. Meyer, K.C. Hart, et al., Activating mutations in the extracellular domain of the fibroblast growth factor receptor 2 function by disruption of the disulfide bond in the third immunoglobulin-like domain, Proc. Natl. Acad. Sci. U. S. A. 95 (1998) 4567–4572.
[92] F. Chen, C. Degnin, M. Laederich, W. Horton, K. Hristova, The A391E mutation enhances FGFR3 activation in the absence of ligand, Biochim. Biophys. Acta 1808 (8) (2011) 2045–2050.
[93] M.T. Chung, B. Levi, J.S. Hyun, et al., Pierre Robin sequence and Treacher Collins hypoplastic mandible comparison using three-dimensional morphometric analysis, J. Craniofac. Surg. 23 (7 Suppl 1) (2012) 1959–1963, https://doi.org/10.1097/SCS.0b013e318258bcf1.
[94] M.T. McDonald, J.L. Gorski, Nager acrofacial dysostosis, J. Med. Genet. 30 (1993) 779–782.
[95] G.H. Sperber, G.H. Sperber, G.D. Guttmann, S.M. Sperber, G.D. Gutterman, Craniofacial Development, PMPH-USA, 2001.

2. Article 2

Morice *et al*. Craniofacial growth and function in achondroplasia: a multimodal 3D study on 15 patients. Orphanet Journal of Rare Diseases. *Accepté, sous presse.*

a) Introduction

L'achondroplasie est la chondrodysplasie liée à FGFR3 la plus fréquente, due dans plus de 97 % des cas, à une mutation gain de fonction G380R affectant le domaine transmembranaire du récepteur FGFR3 (Rousseau et al, 1994, Shiang et al, 1994, Horton et al, 2002).

Le phénotype est dominé par la présence d'un nanisme rhizomélique sévère, et par des anomalies craniofaciales dont la caractérisation et la corrélation avec la sévérité du syndrome d'apnées du sommeil restent à préciser. En effet, dans ce cadre, le syndrome d'apnées obstructives du sommeil est d'origine multifactorielle : facteurs obstructifs des voies aériennes supérieures (sténose choanale, hypertrophie des végétations adénoïdes et amygdalienne, macroglossie), hypotonie des muscles des voies aériennes, rétrusion de l'étage moyen de la face (Julliand et al, 2012 ; Tenconi et al, 2017 ; Holzman et al, 2008, Onodera et al, 2006). La correction chirurgicale des facteurs obstructifs des voies aériennes supérieures reste souvent insuffisante pour normaliser le syndrome d'apnées obstructives du sommeil (Julliand et al, 2012, Sisk et al, 1999). Une hypothèse explicative peut être la persistance des anomalies squelettiques craniofaciales, en particulier la rétrusion maxillaire et la réduction des dimensions antéropostérieures de la base du crâne. La corrélation entre les modifications squelettiques craniofaciales et la sévérité des apnées obstructives du sommeil n'a jamais été confirmée dans l'achondroplasie. Or, compte tenu du développement de nouvelles stratégies thérapeutiques dans l'achondroplasie, dont certaines sont actuellement en cours de phase clinique chez les patients porteurs d'achondroplasie (analogue du CNP (vosoritide, Biomarin), inhibiteurs de tyrosine kinases (infigratinib, QED Therapeutics)), la question de l'impact de ces traitements sur le phénotype craniofacial et les conséquences fonctionnelles (apnées obstructives) impose la compréhension précise du phénotype craniofacial et de ses conséquences fonctionnelles en premier lieu à l'état basal, sans traitement. Il était donc indispensable de mettre en place une étude visant à répondre à ces questions. De ce fait, nous avons mis en place une étude avec analyses multimodales à partir des données cliniques, polysomnographiques, céphalométriques, et morphométriques (scanners) d'une cohorte de patients porteurs d'achondroplasie, en cours de croissance, dans le but d'analyser le phénotype craniofacial à différents âges au cours de la croissance, et d'évaluer l'évolution du phénotype avec l'âge, ainsi que ses corrélations avec la sévérité des apnées obstructives du sommeil.

b) Abstract

L'achondroplasie est la chondrodysplasie liée à FGFR3 la plus fréquente. L'achondroplasie est caractérisée par la présence d'un nanisme rhizomélique, d'anomalies craniofaciales, de sténose du foramen magnum et d'anomalies fonctionnelles en résultant, il s'agit du syndrome d'apnées du sommeil.

La corrélation des anomalies craniofaciales avec le syndrome d'apnées obstructives du sommeil n'est pas établie à ce jour. Cette étude avait pour objectif de mieux caractériser la croissance et les anomalies craniofaciales, et de rechercher des facteurs de corrélation anatomofonctionnelle, entre les anomalies craniofaciales et la sévérité du syndrome d'apnées obstructives du sommeil.

Pour répondre à cet objectif, une étude multimodale a été réalisée à partir d'une cohorte pédiatrique de 15 patients achondroplases (âge moyen 7,8 ± 3,3 ans), à l'aide des données cliniques et d'analyse du sommeil, de céphalométries 2D, et d'analyses par morphométrie géométrique 3D, à partir de scanners craniofaciaux de patients et de témoins (âge moyen au scanner 4,9 ± 4,9 et 3,7 ± 4,2 ans, respectivement).

Le phénotype craniofacial était caractérisé par la présence de rétrusion maxillo-zygomatique, d'ensellure nasale marquée, et de proéminence du front. Les analyses céphalométriques 2D ont montré chez tous les patients la présence de rétrusion maxillomandibulaire, avec excès vertical du tiers inférieur de la face, et de modifications des angles de la base du crâne.

L'étude scanographique a montré une fusion prématurée constante des synchondroses de la base du crâne. Les analyses par morphométrie géométriques 3D ont permis de mettre en évidence la présence d'un phénotype craniofacial plus sévère chez les patients plus âgés, en particulier au niveau de l'étage moyen de la face (rétrusion maxillaire), et au niveau de la base du crâne (fermeture de l'angle spheno occipital). Au niveau mandibulaire, la branche montante et la branche horizontale présentaient des modifications morphologiques plus importantes chez les patients plus âgés, caractérisées par un raccourcissement relatif de la hauteur ramique et condylienne, et de la longueur antéropostérieure de la branche horizontale.

Enfin, nous avons montré une corrélation significative entre la sévérité de la rétrusion maxillomandibulaire et le syndrome d'apnées obstructives du sommeil ($p < 0,01$).

Notre étude a montré la présence d'aggravation du phénotype craniofacial et mandibulaire avec l'âge, ainsi qu'une corrélation anatomofonctionnelle significative entre la sévérité du phénotype de l'étage moyen de la face et de la mandibule et les apnées obstructives du sommeil.

c) Article

Craniofacial growth and function in achondroplasia: a multimodal 3D study on 15 patients

Short title Craniofacial growth in achondroplasia

Anne **Morice** (1,2,3), Maxime **Taverne** (2), Sophie **Eché** (1), Lucie **Griffon** (4), Brigitte **Fauroux** (4), Nicolas **Leboulanger** (5), Vincent **Couloigner** (5), Geneviève **Baujat** (3,6), Valérie **Cormier-Daire** (3,6), Arnaud **Picard** (1), Laurence **Legeai-Mallet** (3), Natacha **Kadlub** (1), Roman Hossein **Khonsari** (1,2,3)

1. Service de chirurgie maxillofaciale et chirurgie plastique, Hôpital Necker - Enfants Malades, Assistance Publique - Hôpitaux de Paris; Faculté de Médecine, Université Paris Cité; Paris, France
2. Laboratoire 'Forme et Croissance du Crâne', Hôpital Necker - Enfants Malades, Assistance Publique - Hôpitaux de Paris; Faculté de Médecine, Université Paris Cité; Paris, France
3. Molecular and Physiopathological Bases of Osteochondrodysplasia. INSERM UMR 1163, Imagine Institute, Paris, France.
4. Unité de ventilation non invasive et du sommeil de l'enfant, Hôpital Necker - Enfants Malades, Assistance Publique - Hôpitaux de Paris; Faculté de Médecine, Université Paris Cité, EA VIFASOM; Paris, France
5. Service d'oto-rhino-laryngologie et chirurgie cervico-faciale, Hôpital Necker - Enfants Malades, Assistance Publique - Hôpitaux de Paris; Faculté de Médecine, Université Paris Cité, Paris, France
6. Centre de Référence des Maladies Osseuses Constitutionnelles, Service de Médecine Génomique des Maladies Rares, Hôpital Universitaire Necker-Enfants Malades, Paris, France

Keywords achondroplasia; *FGFR3*; sleep apnoea; geometric morphometrics; cephalometrics; principal component analysis; craniofacial growth

Corresponding author Dr Anne Morice, Service de chirurgie maxillofaciale et chirurgie plastique, Hôpital Necker - Enfants Malades, 149 rue de Sèvres 75015 Paris, France

tel 0171396754 email anne.morice2@aphp.fr

Abstract

Background

Achondroplasia is the most frequent FGFR3-related chondrodysplasia, leading to rhizomelic dwarfism, craniofacial anomalies, stenosis of the foramen magnum, and sleep apnea. Craniofacial growth and its correlation with obstructive sleep apnea syndrome has not been assessed in achondroplasia. In this study, we provide a multimodal analysis of craniofacial growth and anatomo-functional correlations between craniofacial features and the severity of obstructive sleep apnea syndrome.

Methods

A multimodal study was performed based on a paediatric cohort of 15 achondroplasia patients (mean age, 7.8±3.3 years), including clinical and sleep study data, 2D cephalometrics, and 3D geometric morphometry analyses, based on CT-scans (mean age at CT-scan: patients, 4.9±4.9 years; controls, 3.7±4.2 years).

Results

Craniofacial phenotype was characterized by maxillo-zygomatic retrusion, deep nasal root, and prominent forehead. 2D cephalometric studies showed constant maxillo-mandibular retrusion, with excessive vertical dimensions of the lower third of the face, and modifications of cranial base angles. All patients with available CT-scan had premature fusion of skull base synchondroses. 3D morphometric analyses showed more severe craniofacial phenotypes associated with increasing patient age, predominantly regarding the midface - with increased maxillary retrusion in older patients - and the skull base - with closure of the spheno-occipital angle. At the mandibular level, both the corpus and ramus showed shape modifications with age, with shortened anteroposterior mandibular length, as well as ramus and condylar region lengths. We report a significant correlation between the severity of maxillo-mandibular retrusion and obstructive sleep apnea syndrome ($p<0.01$).

Conclusions

Our study shows more severe craniofacial phenotypes at older ages, with increased maxillomandibular retrusion, and demonstrates a significant anatomo-functional correlation between the severity of midface and mandible craniofacial features and obstructive sleep apnea syndrome.

Keywords

Achondroplasia; *FGFR3*; sleep apnoea; geometric morphometrics; cephalometrics; principal component analysis; craniofacial growth

Background

Achondroplasia (ACH, OMIM 100800) is the most frequent form of chondrodysplasia, occurring with an incidence ranging from 1/30 000 to 1/10 000[1,2]. Clinical presentation is characterized by rhizomelic dwarfism and craniofacial anomalies, including macrocephaly, frontal bossing, midface retrusion, mandibular malformations, and cranio-vertebral junction anomalies[1–4].

Achondroplasia is due to activating mutations in the Fibroblast Growth Factor Receptor 3 gene (*FGFR3*), consisting in a glycine-to-arginine substitution in the transmembrane domain of the receptor (position 380) in more than 97% of cases[5,6]. Activating *FGFR3* mutations lead to disorganisation of growth plate cartilage, premature fusion of the skull base synchondroses and impaired bone elongation[3,7–10].

The exact effect of *FGFR3* activating mutations on craniofacial skeletal phenotype and growth in ACH is not well understood. A better characterization of skull bone anomalies using 3D renderings could be of use to describe the multiple craniofacial anomalies occurring in this condition. In clinical practice, describing skull growth and form in ACH is crucial to evaluate the functional consequences of midfacial retrusion, mandibular malformations, in order to establish evidence-based treatment plans. Obstructive and central sleep apnea are among the most alarming functional issues in ACH, affecting 60% of patients[11,12], and have been related to a sagittal shortening of the cranial base and stenosis of the foramen magnum[13]. Obstructive sleep apnea (OSA)[14] in ACH is partially due to midfacial retrusion. Currently, the relationship between skeletal craniofacial shape and functional respiratory anomalies is not well understood. Deciphering the craniofacial morphology and its growth in patient with ACH could help assess the beneficial effects of promising medical treatments that are currently being developed to counteract the effects of activating *FGFR3* mutations[15,16].

The aim of this study was to better characterise and quantify the skeletal craniofacial phenotype in a cohort of 15 ACH patients, using clinical evaluation, 2D cephalometrics and 3D geometric morphometrics. We also investigated the relationship between craniofacial shape and sleep study parameters, to understand whether craniofacial anomalies could be predictive of the severity of obstructive sleep apnea.

Methods

Patients

All ACH patients were initially managed in the National Reference Centres for Congenital Bone Diseases (Centre de Référence Maladies Rares MOC) and for Cleft and Maxillofacial Malformations (Centre de Référence Maladies Rares MAFACE), located within Necker hospital. This retrospective study included 15 ACH patients from 2017 to 2021 with confirmed *FGFR3* gain-of-function mutations. We analysed clinical and orthodontics evaluation and photographs, respiratory polygraphic (PG) results, lateral cephalograms, and craniofacial computed tomographic (CT) scans (n=11), being both performed before any skeletal craniofacial procedure, including orthodontic treatments. Patients whose ages at PG and at cephalograms were not similar (tolerance of 15 months maximum, i.e 20% of age difference), were excluded from the study.

To account for facial characteristics and to screen for potential clinical predictive factors of OSA, we used three morphological features - maxillo-zygomatic retrusion, deep nasal root, prominent forehead - with three grades of severity. Facial profile was sorted into three types (convex, concave, or flat) (Figure 1). Occlusion was defined using the Angle classification[26].

Controls

Controls (n=11) were selected among age and gender-matched patients without any reported craniofacial anomalies. These patients underwent CT-scans performed within a short delay after benign trauma or infections that did not affect the studied regions.

Cephalometric analysis

Cephalometric analysis was performed according to Delaire's principles[17], using lateral cephalograms, with the software *DELAIRE CEPHALOMETRIE* (Blued'IS, Béthemont la Forêt, France). Fourteen landmarks were manually placed on each lateral cephalogram, defining 12 lines. Cranial and facial cephalometric analyses are described in supplementary data section (Figure S1 and Table S1).

Investigation of skull and mandible shape

An initial macroscopic analysis aimed at detecting potential premature fusion of skull vault sutures and skull base synchondroses, graded as follows: grade 1 (open), grade 2 (partially closed), and grade 3 (completely closed)[18–20]. Twenty landmarks were placed on the skull and twenty-three landmarks were placed on the mandible (Figure 2, Table S2) using Avizo 2020 (Thermo Fisher Scientific, Waltham, MA, USA). Landmarks positioning was realized by the same expert, and preliminary study of intrarater reliability was performed to ensure repeatability of landmark annotation. Concretely, landmarks were placed 5 times on the skull and mandible of 3 patients. Three-dimensional coordinates were aligned and scaled by mean of a Procrustes superimposition, and Procrustes coordinates were compared among individuals using a multivariate analysis of variance with permutation procedure (1000 iterations). This enabled us to assess the relative importance of the variance due to intrarater bias and the variance existing between individuals. The tests resulted in clear differences between individuals (all $p < 0.05$), suggesting that intrarater bias was marginal. Landmarks supporting most of the intrarater variance were identified by displaying the thin-plate spline deformations along the axes of a Principal Component Analysis computed on the repeated landmarks of each individual. Special attention was further paid to these landmarks when the definitive annotation started. All computations and statistical analyses were performed using R[21]. Landmarks were aligned using Procrustes superimposition (*procSym*, *Morpho* package)[22], either with (1) standardisation of overall size (generating Procrustes coordinates), and (2) without scaling (generating Boas coordinates). With and without scaling, the 3D coordinates of the aligned points were combined into matrices to perform subsequent multivariate statistical analyses. All following analyses that generated theoretical 3D shapes used the mandible and the skull of a control individual as the reference shape. This reference shape was obtained by segmenting the CT-scan images of the individual with Avizo and by exporting the constructed volumes as 3D surface objects. Growth trajectories within each group of subjects were estimated from two-blocks partial least-squares regressions (2b-PLS), using *pls2B* from the *Morpho* package[22]. The first block corresponded to the Procrustes or Boas coordinates, and the second block corresponded to the log10-transformed age in years. Theoretical morphological variations along the statistically significant axis of covariation between shape and age were displayed using *tps3d* (*Morpho* package)[22]. Patterns of morphological changes during growth were compared between groups of individuals, first qualitatively, then quantitatively using the *compare.pls* (*geomorph* package)[23–25]. The covariation axes of the 2b-PLS regressions of Procrustes coordinates relative to age were used to extract theoretical morphologies at 6 different ages in each group: 0.5, 1, 3, 6, 9 and 12

years of age. Procrustes distances were computed for each landmark between the theoretical shapes in the two groups of patients, to estimate possible aggravation, defined as the increase in morphological differences between controls and patients with age. Deformation was then averaged within subsets of landmarks corresponding to 5 anatomical regions (Figure 2). For the skull, three areas were considered: face (LM 1-13), cranial vault (LM 14-17), and skull base (LM 18-20). For the mandible, we considered two areas: mandibular ramus (LM 1-5, 11-19, 22) and mandibular corpus (the remaining landmarks). For each of these 5 anatomical regions, a logarithmic equation describing the evolution of deformation with age was generated. These growth equations enabled predicting deformation variations with age. The relationship between the intensity of morphological deformation and indices of apnea (see below, apnea-hypopnea index = AHI and obstructive AHI = OAHI) was investigated by computing stepwise regressions (using *stepAIC* from the *MASS* package)[26] between AHI or OAHI and the deformation of the five previously defined anatomical areas.

Sleep parameters

Overnight PG with the recording of nasal flow, respiratory movements (bands), tracheal sound, body position, electrocardiogram, heart rate, pulse oximetry (SpO_2), and transcutaneous carbon dioxide pressure (PtcCO2) were performed in room air (American Thoracic Society, 1996). Obstructive, central, mixed apnea and hypopnea were defined as previously described[11,12]. The AHI was calculated as the sum of the apnea and hypopnea events per hour of total sleep. Sleep study was considered normal for AHI < 1.5 /hour[27]. $PtcCO_2$ was recorded simultaneously by a Sentec monitor (Sentec, Therwill, Switzerland). The oxygen desaturation index (ODI) was considered abnormal when >5 /hour. All available PG from all patients were considered to evaluate the evolution of sleep apnea during growth and after airways surgery.

Relationships between cephalometric and sleep parameters

The correlation between each quantitative sleep parameter individually and all cephalometric variables was investigated through stepwise multiple regressions (using *step.AIC* from the *MASS* package. This enabled the best model to be retained by minimising the Akaike Information Criterion (AIC). Hence, the relative contributions of the explanatory variables to the variation of the dependent variable were assessed by computing the standardised (beta) coefficients.

Non-parametric three-way multivariate analyses of variance (MANOVAs with permutation procedure) enabled the estimation of the effects of the severity of maxillo-zygomatic retrusion, age and sex on the cephalometric and sleep parameters, using *procD.lm* from the *geomorph* package. Univariate pairwise permutation tests (alternative to the parametric univariate analyses of variance - ANOVA - and to *post-hoc* tests) were computed with *pairwise PermutationTest* from the *rcompanion* package[28]. These analyses aimed to investigate the effect of the factors that had shown significant influence in earlier multivariate analyses on individual cephalometric variables separately, and to perform pairwise mean comparison. The procedure applied a Bonferroni adjustment of the *p-value* to balance the biases of multiple comparisons.

Results

Patients

Fifteen ACH patients were included. Mean age at initial clinical evaluation was 7.8±3.3 years; female / male ratio was 5/10. Genetic studies revealed the presence of a G380R mutation in *FGFR3* gene in all tested patients (n=13). In the two remaining patients, born more than 15 years before the time of the study (i.e. 2021), molecular screening had not been performed, as genetic molecular confirmation was not mandatory at this period in these cases of typical clinical presentation of ACH. All patients presented a severe rhizomelic dwarfism, characterized by short limbs and trunk.

Craniofacial morphological multimodal assessment

Clinical assessment

Four patients presented i) mild, eight ii) moderate and three iii) severe maxillo-zygomatic retrusion (Figure 1). Nasal root was deeply depressed in eleven patients and was less depressed in four patients. Forehead was flattened in 3/15, otherwise moderate convexity or marked prominent forehead affected 7/15 and 5/15 patients respectively. Profile was concave in 10/15, flat in 4/15, and convex in 1/15 patients.

Cephalometric analysis

Mean age at cephalometric analysis was 7.9±3.2 years and was not statistically different from mean age at clinical evaluation. Maxillary retrusion (maxillary retroposition) and

retrognathism (mandibular retroposition), in relation to cranio-adapted F1, affected all patients (n=15). Skeletal Angle class was predominantly type III (n=10/15), and less frequently I or II (n=3 and 2/15, respectively). Gonial angle was mostly obtuse (n=13) (relative to F3/F7 angle) and acute in 2/15 patients. All patients had excessive vertical dimension of the lower third of the face. Cranial base angles were abnormal in all patients, the anterior angle being obtuse (> 22°) in 8/15 patients, and the posterior angle acute (< 115°) in 13/15 (Table 1), accounting for modifications of the cranial base shape due to premature fusion of the skull base synchondroses (see below).

Craniofacial shape and growth: 3D-CT assessment

Cranial sutures and skull base synchondroses

Craniofacial CT-scans were available for 11/15 patients (female/male ratio: 3/8), with a mean age of 4.9±4.9 years (range 0,2 - 13.6). Premature fusion of the squamo-sphenoidal suture affected 8/11 patients: either *in a partial* or *complete form* (4 patients each). A large anterior fontanelle was observed in 5/11 patients (all aged under 2 years), and 2/11 patients presented a mild fontanelle closure delay (ages 2.6 and 2.8 years).

All 11/15 patients presented with premature fusions (1) of the intra-sphenoidal synchondrosis (ISS) with 10/11 in a *complete* form (grade 3) and in 1/11 a *partial* form (grade 2); (2) of the spheno-occipital synchondrosis (SOS) with 9/11 in a *complete* (grade 3) and 2/11 in a *partial* form (grade 2), and (3) of the intra-occipital synchondrosis (IOS) bilaterally with 8/11 in a *complete* form (grade 3) and 3/11 in a *partial* form (grade 3). A *complete* fusion of the spheno-ethmoidal synchondrosis (grade 3) was observed in 7/11 patients, though it remained open (grade 1) in 4/11 patients.

Growth trajectories

Both standardized (Procrustes coordinates) and non-standardized (Boas coordinates) skull and mandible shapes strongly covaried (rPLS > 0.9) with age within the ACH group and the control group (Table S3, Figure 3). The strength of the covariation, provided by the rPLS index, was never significantly different between the two groups of patients, suggesting that intra-group variability in phenotype relative to age was comparable in the two cohorts.

The 2b-PLS regressions between Boas coordinates of the skull and age showed that, compared with controls, the growth of the skull in ACH was characterized by an overall

retrusion of the midface and a forward tilting of the anterior aspect of the skull base, leading to a tightening of the space between skull base and the posterior part of the maxilla (Figure 3).

More precisely, facial shape in ACH was characterised by a deep nasal root and a maxillo-zygomatic retrusion. The angulation of the skull base at the site of the SOS (with subsequent forward and downward tilting of the basisphenoid) and reduction of the skull base antero-posterior dimensions were associated with a shortening of the skull length. The orbits were vertically more elongated than in the control group. The skull vault was higher in the frontal region (which is mostly described by cephalometric landmark FPmid (Figures 2 and 3 and Table S2), in older patients when compared with controls. Growth anomalies were also highlighted by 2b-PLS regressions between Procrustes skull coordinates and age, suggesting that these were not only due to size, but rather corresponded to disease-specific phenomena.

The 2b-PLS regressions between Boas coordinates of the mandible and age showed that mandible growth in ACH was characterized by a backwards shift of the symphysis and greater symphysis height (defined as the distance between cephalometric landmarks 8 Pog and InfDe, see Figures 2, 3 and Table S2). Additionally, in older patients when compared with younger ones, the mandibular ramus was narrower and more vertical overall, the notch of the sigmoid was more profound, the coronoid process and the condyle were more vertically positioned, and the segment between the retromolar region and the mandibular ramus was more concave. A decrease in the overall antero-posterior length of the mandible seemed to occur before teenage years, characterized by the shortening and verticalization of the condyle in older ACH patients. This decrease in length did not seem to occur in the first years of life. Similar results were obtained after scaling, suggesting that size moderately affected these morphological variations.

Phenotypic aggravation with age

Skull vault showed the highest level of deformation between controls and patients (Figure 4). Skull height increase was one of the main features of ACH. Nevertheless, the skull base and the face showed the most significant levels of aggravation with age (approximately +75% to +106% of phenotypic deformation from 6 months to 12 years old, respectively) (Table S4). The facial landmarks that showed the greatest aggravation in older patients when compared with younger ones were those surrounding the nostrils (InfExOL, InfNasApR, InfNasApL, InfNasMid, Figure 2, Table S4).

Both the mandibular ramus and corpus showed comparable levels of phenotypic deformation between controls and patients. The most pronounced levels of aggravation were in the mandibular corpus (+119% of phenotypic deformation). When considering landmarks separately and not by anatomical region, it appeared that not all landmarks showed the same levels of aggravation with age. Overall, disparity in the levels of aggravation among landmarks was increased in older patients when compared with younger ones (Figure 4). Within the mandibular ramus, the areas experiencing the greatest deformation were the coronoid process, the condyle and the gonion (CorR, CoExtR, GoR, CorL, CoExtL, GoL); and within the mandibular corpus, the most inferior part of the chin (MeR, MeL, Figure 2 and Table S4).

No significant model was retained from the stepwise regressions between the intensity of shape deformation and indices of apnea (all $p > 0.05$).

Functional assessment: obstructive sleep apnea syndrome

Polygraphic results and upper airway surgery

Mean age at sleep study was 7.8±3.2 years, which was not statistically different from mean age at cephalometric study (difference 0,1491±1,198). Sleep anomalies affected 80% of patients, with 33% patients having severe obstructive sleep apnea syndrome (AHI >= 10 events/hour) (Tables S5 and S6). Abnormal desaturations were observed in 13/15 patients. Apneas were mostly obstructive; the median index of central apnea was 0 (range 0 - 2.2). In our series, cranio-vertebral decompression had been performed in 4/15 patients with central apnea due to foramen magnum stenosis. In these cases, sleep analyses selected for the present study were performed after cranio-vertebral decompression.

Fourteen out of 15 patients benefited from upper airways surgery, mostly adeno-tonsillectomy and turbinectomy (Table S5). One out of 15 patients with severe ventilation disorders of multiple origins (pulmonary hypoplasia, obstructive apnea and central apnea due to upper spinal cord compression) had a tracheostomy and a cranio-vertebral decompression at the age of one and was decannulated two weeks post-operatively. Six out of 15 patients benefited from non-invasive continuous positive airway pressure (CPAP) ventilation, starting at the mean age of 4.9±3.2 years, and CPAP had been stopped following a normal sleep study without CPAP in 3/6 of them (mean age 9±1.7 years). In average, higher values of AHI and OAHI were observed at the ages 1-3 (19.5±42.1, 13.5±28.9 evens/hour, respectively) and 6-9

years of age (19.1±42.2, 15.2±30.3 events/hour, respectively) than at other ages (Figure 5), although not significantly (p=0.9, Kruskal-Wallis's test).

Craniofacial phenotype and sleep disorders: anatomo-functional correlation

Stepwise regressions between each sleep parameter and the set of cephalometric variables retained three statistically significant models (Table S7). Greater AHI and OAHI values were both associated with more pronounced maxillary retrusion and retrognathism, and with smaller C1-C2 values. When maxillary and mandibular retrusion increased, SpO2 min decreased. Non-parametric MANOVAs with permutation detected no relationship between sleep study parameters and the severity of maxillo-zygomatic retrusion, sex, and age (all $p > 0.05$, Table S8). Cephalometric parameters were influenced by the grade of maxillo-zygomatic retrusion ($p = 0.034$; $R^2 = 0.157$; $F = 2.538$; $Z = 1.904$) and sex ($p = 0.011$; $R^2 = 0.178$; $F = 2.874$; $Z = 2.287$). More specifically, the univariate pairwise permutation tests did not reveal any significant relationship between the severity of maxillo-zygomatic retrusion and cephalometric parameters considered separately (Table S9). However, levels of maxillary retrusion and values of C1-C4 angles differed between sexes, with boys presenting with more severe maxillary retrusion and lower C1-C4 angle values than girls.

Discussion

FGFR3 is involved in craniofacial membranous and endochondral ossification processes[3,29]. Gain-of-function *FGFR3* mutations lead to dwarfism (ACH, hypochondroplasia, and thanatophoric dysplasia)[5,30,31] but also craniofacial suture fusions (craniosynostoses: Muenke syndrome and Crouzon syndrome with *acanthosis nigricans*)[32,33].

Even though all the ACH patients reported here presented similar craniofacial features (frontal bossing, macrocephaly, maxillary retrusion, deep nasal root, and prognathism)[3,4,34], we observed three grades of facial phenotype severity – 'mild', 'moderate' or 'severe' –, suggesting a phenotypic disparity in a genetic disease due in >95% to a same G380R *FGFR3* mutation. All patients presented maxilla and mandible retrusion, an opening of gonial angle, a closure of the posterior skull base angles and a vertically elongated chin, confirming previous findings in ACH[34,35].

Our 3D morphometric analyses suggested an aggravation of the craniofacial phenotype with age, even though our study is not longitudinal. The most affected craniofacial region was the midface, characterised by an increased maxillary retrusion and a deeper nasal root in older

patients when compared with younger ones. Aggravation of midface retrusion was most probably related to the premature fusion of skull base synchondroses secondary to activating *FGFR3* mutations that impair cartilage homeostasis[3,36], as observed in ACH mouse models. Normal synchondrosis fusion in humans follows a specific age-related sequence: ISS before the age of 2, IOS before the age of 7, spheno-ethmoidal synchondrosis before the age of 9, and SOS before puberty[20,37,38]. Premature fusion of skull base synchondroses was always observed in our series, at the site of ISS, SOS and IOS. Gradual premature fusion of skull base synchondroses contributes to anteroposterior facial growth restriction and subsequent maxillary and midfacial retrusion[19,20,39]. In our series, we observed abnormal angulations at the site of the SOS. These skull angle modifications may be related to the premature fusion of the skull base synchondroses, but we cannot exclude the influence of intrinsic brain anomalies, especially of the temporal region, as already reported in *FGFR* mutations[40,41]. In addition, shape changes of the foramen magnum may also be involved in skull base anomalies, with secondary repercussions on the midface[3,42].

Premature fusion of skull vault sutures was observed in 80% of the patients at the squamo-sphenoidal suture, and all patients under the age of 2 had a large anterior fontanelle, indicating potential anomalies in the membranous ossification of the skull vault[3]. In addition, brain anomalies and potential increased intracranial pressure may also worsen skull shape deformations and impair fontanelle closure and frontal bone ossification. However, previous *ex vivo* studies conducted on a mouse model of ACH, $Fgfr3^{Y367Y/+}$, showed that the ossification delay of skull vault occurred independently of brain and cranial base parameters, suggesting an intrinsic influence of *FGFR3* gain-of-function mutations on membranous ossification[3]. Premature synostosis of one cranial suture constrains cranial growth at the site of the suture, and continuous growth of the underlying brain induces compensatory skull vault growth at the site of other non-fused cranial sutures, leading to skull deformations. Both the premature fusion of cranial sutures and ossification delays of frontal bones may play a role in the prominent forehead observed in ACH patients. In addition, this excessive frontal convexity is also accentuated by the presence of a nasal root depression at the nasofrontal junction, associated with the restricted anteroposterior growth of the skull base.

Obstructive sleep apnea in ACH can be related to multiple anomalies: volume reduction of the upper respiratory tract and nasopharyngeal stenosis (choanal stenosis, adenoids, and tonsils hypertrophy, as well as macroglossia), and airway muscles hypotonia[11,12,14,35]. Here we report two main age periods associated with higher values of AHI and OAHI, i.e 1-3 and 6-9 years,

corresponding to the physiological higher incidence of adenoid and tonsils hypertrophy, respectively. Although an influence of nasopharyngeal obstructive factors in persisting obstructive sleep apnea has been reported in ACH, the surgical correction of these anomalies is often insufficient to treat apnea[11,43]. This is possibly because bony anomalies including short skull base and midface retrusion persist. However, a correlation between craniofacial skeletal shape modifications and severity of OSA had never been confirmed in children with ACH. Here, we report significant correlations between maxillo-mandibular anomalies and AHI, OAHI, and hypoxia: greater AHI and OAHI and lower SpO_2 min values were both associated with severe maxillary retrusion and retrognathism. In addition, higher AHI and OAHI significantly correlated with smaller C1-C2 angle values, highlighting correlation between skull base changes, maxillo-mandibular retrusion, and severity of obstructive sleep apnea. However, we cannot exclude structural and functional upper respiratory tract anomalies in ACH. Although it has been shown that *FGFR2* activating mutations lead to abnormal tracheal formation and segmentation[44–46], there is no data available documenting the impact of *FGFR3* activating mutations on respiratory tract formation. Therefore, a potential intrinsic impact of *FGFR3* mutations on airway formation, development, and function remains to be elucidated.

In addition to premature fusion of skull base synchondroses leading to anteroposterior craniofacial growth limitation, reduction of the nasopharyngeal airway flow itself also contributes to impair transverse and sagittal facial growth, as observed in mouth-breather non-syndromic children presenting chronic nasal obstruction[47]. In this context, functional defects due to *FGFR*-related anatomical anomalies most probably add to the ongoing effects of the *FGFR3* activating mutation in the aggravation of the phenotype with age.

The presence of an anatomo-functional correlation between maxillo-mandibular retrusion and OSA in ACH objectively stresses the clinical need for a specialized multidisciplinary follow-up in this condition with systematic craniomaxillofacial and orthodontic evaluations. Although the benefit of maxillary expansion in releasing nasal obstruction remains unclear, this orthodontic treatment is often recommended to treat palatal transversal insufficiency in ACH after the age of 6. Maxillary advancement is sometimes required, using either controversial orthodontic appliances (Delaire facemasks[48]) in the less severe cases, or surgery, in the cases of severe maxillary retrusion or functional symptoms (OSA, snoring). CPAP face masks may limit the feasibility of these treatments because of the external forces applied on

the midface during maxillary advancement. Development of new CPAP appliances minimizing pressure on the midface should thus be considered in ACH patients[49].
Two patients benefited from maxillary expansion and/or maxillary protraction appliance (Delaire facemasks[8]). One of these patients underwent an interceptive Le Fort I osteotomy with distraction at the age of 10. All these procedures had been performed after 2D and 3D analyses used in the present study. At the time of the study (i.e. 2021), orthodontic treatment was also planned for five patients, and interceptive Le Fort I osteotomy with distraction was considered for two patients. Systematic re-assessment during growth was decided otherwise. Although our sample did not allow us to address this question, future studies should investigate the impact of orthodontic treatments and orthognathic surgery on OSA.
The limitations of our study are due to the small cohort with available cephalometric analyses, CT-scans, and sleep studies performed within the same short period of time to allow correlation studies. A longitudinal follow-up during growth, at different timepoints, will be necessary to confirm craniofacial phenotype modifications with age, and its correlations with the evolution of sleep disorders.
More generally, larger multicentric and prospective cohorts will be useful in future to understand whether and how additional potential factors (such as upper airway hypotonia or collapse, and macroglossia) could contribute to OSA in ACH.

Conclusions

This study highlighted that achondroplasia leads to different degrees of craniofacial morphological and functional severity. We showed for the first time that more severe craniofacial phenotypes occur in older patients than in younger ones, which suggests an aggravation of craniofacial phenotypes during growth. We furthermore demonstrated an anatomo-functional correlation between the severity of maxillo-mandibular retrusion and OSA.
FGFR-related conditions due to activating mutations may soon benefit from medical treatments that will hopefully reduce the need for invasive surgical procedures. In this context, precise knowledge on the natural history of these conditions including ACH is crucial for adapting future treatment and assessing their efficiency, especially in resolving functional anomalies like OSA.

Abbreviations

ACH: achondroplasia; CPAP: Continuous Positive Airway Pressure; FGFR: Fibroblast Growth; OSA: obstructive sleep apnea; AHI: Apnea Hypopnea Index; OAHI: Obstructive Apnea Hypopnea Index;
SpO_2: pulse oximetry; PtcCO2: transcutaneous carbon dioxide pressure; ISS: intra-sphenoidal synchondrosis; SOS: spheno-occipital synchondrosis.

Figure legends:

Figure 1. Clinical grading of morphological severity: maxillo-zygomatic retrusion: mild (patient A), moderate (patient B) and severe (patient C), normal nasal root (patient A), deep nasal root with moderate nasal bone hypoplasia (patient B), totally flattened nasal root with severe nasal bone hypoplasia (patient C), forehead: flattened (patient A), moderate convexity (patient B), markly prominent forehead (patient C).

Figure 2. Anatomical landmarks placed on the skull (frontal and lower views; midline sagittal section) and mandible (frontal and lateral views). Landmarks 13-22 on the mandible are not visible, since they are symmetrically placed on the left side of the mandible. Color code for the skull: face = dark green; cranial vault = orange; skull base midline = purple. Color code for the mandible: mandibular corpus = blue; mandibular ramus = light green.

Figure 3: 2b-PLS regressions between skull morphology and age (3A), and between mandibular morphology and age (3B), describing growth trajectories in patients and controls, before (Boas coordinates) and after scaling (Procrustes coordinates). Numbers refer to age in years. Skull deformation series correspond to theoretical intermediate shapes along the covariation axis (negative values on the left side).

Figure 4: Patterns of phenotypic aggravation with age. Aggravation was defined as the increase of Procrustes distance for each landmark between controls and patients, by comparing the general growth trajectory of each group which was provided by the two-blocks partial least-squares regressions between Procrustes coordinates and age. Aggravation was averaged by anatomical region within both skull and mandible. In each graph, the x-axis was age in years (yo), and the y-axis was the Procrustes distance (no unit). The lower part of the figure represents theoretical morphological deformation of the skull (frontal and inferior views) and mandible (frontal and dorsal views) at 6 different ages (from 6 months to 12 years old), with landmarks highlighted in a gradient of color providing information about the intensity of the deformation in patients (Procrustes distance).

Figure 5. AHI and OAHI before and after upper airway surgery, per age groups. Values obtained from patients who required non-invasive CPAP ventilation at the time of the sleep study are labeled (a unique symbol is used for each patient). AHI: apnea hypopnea index, OAHI: obstructive apnea hypopnea index.

Supplementary Figures and Tables

Figure S1 and Table S1: Cephalometric studies according Delaire[17]: definition of landmarks, lines, and distances

Table S2: 3D morphometric studies: anatomical skull and mandible landmarks.

Table S3: Two-block partial least-square regressions (2bPLS) aiming at describing trends of covariation between skull and mandible shape and age, within patient or control groups. Last column displays the comparison of rPLS between the two groups (rPLS: coefficient of covariation, P: p-value, BOAS: aligned landmark coordinates before scaling, PROCRUSTES: aligned landmark coordinates after scaling). Bold values indicate p-values < 0.05.

Table S4: Differences in Procrustes distances at each landmark between controls and patients. Theoretical shape information at 6 ages extracted from the axis of covariation given by the two-block partial least-square regressions between Procrustes coordinates of skulls or mandibles and age (in years, yo) within each group of subjects.

Table S5: Characteristics of the patients: respiratory data and interventions

Table S6: Respiratory polygraphy data of the 15 patients

Table S7: Stepwise multiple regressions between sleep parameters and cephalometric parameters. Each model assessed one sleep study parameter (AHI, OAHI, % of time with $PtcCO_2$ > 50 mmHg, Maximal $PtcCO_2$ (mmHg), SpO_2 min, and oxygen desaturation index) versus all cephalometric parameters. The contributions of individual explanatory variables were estimated according to the slope of the correlation, the standardized coefficient (β coeff), the t-statistics, and the p-value of simple regressions (Pr). Statistically significant values are indicated in bold. Adj-R^2: adjusted Pearson's determination coefficient.

Table S8: Results of the non-parametric three-way multivariate analyses of variance (MANOVAs with permutation procedure) between sets of sleep and cephalometric parameters and the maxilla-zygomatic retrusion grade, sex and patient age. These include the effect of each explanatory variable individually and all possible interactions between them. Df: degree of freedom; R^2: Pearson's determination coefficient; F: F-statistic; Z: Z-scores; Pr: p-value associated with the F test. Bold values indicate significant results.

Table S9: Univariate pairwise permutation tests between the maxilla-zygomatic retrusion grade (MZR) or sex (the two factors that multivariate permutation tests revealed to be significantly influencing cephalometrics, see Table S2) and each of the cephalometric variables.

Table legends

Table 1. Cephalometric analyses (n=15 patients). SD: standard deviation. For the definition of the cephalometric parameters (C1, F1, F1M, F1m, C2, C4), see Figure 1/ Suppl Table 1.

		Mean ± SD	Definition
Age (years)		7.9±3.2	
C1/F1 angle (degrees)		87.8±5.3	
Maxillo-mandibular position	Maxillary position C1/f1M angle (relative to F1)	- 10.3±4.9	maxillary retrusion (n=15)
	Mandibular position (C1/f1m angle) (relative to F1)	- 8±4.3	retrognathism (n=15)
	Maxillo-mandibular discordance (f1M/1m angle)	- 2.2±4.4	Angle class I/II/III (n=3/2/10)
Gonial angle (degrees)		129.6±20.32	open n=13, closed n=2 (relative to F3^F7 angle)
Vertical excess of the lower third of the face (%)		+ 6±0.02	lower facial excess (n=15)
Cranial base angles (degrees)	C1/C2 angle	23.8±4.53 (20-22)	anterior angle of the cranial base (open n=8, closed n=5, normal n=1)
	C1/C4 angle	111.2±11.3 (115-120)	posterior angle of the cranial base (open n=1, closed n=13, normal n=1)

Figure 1. Clinical grading of morphological severity: maxillo-zygomatic retrusion: mild (patient A), moderate (patient B) and severe (patient C), normal nasal root (patient A), deep nasal root with moderate nasal bone hypoplasia (patient B), totally flattened nasal root with severe nasal bone hypoplasia (patient C), forehead: flattened (patient A), moderate convexity (patient B), markly prominent forehead (patient C).

Figure 2. Anatomical landmarks placed on the skull (frontal and lower views; midline sagittal section) and mandible (frontal and lateral views). Landmarks 13-22 on the mandible are not visible, since they are symmetrically placed on the left side of the mandible. Color code for the skull: face = dark green; cranial vault = orange; skull base midline = purple. Color code for the mandible: mandibular corpus = blue; mandibular ramus = light green.

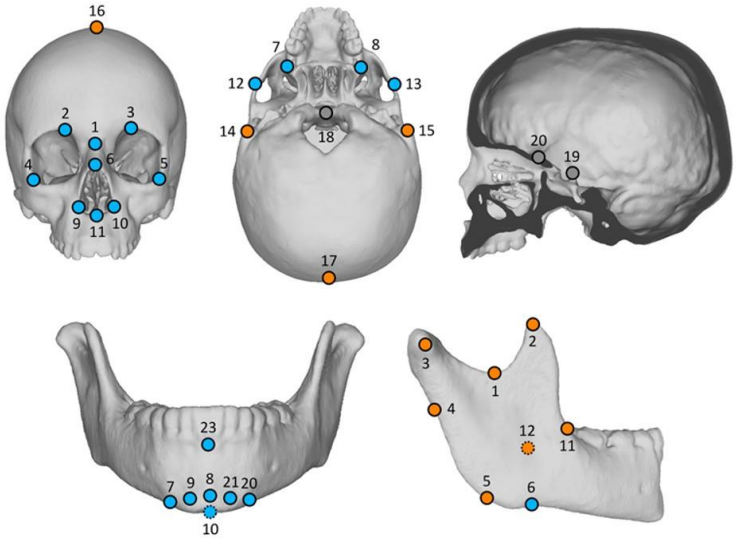

Figure 3: 2b-PLS regressions between skull morphology and age (3A), and between mandibular morphology and age (3B), describing growth trajectories in patients and controls, before (Boas coordinates) and after scaling (Procrustes coordinates). Numbers refer to age in years. Skull deformation series correspond to theoretical intermediate shapes along the covariation axis (negative values on the left side).

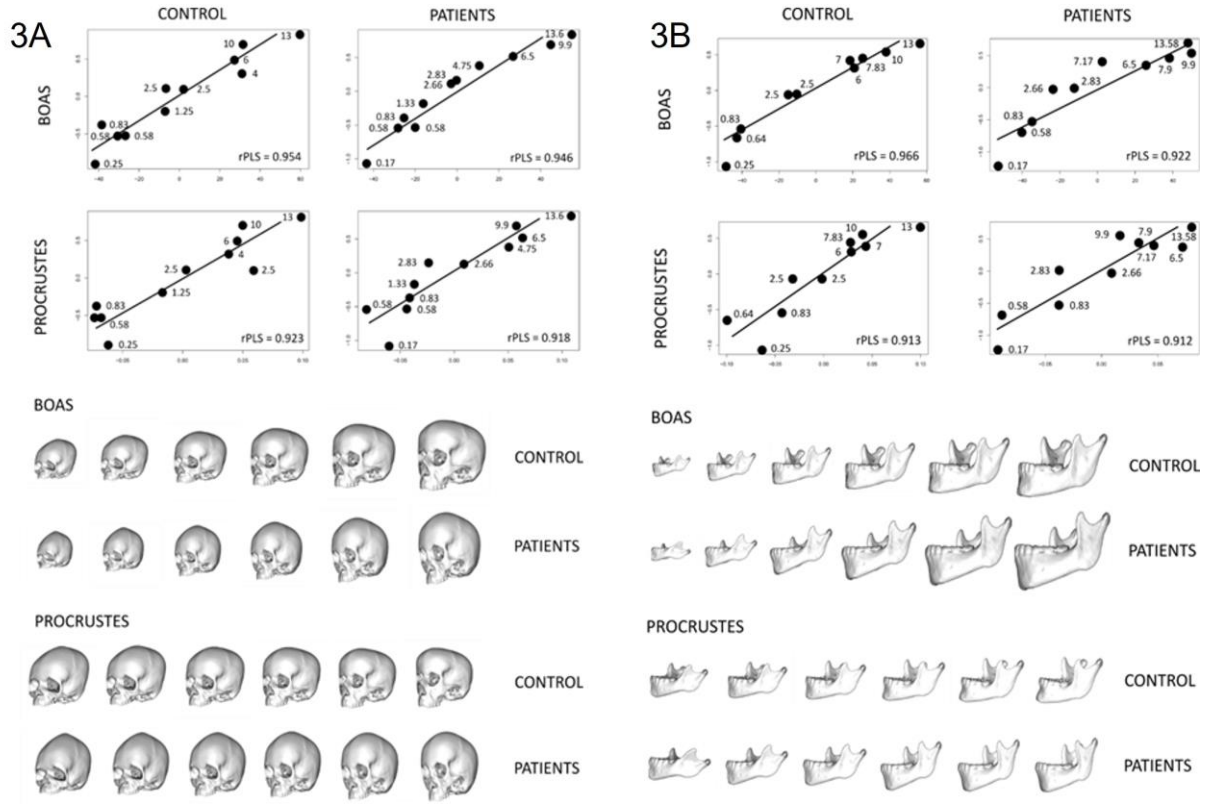

Figure 4: Patterns of phenotypic aggravation with age. Aggravation was defined as the increase of Procrustes distance for each landmark between controls and patients, by comparing the general growth trajectory of each group which was provided by the two-blocks partial least-squares regressions between Procrustes coordinates and age. Aggravation was averaged by anatomical region within both skull and mandible. In each graph, the x-axis was age in years (yo), and the y-axis was the Procrustes distance (no unit). The lower part of the figure represents theoretical morphological deformation of the skull (frontal and inferior views) and mandible (frontal and dorsal views) at 6 different ages (from 6 months to 12 years old), with landmarks highlighted in a gradient of color providing information about the intensity of the deformation in patients (Procrustes distance).

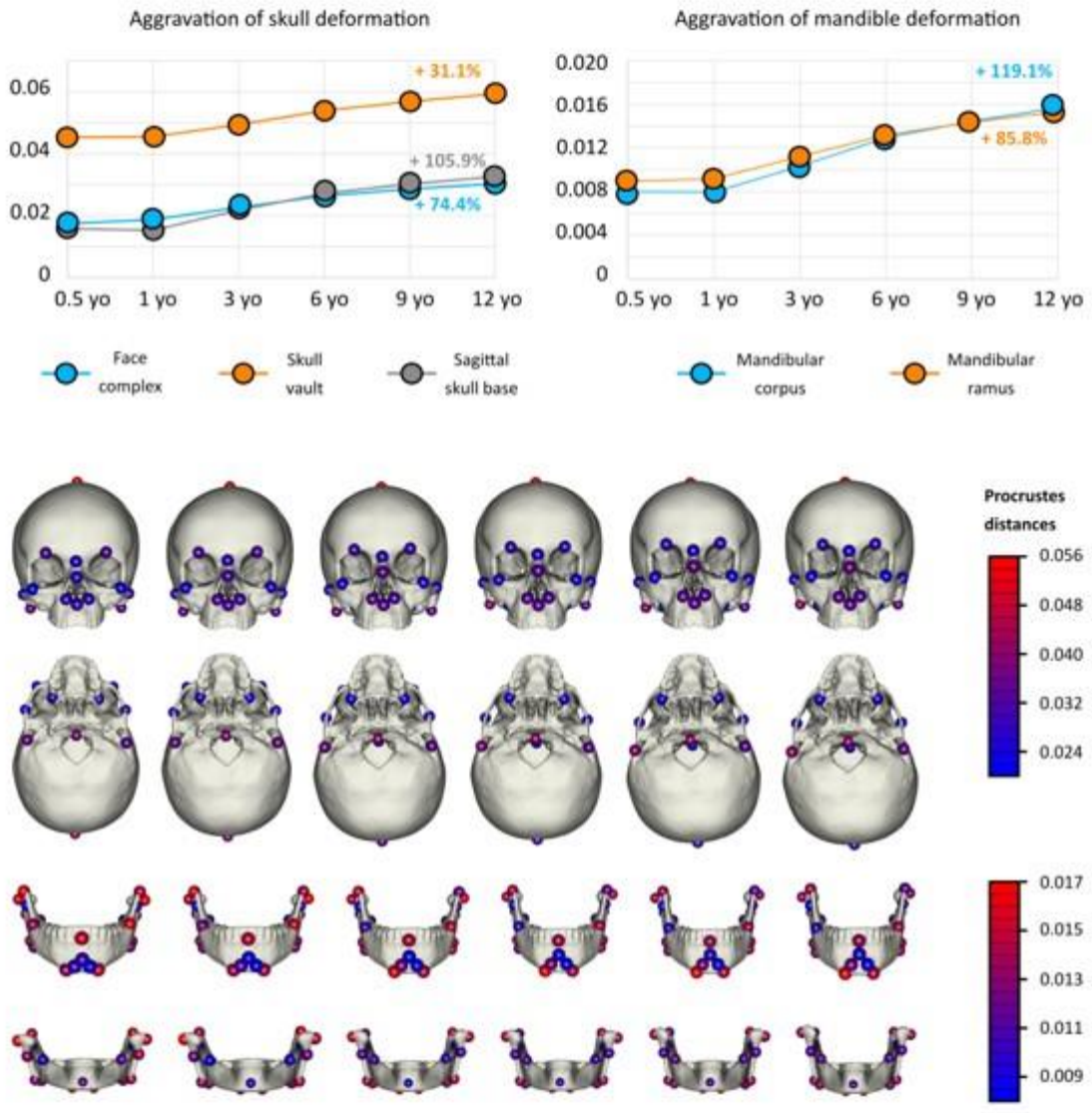

Figure 5. AHI and OAHI before and after upper airway surgery, per age groups. Values obtained from patients who required non-invasive CPAP ventilation at the time of the sleep study are labeled (a unique symbol is used for each patient). AHI: apnea hypopnea index, OAHI: obstructive apnea hypopnea index.

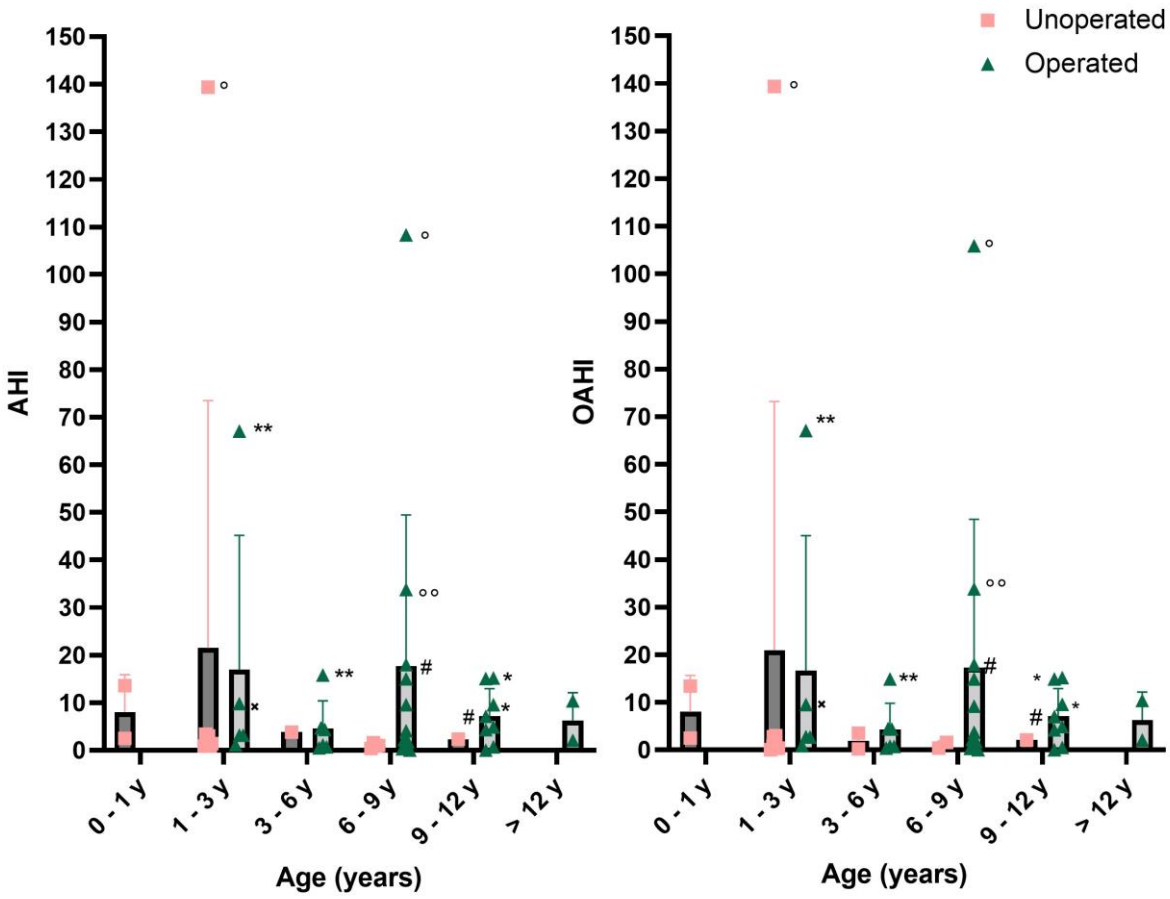

Figure S1 and Table S1: Cephalometric studies according Delaire[17]: definition of landmarks, lines, and distances

Symbol	Definition	Symbol	Definition
Na	Nasion	C1	M-Cp
M	Junction of the nasal, frontal and maxillary bones	C2	Perpendicular to C1, at its center
FM	Frontomaxillary articulation	C3	M-Clp
Cla	Anterior Clinoid process	C4	Cp-Clp
Clp	Posterior Clinoid process	F1	Perpendicular to C3, at FM
Cp	Posterior tangent of the condyle	F2	Pts-Pti
Ara	Articulare anterior	F3	Parallel to F2, tangential to Cp
Od	Odontoid	F4	Parallel to C3 through ANS
Pti	Inferior pterygoid point	F5	Perpendicular to C4 through ANS (from Na' to Me' (ANS-Me' = 55% of Na'-Me')
Pts	Superior pterygoid point		
ANS	Anterior nasal spine		
Np	Nasopalatine foramen	F6	ENA-Go
Go	Gonion	F7	Om-midlle of ANS-Me'
Me	Menton point	F8	Parralel to C1 through Go

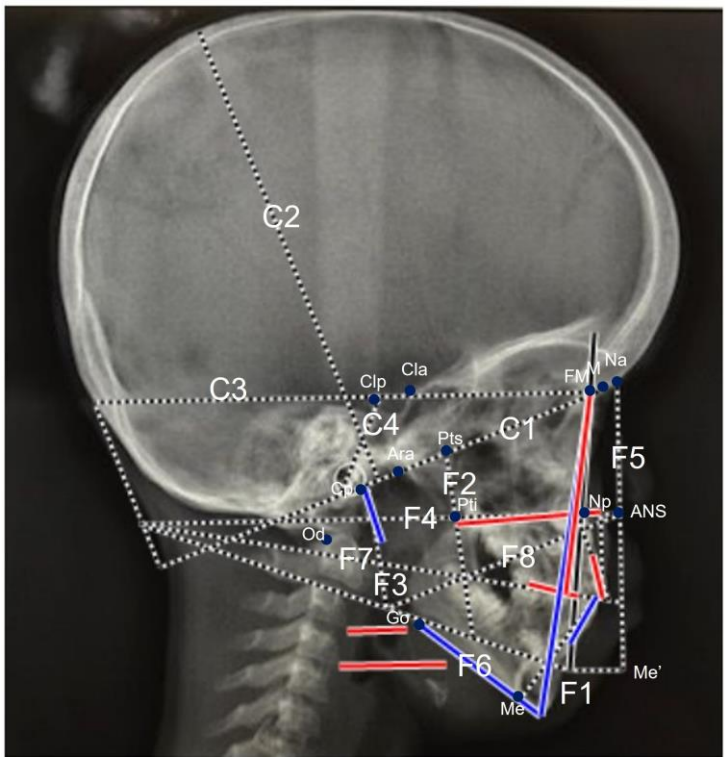

Table S2: 3D morphometric studies: anatomical skull and mandible landmarks.

LM n°	Symbol	Mandible	Symbol	Skull
1	SigR	Sigmoid notch (right side)	NaS	Most superior point of nasal bones at midline
2	CorR	Coronoid process (right side)	SupOrbR	Supra-orbitale point (right side)
3	CoExtR	Most external point of the condyle (right side)	SupOrbL	Supra-orbitale point (left side)
4	ColR	Most posterior point of the condyle neck at the intersection of the sigmoid notch line (right side)	InfExOR	Infero-external angle of the orbit (right side)
5	GoR	Gonion (right side)	InfExOL	Infero-external angle of the orbit (left side)
6	AntGoR	Antegonial (right side)	InfNas	Inferior point of the anterior nasal spine
7	MeR	Menton (right side)	MaxTubR	Maxillary tuberosity (right side)
8	Pog	Pogonion	MaxTubL	Maxillary tuberosity (left side)
9	GnR	Gnathion (right side)	InfNasApR	Infero-lateral angle of the nasal aperture (right side)
10	Symp	Symphysis	InfNasApL	Infero-lateral angle of the nasal aperture (left side)
11	RetMolExtR	Retromolar external (right side)	InfNasMid	Most inferior point of the nasal bones at the midline
12	SpixR	Spix (right side)	ExZygoR	Most external point of the zygomatic arch (right side)
13	Spix L	Spix (left side)	ExZygoL	Most external point of the zygomatic arch (left side)
14	SigL	Sigmoid notch (left side)	InfMastoR	Most inferior point of the mastoid process (right side)
15	CorL	Coronoid process (left side)	InfMastoL	Most inferior point of the mastoid process (left side)
16	CoExtL	Most external point of the condyle (left side)	FPmid	Fronto-parietal junction at the midline
17	ColL	Most posterior point of the condyle neck at the intersection of the sigmoid notch line (left side)	OPmid	Occipito-parietal junction at the midline
18	GoL	Gonion (left side)	AntForMid	Most anterior point of the foramen magnum on the midline
19	AntGoL	Antegonial (left side)	SeMid	Dorsum sella on the midline
20	MeL	Menton (left side)	PostCriMid	Most posterior part of the cribriform plate on the midline
21	GnL	Gnathion (left side)		
22	RetMolExtL	Retromolar external (left side)		
23	InfDe	Infradentale		

Table S3: Two-block partial least-square regressions (2bPLS) aiming at describing trends of covariation between skull and mandible shape and age, within patient or control groups. Last column displays the comparison of rPLS between the two groups (rPLS: coefficient of covariation, P: p-value, BOAS: aligned landmark coordinates before scaling, PROCRUSTES: aligned landmark coordinates after scaling). Bold values indicate p-values < 0.05.

SHAPE vs. AGE		Patients		Control		Patients vs. Control
		rPLS	P	rPLS	P	P
BOAS	Mandible	0,922	0,001	0,966	0,001	0,764
	Skull	0,946	0,001	0,954	0,001	0,971
PROCRUSTES	Mandible	0,912	0,001	0,913	0,001	0,986
	Skull	0,918	0,001	0,923	0,001	0,673

Table S4: Differences in Procrustes distances at each landmark between controls and patients. Theoretical shape information at 6 ages extracted from the axis of covariation given by the two-block partial least-square regressions between Procrustes coordinates of skulls or mandibles and age (in years, yo) within each group of subjects.

		0.5 yo	1 yo	3 yo	6 yo	9 yo	12 yo
SKULL	LM1	0.0146	0.0160	0.0189	0.0212	0.0225	0.0236
	LM2	0.0271	0.0269	0.0277	0.0288	0.0296	0.0303
	LM3	0.0271	0.0273	0.0279	0.0286	0.0291	0.0295
	LM4	0.0056	0.0086	0.0139	0.0175	0.0195	0.0210
	LM5	0.0105	0.0115	0.0131	0.0143	0.0149	0.0154
	LM6	0.0193	0.0250	0.0339	0.0398	0.0430	0.0455
	LM7	0.0163	0.0122	0.0116	0.0154	0.0182	0.0205
	LM8	0.0192	0.0114	0.0112	0.0192	0.0242	0.0281
	LM9	0.0208	0.0257	0.0333	0.0384	0.0411	0.0432
	LM10	0.0177	0.0228	0.0309	0.0363	0.0393	0.0415
	LM11	0.0178	0.0240	0.0342	0.0409	0.0447	0.0475
	LM12	0.0118	0.0138	0.0182	0.0215	0.0234	0.0248
	LM13	0.0184	0.0187	0.0201	0.0216	0.0226	0.0234
	LM14	0.0322	0.0331	0.0419	0.0507	0.0561	0.0604
	LM15	0.0313	0.0320	0.0363	0.0408	0.0436	0.0459
	LM16	0.0713	0.0757	0.0840	0.0902	0.0938	0.0966
	LM17	0.0464	0.0413	0.0356	0.0341	0.0342	0.0347
	LM18	0.0372	0.0409	0.0490	0.0553	0.0590	0.0619
	LM19	0.0051	0.0020	0.0048	0.0084	0.0105	0.0120
	LM20	0.0053	0.0029	0.0115	0.0178	0.0213	0.0240
MANDIBLE	LM1	0.0021	0.0024	0.0029	0.0033	0.0035	0.0036
	LM2	0.0138	0.0141	0.0165	0.0190	0.0205	0.0218
	LM3	0.0126	0.0129	0.0154	0.0178	0.0194	0.0206
	LM4	0.0106	0.0083	0.0084	0.0107	0.0124	0.0138
	LM5	0.0110	0.0125	0.0153	0.0173	0.0185	0.0194
	LM6	0.0079	0.0089	0.0122	0.0149	0.0165	0.0178
	LM7	0.0098	0.0113	0.0187	0.0247	0.0282	0.0309
	LM8	0.0048	0.0022	0.0022	0.0049	0.0063	0.0075
	LM9	0.0046	0.0064	0.0104	0.0133	0.0149	0.0162
	LM10	0.0076	0.0045	0.0048	0.0082	0.0103	0.0119
	LM11	0.0100	0.0086	0.0073	0.0074	0.0078	0.0082
	LM12	0.0067	0.0039	0.0058	0.0094	0.0115	0.0132
	LM13	0.0042	0.0027	0.0077	0.0118	0.0141	0.0158
	LM14	0.0046	0.0059	0.0081	0.0095	0.0103	0.0108
	LM15	0.0121	0.0111	0.0112	0.0123	0.0132	0.0140
	LM16	0.0147	0.0159	0.0180	0.0195	0.0203	0.0209
	LM17	0.0095	0.0081	0.0082	0.0097	0.0109	0.0120
	LM18	0.0085	0.0104	0.0139	0.0164	0.0178	0.0189
	LM19	0.0079	0.0102	0.0149	0.0183	0.0202	0.0217
	LM20	0.0124	0.0123	0.0159	0.0198	0.0221	0.0241
	LM21	0.0037	0.0057	0.0093	0.0117	0.0131	0.0141
	LM22	0.0093	0.0128	0.0201	0.0253	0.0282	0.0304
	LM23	0.0105	0.0111	0.0163	0.0209	0.0237	0.0259

Table S5: Characteristics of the patients: respiratory data and interventions

	Total population n = 15
Age at sleep study (years), mean ± SD, [min;max]	7.8 ± 3.2, [3.9;17.6]
Male/Female (number)	10/5
Prior upper airway surgery (n, %)	14
Adenoidectomy (n)	14
Turbinoplasty (n)	11
Tonsillectomy (n)	9
Other (epiglottoplasty, pharyngoplasty, tongue base reduction, or tracheostomy (n)	4

Table S6: Respiratory polygraphy data of the 15 patients

Respiratory events	
Median AHI (events/hours), [min;max]	2.3 [0;108.3]
AHI ≤ 1 events/h, n (%)	3 (20)
AHI > 1 and ≤ 5 events/h, n (%)	6 (40)
AHI > 5 and < 10 events/h, n (%)	1 (6.7)
AHI ≥ 10 events/h, n (%)	5 (33.3)
Median central AI (events/hours), [min;max]	0 [0;2.4]
Median obstructive AI (events/hours), [min;max]	2.2 [0;105.9]
Obstructive AI > 5 events/h, n (%)	1 (6.7)
Obstructive AI > 10 events/h, n (%)	5 (33.3)
Nocturnal gas exchange	
Mean SpO_2 (%), median [min;max]	97.5 [95;99]
Minimal SpO_2 (%): median [min;max]	90 [69;95]
% of time with SpO_2 < 90% (%)	0 [0;5]
Patients with > 10% of time with a SpO_2 < 90%, n (%)	0
Median 3% ODI (events/hours), [min;max]	27 [1;514]
ODI > 5 events/h, n (%)	13 (86.6)
Mean $PtcCO_2$ (mmHg): median [min;max]	31 [34;50]
Maximal $PtcCO_2$ (mmHg): median [min;max]	46 [39;57]
% of time with $PtcCO_2$ > 50 mmHg (%): median [min;max]	0 [0;16]
Patients with > 10% of time with a $PtcCO_2$ > 50 mmHg, n (%)	3 (20)

Table S7: Stepwise multiple regressions between sleep parameters and cephalometric parameters. Each model assessed one sleep study parameter (AHI, OAHI, % of time with $PtcCO_2$ > 50 mmHg, Maximal $PtcCO_2$ (mmHg), SpO_2 min, and oxygen desaturation index) versus all cephalometric parameters. The contributions of individual explanatory variables were estimated according to the slope of the correlation, the standardized coefficient (β coeff), the t-statistics, and the p-value of simple regressions (Pr). Statistically significant values are indicated in bold. Adj-R^2: adjusted Pearson's determination coefficient.

IAH ~ cephalo						IAHO ~ cephalo					
Model: ~ IAH	p-value	0,005	adj-R^2	0,739		Model: ~ IAHO	p-value	0,002	adj-R^2	0,794	
Variable	Slope	β coeff	t-value	Pr (> |t|)		Variable	Slope	β coeff	t-value	Pr (> |t|)	
C1.F1	-	-	-	-		C1.F1	0,426	0,27	1,917	0,092	
Retromaxillia	-1,227	-0,87	-6,136	< 0,001		Retromaxillia	-1,538	-1,09	-6,734	< 0,001	
Retrognathia	-0,923	-0,67	-4,508	0,002		Retrognathia	-0,98	-0,71	-5,117	< 0,001	
Gonial_Angle	0,201	0,13	1,245	0,248		Gonial_Angle	-	-	-	-	
Maxillomand_rel	-0,282	-0,21	-1,952	0,087		Maxillomand_rel	-0,215	-0,16	-1,503	0,171	
C1.C4	-0,249	-0,16	-1,105	0,301		C1.C4	-0,226	-0,15	-1,084	0,310	
C1.C2	-0,578	-0,41	-2,925	0,019		C1.C2	-0,453	-0,32	-2,469	0,039	
tps_PtCO2 ~ cephalo						SpO2_min ~ cephalo					
Model: ~ tpsPtCO2	p-value	0,141	adj-R^2	0,094		Model: ~ SpO2_min	p-value	0,031	adj-R^2	0,414	
Variable	Slope	β coeff	t-value	Pr (> |t|)		Variable	Slope	β coeff	t-value	Pr (> |t|)	
C1.F1	-	-	-	-		C1.F1	-	-	-	-	
Retromaxillia	-	-	-	-		Retromaxillia	0,374	0,26	3,265	0,008	
Retrognathia	-0,496	-0,36	-1,567	0,141		Retrognathia	0,374	0,27	3,294	0,007	
Gonial_Angle	-	-	-	-		Gonial_Angle	-	-	-	-	
Maxillomand_rel	-	-	-	-		Maxillomand_rel	-	-	-	-	
C1.C4	-	-	-	-		C1.C4	-	-	-	-	
C1.C2	-	-	-	-		C1.C2	0,119	0,09	1,310	0,217	
PtcCO2_max ~ cephalo						desat_index ~ cephalo					
Model: ~ PtcCO2_max	p-value	0,069	adj-R^2	0,173		Model: ~ desat_index	p-value	0,079	adj-R^2	0,351	
Variable	Slope	β coeff	t-value	Pr (> |t|)		Variable	Slope	β coeff	t-value	Pr (> |t|)	
C1.F1	-	-	-	-		C1.F1	-	-	-	-	
Retromaxillia	-	-	-	-		Retromaxillia	-0,87	-0,61	-2,823	0,018	
Retrognathia	-	-	-	-		Retrognathia	0,372	-0,27	-1,212	0,253	
Gonial_Angle	-	-	-	-		Gonial_Angle	0,304	0,20	1,224	0,249	
Maxillomand_rel	-	-	-	-		Maxillomand_rel	-	-	-	-	
C1.C4	-0,056	-0,04	-1,980	0,069		C1.C4	-	-	-	-	
C1.C2	-	-	-	-		C1.C2	-0,457	-0,33	-1,863	0,092	

Table S8: Results of the non-parametric three-way multivariate analyses of variance (MANOVAs with permutation procedure) between sets of sleep and cephalometric parameters and the maxilla-zygomatic retrusion grade, sex and patient age. These include the effect of each explanatory variable individually and all possible interactions between them. Df: degree of freedom; R^2: Pearson's determination coefficient; F: F-statistic; Z: Z-scores; Pr: p-value associated with the F test. Bold values indicate significant results.

Model : MANOVA (Variables polysomno ~ Maxillo-zygomatic retrusion * Sex * Age)

Expl. Var	Df	R^2	F	Z	Pr (> F)
MZR	1	0,021	0,211	-1,165	0,879
Sex	1	0,108	1,089	0,319	0,377
Age	1	0,010	0,103	-1,555	0,945
MZR : Sex	1	0,002	0,020	-2,667	0,996
MZR : Age	1	0,057	0,576	-0,241	0,581
Sex : Age	1	0,053	0,531	-0,316	0,618
MZR : Sex : Age	1	0,052	0,518	-0,299	0,605

Model : MANOVA (Variables cephalo ~ Maxillo-zygomatic retrusion_grade * Sex * Age)

Expl. Var	Df	R^2	F	Z	Pr (> F)
MZR	1	0,157	2,538	1,904	0,034
Sex	1	0,178	2,874	2,287	0,011
Age	1	0,042	0,686	-0,384	0,654
MZR : Sex	1	0,021	0,346	-1,389	0,919
MZR : Age	1	0,053	0,864	0,016	0,516
Sex : Age	1	0,066	1,061	0,240	0,409
MZR : Sex : Age	1	0,049	0,808	-0,047	0,528

Table S9: Univariate pairwise permutation tests between the maxilla-zygomatic retrusion grade (MZR) or sex (the two factors that multivariate permutation tests revealed to be significantly influencing cephalometrics, see Table S2) and each of the cephalometric variables.

Factor			C1.F1	Retromaxillia	Retrognathia	Gonial angle	Maxillomand_rel	C1.C4	C1.C2
MZR	Medians	Grade 1	0,650	-0,281	0,65	-0,161	0,909	0,344	0,800
		Grade 2	0,408	0,284	0,408	-0,371	-0,328	-0,524	0,131
		Grade 3	-0,412	0,961	-0,412	-0,491	-0,141	0,185	-0,906
	Test 1 vs 2	Statistic	-0,623	-0,786	0,317	0,097	1,879	1,301	0,469
		p-value	1,000	1,000	1,000	1,000	0,181	0,579	1,000
	Test 1 vs 3	Statistic	-2,257	-1,996	0,95	0,509	1,419	-0,116	1,252
		p-value	0,072	0,138	1,000	1,000	0,468	1,000	0,632
	Test 2 vs 3	Statistic	-2,156	-1,708	0,989	0,412	-0,222	-1,525	1,446
		p-value	0,093	0,263	0,968	1,000	1,000	0,382	0,445
Sex	Medians	Females	-0,176	-0,141	0,757	0,468	0,000	0,785	-0,009
		Males	0,035	0,412	-0,412	-0,615	0,069	-0,524	0,400
	Test F vs M	Statistic	-1,153	-1,144	2,280	1,597	0,674	2,440	-0,576
		p-value	0,249	0,253	0,023	0,110	0,500	0,015	0,564

References

1. Horton WA, Hall JG, Hecht JT. Achondroplasia. *The Lancet*. 2007;370(9582):162-172. doi:10.1016/S0140-6736(07)61090-3
2. Baujat G, Legeai-Mallet L, Finidori G, Cormier-Daire V, Le Merrer M. Achondroplasia. Best Pract Res Clin Rheumatol. 2008 Mar;22(1):3-18. doi: 10.1016/j.berh.2007.12.008. PMID: 18328977.
3. Di Rocco F, Biosse Duplan M, Heuzé Y, Kaci N, Komla-Ebri D, Munnich A, Mugniery E, Benoist-Lasselin C, Legeai-Mallet L. FGFR3 mutation causes abnormal membranous ossification in achondroplasia. Hum Mol Genet. 2014 Jun 1;23(11):2914-25. doi: 10.1093/hmg/ddu004. Epub 2014 Jan 12. PMID: 24419316.
4. Biosse Duplan M, Komla-Ebri D, Heuzé Y, Estibals V, Gaudas E, Kaci N, Benoist-Lasselin C, Zerah M, Kramer I, Kneissel M, Porta DG, Di Rocco F, Legeai-Mallet L. Meckel's and condylar cartilages anomalies in achondroplasia result in defective development and growth of the mandible. Hum Mol Genet. 2016 Jul 15;25(14):2997-3010. doi: 10.1093/hmg/ddw153. Epub 2016 Jun 3. PMID: 27260401; PMCID: PMC5181594.
5. Rousseau F, Bonaventure J, Legeai-Mallet L, Pelet A, Rozet JM, Maroteaux P, Le Merrer M, Munnich A. Mutations in the gene encoding fibroblast growth factor receptor-3 in achondroplasia. Nature. 1994 Sep 15;371(6494):252-4. doi: 10.1038/371252a0. PMID: 8078586.
6. Horton WA, Lunstrum GP. Fibroblast growth factor receptor 3 mutations in achondroplasia and related forms of dwarfism. Rev Endocr Metab Disord. 2002 Dec;3(4):381-5. doi: 10.1023/a:1020914026829. PMID: 12424440.
7. Legeai-Mallet L, Benoist-Lasselin C, Munnich A, Bonaventure J. Overexpression of FGFR3, Stat1, Stat5 and p21Cip1 correlates with phenotypic severity and defective chondrocyte differentiation in FGFR3-related chondrodysplasias. Bone. 2004 Jan;34(1):26-36. doi: 10.1016/j.bone.2003.09.002. PMID: 14751560.
8. Wang Q, Green RP, Zhao G, Ornitz DM. Differential regulation of endochondral bone growth and joint development by FGFR1 and FGFR3 tyrosine kinase domains. Development. 2001 Oct;128(19):3867-76. PMID: 11585811.
9. Segev O, Chumakov I, Nevo Z, Givol D, Madar-Shapiro L, Sheinin Y, Weinreb M, Yayon A. Restrained chondrocyte proliferation and maturation with abnormal growth plate vascularization and ossification in human FGFR-3(G380R) transgenic mice. Hum Mol Genet. 2000 Jan 22;9(2):249-58. doi: 10.1093/hmg/9.2.249. PMID: 10607835.
10. Matsushita T, Wilcox WR, Chan YY, Kawanami A, Bükülmez H, Balmes G, Krejci P, Mekikian PB, Otani K, Yamaura I, Warman ML, Givol D, Murakami S. FGFR3 promotes synchondrosis closure and fusion of ossification centers through the MAPK pathway. Hum Mol Genet. 2009 Jan 15;18(2):227-40. doi: 10.1093/hmg/ddn339. Epub 2008 Oct 15. PMID: 18923003; PMCID: PMC2638772.
11. Julliand S, Boulé M, Baujat G, Ramirez A, Couloigner V, Beydon N, Zerah M, di Rocco F, Lemerrer M, Cormier-Daire V, Fauroux B. Lung function, diagnosis, and treatment of sleep-disordered breathing in children with achondroplasia. Am J Med Genet A. 2012 Aug;158A(8):1987-93. doi: 10.1002/ajmg.a.35441. Epub 2012 Jun 18. PMID: 22711495.

12. Tenconi R, Khirani S, Amaddeo A, Michot C, Baujat G, Couloigner V, De Sanctis L, James S, Zerah M, Cormier-Daire V, Fauroux B. Sleep-disordered breathing and its management in children with achondroplasia. Am J Med Genet A. 2017 Apr;173(4):868-878. doi: 10.1002/ajmg.a.38130. Epub 2017 Feb 27. PMID: 28239978.
13. Reid CS, Pyeritz RE, Kopits SE, Maria BL, Wang H, McPherson RW, Hurko O, Phillips JA 3rd, Rosenbaum AE. Cervicomedullary compression in young patients with achondroplasia: value of comprehensive neurologic and respiratory evaluation. J Pediatr. 1987 Apr;110(4):522-30. doi: 10.1016/s0022-3476(87)80542-5. PMID: 3559799.
14. Holzman, R. S., Mancuso, T. J., & Polaner, D. M. (2008). A Practical Approach to Pediatric Anesthesia. 1st Edition. Philadelphia, USA: Lippincott Williams and Wilkins.
15. Legeai-Mallet L, Savarirayan R. Novel therapeutic approaches for the treatment of achondroplasia. Bone. 2020 Dec;141:115579. doi: 10.1016/j.bone.2020.115579. Epub 2020 Aug 11. PMID: 32795681.
16. Fafilek B, Bosakova M, Krejci P. Expanding horizons of achondroplasia treatment: current options and future developments. Osteoarthritis Cartilage. 2021 Dec 2:S1063-4584(21)00980-8. doi: 10.1016/j.joca.2021.11.017. Epub ahead of print. PMID: 34864168.
17. Delaire J, Schendel SA, Tulasne JF. An architectural and structural craniofacial analysis: a new lateral cephalometric analysis. Oral Surg Oral Med Oral Pathol. 1981 Sep;52(3):226-38. doi: 10.1016/0030-4220(81)90252-8. PMID: 6945527.
18. Rijken BFM, Lequin MH, de Rooi JJ, van Veelen MC, Mathijssen IMJ. Foramen magnum size and involvement of its intraoccipital synchondroses in Crouzon syndrome. Plast Reconstr Surg. 2013 Dec;132(6):993e-1000e. doi: 10.1097/PRS.0b013e3182a8077e. PMID: 24281646.
19. Tahiri Y, Paliga JT, Vossough A, Bartlett SP, Taylor JA. The spheno-occipital synchondrosis fuses prematurely in patients with Crouzon syndrome and midface hypoplasia compared with age- and gender-matched controls. J Oral Maxillofac Surg. 2014 Jun;72(6):1173-9. doi: 10.1016/j.joms.2013.11.015. Epub 2013 Nov 22. PMID: 24480760.
20. Coll G, Sakka L, Botella C, Pham-Dang N, Collet C, Zerah M, Arnaud E, Di Rocco F. Pattern of Closure of Skull Base Synchondroses in Crouzon Syndrome. World Neurosurg. 2018 Jan;109:e460-e467. doi: 10.1016/j.wneu.2017.09.208. Epub 2017 Oct 10. PMID: 29024761.
21. R Core Team. (2021). R: A language and environment for statistical computing. R Foundation for Statistical Computing, Vienna, Austria. URL https://www.R-project.org/.
22. Schlager, S. (2017). Morpho and Rvcg – Shape Analysis in R. In Zheng G, Li S, Szekely G (eds.), Statistical Shape and Deformation Analysis, 217–256. Academic Press.
23. Adams D, Collyer M, Kaliontzopoulou A, Baken E. (2021). Geomorph: Software for geometric morphometric analyses. R package version 4.0.
24. Baken E, Collyer M, Kaliontzopoulou A, Adams D. (2021). gmShiny and geomorph v4.0: new graphical interface and enhanced analytics for a comprehensive morphometric experience.
25. Collyer ML, Adams DC. (2021). RRPP: Linear Model Evaluation with Randomized Residuals in a Permutation Procedure, R package version 0.6.2.
26. Venables WN, Ripley BD. (2002). Modern Applied Statistics with S, Fourth edition. Springer, New York.

27. Uliel, S., Tauman, R., Greenfeld, M., & Sivan, Y. (2004). Normal polysomnographic respiratory values in children and adolescents. Chest, 125(3), 872-878.
28. Mangiafico S. (2021). Rcompanion: Functions to support extension education program evaluation in R.
29. Ornitz DM, Marie PJ. Fibroblast growth factor signaling in skeletal development and disease. Genes Dev. 2015 Jul 15;29(14):1463-86. doi: 10.1101/gad.266551.115. PMID: 26220993; PMCID: PMC4526732.
30. Rousseau F, Bonaventure J, Legeai-Mallet L, Schmidt H, Weissenbach J, Maroteaux P, Munnich A, Le Merrer M. Clinical and genetic heterogeneity of hypochondroplasia. J Med Genet. 1996 Sep;33(9):749-52. doi: 10.1136/jmg.33.9.749. PMID: 8880574; PMCID: PMC1050728.
31. Bellus GA, McIntosh I, Smith EA, Aylsworth AS, Kaitila I, Horton WA, Greenhaw GA, Hecht JT, Francomano CA. A recurrent mutation in the tyrosine kinase domain of fibroblast growth factor receptor 3 causes hypochondroplasia. Nat Genet. 1995 Jul;10(3):357-9. doi: 10.1038/ng0795-357. PMID: 7670477.
32. M. Muenke, K.W. Gripp, D.M. McDonald-McGinn, K. Gaudenz, L.A. Whitaker, S.P. Bartlett, et al., A unique point mutation in the fibroblast growth factor receptor 3 gene (FGFR3) defines a new craniosynostosis syndrome, Am. J. Hum. Genet. 60 (3) (1997 Mar) 555–564.
33. Meyers GA, Orlow SJ, Munro IR, Przylepa KA, Jabs EW. Fibroblast growth factor receptor 3 (FGFR3) transmembrane mutation in Crouzon syndrome with acanthosis nigricans. Nat Genet. 1995 Dec;11(4):462-4. doi: 10.1038/ng1295-462. PMID: 7493034.
34. Cohen MM, Walker GF, Phillips C. A morphometric analysis of the craniofacial configuration in achondroplasia. *J Craniofac Genet Dev Biol Suppl*. 1985;1:139-165.
35. Onodera K, Niikuni N, Chigono T, Nakajima I, Sakata H, Motizuki H. Sleep disordered breathing in children with achondroplasia. *Int J Pediatr Otorhinolaryngol*. 2006;70(3):453-461. doi:10.1016/j.ijporl.2005.07.016
36. Komla-Ebri D, Dambroise E, Kramer I, Benoist-Lasselin C, Kaci N, Le Gall C, Martin L, Busca P, Barbault F, Graus-Porta D, Munnich A, Kneissel M, Di Rocco F, Biosse-Duplan M, Legeai-Mallet L. Tyrosine kinase inhibitor NVP-BGJ398 functionally improves FGFR3-related dwarfism in mouse model. J Clin Invest. 2016 May 2;126(5):1871-84. doi: 10.1172/JCI83926. Epub 2016 Apr 11. PMID: 27064282; PMCID: PMC4855917.
37. Madeline LA, Elster AD. Postnatal development of the central skull base: normal variants. Radiology. 1995 Sep;196(3):757-63. doi: 10.1148/radiology.196.3.7644640. PMID: 7644640.
38. Wei, X., Hu, M., Mishina, Y., & Liu, F. (2016). Developmental regulation of the growth plate and cranial synchondrosis. Journal of dental research, 95(11), 1221-1229.
39. Goldstein, J. A., Paliga, J. T., Wink, J. D., Bartlett, S. P., Nah, H. D., & Taylor, J. A. (2014). Earlier evidence of spheno-occipital synchondrosis fusion correlates with severity of midface hypoplasia in patients with syndromic craniosynostosis. Plastic and reconstructive surgery, 134(3), 504-510.
40. Mondal A, Mandal B, Das RN, Chatterjee U, Mukherjee S. Thanatophoric dysplasia type 1 with temporal lobe dysplasia: Report of a case along with differential diagnosis. Indian

J Pathol Microbiol. 2021 Oct-Dec;64(4):776-779. doi: 10.4103/IJPM.IJPM_917_20. PMID: 34673602.
41. Khonsari RH, Delezoide AL, Kang W, Hébert JM, Bessières B, Bodiguel V, Collet C, Legeai-Mallet L, Sharpe PT, Fallet-Bianco C. Central nervous system malformations and deformations in FGFR2-related craniosynostosis. Am J Med Genet A. 2012 Nov;158A(11):2797-806. doi: 10.1002/ajmg.a.35598. Epub 2012 Sep 17. PMID: 22987770.
42. DiMario, F. J., Ramsby, G. R., Burleson, J. A., & Greensheilds, I. R. (1995). Brain morphometric analysis in achondroplasia. Neurology, 45(3), 519-524.
43. Sisk, E. A., Heatley, D. G., Borowski, B. J., Leverson, G. E., & Pauli, R. M. (1999). Obstructive sleep apnea in children with achondroplasia: surgical and anesthetic considerations. Otolaryngology—Head and Neck Surgery, 120(2), 248-254.
44. Eswarakumar, V. P., Horowitz, M. C., Locklin, R., Morriss-Kay, G. M., & Lonai, P. (2004). A gain-of-function mutation of Fgfr2c demonstrates the roles of this receptor variant in osteogenesis. Proceedings of the National Academy of Sciences, 101(34), 12555-12560.
45. Lam, A. S., Liu, C. C., Deutsch, G. H., Rivera, J., Perkins, J. A., Holmes, G., … & Dahl, J. P. (2021). Genotype–phenotype correlation of tracheal cartilaginous sleeves and Fgfr2 mutations in mice. The Laryngoscope, 131(4), E1349-E1356.
46. Hines, E. A., Jones, M. K. N., Harvey, J. F., Perlyn, C., Ornitz, D. M., Sun, X., & Verheyden, J. M. (2019). Crouzon syndrome mouse model exhibits cartilage hyperproliferation and defective segmentation in the developing trachea. Science China Life Sciences, 62(10), 1375-1380.
47. Faria, P. T. M., Ruellas, A. C. D. O., Matsumoto, M. A. N., Anselmo-Lima, W. T., & Pereira, F. C. (2002). Dentofacial morphology of mouth breathing children. Brazilian Dental journal, 13(2), 129-132.
48. Delaire, J. (1997). Maxillary development revisited: relevance to the orthopaedic treatment of Class III malocclusions. Eur J Orthod 19(3):289-311.
49. Khirani S, Amaddeo A, Griffon L, Lanzeray A, Teng T, Fauroux B. Follow-Up and Monitoring of Children Needing Long Term Home Ventilation. Front Pediatr. 2020 Jun 22;8:330. doi: 10.3389/fped.2020.00330. PMID: 32656168; PMCID: PMC7322995.

Declaration section:

Ethics approval and consent to participate

The study was performed in accordance with the rules of local ethics committees (Comité d'Ethique Necker Enfants Malades). An informed consent to participate in the study was obtained from patient's parents.

Consent for publication

A written informed consent for publication was obtained from patient's parents prior to submission.

Availability of data and materials

All data generated or analysed during this study are included in this published article (and its supplementary information files).

Competing interests

The authors declare that they have no competing interests.

Funding

Not applicable.

Authors' contributions

Anne Morice contributed to the conception, design of the study, acquisition, analyses, and data interpretation, and has drafted the work.
Maxime Taverne contributed to the design of the study, the analyses and data interpretation and participated in the drafting of the work.
Sophie Eche and Lucie Griffon contributed to data collection, acquisition and analyses.
Nicolas Leboulanger, Vincent Couloigner, Geneviève Baujat, Valérie Cormier-Daire and Arnaud Picard contributed to the acquisition and interpretation of the data.
Brigitte Fauroux contributed to the study design, the data interpretation, and to the revision of the work.
Laurence Legeai-Mallet contributed to the data interpretation and the critical revision of the work.

Natacha Kadlub contributed to the study design, the data collection and interpretation, and the critical revision of the work.
Roman Hossein Khonsari contributed to the study design, data interpretation and the critical revision of the work.
All coauthors have approved the submitted version and agreed both to be personally accountable for the author's own contributions and to ensure that questions related to the accuracy or integrity of any part of the work, even ones in which the author was not personally involved, are appropriately investigated, resolved, and the resolution documented in the literature.

Acknowledgements
Special thanks to Necker - Enfants Malades hospital consultants who contributed to data collection: Pr. Nathalie Boddaert (medical imaging), Dr Giovanna Paternoster (neurosurgery), and to Pr. Martin Biosse-Duplan (dentist, Bretonneau hospital, Paris).
Anne Morice's PhD position was supported by a 'Poste d'Accueil' grant from INSERM, France, and from an 'Impulsion Recherche' grant from the 'Filière de Santé Maladies Rares TeteCou'.
Maxime Taverne's post-doctoral position was supported by a 2020 'Emergence' grant from the 'Mairie de Paris'.

3. Conclusions et perspectives

Nous avons montré, dans le cadre de l'achondroplasie, que le phénotype craniofacial et mandibulaire était plus sévère chez les patients en fin de croissance que chez les plus jeunes. Nos résultats montrent également dans ce cadre, une corrélation significative entre la sévérité de la rétrusion maxillomandibulaire et la sévérité du syndrome d'apnées obstructives du sommeil. Nous allons poursuivre cette étude, avec l'évaluation de l'impact des mesures orthodontiques et orthognatiques visant à corriger la rétrusion maxillaire, sur le syndrome d'apnées obstructives du sommeil.

Nos études morphométriques ont montré que les mutations activatrices gain-de-fonction dans les gènes *FGFR2* et *FGFR3* perturbent la morphologie mandibulaire à la fois dans le cadre des chondrodysplasies et dans celui des craniosténoses. Les différences phénotypiques significatives observées selon le syndrome (écart intercondylien, hauteur ramique, angle gonique et écart intergoniaque, hauteur symphysaire), renforcent l'hypothèse de corrélation génotype phénotype dans ce contexte.

Nos résultats confirment que les mutations activatrices *FGFR2* et *FGFR3* perturbent la formation et la croissance mandibulaire. Cet impact avait déjà été démontré dans des modèles murins d'achondroplasie, et de craniosténose FGFR2 (syndrome d'Apert, Crouzon et Pfeiffer). Nous avons comme perspective de conduire des études similaires dans l'hypochondroplasie. De multiples mutations ont été associées à l'hypochondroplasie, et une grande variabilité phénotypique est observée. L'étude de la morphologie craniofaciale et mandibulaire chez les patients porteurs d'hypochondroplasie permettra de mettre en évidence d'éventuelles corrélations génotype phénotype, et une meilleure compréhension de l'impact de ces mutations dans le cadre du développement craniofacial et mandibulaire.

B. Partie 2 : données expérimentales : modèle murin d'hypochondroplasie

1. Article 3

Hypochondroplasia gain-of-function mutation in FGFR3 causes defective bone mineralization in mice

Léa Loisay [1*], Davide Komla-Ebri [2,3*], Anne Morice [1], Yann Heuze [4], Camille Viaut[1], Amélie de la Séglière[1],Danny Chan[5], Lamouroux Audrey[6], Genevieve Baujat[1,7], J. H. Duncan Bassett[2], Graham R. Williams [2], Laurence Legeai-Mallet[1#]

1-Université de Paris Cité, *Imagine* Institute, Laboratory of Molecular and Physiopathological Bases of Osteochondrodysplasia. INSERM UMR 1163, Paris, France.

2- Molecular Endocrinology Laboratory, Department of Metabolism Digestion and Reproduction, Imperial College London, W12 0NN London, United Kingdom.

3- UCB Pharma, Slough, UK

4-UMR5199 PACEA, CNRS, MC, Université de Bordeaux, Pessac, France.

5-School of Biomedical Sciences, The University of Hong Kong, Hong Kong, China

6- Department of Medical genetics, CHU Arnaud De Villeneuve, Montpellier, France

7-Department of Medical genetics. French Reference Center for Skeletal Dysplasia, AP-HP, Necker Enfants Malades Hospital, Paris, France.

*Equally contributors

Hypochondroplasia gain-of-function mutation in FGFR3 causes defective bone mineralization in mice

Authors

Léa Loisay [1*], Davide Komla-Ebri [2,3*], Anne Morice [1], Yann Heuze [4], Camille Viaut[1], Amélie de la Seiglière[1], Danny Chan[5], Lamouroux Audrey[6], Genevieve Baujat[1,7], J. H. Duncan Bassett[2], Graham R. Williams [2], Laurence Legeai-Mallet[1#]

1-Université de Paris Cité, *Imagine* Institute, Laboratory of Molecular and Physiopathological Bases of Osteochondrodysplasia. INSERM UMR1163, Paris, France.

2- Molecular Endocrinology Laboratory, Department of Metabolism Digestion and Reproduction, Imperial College London, W12 0NN London, United Kingdom.

3- UCB Pharma, Slough, UK

4-UMR5199 PACEA, CNRS, MC, Université de Bordeaux, Pessac, France.

5-School of Biomedical Sciences, The University of Hong Kong, Hong Kong, China

6- Department of Medical genetics, CHU Arnaud De Villeneuve, Montpellier, France

7-Department of Medical genetics. French Reference Center for Skeletal Dysplasia, AP-HP, Necker Enfants Malades Hospital, Paris, France.

*Equally contributors

Abstract (168 words)

Hypochondroplasia (HCH) is a mild dwarfism caused by missense mutations in Fibroblast Growth Factor Receptor 3 (FGFR3), with the majority of cases resulting from a heterozygous p.Asn540Lys gain-of-function mutation. Here, we report the generation and characterization of the first mouse model (*Fgfr3*$^{Asn534Lys/+}$) of HCH. *Fgfr3*$^{Asn534Lys/+}$ mice exhibited progressive dwarfism and impairment of the synchondroses of the cranial base resulting in defective formation of the foramen magnum. The appendicular and axial skeletons were both severely affected and we demonstrated an important role of FGFR3 in regulation of cortical and trabecular bone structure. Trabecular bone mineral density (BMD) of long bones, and vertebral body was decreased, but cortical bone BMD increased with age in both tibiae and femurs. These findings demonstrate that bones in *Fgfr3*$^{Asn534Lys/+}$ mice due to FGFR3 activation exhibit some characteristics of osteoporosis. These findings highlight the deleterious impact of *Fgfr3* gain of function mutation for long bone modelling during development and aging, and have an important impact on the management of adult patients with hypochondroplasia.

Introduction

Hypochondroplasia (HCH; MIM#146000) is an autosomal dominant skeletal disorder characterized by short-limbed dwarfism. The clinical and radiological features of this dwarfism are milder than achondroplasia (ACH, MIM # 100800), a severe form of dwarfism and those of thanatophoric dysplasia (TDI, MIM # 187600, TDII, MIM # 187601), a lethal dwarfism. HCH is characterized by disproportionate short stature, rhizomelic short arms and legs, mild and joint laxity. Macrocephaly, prognathism, premature fusion of synchondroses and foramen magnum stenosis are frequently reported in FGFR3-related chondrodysplasia (1–4). The radiologic features include shortening of the long bones with mild metaphyseal flare, narrowing of the inferior lumbar interpedicular distance, short broad femoral neck and squared shortened ilia. Spinal defects are frequently reported in children and adults ACH and HCH patients and are characterized by kyphosis, scoliosis and lumbar lordosis due to anomalies of the vertebral bodies, and intervertebral discs (IVD) (5). Obstructive apnea and intellectual disability are also observed in HCH (6).

These clinical signs are generally less pronounced in HCH than those seen with ACH and may not be apparent until early or middle childhood. The incidence and prevalence of HCH is similar to ACH which occurs in 1 in 15 000 newborns; more than 250 000 people worldwide have been diagnosed with HCH. Most HCH cases (70%) are caused by a common heterozygous gain-of-function mutation (p.Asn540Lys) in the tyrosine kinase domain of fibroblast growth factor receptor 3 (FGFR3) (7, 8). This receptor tyrosine kinase (RTK) is a cell surface receptor that binds and responds to fibroblast growth factors (FGFs). These ligands bind to FGFR3, forming cross-linked dimers that trigger tyrosine kinase activation of FGFR3. Structural characterization studies highlighted the activating effect of the p.Asn540Lys mutation. This mutation drives the receptor into the active state by disengaging the autoinhibitory molecular brake at the kinase hinge domain (9, 10). Recently, it was demonstrated that thermostability of the receptor explains mild skeletal phenotype of HCH compared to less activating mutations localized in the activating loop responsible for more severe dwarf phenotype (11).

FGFR3 is a negative regulator of bone growth (12, 13) and missense *FGFR3* mutations induce defective long bone elongation mainly due to abnormal proliferation and differentiation of growth plate chondrocytes. Many intracellular signaling pathways are triggered by FGFR3, among them the MAPK (mitogen-activated protein kinase) pathway has been shown to regulate chondrocyte differentiation and the STAT (signal transducer and activator of transcription

protein) pathway regulates chondrocyte proliferation (14). Their impact on chondrogenesis has also been clearly shown in several *Fgfr3* mouse models recapitulating ACH, TDI and TDII (15–21). FGF signaling controls not only chondrogenesis but also osteogenesis. FGFR1 and FGFR2 and FGFR3 are expressed in osteogenic lineages, perichondrium and periosteum (22), and in osteocytes isolated from cortical bone (23). Mice lacking *Fgfr1* and *Fgfr2* in mature osteoblasts or osteocytes display increased cortical bone remodeling and high bone mass (24), thus, suggesting a critical homeostatic role for FGFRs in developing and adult bone. The role of FGFR3 in bone formation has been studied in a knock-out mouse model ($Fgfr3^{-/-}$), which displayed decreased trabecular bone mass (25) and in a knock-out zebrafish model ($fgfr3^{lof/lof}$) which displayed a defect in the craniofacial skeleton formation (26). *Fgfr3* activation in mouse models of ACH ($Fgfr3^{G369C/+}$, $Fgfr3^{G380R/G380R}$, $Fgfr3^{Y367C/+}$) also exhibited bone formation and femoral bone mass decrease and alteration of bone microarchitecture in growing and adult mice (20, 27, 28).

It is currently well accepted that *Fgfr3* gain-of-function mutations play a key role in the formation of the skeleton in both chondrodysplasia and craniosynostosis (29). Among the FGFR3-related osteochondrodysplasia, numerous laboratories have developed research programs using *Fgfr3* knock-in mouse models to understand biological mechanisms responsible for ACH and to offer therapeutic approaches for these disorders (14, 30). Conversely, very limited experimental and clinical studies have been conducted to determine the key features of the hypochondroplasia phenotype. So far, the lack of mouse models has ~~so far~~ restricted the progression in understanding the pathogenesis of HCH.

In this study, we generated the first mouse model of HCH, expressing a homologous mutation to that most frequently found in HCH patients p.Asn540Lys. This HCH mouse model ($Fgfr3^{Asn534Lys/+}$) ubiquitously expresses the mutant N534K FGFR3 protein, exhibits a mild dwarfism. Thus, the $Fgfr3^{Asn534Lys/+}$ mouse model offers a unique opportunity to study the impact of FGFR3 gain-of-function mutation in both endochondral and membranous ossification processes and to decipher its impact on skeletal development during childhood and adulthood. Here, we demonstrate that the presence of the *Fgfr3* p.Asn534Lys mutation impairs the function of both long bone cartilage and cranial synchondroses resulting in defective bone growth and foramen magnum formation. Similarly, the spine was severely affected with abnormalities of the intervertebral discs visible from birth and throughout adulthood. Unexpectedly, analysis of osteogenesis, in adult $Fgfr3^{Asn534Lys/+}$ mice, demonstrated opposing effects of the p.Asn534Lys mutation in the trabecular and cortical compartments of long bones.

As observed previously in juvenile ACH and TD mice (20, 27, 28), the HCH gain of function mutation resulted in decreased trabecular bone mineral density (BMD) in tibia and femur and vertebral bodies. However, in contrast, we observed increased tibial and femoral cortical BMD in adult *Fgfr3*$^{Asn534Lys/+}$ mice, and demonstrated that long bones are brittle with reduced toughness. These data suggest that the N534K mutation results in differential regulation of mature osteoblasts or osteocytes in trabecular and cortical bone. Consistent with this, transcriptional profiling of the femoral cortical bone demonstrated a downregulation of markers of the osteoblast lineage and high-resolution micro-Computed Tomographic (μCT) analyses of cortical bone highlighted anomalies of the osteocyte lacunae in the *Fgfr3*$^{Asn534Lys/+}$ mouse model of HCH.

Taken together these data suggest that HCH patients may have a previously unrecognised increased risk of fracture and this may have important implications for their medical follow up and treatment during adulthood and ageing.

Results

Fgfr3$^{Asn534Lys/+}$ mice display a dwarf phenotype that recapitulates the clinical features of HCH patients

The skeletal phenotype of HCH patients harboring the Asn540Lys mutation was investigated by X-ray (Figure 1A). Shortened long bones with moderate rhizomelia (≤ 1 percentile) are visible by 34 weeks of gestation and metaphyseal enlargement, trident acetabula and squared ilia were also identified (Figure 1A). The X-rays of 3-, 5- and 8-year-old HCH patients suggested significant variability in the clinical features of HCH (Figure 1A, b-d). In the 3 and 5-year-old female patients (Figure 1A b and c) the height was -2SD (standard deviation) below the age and sex matched mean and long bones were short and broad. By contrast, in the 8-year-old male patient (Figure 1A d) the height was -4SD below the age and sex matched mean and the fibula was disproportionately long with obliquity of the distal tibia metaphyseal growth plate. The carpal bone age was also determined using the standard Greulich and Pyle atlas and was delayed in all patients. Furthermore, ulnar styloid is not mineralized yet at this age but we noted in the 3 patients the slight internal metaphysis enlargement of the distal ulna, with obliquity of the metaphyseal line, which lead to the styloid aspect frequently reported in older HCH patients (Figure 1B).

To further understand the impact of p. Asn540Lys on the skeleton during growth, we generated the first mouse model of HCH using Cre-loxP gene targeting. We introduced the most frequent HCH FGFR3 mutation p.Asn534Lys (corresponding to Asn540Lys in human) in the knock-in

Fgfr3$^{Asn534Lys/+}$ mouse model. Excision of the loxP cassette of the mouse line *Fgfr3*$^{+/loxp\ Asn534Lys}$ was achieved using the mouse line CMV-cre (31) (Supplemental Figure 1A). We confirmed the presence of the heterozygous Asn534Lys mutation in *Fgfr3*$^{+/Asn534Lys}$ (*Hch*) mice by DNA sequencing (Supplemental Figure 1B). Detailed skeletal phenotyping of the *Hch* mice was performed at multiple time points from birth to adulthood. X-ray analysis demonstrated a progressive skeletal phenotype in *Fgfr3*$^{Asn534Lys/+}$ mice from post-natal day 7 (P7) until P180 (Figure 1C). Studying tibia and femur lengths at birth, we noted a reduced length in *Fgfr3*$^{Asn534Lys/+}$ compared to *Fgfr3*$^{+/+}$ mice (-6.93% p=0.03 and -7.09% p=0.01) (Figure 1D). Long bones length remained consistently reduced across all analyzed time-points with the largest difference recorded at P60 (-28.33% in femurs p<0.0001, -28.65% in tibiae p<0.0001) (Figure 1E, Table 1). Body weight and naso-anal length were also decreased in *Fgfr3*$^{Asn534Lys/+}$ mice (Figure 1E, Table 1). At P60 body weight was reduced by 35% in *Fgfr3*$^{Asn534Lys/+}$ compared to controls (p<0.0001) (Figure 1E). The phenotype severity was progressive with the naso-anal length being similar to control at P7 (p=0.451) but reduced by 12% at P21 (p=0.0056), 14% at P60 (p<0.0001) and 9% at P180 (p<0.0001). These macroscopic and X-rays analyses demonstrate that the *Fgfr3*$^{Asn534Lys/+}$ mice recapitulate the phenotype of human HCH and exhibit a progressive dwarfism from birth and throughout adulthood.

Fgfr3$^{Asn534Lys/+}$ mice have important craniofacial abnormalities

We previously demonstrated craniofacial abnormalities in achondroplasia mouse model (32). Consistent with this, *Fgfr3*$^{Asn534Lys/+}$ mice exhibited abnormal skull morphology at P14 (Figure 2A). Mutant mice had a dome shaped-skull compared to wild-type mice length (-8.85%, p<0.0001), width (+3.82%, p=0.0070) and centroid size (-5,34%, p=0.0002) (Figure 2B, Supplemental Table 1). Geometric morphometric analyses of cranial landmark coordinates confirmed significant shape differences between *Fgfr3*$^{Asn534Lys/+}$ mice and WT littermates (d=0.0926, p<0.0001) (Supplemental Figure 2A, Supplemental Table 1). Overall, *Fgfr3*$^{Asn534Lys/+}$ mice displayed a more globular skull shape with increased width and reduced length. Most of the differences were due to the size effect as seen with the decreased of centroid size measurement in *Fgfr3*$^{Asn534Lys/+}$ mice (Figure 2B-2C, Supplemental Figure 2A) which is a composite size measurement of the landmarks summary (33, 34). Allometry explained 73.3% of the shape variation expressed on PC1 and 56.1% of the total cranial shape variation distributed along PC1 to PC17 (Figure 2C, Supplemental Figure 2A). These results suggest that *Fgfr3*$^{Asn534Lys/+}$ mouse display abnormal craniofacial endochondral and intramembranous

ossification. Our previous work demonstrated mandibular defects in both mouse model (35) and patients with ACH (Morice et al 2020). The mandible is formed by both intramembranous and endochondral ossification. Geometric morphometric analyses of maxillomandibular landmark coordinates confirmed significant shape differences between *Fgfr3*$^{Asn534Lys/+}$ mice and controls (Supplemental Figure 2B) (d=0.0805, p<0.001). 3D representations of PCA (principal component) result show that, in *Fgfr3*$^{Asn534Lys/+}$ mice, the mandible was prognathic, and the intercondylar and intergonial distances were relatively wider compared to controls (Figure 2D). Our previous work shows a premature closure of the synchondroses in the *Fgfr3*$^{Y367C/+}$ mouse (36). Interestingly, skull base µCT and histological analyses revealed spheno-occipital synchondroses (SOS) and intrasphenoidal synchondrosis (ISS) fusion and partial fusion of the intra-occipital synchondroses (IOS) in *Fgfr3*$^{Asn534Lys/+}$ mice at P14 whereas synchondroses are patent in control animals (Figure 2E). Consistent with premature synchondrosis fusion, skull base length was decreased by 21% (p<0.0001) and foramen magnum area by 19% (p<0.0001) in *Fgfr3*$^{Asn534Lys/+}$ mice compared to controls (Figure 2F, Table 2). Additionally, foramen magnum shape was also abnormal in *Fgfr3*$^{Asn534Lys/+}$ mice (Figure 2G). These analyses demonstrate that *Fgfr3*$^{Asn534Lys/+}$ mice have abnormal endochondral ossification that results in premature fusion of the skull synchondroses (primary cartilage joints) leading to multiple craniofacial anomalies.

Fgfr3$^{Asn534Lys/+}$ mice have abnormally shaped vertebrae and intervertebral discs that exhibit reduced vertebral bone mass and strength

We previously reported that *Fgfr3* activating mutations lead to abnormalities in both vertebra and IVD in *Fgfr3*$^{Y367C/+}$ mouse model (36). For this reason, we hypothesized that the activating mutation p.Asn534Lys could affect the axial skeleton. µCT analysis of the 5th lumbar vertebrae and IVDs in 10-week-old male mice demonstrated 12% reduction in vertebral body length (p<0.0001) (Figure 3A), 8% reduction in interpedicular distance (p=0.0037) (Figure 3B), and 14% reduction in canal area (p=0.037) in *Fgfr3*$^{Asn534Lys/+}$ mice compared to WT littermates. Furthermore, morphometric analysis demonstrated that L5 vertebrae from *Fgfr3*$^{Asn534Lys/+}$ and WT mice differed significantly in shape PC1 (35.980% of the total variance) and PC2 (19,856% of the total variance) (d=0.0872, p=0.0005) (Supplemental Figure 3B). Vertebral trabecular bone parameters showed 18% reduction in bone volume per tissue volume (BV/TV) (p<0.0001), 15% decrease in trabecular thickness (Tb.Th) (p<0.0001), and 7% reduction in BMD (p<0.0001) in *Fgfr3*$^{Asn534Lys/+}$ compared to WT mice (Figure 3C, Supplemental table 3).

Consistent with these findings, lumbar vertebrae biomechanical testing demonstrated a 22% reduction in maximum load ($p<0.04$) and a 34% ($p<0.0044$) decrease in stiffness in *Fgfr3*$^{Asn534Lys/+}$ compared to WT mice (Figure 3D). These data demonstrate that *Fgfr3*$^{Asn534Lys/+}$ mice have reduced vertebral bone mass and strength and suggest that HCH patients may be at increased risk of vertebral fractures.

Intervertebral disc (IVD), which is a cartilaginous joint localized between vertebral bodies, is severely affected in patient with ACH (5). Thus, we examined the IVD structure on histological sections of *Fgfr3*$^{Asn534Lys/+}$ and control mice at P14. Histological analysis of L5 to L6 lumbar vertebra sections, stained with Safranin-O or hematoxylin and eosin, demonstrated IVD deformation with "reversed herniation" of the inner annulus fibrosus (AF) into the nucleus pulposus (NP) region (Figure 3E). This NP "reversed herniation" was visible in histological sections from P1 to P90 (Supplemental Figure 3B). To confirm FGFR3 role in IVD, we perform FGFR3 immunostaining on P14 mice IVD. FGFR3 is normally expressed in NP and AF in WT littermates. We notice an overexpression of FGFR3 in *Fgfr3*$^{Asn534Lys/+}$mice (Supplemental Figure 3C). To quantify this IVD abnormality, we performed High-Resolution Episcopic Microscopy (HREM). 3D rendering of the L5 lumbar vertebral body and IVD demonstrated that the NP was abnormally shaped (sphericity 0.75 vs 0.65) in *Fgfr3*$^{Asn534Lys/+}$ compared to WT mice ($p<0.008$) (Figure 3F). These data show that FGFR3 is involved in IVD development and *Fgfr3*$^{Asn534Lys/+}$mice have IVD abnormalities. Those results suggest that HCH patients may be at increased risk of developing a degenerative disc disease.

Fgfr3$^{Asn534Lys/+}$ mice have impaired chondrocyte differentiation due to increased MAPK signalling

We next sought to study chondrocyte proliferation and differentiation in the cartilage growth plate. It is well known that the endochondral bone formation is severely affected by *FGFR3* activating mutations and this was demonstrated in various *Fgfr3* mouse models of ACH and TD (17–19, 21). We found no obvious difference in *Fgfr3*$^{Asn534Lys/+}$ epiphyseal growth plate structures of femur compared to controls at P7, thus confirming the absence of severe skeletal phenotype after birth (data not shown). Histological analysis of growth plate sections at P14 and P21 demonstrated progressive disorganization of the growth plate in *Fgfr3*$^{Asn534Lys/+}$ mice compared to WT from P14 that was characterized by reduced hypertrophic zone width and delayed secondary ossification center (SOC) formation (Figure 4A). µCT analysis confirmed a 43% reduction in SOC volume per epiphyseal volume at P14 in *Fgfr3*$^{Asn534Lys/+}$ mice

(p=0,0159) (Figure 4B). To determine the underlying cellular mechanism, we investigated chondrocyte differentiation by expression of the late-stage differentiation marker collagen type X, which demonstrated smaller hypertrophic chondrocytes due to a lack of cell swelling in *Fgfr3*$^{Asn534Lys/+}$ mice compared to WT (Figure 3C) and a 20% reduction in the total area of collagen type X positive cells (p=0.0401) (Figure 4C).

By contrast, chondrocyte proliferation in *Fgfr3*$^{Asn534Lys/+}$ mice investigated by both Ki67 staining and BrdU incorporation did not differ from controls at either P14 or P21 (Figure 4D). To further examine the underlying molecular mechanism we analyzed Erk1/2 phosphorylation *in vivo* and *in vitro* as MAPK activation is known to inhibit chondrocyte differentiation in ACH and TD (36–38). pErk1/2 immunostaining was increased by 13% in growth plate sections from *Fgfr3*$^{Asn534Lys/+}$ mice compared to WT (p=0.048) (Figure 4E). Consistent with this, fibroblast growth factor 2 (FGF2) treatment of primary chondrocyte cultures from *Fgfr3*$^{Asn534Lys/+}$ mice resulted in increased and sustained Erk1/2 phosphorylation compared to control cells (p<0.05) (Figure 4E). These data demonstrate that anomalies of the growth plate of *Fgfr3*$^{Asn534Lys/+}$ mice are predominantly a consequence of impaired chondrocyte differentiation and hypertrophy rather than major abnormal proliferation.

Long bones from *Fgfr3*$^{Asn534Lys/+}$ mice have reduced trabecular bone volume but increased cortical bone volume and mineralization

To determine the effect of the *Hch* mutation in the appendicular skeleton, µCT analyses of femurs (Figure 5, Supplemental Figure 4, Supplemental Tables 2, 4) and tibiae (Figure 6, Supplemental Figure 5, Supplemental Tables 2, 5) from WT and *Fgfr3*$^{Asn534Lys/+}$ mice were performed at P42, P70, P180. Trabecular analysis of femurs showed reduced BV/TV (30-42%, p=0.0038 to p<0.0002), decreased Tb.N (10-17%, p=0.0007 to p<0.0001) and increased Tb.Sp (12-28%, p=0.0342 to p<0.0001) at all ages, decreased Tb.Th (13-17%, p=0.0009 to p<0.0001) at P70 and P180 and decreased trabecular BMD (4% p=0.0013), at P70 (Figure 5B, Supplemental Figure 4). BMD (p=0.787) and Tb.Th (p=0.4208) were not significantly different in P42 mice which indicate that the phenotype was more severe in older animals.

Interestingly, none of the tibia trabecular bone measurement was different at P42, whereas we detected results from tibia trabecular analysis similar to femurs (Figure 6B, Supplemental Figure 4) at P70 and P180. We observed reduced BV/TV (24-38%, p<0.0001) and Tb.Th (7-15%, p<0.001).

We also evaluated the cortical bone parameters of femoral and tibial mid-shafts (Figure 5C, 6C) (Supplemental Figure 4 data from P42 to P180). Femur and tibia cortical analysis showed decreased total diameter (8-11%, p=0.0003 to p<0.0001) at all ages.

Surprisingly, in the femoral bone, we observed an increase of cortical BMD (6-10%, p=0.002 to p<0.0001) at all ages in mutant compared to wild-type mice (Figure 5C, Supplemental Table 4), whereas a higher BMD was observed in tibia only at P180 (6%, p=0.0077) in mutants (Figure 6C). We also observed an increased cortical bone volume per tissue volume (17%, p<0.0001) and C.Th/Total diameter (4-9%, p<0.0001) at P180, for both femur (Figure 5C, Supplemental Figure 5) and tibia (Figure 6C, Supplemental Figure 5).

Altogether, these results suggest that a high cortical bone mineral density is a novel pathological feature of HCH, concordant with the lower cortical BMD observed in the *Fgfr3* knock-out model (25).

Fgfr3$^{+/Asn534Lys}$ mice display osteoblast and osteocyte abnormalities

To further investigate the cellular and molecular mechanisms underlying these skeletal abnormalities in *Fgfr3*$^{+/Asn534Lys}$ mice, we investigated osteoblastic and osteoclastic markers expression. We performed RT-qPCR using RNA isolated from femur cortical bone. Osteoblast lineage characteristic gene expressions were decreased in *Fgfr3*$^{+/Asn534Lys}$ samples compared to WT. These genes included *Osterix (OSX*) (p=0.0411), Runt-related transcription factor 2 (*Runx2*) (p=0.0006), *Osteocalcin (Ocn*) (p=0.0262) and *Collagen type I (Col I*) (p=0.0047). By contrast, negative regulators of WNT signaling, including *Sclerostin* (*SOST*) (p=0.9372) and Dickkopf WNT Signaling Pathway Inhibitor 1 (*DKK1*) (p=0.2468) did not differ. (Figure 7A). The expression of the osteoclast marker, *Tartrate-Resistant Acid Phosphatase (TRAP*), did not differ between *Fgfr3*$^{+/Asn534Lys}$ and WT mice (p=0.5350) (Figure 7A). Furthermore, analysis of TRAP-stained distal femur sections from *Fgfr3*$^{+/Asn534Lys}$ and WT mice at P60 showed no difference in osteoclast parameters (Figure 7B).

To investigate the osteocyte cortical lacunar network, we performed high-resolution µCT analyses of femur midshaft cortical bone from *Fgfr3*$^{+/Asn534Lys}$ and WT male mice at P180. *Fgfr3*$^{+/Asn534Lys}$ mice showed a 40% decrease in cortical microporosity (Ct.µPo.) (p<0.0001), 29% decrease in lacunae number per bone volume (Lc.N/BV) (p=0.0002), and 16% decrease in median lacunae volume (Lc.V) (p<0.0001) compared to WT (Figure 7C). The distribution of lacuna sizes also differed in mutant mice displaying a higher percentage of small lacunae (100-200 µm^3): 55% in *Fgfr3*$^{+/Asn534Lys}$ vs 41% in WT and a lower percentage of large lacunae (400-2000 µm^3): 10% in *Fgfr3*$^{+/Asn534Lys}$ vs 15% in WT (Figure 7C). Furthermore, the lacuna

shape showed increased sphericity (Lc.Sph) in mutant mice with a median of 0.579 in *Fgfr3*$^{+/Asn534Lys}$ vs 0.574 in WT mice (p<0.0001) (Figure 7C).

Together, these data demonstrate that *Fgfr3* p.Asn534Lys mutation results in abnormal osteoblast and osteocyte functions that lead to contrasting effects in trabecular and cortical bone.

Long bones from *Fgfr3*$^{Asn534Lys/+}$ mice have reduced strength and stiffness

To determine the effect of the FGFR3 p.Asn534Lys mutation on long bone strength, 3-point bend testing of tibia (Figure 8, Supplemental Table 6) from WT and *Fgfr3*$^{Asn534Lys/+}$ mice at P42, P70, P180 was performed. Biomechanical analysis showed reduced yield load (18-38%, p=0.0077 to p<0.0001), maximum load (24-37%, p=0.0126 to p<0.0001) and stiffness (37-53%, p=0.0014 to p<0.0001) at all, ages, and reduced toughness (Energy dissipated at Fracture) (37%, p<0.0001) and plastic work to total work (21%, p<0.0001) at P180. These data demonstrate that long bones in *Fgfr3*$^{Asn534Lys/+}$ mice are weak and flexible. In older animals the increased cortical thickness and mineralization also results in reduced toughness and a brittle phenotype. The latter finding was of particular interest since it demonstrated that a higher cortical bone mineral density in 6-months old tibiae was detrimental to their biomechanical performance.

Discussion

HCH is the mildest form of FGFR3-related chondrodysplasia. It was reported that patients who have the most frequent mutations (Asn540Lys) have a more severe form of dwarfism (8, 39–41). Currently, little is known about bone phenotype and growth in children with HCH. Various studies have described HCH patients with short stature, body disproportion, and relative macrocephaly (42). Our study was designed to elucidate the impact of the most common HCH mutation (Asn540Lys) on skeletal development and adult bone maintenance and strength, these functions remain completely unknown. To conduct this research program, we generated the first *Fgfr3*$^{Asn534Lys/+}$ mouse model expressing the Asn534Lys gain-of-function mutation.

FGFR3 regulates a wide range of physiological processes and its aberrant signaling has been linked to dwarfism (14), overgrowth (43) and several types of malignancies (44–46). Analysis of kinase activity of selected FGFR3 variants harboring missense mutations showed that Asn540Lys mutation resulted in a large increase of auto-phosphorylation (47). We confirmed

enhanced activation of this variant and MAPK pathway *in vitro* using primary chondrocytes isolated from the *Fgfr3*$^{Asn534Lys/+}$ rib cages and *in vivo* with pErk1/2 immunostaining.

We attempted to elucidate some HCH phenotypic traits. First, the dwarf phenotype observed in *Hch* mutant is more pronounced in older animals which is similar to the human pathology (8, 48). We confirmed that activating HCH mutation modified *Fgfr3*$^{Asn534Lys/+}$ mice skull shape by inducing macrocephaly and prognathism. Interestingly, we observed a significant decrease of the foramen magnum area due to a premature fusion of the synchondroses also observed in another FGFR3 gain-of-function mouse model (36). These findings are consistent with previous data demonstrating that FGFR3 and MAPK downstream signaling in chondrocyte promotes foramen magnum stenosis (49). Overall, these data identify important craniofacial abnormalities in *Fgfr3*$^{Asn534Lys/+}$mice and suggest that similar anomalies may be present in HCH patients.

During growth, we observed defects of the axial skeleton with structural anomalies of the IVD. Concomitant low bone mineral density of the lumbar vertebrae is also observed at adult stages. Interestingly, IVD normal architecture loss suggests that these anomalies are due to the key role of FGFR3 in controlling IVD development with an impact on NP and AF formation during embryonic development. Recently, FGFR3 has been described to be indispensable to NP development and proliferation (50). This phenotypic trait has not been described in HCH and could be further clinically explored.

As expected, FGFR3 strong activity impaired the endochondral ossification thus inducing a dysregulation of chondrocyte differentiation. The absence of visible defective proliferation during the post-natal period confirms that the reduced bone growth in *Hch* mouse model is due to the impairment of hypertrophic chondrocytes enlargement modulating by increased Erk1/2 activation (51). In the future, it will be relevant to investigate whether *Hch* hypertrophic chondrocytes undergo apoptosis and autophagic processes (52) and/or transdifferentiate into osteoblasts (53).

Usually, studies concerning FGFR3-related chondrodysplasias were mostly focused on growth plate cartilage from birth to puberty in young animals. Here, one of our concerns was to decipher the bone formation during adult period in *Hch* mouse model.

Previously, low BMD of the long bone (20, 28, 54) and an increased number of osteoclasts (27) in young animals expressing an *Fgfr3* gain-of-function mutation (G369C/+) was reported. However, *Fgfr3* knock-out mice showed osteopenia, reduced cortical thickness and an increased number of osteoclasts (25, 56). In contrast, *Fgfr3* deletion restricted to chondrocytes leads to increased bone mass by up-regulating osteogenesis and inhibiting osteoclastogenesis

(54). Finally, *Fgfr3* deficiency in osteoclast lineage cells lead to increased bone mass and impaired bone regeneration by inhibiting osteoclasts bone resorption activity (57). Taking advantage of the ubiquitous expression of *Fgfr3* pAsn534Lys gain-of-function mutation in *Hch* mice, we deeply analyzed the bone phenotype and demonstrated that *Fgfr3* activation did not modify osteoclasts expression, however it decreased bone mineral density (BMD), reduced BV/TV in the femur trabecular bone. Moreover, bone formation modifications were less obvious for the tibia. Femur mineralization is highly affected from 6 weeks to 6 months of age in mutant compared to control. However, we observed a less established bone phenotype in tibia between two months and six months of age, demonstrating that the proximo-distal differentiation of limb segments influenced distal trabecular bone formation. These data could be explained by the human pathology describing HCH as rhizomelic dwarfism.

As observed in long bones, we noted a BMD decrease in vertebrae. While, performing compression tests on the lumbar vertebral bodies, we revealed a trabecular bone fragility in $Fgfr3^{Asn534Lys/+}$ mice. These data with the presence of IVD anomalies should be compared to the human pathology. The low BMD we observed in *Hch* mice is concordant with low lumbar BMD reported in HCH patients (58).

In long bones, it is well known that cortical and trabecular bone should be considered as two separate bone compartments. Trabecular bone derives directly from the growth plate. In the opposite, cortical bone derives from periosteum mesenchymal cells which differentiate into osteoblasts. Here, we studied femur and tibia cortical bone. Surprisingly, we observed in *Hch* mice that cortical bone BMD and BV/TV were significantly increased for both femurs and tibiae. This increased cortical mineralization of tibia and femur was more pronounced at 6 months of age but as described for the trabecular bone, the phenotype was more severe in femur than in tibia. To provide unique insights and valuable information regarding cortical bone in *Hch* we performed a biomechanical three-point bending test on tibiae and we observed a higher fragility in *Hch* tibiae than in WT. Considering these findings, we confirmed that trabecular bone formation is tightly regulated by growth plate and paracrine actions on the osteogenesis whereas the cortical bone is under control of the cells coming from the periosteum. The exact role of FGFRs in the regulation of osteocytes survival or apoptosis is poorly understood. Recently, the role of *Fgfr1* was reported in mouse models lacking *Fgfr1* alone or *Fgfr1/Fgfr2* in mature osteoblasts showing a dramatic bone mass increase. The authors suggested that the viability/death of osteocytes were controlled by *Fgfr1* (24). Interestingly, a volumetric bone mineral density (vBMD) study in patients with ACH showed higher cortical vBMD and lower trabecular vBMD in the tibia, confirming our data obtained from *Hch* mouse model (59).

Here, our data suggest that the *Fgfr3* gain-of-function mutation deregulates the osteoblastic function by promoting defective cortical bone mineralization associated with impairment of bone markers and in the opposite decreasing trabecular bone mineralization. Lacunae high-resolution analyses demonstrated HCH mutation impact on osteocytes. Therefore, we can reasonably hypothesize that deregulated osteocytes may play a key role in cortical bone abnormal mineralization. As a result of osteoblastic lineage altered regulation, the osteogenesis is defective leading to a weak and brittle bone. These various dysfunctions of osteoblast lineage in long bones seem to be more pronounced with ageing. We can hypothesize that this increase in cortical bone mass observed in our *Fgfr3* gain-of-function mouse model could be associated with a decreased expression of *Fgfr1* in mature osteoblasts. It is likely that the dysregulation of *Fgfr1* could be more important in cortical bone than in trabecular bone. Future studies will be required to determine the relative contribution and the distinct roles of *Fgfr1*, *Fgfr2* and *Fgfr3* to bone growth regulation. In our study, *Hch* mutation downregulates osteoblastogenesis and not osteoclastogenesis. We know that FGFR3 is involved in osteoblastogenesis. Indeed, fgfr3 loss-of-function downregulates suture formation in a zebrafish model with an extracellular matrix dysregulation (26). On the other hand, FGFR3 can moderate osteoblastogenesis through activation of downstream signaling pathways which are known to be involved in osteoblastogenesis. *Stat1* null mice present a higher cortical BMD and dysregulates *Fgfr3* expression in osteoblast (60). Some new findings show that *Fgfr3* is present in osteocyte RNA (61) and this publication reveals a gene expression difference between femur and tibia which can explain our finding in *Hch* mouse model. Finally, others studies indicated defective cortical bone formation may be under control of MAPK and the suppressor of cytokine signaling (SOCS) and showed that FGFR3 and SOCS3 are tightly linked in bone maturation (62, 63). These data may be consistent with our present findings suggesting overactivation of FGFR3 by gain-of-function mutation can lead to SOCS3 overexpression thus inducing higher corticalisation in long bone, but additional studies are needed to fully elucidate and separate the role of FGFR3 in trabecular and cortical bone.

Our findings show that *Hch* bone has some characteristics of osteoporotic bones, suggesting that HCH patients may present osteoporotic traits with a higher risk fracture in old age. Interestingly, recent studies described osteoporosis in patients with ACH and HCH (58, 64). However, other studies need to be conducted in a larger series of adult HCH patients to confirm those clinical observations. If our findings in *Hch* match clinical findings, special attention will be demanded in designing a pharmacological treatment of osteoporosis for these patients because of the opposite mineralization densities detected in trabecular and cortical bone. These

data highlight the deleterious effect of FGFR3 gain-of-function mutation on long bone modelling during development and ageing which may have a major impact on the management of adult patients with HCH.

Methods

Generation of *Fgfr3*$^{Asn534Lys/+}$ mice

A targeting vector was constructed containing the Asn534Lys (corresponding to Asn540Lys in human) mutation in exon 12 of *Fgfr3* and the loxP flanked neo/STOP cassette. The construct was injected in blastocysts and the presence of the targeted allele was screened in chimeric mice. Finally, the excision of the loxP cassette of the mouse line *Fgfr3*$^{+/\ loxp\ Asn534Lys}$ was achieved using the mouse line CMV-cre (31). *Fgfr3*^{loxAsn534Lys} ES cells (SY05) were injected into blastocysts from grey C57Bl/N mice by Polygene. The resulting chimerae were bred with C57Bl/6N mice to obtain *Fgfr3*$^{loxAsn534Lys/+}$ mice. In *Fgfr3*$^{loxAsn534Lys/+}$ mice, the mutation is located in exon 12 of *Fgfr3* gene and in intron 10, a neomycin box was inserted. *Fgfr3*$^{loxAsn534Lys/+}$ mice were bred with *CMV-Cre* mice (C57BL/6J) in order to delete the neomycin box and obtain *Fgfr3*$^{Asn534Lys/+}$ mice.
Genomic DNA was isolated from tail using NucleoSpin Tissue kit (Macherey-Nagel) according the manufacturer's instructions. The mice were genotyped using the following primers: 5'-GTGGGGGTTCTGCGGTTGG-3' and 5'-TGACAGGCTTGGCAGTACGG-3' for isolate WT and mutant mice, 5'AACCTCTACAAATGTGGTATGGCTG-3' and 5'-CCGCTTCCTCGTGCTTTACGGTA-3' for the neomycin box. For all analyses wild-type littermates were used as controls, and both male and female were used during longitudinal analyses. At P7, P14 and P21 WT and mutant mice received intraperitoneal injection of BrdU labelling reagent (00-0103, Invitrogen) at 10 µL per 1g body weight, 2 hours before sacrifice. Long bones were measured by caliper (VWRi819-0013, VWR International).

X ray microradiography

X-ray radiography imaging was performed immediately post-mortem using a Faxitron UltraFocus digital X-ray radiography system (Faxitron Bioptics, Tucson, AZ, USA). Ventral images were taken at 1x.

Sequence analysis

The exons were amplified with specific primer 5'-TAAGCCTCTTGGAGAAGGCTGCTTTG-3' and 5'- CATTCCCTAGCTCAGGCAAAC-3' targeting exon 12 of *Fgfr3* containing C1602->A mutation. Amplification products were purified by ExoProStar 1-Step (Amersham) and directly sequenced with the Big Dye Terminator v3.1 Cycle Sequencing Ready Reaction kit (Applied Biosystems) on an automatic sequencer (3500xL Applied Biosystems). Sequence analyses were performed with Sequencing 6 software (Applied Biosystems).

Whole body alizarin red and alcian blue staining

P1 mice were skinned, fixed in 95% ethanol and stained with Alcian Blue 8GX and Alizarin Red (Sigma Aldrich MO). Whole skeleton were cleared by potassium hydroxide treatment and stored in glycerol 100% according to standard protocols (65). Measurements were performed using ImageJ software (Rasband, W.S., ImageJ, U. S. National Institutes of Health, Bethesda, Maryland, USA, https://imagej.nih.gov/ij/, 1997-2018).

Morphometric analyses

The samples consist of nine P14 *Fgfr3*$^{N534K/+}$ mice and nine WT. Micro-Computed Tomography imaging of the skull and mandibles were performed using a Skyscan 1172 (Bruker, Kontich, Belgium). Samples were fixed in 70% ethanol and scanned with settings of 80 kV, 100 µA, 17.99 µm pixel resolution, 0.5° rotation steps with a 0.5-mm Aluminum filter. Three-dimensional (3D) reconstructions were generated using NRecon software (Skyscan). Visual adjustments of the cortical bone density threshold were done for each CT-scan, without smoothing factors to keep the correct contours and avoid any loss of information concerning anatomical variations. The 3D surface mesh was obtained using Avizo® (ThermoFisher, MA, USA) software for each specimen and then used for landmark positioning.

Landmark 3D coordinates were analyzed by geometric morphometric methods, including standardization for position, scale, and orientation through Procrustes superimposition (66). Positions of the landmarks are provided in Supplemental Figure 1. Error measurement was assessed with a Procrustes ANOVA analysis and showed no significant differences in landmark positioning, allowing valid comparative analyses of shape variation among specimens. After Procrustes superimposition, the resulting 3D Procrustes shape coordinates were evaluated by principal component analysis. Wireframes were used to visualize the shape differences corresponding to the skull associated with specific scores on principal component (PC) 1. Centroid size (CS), the square root of the sum of squared distances of the landmarks from their centroid, was used as a proxy for size (Dryden and Mardia 1998). The influence of size on shape (i.e. allometry) was tested with multiple multivariate regression. Procrustes distances (d) separating groups in the morphospace were computed and significance was assessed using permutation tests (10,000 permutation rounds). A significant value of d was interpreted as significant shape differences between the two groups compared. The geometric morphometric analyses were performed with MorphoJ v. 1.06 (Dryden et al. 2008).

Foramen magnum area was evaluated using Radinsky formula (1/4π*mediosagittal foramen magnum distance*transversal foramen magnum distance) (68).

Linear skull measurements were performed using ImageJ software (Rasband, W.S., ImageJ, U. S. National Institutes of Health, Bethesda, Maryland, USA, https://imagej.nih.gov/ij/, 1997-2018). For mandibular morphometry analyses, thirty anatomical landmarks (fifteen per mandible, including the incisors) were defined in order to model the shape of the mandible and were placed using Avizo® by the same author. In addition, ten anatomical landmarks were defined on the maxilla (including incisors and nasal bones (five per side) to better analyze the relationship between the maxilla and the mandible. In total forty landmarks were placed for each specimen. Positions of the landmarks are provided in supplemental Figure. 1. To confirm statistically shape differences, ANalysis Of VAriance (ANOVA) was performed considering the genotype as classifier. For vertebrae morphometric analyses images were acquired in 70% ethanol using a Scanco uCT50 scanner (scans were performed at 70kV, 200µA, 0.5mm aluminium filter). 3D surface mesh generation and 32 landmarks positioning for each specimen were performed with Avizo® (ThermoFisher, MA, USA). The influence of size on shape (i.e. allometry) was tested with multiple multivariate regression. Procrustes distances separating groups in the morphospace were computed and significance was assessed using permutation tests (10,000 permutation rounds).

HREM

After dissection, samples were fixed in 4% paraformaldehyde during 24h. Fixed tissues were rinsed twice with phosphate buffered saline and dehydrated through a graded series of methanol baths (20%, 30%, 40%, 50%, 60%, 70%, 80%, 90% and 95%) for 4 hours. After dehydration,

the samples are embedded in methacrylate resin (JB4, polysciences) containing eosin and acridine orange as contrast agents (69). Images of the surface of the resin block were acquired repeatedly after removal of 1.56µm thick section using the Optical High-Resolution Episcopic Microscope (Indigo Scientific). The 3D images acquired by HREM were analyzed using Imaris software (Bitplane). For HREM analyses, P14 mice were used WT n=5, *Fgfr3*$^{Asn534Lys/+}$ n=5 both male and female mice)

Western Blots

Primary chondrocytes from P1 *Fgfr3*$^{Asn534Lys/+}$ ribs and control littermates were harvested using previously described methods (37) and cultured in DMEM/F12 + 10% SVF. Cells were cultured without serum during 24h and then supplemented with FGF2 (100ng.mL^{-1}) (FGF-basic, Peprotech). Whole-chondrocyte lysates were prepared using RIPA buffer supplemented with protease-inhibitor cocktail tablets (cOmplete Mini, EDTA-free, Roche). Proteins were incubated and gently mixed on wheel-type tube rotor at 11 rpm for 2h at 4 °C. Proteins were isolated by centrifugation at 11,000 rpm for 20 min at 4 °C, then denatured with β-mercaptoethanol 2.5% at 95 °C 10 min. Extracted proteins were subjected to NuPAGE 4–12% (Life Technologies and transferred onto PVDF membranes (Millipore) Using standard protocols, blots were probed with primary antibodies such as rabbit anti-phospho-Erk1–2 (Cell Signaling #4370, 1:2,000), mouse anti-total Erk1–2 (Cell Signaling #4696, 1:1,000) and mouse anti-actin (Millipore, MAB1501, 1:5,000) antibodies. Proteins of interest were detected with horseradish peroxidase (HRP)-conjugated antibodies (Cell Signaling #7074 and #7076, 1:10,000) and visualized with the ECL (ThermoFisher, MA, USA). The obtained immunoreactivities were determined and calculated using ImageJ software using the 'Gels and Plot lanes' plug-in.

RT-PCR

Cortical bones were isolated from male mouse femur at P70. Bone marrow was flushed. Cortical bones were placed in RNAlater (Invitrogen) during 24h at 4°C, then bones were placed in liquid nitrogen and crushed. TriZOL reagent (Invitrogen) was used to separate RNA from DNA then purified with Qiagen RNeasy Mini kit following the manufacturer's instructions (Qiagen). 200 µg of each RNA were converted into cDNA using the SuperScript III First-Strand (Invitrogen). Quantitative real-time PCR expression analysis was performed using a 7300 (Applied Biosystem) and ABsolute SYBR Green ROX mix (ABgene). The sets of primers used were: *Runx2* : forward: 5′-TGGCCACTTACCACAGAGCTATT-3′; reverse: 5′-AGGTTTAGAGTCATCAAGCTTCTGTC-3′, *ColI* : forward: 5′-CTCAGAGGCGAAGGCAACA-3′; reverse: 5′-TGACTGTCTTGCCCCAAGTTC-3′); *Osteocalcin* : forward: 5′-TGGCTGCGCTCTGTCTCT-3′; reverse: 5′-TTATTGCCCTCCTGCTTGG-3′); *Osteopontin* : forward: 5′-CGGCCGAGGTGATAGCTT -3′; reverse: 5′-TCCTCATCTGTGGCATCA-3′; *Trap* :forward: 5′-CGACCATTGTTAGCCACATACG -3′; reverse: 5′-ACACCGTTCTCGTCCTGAAG-3′; *Gapdh* : forward: 5′-GGGCTGGCATTGCTCTCA -3′; reverse: 5′-GGTCCACCACCCTGTTGCT-3′; *Osterix* : forward: 5′-CGCTTTGTGCCTTTGAAAT -3′; reverse: 5′-CCGTCAACGACGTTATGC-3; *Dkk1* forward: 5'-TCCCAGAAGAACCACACTGACTTC-3' ; reverse ; 5'-TCTTGGACCAGAAGTCTCTTGCAC-3' ; *Sost :* forward : 5'-ATCCCAGGGCTTGGAGAGTA-3'; reverse : 5'ACATCTTTGGCGTCATAGGG-3'.

Histology

All bones were collected in 4% paraformaldehyde, fully decalcified in 0.5M EDTA (pH 8.0) and paraffin embedded. 5 µm serial sections were used for hematoxylin and eosin (H&E), Safranin O staining or immunochemistry. All slices were deparaffinized in neo-clear solution (Millipore) and then rehydrated to perform standard immunostaining protocols. For Mouse Anti-Collagen Type X (ColX) antibody (1:100, Quartett, 1-CO097-05), pepsin was used for antigen retrieval (Sigma-Aldrich Co, St. Louis, MO, USA) during 2 hours at 37°C. P-p44/42 labellings were performed using the standard protocol with P-p44/42 MAPK (1:100, Cell Signaling #4370) incubation overnight at 4°C. Immunostaining revelation was performed using Dako Envision Kit (Dako North America, Inc, CA, USA).

For BrdU immunostaining, a heat antigen retrieval was performed using citrate buffer (pH 6.0) and DNA denaturation was performed using HCl 2 mol/L for 30 minutes at 37°C. Primary antibody incubation with Rat anti-BrdU antibody (1:1,000 ab6326, abcam) was performed overnight at 4°C. Immunostaining revelation was performed using anti-Rat Alexa Fluor 594 antibody (Invitrogen) and counterstaining with DAPI (Prolong gold anti fade reagent, Invitrogen). Images were captured with an Olympus PD70-IX2-UCB microscope. Labeled cells were counted using ImageJ software (Rasband, W.S., ImageJ, U. S. National Institutes of Health, Bethesda, Maryland, USA, https://imagej.nih.gov/ij/, 1997-2018).

Osteoclasts were quantified on paraffin sections deparaffinized in xylene (Merck) and stained for TRAP activity. Images were acquired on a Leica DM LB2 microscope. For each sample osteoclasts were determined in an equivalent ROI in trabecular bone.

Microcomputed tomographic analyses and imaging of long bones and vertebrae

Male femurs, tibiae (WT P42 n=9, P70 n=12, P180 n=9; *Fgfr3*$^{Asn534Lys/+}$: P42 n=8, P70 n=10, P180 n=10) and vertebrae (*Fgfr3*$^{+/+}$*:* P70 n=12, *Fgfr3*$^{Asn534Lys/+}$: P70 n=10, P180 n=10) images were acquired in 70% ethanol using a Scanco uCT50 scanner (scans were performed at 70kV, 200µA, 0.5mm aluminium filter).

In femurs, cortical bone parameters were determined at 10µm voxel resolution of a region of interest equal to 6-7% of the femur length centered in the mid-shaft bone 56% along the proximo-distal length of the femur, and trabecular parameters were obtained at 5µm voxel resolution in a region of interest (8-9.5% of the femur length in size) beginning 100µm proximal to the distal growth plate.

Similarly, in tibiae values for the compact bone were obtained at 10µm voxel resolution of a region of interest equivalent to 5.5-6% of the tibia length centered at 50% along the length of the tibia, and trabecular parameters were determined at 5µm voxel resolution in a region of interest corresponding to 5.5-6% of the tibia length located at 100µm from the end of the proximal growth plate.

Trabecular bone parameters of lumbar vertebrae 5 (L5) have been determined at 5µm voxel resolution analysing the vertebral body region delimited by the two cartilage endplates (Supplemental table 2).

Analyses and 3D rendering for trabecular and cortical bone were performed using Scanco µCT V6.1 software Evaluation and 3D display programs (Scanco Medical, Brüttisellen, Switzerland). Whole bone 3D imaging was produced with Drishti v2.6.5 (National Computational Infrastructure National Facility, The Australian National University, Canberra, Australia).

µCT analysis of osteocyte lacunae

Osteocyte lacuna parameters and images were obtained by µCT using a Scanco µCT50 as previously mentioned. Scans of a 0.25mm region of interest centred on the cortical bone

midshaft at 56% along proximo-distal length were run at a voxel resolution of 1 µm. µCT data was reconstructed using a segmentation threshold of 350 (851.7 mg $HAcm^{-3}$) for all samples (male P180 WT n = 9, *Fgfr3*^{Asn534Lys} n = 10). DICOM images of pores and cortical bones were produced with the Scanco Image Processing Language (IPL). Stack images were processed using Fiji (70) and analyses of lacunae volumes (Lc. V) were performed with BoneJ tool Particle Analyzer (71). Pores with volumes inferior to 100µm^3 and larger than 2000µm^3 were excluded from the analyses in accordance with previous studies (61, 72). The sphericity of the particles (Lc. Sph) was determined using the 3D Shape Measure plugin of Fiji (73). 3D rendering of the osteocyte lacunae was obtained using the Volume Viewer plugin of Fiji.

Biomechanical testing

Tibial three-point bend testing (WT P42 n=9, P70 n=12, P180 n=9*;* *Fgfr3*$^{Asn534Lys/+}$: P42 n=8, P70 n=10, P180 n=10) was performed using an Instron 5543 load frame and 100 N load cell (Instron Limited, High Wycombe, United Kingdom). Bones were positioned horizontally on their dorsal surface and centred on supports with a span of 8 mm. Load was applied vertically to the mid-shaft with a constant rate of displacement of 2 mm/min until fracture and data were collected by using BlueHill 3 software (Instron Limited, High Wycombe, United Kingdom).
Lumbar vertebrae 5 (WT*:* P70 n=12, *Fgfr3*$^{Asn534Lys/+}$*:* P70 n=10, P180 n=10) were processed using a HS Micro-Motor L50 (Henri Schein, Gillingham, United Kingdom) harboring a H259 dentist drill (Komet Dental - Gebr. Brasseler GmbH & Co. KG, Lemgo, Germany) to erode all vertebral structure but the vertebral body. L5 vertebral centra have been tested for compression using an Instron 5543 load frame and 500 N load cell (Instron Limited, High Wycombe, United Kingdom). To determine biomechanical variables for bone strength and toughness, the tested vertebral body was placed standing on a support while the load was applied vertically to the top of the vertebral body with a constant rate of displacement of 0.03 mm/s and data were acquired with BlueHill 3 software (Instron Limited, High Wycombe, United Kingdom).

Statistics

Variables from all experiments were assessed for normality with Anderson-Daarling, Shapiro-Wilk, Kolmogorov and D'agastino&Pearson tests. Data that were normally distributed were expressed as mean ± SD. For analyses involving 2 groups, parametric 2-tailed Student's t-test was used. When 3 or more groups were analyzed, ANOVA with Bonferroni's post hoc test was performed. When data were not normally distributed, Mann-Whitney test was used when 2 groups were analyzed (values are shown as mean ± SD).
For Lacunae volume and sphericity (Lc. Sph) distribution, represented with a Violin plot, were determined by permutations of an equivalent number of lacunae from each sample. The volume and sphericity distribution for each mutant was compared to WT using a two-tailed Kolmogorov-Smirnov analysis (GraphPad Prism v8). Differences between mutant and WT were considered valid if significant after 10 rounds of permutations.

The significance threshold was set at $p \leq 0.05$ ($*0.01 < p < 0.05$, $**0.001 < p < 0.01$, $***0.0001 < p < 0.001$, $****p < 0.0001$). Statistical analyses were performed using GraphPad Prism (version 9).

Study approval

All procedures were approved by the French Animal Care and Use Committee with the APAFIS number: # 26995.

Authors contribution

LL and DKE contributed equally to the work and should be considered co–first authors. LL and DKE designed and performed the experiments and LLM directed the research. AM, CV, AS performed the experiments. LL, DKE, AM and YH analyzed the results and made the figures. AL, GB gave the human X-RAY. DC, JHDB, GRW participated in the project design. LL, DKE and LLM wrote the manuscript. All authors reviewed and critically edited the manuscript.

Legends

Figure 1: The hypochondroplasia mutation induces a dwarf phenotype in both human and mouse model

(**A**) X-rays of foetus (34 weeks of gestation) showing metaphyseal enlargement, trident acetabula and squared ilia (red arrow) and a relative early cuboid ossification center appearance. X-rays of HCH patients (b: three-year-old female) showing slight tibial bending with elongation of the distal fibula, obliquity of the distal tibia metaphyseal growth plate of (c: five year old female). The leg bones are mildly short and the metaphysis are wide. We noted an elongation of the distal fibula and broad internal ossified epiphyseal centers of the knee (d: male eight years of age) iliac bones are squared and acetabular roofs are horizontal (scale bar = 5 cm). (**B**) X-rays of patient hand extremities (a: three years old female, b: five years old male, c: eight years old male). We observed a bone carpal age delay (red arrows), a relative short and broad phalange (particularly the proximal and middle phalanges), prominent ulnar styloid process (scale bar = 5cm). (**C**) X-rays of both male and female *Fgfr3*$^{Asn534Lys/+}$ mice and their control littermates from 7 days to 180 days of age showing a progressive skeletal phenotype in *Fgfr3*$^{Asn534Lys/+}$ mice compared to *Fgfr3*$^{+/+}$ (scale bar=1cm). (**D**) Alizarin red/Alcian blue staining of mice femurs and tibia at post-natal day 1. Graphical representation of femur and tibia length. Scale bars = 1mm. (*Fgfr3*$^{+/+}$ n=6 and *Fgfr3*$^{Asn534Lys/+}$ n=7) (**E**) Graphical representation of the body weight, naso-anal, femur and tibia length of *Fgfr3*$^{Asn534Lys/+}$ and *Fgfr3*$^{+/+}$ male and female mice during development (postnatal day1, 7, 14, 21, 28, 42, 60 and 180).

Figure 2: The *Fgfr3*$^{Asn534Lys/+}$ mice exhibit craniofacial anomalies

(**A**) Representative *Fgfr3*$^{+/+}$ and *Fgfr3*$^{Asn534Lys/+}$ skull bone µCT images from P14 mice in transversal and sagittal orientations (scale bar= 5mm). (**B**) Graphical representation of the skull length, skull width and centroid size of *Fgfr3*$^{Asn534Lys/+}$ (n=9) and *Fgfr3*$^{+/+}$ mice (n=9) at P14. ** p<0.01 **** p<0.0001 Student's t-test. (**C**) 3D representations showing variations of skull shape relationships between *Fgfr3*$^{Asn534Lys/+}$ and *Fgfr3*$^{+/+}$ mice at P14 using Canonical Variate. (**D**) 3D representations showing variations of mandibular shape and maxillomandibular relationships between mutants and controls using PC analysis (*Fgfr3*$^{+/+}$ n=9 *Fgfr3*$^{Asn534Lys/+}$ n=9). (**E**) Representative *Fgfr3*$^{+/+}$ and *Fgfr3*$^{Asn534Lys/+}$ skull base µCT images from P14 mice in sagittal orientation. Complete fusion of the SOS and ISS and partial fusion of IOS in *Fgfr3*$^{Asn534Lys/+}$. (**F**) Graphical representation of the skull base length and foramen magnum area. (*Fgfr3*$^{+/+}$ n=9, *Fgfr3*$^{Asn534Lys/+}$ n=9 **** p<0.0001 Student's t-test. (**G**) Representative *Fgfr3*$^{+/+}$ and *Fgfr3*$^{Asn534Lys/+}$ foramen magnum µCT images from 2 weeks-old mice.

Figure 3: HCH mutation affects the structure of vertebral body and intervertebral disc

(**A**) Three-dimensional rendering of 10-week-old *Fgfr3*$^{+/+}$ and *Fgfr3*$^{Asn534Lys/+}$ male mice lumbar vertebrae 5. In red is highlighted the Region of Interest (ROI) on the vertebral body analyzed by microcomputed tomography. Scale bar = 0.5mm. Graphical representation of the

vertebral body (VB) length. ****p<0.0001 Student's t-test. (**B**) Graphical representation of L5 interpedicular distance, L5 canal area, pedicle length of 10-week-old *Fgfr3*$^{+/+}$ and *Fgfr3*$^{Asn534Lys/+}$ male mice. Scale bar = 0.5mm. **p<0.001 Student's t-test. (**C**) Dot plots for the trabecular bone parameters studied on WT (n=12) and *Hch* (n=10) mice: bone mineral density (BMD), ratio of bone volume on tissue volume (BV/TV), trabecular number (Tb.N), trabecular space (Tb.Sp), trabecular thickness (Tb.Th). ns=not significant, *p<0.05, ***p<0.001 Student's t-test. (**D)** Schematic representation of the set up required for lumbar vertebra compression. Representative load displacement curves (white arrow head = Yield Load; black arrow head = Maximum Load; dotted line = Stiffness) and histograms for the mechanical parameters of WT and *Hch* vertebrae: Yield Load, Maximum Load and Stiffness. ns= not significant, *p<0.05, **p<0.01 Student's t-test. (**E**) Safranin-O staining of lumbar intervertebral disc (IVD) (L5-L6) in P14 mice (scale bar=250µm). (**F**) HREM 3D reconstruction and visualization of IVD and lumbar vertebrae (scale bar=1000µm). Graphical representation of Nucleus Pulposus (NP) Sphericity (WT n=5; *Hch* n=5) and NP on IVD volume (WT n=5; *Hch* n=5). ns= not significant, **p<0.01 Mann-Whitney test.

Figure 4: Analyses of the cartilage growth plate and the secondary ossification center
(**A**) H&E femur distal growth plate at P14 and P21 showing secondary ossification center delay and reduced hypertrophic cartilage area (scale bar=200µm and 50µm). (**B**) Collagen type X (Col X) immunostaining (scale bar=50µm), graphical representation of mean cells area in Col X-labelled zone (WT n=7 and *Fgfr3*$^{Asn534Lys/+}$ mice n= 6, *p<0.05 Mann-Whitney test). (**C**) HREM 3D reconstruction and visualization of secondary ossification center of the distal femur (scale bar=1000µm) and graphical representation of the volume of the SOC/epiphysis ratio (*Fgfr3*$^{+/+}$ (n=5) and *Fgfr3*$^{Asn534Lys/+}$ mice (n=5), *p<0.05 Mann-Whitney test). (**D**) Ki67 positive cells/Dapi at p14 in *Fgfr3*$^{+/+}$ (n=6) and *Fgfr3*$^{Asn534Lys/+}$ (n=7) mice, BrdU positive cells/Dapi at p14 in *Fgfr3*$^{+/+}$ (n=7) and *Fgfr3*$^{Asn534Lys/+}$ (n=7), BrdU positive cells/Dapi at p21 in *Fgfr3*$^{+/+}$ (n=5) and *Fgfr3*$^{Asn534Lys/+}$ (n=5) (ns= not significant, Mann-Whitney test). (**E**) p-Erk1/2 immunostaining on P14 growth plate. Graphical representation of relative intensity of p-Erk1/2 on *Fgfr3*$^{+/+}$ (n=5) and *Fgfr3*$^{Asn534Lys/+}$ (n=7) growth plates Mann-Withney test, *p<0.05. (**F**) Representative immunoblots of p-Erk1/2 on Erk1/2 quantification from primary chondrocytes with FGF2 stimulation over time (0, 5, 30, 60, 120 min) from 4 separate independent western blots with (n=5 mice per group), graphical representation of p-Erk1/2/Erk1/2 during time (* p<0.05 Sidak's multiple comparison test).

Figure 5: The microarchitecture of the femur is affected in *Fgfr3*$^{Asn534Lys/+}$ mice
(**A**) Three-dimensional visualization of representative P70 *Fgfr3*$^{+/+}$ and *Fgfr3*$^{Asn534Lys/+}$ male femurs. Highlighted in red the ROI selected for the trabecular bone analyses, while the area in green points out the ROI chosen for the cortical bone studies (scale bars=1mm). Dot plots show the differences in size at P42 (*Fgfr3*$^{+/+}$ n=9, *Fgfr3*$^{Asn534Lys/+}$ n=8), P70 (*Fgfr3*$^{+/+}$ n=12, *Fgfr3*$^{Asn534Lys/+}$ n=10) and P180 (*Fgfr3*$^{+/+}$ n=9, *Fgfr3*$^{Asn534Lys/+}$ n=10) of the femurs analyzed. (****p<0.0001 2-way ANOVA and Bonferroni's post-hoc test). (**B)** Histograms for the trabecular bone parameters of P42, P70 and P180 femurs obtained by µCT: bone mineral density (BMD), ratio of bone volume on tissue volume (BV/TV), trabecular number (Tb.N), trabecular space (Tb.Sp), trabecular thickness (Tb.Th). ns= not significant (* p<0.05, **p<0.01, ***p<0.001, ****p<0.0001 2-way ANOVA and Bonferroni's post-hoc test). (**C)** Dot plots for the cortical bone parameters of P42, P70 and P180 femurs obtained by µCT: bone mineral density (BMD), ratio of bone volume on tissue volume (BV/TV), cortical thickness (C.Th), tissue diameter (T.Dm) and cortical thickness as percentage of tissue diameter

(C.Th/T.Dm) ns= not significant (* p<0.05, **p<0.01, ***p<0.001, ****p<0.0001 2-way ANOVA and Bonferroni's post-hoc test).

Figure 6: Microcomputed tomographic analyses of the tibia in *Fgfr3*$^{Asn534Lys/+}$ mice

(A) Three-dimensional imaging of representative P70 *Fgfr3*$^{+/+}$ and *Fgfr3*$^{Asn534Lys/+}$ male tibiae. Highlighted in red the ROI selected for the trabecular bone analyses, whereas the area in green points out the ROI chosen for the cortical bone studies (scale bars = 1mm). The histograms show the differences in size at P42 (*Fgfr3*$^{+/+}$ n=9, *Fgfr3*$^{Asn534Lys/+}$ n=8), P70 (*Fgfr3*$^{+/+}$ n=12, *Fgfr3*$^{Asn534Lys/+}$ n=10) and P180 (*Fgfr3*$^{+/+}$ n=9, *Fgfr3*$^{Asn534Lys/+}$ n=10) of the tibiae analyzed (****p<0.0001 2-way ANOVA and Bonferroni's post-hoc test). (**B)** Dot plots for the trabecular bone parameters of P42, P70 and P180 tibiae obtained by µCT: bone mineral density (BMD), ratio of bone volume on tissue volume (BV/TV), trabecular number (Tb.N), trabecular space (Tb.Sp), trabecular thickness (Tb.Th). ns= not significant (* p<0.05, **p<0.01, ***p<0.001, ****p<0.0001 2-way ANOVA and Bonferroni's post-hoc test). (**C)** Histograms for the cortical bone parameters of P42, P70 and P180 femurs obtained by µCT: bone mineral density (BMD), ratio of bone volume on tissue volume (BV/TV), cortical thickness (C.Th), tissue diameter (T.Dm) and cortical thickness as percentage of tissue diameter (C.Th/T.Dm) ns= not significant (**p<0.01, ***p<0.001, ****p<0.0001 2-way ANOVA and Bonferroni's post-hoc test).

Figure 7. Defective bone homeostasis

(**A**) qRT-PCR analysis of femoral cortical bone. Relative expressions performed in *Fgfr3*$^{+/+}$ (n= 7) and *Fgfr3*$^{Asn534Lys/+}$ (n= 6) are shown (*p<0.05, **p<0.01, ***p<0.001, Mann-Whitney test). (**B**) Histological sections of WT and *Fgfr3*$^{Asn564Lys/+}$ decalcified 2-months old male femurs stained for tartrate-resistant acid phosphatase (TRAP). Black arrow heads point out red TRAP-stained osteoclasts (scale bars=200µm). Graphs show osteoclast surface per mm of bone surface (Oc.S/BS), number of osteoclasts per mm of bone surface (N.Oc/BS), number of osteoclasts per mm^2 of bone (N.Oc/BV) and number of osteoclasts per mm^2 of tissue area analyzed (N.OC/TV) (mean ± SD, n = 5 per genotype, ns= not significant, Mann-Whitney test). Dashed lines outline the ROI of the trabecular area that was quantified. (**C**) µCT images representative of osteocyte lacunae in femoral cortical bone of 6-month old male WT (n = 9) and *Fgfr3*$^{Asn564Lys/+}$ (n = 10) mice highlighting small (100-200 µm^3) and large lacunae (400-2000 µm^3) (scale bar=250µm). Graphs show osteocyte lacunae number per bone volume (Lc.N/BV), cortical microporosity (%) (*** p<0.001, **** p<0.0001, Mann-Whitney test) and relative frequency distribution of lacunae volumes (Lc.V) in WT and mutant mice. Violin plots show distribution of lacunae volumes (Lc.V) and lacunae sphericity (Lc.Sph) in WT and *Fgfr3*$^{Asn564Lys/+}$ animals (*** p<0.001, **** p<0.0001, two-tailed Kolmogorov-Smirnov test).The percentage of number of lacunae (Lc. N %) was obtained by binning the osteocyte lacunae based on the illustrated range of volumes.

Figure 8: Evaluation of bone strength in tibiae

(A) Schematic representation of a three-point bend test on tibia and representative load displacement curves of tibiae from male P42, P70 and P180 *Fgfr3*$^{+/+}$ and *Fgfr3*$^{Asn534Lys/+}$ mice (white arrow head = Yield Load; black arrow head = Maximum Load; black arrow = Fracture Load, dotted line = Stiffness, colored area under curve = Energy Dissipated prior to fracture). (**B)** Histograms for the biomechanical parameters of *Fgfr3*$^{+/+}$ (P42 n=9, P70 n=12, P180 n=9) and *Fgfr3*$^{Asn534Lys/+}$ (P42 n=8, P70 n=10, P180 n=10) tibiae: Yield Load, Maximum Load, Fracture Load, Stiffness, percentage of Energy Dissipated prior to Fracture (toughness), Plastic Work as percentage of Total Work. ns= not significant (**p<0.01, ***p<0.001, ****p<0.0001 2-way ANOVA and Bonferroni's post-hoc test).

Table 1: Measurements of the naso-anal, bones size and weight of male and female mice at Postnatal day 1, 7, 14, 21, 28, 42, 60 and 180 Student's t-test.

Supplemental Figure 1

(**A**) Generation of the dwarf *Fgfr3*$^{Asn534Lys/+}$ mouse. The point mutation Asn534Lys is localized in mouse exon 12. *Fgfr3*$^{Asn534Lys/+}$ mice were crossed with CMV-Cre mice to remove the NEO cassette gene. (**B**) The presence of the heterozygous mutation p.Asn534Lys in DNA isolated from tail.

(C) Graphical representation of the humerus and ulna length of *Fgfr3*$^{Asn534Lys/+}$ and *Fgfr3*$^{+/+}$ male and female mice during development (postnatal day 1, 7, 14, 21, 28, 42, 60 and 180) Student's t-test.

Supplemental Figure 2

(**A**) Definitions and positioning of the 57 anatomical landmarks per specimen digitized on three-dimensional models on mouse skull. Comparison of skull shape between mutants and controls: plots of Principal Components (PC) scores for PC1 and PC2 with corresponding variances (in %) (*Fgfr3*$^{Asn534Lys/+}$ n=9 and *Fgfr3*$^{+/+}$ n=9). (**B**) Definitions and positioning of the 40 anatomical landmarks per specimen digitized on three-dimensional models: mandibular anatomical landmarks (n=20 per mandible); maxillar anatomical landmarks (n=10 per side). Comparison of mandibular shape and relationship to the maxilla between mutants and controls: plots of Principal Components (PC) scores for PC1 and PC2 with corresponding variances (in %) (*Fgfr3*$^{Asn534Lys/+}$ n=9 and *Fgfr3*$^{+/+}$ mutants n=9). Results were statistically significant ($p < 0.01$) Student's t-test.

Supplemental Figure 3

(**A)** Definitions and positioning of the 32 anatomical landmarks per specimen digitized on three-dimensional models on mouse L5 lumbar vertebrae. Comparison of L5 lumbar vertebrae shape between *Fgfr3*$^{+/+}$*:* P70 n=7, *Fgfr3*$^{Asn534Lys/+}$: P70 n=8 male mice plots of Principal Components (PC) scores for PC1 and PC2 with corresponding variances (in %). (**B**) H&E staining of L5 to L6 lumbar vertebrae intervertebral disc form 1 day-of-age to 3 months-of-age (scale bar=200µm)**. (C)** Representative images of FGFR3 immunostaining.

Supplemental Figure 4

Representative µCT images of femur and tibia trabecular bone from *Fgfr3*$^{+/+}$ and *Fgfr3*$^{Asn534Lys/+}$ mice at P42, P70 and P183 (scale bars=1mm).

Supplemental Figure 5

Representative µCT images of femur and tibia cortical bone from *Fgfr3*$^{+/+}$ and *Fgfr3*$^{Asn534Lys/+}$ mice at P42, P70 and P183 (scale bars=1mm).

Supplemental Table 1

Skull analyses on P14 mice, Student's t-test.

Supplemental Table 2

Selection of region of interests (ROIs) for µCT analyses of lumbar vertebrae, femurs and tibiae.

Supplemental Table 3
Lumbar vertebrae 5 measurements obtained with µCT are presented classified by genotype and age. Values are expressed as mean ± standard deviation. The difference among WT and *Hch* mice is also presented in percentage and the relative p-value is also reported.

Supplemental Table 4
Femur measurements obtained with µCT are presented classified by genotype and age. Values are expressed as mean ± standard deviation. The difference among WT and *Hch* mice is also presented in percentage and the relative p-value is also reported.

Supplemental Table 5
Tibia measurements obtained with µCT are presented classified by genotype and age. Values are expressed as mean ± standard deviation. The difference among WT and *Hch* mice is also presented in percentage and the relative p-value is also reported.

Supplemental Table 6
Biomechanical test data. The table presents the data of our studies sorted per genotype and age. They are expressed as mean ± standard deviation. The variations across WT and *Hch* mice are expressed in percentage and their p-values are listed.

References

1. Hecht JT, et al. Growth of the foramen magnum in achondroplasia. *Am. J. Med. Genet.* 1989;32(4):528–535.
2. Horton WA, Hall JG, Hecht JT. Achondroplasia. *Lancet Lond. Engl.* 2007;370(9582):162–172.
3. Meyers GA, et al. Fibroblast growth factor receptor 3 (FGFR3) transmembrane mutation in Crouzon syndrome with acanthosis nigricans. *Nat. Genet.* 1995;11(4):462–464.
4. Baujat G, et al. Achondroplasia. *Best Pract. Res. Clin. Rheumatol.* 2008;22(1):3–18.
5. Huet T, et al. Lumbar spinal stenosis and disc alterations affect the upper lumbar spine in adults with achondroplasia. *Sci. Rep.* 2020;10(1):4699.
6. Linnankivi T, et al. Neuroimaging and neurological findings in patients with hypochondroplasia and FGFR3 N540K mutation. *Am. J. Med. Genet. A.* 2012;158A(12):3119–3125.
7. Bellus GA, et al. A recurrent mutation in the tyrosine kinase domain of fibroblast growth factor receptor 3 causes hypochondroplasia. *Nat. Genet.* 1995;10(3):357–359.
8. Rousseau F, et al. Clinical and genetic heterogeneity of hypochondroplasia. *J. Med. Genet.* 1996;33(9):749–752.
9. Patani H, et al. Landscape of activating cancer mutations in FGFR kinases and their differential responses to inhibitors in clinical use. *Oncotarget* 2016;7(17):24252–24268.
10. Chen H, et al. A 'Molecular Brake' in the Kinase Hinge Region Regulates the Activity of Receptor Tyrosine Kinases. *Mol. Cell* 2007;27(5):717–730.
11. Marsiglia WM, et al. A Conserved Allosteric Pathway in Tyrosine Kinase Regulation. *Structure* 2019;27(8):1308-1315.e3.
12. Deng C, et al. Fibroblast growth factor receptor 3 is a negative regulator of bone growth. *Cell* 1996;84(6):911–921.
13. Colvin JS, et al. Skeletal overgrowth and deafness in mice lacking fibroblast growth factor receptor 3. *Nat. Genet.* 1996;12(4):390–397.

14. Ornitz DM, Legeai-Mallet L. Achondroplasia: Development, pathogenesis, and therapy. *Dev. Dyn. Off. Publ. Am. Assoc. Anat.* 2017;246(4):291–309.
15. Naski MC, et al. Repression of hedgehog signaling and BMP4 expression in growth plate cartilage by fibroblast growth factor receptor 3. *Development* 1998;125(24):4977–4988.
16. Wang Y, et al. A mouse model for achondroplasia produced by targeting fibroblast growth factor receptor 3. *Proc. Natl. Acad. Sci.* 1999;96(8):4455–4460.
17. Pannier S, et al. Delayed bone age due to a dual effect of FGFR3 mutation in Achondroplasia. *Bone* 2010;47(5):905–915.
18. Iwata T, et al. Highly activated Fgfr3 with the K644M mutation causes prolonged survival in severe dwarf mice. *Hum. Mol. Genet.* 2001;10(12):1255–1264.
19. Chen L, et al. Gly369Cys mutation in mouse *FGFR3* causes achondroplasia by affecting both chondrogenesis and osteogenesis. *J. Clin. Invest.* 1999;104(11):1517–1525.
20. Lee Y-C, et al. Knock-in human FGFR3 achondroplasia mutation as a mouse model for human skeletal dysplasia. *Sci. Rep.* 2017;7(1):43220.
21. Li C, et al. A Lys644Glu substitution in fibroblast growth factor receptor 3 (FGFR3) causes dwarfism in mice by activation of STATs and ink4 cell cycle inhibitors. *Hum. Mol. Genet.* 1999;8(1):35–44.
22. Delezoide AL, et al. Spatio-temporal expression of FGFR 1, 2 and 3 genes during human embryo-fetal ossification. *Mech. Dev.* 1998;77(1):19–30.
23. Miyagawa K, et al. Dysregulated Gene Expression in the Primary Osteoblasts and Osteocytes Isolated from Hypophosphatemic Hyp Mice. *PLOS ONE* 2014;9(4):e93840.
24. McKenzie J, et al. Osteocyte Death and Bone Overgrowth in Mice Lacking Fibroblast Growth Factor Receptors 1 and 2 in Mature Osteoblasts and Osteocytes. *J. Bone Miner. Res.* 2019;34(9):1660–1675.
25. Valverde-Franco G, et al. Defective bone mineralization and osteopenia in young adult FGFR3−/− mice. *Hum. Mol. Genet.* 2004;13(3):271–284.
26. Dambroise E, et al. Fgfr3 Is a Positive Regulator of Osteoblast Expansion and Differentiation During Zebrafish Skull Vault Development. *J. Bone Miner. Res.* 2020;35(9):1782–1797.
27. Su N, et al. Gain-of-function mutation in FGFR3 in mice leads to decreased bone mass by affecting both osteoblastogenesis and osteoclastogenesis. *Hum. Mol. Genet.* 2010;19(7):1199–1210.
28. Mugniery E, et al. An activating Fgfr3 mutation affects trabecular bone formation via a paracrine mechanism during growth. *Hum. Mol. Genet.* 2012;21(11):2503–2513.
29. Ornitz DM, Marie PJ. Fibroblast growth factors in skeletal development. *Curr. Top. Dev. Biol.* 2019;133:195–234.
30. Legeai-Mallet L, Savarirayan R. Novel therapeutic approaches for the treatment of achondroplasia. *Bone* 2020;115579.
31. Metzger D, et al. Conditional site-specific recombination in mammalian cells using a ligand-dependent chimeric Cre recombinase.. *Proc. Natl. Acad. Sci. U. S. A.* 1995;92(15):6991–6995.
32. Di Rocco F, et al. FGFR3 mutation causes abnormal membranous ossification in achondroplasia. *Hum. Mol. Genet.* 2014;23(11):2914–2925.
33. Kawakami M, Yamamura K. Cranial bone morphometric study among mouse strains. *BMC Evol. Biol.* 2008;8(1):73.
34. Toussaint N, et al. A landmark-free morphometrics pipeline for high-resolution phenotyping: application to a mouse model of Down syndrome. *Development* 2021;148(18):dev188631.
35. Biosse Duplan M, et al. Meckel's and condylar cartilages anomalies in achondroplasia result in defective development and growth of the mandible. *Hum. Mol. Genet.*

2016;25(14):2997–3010.
36. Komla-Ebri D, et al. Tyrosine kinase inhibitor NVP-BGJ398 functionally improves FGFR3-related dwarfism in mouse model. *J. Clin. Invest.* 2016;126(5):1871–1884.
37. Martin L, et al. Constitutively-active FGFR3 disrupts primary cilium length and IFT20 trafficking in various chondrocyte models of achondroplasia. *Hum. Mol. Genet.* 2018;27(1):1–13.
38. Tsang M, Dawid IB. Promotion and Attenuation of FGF Signaling Through the Ras-MAPK Pathway. *Sci. Signal.* 2004;2004(228):pe17–pe17.
39. Heuertz S, et al. Novel FGFR3 mutations creating cysteine residues in the extracellular domain of the receptor cause achondroplasia or severe forms of hypochondroplasia. *Eur. J. Hum. Genet. EJHG* 2006;14(12):1240–1247.
40. Thauvin-Robinet C, et al. Hypochondroplasia and stature within normal limits: Another family with an Asn540Ser mutation in the fibroblast growth factor receptor 3 gene. *Am. J. Med. Genet. A.* 2003;119A(1):81–84.
41. Prinster C, et al. Comparison of clinical-radiological and molecular findings in hypochondroplasia. *Am. J. Med. Genet.* 1998;75(1):109–112.
42. Arenas MA, Pino M del, Fano V. FGFR3-related hypochondroplasia: longitudinal growth in 57 children with the p.Asn540Lys mutation. *J. Pediatr. Endocrinol. Metab.* 2018;31(11):1279–1284.
43. Toydemir RM, et al. A Novel Mutation in FGFR3 Causes Camptodactyly, Tall Stature, and Hearing Loss (CATSHL) Syndrome. *Am. J. Hum. Genet.* 2006;79(5):935–941.
44. Chesi M, et al. Frequent translocation t(4;14)(p16.3;q32.3) in multiple myeloma is associated with increased expression and activating mutations of fibroblast growth factor receptor 3. *Nat. Genet.* 1997;16(3):260–264.
45. di Martino E, et al. Mutant fibroblast growth factor receptor 3 induces intracellular signaling and cellular transformation in a cell type- and mutation-specific manner. *Oncogene* 2009;28(48):4306–4316.
46. Lew ED, et al. The precise sequence of FGF receptor autophosphorylation is kinetically driven and is disrupted by oncogenic mutations. *Sci. Signal.* 2009;2(58):ra6.
47. Farrell B, Breeze AL. Structure, activation and dysregulation of fibroblast growth factor receptor kinases: perspectives for clinical targeting. *Biochem. Soc. Trans.* 2018;46(6):1753–1770.
48. Bober MB, et al. Hypochondroplasia. In: Adam MP et al eds. *GeneReviews®*. Seattle (WA): University of Washington, Seattle; 1993:
49. Matsushita T, et al. FGFR3 promotes synchondrosis closure and fusion of ossification centers through the MAPK pathway. *Hum. Mol. Genet.* 2009;18(2):227–240.
50. Xu M, et al. Expansion of FGFR3-positive nucleus pulposus cells plays important roles in postnatal nucleus pulposus growth and regeneration. *Stem Cell Res. Ther.* 2022;13(1):227.
51. Hallett SA, et al. Chondrocytes in the resting zone of the growth plate are maintained in a Wnt-inhibitory environment. *eLife* 2021;10:e64513.
52. Luo P, et al. The Role of Autophagy in Chondrocyte Metabolism and Osteoarthritis: A Comprehensive Research Review. *BioMed Res. Int.* 2019;2019:5171602.
53. Jing Y, et al. Chondrogenesis Defines Future Skeletal Patterns Via Cell Transdifferentiation from Chondrocytes to Bone Cells. *Curr. Osteoporos. Rep.* 2020;18(3):199–209.
54. Wen X, et al. Chondrocyte FGFR3 Regulates Bone Mass by Inhibiting Osteogenesis. *J. Biol. Chem.* 2016;291(48):24912–24921.
55. Lee C-H, et al. Development and validation of a subject-specific finite element model of the functional spinal unit to predict vertebral strength. *Proc. Inst. Mech. Eng. [H]*

2017;954411917708806.
56. Eswarakumar VP, et al. The IIIc alternative of Fgfr2 is a positive regulator of bone formation. *Development* 2002;129(16):3783–3793.
57. Su N, et al. Deletion of FGFR3 in Osteoclast Lineage Cells Results in Increased Bone Mass in Mice by Inhibiting Osteoclastic Bone Resorption. *J. Bone Miner. Res.* 2016;31(9):1676–1687.
58. Matsushita M, et al. Low bone mineral density in achondroplasia and hypochondroplasia. *Pediatr. Int.* 2016;58(8):705–708.
59. Liang H, et al. Evaluation of Volumetric Bone Mineral Density, Bone Microarchitecture, and Bone Strength in Patients with Achondroplasia Caused by FGFR3 c.1138G > A Mutation. *Calcif. Tissue Int.* [published online ahead of print: October 19, 2022]; doi:10.1007/s00223-022-01027-2
60. Xiao L, et al. Stat1 Controls Postnatal Bone Formation by Regulating Fibroblast Growth Factor Signaling in Osteoblasts. *J. Biol. Chem.* 2004;279(26):27743–27752.
61. Youlten SE, et al. Osteocyte transcriptome mapping identifies a molecular landscape controlling skeletal homeostasis and susceptibility to skeletal disease. *Nat. Commun.* 2021;12(1):2444.
62. Liu X, et al. Deleting Suppressor of Cytokine Signaling-3 in chondrocytes reduces bone growth by disrupting mitogen-activated protein kinase signaling. *Osteoarthritis Cartilage* 2019;27(10):1557–1563.
63. Isojima T, Sims NA. Cortical bone development, maintenance and porosity: genetic alterations in humans and mice influencing chondrocytes, osteoclasts, osteoblasts and osteocytes. *Cell. Mol. Life Sci.* 2021;78(15):5755–5773.
64. Arita ES, et al. Assessment of osteoporotic alterations in achondroplastic patients: a case series. *Clin. Rheumatol.* 2013;32(3):399–402.
65. Rigueur D, Lyons KM. Whole-Mount Skeletal Staining. *Methods Mol. Biol. Clifton NJ* 2014;1130:113–121.
66. Rohlf FJ, Slice D. Extensions of the Procrustes Method for the Optimal Superimposition of Landmarks. *Syst. Biol.* 1990;39(1):40–59.
67. Klingenberg CP. MorphoJ: an integrated software package for geometric morphometrics. *Mol. Ecol. Resour.* 2011;11(2):353–357.
68. Kamath VG, et al. Binary Logistic Regression Analysis of Foramen Magnum Dimensions for Sex Determination. *Anat. Res. Int.* 2015;2015. doi:10.1155/2015/459428
69. Mohun TJ, Weninger WJ. Embedding Embryos for High-Resolution Episcopic Microscopy (HREM). *Cold Spring Harb. Protoc.* 2012;2012(6):pdb.prot069583.
70. Schindelin J, et al. Fiji - an Open Source platform for biological image analysis. *Nat. Methods* 2012;9(7):10.1038/nmeth.2019.
71. Doube M, et al. BoneJ: free and extensible bone image analysis in ImageJ. *Bone* 2010;47(6):1076–1079.
72. Hemmatian H, et al. Aging, Osteocytes, and Mechanotransduction. *Curr. Osteoporos. Rep.* 2017;15(5):401–411.
73. Ollion J, et al. TANGO: a generic tool for high-throughput 3D image analysis for studying nuclear organization. *Bioinforma. Oxf. Engl.* 2013;29(14):1840–1841.

Figure 1: The hypochondroplasia mutation induces a dwarf phenotype in both human and mouse model

(**A**) X-rays of foetus (34 weeks of gestation) showing metaphyseal enlargement, trident acetabula and squared ilia (arrow) and a relative early cuboid ossification center appearance. X-rays of HCH patients (b: female three years old) showing slight tibial bending with elongation of the distal fibula, obliquity of the distal tibia metaphyseal growth plate of (c: female 5 years old) The leg bones are mildly short and the metaphysis are wide, we noted elongation of the distal fibula and broad internal ossified epiphyseal centers of the knee (d: male 8 years of age) the iliac bones are squared and acetabular roofs are horizontal Scale bar = 5 cm. (**B**) X-rays of the hand extremities, patient (a: female 3 years old, b: male 5 years old, c: male 8 years old). we observed a bone carpal age delay (arrows) and a relative short and broad phalange (particularly the proximal and middle phalanges) and prominent ulnar styloid process Scale bar = 5cm. (**C**) X-rays of *Fgfr3*$^{Asn534Lys/+}$ both male and female mice and its control littermates from 7 days to 180 days of age showing a progressive skeletal phenotype in *Fgfr3*$^{Asn534Lys/+}$ mice compared to *Fgfr3*$^{+/+}$. Scale bar = 1cm. (**D**) Alizarin red/Alcian blue staining of mice femurs and tibia at post-natal day 1. Graphical representation of femur and tibia length. Scale bars = 1mm. (*Fgfr3*$^{+/+}$ n=6 and *Fgfr3*$^{Asn534Lys/+}$ n=7) (**E**) Graphical representation of the body weight, naso-anal, femur and tibia length of *Fgfr3*$^{Asn534Lys/+}$ and *Fgfr3*$^{+/+}$ male and female mice during development (postnatal day1, 7, 14, 21, 28, 42, 60 and 180).

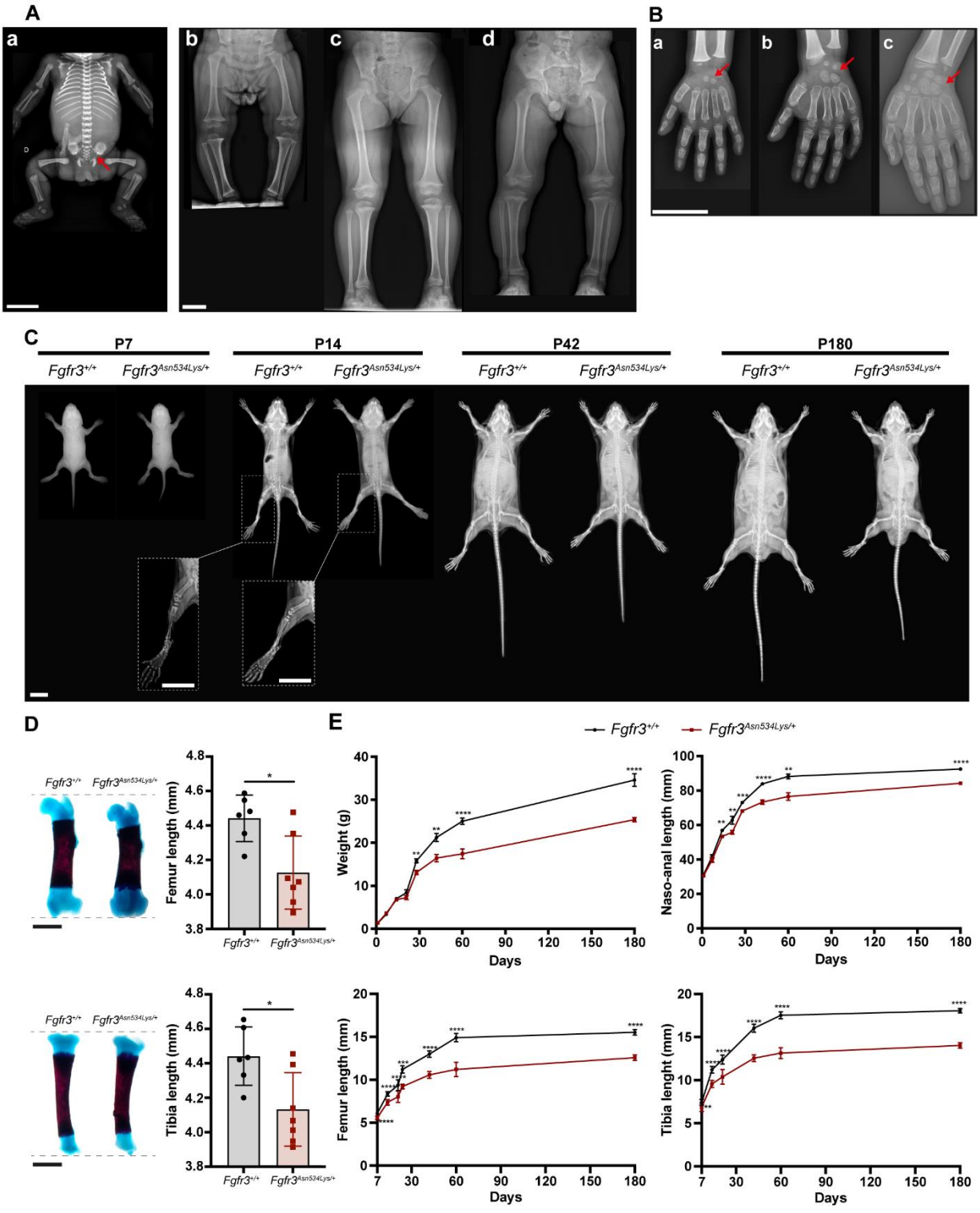
A
a
b
c
d
B
a
b
c
C
P7
P14
P42
P180
Fgfr3+/+
Fgfr3Asn534Lys/+
D
Femur length (mm)
Tibia length (mm)
E
Weight (g)
Naso-anal length (mm)
Femur length (mm)
Tibia lenght (mm)
Days

Figure 2: The *Fgfr3*$^{Asn534Lys/+}$ mice exhibit craniofacial anomalies

(**A**) Representative *Fgfr3*$^{+/+}$ and *Fgfr3*$^{Asn534Lys/+}$ skull bone µCT images from P14 mice in transversal and sagittal orientations. Scale bars: 5mm. (**B**) Graphical representation of the skull length, skull width and centroid size of *Fgfr3*$^{Asn534Lys/+}$ n= 9 and *Fgfr3*$^{+/+}$ mice n=9 at P14. ** p<0.01 **** p<0.0001 t-student test. (**C**) 3D representations showing variations of skull shape relationships between *Fgfr3*$^{Asn534Lys/+}$ and *Fgfr3*$^{+/+}$ mice at P14 using Canonical Variate. (**D**) 3D representations showing variations of mandibular shape and maxillomandibular relationships between mutants and controls using PC analysis (*Fgfr3*$^{+/+}$ n=9 *Fgfr3*$^{Asn534Lys/+}$ n=9). (**E**) Representative *Fgfr3*$^{+/+}$ and *Fgfr3*$^{Asn534Lys/+}$ skull base µCT images from P14 mice in sagittal orientation. Complete fusion of the SOS and ISS and partial fusion of IOS in *Fgfr3*$^{Asn534Lys/+}$. (**F**) Graphical representation of the skull base length and foramen magnum area. (*Fgfr3*$^{+/+}$ n=9, *Fgfr3*$^{Asn534Lys/+}$ n=9 **** p<0.0001 t-student test. (**G**) Representative *Fgfr3*$^{+/+}$ and *Fgfr3*$^{Asn534Lys/+}$ foramen magnum µCT images from 2 weeks-old mice.

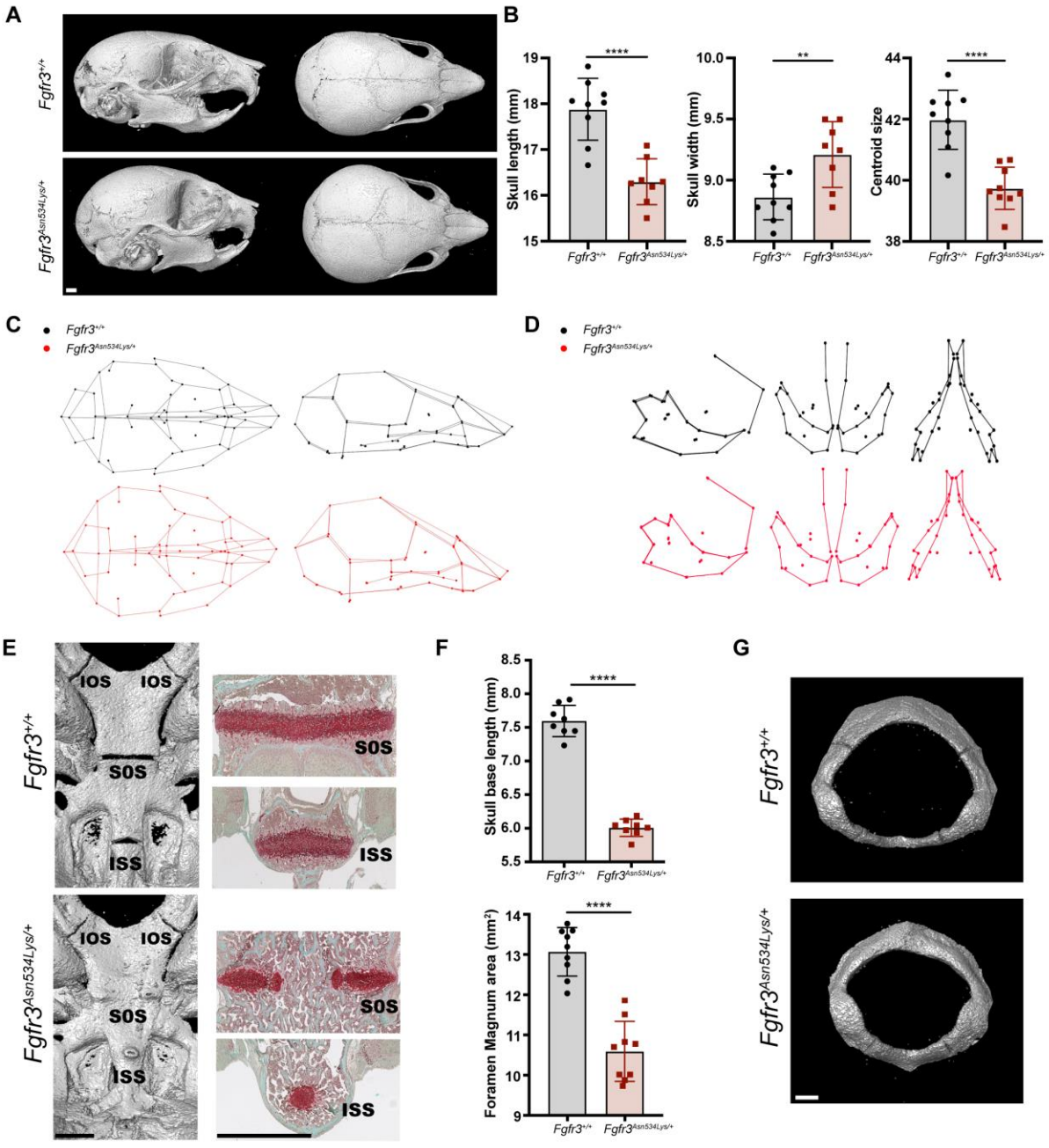
A
Fgfr3+/+
Fgfr3Asn534Lys/+
B
Skull length (mm)
Skull width (mm)
Centroid size
****
**
****
Fgfr3+/+
Fgfr3Asn534Lys/+
C
Fgfr3+/+
Fgfr3Asn534Lys/+
D
Fgfr3+/+
Fgfr3Asn534Lys/+
E
Fgfr3+/+
Fgfr3Asn534Lys/+
IOS
SOS
ISS
F
Skull base length (mm)
Foramen Magnum area (mm²)
****
****
Fgfr3+/+
Fgfr3Asn534Lys/+
G
Fgfr3+/+
Fgfr3Asn534Lys/+

Figure 3: HCH mutation affects the structure of vertebral body and intervertebral disc
(**A**) Three-dimensional rendering of 10-weeks-old *Fgfr3*$^{+/+}$ and *Fgfr3*$^{Asn534Lys/+}$ male mice lumbar vertebrae 5. In red is highlighted the Region of Interest (ROI) on the vertebral body analyzed by microcomputed tomography. Scale bar = 0.5mm. Graphical representation of the vertebral body (VB) length. ****p<0.0001 (**B**) Graphical representation of L5 interpedicular distance, L5 canal area, pedicle length of 10-weeks-old *Fgfr3*$^{+/+}$ and *Fgfr3*$^{Asn534Lys/+}$ male mice. Scale bar = 0.5mm. **p<0.001 (**C**) Dot plots for the trabecular bone parameters studied on WT (n=12) and *Hch* (n=10) mice: bone mineral density (BMD), ratio of bone volume on tissue volume (BV/TV), trabecular number (Tb.N), trabecular space (Tb.Sp), trabecular thickness (Tb.Th). ns=not significant, *p<0.05, ***p<0.001 Student's t-test. (**D**) Schematic representation of the set up required for lumbar vertebra compression. Representative load displacement curves (white arrow head = Yield Load; black arrow head = Maximum Load; dotted line = Stiffness) and histograms for the mechanical parameters of WT and *Hch* vertebrae: Yield Load, Maximum Load and Stiffness. ns= not significant, *p<0.05, **p<0.01 Student's t-test. (**E**) Safranin-O staining of lumbar intervertebral disc (IVD) (L5-L6) in P14 mice Scale bar = 250µm (**F**) HREM 3D reconstruction and visualization of IVD and lumbar vertebrae Scale bar = 1000µm. Graphical representation of Nucleus Pulposus (NP) Sphericity (WT n=5; *Hch* n=5) and NP on IVD volume (WT n=5; *Hch* n=5). ns= not significant, **p<0.01 Mann-Whitney test.

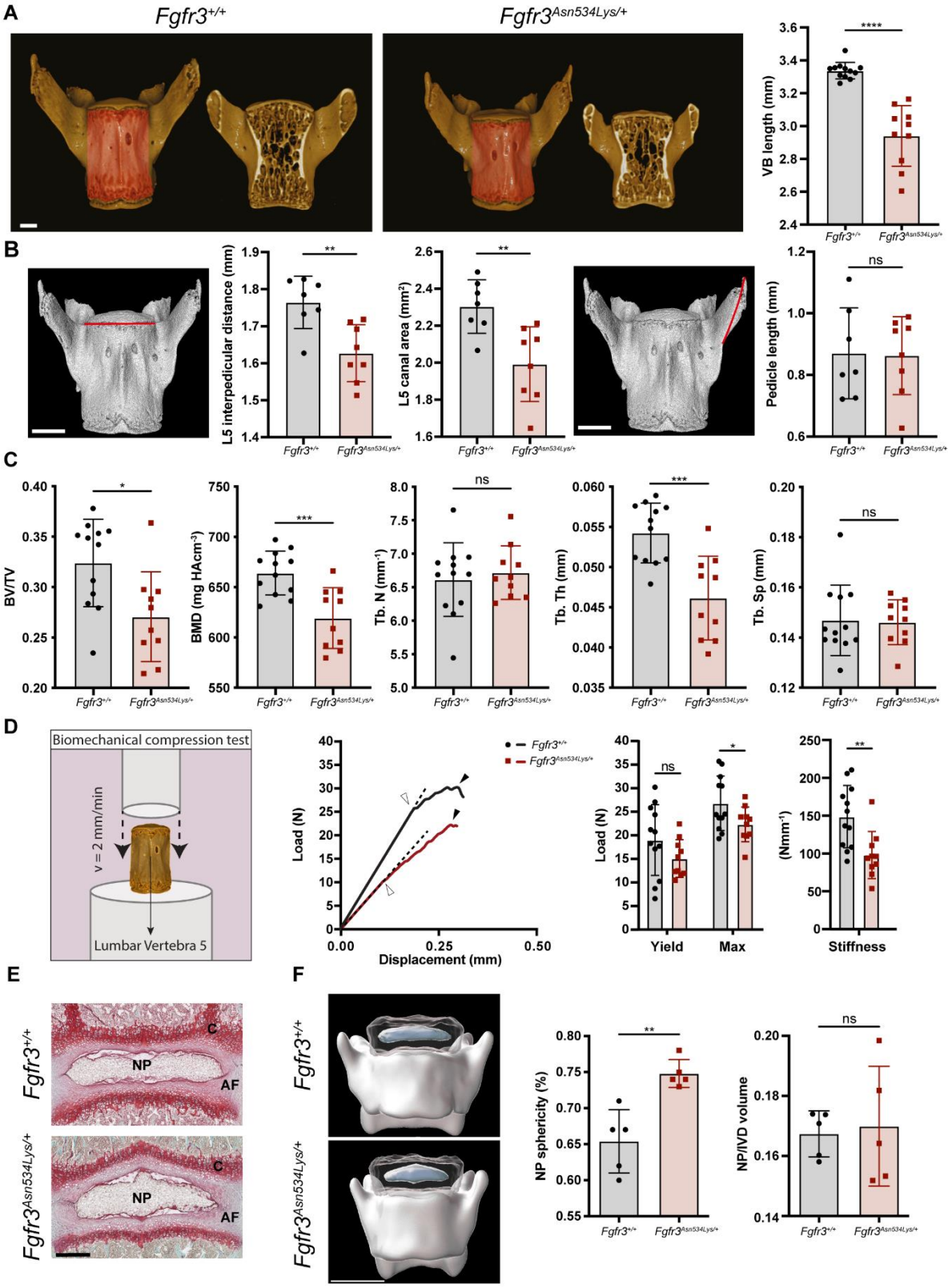
A
Fgfr3+/+
Fgfr3Asn534Lys/+
VB length (mm)
****
B
L5 interpedicular distance (mm)
**
L5 canal area (mm²)
**
Pedicle length (mm)
ns
C
BV/TV
*
BMD (mg HAcm-3)
***
Tb. N (mm-1)
ns
Tb. Th (mm)
***
Tb. Sp (mm)
ns
D
Biomechanical compression test
v = 2 mm/min
Lumbar Vertebra 5
Load (N)
Displacement (mm)
Yield
Max
Stiffness
E
C
NP
AF
F
NP sphericity (%)
NP/IVD volume

Figure 4: Analyses of the cartilage growth plate and the secondary ossification center
(**A**) H&E femur distal growth plate at P14 and P21 showing secondary ossification center delay and reduced hypertrophic cartilage area (Scale bar = 200µm and 50µm). (**B**) Collagen type X (Col X) immunostaining (Scale bar = 50µm), graphical representation of mean cells area in Col X-labelled zone (WT n=7 and $Fgfr3^{Asn534Lys/+}$ mice n= 6, *p<0.05 Mann-Whitney test.
(**C**) HREM 3D reconstruction and visualization of secondary ossification center of the distal femur Scale bar = 1000µm and graphical representation of the volume of the SOC/epiphysis ratio ($Fgfr3^{+/+}$ n=5 and $Fgfr3^{Asn534Lys/+}$ mice n=5, *p<0.05 Mann-Whitney test). **D**) KI67 positive cells/Dapi at p14 in $Fgfr3^{+/+}$ (n=6) and $Fgfr3^{Asn534Lys/+}$ (n=7) mice, BrdU positive cells/Dapi at p14 in $Fgfr3^{+/+}$ (n=7) and $Fgfr3^{Asn534Lys/+}$ (n=7), BrdU positive cells/Dapi at p21 in $Fgfr3^{+/+}$ (n=5) and $Fgfr3^{Asn534Lys/+}$ (n=5) (ns= not significant, Mann-Whitney test) (**E**) p-Erk1/2 immunostaining on P14 growth plate. Graphical representation of relative intensity of p-Erk1/2 on $Fgfr3^{+/+}$ (n=5) and $Fgfr3^{Asn534Lys/+}$ (n=7) growth plates Mann-Withney test, *p<0.05. (**F**) Representative immunoblots of p-ERK1/2 on ERK1/2 quantification from primary chondrocytes with FGF2 stimulation over time (0, 5, 30, 60, 120 min) from 4 separate independent western blot with (n=5 mice per group), graphical representation of p-Erk1/2/Erk1/2 during time * p<0.05 Sidak's multiple comparison test.

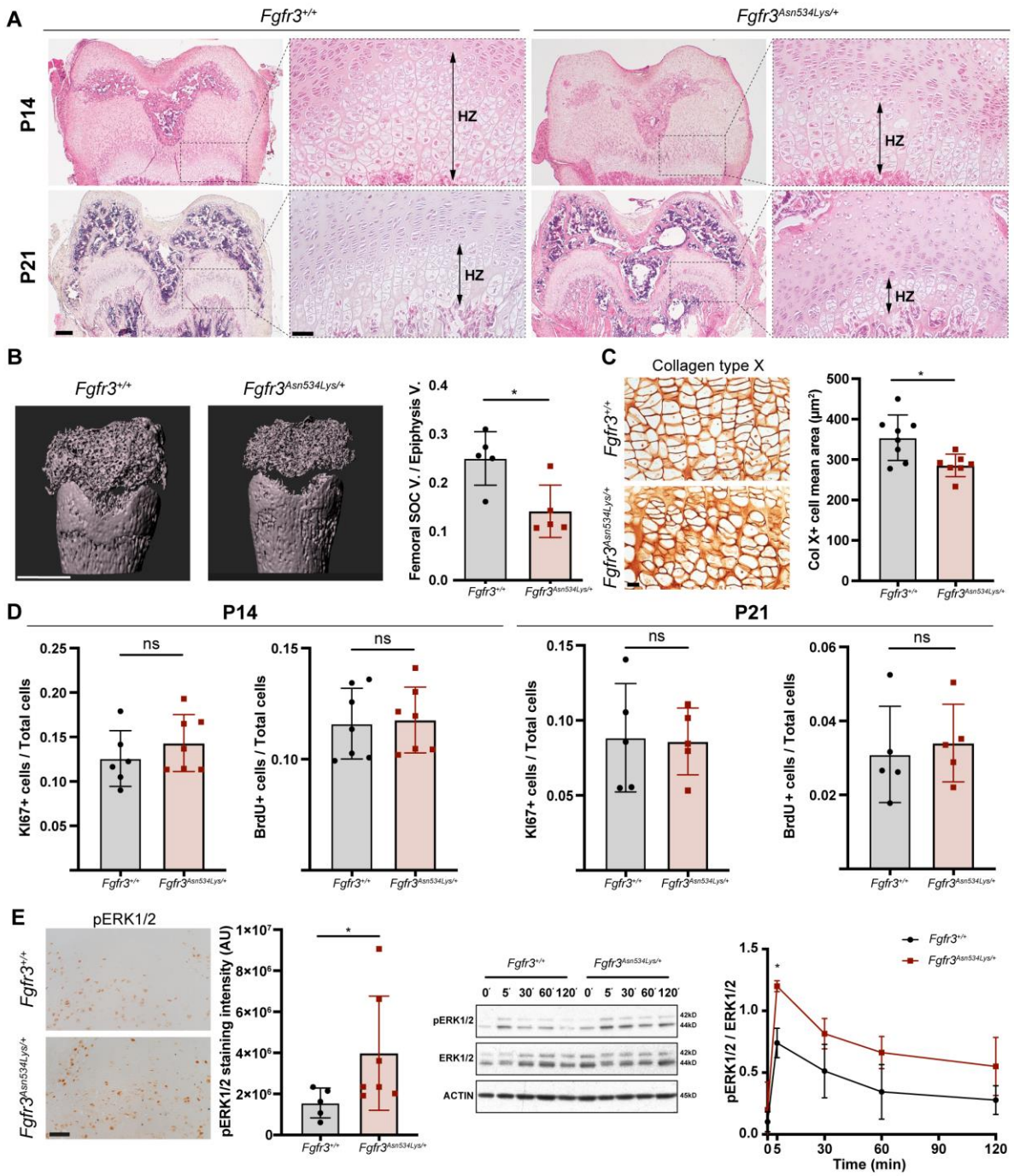
A
Fgfr3+/+
Fgfr3Asn534Lys/+
P14
P21
HZ
B
Fgfr3+/+
Fgfr3Asn534Lys/+
Femoral SOC V. / Epiphysis V.
C
Collagen type X
Col X+ cell mean area (µm²)
D
P14
P21
KI67+ cells / Total cells
BrdU+ cells / Total cells
ns
E
pERK1/2
pERK1/2 staining intensity (AU)
ERK1/2
ACTIN
Time (min)

Figure 5: The microarchitecture of the femur is affected in *Fgfr3*$^{Asn534Lys/+}$ mice

(**A**) Three-dimensional visualisation of representative P70 *Fgfr3*$^{+/+}$ and *Fgfr3*$^{Asn534Lys/+}$ male femurs. Highlighted in red the ROI selected for the trabecular bone analyses, while the area in green points out the ROI chosen for the cortical bone studies. Scale bars = 1mm. Dot plots show the differences in size at P42 (*Fgfr3*$^{+/+}$ n=9, *Fgfr3*$^{Asn534Lys/+}$ n=8), P70 (*Fgfr3*$^{+/+}$ n=12, *Fgfr3*$^{Asn534Lys/+}$ n=10) and P180 (*Fgfr3*$^{+/+}$ n=9, *Fgfr3*$^{Asn534Lys/+}$ n=10) of the femurs analyzed. ****p<0.0001 2-way ANOVA and Bonferroni's post-hoc test. (**B)** Histograms for the trabecular bone parameters of P42, P70 and P180 femurs obtained by µCT: bone mineral density (BMD), ratio of bone volume on tissue volume (BV/TV), trabecular number (Tb.N), trabecular space (Tb.Sp), trabecular thickness (Tb.Th). ns= not significant, * p<0.05, **p<0.01, ***p<0.001, ****p<0.0001 2-way ANOVA and Bonferroni's post-hoc test. (**C**) Dot plots for the cortical bone parameters of P42, P70 and P180 femurs obtained by µCT: bone mineral density (BMD), ratio of bone volume on tissue volume (BV/TV), cortical thickness (C.Th), tissue diameter (T.Dm) and cortical thickness as percentage of tissue diameter (C.Th/T.Dm) ns= not significant, * p<0.05, **p<0.01, ***p<0.001, ****p<0.0001 2-way ANOVA and Bonferroni's post-hoc test.

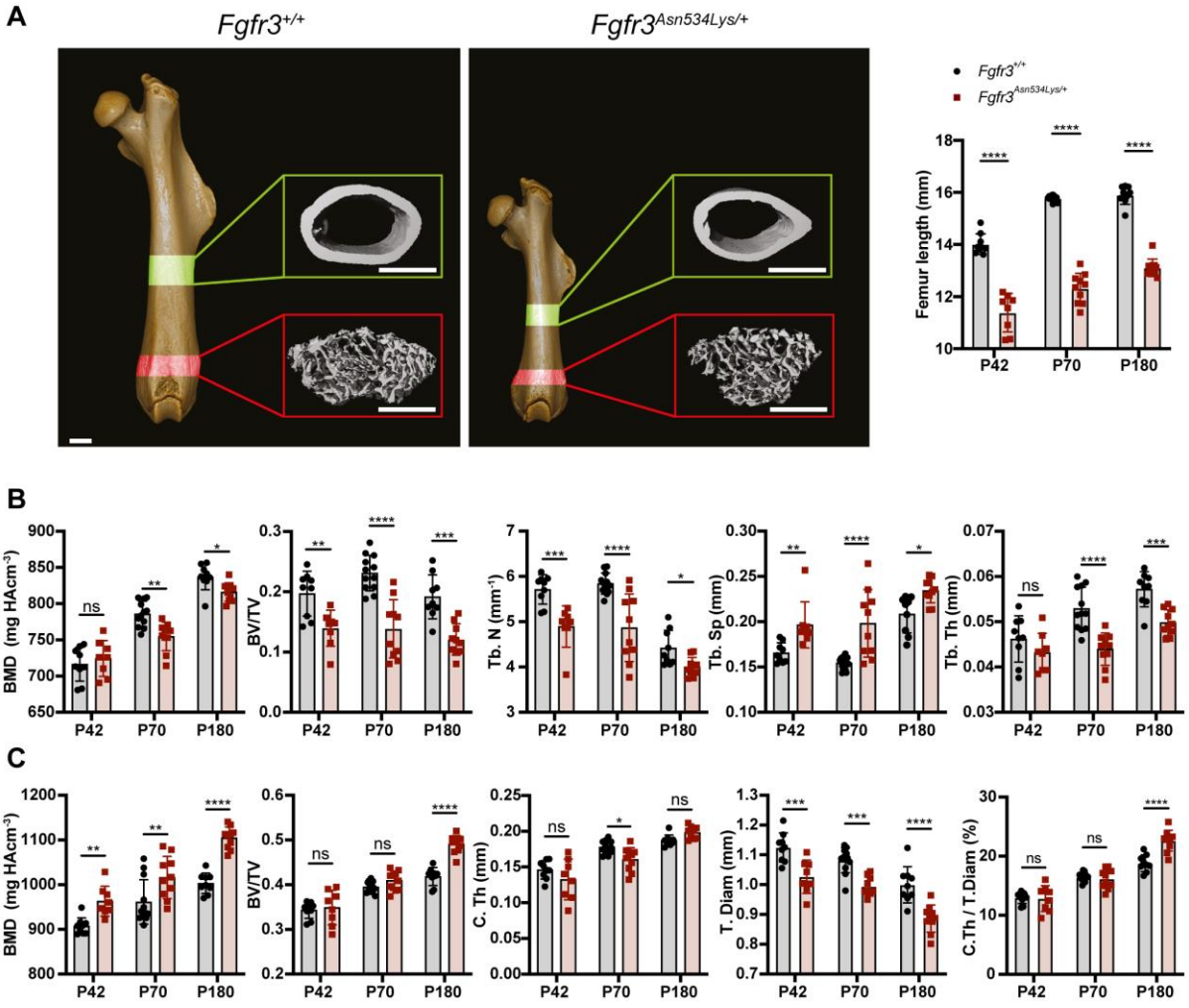
A
Fgfr3+/+
Fgfr3Asn534Lys/+
Femur length (mm)
P42
P70
P180
B
BMD (mg HAcm-3)
BV/TV
Tb. N (mm-1)
Tb. Sp (mm)
Tb. Th (mm)
C
BMD (mg HAcm-3)
BV/TV
C. Th (mm)
T. Diam (mm)
C.Th / T.Diam (%)

Figure 6: Microcomputed tomographic analyses of the tibia in *Fgfr3*$^{Asn534Lys/+}$ mice
(A) Three-dimensional imaging of representative P70 *Fgfr3*$^{+/+}$ and *Fgfr3*$^{Asn534Lys/+}$ male tibiae. Highlighted in red the ROI selected for the trabecular bone analyses, whereas the area in green points out the ROI chosen for the cortical bone studies. Scale bars = 1mm. The histograms show the differences in size at P42 (*Fgfr3*$^{+/+}$ n=9, *Fgfr3*$^{Asn534Lys/+}$ n=8), P70 (*Fgfr3*$^{+/+}$ n=12, *Fgfr3*$^{Asn534Lys/+}$ n=10) and P180 (*Fgfr3*$^{+/+}$ n=9, *Fgfr3*$^{Asn534Lys/+}$ n=10) of the tibiae analyzed. ****p<0.0001 2-way ANOVA and Bonferroni's post-hoc test. (**B)** Dot plots for the trabecular bone parameters of P42, P70 and P180 tibiae obtained by µCT: bone mineral density (BMD), ratio of bone volume on tissue volume (BV/TV), trabecular number (Tb.N), trabecular space (Tb.Sp), trabecular thickness (Tb.Th). ns= not significant, * p<0.05, **p<0.01, ***p<0.001, ****p<0.0001 2-way ANOVA and Bonferroni's post-hoc test. (**C)** Histograms for the cortical bone parameters of P42, P70 and P180 femurs obtained by µCT: bone mineral density (BMD), ratio of bone volume on tissue volume (BV/TV), cortical thickness (C.Th), tissue diameter (T.Dm) and cortical thickness as percentage of tissue diameter (C.Th/T.Dm) ns= not significant, **p<0.01, ***p<0.001, ****p<0.0001 2-way ANOVA and Bonferroni's post-hoc test.

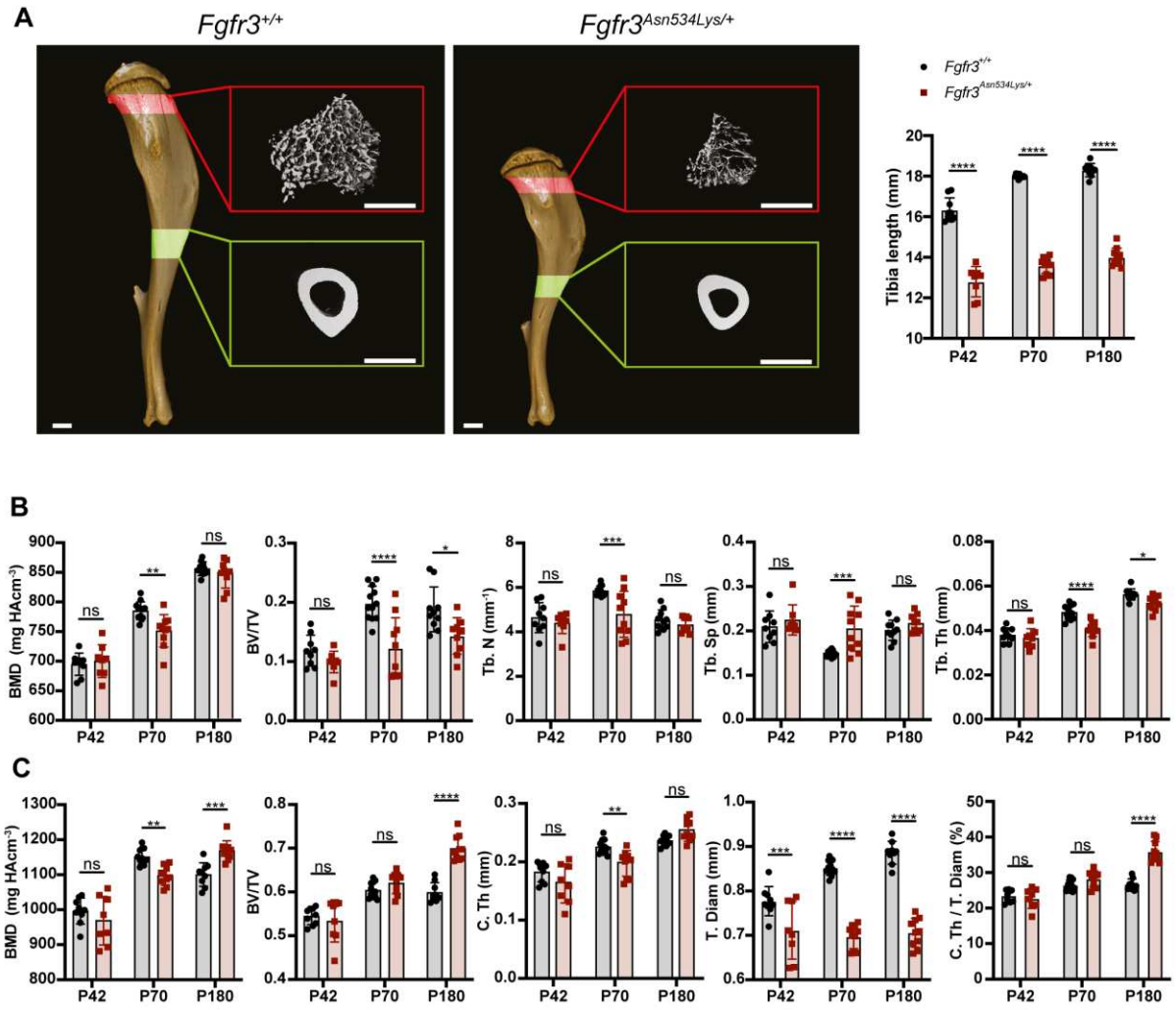
A
Fgfr3+/+
Fgfr3Asn534Lys/+
Fgfr3+/+
Fgfr3Asn534Lys/+
Tibia length (mm)
P42
P70
P180
B
BMD (mg HAcm-3)
BV/TV
Tb. N (mm-1)
Tb. Sp (mm)
Tb. Th (mm)
C
BMD (mg HAcm-3)
BV/TV
C. Th (mm)
T. Diam (mm)
C. Th / T. Diam (%)

Figure 7. Defective bone homeostasis

(**A**) qRT-PCR analysis of femoral cortical bone. Relative expressions performed in *Fgfr3*$^{+/+}$ (n= 7) and *Fgfr3*$^{Asn534Lys/+}$ (n= 6) are shown (*p<0.05, **p<0.01, ***p<0.001, Mann-Whitney test) (**B**) Histological sections of WT and *Fgfr3*$^{Asn564Lys/+}$ decalcified 2-months old male femurs stained for tartrate-resistant acid phosphatase (TRAP). Black arrow heads point out red TRAP-stained osteoclasts. Scale bars = 200µm. Graphs show osteoclast surface per mm of bone surface (Oc.S/BS), number of osteoclasts per mm of bone surface (N.Oc/BS), number of osteoclasts per mm^2 of bone (N.Oc/BV) and number of osteoclasts per mm^2 of tissue area analyzed (N.OC/TV) (mean ± SD, n = 5 per genotype, ns= not significant, Mann-Whitney test). Dashed lines outline the ROI of the trabecular area that was quantified. (**C**) µCT images representative of osteocyte lacunae in femoral cortical bone of 6-months old male WT (n = 9) and *Fgfr3*$^{Asn564Lys/+}$ (n = 10) mice highlighting small (100-200 µm^3) and large (400-2000 µm^3). Scale bar = 250µm. Graphs show osteocyte lacunae number per bone volume (Lc.N/BV), cortical microporosity (%) (*** p<0.001, **** p<0.0001, Mann-Whitney test) and relative frequency distribution of lacunae volumes (Lc.V) in WT and mutant mice. Violin plots show distribution of lacunae volumes (Lc.V) and lacunae sphericity (Lc.Sph) in WT and *Fgfr3*$^{Asn564Lys/+}$ animals (*** p<0.001, **** p<0.0001, two-tailed Kolmogorov-Smirnov test).The percentage of number of lacunae (Lc. N %) was obtained by binning the osteocyte lacunae based on the illustrated range of volumes.

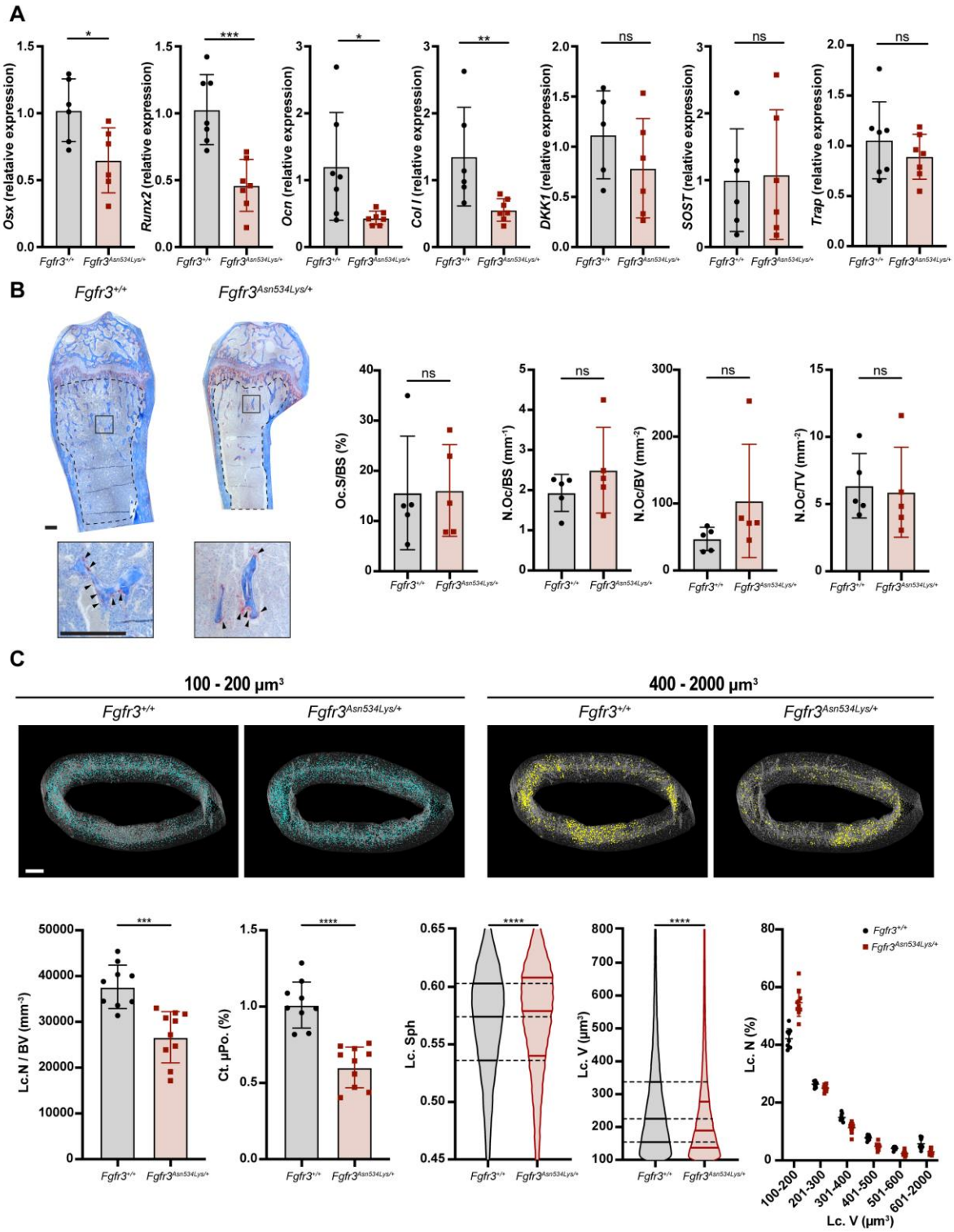
A
Osx (relataive expression)
Runx2 (relative expression)
Ocn (relative expression)
Col I (relative expression)
DKK1 (relative expression)
SOST (relative expression)
Trap (relative expression)
*
***
*
**
ns
ns
ns
Fgfr3+/+
Fgfr3Asn534Lys/+
B
Fgfr3+/+
Fgfr3Asn534Lys/+
Oc.S/BS (%)
N.Oc/BS (mm-1)
N.Oc/BV (mm-2)
N.Oc/TV (mm-2)
ns
C
100 - 200 µm3
400 - 2000 µm3
Fgfr3+/+
Fgfr3Asn534Lys/+
Lc.N / BV (mm-3)
Ct. µPo. (%)
Lc. Sph
Lc. V (µm3)
Lc. N (%)
***
****
100-200
201-300
301-400
401-500
501-600
601-2000
Lc. V (µm3)

Figure 8: Evaluation of bone strength in tibiae

(A) Schematic representation of a three-point bend test on tibia and representative load displacement curves of tibiae from male P42, P70 and P180 *Fgfr3*$^{+/+}$ and *Fgfr3*$^{Asn534Lys/+}$ mice (white arrow head = Yield Load; black arrow head = Maximum Load; black arrow = Fracture Load, dotted line = Stiffness, colored area under curve = Energy Dissipated prior to fracture). (**B)** Histograms for the biomechanical parameters of *Fgfr3*$^{+/+}$ (P42 n=9, P70 n=12, P180 n=9) and *Fgfr3*$^{Asn534Lys/+}$ (P42 n=8, P70 n=10, P180 n=10) tibiae: Yield Load, Maximum Load, Fracture Load, Stiffness, percentage of Energy Dissipated prior to Fracture (toughness), Plastic Work as percentage of Total Work. ns= not significant, $^{**}p<0.01$, $^{***}p<0.001$, $^{****}p<0.0001$ 2-way ANOVA and Bonferroni's post-hoc test.

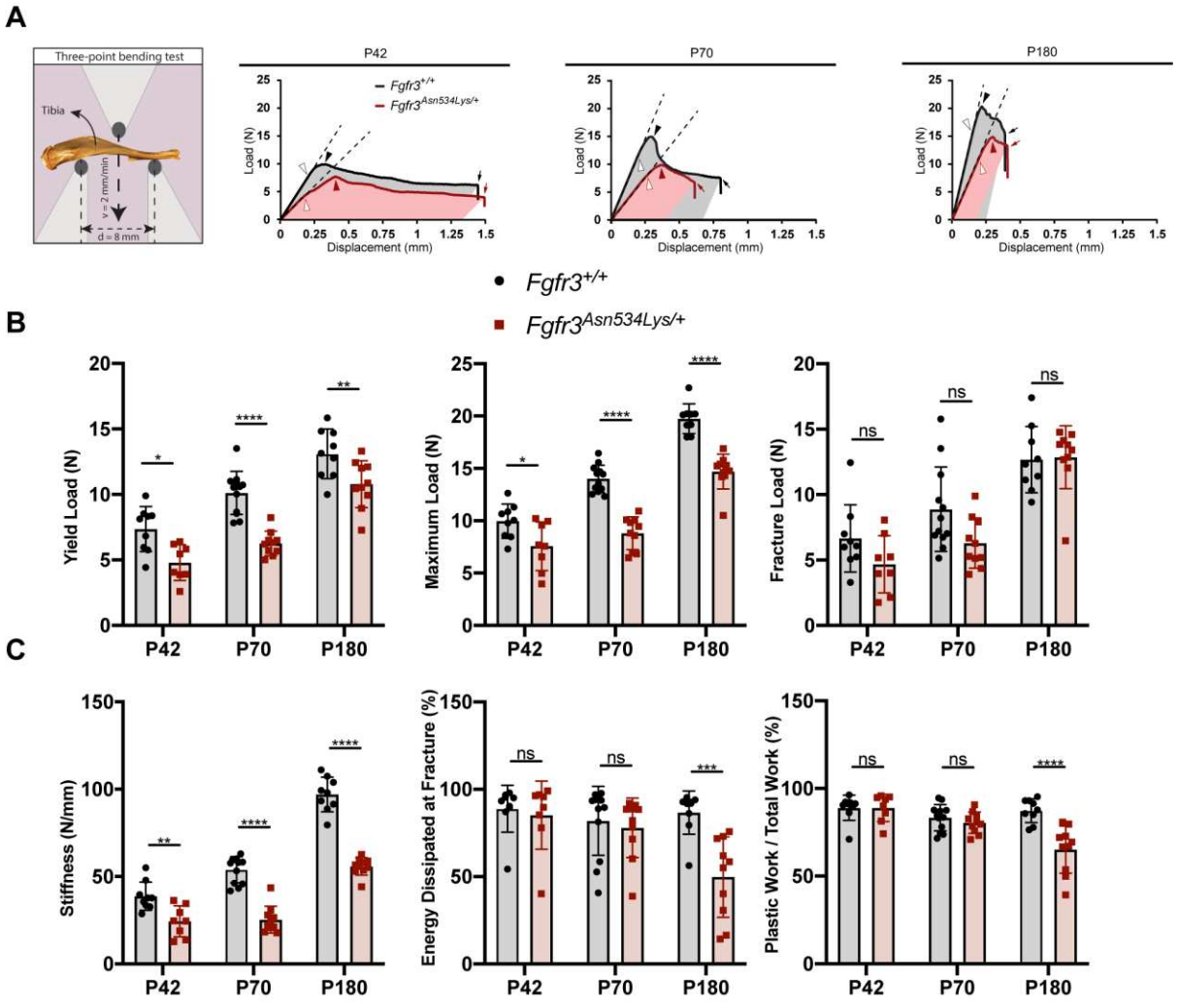
A
Three-point bending test
Tibia
v = 2 mm/min
d = 8 mm
P42
P70
P180
Fgfr3+/+
Fgfr3Asn534Lys/+
Load (N)
Displacement (mm)
B
Yield Load (N)
Maximum Load (N)
Fracture Load (N)
C
Stiffness (N/mm)
Energy Dissipated at Fracture (%)
Plastic Work / Total Work (%)
ns

Table 1: Measurements of the naso-anal, bones size and weight of male and female mice at Postnatal day 1, 7, 14, 21, 28, 42, 60 and 180. t student statistical test.

Table 1: Measurements of the naso-anal, bones size and weight of male and female mice at Postnatal day 1, 7, 14, 21, 28, 42, 60 and 180

Days of age	1		7		14		21		28		42		60		180	
Genotype	*Fgfr3* $^{+/+}$	*Fgfr3* $^{Asn534Lys/+}$	*Fgfr3* $^{+/+}$	*Fgfr3* $^{Asn534Lys/+}$	*Fgfr3* $^{+/+}$	*Fgfr3* $^{Asn534Lys/+}$	*Fgfr3* $^{+/+}$	*Fgfr3* $^{Asn534Lys/+}$	*Fgfr3* $^{+/+}$	*Fgfr3* $^{Asn534Lys/+}$	*Fgfr3* $^{+/+}$	*Fgfr3* $^{Asn534Lys/+}$	*Fgfr3* $^{+/+}$	*Fgfr3* $^{Asn534Lys/+}$	*Fgfr3* $^{+/+}$	*Fgfr3* $^{Asn534Lys/+}$
Mice number (n)	10	13	7	11	7	10	7	10	10	9	10	12	14	18	11	12
Weight (g)																
mean	1,36	1,38	3,41	3,65	7,01	6,77	8,69	7,02	15,83	13,12	21,24	16,44	25,02	18,06	34,60	25,39
standard deviation ±	0,14	0,17	0,45	0,37	0,95	0,88	2,18	1,93	1,49	1,54	3,02	2,98	2,81	4,30	4,65	1,58
difference (%)	1,99		6,66		-3,58		-14,63		-18,70		-25,46		-35,56		-30,68	
p value	0,7534		0,3623		0,4173		0,0926		0,0003		0,0036		<0,0001		<0,0001	
Naso-anal length (mm)																
mean	31,22	30,54	41,69	39,76	56,91	53,37	62,75	55,76	73	68,11	83,86	73,29	88,17	76,55	92,45	84,19
standard deviation ±	1,19	1,05	2,88	4,78	2,56	2,26	6,09	3,49	2,79	2,15	2,82	4,33	3,44	6,08	2,85	3,29
difference (%)	-2,22		-4,75		-6,43		-11,80		-6,93		-13,46		-14,12		-9,36	
p value	0,1862		0,451		0,0185		0,0056		0,0005		<0,0001		<0.0001		<0,0001	
mice number (n)	0	0	7	12	8	12	9	11	0	0	10	12	6	8	11	11
Femur length (mm)																
mean			6,10	5,58	8,36	7,38	9,37	8,02			12,99	10,58	14,90	11,20	15,52	12,58
standard deviation ±			0,20	0,07	0,34	0,27	0,67	0,63			0,39	0,37	0,83	0,49	0,32	0,33
difference (%)			-8,94		-12,41		-15,55				-20,47		-28,33		-20,93	
p value			0,000007		0,000006		0,000224				<0,000001		0,000002		<0,000001	
Tibia length (mm)																
mean			7,43	6,85	11,22	9,56	12,37	10,37			16,03	12,54	17,53	13,14	18,06	14,02
standard deviation ±			0,49	0,34	0,40	0,39	0,86	0,52			0,38	0,47	0,64	0,41	0,32	0,25
difference (%)			-8,05		-15,90		-17,63				-24,46		-28,65		-25,20	
p value			0,0131		<0,0001		<0,0001				<0,0001		<0,0001		<0,0001	
Humerus length (mm)																
mean			6,03	5,66	7,55	6,86	8,14	7,18			10,89	8,98	11,76	9,29	12,31	10,59
standard deviation ±			0,16	0,20	0,26	0,36	0,53	0,45			0,32	0,31	0,61	0,30	0,15	0,17
difference (%)			-6,20		-9,57		-12,53				-19,18		-23,41		-14,94	
p value			0,000063		0,00006		0,000414				<0,000001		<0,000001		<0,000001	
Ulna length (mm)																
mean			7,41	6,78	9,67	8,65	10,42	9,24			12,65	10,69	13,61	10,97	13,57	11,62
standard deviation ±			0,28	0,39	0,43	0,52	0,66	0,71			0,30	0,56	0,52	0,47	0,31	0,33
difference (%)			-8,80		-11,17		-12,03				-16,79		-21,48		-15,50	
p value			0,000137		0,000133		0,001182				<0,000001		<0,000001		<0,000001	

Supplemental Figure 1

(**A**) Generation of the dwarf *Fgfr3*$^{Asn534Lys/+}$ mouse. The point mutation Asn534Lys is localized in mouse exon 12. *Fgfr3*$^{Asn534Lys/+}$ mice were crossed with CMV-Cre mice to remove the NEO gene. (**B**) The presence of the heterozygous mutation p.Asn534Lys in DNA isolated from tail. **(C)** Graphical representation of the humerus and ulna length of *Fgfr3*$^{Asn534Lys/+}$ and *Fgfr3*$^{+/+}$ male and female mice during development (postnatal day 1, 7, 14, 21, 28, 42, 60 and 180) T student statistical test.

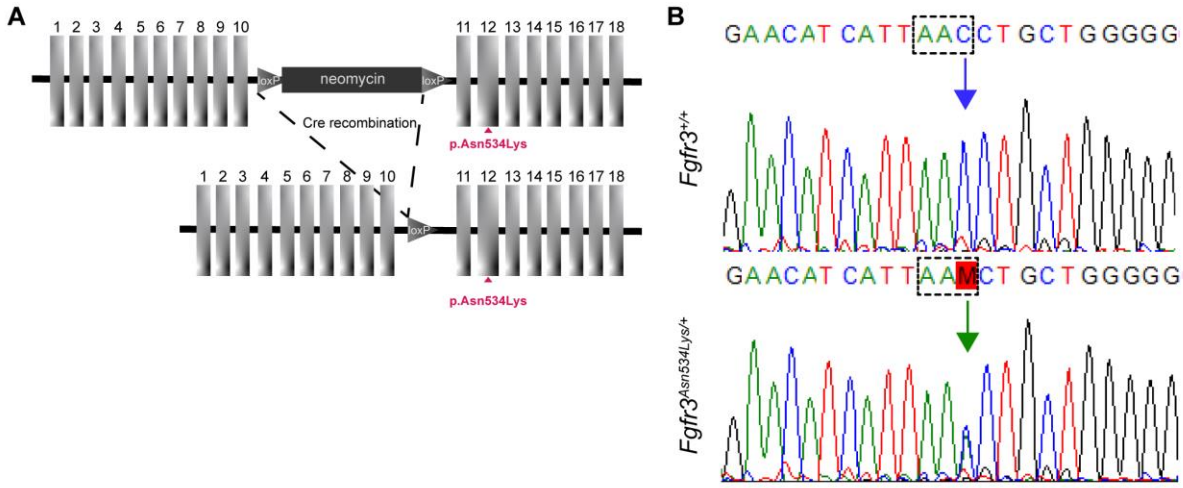
A
1 2 3 4 5 6 7 8 9 10
loxP
neomycin
loxP
11 12 13 14 15 16 17 18
Cre recombination
p.Asn534Lys
1 2 3 4 5 6 7 8 9 10
11 12 13 14 15 16 17 18
loxP
p.Asn534Lys
B
GAACAT CATT AAC CT GCT GGGGG
Fgfr3+/+
GAACAT CATT AAT CT GCT GGGGG
Fgfr3Asn534Lys/+

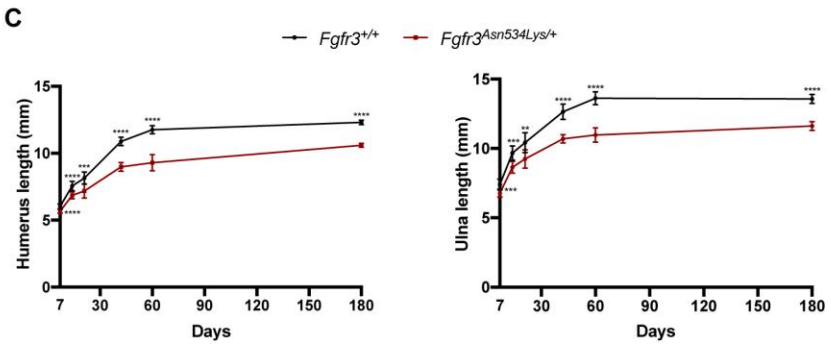
C
Fgfr3+/+
Fgfr3Asn534Lys/+
Humerus length (mm)
Ulna length (mm)
Days
0
5
10
15
7
30
60
90
120
150
180

Supplemental Figure 2

(**A**) Definitions and positioning of the 57 anatomical landmarks per specimen digitized on three-dimensional models on mouse skull. Comparison of skull shape between mutants and controls: plots of Principal Components (PC) scores for PC1 and PC2 with corresponding variances (in %) (*Fgfr3*$^{Asn534Lys/+}$ n=9 and *Fgfr3*$^{+/+}$ n=9). (**B**) Definitions and positioning of the 40 anatomical landmarks per specimen digitized on three-dimensional models: mandibular anatomical landmarks (n=20 per mandible); maxillar anatomical landmarks (n=10 per side). Comparison of mandibular shape and relationship to the maxilla between mutants and controls: plots of Principal Components (PC) scores for PC1 and PC2 with corresponding variances (in %) (*Fgfr3*$^{Asn534Lys/+}$ n=9 and *Fgfr3*$^{+/+}$ mutants n=9) Results were statistically significant ($p < 0.01$).

A

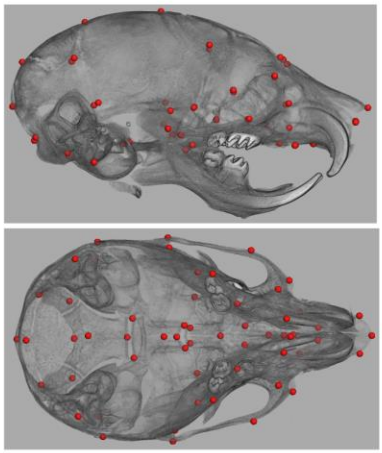

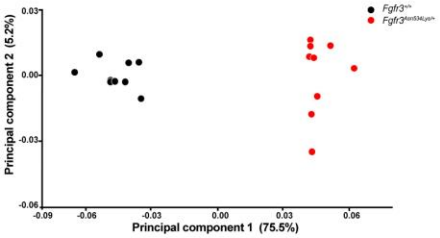
Fgfr3+/+
Fgfr3Ser534Leu/+
Principal component 2 (5.2%)
0.03
0.00
-0.03
-0.06
-0.09
-0.06
-0.03
0.00
0.03
0.06
Principal component 1 (75.5%)

B

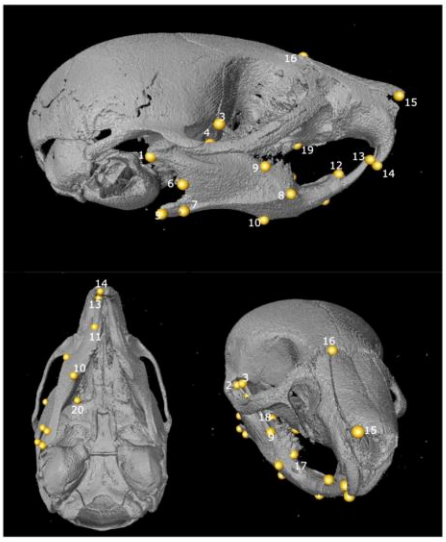
16
15
3
4
19
1
13
9
12
14
6
8
7
10
14
13
11
10
20
16
3
2
18
15
17

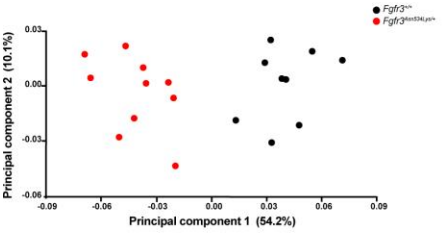
Fgfr3+/+
Fgfr3Ser534Leu/+
Principal component 2 (10.1%)
0.03
0.00
-0.03
-0.06
-0.09
-0.06
-0.03
0.00
0.03
0.06
0.09
Principal component 1 (54.2%)

Supplemental Figure 3

(**A)** Definitions and positioning of the 32 anatomical landmarks per specimen digitized on three-dimensional models on mouse L5 lumbar vertebrae. Comparison of L5 lumbar vertebrae shape between *Fgfr3*$^{+/+}$*:* P70 n=7, *Fgfr3*$^{Asn534Lys/+}$: P70 n=8 male mice plots of Principal Components (PC) scores for PC1 and PC2 with corresponding variances (in %).
(**B**) H&E staining of L5 to L6 lumbar vertebrae intervertebral disc form 1 day-of-age to 3 months-of-age. Scale bar = 200µm
(C) Representative images of FGFR3 immunostaining

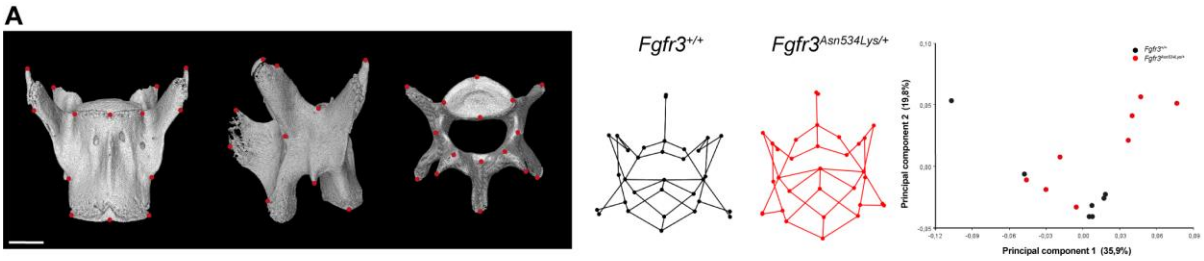
A
Fgfr3+/+
Fgfr3Asn534Lys/+
Principal component 2 (19,8%)
Principal component 1 (35,9%)

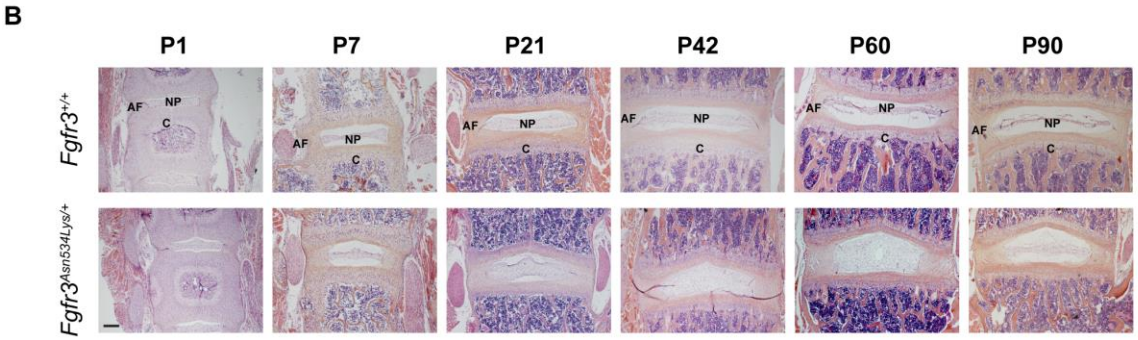
B
P1
P7
P21
P42
P60
P90
Fgfr3+/+
Fgfr3Asn534Lys/+
AF
NP
C

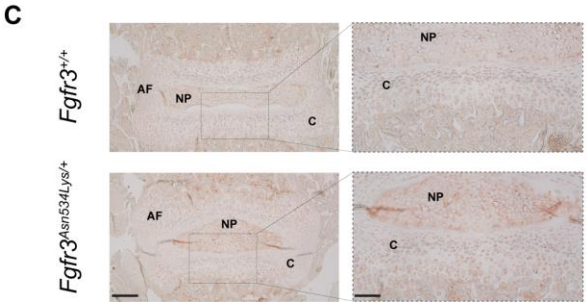
C
Fgfr3+/+
Fgfr3Asn534Lys/+
AF
NP
C

Supplemental Figure 4
Representative μCT images of femur and tibia trabecular bone from *Fgfr3*$^{+/+}$ and *Fgfr3*$^{Asn534Lys/+}$ mice at P42, P70 and P183. Scale bars = 1mm

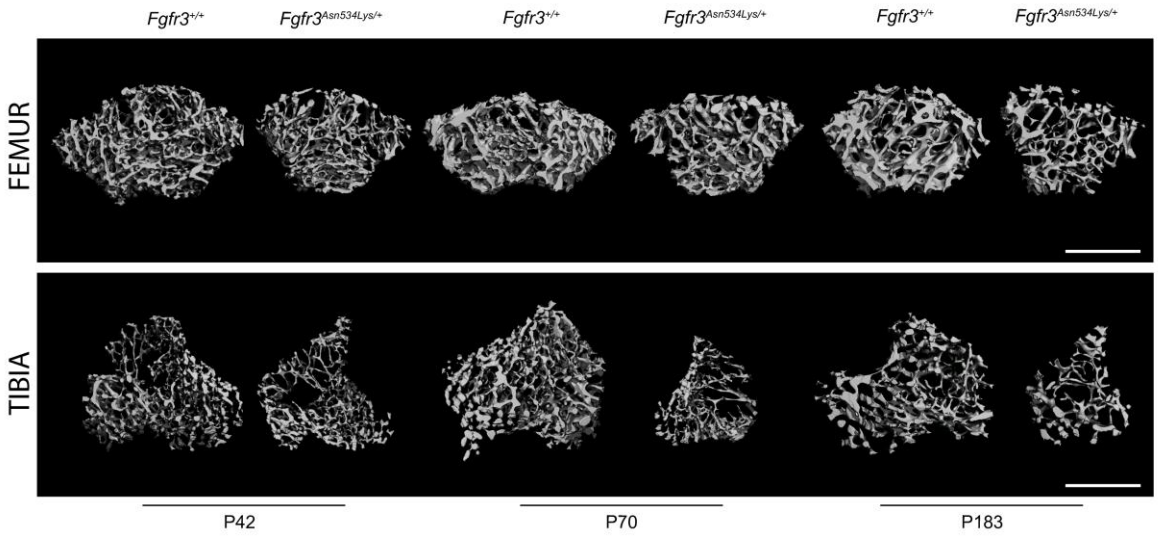
Fgfr3+/+
Fgfr3Asn534Lys/+
Fgfr3+/+
Fgfr3Asn534Lys/+
Fgfr3+/+
Fgfr3Asn534Lys/+
FEMUR
TIBIA
P42
P70
P183

Supplemental Figure 5
Representative μCT images of femur and tibia cortical bone from *Fgfr3*$^{+/+}$ and *Fgfr3*$^{Asn534Lys/+}$ mice at P42, P70 and P183. Scale bars = 1mm

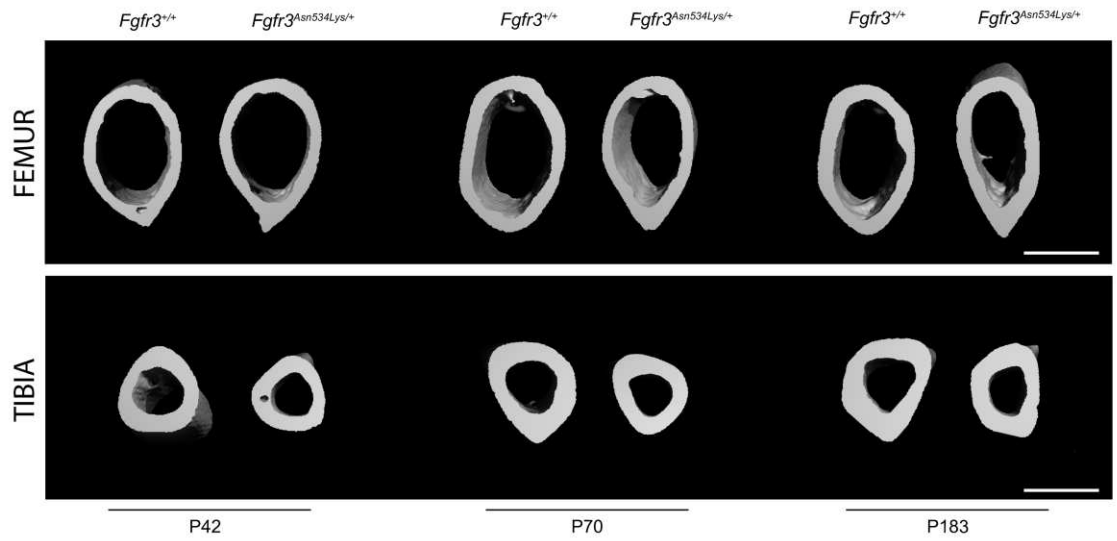
Fgfr3+/+
Fgfr3Asn534Lys/+
Fgfr3+/+
Fgfr3Asn534Lys/+
Fgfr3+/+
Fgfr3Asn534Lys/+
FEMUR
TIBIA
P42
P70
P183

Supplemental Table 1
Skull analyses on P14 mice, t-student statistical test.

Supplementary Table 1: skull analyses on P14 mice

Days of age	14	
Genotype	*Fgfr3*$^{+/+}$	*Fgfr3*$^{Asn534Lys/+}$
Mice number (n)	9	8
skull length		
mean	17,88	16,3
standard deviation ±	0,6756	0,4993
difference (%)	8,836689038	
p value	<0,0001	
skull width		
mean	8,862	9,21
standard deviation ±	0,1869	0,2692
difference (%)	-3,926878808	
p value	0,007	
centroid size		
mean	41,98	39,74
standard deviation ±	0,9691	0,69
difference (%)	5,335874226	
p value	<0,0001	
skull base length		
mean	7,596	6,008
standard deviation ±	0,2319	0,129
difference (%)	21	
p value	0,02	
foramen magnum area		
mean	13,07	10,59
standard deviation ±	0,6024	0,7466
difference (%)	20	
p value	<0,0001	

Supplemental Table 2
Selection of region of interests (ROIs) for μCT analyses of lumbar vertebrae, femurs and tibiae.

Supplementary Table 2: Region Of Interests selected for microcomputed tomographic analyses.
ROIs expressed as % of total bone length, minimum and maximum size per group.

			P42			P70			P180		
Analysis	**Bone**	**Genotype & Treatment**	**Bone %**	**Min size (µm)**	**Max size (µm)**	**Bone %**	**Min size (µm)**	**Max size (µm)**	**Bone %**	**Min size (µm)**	**Max size (µm)**
Trabecular Analysis	Lumbar Vertebra 5	*Fgfr3* $^{+/+}$				100%*	3260	3460			
		Fgfr3 $^{Asn534Lys/+}$					2605	3165			
	Femur	*Fgfr3* $^{+/+}$	7,0%	955	1040	6,0%	935	955	6,0%	905	975
		Fgfr3 $^{Asn534Lys/+}$		765	855		685	795		765	840
	Tibia	*Fgfr3* $^{+/+}$	6,0%	945	1040	6,0%	1070	1090	5,5%	975	1040
		Fgfr3 $^{Asn534Lys/+}$		700	825		780	845		740	820
Cortical Analysis	Femur	*Fgfr3* $^{+/+}$	9,5%	1290	1410	8,5%	1320	1350	8,0%	1210	1300
		Fgfr3 $^{Asn534Lys/+}$		980	1160		970	1130		1030	1120
	Tibia	*Fgfr3* $^{+/+}$	9,5%	1500	1640	8,5%	1510	1540	8,0%	1420	1510
		Fgfr3 $^{Asn534Lys/+}$		1110	1310		1100	1200		1080	1190

** For Lumbar Vertebrae the full Vertebral Body (in between the two cartilaginous end plates) has been selected as ROI*

Supplemental Table 3

Lumbar vertebrae 5 measurements obtained with µCT are presented classified by genotype and age. Values are expressed as mean ± standard deviation. The difference among WT and *Hch* mice is also presented in percentage and the relative p-value is also reported.

			P70			
			Fgfr3$^{+/+}$ **n**=11; *Fgfr3*$^{Asn534Lys/+}$ **n**=10			
		genotype	**mean**	**standard deviation ±**	**difference (%)**	**p-value**
Trabecular	**TV (mm^3)**	*Fgfr3*$^{+/+}$	2,893	0,1775	-26,23574144	<0.0001
		Fgfr3$^{Asn534Lys/+}$	2,134	0,4106		
	BV/TV	*Fgfr3*$^{+/+}$	0,3508	0,02244	-17,64538198	<0.0001
		Fgfr3$^{Asn534Lys/+}$	0,2889	0,03187		
	Tb.N (mm^{-1})	*Fgfr3*$^{+/+}$	6,527	0,175	-0,536234104	0,7922
		Fgfr3$^{Asn534Lys/+}$	6,492	0,4171		
	Tb.Th (mm)	*Fgfr3*$^{+/+}$	0,06207	0,003405	-14,62864508	<0.0001
		Fgfr3$^{Asn534Lys/+}$	0,05299	0,0031		
	Tb.Sp (mm)	*Fgfr3*$^{+/+}$	0,1576	0,005307	-0,253807107	0,8933
		Fgfr3$^{Asn534Lys/+}$	0,1572	0,01042		
	BMD (mgHAcm^{-3})	*Fgfr3*$^{+/+}$	646,1	16,84	-6,531496672	<0.0001
		Fgfr3$^{Asn534Lys/+}$	603,9	12,75		
	Vertebral body size (mm)	*Fgfr3*$^{+/+}$	3,338	0,05025	-11,89334931	<0.0001
		Fgfr3$^{Asn534Lys/+}$	2,941	0,1842		

Supplemental Table 4

Femur measurements obtained with μCT are presented classified by genotype and age. Values are expressed as mean ± standard deviation. The difference among WT and *Hch* mice is also presented in percentage and the relative p-value is also reported.

Supplementary Table 4: Femur - Descriptive statistics and 2-way ANOVA with Bonferroni's test p-values of microcomputed tomographic analyses

			P42				P70				P180			
			Fgfr3 $^{+/+}$ n=9; *Fgfr3* $^{Asn534Lys/+}$ n=8				*Fgfr3* $^{+/+}$ n=12; *Fgfr3* $^{Asn534Lys/+}$ n=10				*Fgfr3* $^{+/+}$ n=9; *Fgfr3* $^{Asn534Lys/+}$ n=10			
		genotype	mean	standard deviation ±	difference (%)	p-value	mean	standard deviation ±	difference (%)	p-value	mean	standard deviation ±	difference (%)	p-value
Trabecular	TV (mm^3)	*Fgfr3* $^{+/+}$	2,196	0,1748	-20,67395264	<0.0001	2,338	0,1166	-24,8502994	<0.0001	2,441	0,1993	-28,10323638	<0.0001
		Fgfr3 $^{Asn534Lys/+}$	1,742	0,3111			1,757	0,2102			1,755	0,1118		
	BV/TV	*Fgfr3* $^{+/+}$	0,197	0,03725	-29,69543147	0,0038	0,231	0,02938	-40,47619048	<0.0001	0,1916	0,03649	-37,36951983	0,0002
		Fgfr3 $^{Asn534Lys/+}$	0,1385	0,02993			0,1375	0,04843			0,12	0,02594		
	Tb.N (mm^{-1})	*Fgfr3* $^{+/+}$	5,713	0,3253	-14,3182216	0,0007	5,843	0,2331	-16,70374807	<0.0001	4,418	0,3919	-9,416025351	0,118
		Fgfr3 $^{Asn534Lys/+}$	4,895	0,4552			4,867	0,7461			4,002	0,2078		
	Tb.Th (mm)	*Fgfr3* $^{+/+}$	0,0462	0,005121	-6,515151515	0,4208	0,05291	0,004729	-16,95331695	<0.0001	0,05718	0,00389	-12,88912207	0,0009
		Fgfr3 $^{Asn534Lys/+}$	0,04319	0,004262			0,04394	0,003564			0,04981	0,002846		
	Tb.Sp (mm)	*Fgfr3* $^{+/+}$	0,1656	0,01105	18,59903382	0,0136	0,1544	0,00697	28,30310881	<0.0001	0,2085	0,02071	12,32613909	0,0342
		Fgfr3 $^{Asn534Lys/+}$	0,1964	0,02539			0,1981	0,03735			0,2342	0,01347		
	BMD ($mgHAcm^{-3}$)	*Fgfr3* $^{+/+}$	716,4	23,37	1,102735902	0,787	785,8	17,55	-3,957750064	0,0013	837	17,76	-2,508960573	0,0658
		Fgfr3 $^{Asn534Lys/+}$	724,3	24,79			754,7	19,69			816	12,72		
Cortical	TV (mm^3)	*Fgfr3* $^{+/+}$	2,588	0,2834	-36,32148377	<0.0001	2,815	0,1151	-40	<0.0001	2,779	0,2012	-33,86110112	<0.0001
		Fgfr3 $^{Asn534Lys/+}$	1,648	0,395			1,689	0,2635			1,838	0,0978		
	BV/TV	*Fgfr3* $^{+/+}$	0,3436	0,01857	1,51338766	>0.9999	0,3953	0,01218	3,491019479	0,4602	0,4182	0,02015	17,28837877	<0.0001
		Fgfr3 $^{Asn534Lys/+}$	0,3488	0,03887			0,4091	0,02155			0,4905	0,01945		
	C.Th (mm)	*Fgfr3* $^{+/+}$	0,1461	0,0128	-9,240246407	0,2	0,1778	0,008771	-9,673790776	0,0279	0,1872	0,007673	6,784188034	0,205
		Fgfr3 $^{Asn534Lys/+}$	0,1326	0,02835			0,1606	0,01634			0,1999	0,009674		
	Ma.Dm (mm)	*Fgfr3* $^{+/+}$	0,9786	0,04484	-8,634784386	0,0007	0,904	0,03774	-7,842920354	0,0013	0,8125	0,06199	-15,53230769	<0.0001
		Fgfr3 $^{Asn534Lys/+}$	0,8941	0,03273			0,8331	0,03214			0,6863	0,04878		
	BMD ($mgHAcm^{-3}$)	*Fgfr3* $^{+/+}$	907,5	18,48	6,126721763	0,0075	961,5	49,76	5,668226729	0,0026	1003	22,73	10,16949153	<0.0001
		Fgfr3 $^{Asn534Lys/+}$	963,1	33,52			1016	47,33			1105	24,49		
	T.Dm (mm)	*Fgfr3* $^{+/+}$	1,125	0,04918	-8,711111111	0,0003	1,082	0,04189	-8,160813309	0,0002	0,9997	0,06078	-11,34340302	<0.0001
		Fgfr3 $^{Asn534Lys/+}$	1,027	0,05577			0,9937	0,03125			0,8863	0,04534		
	C.Th / T.Dm (%)	*Fgfr3* $^{+/+}$	12,99	0,9997	-0,16	>0.9999	16,44	0,7112	-0,28	>0.9999	18,79	1,413	3,83	<0.0001
		Fgfr3 $^{Asn534Lys/+}$	12,83	2,189			16,16	1,633			22,62	1,76		
	Full bone Length (mm)	*Fgfr3* $^{+/+}$	14,02	0,3907	-18,83024251	<0.0001	15,78	0,1156	-21,92648923	<0.0001	15,9	0,3589	-17,54716981	<0.0001
		Fgfr3 $^{Asn534Lys/+}$	11,38	0,7412			12,32	0,5796			13,11	0,332		

Supplemental Table 5

Tibia measurements obtained with μCT are presented classified by genotype and age. Values are expressed as mean ± standard deviation. The difference among WT and *Hch* mice is also presented in percentage and the relative p-value is also reported.

Supplementary Table 5: Tibia - Descriptive statistics and 2-way ANOVA with Bonferroni's test p-values of microcomputed tomographic analyses

			P42				P70				P180			
			Fgfr3 $^{+/+}$ n=9; *Fgfr3* $^{Asn534Lys/+}$ n=8				*Fgfr3* $^{+/+}$ n=12; *Fgfr3* $^{Asn534Lys/+}$ n=10				*Fgfr3* $^{+/+}$ n=9; *Fgfr3* $^{Asn534Lys/+}$ n=10			
		genotype	mean	standard deviation ±	difference (%)	p-value	mean	standard deviation ±	difference (%)	p-value	mean	standard deviation ±	difference (%)	p-value
Trabecular	TV (mm^3)	*Fgfr3* $^{+/+}$	2,301	0,3118	-46,06692742	<0.0001	2,736	0,202	-46,56432749	<0.0001	2,176	0,4041	-49,08088235	<0.0001
		Fgfr3 $^{Asn534Lys/+}$	1,241	0,2278			1,462	0,3008			1,108	0,0652		
	BV/TV	*Fgfr3* $^{+/+}$	0,1184	0,02636	-16,26689189	0,7526	0,1987	0,02861	-38,34927026	<0.0001	0,1883	0,03787	-24,00424854	0,0198
		Fgfr3 $^{Asn534Lys/+}$	0,09914	0,01818			0,1225	0,05145			0,1431	0,03077		
	Tb.N (mm^{-1})	*Fgfr3* $^{+/+}$	4,641	0,6775	-5,23594053	>0.9999	5,852	0,217	-18,11346548	0,0003	4,542	0,4489	-4,799647732	>0.9999
		Fgfr3 $^{Asn534Lys/+}$	4,398	0,477			4,792	1,035			4,324	0,3388		
	Tb.Th (mm)	*Fgfr3* $^{+/+}$	0,0379	0,003189	-3,667546174	>0.9999	0,04822	0,003218	-15,45002074	<0.0001	0,05625	0,002492	-7,04	0,0354
		Fgfr3 $^{Asn534Lys/+}$	0,03651	0,004308			0,04077	0,003519			0,05229	0,003301		
	Tb.Sp (mm)	*Fgfr3* $^{+/+}$	0,2094	0,03547	7,258834766	0,9389	0,1504	0,007008	36,30319149	0,0004	0,2015	0,02273	7,642679901	0,8387
		Fgfr3 $^{Asn534Lys/+}$	0,2246	0,03404			0,205	0,05082			0,2169	0,02043		
	BMD ($mgHAcm^{-3}$)	*Fgfr3* $^{+/+}$	694,9	18,81	0,777090229	0,9333	785,2	15,02	-4,304635762	0,0012	856,3	11,54	-1,132780568	0,4941
		Fgfr3 $^{Asn534Lys/+}$	700,3	27,67			751,4	27,19			846,6	23,06		
Cortical	TV (mm^3)	*Fgfr3* $^{+/+}$	1,446	0,1554	-35,45643154	<0.0001	1,749	0,08256	-46,42081189	<0.0001	1,897	0,1137	-44,80759093	<0.0001
		Fgfr3 $^{Asn534Lys/+}$	0,9333	0,2306			0,9371	0,1268			1,047	0,0986		
	BV/TV	*Fgfr3* $^{+/+}$	0,5447	0,0193	-2,037818983	>0.9999	0,6041	0,01764	2,714782321	0,5061	0,5992	0,02207	16,75567423	<0.0001
		Fgfr3 $^{Asn534Lys/+}$	0,5336	0,04816			0,6205	0,024			0,6996	0,0282		
	C.Th (mm)	*Fgfr3* $^{+/+}$	0,1826	0,01691	-10,78860898	0,1286	0,2255	0,01185	-12,50554324	0,0041	0,2363	0,009022	7,067287347	0,1996
		Fgfr3 $^{Asn534Lys/+}$	0,1629	0,03363			0,1973	0,0222			0,253	0,01794		
	Ma.Dm (mm)	*Fgfr3* $^{+/+}$	0,5943	0,02531	-7,706545516	0,0024	0,6271	0,02044	-20,28384628	<0.0001	0,6499	0,03031	-30,29696876	<0.0001
		Fgfr3 $^{Asn534Lys/+}$	0,5485	0,03262			0,4999	0,0113			0,453	0,03485		
	BMD ($mgHAcm^{-3}$)	*Fgfr3* $^{+/+}$	568,8	22,66	-2,549226442	0,3795	1151	21,96	-4,604691573	0,0045	1101	33,73	6,176203451	0,0007
		Fgfr3 $^{Asn534Lys/+}$	554,3	57,66			1098	26,77			1169	29,24		
	T.Dm (mm)	*Fgfr3* $^{+/+}$	0,7769	0,03277	-8,430943493	0,0009	0,8526	0,01703	-18,22660099	<0.0001	0,8861	0,02558	-20,31373434	<0.0001
		Fgfr3 $^{Asn534Lys/+}$	0,7114	0,06485			0,6972	0,02703			0,7061	0,0325		
	C.Th / T.Dm (%)	*Fgfr3* $^{+/+}$	23,48	1,723	-0,78	>0.9999	26,46	1,469	1,77	0,1821	26,69	1,537	9,2	<0.0001
		Fgfr3 $^{Asn534Lys/+}$	22,7	2,804			28,23	2,271			35,89	2,863		
	Full bone Length (mm)	*Fgfr3* $^{+/+}$	16,34	0,5855	-21,66462668	<0.0001	18,01	0,08908	-24,54192115	<0.0001	18,3	0,3267	-23,49726776	<0.0001
		Fgfr3 $^{Asn534Lys/+}$	12,8	0,7467			13,59	0,3869			14	0,4423		

Supplemental Table 6

Biomechanical test data. The table presents the data of our studies sorted per genotype and age. They are expressed as mean ± standard deviation. The variations across WT and *Hch* mice are expressed in percentage and their p-values are listed.

Supplementary Table 6: Tibia - Descriptive statistics and 2-way ANOVA with Bonferroni's test p-values of destructive 3-point bending test analyses

			P42				P70				P180			
			Fgfr3 $^{+/+}$ n=9; *Fgfr3* $^{Asn534Lys/+}$ n=8				*Fgfr3* $^{+/+}$ n=12; *Fgfr3* $^{Asn534Lys/+}$ n=10				*Fgfr3* $^{+/+}$ n=9; *Fgfr3* $^{Asn534Lys/+}$ n=10			
		genotype	mean	standard deviation ±	difference (%)	p-value	mean	standard deviation ±	difference (%)	p-value	mean	standard deviation ±	difference (%)	p-value
Fracture	Yield Load (N)	*Fgfr3* $^{+/+}$	7,357	1,723	-34,90553215	0,0049	10,11	1,637	-38,1206726	≤0.0001	13,1	1,885	-17,63358779	0,0077
		Fgfr3 $^{Asn534Lys/+}$	4,789	1,364			6,256	0,9319			10,79	1,791		
	Maximum Load (N)	*Fgfr3* $^{+/+}$	9,963	1,64	-24,06905551	0,0126	14	1,306	-37,13571429	≤0.0001	19,75	1,427	-25,56962025	≤0.0001
		Fgfr3 $^{Asn534Lys/+}$	7,565	2,317			8,801	1,563			14,7	1,669		
	Fracture Load (N)	*Fgfr3* $^{+/+}$	6,651	2,575	-29,78499474	0,3462	8,88	3,228	-29,13288288	0,0642	12,67	2,529	1,499605367	>0.9999
		Fgfr3 $^{Asn534Lys/+}$	4,67	2,186			6,293	1,911			12,86	2,402		
	Stiffness (Nmm^{-1})	*Fgfr3* $^{+/+}$	38,75	8,105	-37,00645161	0,0014	53,95	7,539	-52,99351251	≤0.0001	97,01	9,889	-42,45954025	≤0.0001
		Fgfr3 $^{Asn534Lys/+}$	24,41	8,848			25,36	7,662			55,82	5,003		
	Energy Dissipated at Fracture (%)	*Fgfr3* $^{+/+}$	88,85	13,45	-3,7	>0.9999	81,93	19,76	-3,99	>0.9999	86,71	12,38	-36,92	0,0001
		Fgfr3 $^{Asn534Lys/+}$	85,15	19,49			77,94	17			49,79	23,05		
	Plastic Work / Total Work (%)	*Fgfr3* $^{+/+}$	88,96	7,198	-0,02	>0.9999	83,31	7,502	-2,78	>0.9999	87,31	6,726	-20,87	≤0.0001
		Fgfr3 $^{Asn534Lys/+}$	88,94	7,809			80,53	6,836			66,44	9,939		

2. Article 4

Systemic inhibition of FGFR3 in a mouse model of mandibular fracture corrects defects in bone formation and repair. Soumission prévue au Journal of Clinical Investigation.

Morice Anne[1,2,3], de La Seiglière Amélie[3], Loisay Léa[3], Kaci Nabil[3], Hossein Khonsari[1,2,3], Bensidhoum Morad[4], Puig Lombardi Emilia[5], Legeai Mallet Laurence[3].

1. Service de chirurgie maxillofaciale et chirurgie plastique, Hôpital Necker - Enfants Malades, Assistance Publique - Hôpitaux de Paris ; Faculté de Médecine, Université Paris Cité ; Paris, France
2. Centre de Référence Maladies Rares Fentes et Malformations Faciales (MAFACE), Filière Maladies Rares TeteCou, France.
3. Molecular and Physiopathological Bases of Osteochondrodysplasia. INSERM UMR 1163, Imagine Institute, Paris, France.
4. B3OA UMR CNRS 7052, Université Paris Cité CNRS, Paris, France.
5. Bioinformatics Core Platform, Imagine Institute, INSERM UMR1163 and Structure Fédérative de Recherche Necker, INSERM US24/CNRS UAR3633, Université Paris Cité, F-75015 Paris, France

a) Introduction

L'hypochondroplasie (HCH) (OMIM 14600) est une maladie autosomique dominante, qui appartient à la famille des chondrodysplasies liées à des mutations hétérozygotes activatrices gain-de-fonction dans le gène FGFR3. L'hypochondroplasie est charactérisée par un nanisme rhizomélique modéré, avec petite taille disproportionnée avec membres courts et une macrocéphalie (Maroteaux and Falzon, 1988 ; Walker *et al*, 1971). Une grande variabilité phénotypique est observée chez les patients, des formes mineures à sévères. Dans les formes sévères, le diagnostic avec l'achondroplasie (OMIM 100800) peut être difficile à établir cliniquement (Rousseau *et al*, 1996, Flynn and Pauli, 2003). Le phénotype craniofacial dans l'hypochondroplasie a des caractéristiques communes retrouvées dans l'achondroplasie, soit la macrocéphalie, la présence d'un front bombé, la rétrusion de l'étage moyen de la face et un prognathisme relatif. Ces anomalies craniofaciales s'expriment à des degrés variables, des formes subnormales à sévères. De nombreuses mutations hétérozygotes ont été identifiées dans l'hypochondroplasie, parmi elles, la mutation récurrente gain-de-fonction p.Asn540Lys est la plus fréquente, elle est retrouvée dans environ 60 à 70 % des cas, affectant le domaine tyrosine kinase du récepteur FGFR3 (Bellus *et al*, 1995, Ornitz and Legeai-Mallet, 2017, Bober *et al*, 2020). Cette mutation est à l'origine d'une phosphorylation excessive des domaines tyrosine kinases, indépendamment de la présence des ligands FGFs (Raffioni *et al*, 1998).

Le premier modèle murin *Hch* a été généré par Loisay et al (Loisay et al, 2022, en révision), il s'agit d'un modèle murin exprimant la mutation p.Asn534Lys/+ (*Fgfr3*$^{N534K/+}$) homologue à la mutation la plus fréquente, p.Asn540Lys retrouvée en pathologie humaine. Ce modèle murin *Hch* présente un nanisme modéré, mimant la pathologie humaine (Article 3). Le phénotype craniofacial des patients HCH est caractérisé par la présence d'une macrocéphalie, d'une rétrusion de l'étage moyen de la face, et un prognathisme mandibulaire. Ces anomalies sont en rapport avec la fusion prématurée des synchondroses de la base du crâne observée à P14 dans le modèle murin *Fgfr3*$^{N534K/+}$ (Article 3, Loisay et al, 2022, en révision). D'autres modèles murins exprimant des mutations gain-de-fonction de *Fgfr2* et *Fgfr3*, associées à des formes de craniosynostoses ou de chondrodysplasies, présentent également des anomalies de formation et de croissance mandibulaire (Motch Perrine *et al*, 2019, Biosse Duplan *et al*, 2016). Deux modes d'ossification contrôlent la formation mandibulaire : l'ossification de la branche horizontale repose essentiellement sur le mode d'ossification membranaire, et la formation de la branche montante, du condyle et de la symphyse dépend du mode d'ossification endochondrale. La formation mandibulaire dépend de la présence du cartilage de Meckel, il s'agit d'un cartilage primaire transitoire présent en anténatal, servant de tuteur à l'ossification mandibulaire, et de la présence de cartilages secondaires (condyliens, de l'angle mandibulaire et de la symphyse) participant à la croissance post natale de la mandibule (Rice *et al*, 2003).

La réparation osseuse combine à la fois des mécanismes de formation et de résorption d'un cartilage transitoire pendant la formation du cal de réparation. Ce cartilage présent au sein du cal est remplacé par de l'os trabéculaire permettant la formation du cal osseux pontant la zone osseuse fracturée (Gambari *et al*, 2019). Précédemment, l'impact des mutations activatrices dans le gène *Fgfr3* a été étudié dans plusieurs modèles murins *Fgfr3*, les souris mutantes présentaient un retard sévère de consolidation osseuse avec pseudarthrose après fracture non stabilisée des os longs (Su *et al*, 2008, Chen *et al*, 2017, Julien *et al*, 2020). Malgré ces résultats, à ce jour, nous n'avons aucune donnée expérimentale rapportant l'impact des mutations *Fgfr3* activatrices dans le cadre de la formation et la réparation osseuse mandibulaire. Dans ce projet de thèse, nous avons analysé la formation et la réparation osseuse mandibulaire dans le modèle murin d'hypochondroplasie *Fgfr3*$^{N534K/+}$, et avons identifié des gènes clés contrôlant la formation du cal de réparation. Enfin, nous avons testé l'effet pharmacologique de deux antagonistes de FGFR3 (BMN111 et BGJ398), nous avons montré que ces traitements restauraient un processus de réparation osseuse endochondrale normal, et qu'ils permettaient d'accélérer le remodelage osseux, après fracture non stabilisée de la mandibule chez les souris mutantes *Hch*.

b) Abstract

Les mutations gain-de-fonction dans le gène FGFR3 ont été associées à une famille de chondrodysplasie. Le rôle exact de FGFR3 au cours de la formation et la réparation osseuse n'a pas été élucidé à ce jour. Ici, nous rapportons les analyses du modèle murin d'hypochondroplasie (*Fgfr3*$^{N534K/+}$) présentant des anomalies craniofaciales. La différenciation et la maturation chondrocytaire sont significativement impactées au sein des cartilages mandibulaires primaire (Meckel) et secondaires (condyliens), à l'origine de défauts de croissance et d'anomalies morphologiques mandibulaires. La réparation osseuse a été étudiée dans ce modèle après fractures mandibulaires non stabilisées. Nous avons observé un retard de consolidation avec pseudarthrose, une réduction de la différenciation chondrocytaire au sein du cartilage transitoire du cal de réparation, et des défauts microarchitecturaux des cals de réparation chez les souris mutantes *Hch*. Une étude comparative de transcriptomique spatiale réalisée au sein des zones de cartilage et de l'os nouvellement formé des cals de réparation, a révélé une diminution significative de l'expression de gènes exprimés par les chondrocytes matures ou en phase de transdifférenciation en ostéoblastes, il s'agit de *Col11, Col1a, Dmp1, Phospho1, Hmgb2*. Nous avons également montré la présence d'un défaut d'homéostasie osseuse, caractérisée par des anomalies d'expression de gènes impliqués dans les mécanismes d'autophagie et d'apoptose, *Smad1, Comp,* et *Birc2*. Nous avons mis en évidence la surexpression des gènes *Dusp3*, *Dusp9*, et *Socs3*, impliqués dans la régulation négative de la voie MAPKinase, qui est suractivée en aval de l'activation de FGFR3 mutée. Enfin, nous avons testé deux antagonistes de FGFR3, le BGJ 398, un inhibiteur des tyrosines kinases, et le BMN111, un analogue du CNP, au cours de la réparation osseuse après fracture non stabilisée des mandibules. Nous avons montré que ces traitements restauraient un processus de consolidation osseuse normal, et qu'ils accéléraient le remodelage osseux des cals de réparation.

Nos résultats confirment l'impact des mutations activatrices dans le gène *Fgfr3* au cours de la réparation osseuse endochondrale et donnent des perspectives thérapeutiques majeures chez les patients porteurs d'ostéochondrodysplasies liées à FGFR3.

c) Article

Systemic inhibition of FGFR3 in a mouse model of mandibular fracture corrects defects in bone formation and repair

Morice Anne[1,2,3], de La Seiglière Amélie[3], Loisay Léa[3], Kaci Nabil[3], Khonsari Roman Hossein[1,2,3], Bensidhoum Morad[4], Puig Lombardi Emilia[5], Legeai Mallet Laurence[3].

1. Service de chirurgie maxillofaciale et chirurgie plastique, Hôpital Necker - Enfants Malades, Assistance Publique - Hôpitaux de Paris ; Faculté de Médecine, Université Paris Cité ; Paris, France
2. Centre de Référence Maladies Rares Fentes et Malformations Faciales (MAFACE), Filière Maladies Rares TeteCou, France.
3. Molecular and Physiopathological Bases of Osteochondrodysplasia. INSERM UMR 1163, Imagine Institute, Paris, France.
4. B3OA UMR CNRS 7052, Université Paris Cité CNRS, Paris, France.
5. Bioinformatics Core Platform, Imagine Institute, INSERM UMR1163 and Structure Fédérative de Recherche Necker, INSERM US24/CNRS UAR3633, Université Paris Cité, F-75015 Paris, France

Abstract

FGFR3 gain of function mutations are implicated in osteochondrodysplasia and faciocraniosynostoses, two groups of conditions that may require various craniofacial surgery procedures on the bones of the skull and on the jaws. Ideally, evidence-based treatment plans for these patients have to based on a precise understanding of craniofacial growth processes, and on the elucidation of potential anomalies in bone consolidation after osteotomies. However the role of *FGFR3* during mandibular bone formation and bone repair has not been elucidated yet. Here, we report the analysis of a mouse model of hypochondroplasia ($Fgfr3^{N534K/+}$) with craniofacial anomalies. Chondrocyte differentiation and maturation was impaired in primary (Meckel) and secondary (condylar) cartilages, leading to growth defects and mandibular morphological changes. Bone repair was studied following non-stabilized mandibular fractures. We observed delayed bone consolidation, pseudarthrosis, reduction of chondrocyte differentiation, and microarchitectural defects of the calluses in $Fgfr3^{N534K/+}$ mice. A spatial transcriptomics comparaison of gene expression in bone and cartilage area of the callus revealed a significant decrease in the expression of genes expressed by mature chondrocytes or in the phase of transdifferentiation into osteoblasts (*Col11, Col1a, Dmp1, Phospho1, Hmgb2*). We also observed a defect of bone homeostasis, characterized by disturbances in gene expression involved in autophagy and apoptosis mechanisms (*Smad1, Comp, Birc2*). *Dusp3*, *Dusp9*, and *Socs3* genes involved in the downregulation of the MAPKinase pathway, which was highly activated by FGFR3, were overexpressed. Moreover, we demonstrated that a tyrosine kinase inhibitor (BGJ398) and a CNP analog (BMN111) rescued the defective endochondral bone repair and restored bone callus formation in $Fgfr3^{N534K/+}$ mice. Our findings highlight the impact of *Fgfr3* activating mutations during endochondral bone repair and provide major therapeutic perspectives in patients with *FGFR3*-related osteochondrodysplasias, both for potential pharmacological approaches and for the establishment of treatment plans based on the understanding of craniofacial growth processes.

Introduction

Hypochondroplasia (HCH) (OMIM 14600) is an autosomal dominant disorder, belonging to the family of *FGFR3*-related chondrodysplasias, due to *FGFR3* heterozygous gain-of-function mutations. HCH is characterized by a moderate rhizomelic dwarfism, with disproportionate short stature, short limbs and macrocephaly (Maroteaux and Falzon, 1988 ; Walker *et al*, 1971). High variability in severity is reported, from mild to severe forms. In severe cases, differential diagnosis with achondroplasia (OMIM 100800) is sometimes difficult to establish clinically (Rousseau *et al*, 1996, Flynn and Pauli, 2003). Craniofacial phenotype in HCH shares features with achondroplasia, i.e. macrocephaly, frontal bossing, midfacial retrusion and relative prognathism.

Numerous heterozygous mutations have been linked to HCH, among which the recurrent heterozygous gain-of-function mutation, p.Asn540Lys being the most frequent mutation, occurring in around 60 to 70% of the cases, affecting the tyrosine kinase domain of receptor FGFR3 (Bellus *et al*, 1995, Ornitz and Legeai-Mallet, 2017, Bober *et al*, 2020). This mutation leads to high levels of FGFR3 tyrosine kinase domains phosphorylation, independently of the presence of FGF ligands (Raffioni *et al*, 1998).

The first *Hch* mouse model expressed the homologous mutation to human p.Asn540Lys, $Fgfr3^{Asn534Lys/+}$ ($Fgfr3^{N534K/+}$) (Loisay *et al*, under review). This *Hch* mouse model presented a moderate dwarfism, mimicking human pathology. Craniofacial phenotype was characterized by macrocephaly, midfacial retrusion, and mandibular prognathism, due to premature fusion of skull base synchondroses observed at P14 (Loisay *et al*, under review). Other mouse models expressing *Fgfr2* and *Fgfr3* gain-of-function mutations associated with either craniosynostosis or chondrodysplasia also show abnormal mandibular formation and growth (Motch Perrine *et al*, 2019, Biosse Duplan *et al*, 2016). Two ossification processes control the formation of the mandible: the body of the mandible mainly relies on intramembranous ossification, whereas the ramus, the condyle and the symphysis derive from endochondral ossification. Mandibular formation depend on the presence of Meckel's cartilage (MC) (primary cartilage), an antenatal transient cartilage serving as a template for mandibular ossification, and on permanent cartilages (condylar, angular and of the symphysis), the latter allowing post-natal growth of the mandible via endochondral ossification processes (Rice *et al*, 2003). Bone repair processes combine both formation and resorption of a transient cartilage during formation of the soft callus, this cartilage being replaced by bone to form the bone callus allowing bony bridging of

the bone defect (Gambari *et al*, 2019). The impact of *Fgfr3* mutations on bone repair has been previously studied in various *Fgfr3* mouse models, showing severe consolidation delays and defects with pseudarthrosis in non-stabilized fractures of the long bones (Su *et al*, 2008, Chen *et al*, 2017, Julien *et al*, 2020). To the best of our knowledge, there is currently no data available on the role of *Fgfr3* activation in mandibular bone formation and repair. We thus analysed these processes and identified the key genes controlling the formation of the callus in a mouse model of hypochondroplasia. By using two different FGFR3 antagonists, we then assessed the rescue of defective endochondral bone repair and bone callus remodelling following non-stabilized mandibular fracture in *Hch* mouse models.

Results

The hypochondroplasia mouse model, *Fgfr3*$^{N534K/+}$, exhibits abnormal mandibular shape

Mandibular shape is both influenced by skull base shape modifications (extrinsic factors) and intrinsic factors, linked to mandibular cartilage formation and homeostasis (Cottin *et al*, 2017; Ferros *et al*, 2016; Biosse Duplan *et al*; 2016). Mandibular formation is controlled by both membranous and endochondral ossification processes (Rice *et al*, 2003). Meckel's cartilage (MC) is a primary cartilage which induces antenatal mandibular formation. MC is transiently present in the developing mandible and disappears at birth. MC gives rise to the middle ear ossicles (malleus, incus) posteriorly and to the symphysis cartilage anteriorly, while its central part is totally replaced by bone at birth (Scandova *et al*, 2020). To investigate whether *Hch* mutations impacts MC formation and homeostasis in *Fgfr3*$^{N534K/+}$ mouse models (Loisay *et al*, under review), *Fgfr3*$^{N534K/+}$ embryos and control littermates were collected at gestational day E13.5 (early stage of MC formation), E16.5, E18.5, and at three postnatal days (P1, P21 and P42). Histomorphological analyses revealed that MC volume was significantly reduced at E13.5 (-41.1% when compared with control littermates, $p<0.05$) (Figure 1A) while it was increased at E16.5 (+43.7% when compared with control littermates, $p<0.05$) (Figure 1B). At E18.5, we observed a delay in MC resorption in its intermediate part in mutants, although it was completely replaced by mandibular bone at P1 in both mutants and control littermates (data not shown). At P1, macroscopic analyses using alcian blue/alizarin red staining revealed that mandibular length was not significantly different between *Fgfr3*$^{N534K/+}$ mice and control littermates.

At E13.5, Sox9 immunostaining, a specific marker of early chondrocyte differentiation, revealed significantly lower expression in MC in mutants (-71.9% when compared with control littermates, $p<0.01$) (Figure 1A). Using MC Fgfr3 immunostaining, we observed the absence

of Fgfr3 expression in *Fgfr3*$^{N534K/+}$ mice, whereas Fgfr3 expression was detected in control littermates, showing that the onset of Fgfr3 expression was delayed in the MC of *Fgfr3*$^{N534K/+}$ mice. At the same stage, using PCNA to analyse proliferation, we observed an apparent reduction in staining intensity in the MC of mutants (-62.2 % when compared with control littermates) (Supplemental Figure 1). Although this difference was not significant, we cannot exclude that *Fgfr3*$^{N534K/+}$ mutation impacts chondrocyte proliferation at early stages of MC formation. At E16.5, we studied the chondrocyte differentiation process using Collagen X immunostaining, a specific marker for mature chondrocytes called hypertrophic. We showed a significant reduction of hypertrophic chondrocytes area relative to the total cartilage area in mutants (-40.5%, compared to control littermates, $p<0.05$) (Figure 1B). We also observed an overlapping of the expression of Sox9 and Collagen X in the mutants, while it was clearly delimitated in control littermates (Figure 1B). Fgfr3 expression was more intense in *Fgfr3*$^{N534K/+}$ mice than in control littermates (Figure 1B). Overall, these data show that *Fgfr3*$^{N534K/+}$ mutation delays MC formation and resorption, and impacts chondrocyte differentiation during antenatal mandibular formation.

To investigate whether *Fgfr3*$^{N534K/+}$ mutation impacted mandibular morphology and growth, we first evaluated craniofacial and mandibular shapes at an adult age (P42). Using morphometric analyses based on µCT scans, we observed significant reduction of the nasooccipital length ($p<0.005$) and an increase of skull width ($p<0.005$) in mutant mice when compared with control littermates (Figure 1C). We showed a significant reduction of mandibular length ($p<0.005$) and ramus height ($p<0.05$) in mutant mice when compared with control littermates (Figure 1C). We further investigated craniofacial and mandibular shapes modifications using 3D geometric morphometric analyses. *Fgfr3*$^{N534K/+}$ mice displayed a more rounded skull shape, with shorter skull base and retrusion of the maxilla, with relative mandibular prognathism (Figure 1D). Larger mandibular intercondylar and intergonial distances were observed in mutant mice, in relation to the increased skull width (data not shown). Regarding the maxillomandibular shapes, the first 7 PCs (skull) and the first 9 PCs (mandible) represented 90% of total shape variation. Concerning skull and mandibular shape comparisons, a clear separation of mutants and controls was visible along PC1 (39% and 23% of the total variance, concerning the skull and the mandible, respectively) as the result of significant shape differences (Figure 1D) (Procrustes distance d=0,1094; $p<0.001$ (skull), Procrustes distance d=0,0846; $p<0.001$ (mandible)).

To explain this postnatal mandibular growth impairment, we studied the condylar cartilage, a permanent cartilage that participates to endochondral ossification of the upper part of the mandibular ramus during the post natal period (P21). We observed a significantly higher proportion of smaller hypertrophic chondrocytes in mutants (i.e 100-200 μm^2, -26,8% when compared with control littermates, $p<0.005$) and smaller proportion of larger chondrocytes (i.e 200-300 μm^2, +20,6% when compared with control littermates, $p<0.005$) (Figure 1E).

These data demonstrate that the *Fgfr3*$^{N534K/+}$ mutation impacts hypertrophic chondrocyte maturation at the level of condylar cartilages during postnatal growth, and may take part into postnatal mandibular growth limitation.

Overall, we showed that *Fgfr3* plays a key role during mandibular formation, and that the *Fgfr3*$^{N534K/+}$ mutation impacts formation and homeostasis of both primary and secondary cartilages of the mandible at ante- and postnatal stages, disturbing both membranous and endochondral ossification of the mandible.

Fgfr3$^{N534K/+}$ mutation leads to defective mandibular bone repair and formation of pseudarthrosis

Fgfr3 gain-of function mutations impair bone formation and repair (Julien *et al*, 2020; Mugniery *et al*, 2012; Biosse Duplan *et al*, 2016). The endochondral bone repair process promotes the immature chondrocytes proliferation in the early soft callus, induces transdifferentiation of hypertrophic chondrocytes into osteoblasts and stimulates apoptosis to form the bone callus (Galea *et al*, 2021). To address the role of *Fgfr3* in mandibular bone repair, we generated several series of non-stabilized vertical mandibular fractures of the ramus in *Fgfr3*$^{N534K/+}$ mice and their control littermates at an adult age (P42) (Figure 2A). Bone repair and callus formation were assessed at different key points of endochondral bone repair from day 7 to day 28 post-fracture (Figure 2B) (Oryan *et al*, 2016, Schell *et al*, 2017, Sheen and Garla, 2022). Morphometric analyses based on CT-scans revealed that Bone Volume (BV) / Tissue Volume (TV) of the calluses was significantly reduced in *Fgfr3*$^{N534K/+}$ mice from day 10 to day 28 post fracture when compared to control littermates: day 10 (-23%, $p<0.05$), day 14 (-14%, $p<0.01$), day 21 (-14.9%, $p<0.005$), and day 28 (-5.8%, $p<0.05$) (Figure 2C). No significant changes were observed in callus volumes (Figure 2C). Interestingly, we observed a delay in cartilage formation in *Fgfr3*$^{N534K/+}$ mice compared to controls during the endochondral process of bone repair (Figure 2C).

To address on a more global scale whether *Fgfr3*$^{N534K/+}$ mutation impaired callus cartilage formation, we performed further histomorphometry and immunohistology analyses on the bone callus at day 7, day 14 and day 28 post-fracture. Histomorphometric analyses revealed significantly reduced callus cartilage volumes at day 7 post-fracture in *Fgfr3*$^{N534K/+}$ mice compared to control littermates (- 88%, $p<0.01$) (Figure 2D). The expression of PCNA in *Fgfr3*$^{N534K/+}$ mutants was similar to controls (Supplemental Figure 2), thus demonstrating no significant impact of the *Fgfr3*$^{N534K/+}$ mutation on chondrocyte proliferation at this stage of endochondral bone repair. We noted a delay in chondrocyte maturation in *Fgfr3*$^{N534K/+}$ mice compared to controls with a co-expression of Sox9 and Collagen type X (Figure 2D). Fgfr3 was expressed in cartilage callus in both mutants and control littermates (Figure 2D). Similar data were observed at day 14 post-fracture (Figure 2E). To confirm these findings, we compared the expression of Collagen II and Collagen type X. The ratio of Collagen X/Collagen II area was significantly reduced in mutants (-62.8% when compared with control littermates, $p<0.005$) (Figure 2E), demonstrating that *Fgfr3*$^{N534K/+}$ mutation impairs hypertrophic chondrocyte differentiation. Hypertrophic chondrocytes are mainly characterized by a marked volume enlargement. Studying the area of the hypertrophic cells, we noted a significantly higher proportion of smaller chondrocytes (100-200 μm^2, $p<0.05$) compared to the number of larger chondrocytes (300-400 μm^2, $p<0.05$) in mutants (Figure 2E), indicating that the *Fgfr3*$^{N534K/+}$ mutation impairs chondrocyte volume growth. Many factors can be involved in the terminal regulation of chondrocyte differentiation. In particular, VEGF (Vascular Endothelial Growth Factor), a key gene of angiogenesis, secreted by hypertrophic chondrocytes, was highly expressed in mutants compared to controls (Hu and Olsen, 2016; Komatsu and Hadjiargyrou, 2004) (Supplemental Figure 3). In mutants, both proliferative (Sox9) and hypertrophic (Collagen type X) cells expressed Fgfr3, whereas in controls only hypertrophic (Collagen type X) cells expressed Fgfr3 (Figure 2E). Overall, the level of Fgfr3 expression was higher in mutants than in controls.

During endochondral bone repair, hypertrophic chondrocytes have different fates: transdifferentiating into osteoblasts to form the bone callus, or entering apoptosis (Hinton *et al*, 2017). We further investigated whether the *Fgfr3*$^{N534K/+}$ mutation could modify apoptosis in hypertrophic chondrocytes. TUNEL/DAPI staining revealed significantly lower rates of apoptotic cells in the Collagen X positive cartilage area in mutants (-54.9% when compared with control littermates, $p<0.01$) (Figure 2F). To evaluate osteogenesis, we analysed Collagen I expression in the woven bone callus (Marie, 2008). Collagen I immunostaining revealed

significantly higher intertrabecular separation in mutants than in control littermates (+68.7%, $p<0.005$) (Figure 2G) thus demonstrating microarchitectural alterations of the bone callus and confirming the lower BV/TV ratio observed in mutants (Figure 2C).

At day 28 post-fracture, we classified bone repair according a consolidation grade scale (1 to 4) (Figure 2H). Total bony bridging of the mandibular fractures were achieved in all control littermate mice (grade 1 and 2) whereas partial bone union (grade 3) and a complete absence of bone union (grade 4) were observed in 23 % of the mutants (Figure 2H). Consolidation grade 1 (complete union) was never observed in the mutants whereas consolidation grade 2 (complete union with small bone irregularities at the periphery of the bone callus) was found in 54% of mutants (Figure 2H). Histomorphometric analyses of the grade 4 callus showed pseudarthrosis in 6/13 of mutants (Figure 2H). Altogether, the analyses of the bone repair processes from day 7 to day 28 post-fracture demonstrated that the endochondral mandibular bone repair is strongly impaired in the *Fgfr3*$^{N534K/+}$ HCH mouse model, characterized by severe consolidation delays with pseudarthrosis and cartilage resorption delay, due to defective chondrocyte differentiation, apoptosis and altered bone formation and remodelling.

GeoMx spatial whole transcriptomic analyses of the callus cartilage

To decipher the molecular mechanisms affecting mandibular bone repair in the *Fgfr3*$^{N534K/+}$ HCH mouse model, we conducted spatial whole transcriptomic analyses of the callus cartilage and newly formed bone at day 14 post-fracture, in both *Fgfr3*$^{N534K/+}$ mutants and control littermate mice. GeoMx spatial whole transcriptome assays of the callus were performed in two separate regions of interest (ROI): callus cartilage and newly formed bone, corresponding to 27 samples (Supplemental Figures 4A and 4B).

Regarding the callus cartilage, we assayed 19,421 genes across the entire set of ROIs, with 18,125 genes detected in at least 10% of the ROIs and 8,211 genes expressed in over 50% of the ROIs. Unsupervised clustering performed on the normalized read counts for the 18,125 genes expressed in at least 10% of ROIs showed an overview of transcriptome-wide differences in expression between the retained samples (Supplemental Figure 4B). Subsequently, in order to examine specific expression changes between mutant and control ROIs, differential expression analyses were carried out.

Differential expression analysis between *Fgfr3*$^{N534K/+}$ and *Fgfr3*$^{+/+}$ mice from the cartilage ROIs identified 529 genes displaying significant ($p < 0.1$) changes in expression levels. Among them, 268 genes were up-regulated ($\log_2$(fold-change) > 0) in mutant samples relative to

controls, and 261 were down-regulated (log_2(fold-change) < 0); Figure 3A, 3B). Specific markers of chondrocytes were similarly expressed in both mutants and controls at transcriptomic levels, i.e *Col2a1*, *Col10a1*, *Ihh*, *Sox9*, *MAPK3* and *Pth* and *Bglap* (Supplemental Figure 5A).

Collagen 11 (Col11a2), essential for normal chondrocyte differentiation (Bridgewater *et al*, 1998) was downregulated in mutants compared to controls (p=0.003) (Figure 3C). *Col1a1* is an osteoblast marker expressed at all stages of osteoblast differentiation (Amarasekara *et al*, 2021), and by hypertrophic chondrocytes acquiring an osteoblast fate during endochondral bone repair (Hu *et al*, 2017). Interestingly *Col1a1* was significantly downregulated in mutants when compared with control littermates (p=0.01) (Figure 3C), highlighting impaired chondrocyte to osteoblast transdifferentiation in the calluses of mutants at 14 post-fracture. We then investigated the differential expression of genes involved in bone matrix mineralisation. *Dmp1* (Dentin Matrix Acidic Phosphoprotein 1) is a noncollagenous extracellular matrix protein belonging to the SIBLING (small integrin-binding ligand, N-linked glycoproteins) (Fisher *et al*, 2001; Zhang *et al*, 2016) and *Phospho 1* (Phosphatase, orphan 1) is a skeletal tissue-specific phosphatase, involved in matrix mineralisation during skeletal development and in the process of bone repair (Morcos *et al*, 2018). We observed significant lower expression levels of both *Dmp1* and *Phospho 1* in the callus cartilage of $Fgfr3^{N534K/+}$ mice when compared with control littermates (p=0.05, p=0.03, respectively) (Figure 3C), highlighting defective osteoblast differentiation and function and reduced matrix mineralisation in $Fgfr3^{N534K/+}$ mice in endochondral bone repair.

To decipher the underlying mechanisms leading to defective chondrocyte differentiation and bone formation in the bone calluses observed in $Fgfr3^{N534K/+}$ mice, we explored the expression of key regulators of chondrocyte differentiation. *Hmgb2* (High Mobility Group Box 2) regulates chondrocyte hypertrophy by mediating Runt-related transcription factor 2 expression and Wnt signaling (Taniguchi *et al*, 2018). Our results showed significant downregulation of *Hmgb2* in the cartilage callus of mutant mice (p=0.02, Figure 3C) compared to controls, revealing impaired regulation of chondrocyte differentiation at hypertrophic stage.

The role of Indian Hedgehog (*Ihh*) is crucial in the cartilage by stimulating chondrocyte proliferation, promoting chondrocyte hypertrophy and transdifferentiation into osteoblasts (Aghajanian *et al*, 2017; Lee *et al*, 1995) and controling ciliogenesis (Ascenzi *et al*, 2011, Haycraft *et al*, 2007; Kunova Bosakova *et al*, 2018; Martin *et al*, 2022). We observed an

apparently reduced expression of *Ihh* in mutants, although it was not statistically significant (Supplemental Figure 5A). Primary cilia are microtubule-based structures which act as sensors, and transmit and integrate various mechanical and chemical signals that are necessary for tissue development and homeostasis (Anvarian *et al*, 2019; Kopinke *et al*, 2021). We investigated expression of kinesin superfamily proteins (KIFs) which are microtubule-based molecular motors that convert the chemical energy of ATP hydrolysis to the mechanical force of transporting cargos along microtubules (Hirokawa *et al*., 2010, Schliwa *et al*, 2002). Among them, *Kif17* (Kinesin like protein 17) is expressed in the ciliary tip and participates to the anterograde trafficking of ciliary proteins (Funabashi *et al*, 2017; Ishida *et al*, 2022). We found significant lower expression rates of *Kif17* in the cartilage callus of $Fgfr3^{N534K/+}$ mice when compared with control littermates (p=0.03), in favour of defective intraciliary protein trafficking and potentially of mechanosensation and mechanotransduction during bone repair.

Several FGFR3 downstream signalling pathways are well described such as the extracellular signal-regulated kinases (ERK) and p38 mitogen-activated protein kinase (MAPK) pathways, the signal transducer and activation of transcription pathway (STAT), the phosphoinositide 3 kinase-AKT and protein kinase C pathways (Jonquoy *et al*, 2011). We observed increased expression levels of several subsets of MAPKs in the $Fgfr3^{N534K/+}$callus when compared with control littermates, although not significantly at transcriptional levels (Supplemental Figure 5A).

Dusp9, an ERK-specific phosphatase, member of the dual-specificity (threonine/tyrosine) phosphatase superfamily, was significantly upregulated in the cartilage callus in $Fgfr3^{N534K/+}$ mice (p=0.007) (Figure 3C), confirming a negative regulation of excessive MAPK signalling pathway activity, already described in *Fgfr3* mouse models (Komla Ebri *et al*, 2016, Loisay *et al*, under review).

Whole transcriptomic analyses of the newly formed bone of the calluses

Comparative analyses of the transcriptomic data between mutants and controls mice from the newly formed bone ROIs identified 541 genes displaying significant ($p < 0.1$) changes in expression levels. Among them, 282 genes were up-regulated ($\log_2$(fold-change) > 0) in mutant samples relative to controls, and 259 were down-regulated ($\log_2$(fold-change) < 0); Figure 4A, 3B). Specific bone markers were expressed in both mutants and controls at the transcriptomic level, i.e osteoblast markers, such as *Col1a1*, *Osx (Sp7)*, *Runx2*, *Alpl* (Alkaline Phosphatase), *Spp1* (osteopontin) and the osteoclast marker *Tnfrs11a* (RANK) (Supplemental Figure 4B).

Gene-set enrichment analysis of differentially expressed genes based on functional annotation (GO-BP database) showed enrichment in specific pathways (Supplemental Figure 7). We did not find significant differences in the expression of the following osteoblast markers: *Col1a1*, *Osx (Sp7)*, *Runx2*, *Alpl* (Alkaline Phosphatase), *Spp1* (osteopontin), and in the osteoclast marker *Tnfrs11a* (RANK), between $Fgfr3^{N534K/+}$ mice and control littermates (Supplemental Figure 5B).

Bone homeostasis depends on the balance between bone formation and resorption and relies on both biosynthesis and catabolic processes (Harada and Rodan, 2003; Cinque *et al*, 2015). Autophagy is a catabolic process that has a major role in bone tissue homeostasis (Mizushima *et al*, 2011). We thus investigated specific genes implicated during autophagy in the context of bone homeostasis. The BMP (Bone Morphogenetic Protein)/Smad 1/5/8 pathway positively regulates osteoblast differentiation and is activated upon autophagy activation (Li *et al*, 2018). We found significantly lower expression levels of *Smad1* in the bone calluses of $Fgfr3^{N534K/+}$ mice when compared with control littermates (p=0.005) (Figure 4C).

Bone callus formation during endochondral bone repair also depends on the regulation of apoptosis. Although part of the population of hypertrophic chondrocytes transdifferentiates into osteoblasts, another part undergoes apoptosis to allow trabecular bone formation with space for bone marrow (Hu *et al*, 2017).

Interestingly, we observed that the expression of *Comp* (Cartilage Oligomeric Matrix Protein), a key regulator of the structural integrity of the cartilage and a suppressor of apoptosis was significantly lower in mutants compared to controls (p=0.07). *Comp* suppresses apoptosis by inducing the IAP (Inhibitor of Apoptosis Protein) family of survival proteins BIRC3, BIRC2, BIRC5 and XIAP (Gagarina *et al*, 2008). The expression of *Birc2* (p=0.05) was elevated in $Fgfr3^{N534K/+}$ bone callus compared to control littermates (Figure 4C), thus indicating that the $Fgfr3^{N534K/+}$ mutation disturbed apoptotic regulation during the process of endochondral bone callus formation.

As we observed that apoptotic activity was abnormally increased in the bone callus of $Fgfr3^{N534K/+}$ mice, we investigated markers of DNA repair. Human AlkB homolog 2 (Alkbh2) is a DNA repair enzyme that catalyzes the direct reversal of DNA methylation damage through oxidative demethylation. Alkbh2 forms a complex with PCNA (Proliferating Cell Nuclear Antigen), increasing during DNA replication (Fu *et al*, 2015). We found significant lower

expression rates of *Alkbh2* in *Fgfr3*$^{N534K/+}$ mice when compared with control littermates (p=0.005) (Figure 4C), showing defective DNA repair in the forming bone callus.

Finally, we explored negative regulators of MAPK and STAT signalling pathways activated downstream of FGFR3 activation, responsible for defective chondrocyte differentiation and proliferation in *FGFR3* related chondrodysplasias (Ornitz and Marie, 2015; Komla Ebri, 2016). We found significantly higher expression levels of *Dusp3*, a negative regulator of MAPK pathways (Jeffrey *et al*., 2007, Patterson *et al*., 2009) in *Fgfr3*$^{N534K/+}$ mice compared to control littermates (p=0.04) (Figure 4C). We observed significantly increased expression levels of *Socs3* (Suppressor of Cytokine Signaling-3), a negative regulator of STAT3 signaling (Babon and Nicola, 2012) and MAPK (Liu *et al*, 2019) (p=0.01). Overall, our data suggest that both MAPK and STAT pathways are activated in the bone callus in an excessive manner in the HCH mouse model, highlighting the key role of these pathway in *FGFR3*-related disorders.

Finally, gene set enrichment analysis of differentially expressed genes based on functional annotation (Gene Ontology – Biological Process database) showed enrichment in specific pathways (Supplemental Figure 6).

FGFR3 antagonists (BMN111 and BGJ398) rescue the pseudarthrosis phenotype in the hypochondroplasia mouse model *Fgfr3*$^{N534K/+}$

We hypothesized that we could use FGFR3 antagonists to improve the defective endochondral bone repair observed in *Fgfr3*$^{N534K/+}$ mice. Many preclinical and clinical studies have been conducted or are ongoing, dedicated to the treatment of *FGFR3*-related disorders (Legeai-mallet and Savariryan, 2020). In this context, we tested BMN111 (vosoritide, first drug approved for clinical use in achondroplasia), a CNP (C-Natriuretic Peptide) analog inhibing the MAPKinase pathway at the level of Raf1. The positive effect of BMN111 on cartilage growth plate has been demonstrated in many preclinical studies (Lorget *et al*, 2012, Wendt *et al*, 2015, Komla Ebri *et al*, 2016, Di Rocco *et al*, 2014, Biosse Duplan *et al*, 2016). In parrallel, we evaluated the effect of BGJ398 (infigratinib), a tyrosine-kinase inhibitor able to improve cartilage growth and Meckel's cartilage formation (Komla Ebri *et al*, 2016, Di Rocco *et al*, 2014, Biosse Duplan *et al*, 2016). To test our hypotheses, we generated non-stabilized mandibular fractures and treated mice with either BMN111 (0.8 mg/kg) or BGJ398 (4 mg/kg), using subcutaneous injections, 3 times a week, during 14 or 28 days after the fracture performed at 6 weeks of age. Morphometric analyses of the callus based on CT-scans performed at day 14 post-fracture showed a significant increase of BV/TV values of the calluses of mutant mice

treated with BMN111: +29%, p<0.005, and BGJ398: +20.8% compared to non-treated mutant mice, p<0.05 (Figure 5A). Histomorphometric analyses of the callus performed at the same timepoint did not shown any significant modifications of cartilage volume in the two treated mutant groups (BMN111 and BGJ398) compared to non-treated mice (data not shown). Chondrocyte differentiation was significantly improved by both treatments, as shown by the significant increase of the ratio of Collagen X positive chondrocytes area relative to Collagen II positive area (BMN111: +64.9%, p<0.01; BGJ398: +40.6%, p<0.01) in *Fgfr3*$^{N534K/+}$ mice (Figure 5 B). BMN111 treatment reduced the abnormally high expression of Sox9, VEGF and Fgfr3 in *Fgfr3*$^{N534K/+}$ mice whereas the impact of BGJ398 on Sox9 expression was less visible (Figure 5B, Supplemental Figure 7). TUNEL/DAPI positive cells in the hypertrophic chondrocyte area of the callus was significantly increased in both groups of treated mice: BMN111, +268%, p<0.01; BGJ398, +215%, p<0.01, highlighting the restoration of hypertrophic chondrocyte apoptosis following treatment with BMN111 and BGJ398 in *Fgfr3*$^{N534K/+}$ mice (Figure 5B). Interestingly, in the bony part of the callus, Collagen I immunostaining revealed a significant reduction of intertrabecular separation following treatment in both groups: BMN111, -26,5%, p<0.05; BGJ398, -28,7%, p<0.05, in *Fgfr3*$^{N534K/+}$ compared with non-treated mice thus demonstrating increase of bone formation in the calluses at day 14 by FGFR3 antagonists (Figure 5B).

We analysed the fractured mandibles at the end of the bone repair process (day 28 post-fracture). BV/TV was significantly increased in both BMN111 (+24%, p<0.005) and BGJ398 (+17.8%, p<0.01) groups compared to non-treated mice. Calluses volumes were significantly decreased in both treated groups (BMN111: -30.9%, p<0.005; BGJ398: -38.6%, p<0.0001), corresponding to an acceleration of the bone callus remodelling process. Histomorphometric analyses showed complete bony bridging in both groups and an absence of pseudarthrosis in all treated mutant mice (Figure 5C). We further investigated osteoclast activity at the periphery of the calluses using TRAP staining. Osteoclast number was significantly reduced in both groups of treated mutants: BMN111, -66.8%, p<0.05; BGJ398, -43.8%, p<0.05, compared to non-treated mutant mice, showing that bone resorption was stimulated by BMN111 and BGJ398 and confirming the accelerated bone callus remodelling at day 28 post-fracture (Figure 5D).

Overall, these data showed that BMN111 and BGJ398 rescued defective endochondral bone repair due to the *Fgfr3*$^{N534K/+}$ mutation and accelerate boned callus remodelling following non-stabilized mandibular fractures.

Discussion

The specific role of *Fgfr3* in mandibular bone formation and repair has not been studied in depth to date, and it has never been assessed in HCH. Our study reveals that the $Fgfr3^{N534K/+}$ mice mimicking HCH (Loisay *et al*, under review) display altered craniofacial and mandibular phenotypes. We investigated the impact of the $Fgfr3^{N534K/+}$ mutation on MC during the antenatal period. At E13.5, corresponding to the early stage of MC formation following mesenchymal condensation (Ramaesh and Bard, 2003), we showed a significant reduction of the MC area and lower expressions of Sox9 and PCNA in $Fgfr3^{N534K/+}$ mutant mice, highlighting a delay in the onset of MC formation and chondrocyte proliferation. Furthermore, at E16.5, we found significant reduction of the hypertrophic chondrocytes area in MC of $Fgfr3^{N534K/+}$mice, highlighting that $Fgfr3^{N534K/+}$mutation inhibits chondrocyte differentiation. We also demonstrated that MC area was significantly increased in $Fgfr3^{N534K/+}$mice at E16.5. This result corroborates with those observed at stage E18.5 where larger remnants of MC persisted, illustrating a delay in MC resorption.

Despite $Fgfr3^{N534K/+}$ mutation inhibited chondrocyte differentiation before birth in MC, mandibular length was not affected at P1, whereas it was reduced at birth in another $Fgfr3^{Y367C/+}$ achondroplasia mouse model, in line with mild dwarfism observed in *Hch* mice and in humans (Biosse Duplan *et al*, 2016, Morice *et al,* in press, Orphanet 2023).

In adult animals from P14, we found significant size and shape modifications, i.e retrusion of the maxilla, relative mandibular prognathism and reduced mandibular length (Loisay et al under review). Endochondral ossification occurring in the condylar region allows ramus elongation. Noticeably, we report defective chondrocyte maturation in the condylar cartilages thus demonstrating that $Fgfr3^{N534K/+}$ mutation strongly impacts endochondral post-natal ossification of the mandible. All these results account for the increasing severity of the mandibular phenotype with age in *Hch* mice.

It is well known that mandibular shape contributes to facial morphology and influences dental occlusion, masticatory function, speech, and respiratory functions (Pirttiniemi *et al*, 2009; Obwegeser *et al*, 2001). Therefore, patients with *FGFR3*-related chondrodysplasia may require orthodontic treatments and orthognathic maxillary and mandibular bone surgery for morphological and/or functional problems. We investigated the impact of the mutation in the context of endochondral bone repair following non-stabilized fractures of the mandible. The major source for chondrocytes is periosteal mesenchymal progenitors, and these cells invade

the callus concomitantly to vascular invasion, occurring from day 2 post-fracture (Colnot *et al*, 2009; Matthew *et al*, 2014; Grcevic *et al*, 2012). The endochondral bone repair was defective and characterized by defective chondrocyte differentiation and apoptosis in the mandibular callus and led to non-bone union with pseudarthrosis at day 28 post-fracture in nearly half of $Fgfr3^{N534K/+}$ mice, otherwise consolidation and remodeling was constantly delayed. Interestingly, we observed significant microarchitectural alterations of the bone calluses from day 10 to day 28 post-fracture, with lower BV/TV and increased trabecular separation in the woven bone, without excessive bone resorption. Previously, a study using $Prx1^{Cre};Fgfr3^{Y367C/+}$ mutants, showed pseudarthrosis following non-stabilized tibial fractures confirming the putative role of *Fgfr3* in bone repair (Julien *et al*, 2020).

We also performed spatial whole transcriptomic analyses and studied gene expression profiling during a key stage of bone formation in both cartilage and bone callus. We found that *Collagen 11*, which is essential for normal chondrocyte differentiation (Bridgewater *et al*, 1998), was downregulated in $Fgfr3^{N534K/+}$ mice. Furthemore, our analyses revealed downregulation of specific osteoblast markers, normally expressed by hypertrophic chondrocytes acquiring an osteoblast-like cell fate during transdifferentiation, i.e, *Collagen 1*, *Dmp1* (Dentin Matrix Acidic Phosphoprotein 1) and *Phospho 1* (Phosphatase, orphan 1) and participating in bone matrix mineralization (*Dmp1*) (Hu *et al*, 2017, Fisher *et al*, 2001; Zhang *et al*, 2016, Morcos *et al*, 2018). We further explored the expression of a key regulator of chondrocyte differentiation. *Hmgb2* (High Mobility Group Box 2) regulating chondrocyte hypertrophy (Taniguchi *et al*, 2018), was significantly downregulated in $Fgfr3^{N534K/+}$ mice. Few studies have investigated the role of *Hmgb2* during endochondral bone formation, and its role during endochondral bone repair has never been studied. Here, our data suggest that *Hmgb2* downregulation may modulate the defective hypertrophic chondrocyte differentiation due to FGFR3 activation.

Among the genes with altered expression in the cartilage callus of $Fgfr3^{N534K/+}$ mice, of particular interest is the downregulation of *Ihh,* a key regulator of chondrocyte proliferation and differentiation and promoter of chondrocyte to osteoblast transdifferentiation (Aghajanian *et al*, 2017; Lee *et al*, 1995) and of *Kif17* (Kinesin like protein 17) participating to the anterograde trafficking of ciliary proteins (Funabashi *et al*, 2017; Ishida *et al*, 2022). Previously, we have reported defective ciliogenesis and decreased expression of *Ihh* in the $Fgfr3^{Y367C/+}$ mouse model recapitulating achondroplasia, thus inducing a disorganization of the growth plates (Martin *et al*; 2021). These data suggest that $Fgfr3^{N534K/+}$ mutation may lead to defective intraciliary protein trafficking which may in turn disturb chondrocyte organization in

the callus cartilage. We examined the newly formed woven bone of the calluses, interestingly neither levels of osteoblast markers *Col1a1*, *Osx (Sp7)*, *Runx2*, *Alpl* (Alkaline Phosphatase), *Spp1* (osteopontin) nor the osteoclast marker *Tnfrs11a* (RANK) were altered by the activated Fgfr3 signaling. In addition, as bone homeostasis depends on the balance of bone formation and resorption, implying both synthesis and catabolic processes, we investigated the impact of *Fgfr3*$^{N534K/+}$ mutation on autophagy and apoptosis processes (Harada and Rodan, 2003; Cinque *et al*, 2015). The role of FGF/FGFR signalling in the regulation of autophagy has been demonstrated (Cinque *et al*, 2015), and it has been shown that FGFR3 activation inhibits autophagic processes in the context of skeletal bone formation and growth (Wang *et al*, 2015). Defective autophagy leads to endoplasmic reticulum stress, which in turns downregulates the BMP/Smad1/5/8 pathway, and inhibits osteoblast differentiation (Li *et al*, 2018). *Smad1* was significantly downregulated in the bone calluses of *Fgfr3*$^{N534K/+}$ mice. We speculate that downregulation of *Smad 1* could be due to defective autophagy linked to *Fgfr3* overexpression, which in turn may inhibit osteoblast differentiation. We found that apoptosis regulation was altered in the bone calluses of *Fgfr3*$^{N534K/+}$ mice, as shown by the downregulation of *Comp* (Cartilage Oligomeric Matrix Protein), a suppressor of apoptosis (Gagarina *et al*, 2008), expressed in both chondrocytes and osteoblasts in developing and mature tissues (Di Cesare *et al*, 1995 ; Fang *et al*, 2000). Our results also demonstrated altered DNA repair in *Fgfr3*$^{N534K/+}$ mice, as revealed by the downregulation of *Alkbh2*, a DNA repair enzyme that catalyses the direct reversal of DNA methylation damage through oxidative demethylation (Fu *et al*, 2015). Overall, these analyses reveal that *Fgfr3*$^{N534K/+}$ mutation disturbs autophagic and apoptotic processes during bone callus formation. Our findings indicate that altered bone callus formation may be due to *Fgfr3* overexpression on both chondrocyte and osteoblast differentiation via MAPK pathway and via negative regulation of BMP/Smad pathway in response to defective autophagy.

Furthermore, we explored members of the dual-specificity (threonine/tyrosine) phosphatase superfamily (Dusp) (Jeffrey *et al*, 2007, Patterson *et al,* 2009), negative regulators of MAPK and STAT signalling pathways downstream of Fgfr3 (Ornitz and Marie, 2015; Komla Ebri *et al*, 2016). *Dusp9* and *Dusp3*, negative regulators of the MAPK pathway, were upregulated in mutants, in the cartilage and in the bone callus, respectively. Significantly increased expression levels of *Socs3* (Suppressor of Cytokine Signaling-3), a negative regulator of STAT3 signalling (Babon and Nicola, 2012) and MAPK signalling (Liu *et al*, 2019), were observed. Overall, our data suggest that the MAPK pathway is a key signalling pathway that alters chondrocyte

differentiation and bone formation downstream of *Fgfr3* constitutive overactivation during the endochondral bone repair process.

To rescue the defective bone repair processes *in vivo*, we evaluated the action of two FGFR3 antagonists (BGJ398 and BMN111). BGJ398 is a tyrosine kinase inhibitor, inhibiting excessive phosphorylation of tyrosine kinase residues and correcting defective bone growth in the *Fgfr3*$^{Y367C/+}$ mouse model (Komla Ebri *et al*, 2016, Di Rocco *et al*, 2014, Biosse Duplan *et al*, 2016). BMN111 is a CNP analog with a longer half-life than CNP (BioMarin®), inhibiting MAPK signalling, activated downstream FGFR3. The positive effects of BMN111 (vosoritide) on bone growth have been demonstrated in *Fgfr3* mouse models (Lorget *et al*, 2012, Wendt *et al*, 2015), and positive results have been reported in clinical studies in children with achondroplasia (Savarirayan *et al*, 2020). Recently, vosoride has received FDA approval. Interestingly, both BGJ398 and BMN111 treatments resulted the rescie of defective bone repair, allowing normal consolidation. Chondrocyte differentiation and apoptosis were improved in the cartilage callus and microarchitectural alterations of the bone callus were rescued by both treatments. Interestingly, BMN111 mostly rescued chondrocyte differentiation and BGJ398 mostly stimulated osteoblast differentiation and maturation. Both treatments accelerated bone repair, leading to modification of the bone formation / bone resorption balance, in favour of bone apposition to restore mandibular cortical bone. Both treatments corrected the MAPK pathway overactivation. BMN111 is a CNP analog, which inhibits MAPK pathway via the activation of NPR-B receptor (Lorget *et al*, 2012), whereas BGJ398 decreased the Fgfr3 activation and several downstream signalling pathways. In the future, others signalling pathways downstream FGFR3 should be investigated.

In conclusion, a *Fgfr3* gain-of-function mutation impaired endochondral bone formation and repair of the mandible and promoted pseudarthrosis in an *Hch* mouse model. This finding identifies a role of Fgfr3 in the regulation of chondrocyte and osteoblast differentiation during bone repair and further supports the concept that FGFR3 antagonists rescued altered bone callus formation. These data may offer promising therapeutic perspectives to tackle defective bone repair in patients with *FGFR3*-related osteochondrodysplasia, in the context of traumatic bone fractures, and following craniofacial and mandibular osteotomies.

Methods

Mouse model

All the experiments were conducted using *Fgfr3*$^{N534K/+}$ mice (*Fgfr3*$^{Asn534Lys/+}$), a mouse model that mimics clinical features of human hypochondroplasia (Loisay *et al,* under review), and in wild-type littermates used as controls. The mutant mice expressed the Asn534Lys mutation in exon 12 of *Fgfr3* (corresponding to Asn540Lys in human) and the loxP flanked neo/STOP cassette. All mice were on a C57BL/6 background. Mice were genotyped by PCR of external ear DNA. Experimental animal procedures and protocols were approved by the French Animal Care and Use Committee. For all analyses, both male and female wild-type littermates were used as controls.

Non-stabilized mandibular fracture protocol

Adult mutant and control mice (female and males aged 6 weeks) were anesthetized with isoflurane (induction 4%, maintenance 2.5%) and received a pre-operative dose of buprenorphine (0.1 mg/kg) by sub-cutaneous injection. Non-stabilized mandibular fractures were performed using a sub-mandibular approach. A cutaneous incision was performed along the inferior (basilar) border of the right mandible. The masseter muscle was elevated in a subperiosteal plane along the ascending branch of the mandible with a periosteal elevator.

A vertical and complete fracture of the ascending branch was performed from the basilar border to the coronoid notch (between the condylar and the coronoid processes), using a piezotome under saline serum irrigation, and scissors (Figure 2A). The cutaneous approach was closed by silk sutures. Lateral X-rays of the head were performed immediately post-operatively in a sagittal plane, to control the position of the mandibular fracture.

Post-operatively, mice received subcutaneous injections of buprenorphine (0.1 mg/kg), 4 hours after surgery, and at days 1, 2 and 3. During all the post-operative period, mice were fed with soft diet. Food intake, weight and animal activity were monitored every day the first week, and then every two days and as frequently as necessary. In case of an excessive growth of mandibular incisors in mutants (due to shortened skull base, maxillary retrusion and prognathism), dental section was performed when necessary pre- and post-operatively to avoid feeding difficulties. The entire skull and mandibles were collected at 7, 10, 14, 21 and 28 days post-fracture.

X ray microradiography

X-ray radiography imaging was performed immediately after the fracture and post-mortem using a Faxitron UltraFocus digital X-ray radiography system (Faxitron Bioptics, Tucson, AZ, USA). Lateral images of the head and mandibles were taken at 1x.

CT images

Micro-Computed Tomography imaging of the skull and mandibles were performed using a Skyscan 1172 (Bruker, Kontich, Belgium). The samples for geometric morphometrics consisted of skulls and mandibles of mutants and controls aged P42 fixed in 70 % ethanol. For bone repair morphometrics, the samples consisted of mandibles of mutants and controls euthanatized at day 10, 14, 21 and 28 post-fracture, fixed in PFA 4% for 24 hours, and then washed with PBS 1X, and immediately scanned.

Samples were scanned with settings of 80 kV, 100 µA, 23 µm pixel resolution, 0.5° rotation steps with a 0.5 mm Aluminum filter. Three-dimensional (3D) reconstructions were generated using NRecon software (Skyscan). Adjustments of the bone density threshold were done for each CT-scan with the same parameters, without smoothing factors.

For bone repair morphometrics, the region of interest concerned the callus area, which was selected manually using CTAn software (Skyscan). Bone Volume / Tissue Volume (BV/TV) for each callus was automatically calculated using CTAn. To compare the callus volumes between controls and mutants presenting significantly different mandibular sizes, the entire contralateral unfractured mandibular ascending branch was contoured manually from the retromolar area. The ratio Tissue Volume (TV) of the callus / Tissue Volume (TV) of the contralateral ascending branch was calculated for normalization.

For 3D geometric morphometrics, following reconstruction, the 3D surface mesh was obtained using Avizo® (ThermoFisher, MA, USA) for each specimen and then used for landmark positioning of the skull (Supplemental Figure 8A) and mandibles (Supplemental Figure 8B). The listing of the landmarks is provided in Supplemental File 1. 3D Landmark coordinates were analyzed using geometric morphometric approaches, including standardization for position, scale, and orientation through Procrustes superimposition (Rohlf *et al*, 1990). Error measurement was assessed with a Procrustes ANOVA analysis and showed no significant differences in landmark positioning, allowing valid comparative analyses of shape variation among specimens. After Procrustes superimposition, the resulting 3D Procrustes shape

coordinates were evaluated by principal component analysis. Wireframes were used to visualize the shape differences corresponding to the skull associated with specific scores on principal components (PC). Centroid size (CS), the square root of the sum of squared distances of the landmarks from their centroid, was used as a proxy for size (Dryden and Walker, 1999). The influence of size on shape (i.e. allometry) was tested with multiple multivariate regression. Procrustes distances (d) separating groups in the morphospace were computed and significance was assessed using permutation tests (10,000 permutation rounds). A significant value of d was interpreted as significant shape differences between the two groups compared. The geometric morphometric analyses were performed with MorphoJ v. 1.06 (Dryden *et al*., 2008).

Histology

All samples were collected in 4% paraformaldehyde, fully decalcified in 0.5M EDTA (pH 8.0) and embedded in paraffin. Six µm serial sections were performed. All slices were deparaffinized in Neo-clear solution (Millipore) and then rehydrated to perform standard immunostaining protocols. Cuts were stained with haematoxylin and eosin (H&E), Safranin-O/Fast-Green, or Sirus red/Alcian blue according standard protocols.

Histomorphometric analyses were performed on stepped cuts stained with Safranin O for the evaluation of Meckel's cartilage volume, and with Sirus Red/Alcian blue to determine the cartilage and bone volumes of the calluses. A minimum of seven equidistant sections spaced at 120 µm apart throughout the callus was analysed for each callus. Total volumes of the region of interests (cartilage, bone) were estimated according to Cavalieri's principle, as described by Abou-Khalil *et al*, 2014.

Selected adjacent slides were subjected to immunohistochemical staining using standard protocols with antibodies against Collagen I (1:800, 20151-1, Novotec), Collagen II (1:500, 20251, Novotec), Collagen X (1:100, Quartett, 1-CO097-05), Sox 9 (1:1000, ab185230, Abcam), Fgfr3 (1:100, F0425, Sigma), VEGF (1:200, ab46154, Abcam), and PCNA (proliferating cell nuclear antigen) (1:500, ab29, Abcam) using the Dako Envision kit (Dako North America, Inc., CA, USA).

For the Mouse Anti-Collagen Type X (ColX) antibody, pepsin was used for antigen retrieval (Sigma-Aldrich Co, St. Louis, MO, USA) during 2 hours at 37°C for post-natal and callus samples, or during 1 hour for embryo samples. For the Mouse Anti-Collagen Type I (ColI) antibody, hyaluronidase was used for antigen retrieval during 30 minutes at 37°C.

To detect DNA fragmentation, a TUNEL assay (Terminal deoxynucleotidyl transferase dUTP nick end labelling) was performed on 6 µm paraffin slides after deparaffinisation using Promega kit G3250, according to the manufacturer's protocol. Sections were mounted with Fluoromount-G mounting medium with DAPI (4',6-diamidino-2-phénylindole) for nuclear staining (00-4959-52, Life Technologies).

To detect osteoclast activity, TRAP (Tartrate-resistant acid phosphatase) staining was performed on 6 µm paraffin slides after deparaffinisation, using a Sigma kit 38717-1KT, according to manufacturer's protocol. Sections were counterstained with Anilin blue according to standard's protocols.

Macroscopic analyses and linear measurements of the mandibles of mutants and control littermates were performed after Alizarin Red/Alcian Blue staining according to standard protocols.

Images were captured with an Olympus PD70-IX2-UCB microscope (Olympus, Tokyo, Japan), and morphometry was performed with ImageJ software (National Institutes of Health, Bethesda, MD, USA).

Spatial transcriptomic analyses - GeoMx DSP (Digital Spatial Profiler)

Experiments were performed using calluses of mutants and control littermates at 14 days post-fracture, using the same non-stabilized mandibular fracture protocol as previously described. All samples were collected in 4% paraformaldehyde for 4 hours, fully decalcified in EDTA pH 7.4 for 72 hours and paraffin embedded. Six µm serial sections were performed, dried overnight at room temperature, and stored hermetically with dessicant at 4°C before further processing. FFPE mouse samples were baked overnight at 37°C followed by 3 hours of baking at 65°C, then loaded onto a Leica Bond RX Fully Automated Research Stainer for subsequent processing steps. The processing protocol included three major steps: (1) slide baking, (2) antigen retrieval for 20min at 100°C, and (3) treatment with Proteinase K (1.0 µg/mL in 1xPBS) for 15 min. Following these steps, slides were removed from the Leica Bond RX, and a cocktail of GeoMx Mouse Whole Transcriptome Atlas probes (targeting over 19,000 genes) were applied to each slide and allowed to hybridize at 37°C overnight in a humidity chamber. The following day, slides were washed, blocked, and allowed to incubate with a combination of Alexa Fluor 594 Anti-alpha smooth muscle Actin antibody (Abcam antibody ab202368; clone: 1A4) and Syto83 nucleic acid stain. Slides were stained for 1h at room temperature in a humidity chamber. Slides were then washed and loaded onto the GeoMx instrument.

Next-generation sequencing and sequencing data processing

On the GeoMx machine, slides were fluorescently scanned, and ROIs were manually placed in in the newly formed bone and the cartilage. The GeoMx device exposed ROIs to 385 nm light (UV), releasing the indexing oligos. Indexing oligos were collected with a microcapillary and deposited into a 96-well plate. Samples were dried overnight, then resuspended in 10 µL of DEPC-treated water. PCR was performed using 4 µL of each sample and the oligos from each ROI were indexed using unique i5 and i7 dual-indexing systems (Illumina). PCR reactions were purified twice using AMPure XP beads (Beckman Coulter, Inc) according to the manufacturer's protocol. Purified libraries were sequenced on an Illumina NovaSeq 6000. Fastq files were processed using the NanoString GeoMx NGS Pipeline v2.2. Briefly, reads were trimmed to remove low quality bases and adapter sequences. Paired end reads were aligned and stitched, and the barcode and UMI sequences were extracted. Barcodes were matched to known probe barcodes with maximum 1 mismatch allowed. Reads matching the same barcode were deduplicated by UMI. All analyses used UMI deduplicated counts to correct for any PCR amplification bias (Supplemental Figure 4A).

GeoMx spatial whole transcriptome assays were performed using 2 slides, for a total of n=32 regions of interest (or ROIs). After quality control filters were applied, 27 sample ROIs were retained for analysis (Supplemental Figure 4B), as follows: 13 cartilage samples and 14 newly formed bone samples of mandibular calluses selected in both mutant and control groups (mutants: cartilage samples n=7, newly formed samples n=7 ; controls : cartilage samples n=6, newly formed samples n=7). Briefly, quality control for each ROI was performed using a three-step filtering procedure, notably retaining ROIs with a sequencing saturation above 50 to capture full sample diversity, removing outlier probes and keeping genes expressed above the limit of quantification to increase the performance of downstream statistical tests.

Data analysis and visualization. All statistical analyses and data visualizations were performed in R environment. Count data was processed and normalized using the GeoMxTools (v3.2), GeoMxWorkflows (v1.5,) and NanoStringQCPro (v1.30) R/Bioconductor packages. AOIs with fewer than 1000 raw reads, a sequencing saturation <50%, an alignment rate <80% or a segment area <5000 were filtered out of the analysis. For the negative control probes, outlier testing was performed and led to the removal of outlier probes from the analysis prior to collapsing counts. As previously described (Zimmerman *et al*. 2021 *bioRxiv* 2021.09.29.462442), a negative probe was considered to be an outlier following two criteria.

Firstly, if the average count of a probe across all segments was less than 10% of the average count of all negative probes, then the probe was globally (i.e. from all segments) removed. Secondly, if the probe was considered an outlier by the Grubb's test (alpha = 0.01), it was locally (i.e. from that particular segment) removed. If the probe was an outlier by the Grubb's test in over 20% of segments, then it was globally removed. Finally, we calculated the geometric mean of the retained probes in order to collapse the negative probes into a single count value. The limit of quantification (LOQ) for any given gene was defined as 2 standard deviations above the geometric mean of negative probes. Genes were filtered to only those above LOQ in >10% of AOIs. Subsequently, differential expression was performed using DESeq2 (Love *et al*, 2014) in combination with RUVSeq (Risso *et al*, 2014) for normalization by controlling for mouse housekeeping genes. The obtained *p*-values were corrected for multiple testing (Benjamini-Hochberg method) and genes were considered to be significantly differentially expressed when FDR < 10%. Finally, pathway enrichment analysis was performed using GSEA (Subramanian *et al*. 2005) on the Human Molecular Signatures database (MSigDB) collections.

Data availability. All data generated in this study are available at the NCBI Gene Expression Omnibus (GEO), accession number **GSE216899**.

Preclinical *in vivo* experiments

Mutant mice received either BGJ398 (infigratinib (Novartis®), 4 mg/kg, DMSO 4%, isotonic saline serum) or BMN111 (vosoritide (Biosynth®, 0.8 mg/kg, isotonic saline serum), or vehicle using sub-cutaneous injections from the fracture day during either 14 or 28 days post-fracture, three times a week. Non-stabilized mandibular fractures, post-operative follow-up, morphometric analyses (CT-scans, histomorphometry) and immunohistochemistry analyses were performed as previously described.

Statistical analysis

Statistical comparisons were made using GraphPad Prism (V8.00, GraphPad Software, La Jolla, CA, USA). The significance threshold was set at $P<0.05$ (*$0.01 < p < 0.05$, **$0.001 < p < 0.01$, ***$0.0001 < p < 0.001$, ****$p < 0.0001$, Mann-Whitney test).

References

Abou-Khalil R, Yang F, Mortreux M, et al. Delayed bone regeneration is linked to chronic inflammation in murine muscular dystrophy. *J Bone Miner Res*. 2014;29(2):304-315. doi:10.1002/jbmr.2038

Aghajanian P, Xing W, Cheng S, Mohan S. Epiphyseal bone formation occurs via thyroid hormone regulation of chondrocyte to osteoblast transdifferentiation. *Sci Rep*. 2017;7(1):10432. Published 2017 Sep 5. doi:10.1038/s41598-017-11050-1.

Amarasekara DS, Kim S, Rho J. Regulation of Osteoblast Differentiation by Cytokine Networks. *Int J Mol Sci*. 2021;22(6):2851. Published 2021 Mar 11. doi:10.3390/ijms22062851.

Anvarian Z, Mykytyn K, Mukhopadhyay S, Pedersen LB, Christensen ST. Cellular signalling by primary cilia in development, organ function and disease. *Nat Rev Nephrol*. 2019;15(4):199-219. doi:10.1038/s41581-019-0116-9.

Ascenzi MG, Blanco C, Drayer I, et al. Effect of localization, length and orientation of chondrocytic primary cilium on murine growth plate organization. *J Theor Biol*. 2011;285(1):147-155. doi:10.1016/j.jtbi.2011.06.016.

Babon JJ, Nicola NA. The biology and mechanism of action of suppressor of cytokine signaling 3. *Growth Factors*. 2012;30(4):207-219. doi:10.3109/08977194.2012.687375

Bellus GA, McIntosh I, Smith EA, et al. A recurrent mutation in the tyrosine kinase domain of fibroblast growth factor receptor 3 causes hypochondroplasia. *Nat Genet*. 1995;10(3):357-359. doi:10.1038/ng0795-357.

Biosse Duplan M, Komla-Ebri D, Heuzé Y, et al. Meckel's and condylar cartilages anomalies in achondroplasia result in defective development and growth of the mandible. *Hum Mol Genet*. 2016;25(14):2997-3010. doi:10.1093/hmg/ddw153.

Bober MB, Bellus GA, Nikkel SM, Tiller GE. Hypochondroplasia. In: Adam MP, Everman DB, Mirzaa GM, et al., eds. *GeneReviews*®. Seattle (WA): University of Washington, Seattle; July 15, 1999.

Bridgewater LC, Lefebvre V, de Crombrugghe B. Chondrocyte-specific enhancer elements in the Col11a2 gene resemble the Col2a1 tissue-specific enhancer. *J Biol Chem*. 1998;273(24):14998-15006. doi:10.1074/jbc.273.24.14998.

Chen H, Sun X, Yin L, et al. PTH 1-34 Ameliorates the Osteopenia and Delayed Healing of Stabilized Tibia Fracture in Mice with Achondroplasia Resulting from Gain-Of-Function Mutation of FGFR3. *Int J Biol Sci*. 2017;13(10):1254-1265. Published 2017 Sep 21. doi:10.7150/ijbs.21258.

Cinque L, Forrester A, Bartolomeo R, et al. FGF signalling regulates bone growth through autophagy. *Nature*. 2015;528(7581):272-275. doi:10.1038/nature16063.

Colnot C. Skeletal cell fate decisions within periosteum and bone marrow during bone regeneration [published correction appears in J Bone Miner Res. 2009 Apr;24(4):758]. *J Bone Miner Res*. 2009;24(2):274-282. doi:10.1359/jbmr.081003

Cottin, M., Khonsari, R. H., & Friess, M. (2017). Assessing cranial plasticity in humans: The impact of artificial deformation on masticatory and basicranial structures. *Comptes Rendus Palevol*, *16*(5-6), 545-556.

Di Rocco F, Biosse Duplan M, Heuzé Y, et al. FGFR3 mutation causes abnormal membranous ossification in achondroplasia. *Hum Mol Genet*. 2014;23(11):2914-2925. doi:10.1093/hmg/ddu004.

DiCesare PE, Mörgelin M, Carlson CS, Pasumarti S, Paulsson M. Cartilage oligomeric matrix protein: isolation and characterization from human articular cartilage. *J Orthop Res*. 1995;13(3):422-428. doi:10.1002/jor.1100130316

Dryden IL, Oxborrow N, Dickson R. Familial relationships of normal spine shape. *Stat Med*. 2008;27(11):1993-2003. doi:10.1002/sim.3162

Dryden IL, Walker G. Highly resistant regression and object matching. *Biometrics*. 1999;55(3):820-825. doi:10.1111/j.0006-341x.1999.00820.x

Fang C, Carlson CS, Leslie MP, et al. Molecular cloning, sequencing, and tissue and developmental expression of mouse cartilage oligomeric matrix protein (COMP). *J Orthop Res*. 2000;18(4):593-603. doi:10.1002/jor.1100180412

Ferros I, Mora MJ, Obeso IF, Jimenez P, Martinez-Insua A. Relationship between the cranial base and the mandible in artificially deformed skulls. *Orthod Craniofac Res*. 2016;19(4):222-233. doi:10.1111/ocr.12128.

Fisher LW, Torchia DA, Fohr B, Young MF, Fedarko NS. Flexible structures of SIBLING proteins, bone sialoprotein, and osteopontin. *Biochem Biophys Res Commun*. 2001;280(2):460-465. doi:10.1006/bbrc.2000.4146.

Flynn MA, Pauli RM. Double heterozygosity in bone growth disorders: four new observations and review. *Am J Med Genet A*. 2003;121A(3):193-208. doi:10.1002/ajmg.a.20143.

Fu D, Samson LD, Hübscher U, van Loon B. The interaction between ALKBH2 DNA repair enzyme and PCNA is direct, mediated by the hydrophobic pocket of PCNA and perturbed in naturally-occurring ALKBH2 variants. *DNA Repair (Amst)*. 2015;35:13-18. doi:10.1016/j.dnarep.2015.09.008

Funabashi T, Katoh Y, Michisaka S, Terada M, Sugawa M, Nakayama K. Ciliary entry of KIF17 is dependent on its binding to the IFT-B complex via IFT46-IFT56 as well as on its nuclear localization signal. *Mol Biol Cell*. 2017;28(5):624-633. doi:10.1091/mbc.E16-09-0648.

Gagarina V, Carlberg AL, Pereira-Mouries L, Hall DJ. Cartilage oligomeric matrix protein protects cells against death by elevating members of the IAP family of survival proteins. *J Biol Chem*. 2008;283(1):648-659. doi:10.1074/jbc.M704035200

Galea GL, Zein MR, Allen S, Francis-West P. Making and shaping endochondral and intramembranous bones. *Dev Dyn*. 2021;250(3):414-449. doi:10.1002/dvdy.278

Gambari L, Grigolo B, Grassi F. Hydrogen Sulfide in Bone Tissue Regeneration and Repair: State of the Art and New Perspectives. *Int J Mol Sci*. 2019;20(20):5231. Published 2019 Oct 22. doi:10.3390/ijms20205231.

Grcevic D, Pejda S, Matthews BG, et al. In vivo fate mapping identifies mesenchymal progenitor cells. *Stem Cells*. 2012;30(2):187-196. doi:10.1002/stem.780

Harada S, Rodan GA. Control of osteoblast function and regulation of bone mass. *Nature*. 2003;423(6937):349-355. doi:10.1038/nature01660.

Haycraft CJ, Zhang Q, Song B, et al. Intraflagellar transport is essential for endochondral bone formation. *Development*. 2007;134(2):307-316. doi:10.1242/dev.02732.

Hinton RJ, Jing Y, Jing J, Feng JQ. Roles of Chondrocytes in Endochondral Bone Formation and Fracture Repair. *J Dent Res*. 2017;96(1):23-30. doi:10.1177/0022034516668321.Marie PJ. Transcription factors controlling osteoblastogenesis. *Arch Biochem Biophys*. 2008;473(2):98-105. doi:10.1016/j.abb.2008.02.030.

Hirokawa N, Niwa S, Tanaka Y. Molecular motors in neurons: transport mechanisms and roles in brain function, development, and disease. *Neuron*. 2010;68(4):610-638. doi:10.1016/j.neuron.2010.09.039.

Hu DP, Ferro F, Yang F, et al. Cartilage to bone transformation during fracture healing is coordinated by the invading vasculature and induction of the core pluripotency genes. *Development*. 2017;144(2):221-234. doi:10.1242/dev.130807.

Hu DP, Ferro F, Yang F, et al. Cartilage to bone transformation during fracture healing is coordinated by the invading vasculature and induction of the core pluripotency genes. *Development*. 2017;144(2):221-234. doi:10.1242/dev.130807

Hu K, Olsen BR. Osteoblast-derived VEGF regulates osteoblast differentiation and bone formation during bone repair. *J Clin Invest*. 2016;126(2):509-526. doi:10.1172/JCI82585.

Ishida Y, Tasaki K, Katoh Y, Nakayama K. Molecular basis underlying the ciliary defects caused by *IFT52* variations found in skeletal ciliopathies. *Mol Biol Cell*. 2022;33(9):ar83. doi:10.1091/mbc.E22-05-0188.

Jeffrey KL, Camps M, Rommel C, Mackay CR. Targeting dual-specificity phosphatases: manipulating MAP kinase signalling and immune responses. *Nat Rev Drug Discov*. 2007;6(5):391-403. doi:10.1038/nrd2289

Jonquoy A, Mugniery E, Benoist-Lasselin C, et al. A novel tyrosine kinase inhibitor restores chondrocyte differentiation and promotes bone growth in a gain-of-function Fgfr3 mouse model. *Hum Mol Genet*. 2012;21(4):841-851. doi:10.1093/hmg/ddr514.

Julien A, Perrin S, Duchamp de Lageneste O, et al. FGFR3 in Periosteal Cells Drives Cartilage-to-Bone Transformation in Bone Repair. *Stem Cell Reports*. 2020;15(4):955-967. doi:10.1016/j.stemcr.2020.08.005.

Komatsu DE, Hadjiargyrou M. Activation of the transcription factor HIF-1 and its target genes, VEGF, HO-1, iNOS, during fracture repair. *Bone*. 2004;34(4):680-688. doi:10.1016/j.bone.2003.12.024.

Komla-Ebri D, Dambroise E, Kramer I, et al. Tyrosine kinase inhibitor NVP-BGJ398 functionally improves FGFR3-related dwarfism in mouse model. *J Clin Invest*. 2016;126(5):1871-1884. doi:10.1172/JCI83926.

Kopinke D, Norris AM, Mukhopadhyay S. Developmental and regenerative paradigms of cilia regulated hedgehog signaling. *Semin Cell Dev Biol*. 2021;110:89-103. doi:10.1016/j.semcdb.2020.05.029.

Kunova Bosakova M, Varecha M, Hampl M, et al. Regulation of ciliary function by fibroblast growth factor signaling identifies FGFR3-related disorders achondroplasia and thanatophoric dysplasia as ciliopathies. *Hum Mol Genet*. 2018;27(6):1093-1105. doi:10.1093/hmg/ddy031.

Lee K, Deeds JD, Segre GV. Expression of parathyroid hormone-related peptide and its receptor messenger ribonucleic acids during fetal development of rats. *Endocrinology*. 1995;136(2):453-463. doi:10.1210/endo.136.2.7835276.

Legeai-Mallet L, Savarirayan R. Novel therapeutic approaches for the treatment of achondroplasia. *Bone*. 2020;141:115579. doi:10.1016/j.bone.2020.115579

Li H, Li D, Ma Z, et al. Defective autophagy in osteoblasts induces endoplasmic reticulum stress and causes remarkable bone loss. *Autophagy*. 2018;14(10):1726-1741. doi:10.1080/15548627.2018.1483807.

Liu P, Verhaar AP, Peppelenbosch MP. Signaling Size: Ankyrin and SOCS Box-Containing ASB E3 Ligases in Action. *Trends Biochem Sci*. 2019;44(1):64-74. doi:10.1016/j.tibs.2018.10.003

Lorget F, Kaci N, Peng J, et al. Evaluation of the therapeutic potential of a CNP analog in a Fgfr3 mouse model recapitulating achondroplasia. *Am J Hum Genet*. 2012;91(6):1108-1114. doi:10.1016/j.ajhg.2012.10.014.

Love MI, Huber W, Anders S. Moderated estimation of fold change and dispersion for RNA-seq data with DESeq2. *Genome Biol*. 2014;15(12):550. doi:10.1186/s13059-014-0550-8

Marie PJ. Transcription factors controlling osteoblastogenesis. *Arch Biochem Biophys*. 2008;473(2):98-105. doi:10.1016/j.abb.2008.02.030

Maroteaux P, Falzon P. Hypochondroplasie. Revue de 80 cas [Hypochondroplasia. Review of 80 cases]. *Arch Fr Pediatr*. 1988;45(2):105-109.

Martin L, Kaci N, Benoist-Lasselin C, et al. Theobroma cacao improves bone growth by modulating defective ciliogenesis in a mouse model of achondroplasia. *Bone Res*. 2022;10(1):8. Published 2022 Jan 25. doi:10.1038/s41413-021-00177-7.

Matthews BG, Grcevic D, Wang L, et al. Analysis of αSMA-labeled progenitor cell commitment identifies notch signaling as an important pathway in fracture healing. *J Bone Miner Res*. 2014;29(5):1283-1294. doi:10.1002/jbmr.2140

Mizushima N, Komatsu M. Autophagy: renovation of cells and tissues. *Cell*. 2011;147(4):728-741. doi:10.1016/j.cell.2011.10.026.

Morcos MW, Al-Jallad H, Li J, et al. PHOSPHO1 is essential for normal bone fracture healing: An Animal Study. *Bone Joint Res*. 2018;7(6):397-405. Published 2018 Jul 7. doi:10.1302/2046-3758.76.BJR-2017-0140.R2.

Motch Perrine SM, Wu M, Stephens NB, et al. Mandibular dysmorphology due to abnormal embryonic osteogenesis in FGFR2-related craniosynostosis mice. *Dis Model Mech*. 2019;12(5):dmm038513. Published 2019 May 30. doi:10.1242/dmm.038513.

Mugniery E, Dacquin R, Marty C, et al. An activating Fgfr3 mutation affects trabecular bone formation via a paracrine mechanism during growth. *Hum Mol Genet*. 2012;21(11):2503-2513. doi:10.1093/hmg/dds065.

Obwegeser, H. L. (2002). Mandibular growth anomalies. *American journal of orthodontics and dentofacial orthopedics*, *121*(5), 546-547.

Ornitz DM, Legeai-Mallet L. Achondroplasia: Development, pathogenesis, and therapy. *Dev Dyn*. 2017;246(4):291-309. doi:10.1002/dvdy.24479.

Ornitz DM, Marie PJ. Fibroblast growth factor signaling in skeletal development and disease. *Genes Dev*. 2015;29(14):1463-1486. doi:10.1101/gad.266551.115

Oryan A, Alidadi S, Moshiri A. Platelet-rich plasma for bone healing and regeneration. *Expert Opin Biol Ther*. 2016;16(2):213-232. doi:10.1517/14712598.2016.1118458.

Patterson KI, Brummer T, O'Brien PM, Daly RJ. Dual-specificity phosphatases: critical regulators with diverse cellular targets. *Biochem J*. 2009;418(3):475-489. doi:10.1042/bj20082234

Pirttiniemi P, Peltomäki T, Müller L, Luder HU. Abnormal mandibular growth and the condylar cartilage. *Eur J Orthod*. 2009;31(1):1-11. doi:10.1093/ejo/cjn117

Raffioni S, Zhu YZ, Bradshaw RA, Thompson LM. Effect of transmembrane and kinase domain mutations on fibroblast growth factor receptor 3 chimera signaling in PC12 cells. A model for the control of receptor tyrosine kinase activation. *J Biol Chem*. 1998;273(52):35250-35259. doi:10.1074/jbc.273.52.35250.

Ramaesh T, Bard JB. The growth and morphogenesis of the early mouse mandible: a quantitative analysis. *J Anat*. 2003;203(2):213-222. doi:10.1046/j.1469-7580.2003.00210.x

Rice DP, Rice R, Thesleff I. Fgfr mRNA isoforms in craniofacial bone development. *Bone*. 2003;33(1):14-27. doi:10.1016/s8756-3282(03)00163-7.

Risso D, Ngai J, Speed TP, Dudoit S. Normalization of RNA-seq data using factor analysis of control genes or samples. *Nat Biotechnol*. 2014;32(9):896-902. doi:10.1038/nbt.2931

Rohlf FJ, Chang WS, Sokal RR, Kim J. Accuracy of estimated phylogenies: effects of tree topology and evolutionary model. *Evolution*. 1990;44(6):1671-1684. doi:10.1111/j.1558-5646.1990.tb03855.x

Rousseau F, Bonaventure J, Legeai-Mallet L, et al. Clinical and genetic heterogeneity of hypochondroplasia. *J Med Genet*. 1996;33(9):749-752. doi:10.1136/jmg.33.9.749.

Savarirayan R, Tofts L, Irving M, et al. Once-daily, subcutaneous vosoritide therapy in children with achondroplasia: a randomised, double-blind, phase 3, placebo-controlled, multicentre trial [published correction appears in Lancet. 2020 Oct 10;396(10257):1070]. *Lancet*. 2020;396(10252):684-692. doi:10.1016/S0140-6736(20)31541-5.

Schell H, Duda GN, Peters A, Tsitsilonis S, Johnson KA, Schmidt-Bleek K. The haematoma and its role in bone healing. *J Exp Orthop*. 2017;4(1):5. doi:10.1186/s40634-017-0079-3.

Schliwa M, Woehlke G. Molecular motors. *Nature*. 2003;422(6933):759-765. doi:10.1038/nature01601.

Sheen JR, Garla VV. Fracture Healing Overview. In: *StatPearls*. Treasure Island (FL): StatPearls Publishing; May 8, 2022.

Su N, Du X, Chen L. FGF signaling: its role in bone development and human skeleton diseases. *Front Biosci*. 2008;13:2842-2865. Published 2008 Jan 1. doi:10.2741/2890.

Svandova E, Anthwal N, Tucker AS, Matalova E. Diverse Fate of an Enigmatic Structure: 200 Years of Meckel's Cartilage. *Front Cell Dev Biol*. 2020;8:821. Published 2020 Aug 28. doi:10.3389/fcell.2020.00821.

Taniguchi N, Kawakami Y, Maruyama I, Lotz M. HMGB proteins and arthritis. *Hum Cell*. 2018;31(1):1-9. doi:10.1007/s13577-017-0182-x.

Walker BA, Murdoch JL, McKusick VA, Langer LO, Beals RK. Hypochondroplasia. *Am J Dis Child*. 1971;122(2):95-104. doi:10.1001/archpedi.1971.02110020029001.

Wang X, Qi H, Wang Q, et al. FGFR3/fibroblast growth factor receptor 3 inhibits autophagy through decreasing the ATG12-ATG5 conjugate, leading to the delay of cartilage development in achondroplasia. *Autophagy*. 2015;11(11):1998-2013. doi:10.1080/15548627.2015.1091551

Wendt DJ, Dvorak-Ewell M, Bullens S, et al. Neutral endopeptidase-resistant C-type natriuretic peptide variant represents a new therapeutic approach for treatment of fibroblast

growth factor receptor 3-related dwarfism. *J Pharmacol Exp Ther*. 2015;353(1):132-149. doi:10.1124/jpet.114.218560.

Yu K, Karuppaiah K, Ornitz DM. Mesenchymal fibroblast growth factor receptor signaling regulates palatal shelf elevation during secondary palate formation. *Dev Dyn*. 2015;244(11):1427-1438. doi:10.1002/dvdy.24319.

Zhang Q, Lin S, Liu Y, Yuan B, Harris SE, Feng JQ. *Dmp1* Null Mice Develop a Unique Osteoarthritis-like Phenotype. *Int J Biol Sci*. 2016;12(10):1203-1212. Published 2016 Sep 15. doi:10.7150/ijbs.15833.

Zimmerman SM, Fropf R, Kulasekara BR, et al. Spatially resolved whole transcriptome profiling in human and mouse tissue using Digital Spatial Profiling. *Genome Res*. 2022;32(10):1892-1905. doi:10.1101/gr.276206.121

Figure legends

Figure 1. The hypochondroplasia mouse model, *Fgfr3*$^{N534K/+}$ exhibits craniofacial and mandibular shape anomalies

A – Meckel's cartilage (MC) at E13.5: Representative *Fgfr3*$^{+/+}$ and *Fgfr3*$^{N534K/+}$ Sirus red/Alcian blue histological staining of MC (scale bar 200 µm), Sox 9 and FGFR3 immunostaining of MC *Fgfr3*$^{+/+}$ and *Fgfr3*$^{N534K/+}$ (scale bar 100 µm). Measurement of MC area (alcian blue staining) in *Fgfr3*$^{+/+}$ (n=6) and *Fgfr3*$^{N534K/+}$ (n=5) . Graphical representation of Sox9 staining density in MC in *Fgfr3*$^{+/+}$ (n=6) and *Fgfr3*$^{N534K/+}$ (n=5).

B – Meckel's cartilage (MC) at E16.5: Representative *Fgfr3*$^{+/+}$ and *Fgfr3*$^{N534K/+}$ Safranin O/Fast Green histological staining (scale bar 200 µm), Sox 9, Collagen X and Fgfr3 immunohistological staining of MC of *Fgfr3*$^{+/+}$ and *Fgfr3*$^{N534K/+}$ (scale bar 200 µm). Graphical representation of MC area (Safranin O staining) in *Fgfr3*$^{+/+}$ (n=7) and *Fgfr3*$^{N534K/+}$ (n=7). Graphical representation of the ratio hypertrophic area (Collagen X staining) / total MC cartilage area (%) (Safranin O staining) of *Fgfr3*$^{+/+}$ (n=7) and *Fgfr3*$^{N534K/+}$ (n=7) .

C – Representative *Fgfr3*$^{+/+}$ and *Fgfr3*$^{N534K/+}$ skull bone µCT images from P42 mice in transversal orientations (scale bar 3 mm). Graphical representation of naso anal length (mm) , mandibular length (mm), mandibular ramus length (mm), and skull width (mm) of *Fgfr3*$^{+/+}$ (n=7) and *Fgfr3*$^{N534K/+}$ (n=7).

D – 3D representations showing landmarks and associated wireframes variations of skull and mandibular shapes *Fgfr3*$^{+/+}$ and *Fgfr3*$^{N534K/+}$ of P42 mice using PC analysis. Comparison of skull and mandibular shape (Skull: Procrustes distance d=0,1094; p<0.001; Mandible: Procrustes distance d=0,0846; p<0.001) between *Fgfr3*$^{+/+}$ and *Fgfr3*$^{N534K/+}$ mice: plots of Principal Components (PC) scores for PC1 and PC2 (n=7 mice for each genotype). *P<0.05, **P < 0.01, ***P < 0.005.

E – Representative *Fgfr3*$^{+/+}$ and *Fgfr3*$^{N534K/+}$ Safranin O/Fast Green histological staining and Collagen X immunohistological staining of MC of *Fgfr3*$^{+/+}$ and *Fgfr3*$^{N534K/+}$ at P21 (scale bar:

100 µm). Graphical representation of mean percentage of hypertrophic chondrocytes for different size categories (expressed in μm^2) inside the condylar cartilage of *Fgfr3*$^{+/+}$ (n=5) and *Fgfr3*$^{N534K/+}$ (n=6) at P21 (n>50 cells for each genotype).

Figure 2. *Fgfr3*$^{N534K/+}$ mutation leads to defective endochondral mandibular bone repair of the mandible and pseudarthrosis

A – Images of the submandibular cutaneous approach of the mandibular ascending branch. X-Rays of the skull of a P42 *Fgfr3*$^{+/+}$ mouse (sagittal view) showing the direction of the non-stabilized mandibular fracture, from the basilar border to the coronoid notch (⋆).

B – Schematic representation of bone repair analysis following fracture performed at Day 0 (D0), key points of endochondral bone repair, Day 7 (D7), Day (10) (soft callus), Day 14 (D14) (transition between soft and bone callus), Day 21 (D21), and Day 28 (D28) (bone callus).

C – Representative *Fgfr3*$^{+/+}$ and *Fgfr3*$^{N534K/+}$ coronal views (3D reconstructions from µCT scans) of the mandibular fracture site (white arrows) from D10 to D28, showing total bony bridging in *Fgfr3*$^{+/+}$ (D28), and consolidation defect without bone callus (⋆) in *Fgfr3*$^{N534K/+}$ mice (Day 28). Graphical representation of Bone Volume / Tissue Volume (BV/TV) of the calluses of *Fgfr3*$^{+/+}$ and *Fgfr3*$^{N534K/+}$ based on µCT images from Day 10 (D10) to Day 28 (D28) post fracture. Graphical representation of the callus volumes of *Fgfr3*$^{+/+}$ and *Fgfr3*$^{N534K/+}$ from Day 10 (D10) to Day 28 (D28) post fracture. D10, n=10 *Fgfr3*$^{+/+}$, n=8 *Fgfr3*$^{N534K/+}$; D14, n=10 *Fgfr3*$^{+/+}$, n=9 *Fgfr3*$^{N534K/+}$; D21, n=7 *Fgfr3*$^{+/+}$, n=9 *Fgfr3*$^{N534K/+}$; D28, n=12 *Fgfr3*$^{+/+}$, n=14 *Fgfr3*$^{N534K/+}$.

Graphical representation of cartilage volume evolution post-fracture from Day 7 (D7) to Day 28 (D28), based on histomorphometric analyses (Sirus Red / Alcian blue staining)$^{+}$: D7, n=6 *Fgfr3*$^{+/+}$, n=6 *Fgfr3*$^{N534K/+}$; D10, n=6 *Fgfr3*$^{+/+}$, n=6 *Fgfr3*$^{N534K/+}$; D14, n=8 *Fgfr3*$^{+/+}$, n=8 *Fgfr3*$^{N534K/+}$; D21, n=6 *Fgfr3*$^{+/+}$, n=6 *Fgfr3*$^{N534K/+}$; D28, n=10 *Fgfr3*$^{+/+}$, n=13 *Fgfr3*$^{N534K/+}$.

D – Representative *Fgfr3*$^{+/+}$ and *Fgfr3*$^{N534K/+}$ Sirus Red/Alcian Blue histological staining of the calluses at day 7 post-fracture (scale bar 200 µm). Higher magnification of the cartilage callus (blue) (scale bar: 200 µm). Sox9, Fgfr3, Collagen X immunohistological staining of cartilage callus of *Fgfr3*$^{+/+}$ and *Fgfr3*$^{N534K/+}$ (scale bar: 200 µm). Graphical representation of histomorphometric cartilage volume analyses at Day 7 post fracture based on Sirud n=6 *Fgfr3*$^{+/+}$, n=6 *Fgfr3*$^{N534K/+}$. C: cartilage, B: Bone callus.

E – Day 14 post-fracture. Representative *Fgfr3*$^{+/+}$ and *Fgfr3*$^{N534K/+}$ coronal views (3D reconstructions from µCT scans) of the mandibular fracture site showing the bone callus (white arrows). Representative *Fgfr3*$^{+/+}$ and *Fgfr3*$^{N534K/+}$ Sirus Red/Alcian Blue histological staining of the callus. Sox9, Fgfr3 and Collagen X immunohistological staining of cartilage callus of *Fgfr3*$^{+/+}$ and *Fgfr3*$^{N534K/+}$ (scale bar: 200 µm). Graphical representation of the ratio (%) between hypertrophic chondrocyte area (Collagen X staining) and chondrocyte area (collagen II) in *Fgfr3*$^{+/+}$ (n=8) and *Fgfr3*$^{N534K/+}$ (n=8) mice. Collagen X and collagen II stainings were performed on adjacent slides. Graphical representation of the mMean percentage of

hypertrophic chondrocytes for different size categories (expressed in μm^2) in the callus of *Fgfr3*$^{+/+}$ (n=7) and nt *Fgfr3*$^{N534K/+}$ (n=8) (n > 100 cells for each genotype). C: cartilage, B: Bone callus.

F – Representative images of of *Fgfr3*$^{+/+}$ and *Fgfr3*$^{N534K/+}$ TUNEL/DAPI staining in Collagen X positive chondrocytes area (hypertrophic cartilage) at day 14 post-fracture. Graphical representation (%) of the nNumber of TUNEL and DAPI positive cells in the callus of WT *Fgfr3*$^{+/+}$ (n=7) and mutant *Fgfr3*$^{N534K/+}$ (n=8) (scale bar: 100 µm).

G – Representative *Fgfr3*$^{+/+}$ and *Fgfr3*$^{N534K/+}$ Collagen I immunohistological staining (scale bar: 200 µm) at day 14 post-fracture. Graphical representation of of intertrabecular separation quantification in bone callus of *Fgfr3*$^{+/+}$ (n=7) and *Fgfr3*$^{N534K/+}$ (n=8).

Data shown as mean with SD; *P<0.05, **P < 0.01, ***P < 0.005.

H – Representative *Fgfr3*$^{+/+}$ and *Fgfr3*$^{N534K/+}$ coronal views (3D reconstructions from µCT scans) at day 28 post-fracture, showing total bony bridging in *Fgfr3*$^{+/+}$ and absence of bone consolidation in *Fgfr3*$^{N534K/+}$ mice (⋆). Graphical representation of consolidation grades: grade 1 - total bone union; grade 2 - bone union with mild bone defects; grade 3 - partial bone union with important bone defects; grade 4 - non-union. *Fgfr3*$^{+/+}$ (n=12), *Fgfr3*$^{N534K/+}$ (n=13). Representative images of *Fgfr3*$^{+/+}$ and *Fgfr3*$^{N534K/+}$ Sirus Red/Alcian Blue histological staining, without (above) and with polarization (below), vizualisation of fibrosis within the callus (pseudarthrosis) (scale bar: 100 µm). Graphical representation of pseudarthrosis in *Fgfr3*$^{+/+}$ (n=0/10) and *Fgfr3*$^{N534K/+}$ (n=6/13).

Figure 3. Spatial transcriptomic analysis of the cartilage of the calluses of *Fgfr3*$^{N534K/+}$ and *Fgfr3*$^{+/+}$ mice at 14 days post-fracture

A – Volcano plot and B – heatmap representation of the top deregulated (differential expression analysis, $P < 0.1$) genes that are either upregulated (red) or downregulated (blue) in *Fgfr3*$^{N534K/+}$ relative to *Fgfr3*$^{+/+}$ mice.

C – Violin plots showing the expression levels (normalized read counts) of *Col11, Col1a1, Dmp1, Phospho1, Hmgb2, Kif17* and *Dusp9* in *Fgfr3*$^{N534K/+}$ (red) and *Fgfr3*$^{+/+}$ mice (grey). The significance of the deregulation in *Fgfr3*$^{N534K/+}$ mice is indicated by the *P*-values shown on top.

Figure 4. Spatial transcriptomic analysis of the newly formed bone of the calluses of *Fgfr3*$^{N534K/+}$ and *Fgfr3*$^{+/+}$ mice at 14 days post-fracture

A – Volcano plot and B – heatmap representation of the top deregulated (differential expression analysis, $P < 0.1$) genes that are either upregulated (red) or downregulated (blue) in *Fgfr3*$^{N534K/+}$ relative to *Fgfr3*$^{+/+}$ mice.

C – Violin plots showing the expression levels (normalized read counts) of *Smad1, Comp, Birc2, Alkbh2, Dusp3* and *Socs3* in $Fgfr3^{N534K/+}$ (red) and $Fgfr3^{+/+}$ mice (grey). The significance of the deregulation in $Fgfr3^{N534K/+}$ mice is indicated by the *P*-values shown on top.

Figure 5. Defective bone repair and pseudarthrosis in $Fgfr3^{N534K/+}$ mice are rescued by BMN111 and BGJ398.

A – Representative $Fgfr3^{+/+}$ and $Fgfr3^{N534K/+}$ coronal views (3D reconstructions from µCT scans) at day 14 post-fracture. $Fgfr3^{+/+}$ + vehicle (n=10) $Fgfr3^{N534K/+}$ + vehicle, $Fgfr3^{N534K/+}$(n=9) + BMN111 (n=8) and $Fgfr3^{N534K/+}$ + BGJ398 (n=7). Graphical representation of Bone Volume / Tissue Volume (BV/TV) of the calluses of $Fgfr3^{+/+}$ and $Fgfr3^{N534K/+}$: $Fgfr3^{+/+}$ + vehicle (n=10), $Fgfr3^{N534K/+}$ + vehicle (n=9), $Fgfr3^{N534K/+}$ treated with BMN111 (n=8) and $Fgfr3^{N534K/+}$ treated with BGJ398 (n=7 each).

B – Day 14 post-fracture. Representative $Fgfr3^{+/+}$ and $Fgfr3^{N534K/+}$ Sirus Red/Alcian Blue histological staining at day 14 post-fracture. Representative $Fgfr3^{+/+}$ and $Fgfr3^{N534K/+}$ Sox9, Fgfr3, Collagen X, Collagen I and TUNEL/DAPI immunohistological labelling of the callus (scale bar: 200 µm). Graphical representation of the quantification of the ratio Collagen X positive / Collagen II positive chondrocyte, $Fgfr3^{+/+}$ + vehicle (n=8), $Fgfr3^{N534K/+}$ + vehicle (n=8) $Fgfr3^{N534K/+}$ + BMN111 and $Fgfr3^{N534K/+}$ + BGJ398 (n=7, each).

Graphical representation of TUNEL and DAPI positive cells in the hypertrophic chondrocyte area of the callus (%) $Fgfr3^{+/+}$ + vehicle (n=7), $Fgfr3^{N534K/+}$ + vehicle (n=8), $Fgfr3^{N534K/+}$ + BMN111 and (n=8) and $Fgfr3^{N534K/+}$ + BGJ398 (n=7). Graphical representation of the ratio intertrabecular area / total bone callus area ratio (based on collagen I staining), $Fgfr3^{+/+}$+ vehicle (n=6) $Fgfr3^{N534K/+}$ + vehicle (n=8), $Fgfr3^{N534K/+}$ + BMN111 (n=7) and $Fgfr3^{N534K/+}$ + BGJ398 (n=7). ns: non-significant, *P<0.05, **P < 0.01, ***P < 0.005.

C – Day 28 post-fracture. Representative coronal (3D reconstructions from µCT scans) at day 28 post-fracture showing the mandibular fracture site of $Fgfr3^{+/+}$ + vehicle, $Fgfr3^{N534K/+}$ + vehicle, $Fgfr3^{N534K/+}$ + BMN111 and $Fgfr3^{N534K/+}$ + BGJ398 mice.

Graphical representation of Bone Volume / Tissue Volume (BV/TV) of the calluses of $Fgfr3^{+/+}$ and $Fgfr3^{N534K/+}$: n=12 $Fgfr3^{+/+}$ + vehicle, n=14 $Fgfr3^{N534K/+}$ + vehicle, n=9 $Fgfr3^{N534K/+}$ treated with BMN111 and n=10 $Fgfr3^{N534K/+}$ treated with BGJ398. Graphical representation of consolidation grades after 28 days (grade 1: total bone union; grade 2: bone union with mild bone defects; grade 3: partial bone union with important bone defects; grade 4: non-union). $Fgfr3^{+/+}$ + vehicle (n=12), $Fgfr3^{N534K/+}$ + vehicle (n=14), $Fgfr3^{N534K/+}$ + BMN111 (n=9) $Fgfr3^{N534K/+}$ + BGJ398 (n=10) (28 days of treatments for each group).

D – Representative $Fgfr3^{+/+}$ and $Fgfr3^{N534K/+}$ TRAP labelling of the callus TRAP at day 28 post-fracture (scale bar: 100 µm). Graphical representation of the osteoclast number (nb osteoclasts/mm): $Fgfr3^{+/+}$+ vehicle (n=6), $Fgfr3^{N534K/+}$ + vehicle (n=6), $Fgfr3^{N534K/+}$ + BMN111 (n=7) and $Fgfr3^{N534K/+}$ + BGJ398 (n=6). ns: non-significant, *P<0.05, **P < 0.01, ***P < 0.005, ****P<0.0005.

Supplemental data

Supplemental File 1: Skull and mandibular landmarks.

Supplemental Figure 1: Representative PCNA labelling of Meckel's cartilage (MC) at E13.5 (scale bar: 100 µm) of MC in *Fgfr3*$^{+/+}$ and *Fgfr3*$^{N534K/+}$ mice. PCNA quantification. ns: non-significant.

Supplemental Figure 2: Representative PCNA labelling of callus cartilage (MC) at day 7 post-fracture in *Fgfr3*$^{+/+}$ and *Fgfr3*$^{N534K/+}$ mice (scale bar: 100 µm). PCNA quantification. ns: non-significant

Supplemental Figure 3: Representative Collagen type II and VEGF labelling of callus cartilage (MC) at day 14 post fracture of *Fgfr3*$^{+/+}$ and *Fgfr3*$^{N534K/+}$ mice (scale bar: 200 µm).

Supplemental Figure 4: Spatial transcriptomic analyses using GeoMx Mouse Whole Transcriptome Atlas probes. (A) Sequential process for spatial transcriptomic analyses using GeoMx Mouse Whole Transcriptome Atlas probes. (B) Following FFPE mouse sample preparation (see Methods), a cocktail of GeoMx Mouse Whole Transcriptome Atlas probes (targeting over 19,000 genes) was applied to each slide and allowed to hybridize. The following day, slides were washed, blocked, and allowed to incubate with a combination of Alexa Fluor 594 Anti-alpha smooth muscle Actin antibody (Abcam antibody ab202368; clone: 1A4) and Syto83 nucleic acid stain (1). Slides were then washed and loaded onto the GeoMx instrument. On the GeoMx machine, slides were fluorescently scanned, and ROIs were manually placed in the following areas of the callus: newly formed bone and cartilage (2). The GeoMx device exposed ROIs to 385 nm light (UV), releasing the indexing oligos (3). Indexing oligos were collected with a microcapillary and deposited into a 96-well plate and PCR was performed (4 and 5).

(B) Principal Components Analysis (PCA) of transcriptome-wide normalized gene counts for bone and cartilage ROIs. All retained ROIs after quality control filtering are represented, with each unique symbol and color pair indicating genotype and sample type (bone or cartilage), respectively. 27 ROIs and 18,125 genes have been analyzed, representing 4 mutants (H = *Fgfr3*$^{N534K/+)}$ and 4 controls (*WT* = *Fgfr3*$^{+/+}$).

Supplemental Figure 5: Violin plots showing the expression levels (normalized read counts), in *Fgfr3*$^{N534K/+}$ and *Fgfr3*$^{+/+}$ mice, of specific cartilage (A: *Col2a1, Col10a1, Ihh (Indian Hedgehog), Sox9, Mapk3, Pth (Parathormone), Bglap*) and bone markers (B: *Col1a1, Sp7 (Osx), Runx2, Alpl (Alkaline Phosphatase), Spp1 (Osteopontin), Tnfrsf11a (Rank)*).

Supplemental Figure 6: Gene set enrichment analysis based on functional annotation (Gene Ontology – Biological Process pathways) of genes deregulated in (A) cartilage or (B) bone samples from *Fgfr3*$^{N534K/+}$ mice. Dot size represents the number of significantly deregulated (left up- or right down-regulated) genes found in a given pathway. The color scale indicates the significance of the enrichment (hypergeometric tests, adjusted *P*-values).

Supplemental Figure 7: Representative VEGF labelling of callus cartilage (MC) at day 14 post fracture in *Fgfr3*$^{+/+}$ and *Fgfr3*$^{N534K/+}$ (+ vehicle, + BMN111, + BGJ398) mice (scale bar: 200 µm).

Supplemental Figure 8: 3D reconstructions from µCT scans of the skull and the mandible of a P42 wild-type mouse, showing positions of skull and mandibular landmarks used for morphometric geometrics analyses.

Figure 1. The hypochondroplasia mouse model, *Fgfr3*$^{N534K/+}$ exhibits craniofacial and mandibular shape anomalies

A – Meckel's cartilage (MC) at E13.5: Representative *Fgfr3*$^{+/+}$ and *Fgfr3*$^{N534K/+}$ Sirus red/Alcian blue histological staining of MC (scale bar 200 µm), Sox 9 and FGFR3 immunostaining of MC *Fgfr3*$^{+/+}$ and *Fgfr3*$^{N534K/+}$ (scale bar 100 µm). Measurement of MC area (alcian blue staining) in *Fgfr3*$^{+/+}$ (n=6) and *Fgfr3*$^{N534K/+}$ (n=5) . Graphical representation of Sox9 staining density in MC in *Fgfr3*$^{+/+}$ (n=6) and *Fgfr3*$^{N534K/+}$ (n=5).

B – Meckel's cartilage (MC) at E16.5: Representative *Fgfr3*$^{+/+}$ and *Fgfr3*$^{N534K/+}$ Safranin O/Fast Green histological staining (scale bar 200 µm), Sox 9, Collagen X and Fgfr3 immunohistological staining of MC of *Fgfr3*$^{+/+}$ and *Fgfr3*$^{N534K/+}$ (scale bar 200 µm). Graphical representation of MC area (Safranin O staining) in *Fgfr3*$^{+/+}$ (n=7) and *Fgfr3*$^{N534K/+}$ (n=7). Graphical representation of the ratio hypertrophic area (Collagen X staining) / total MC cartilage area (%) (Safranin O staining) of *Fgfr3*$^{+/+}$ (n=7) and *Fgfr3*$^{N534K/+}$ (n=7) .

C – Representative *Fgfr3*$^{+/+}$ and *Fgfr3*$^{N534K/+}$ skull bone µCT images from P42 mice in transversal orientations (scale bar 3 mm). Graphical representation of naso anal length (mm) , mandibular length (mm), mandibular ramus length (mm), and skull width (mm) of *Fgfr3*$^{+/+}$ (n=7) and *Fgfr3*$^{N534K/+}$ (n=7).

D – 3D representations showing landmarks and associated wireframes variations of skull and mandibular shapes *Fgfr3*$^{+/+}$ and *Fgfr3*$^{N534K/+}$ of P42 mice using PC analysis. Comparison of skull and mandibular shape (Skull: Procrustes distance d=0,1094; $p<0.001$; Mandible: Procrustes distance d=0,0846; $p<0.001$) between *Fgfr3*$^{+/+}$ and *Fgfr3*$^{N534K/+}$ mice: plots of Principal Components (PC) scores for PC1 and PC2 (n=7 mice for each genotype). *P<0.05, **P < 0.01, ***P < 0.005.

E – Representative *Fgfr3*$^{+/+}$ and *Fgfr3*$^{N534K/+}$ Safranin O/Fast Green histological staining and Collagen X immunohistological staining of MC of *Fgfr3*$^{+/+}$ and *Fgfr3*$^{N534K/+}$ at P21 (scale bar: 100 µm). Graphical representation of mean percentage of hypertrophic chondrocytes for different size categories (expressed in μm^2) inside the condylar cartilage of *Fgfr3*$^{+/+}$ (n=5) and *Fgfr3*$^{N534K/+}$ (n=6) at P21 (n>50 cells for each genotype).

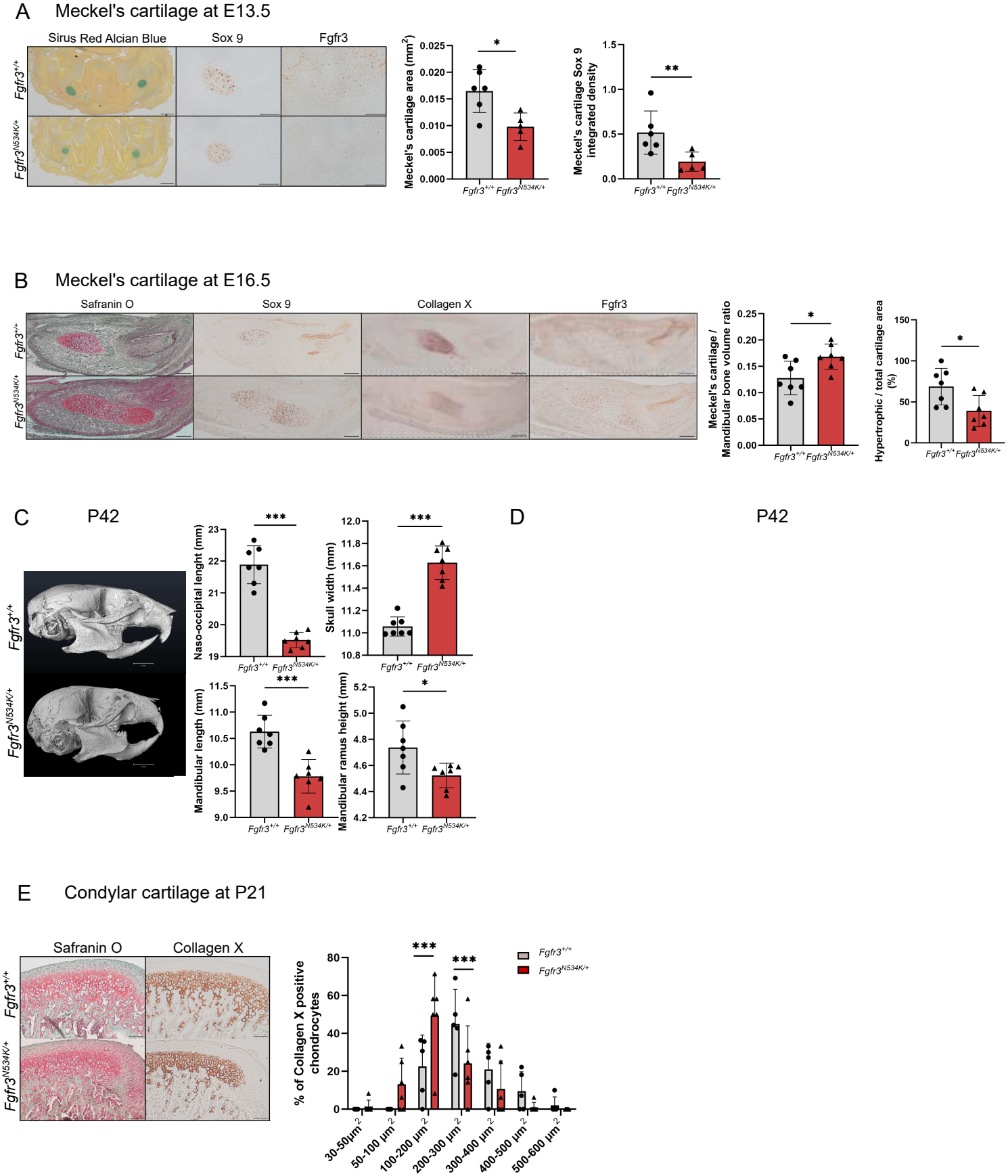
A
Meckel's cartilage at E13.5
Sirus Red Alcian Blue
Sox 9
Fgfr3
Fgfr3+/+
Fgfr3N534K/+
Meckel's cartilage area (mm2)
Meckel's cartilage Sox 9 integrated density
B
Meckel's cartilage at E16.5
Safranin O
Sox 9
Collagen X
Fgfr3
Meckel's cartilage / Mandibular bone volume ratio
Hypertrophic / total cartilage area (%)
C
P42
Naso-occipital lenght (mm)
Skull width (mm)
Mandibular length (mm)
Mandibular ramus height (mm)
D
P42
E
Condylar cartilage at P21
Safranin O
Collagen X
% of Collagen X positive chondrocytes
30-50µm2
50-100 µm2
100-200 µm2
200-300 µm2
300-400 µm2
400-500 µm2
500-600 µm2

Figure 2. *Fgfr3*$^{N534K/+}$ mutation leads to defective endochondral mandibular bone repair of the mandible and pseudarthrosis

A – Images of the submandibular cutaneous approach of the mandibular ascending branch. X-Rays of the skull of a P42 *Fgfr3*$^{+/+}$ mouse (sagittal view) showing the direction of the non-stabilized mandibular fracture, from the basilar border to the coronoid notch (⋆).

B – Schematic representation of bone repair analysis following fracture performed at Day 0 (D0), key points of endochondral bone repair, Day 7 (D7), Day (10) (soft callus), Day 14 (D14) (transition between soft and bone callus), Day 21 (D21), and Day 28 (D28) (bone callus).

C – Representative *Fgfr3*$^{+/+}$ and *Fgfr3*$^{N534K/+}$ coronal views (3D reconstructions from µCT scans) of the mandibular fracture site (white arrows) from D10 to D28, showing total bony bridging in *Fgfr3*$^{+/+}$ (D28), and consolidation defect without bone callus (⋆) in *Fgfr3*$^{N534K/+}$ mice (Day 28). Graphical representation of Bone Volume / Tissue Volume (BV/TV) of the calluses of *Fgfr3*$^{+/+}$ and *Fgfr3*$^{N534K/+}$ based on µCT images from Day 10 (D10) to Day 28 (D28) post fracture. Graphical representation of the callus volumes of *Fgfr3*$^{+/+}$ and *Fgfr3*$^{N534K/+}$ from Day 10 (D10) to Day 28 (D28) post fracture. D10, n=10 *Fgfr3*$^{+/+}$, n=8 *Fgfr3*$^{N534K/+}$; D14, n=10 *Fgfr3*$^{+/+}$, n=9 *Fgfr3*$^{N534K/+}$; D21, n=7 *Fgfr3*$^{+/+}$, n=9 *Fgfr3*$^{N534K/+}$; D28, n=12 *Fgfr3*$^{+/+}$, n=14 *Fgfr3*$^{N534K/+}$.

Graphical representation of cartilage volume evolution post-fracture from Day 7 (D7) to Day 28 (D28), based on histomorphometric analyses (Sirus Red / Alcian blue staining)$^{+}$: D7, n=6 *Fgfr3*$^{+/+}$, n=6 *Fgfr3*$^{N534K/+}$; D10, n=6 *Fgfr3*$^{+/+}$, n=6 *Fgfr3*$^{N534K/+}$; D14, n=8 *Fgfr3*$^{+/+}$, n=8 *Fgfr3*$^{N534K/+}$; D21, n=6 *Fgfr3*$^{+/+}$, n=6 *Fgfr3*$^{N534K/+}$; D28, n=10 *Fgfr3*$^{+/+}$, n=13 *Fgfr3*$^{N534K/+}$.

D – Representative *Fgfr3*$^{+/+}$ and *Fgfr3*$^{N534K/+}$ Sirus Red/Alcian Blue histological staining of the calluses at day 7 post-fracture (scale bar 200 µm). Higher magnification of the cartilage callus (blue) (scale bar: 200 µm). Sox9, Fgfr3, Collagen X immunohistological staining of cartilage callus of *Fgfr3*$^{+/+}$ and *Fgfr3*$^{N534K/+}$ (scale bar: 200 µm). Graphical representation of histomorphometric cartilage volume analyses at Day 7 post fracture based on Sirud n=6 *Fgfr3*$^{+/+}$, n=6 *Fgfr3*$^{N534K/+}$. C: cartilage, B: Bone callus.

E – Day 14 post-fracture. Representative *Fgfr3*$^{+/+}$ and *Fgfr3*$^{N534K/+}$ coronal views (3D reconstructions from µCT scans) of the mandibular fracture site showing the bone callus (white arrows). Representative *Fgfr3*$^{+/+}$ and *Fgfr3*$^{N534K/+}$ Sirus Red/Alcian Blue histological staining of the callus. Sox9, Fgfr3 and Collagen X immunohistological staining of cartilage callus of *Fgfr3*$^{+/+}$ and *Fgfr3*$^{N534K/+}$ (scale bar: 200 µm). Graphical representation of the ratio (%) between hypertrophic chondrocyte area (Collagen X staining) and chondrocyte area (collagen II) in *Fgfr3*$^{+/+}$ (n=8) and *Fgfr3*$^{N534K/+}$ (n=8) mice. Collagen X and collagen II stainings were performed on adjacent slides. Graphical representation of the mMean percentage of hypertrophic chondrocytes for different size categories (expressed in µm^2) in the callus of *Fgfr3*$^{+/+}$ (n=7) and nt *Fgfr3*$^{N534K/+}$ (n=8) (n > 100 cells for each genotype). C: cartilage, B: Bone callus.

F – Representative images of of *Fgfr3*$^{+/+}$ and *Fgfr3*$^{N534K/+}$ TUNEL/DAPI staining in Collagen X positive chondrocytes area (hypertrophic cartilage) at day 14 post-fracture. Graphical representation (%) of the nNumber of TUNEL and DAPI positive cells in the callus of WT *Fgfr3*$^{+/+}$ (n=7) and mutant *Fgfr3*$^{N534K/+}$ (n=8) (scale bar: 100 µm).

G – Representative *Fgfr3*$^{+/+}$ and *Fgfr3*$^{N534K/+}$ Collagen I immunohistological staining (scale bar: 200 µm) at day 14 post-fracture. Graphical representation of of intertrabecular separation quantification in bone callus of *Fgfr3*$^{+/+}$ (n=7) and *Fgfr3*$^{N534K/+}$ (n=8).

Data shown as mean with SD; *P<0.05, **P < 0.01, ***P < 0.005.

H – Representative *Fgfr3*$^{+/+}$ and *Fgfr3*$^{N534K/+}$ coronal views (3D reconstructions from µCT scans) at day 28 post-fracture, showing total bony bridging in *Fgfr3*$^{+/+}$ and absence of bone consolidation in *Fgfr3*$^{N534K/+}$ mice (⋆). Graphical representation of consolidation grades: grade 1 - total bone union; grade 2 - bone union with mild bone defects; grade 3 - partial bone union with important bone defects; grade 4 - non-union. *Fgfr3*$^{+/+}$ (n=12), *Fgfr3*$^{N534K/+}$ (n=13). Representative images of *Fgfr3*$^{+/+}$ and *Fgfr3*$^{N534K/+}$ Sirus Red/Alcian Blue histological staining, without (above) and with polarization (below), vizualisation of fibrosis within the callus (pseudarthrosis) (scale bar: 100 µm). Graphical representation of pseudarthrosis in *Fgfr3*$^{+/+}$ (n=0/10) and *Fgfr3*$^{N534K/+}$ (n=6/13).

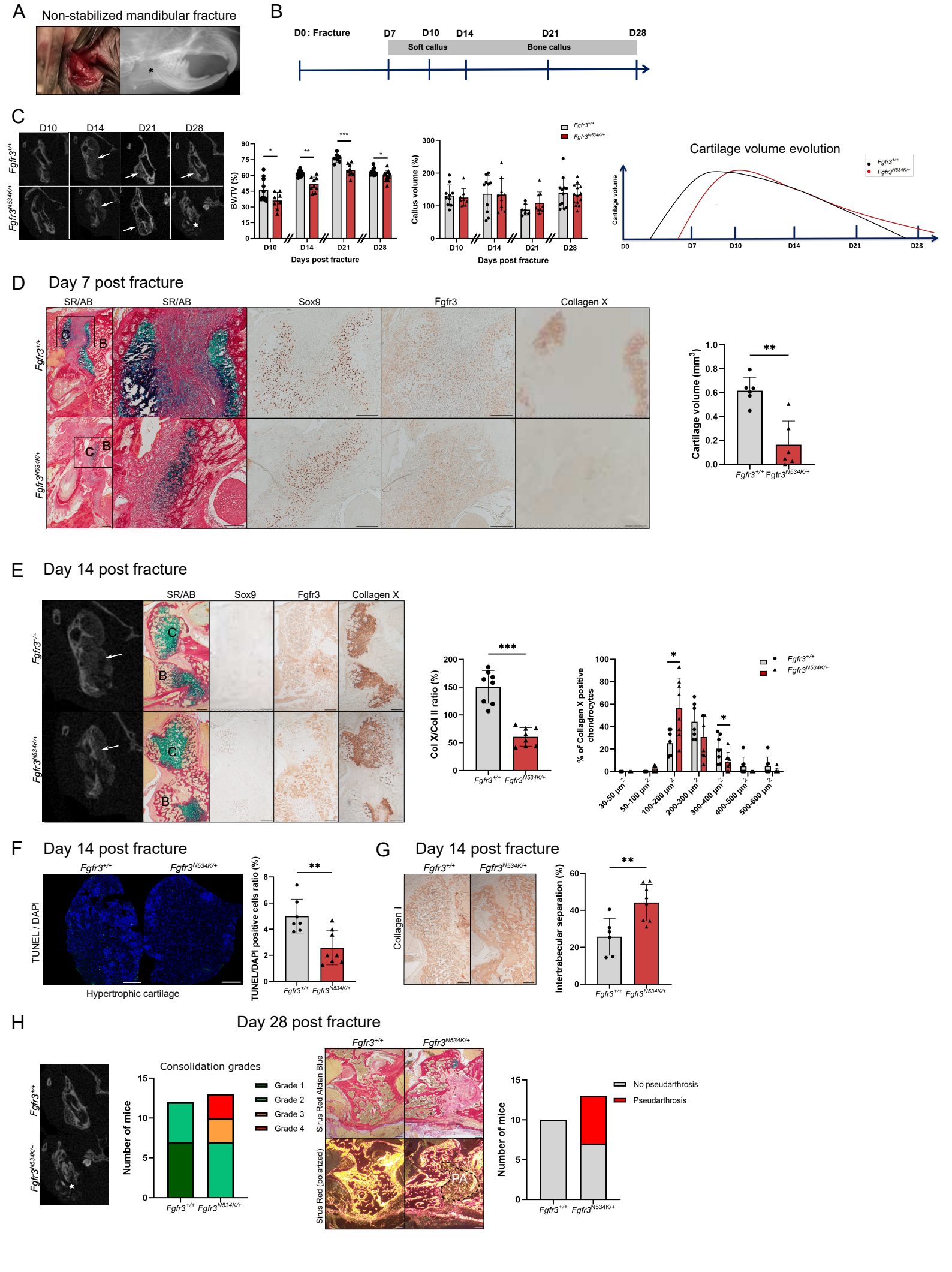
A
Non-stabilized mandibular fracture
B
D0 : Fracture
D7
D10
D14
D21
D28
Soft callus
Bone callus
C
D10
D14
D21
D28
Fgfr3+/+
Fgfr3N534K/+
BV/TV (%)
Days post fracture
Callus volume (%)
Days post fracture
Cartilage volume evolution
Cartilage volume
D
Day 7 post fracture
SR/AB
SR/AB
Sox9
Fgfr3
Collagen X
Cartilage volume (mm3)
E
Day 14 post fracture
SR/AB
Sox9
Fgfr3
Collagen X
Col X/Col II ratio (%)
% of Collagen X positive chondrocytes
30-50 µm2
50-100 µm2
100-200 µm2
200-300 µm2
300-400 µm2
400-500 µm2
500-600 µm2
F
Day 14 post fracture
TUNEL / DAPI
Hypertrophic cartilage
TUNEL/DAPI positive cells ratio (%)
G
Day 14 post fracture
Collagen I
Intertrabecular separation (%)
H
Day 28 post fracture
Consolidation grades
Number of mice
Grade 1
Grade 2
Grade 3
Grade 4
Sirus Red Alcian Blue
Sirus Red (polarized)
PA
No pseudarthrosis
Pseudarthrosis

Figure 3. Spatial transcriptomic analysis of the cartilage of the calluses of *Fgfr3*$^{N534K/+}$ and *Fgfr3*$^{+/+}$ mice at 14 days post-fracture

A – Volcano plot and B – heatmap representation of the top deregulated (differential expression analysis, $P < 0.1$) genes that are either upregulated (red) or downregulated (blue) in *Fgfr3*$^{N534K/+}$ relative to *Fgfr3*$^{+/+}$ mice.

C – Violin plots showing the expression levels (normalized read counts) of *Col11, Col1a1, Dmp1, Phospho1, Hmgb2, Kif17* and *Dusp9* in *Fgfr3*$^{N534K/+}$ (red) and *Fgfr3*$^{+/+}$ mice (grey). The significance of the deregulation in *Fgfr3*$^{N534K/+}$ mice is indicated by the *P*-values shown on top.

A

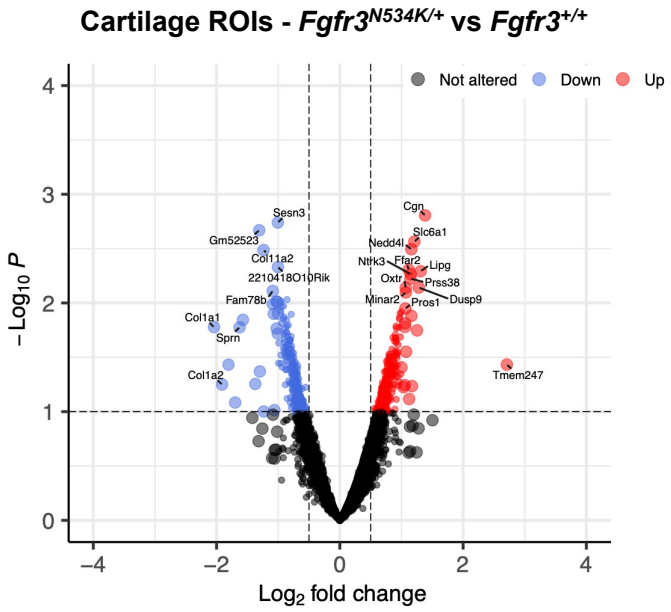
Cartilage ROIs - Fgfr3N534K/+ vs Fgfr3+/+
Not altered
Down
Up
−Log10 P
Log2 fold change
Sesn3
Gm52523
Col11a2
2210418O10Rik
Fam78b
Col1a1
Sprn
Col1a2
Cgn
Slc6a1
Nedd4l
Ntrk3
Ffar2
Lipg
Oxtr
Prss38
Minar2
Pros1
Dusp9
Tmem247

B

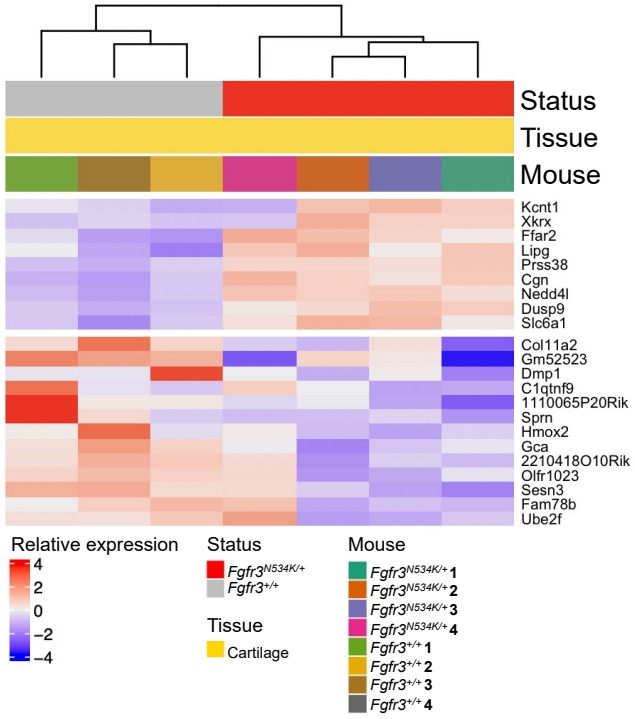
Status
Tissue
Mouse
Kcnt1
Xkrx
Ffar2
Lipg
Prss38
Cgn
Nedd4l
Dusp9
Slc6a1
Col11a2
Gm52523
Dmp1
C1qtnf9
1110065P20Rik
Sprn
Hmox2
Gca
2210418O10Rik
Olfr1023
Sesn3
Fam78b
Ube2f
Relative expression
Cartilage
Fgfr3+/+ 1
Fgfr3+/+ 2
Fgfr3+/+ 3
Fgfr3+/+ 4
Fgfr3N534K/+ 1
Fgfr3N534K/+ 2
Fgfr3N534K/+ 3
Fgfr3N534K/+ 4

C

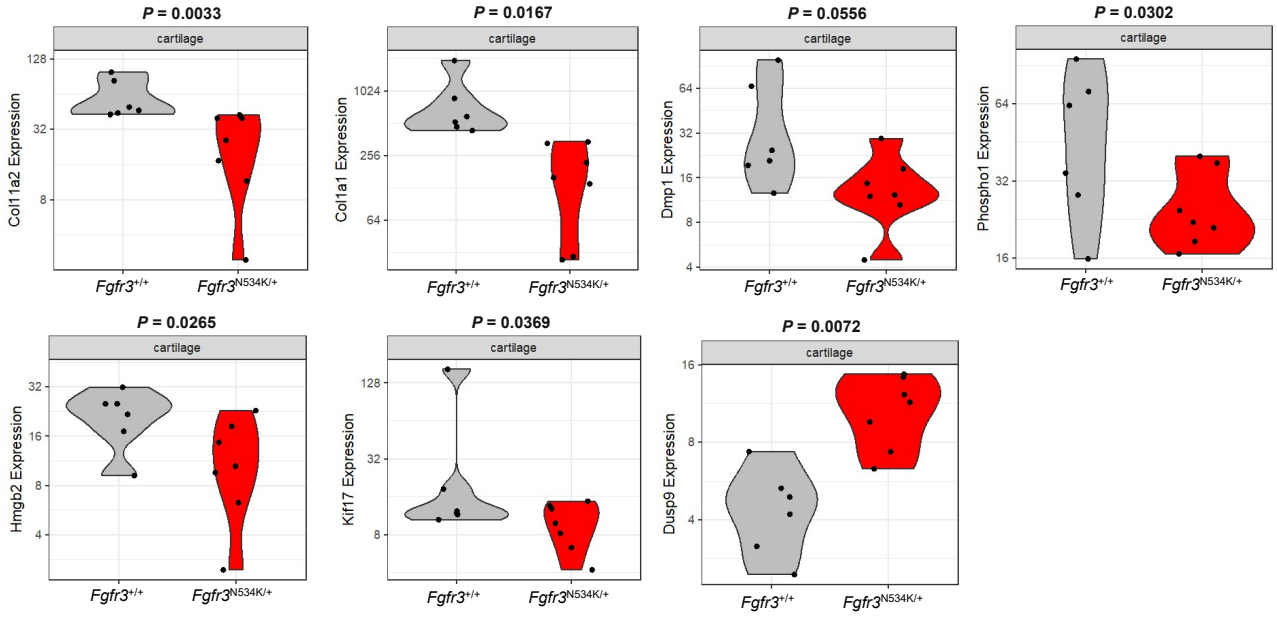
P = 0.0033
P = 0.0167
P = 0.0556
P = 0.0302
P = 0.0265
P = 0.0369
P = 0.0072
cartilage
Col11a2 Expression
Col1a1 Expression
Dmp1 Expression
Phospho1 Expression
Hmgb2 Expression
Kif17 Expression
Dusp9 Expression
Fgfr3+/+
Fgfr3N534K/+

Figure 4. Spatial transcriptomic analysis of the newly formed bone of the calluses of *Fgfr3*$^{N534K/+}$ and *Fgfr3*$^{+/+}$ mice at 14 days post-fracture

A – Volcano plot and B – heatmap representation of the top deregulated (differential expression analysis, $P < 0.1$) genes that are either upregulated (red) or downregulated (blue) in *Fgfr3*$^{N534K/+}$ relative to *Fgfr3*$^{+/+}$ mice.

C – Violin plots showing the expression levels (normalized read counts) of *Smad1, Comp, Birc2, Alkbh2, Dusp3* and *Socs3* in *Fgfr3*$^{N534K/+}$ (red) and *Fgfr3*$^{+/+}$ mice (grey). The significance of the deregulation in *Fgfr3*$^{N534K/+}$ mice is indicated by the *P*-values shown on top.

A

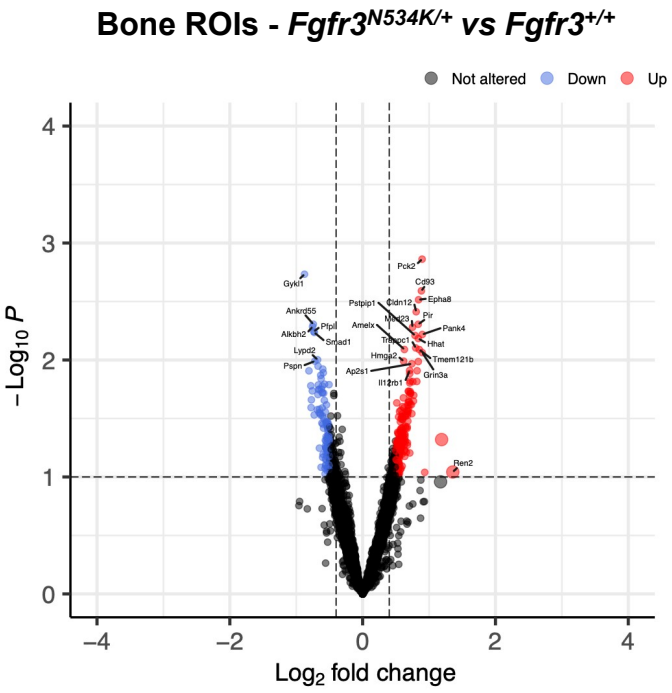
Bone ROIs - Fgfr3N534K/+ vs Fgfr3+/+
Not altered
Down
Up
−Log10 P
Log2 fold change
Pck2
Cd93
Epha8
Pir
Pank4
Hhat
Tmem121b
Grin3a
Ren2
Gykl1
Ankrd55
Ptpl1
Alkbh2
Smad1
Lypd2
Pspn
Pstpip1
Cldn12
Amelx
Mmp23
Tmem160
Hmgn2
Ap2s1
Il12rb1

B

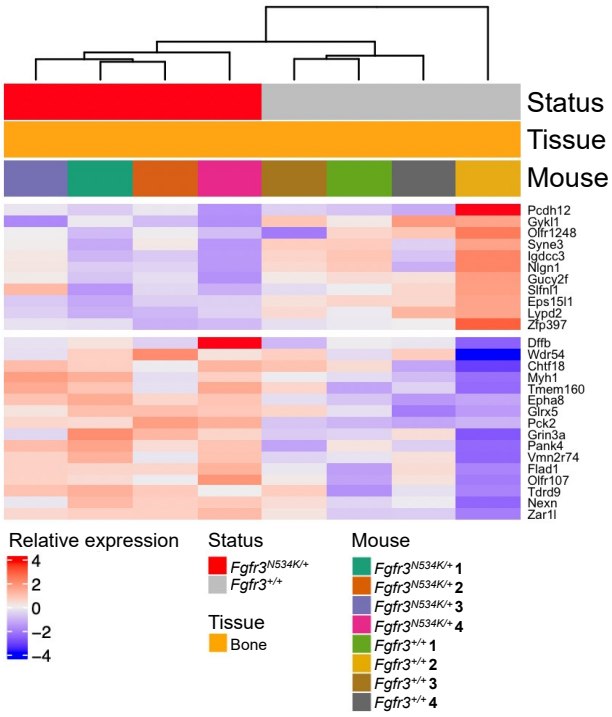
Status
Tissue
Mouse
Pcdh12
Gykl1
Olfr1248
Syne3
Igdcc3
Nlgn1
Gucy2f
Slfnl1
Eps15l1
Lypd2
Zfp397
Dffb
Wdr54
Chtf18
Myh1
Tmem160
Epha8
Glrx5
Pck2
Grin3a
Pank4
Vmn2r74
Flad1
Olfr107
Tdrd9
Nexn
Zar1l
Relative expression
4
2
0
−2
−4
Status
Fgfr3N534K/+
Fgfr3+/+
Tissue
Bone
Mouse
Fgfr3N534K/+ 1
Fgfr3N534K/+ 2
Fgfr3N534K/+ 3
Fgfr3N534K/+ 4
Fgfr3+/+ 1
Fgfr3+/+ 2
Fgfr3+/+ 3
Fgfr3+/+ 4

C

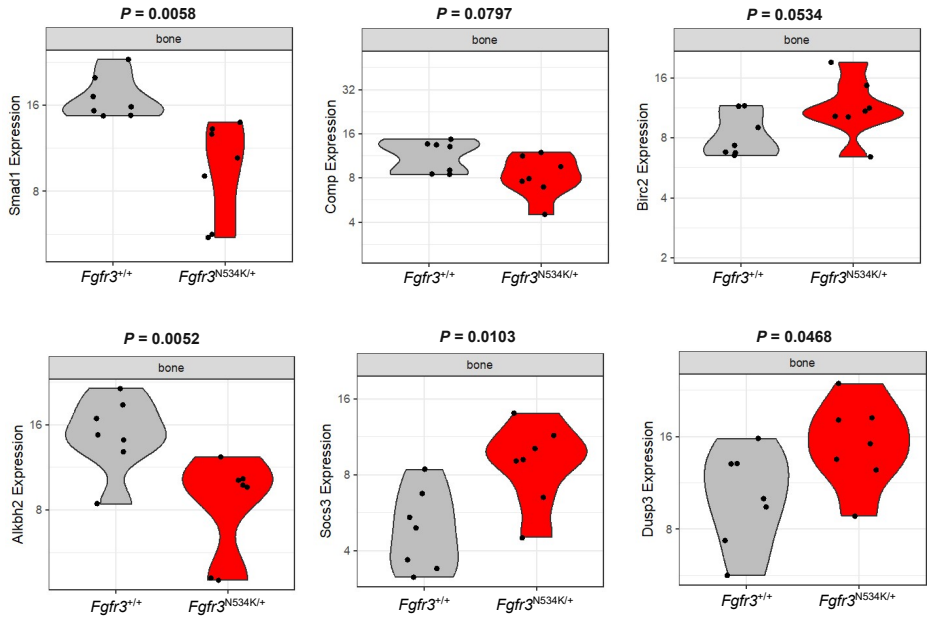
P = 0.0058
P = 0.0797
P = 0.0534
P = 0.0052
P = 0.0103
P = 0.0468
bone
Smad1 Expression
Comp Expression
Birc2 Expression
Alkbh2 Expression
Socs3 Expression
Dusp3 Expression
Fgfr3+/+
Fgfr3N534K/+

Figure 5. Defective bone repair and pseudarthrosis in *Fgfr3*$^{N534K/+}$ mice are rescued by BMN111 and BGJ398.

A – Representative *Fgfr3*$^{+/+}$ and *Fgfr3*$^{N534K/+}$ coronal views (3D reconstructions from µCT scans) at day 14 post-fracture. *Fgfr3*$^{+/+}$ + vehicle (n=10) *Fgfr3*$^{N534K/+}$ + vehicle, *Fgfr3*$^{N534K/+}$(n=9) + BMN111 (n=8) and *Fgfr3*$^{N534K/+}$ + BGJ398 (n=7). Graphical representation of Bone Volume / Tissue Volume (BV/TV) of the calluses of *Fgfr3*$^{+/+}$ and *Fgfr3*$^{N534K/+}$: *Fgfr3*$^{+/+}$ + vehicle (n=10), *Fgfr3*$^{N534K/+}$ + vehicle (n=9), *Fgfr3*$^{N534K/+}$ treated with BMN111 (n=8) and *Fgfr3*$^{N534K/+}$ treated with BGJ398 (n=7 each).

B – Day 14 post-fracture. Representative *Fgfr3*$^{+/+}$ and *Fgfr3*$^{N534K/+}$ Sirus Red/Alcian Blue histological staining at day 14 post-fracture. Representative *Fgfr3*$^{+/+}$ and *Fgfr3*$^{N534K/+}$ Sox9, Fgfr3, Collagen X, Collagen I and TUNEL/DAPI immunohistological labelling of the callus (scale bar: 200 µm). Graphical representation of the quantification of the ratio Collagen X positive / Collagen II positive chondrocyte, *Fgfr3*$^{+/+}$ + vehicle (n=8), *Fgfr3*$^{N534K/+}$ + vehicle (n=8) *Fgfr3*$^{N534K/+}$ + BMN111 and *Fgfr3*$^{N534K/+}$ + BGJ398 (n=7, each).

Graphical representation of TUNEL and DAPI positive cells in the hypertrophic chondrocyte area of the callus (%) *Fgfr3*$^{+/+}$ + vehicle (n=7), *Fgfr3*$^{N534K/+}$ + vehicle (n=8), *Fgfr3*$^{N534K/+}$ + BMN111 and (n=8) and *Fgfr3*$^{N534K/+}$ + BGJ398 (n=7). Graphical representation of the ratio intertrabecular area / total bone callus area ratio (based on collagen I staining), *Fgfr3*$^{+/+}$+ vehicle (n=6) *Fgfr3*$^{N534K/+}$ + vehicle (n=8), *Fgfr3*$^{N534K/+}$ + BMN111 (n=7) and *Fgfr3*$^{N534K/+}$ + BGJ398 (n=7). ns: non-significant, *P<0.05, **P < 0.01, ***P < 0.005.

C – Day 28 post-fracture. Representative coronal (3D reconstructions from µCT scans) at day 28 post-fracture showing the mandibular fracture site of *Fgfr3*$^{+/+}$ + vehicle, *Fgfr3*$^{N534K/+}$ + vehicle, *Fgfr3*$^{N534K/+}$ + BMN111 and *Fgfr3*$^{N534K/+}$ + BGJ398 mice.

Graphical representation of Bone Volume / Tissue Volume (BV/TV) of the calluses of *Fgfr3*$^{+/+}$ and *Fgfr3*$^{N534K/+}$: n=12 *Fgfr3*$^{+/+}$ + vehicle, n=14 *Fgfr3*$^{N534K/+}$ + vehicle, n=9 *Fgfr3*$^{N534K/+}$ treated with BMN111 and n=10 *Fgfr3*$^{N534K/+}$ treated with BGJ398. Graphical representation of consolidation grades after 28 days (grade 1: total bone union; grade 2: bone union with mild bone defects; grade 3: partial bone union with important bone defects; grade 4: non-union). *Fgfr3*$^{+/+}$ + vehicle (n=12), *Fgfr3*$^{N534K/+}$ + vehicle (n=14), *Fgfr3*$^{N534K/+}$ + BMN111 (n=9) *Fgfr3*$^{N534K/+}$ + BGJ398 (n=10) (28 days of treatments for each group).

D – Representative *Fgfr3*$^{+/+}$ and *Fgfr3*$^{N534K/+}$ TRAP labelling of the callus TRAP at day 28 post-fracture (scale bar: 100 µm). Graphical representation of the osteoclast number (nb osteoclasts/mm): *Fgfr3*$^{+/+}$+ vehicle (n=6), *Fgfr3*$^{N534K/+}$ + vehicle (n=6), *Fgfr3*$^{N534K/+}$ + BMN111 (n=7) and *Fgfr3*$^{N534K/+}$ + BGJ398 (n=6). ns: non-significant, *P<0.05, **P < 0.01, ***P < 0.005, ****P<0.0005.

A Day 14 post fracture

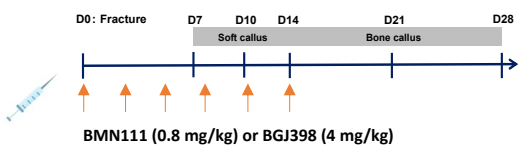

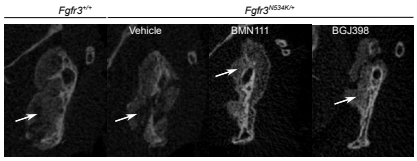

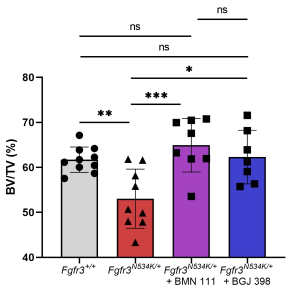

B Day 14 post fracture

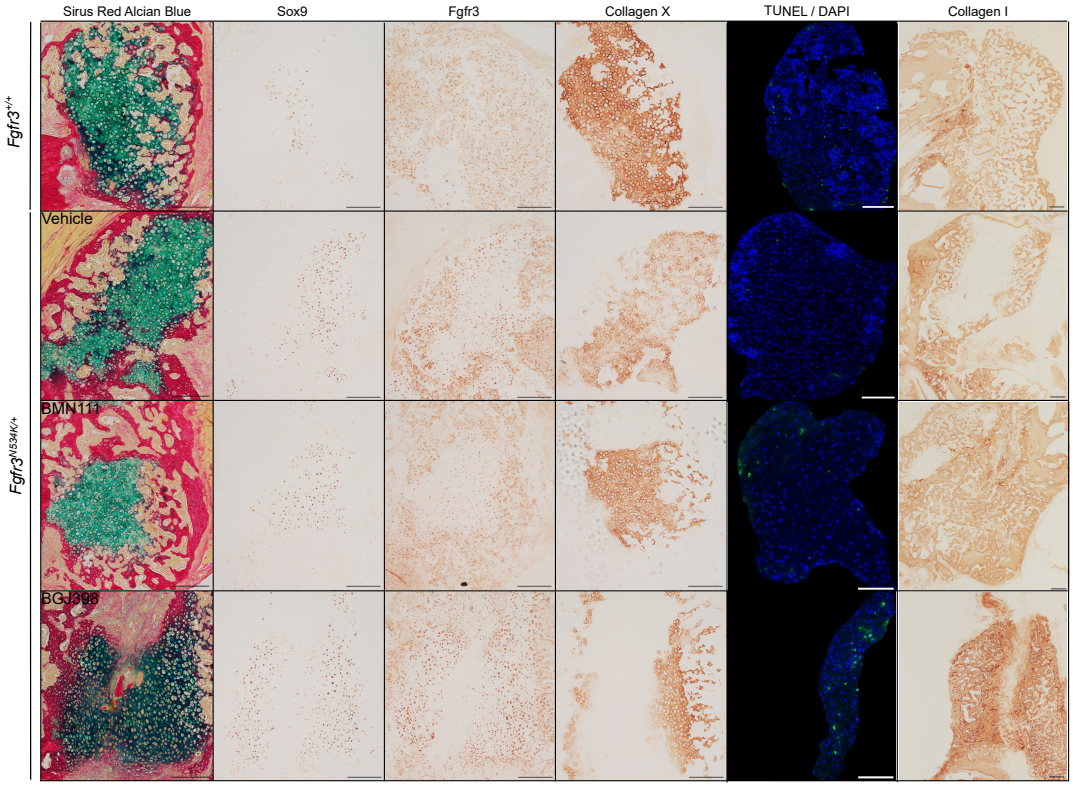

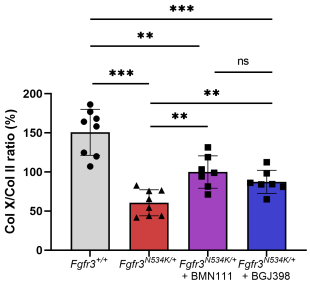

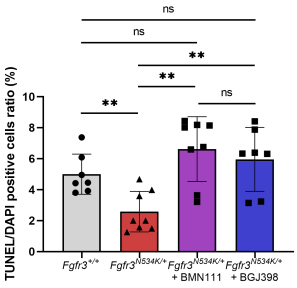

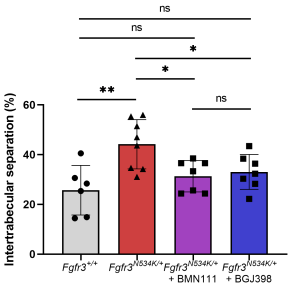

C Day 28 post fracture

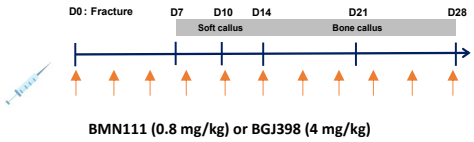

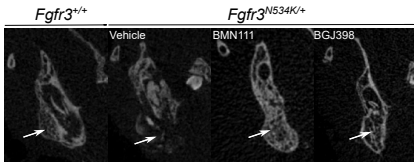

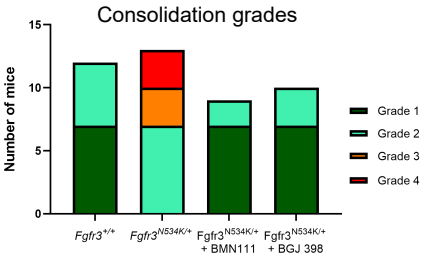

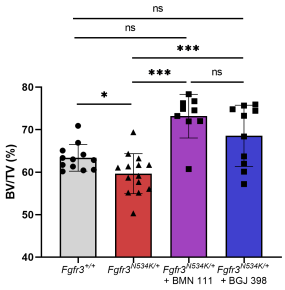

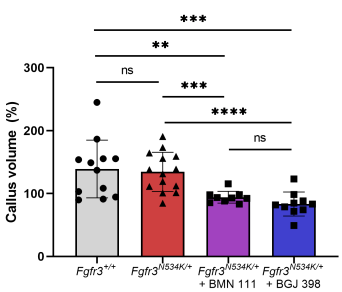

D Day 28 post fracture

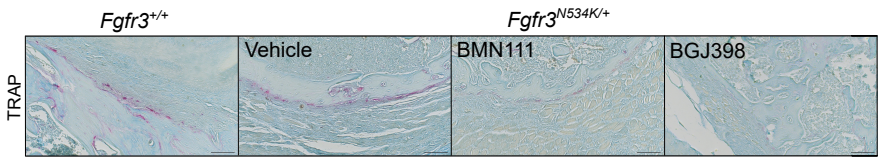

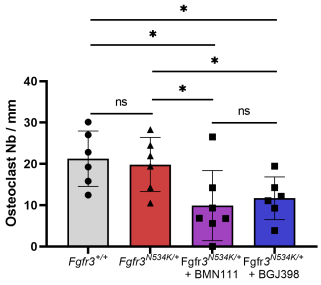

Supplemental File 1: Skull and mandibular landmarks.

Anatomical skull and mandibular landmarks: definition

Skull landmarks

1. Most anterior point on the ectocranial surface of the interparietal on the sagittal plane
2. Most medio-anterior point of the parietal (L)
3. Most medio-anterior point of the parietal (R)
4. Most postero-medial point of the nasal bone (L)
5. Most postero-medial point of the nasal bone (R)
6. Most postero-lateral point of the nasal bone (L)
7. Most postero-lateral point of the nasal bone (R)
8. Most antero-medial point of the nasal bone (L)
9. Most antero-medial point of the nasal bone (R)
10. Most supero-anterior point of the maxilla accounting for the lateral part of the nasal aperture (L)
11. Most supero-anterior point of the maxilla accounting for the lateral part of the nasal aperture (R)
12. Mid-point on the posterior margin of the foramen magnum, taken on squamous occipital
13. Mid-point on the anterior margin of the foramen magnum, taken on basioccipital (basisphenoid)
14. Most infero-lateral point on the squamous occipital (L)
15. Most infero-lateral point on the squamous occipital (R)
16. Most posterior point (midline) on the ectocranial surface of the interparietal
17. Most lateral point of the ectocranial surface of the interparietal (left)
18. Most lateral point of the ectocranial surface of the interparietal (right)
19. Most antero-lateral point on the corner of the basioccipital (L)
20. Most antero-lateral point on the corner of the basioccipital (R)
21. Most anterolateral point on the sphenoid (L)
22. Most anterolateral point on the sphenoid (R)
23. Most antero-medial point on the body of the presphenoid
24. Most lateral point of the junction between the posterior edge of the palatine plate and the pterygoid plate (L)
25. Most lateral point of the junction between the posterior edge of the palatine plate and the pterygoid plate (R)
26. Most posterior point of the anterior palatine foramen (L)
27. Most posterior point of the anterior palatine foramen (R)
28. Most anterior point of the anterior palatine foramen (L)
29. Most anterior point of the anterior palatine foramen (R)
30. Most infero-medial point of the premaxillary-maxillary suture, taken on premaxilla (L)
31. Most infero-medial point of the premaxillary-maxillary suture, taken on premaxilla (R)
32. Most lateral point on the margin of the premaxillary-maxillary suture, taken on premaxilla, at the midline (L)
33. Most lateral point on the margin of the premaxillary-maxillary suture, taken on premaxilla, at the midline (R)
34. Most inferior point of the infraorbital hiatus (L)
35. Most inferior point of the infraorbital hiatus (R)
36. Most distal point of the infraorbital hiatus (L)
37. Most distal point of the infraorbital hiatus (R)
38. Most superior point on the squamous temporal, intersection of the coronal suture (L)
39. Most superior point on the squamous temporal, intersection of the coronal suture (R)
40. Most lateral intersection of the frontal and parietal, taken on the frontal (L)
41. Most lateral intersection of the frontal and parietal, taken on the frontal (R)
42. Most superior point of the infraorbital hiatus (L)
43. Most superior point of the infraorbital hiatus (R)
44. Intersection of zygoma with zygomatic process of maxilla, taken on zygoma (L)
45. Intersection of zygoma with zygomatic process of maxilla, taken on zygoma (R)
46. Intersection of zygoma with zygomatic process of temporal, taken on zygoma (L)
47. Intersection of zygoma with zygomatic process of temporal, taken on zygoma (R)
48. Basis of the zygomatic process of the temporal (L)
49. Basis of the zygomatic process of the temporal (R)
50. Most posterior point on the posterior extension of the forming squamosal (L)
51. Most posterior point on the posterior extension of the forming squamosal (R)

Mandibular landmarks

1 Posterior tip of the mandibular condyle
2 Anterior tip of the mandibular condyle
3 Tip of the coronoid process
4 Greater concavity of the sigmoid notch
5 Tip of the mandibular angle
6 Greater concavity of the ramus
7 Masseter posterior insertion
8 Masseter anterior insertion
9 Anterior tip of the external oblique line
10 Most inferior point of the basilar contour (posterior)
11 Most inferior point of the basilar contour (anterior)
12 Most posterior point of the mandibular incisor on the inferior side
13 Tip of the mandibular incisor
14 Tip of the maxillary incisor
15 Most anterior point of the first mandibular molar
16 Most posterior point of the third mandibular molar
17 ➔ 29: Contralateral mandibular landmarks

Supplemental Figure 1: Representative PCNA labelling of Meckel's cartilage (MC) at E13.5 (scale bar: 100 µm) of MC in *Fgfr3*$^{+/+}$ and *Fgfr3*$^{N534K/+}$ mice. PCNA quantification. ns: non-significant.

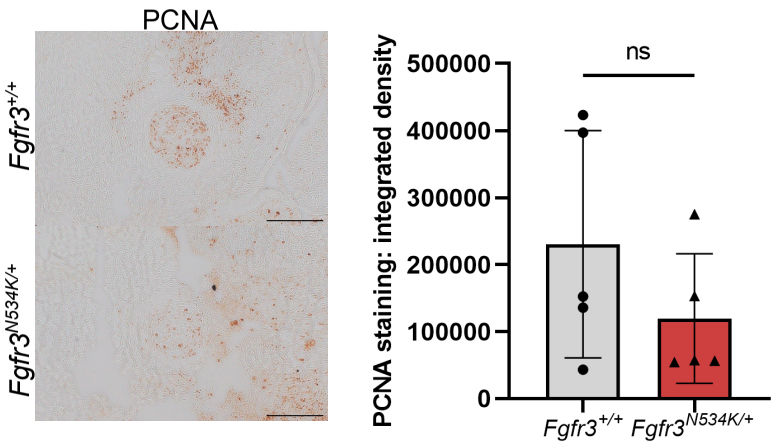
PCNA
Fgfr3+/+
Fgfr3N534K/+
PCNA staining: integrated density
500000
400000
300000
200000
100000
0
ns
Fgfr3+/+
Fgfr3N534K/+

Supplemental Figure 2: Representative PCNA labelling of callus cartilage (MC) at day 7 post-fracture in *Fgfr3*$^{+/+}$ and *Fgfr3*$^{N534K/+}$ mice (scale bar: 100 µm). PCNA quantification. ns: non-significant.

Day 7 post fracture

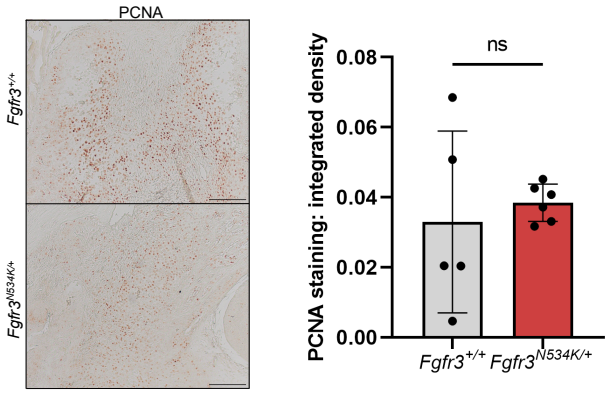

Supplemental Figure 3: Representative Collagen type II and VEGF labelling of callus cartilage (MC) at day 14 post fracture of *Fgfr3*$^{+/+}$ and *Fgfr3*$^{N534K/+}$ mice (scale bar: 200 µm).

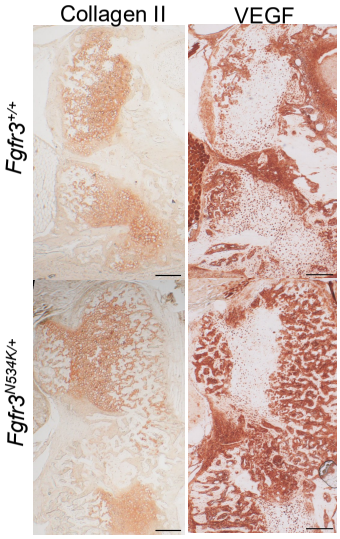
Collagen II
VEGF
Fgfr3+/+
Fgfr3N534K/+

Supplemental Figure 4: Spatial transcriptomic analyses using GeoMx Mouse Whole Transcriptome Atlas probes. (A) Sequential process for spatial transcriptomic analyses using GeoMx Mouse Whole Transcriptome Atlas probes. (B) Following FFPE mouse sample preparation (see Methods), a cocktail of GeoMx Mouse Whole Transcriptome Atlas probes (targeting over 19,000 genes) was applied to each slide and allowed to hybridize. The following day, slides were washed, blocked, and allowed to incubate with a combination of Alexa Fluor 594 Anti-alpha smooth muscle Actin antibody (Abcam antibody ab202368; clone: 1A4) and Syto83 nucleic acid stain (1). Slides were then washed and loaded onto the GeoMx instrument. On the GeoMx machine, slides were fluorescently scanned, and ROIs were manually placed in the following areas of the callus: newly formed bone and cartilage (2). The GeoMx device exposed ROIs to 385 nm light (UV), releasing the indexing oligos (3). Indexing oligos were collected with a microcapillary and deposited into a 96-well plate and PCR was performed (4 and 5).

(B) Principal Components Analysis (PCA) of transcriptome-wide normalized gene counts for bone and cartilage ROIs. All retained ROIs after quality control filtering are represented, with each unique symbol and color pair indicating genotype and sample type (bone or cartilage), respectively. 27 ROIs and 18,125 genes have been analyzed, representing 4 mutants (H = $Fgfr3^{N534K/+)}$ and 4 controls ($WT = Fgfr3^{+/+}$).

A

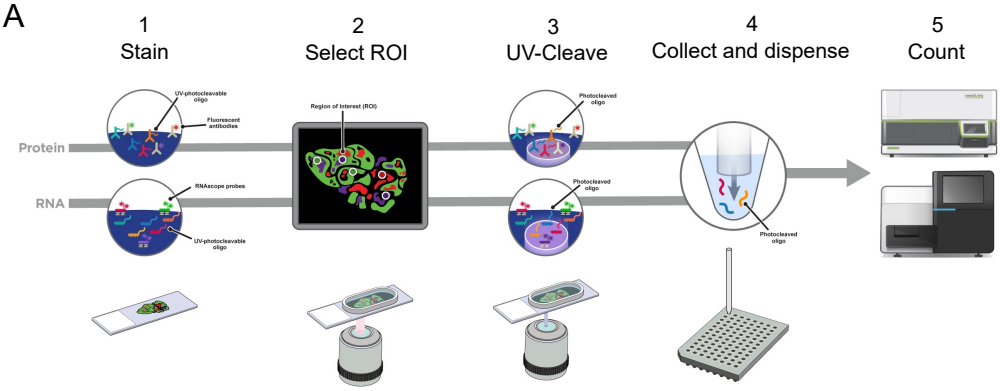
1
Stain
2
Select ROI
3
UV-Cleave
4
Collect and dispense
5
Count
Protein
RNA

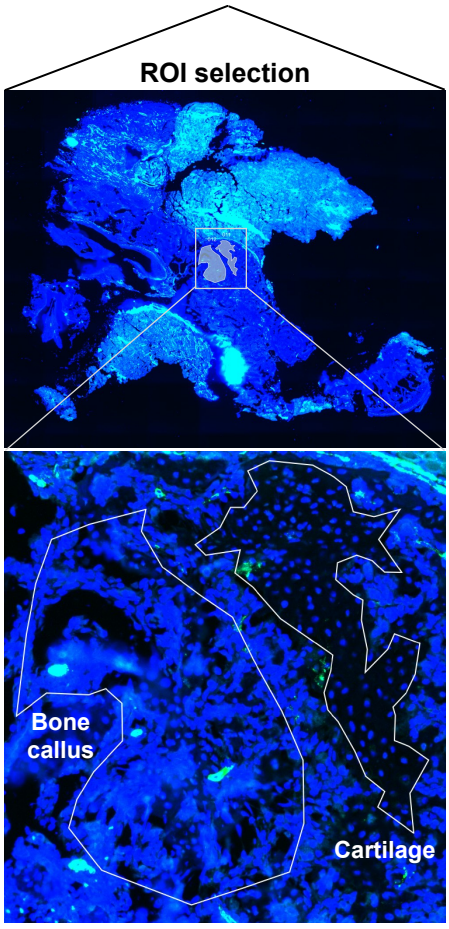
ROI selection
Bone callus
Cartilage

B

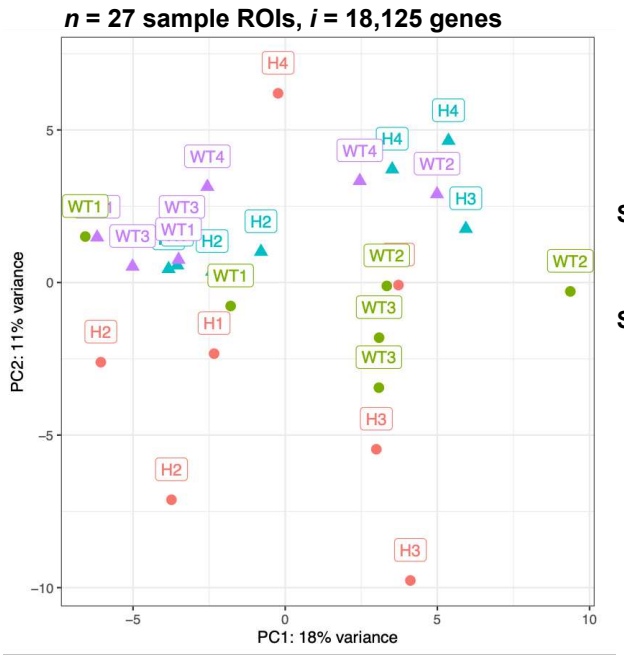
n = 27 sample ROIs, i = 18,125 genes
PC2: 11% variance
PC1: 18% variance
Segment
Cartilage
Bone
Status
Cartilage Fgfr3N534K/+
Cartilage Fgfr3+/+
Bone Fgfr3N534K/+
Bone Fgfr3+/+

Supplemental Figure 5: Violin plots showing the expression levels (normalized read counts), in *Fgfr3*$^{N534K/+}$ and *Fgfr3*$^{+/+}$ mice, of specific cartilage (A: *Col2a1, Col10a1, Ihh (Indian Hedgehog), Sox9, Mapk3, Pth (Parathormone), Bglap*) and bone markers (B: *Col1a1, Sp7 (Osx), Runx2, Alpl (Alkaline Phosphatase), Spp1 (Osteopontin), Tnfrsf11a (Rank)*).

A

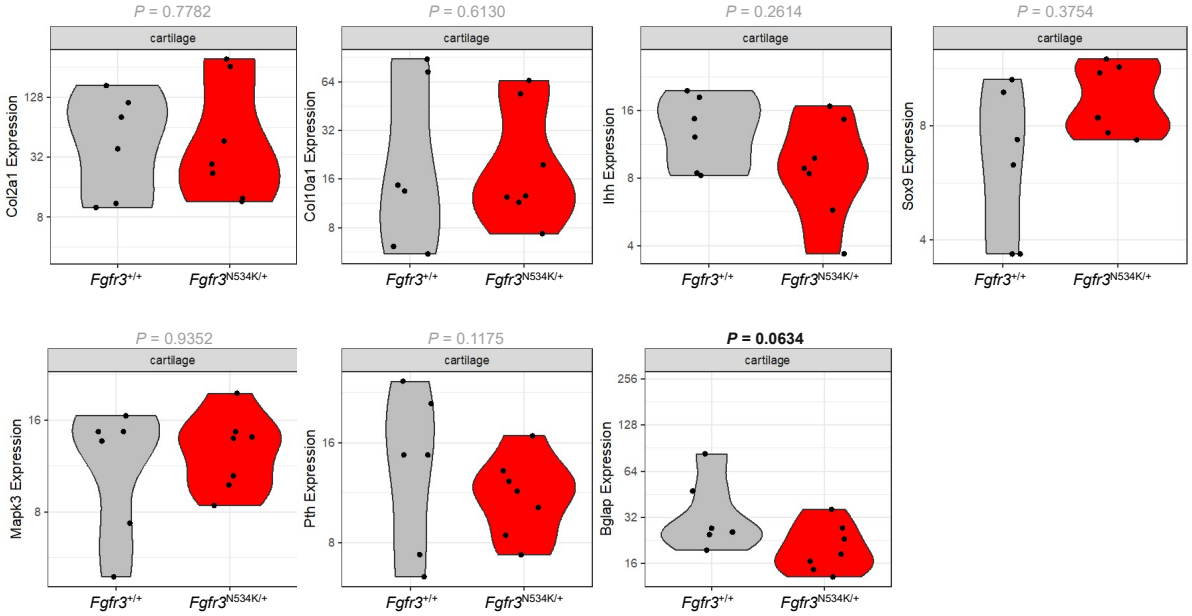
P = 0.7782
cartilage
Col2a1 Expression
128
32
8
Fgfr3+/+
Fgfr3N534K/+
P = 0.6130
cartilage
Col10a1 Expression
64
32
16
8
Fgfr3+/+
Fgfr3N534K/+
P = 0.2614
cartilage
Ihh Expression
16
8
4
Fgfr3+/+
Fgfr3N534K/+
P = 0.3754
cartilage
Sox9 Expression
8
4
Fgfr3+/+
Fgfr3N534K/+
P = 0.9352
cartilage
Mapk3 Expression
16
8
Fgfr3+/+
Fgfr3N534K/+
P = 0.1175
cartilage
Pth Expression
16
8
Fgfr3+/+
Fgfr3N534K/+
P = 0.0634
cartilage
Bglap Expression
256
128
64
32
16
Fgfr3+/+
Fgfr3N534K/+

B

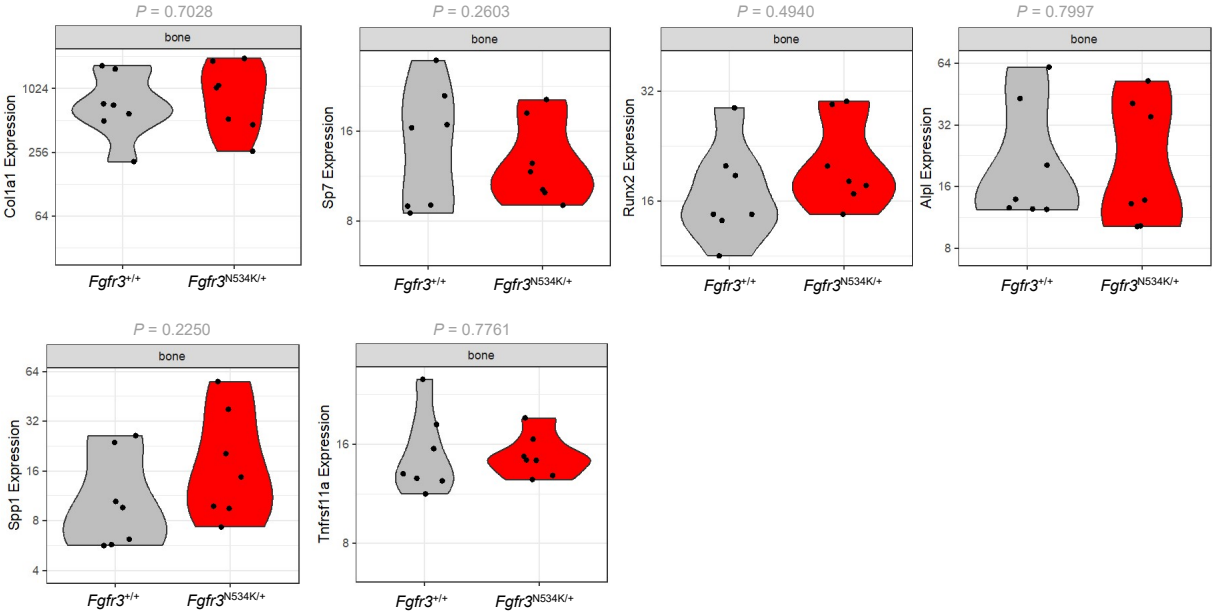
P = 0.7028
bone
Col1a1 Expression
1024
256
64
Fgfr3+/+
Fgfr3N534K/+
P = 0.2603
bone
Sp7 Expression
16
8
Fgfr3+/+
Fgfr3N534K/+
P = 0.4940
bone
Runx2 Expression
32
16
Fgfr3+/+
Fgfr3N534K/+
P = 0.7997
bone
Alpl Expression
64
32
16
8
Fgfr3+/+
Fgfr3N534K/+
P = 0.2250
bone
Spp1 Expression
64
32
16
8
4
Fgfr3+/+
Fgfr3N534K/+
P = 0.7761
bone
Tnfrsf11a Expression
16
8
Fgfr3+/+
Fgfr3N534K/+

Supplemental Figure 6: Gene set enrichment analysis based on functional annotation (Gene Ontology – Biological Process pathways) of genes deregulated in (A) cartilage or (B) bone samples from *Fgfr3*$^{N534K/+}$ mice. Dot size represents the number of significantly deregulated (left up- or right down-regulated) genes found in a given pathway. The color scale indicates the significance of the enrichment (hypergeometric tests, adjusted *P*-values).

Cartilage ROIs

A

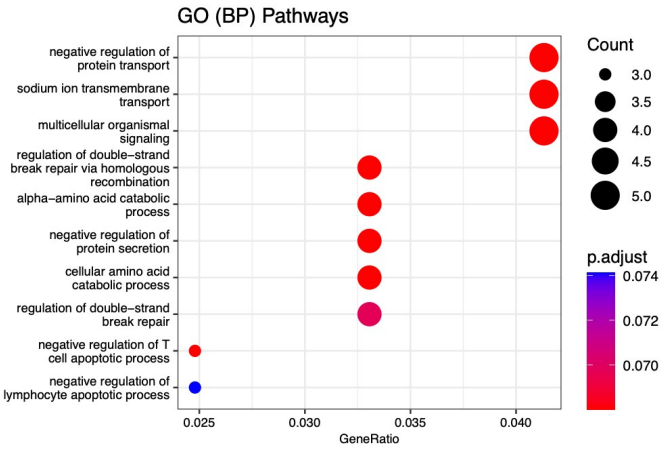

B

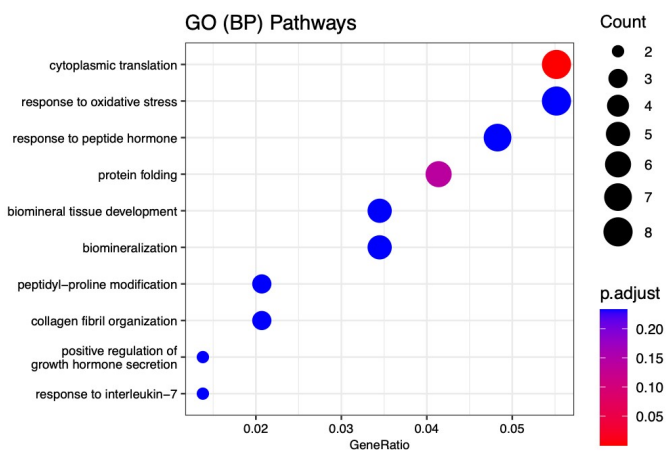

Bone callus ROIs

C

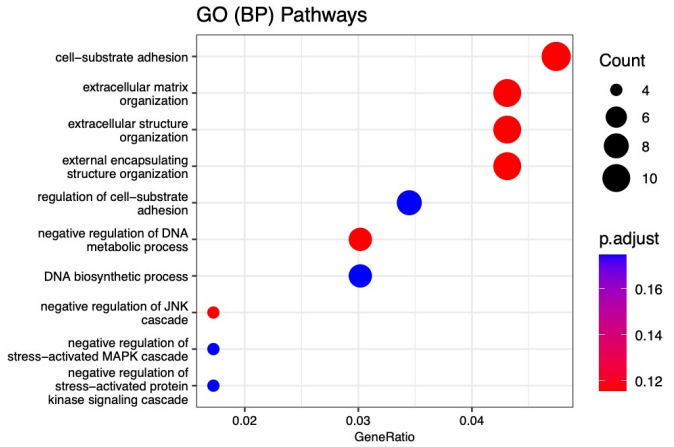

D

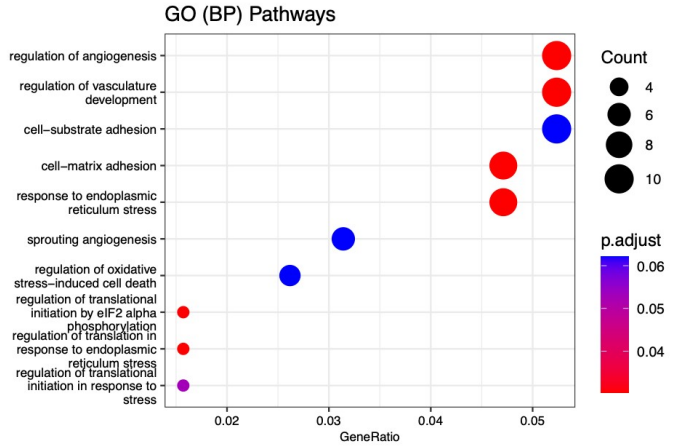

Supplemental Figure 7: Representative VEGF labelling of callus cartilage (MC) at day 14 post fracture in *Fgfr3*$^{+/+}$ and *Fgfr3*$^{N534K/+}$ (+ vehicle, + BMN111, + BGJ398) mice (scale bar 200 µm).

Day 14 post fracture

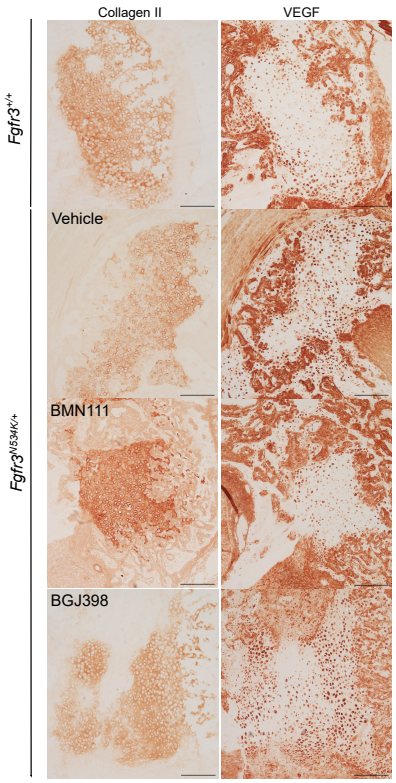

Supplemental Figure 8: 3D reconstructions from μCT scans of the skull and the mandible of a P42 wild-type mouse, showing positions of skull and mandibular landmarks used for morphometric geometrics analyses.

A

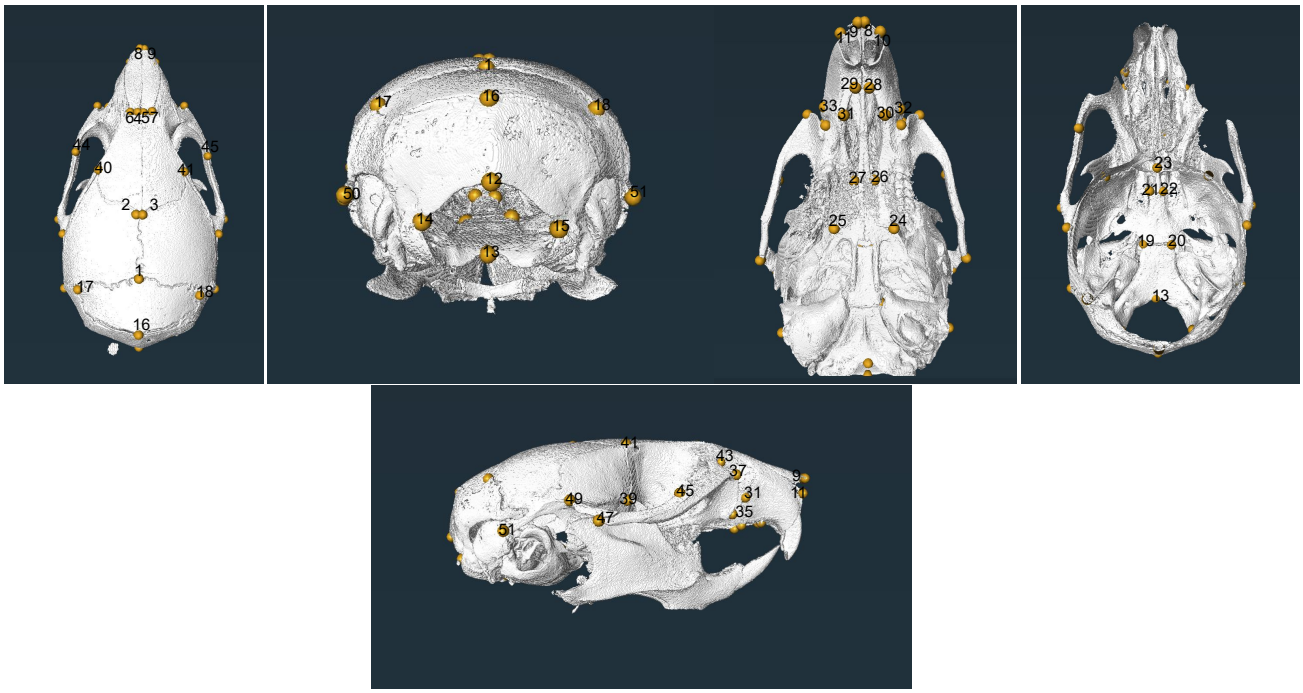
8 9
6 4 5 7
44
45
40
41
2 3
1
17
18
16
17
16
18
50
12
51
14
15
13
29 28
33 31 30 32
27 26
25
24
23
21 22
19 20
13
41
43
37
9
11
49
39
45
31
35
47
51

B

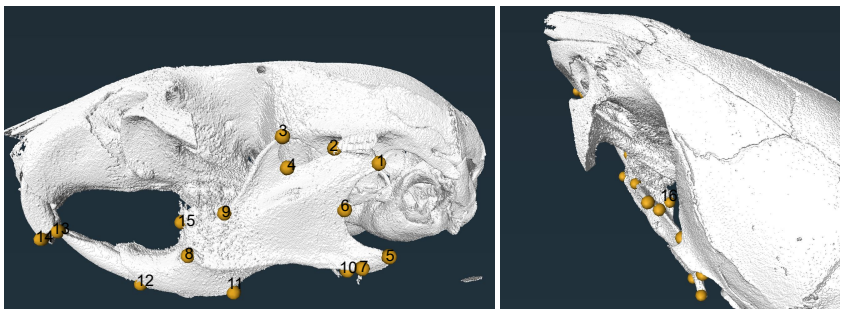
3
2
4
1
15
9
6
14
13
8
5
12
11
10 7
16

3. Conclusions et perspectives

Le premier modèle murin d'hypochondroplasie, *Fgfr3*$^{N534K/+}$, a été généré au sein de notre laboratoire (Loisay et al, 2022, en révision). Il présente un phénotype de nanisme modéré, avec anomalies craniofaciales mimant la pathologie humaine. Nous avons observé des anomalies microarchitecturales osseuses au sein du squelette axial et appendiculaire, il s'agit d'un phénotype ostéoporotique se majorant avec l'âge des souris mutantes (Loisay et al, 2022, en révision). Nos analyses ont montré que cette mutation activatrice *Fgfr3*$^{N534K/+}$ impactait fortement la formation et la croissance postnatale de la mandibule, ainsi que la réparation osseuse dans un contexte de réparation endochondrale, après fractures non stabilisées des mandibules. Ces anomalies majeures de réparation osseuse étaient restaurées après traitement par antagonistes de FGFR3, le BGJ398 (inhibiteur des tyrosines kinases) et le BMN111 (analogue du CNP). Nos analyses montrent que le traitement par BMN111 restaurait surtout la différentiation chondrocytaire, et que le traitement par BGJ398 stimulait essentiellement la différenciation et la maturation ostéoblastique. Les deux traitements corrigent l'hyperactivation de la voie des MAPKinases en aval de FGFR3. Nos analyses de transcriptomique spatiale ont permis de mettre en évidence des anomalies d'expression de gènes clés exprimés par les chondrocytes matures et en phase de transdifférenciation en ostéoblastes, et de gènes impliqués dans les mécanismes d'autophagie et d'apoptose. Dans le futur, ces mêmes analyses réalisées au sein des cals de réparation de souris traitées par BGJ398 et BMN111 permettront de confirmer, sur le plan moléculaire et cellulaire, l'action de ces traitements au cours de la réparation osseuse. Enfin, l'étude de la morphologie et des caractéristiques microarchitecturales des mandibules non fracturées au cours du vieillissement permettra de mieux comprendre l'impact de cette mutation *Fgfr3*$^{N534K/+}$ au cours du remodelage osseux mandibulaire.

IV. Discussion

Impact des mutations activatrices dans les gènes FGFRs au cours de la croissance mandibulaire en pathologie humaine

La première partie de ce projet de thèse avait pour but de mieux comprendre l'impact des mutations activatrices dans les gènes FGFRs au cours de la formation et la croissance mandibulaire. Les gènes FGFR2 et FGFR3 sont exprimés au sein des cartilages primaire (Meckel) et secondaires (condyliens, angulaires et symphysaire) et de l'os mandibulaire au cours de la formation mandibulaire. L'impact des mutations activatrices de FGFR2 et FGFR3 restaient à préciser en pathologie humaine. A partir d'analyses morphométriques 3D comparatives réalisées à partir de scanners mandibulaires de patients porteurs de craniosténoses FGFR2 (syndromes de Crouzon et d'Apert) et FGFR3 (syndrome de Muenke, syndrome de Crouzon avec acanthosis nigricans), de patients achondroplases (FGFR3) et de témoins, nous avons montré des modifications significatives de la morphologie mandibulaire, spécifiques selon le type de syndrome, en faveur de corrélations génotype phénotype. Les patients porteurs de craniosténoses FGFR2 et FGFR3 présentent des fusions prématurées des sutures crâniennes affectant les sutures coronales, associées parfois à la fusion d'autres sutures crâniennes, selon le type de syndrome et la sévérité, ainsi qu'une fusion prématurée des synchondroses de la base du crâne. Nous avons montré à partir de l'étude d'une cohorte de patients achondroplases porteurs d'une mutation $Fgfr3^{G380R/+}$, la mutation la plus fréquemment retrouvée dans l'achondroplasie, la présence de fusions prématurées des synchondroses de la base du crâne et des sutures squamo-sphénoïdales, démontrant l'impact de cette mutation au cours de l'ossification endochondrale et membranaire. Les patients porteurs de craniosténoses FGFR2 et FGFR3 et les patients achondroplases présentent une rétrusion de l'étage moyen de la face de sévérité variable et un prognathisme relatif. La morphologie mandibulaire dépend à la fois de facteurs extrinsèques, en rapport avec la morphologie de la base du crâne, et de l'étage moyen de la face, ainsi que de facteurs intrinsèques, dépendants des processus d'ossification endochondrale et membranaire s'exerçant en période anténatale et postnatale au sein de la mandibule.

Ainsi, nos résultats mettent en exergue l'impact direct des mutations activatrices FGFR2 et FGFR3 au cours de la formation et la croissance mandibulaire, se surajoutant à l'impact

extrinsèque des modifications du crâne et de la base du crâne induites par les fusions prématurées des sutures crâniennes et des synchondroses de la base du crâne.

L'impact de ces anomalies craniofaciales et mandibulaires est à la fois morphologique et fonctionnel. Le syndrome d'apnée obstructive du sommeil est une conséquence fonctionnelle majeure des anomalies morphologiques craniomaxillofaciales et mandibulaires dans ces syndromes. Dans le cadre des craniosténoses FGFRs, l'avancement chirurgical frontofacial permet de corriger le syndrome d'apnées obstructives du sommeil (Khonsari et al, 2020). Dans le cadre de l'achondroplasie, la corrélation anatomofonctionnelle entre la sévérité des anomalies morphologiques craniofaciales et mandibulaires et la sévérité des apnées obstructives du sommeil n'a jamais été confirmée. A partir d'analyses multimodales dans notre cohorte de patients achondroplases, nous avons montré une corrélation significative entre la sévérité du syndrome d'apnées obstructives du sommeil et la sévérité de la rétrusion maxillomandibulaire. Ces résultats constituent un argument supplémentaire en faveur de la correction chirurgicale des anomalies maxillomandibulaires des patients porteurs d'ostéochondrodysplasies, à la fois sur le plan morphologique et fonctionnel (apnées obstructives). Nous avons précédemment montré des différences significatives en termes d'ossification post chirurgicale au niveau de la base du crâne et de la voûte crânienne chez des patients porteurs de craniosténoses FGFRs, selon la mutation dans le gène FGFR2 (Morice et al, 2017 ; Oyama et al ; 2009 ; Bouaoud et al, 2020). Nos données sont également en faveur d'une aggravation du phénotype craniofacial et mandibulaire avec l'âge chez les patients porteurs d'achondroplasie. Cette aggravation du phénotype craniofacial et mandibulaire peut être à la fois expliquée par les fusions progressives des synchondroses de la base du crâne au cours de la croissance craniofaciale, et par l'impact intrinsèque de la mutation activatrice de *FGFR3* sur les cartilages condyliens. Ces cartilages jouent en effet un rôle majeur au cours de la croissance post natale de la mandibule, car ils permettent l'élongation de la branche montante mandibulaire.

L'étude de modèles murins adaptés mimant la pathologie humaine est essentielle pour mieux comprendre l'impact de ces mutations au cours de la formation et de la réparation osseuse mandibulaire. Ceci n'a jamais été étudié dans le contexte de l'hypochondroplasie. Ces questions ont fait l'objet de la deuxième partie de ce projet de thèse.

Impact des mutations activatrices FGFRs au cours de la formation et la réparation osseuse mandibulaire : apport du modèle murin d'hypochondroplasie, *Fgfr3*$^{N534K/+}$

L'impact des mutations activatrices de *Fgfr3* a été montré au cours de la formation mandibulaire dans notre modèle murin d'achondroplasie, *Fgfr3*$^{Y367C/+}$ (Biosse Duplan et al, 2016). Cette mutation entraîne un défaut de différenciation et de maturation chondrocytaire au sein du cartilage de Meckel et des cartilages condyliens, à l'origine d'hypoplasie et d'anomalies morphologiques mandibulaires significatives (Biosse Duplan et al, 2016). Nous avons généré le premier modèle murin *Hch* mimant l'hypochondroplasie, exprimant la mutation *Fgfr3*$^{Asn534Lys/+}$ (*Fgfr3*$^{N534K/+}$) homologue à la mutation la plus fréquente, p.Asn540Lys retrouvée en pathologie humaine. Ce modèle murin mime la pathologie humaine, il présente un phénotype de nanisme modéré et des anomalies craniofaciales caractérisées par une macrocéphalie, une rétrusion de l'étage maxillaire, et une tendance au prognathisme mandibulaire. Nous avons montré chez les souris mutantes *Hch,* un retard à la mise en place du cartilage de Meckel, un défaut de différentiation chondrocytaire et un retard de résorption de ce cartilage présent uniquement en anténatal. Alors qu'une hypoplasie mandibulaire était constatée dès la période postnatale immédiate dans le modèle murin d'achondroplasie *Fgfr3*$^{Y367C/+}$, nous avons observé une réduction significative des longueurs mandibulaires à partir du stade P14. Ces résultats montrent que l'impact de la mutation *Fgfr3*$^{N534K/+}$ (*Hch*) est plus modéré et s'exprime de façon plus tardive au cours de la croissance mandibulaire que la mutation *Fgfr3*$^{Y367C/+}$ (*Ach*), corroborant le caractère progressif et modéré du nanisme rhizomélique observé chez les patients porteurs d'hypochondroplasie. Dans le modèle *Hch*, nous avons montré que les modifications morphologiques mandibulaires s'aggravaient au cours de la croissance. Nous avons observé en période postnatale, un défaut de différenciation et de maturation chondrocytaire au sein des cartilages condyliens, participant au défaut de croissance postnatal de la mandibule.

Nous avons montré que les souris mutantes *Hch* adultes présentaient un phénotype ostéoporotique, s'aggravant avec l'âge, montrant l'impact de la mutation *Fgfr3*$^{N534K/+}$au cours du remodelage osseux. Les analyses morphométriques et histologiques des mandibules chez les souris mutantes *Hch* réalisées à différents stades au cours du vieillissement permettront de préciser l'impact de cette mutation *Hch* au niveau mandibulaire, et notamment au niveau des cartilages condyliens qui sont des cartilages permanents.

Dans un deuxième temps, nous avons étudié l'impact de la mutation *Fgfr3*$^{N534K/+}$ dans le contexte de réparation osseuse endochondrale après fractures mandibulaires non stabilisées.

Nous avons montré un retard important de consolidation osseuse, avec pseudarthrose chez les souris mutantes *Hch*. Des résultats similaires ont été observés au niveau des os longs après fractures non stabilisées dans des modèles murins d'achondroplasie (Su *et al*, 2008, Chen *et al*, 2017, Julien *et al*, 2020).

Nous avons montré dans le modèle *Hch*, la présence d'un retard de mise en place et un retard de résorption du cartilage du cal de réparation, en lien avec un défaut de différenciation chondrocytaire, et un défaut d'apoptose des chondrocytes hypertrophiques. Bien que nous n'ayons pas observé de différences significatives concernant le volume cartilagineux des cals de réparation entre 10 et 21 jours post fracture, des plages cartilagineuses persistantes étaient observées au sein des cals de réparation chez les souris mutantes présentant une discontinuité osseuse et de la pseudarthrose. Ces données montrent que la pseudarthrose est une conséquence directe de l'impact de la mutation $Fgfr3^{N534K/+}$ au cours du processus de réparation osseuse endochondrale. La pseudarthrose concernait environ 50 % des souris mutantes *Hch*, alors qu'elle affectait plus fréquemment et de façon plus sévère les souris mutantes $Prx1^{Cre};Fgfr3^{Y367C/+}$ mimant l'achondroplasie après fracture non stabilisées des tibias (Julien et al, 2020). Tout d'abord, le phénotype pseudarthrosique modéré observé après fracture mandibulaire dans le modèle *Hch* peut être expliqué par les contraintes mécaniques faibles qui s'exerçaient au niveau des cals de réparation mandibulaire, contrastant avec les contraintes mécaniques importantes s'exerçant au niveau des os longs (Julien et al, 2020). Il a été montré dans un contexte non pathologique, que le volume des cals de réparation était plus important après fracture non stabilisée des os longs qu'après fracture mandibulaire, démontrant que des contraintes mécaniques importantes exacerbent le processus de réparation osseuse endochondrale (Yu et al, 2012).

De plus, la mutation $Fgfr3^{Y367C/+}$ (*Ach*) impacte à la fois la prolifération et la différenciation chondrocytaire dans le contexte de réparation osseuse endochondrale (Julien et al, 2020). Nos résultats montrent un défaut de différenciation chondrocytaire au sein du cartilage des cals de réparation, mais nous n'avons pas mis en évidence un défaut de prolifération chondrocytaire au début de la formation du cartilage du cal (J7 post fracture). Les effets moléculaires différenciels de ces mutations activatrices distinctes au sein du gène *Fgfr3* peuvent également expliquer le phénotype pseudarthrosique plus modéré dans notre modèle murin *Hch*.

Pour mieux comprendre l'impact de la mutation $Fgfr3^{N534K/+}$ au cours du processus de réparation osseuse endochondrale, nous avons mené des études comparatives de transcriptomique spatiale à un stade majeur (J14 post fracture), correspondant au stade de transition entre le cal cartilagineux et le cal osseux. Au sein du cartilage du cal, nous avons

montré une diminution de l'expression du *Collagen 11*, essentiel à la différenciation chondrocytaire (Bridgewater *et al*, 1998) chez les souris *Fgfr3*$^{N534K/+}$. De plus, nos analyses ont montré la régulation négative de marqueurs ostéoblastiques spécifiques, normalement exprimés par les chondrocytes hypertrophiques, qui acquièrent des caractéristiques « osteoblast-like » au cours de la transdifférenciation des chondrocytes en ostéoblastes. Il s'agit de *Collagen 1*, et de gènes impliqués dans le processus de minéralisation osseuse, *Dmp1* (Dentin Matrix Acidic Phosphoprotein 1) et *Phospho 1* (Phosphatase, orphan 1) (Hu *et al*, 2017, Fisher *et al*, 2001, Zhang *et al*, 2016, Morcos *et al*, 2018). Nos résultats montrent également chez les souris *Hch,* la diminution significative de l'expression de *Hmgb2* (High Mobility Group Box 2), régulant l'hypertrophie chondrocytaire (Taniguchi *et al*, 2018). Le rôle de *Hmgb2* n'a jamais été étudié au cours de la réparation osseuse. A partir des données existantes concernant le rôle de *Hmgb2* au cours de la formation osseuse, nous avons pour hypothèse que l'expression significativement diminuée de *Hmgb2* au sein du cartilage du cal pourrait perturber l'hypertrophie chondrocytaire secondaire à la mutation activatrice *Fgfr3*$^{N534K/+}$. Parmi les gènes clés de la régulation du processus d'ossification et de réparation osseuse endochondrale, l'expression de *Ihh*, un régulateur clé de la prolifération et la différentiation chondrocytaire, et stimulant la transdifférenciation chondrocytaire en ostéoblaste (Aghajanian *et al*, 2017 ; Lee *et al*, 1995), a été retrouvée diminuée chez les souris mutantes *Hch*. Même si cette différence n'était pas significative dans nos analyses, nous ne pouvons pas exclure l'impact majeur de la diminution de l'expression de *Ihh* au cours de la différenciation chondrocytaire et de la transdifférenciation chondrocytaire en ostéoblastes dans notre modèle murin *Hch*.

Nous avons retrouvé la diminution significative de l'expression d'un gène s'exprimant au sein du cil primaire participant au transport antérograde des protéines ciliaires, il s'agit de *Kif17* (Kinesin like protein 17) (Funabashi *et al*, 2017, Ishida *et al*, 2022). Nous avons précédemment montré l'impact significatif de la mutation *Fgfr3*$^{Y367C/+}$ (*Ach*) au niveau du cil primaire des chondrocytes au sein des plaques de croissance (Martin et al, 2021). Nos résultats suggèrent que le cil primaire chondrocytaire est également affecté dans notre modèle murin *Hch* et que cette perturbation pourrait participer au défaut de mise en place du cartilage du cal de réparation. Des analyses complémentaires sont nécessaires pour compléter cette hypothèse.

Les analyses transcriptomiques réalisées au sein de l'os du cal nouvellement formé, ont confirmé l'expression de gènes spécifiques des tissus osseux, il s'agit de marqueurs ostéoblastiques *Collagen1a1*, *Osterix (Sp7)*, *Runx2*, *Alpl* (Alkaline Phosphatase), *Spp1* (osteopontin) et ostéoclastique, *Tnfrs11a* (RANK). Nous n'avons pas trouvé de différence significative d'expression de ces gènes entre mutants et contrôles. L'homéostasie osseuse

dépend de la balance entre formation et résorption osseuse, impliquant à la fois des processus de biosynthèse et des processus cataboliques. Le rôle de l'interaction FGF/FGFR a été montré dans la régulation de l'autophagie (Cinque *et al*, 2015). En particulier, il a été démontré que l'activation de FGFR3 inhibait les processus d'autophagie dans le contexte de formation et de croissance osseuse (Wang *et al*, 2015). Le défaut d'autophagie entraîne un stress au niveau du réticulum endoplasmique, ce qui en retour régule négativement la voie BMP/Smad1/5/8, à l'origine d'une diminution de la différenciation ostéoblastique via Runx2 (Li *et al*, 2018). L'expression de *Smad1* était significativement diminuée chez les souris *Hch.* Nous avons pour hypothèse que la diminution de l'expression de *Smad1* pourrait être due à un défaut d'autophagie dans ce contexte d'activation excessive de Fgfr3, ce qui par voie de conséquence pourrait participer au défaut de différenciation et de maturation ostéoblastique et expliquer les défauts microarchitecturaux observés au sein de l'os nouvellement formé des cals de réparation. De plus, nos résultats sont en faveur d'une perturbation de la régulation de l'apoptose au sein de l'os des cals de réparation chez les souris *Hch.* Nous avons montré la diminution significative de l'expression de *Comp* (Cartilage Oligomeric Matrix Protein), exprimé par les chondrocytes et les ostéoblastes, qui a un rôle de suppression de l'apoptose (Gagarina *et al*, 2008 ; Di Cesare *et al*, 1995 ; Fang *et al*, 2000). Nos résultats suggèrent que le processus apoptotique est exacerbé au sein de l'os des cals nouvellement formé. De plus, nos résultats sont en faveur d'un défaut de réparation de l'ADN au sein des cals de réparation. En effet, l'expression de *Alkbh2*, une enzyme participant à la correction des dommages de l'ADN par déméthylation (Fu *et al*, 2015) était significativement diminuée au sein de l'os des cals de réparation dans notre modèle *Hch*.
Au total, nos résultats montrent que la mutation $Fgfr3^{N534K/+}$ perturbe l'homéostasie osseuse au sein de l'os nouvellement formé des cals de réparation. Les défauts microarchitecturaux observés au sein des cals de réparation pourraient être induits à la fois par l'impact direct de la mutation $Fgfr3^{N534K/+}$ au cours de la transdifférenciation chondrocytaire en ostéoblaste via la voie des MAPKinases, et de façon indirecte par la régulation négative de la voie BMP/Smad, en réponse au défaut d'autophagie. L'exploration fine des acteurs impliqués dans les mécanismes d'autophagie et d'apoptose dans notre modèle *Hch* au cours de la réparation osseuse permettra de préciser l'impact de la mutation $Fgfr3^{N534K/+}$ dans ces processus. Enfin, nous avons montré l'augmentation significative de l'expression de gènes impliqués dans la régulation négative des voies de signalisation situées en aval de l'activation de FGFR3. Il s'agit de *Dusp 9* et *Dusp3* (dual-specificity (threonine/tyrosine) phosphatases spécifiques de ERK), régulateurs négatifs de la voie des MAPKinases (Jeffrey *et al*., 2007, Patterson *et al*., 2009), dont l'expression était fortement augmentée au sein du cartilage (*Dusp9*) et de l'os du cal

(*Dusp3*). Nous avons également mis en évidence la surexpression de *Socs3* (*Suppressor of Cytokine Signaling-3*) au sein de l'os des cals des souris *Hch*. *Socs3* est un régulateur négatif de la voie STAT3 (Babon and Nicola, 2012) et de la voie des MAPKinases (Liu *et al*, 2019). Ces résultats suggèrent que la suractivation de la voie des MAPKinases retrouvée à la fois au sein du cartilage et de l'os des cals de réparation, pourrait constituer une cible thérapeutique pour restaurer un processus de réparation osseuse endochondrale normal.

Approches précliniques : restauration d'un processus de réparation osseuse endochondrale normal après traitement par antagonistes de FGFR3

Compte tenu de nos résultats, nous avons eu pour hypothèse que des antagonistes de FGFR3 pourraient restaurer un processus de réparation osseuse endochondrale dans notre modèle murin *Hch*. Nous avons testé les effets de deux antagonistes de FGFR3, le BMN111 (vosoritide), un analogue du CNP, et le BGJ398 (infigratinib), un inhibiteur des tyrosines kinases, actuellement évalués en phase clinique chez les patients achondroplases, dans le cadre de la croissance osseuse. Le BGJ398 inhibe la phosphorylation excessive des résidus tyrosines kinases, et a une action de régulation négative de plusieurs voies de signalisation en aval de FGFR3 dont la voie des MAPKinases. Son effet bénéfique au cours de la croissance osseuse a été confirmé dans notre modèle murin d'achondroplasie, $Fgfr3^{Y367C/+}$(Komla Ebri *et al*, 2016, Di Rocco *et al*, 2014, Biosse Duplan *et al*, 2016). Le BMN111 est un analogue du CNP, qui via l'interaction avec le récepteur NPR-B, a une action d'inhibition de la voie des MAPKinases. L'effet positif du BMN111 au cours de la croissance osseuse a été confirmé au cours d'études précliniques à partir de modèles murins d'achondroplasie (Lorget *et al*, 2012, Wendt *et al*, 2015), et chez les patients achondroplases (Savarirayan *et al*, 2020). Le BMN111 a reçu récemment l'autorisation de la FDA. Nous avons observé après traitement par BGJ398 et BMN111 la restauration d'un processus de consolidation osseuse endochondrale normal après fracture non stabilisée des mandibules chez les souris *Hch*. Ces traitements amélioraient significativement la différenciation chondrocytaire et l'apoptose des chondrocytes hypertrophiques, corrigeaient les défauts microarchitecturaux des cals de réparation et accéléraient le remodelage osseux des cals. Bien que ces deux traitements améliorent le processus de réparation osseuse, nos résultats suggèrent des différences d'action des ces deux antagonistes de FGFR3. La restauration du processus de différenciation chondrocytaire était plus importante chez les souris *Hch* traitées par BMN111, et nous avons pour hypothèse que la correction du défaut de consolidation chez les souris traitées par BGJ398 pourrait être lié à une stimulation directe de la différenciation et de la maturation ostéoblastique par ce traitement. Ces deux traitements accéléraient le processus

de remodelage osseux des cals, avec modification de la balance formation / résorption osseuse, en faveur de l'apposition osseuse permettant de restaurer la continuité osseuse corticale sur le site de fracture.

V. Conclusions

En conclusion, nous avons montré que la mutation gain-de-fonction dans le gène *Fgfr3* entraîne des anomalies de formation osseuse mandibulaire et un défaut majeur de réparation osseuse mandibulaire avec pseudarthrose dans le modèle murin *Hch,* liés à l'impact de la mutation $Fgfr3^{N534K/+}$ au cours des processus d'ossification endochondrale. Nos résultats démontrent le rôle majeur de *FGFR3* dans la régulation de la différenciation chondrocytaire et ostéoblastique et l'effet bénéfique d'antagonistes de FGFR3 au cours de la réparation osseuse. Ces données ouvrent des perspectives thérapeutiques prometteuses chez les patients porteurs d'ostéochondrodysplasies liées à FGFR3 présentant des défauts de réparation osseuse, dans le contexte traumatique ou après chirurgie programmée (ostéotomies craniomaxillofaciales et mandibulaires).

Gène (MIM)	Mode de transmission	Syndrome (MIM)	Suture(s) typiquement fusionnée(s)	Traits phénotypiques majeurs
ASXL1 (612990)	AD (n)	Syndrome Bohring-Opitz (605039)	Métopique	Naevus flammeus du front, déviation ulnaire, flexion des poignets et des articulations métacarpalophalangiennes, retard intellectual sévère
CDC45 (603465)	AR		Coronale	Paupières fines, hypoplasie des oreilles, petite taille
COLEC11 (612502)	AR	3MC syndrome 2 (265050)	Métopique	Hypertélorisme, ptosis palpebral, incurvation des sourcils, fente labiale/palatine, surdité, synostose radioulnaire, anomalies génitales et vésico urinaires
EFNB1 (300035)	Dominant lié à l'X	Craniofrontonasal (304110)	Coronales	Hypertélorisme, encoche de la pointe nasale, anomalies du thorax, anomalies des ongles (stries longitudinales), anomalies phénotypiques plus sévères chez les individus de sexe féminin hétérozygotes
ERF (611888)	AD	ERF-related craniosynostosis (600775)	Multisuturaire	Exorbitisme, hypoplasie de l'étage moyen de la face, malformation de Chiari type I, initiation post natale de la fusion prématurée des sutures crâniennes
FGFR1 (136350)	AD	Syndrome de Pfeiffer (101600)	Coronales	Elargissement et déviation du pouce et de l'hallux, bradydactylie, syndactilies cutanées
FGFR1	AD (n)	Dysplasie osteoglophonic (166250)	Multisuturaire	Arcades sourcillières proéminentes, dépression de l'arête nasale, nanisme rhizomélique, lésions métaphysaires ostéolytiques
FGFR2 (176943)	AD (n)	Syndrome d'Apert (101200)	Coronal Multisuturaire	Hypoplasie de l'étage moyen de la face, dilatation des ventricules cérébraux, syndactilies complexes des mains et des pieds
FGFR2	AD (n)	Syndrome de Beare-Stevenson (123790)	Multisuturaire	Atrésie choanale, moignon ombilical proéminent, sillons cutanées du scalp et du cou, acanthosis nigricans
FGFR2	AD	Syndrome de Crouzon (123500)	Multisuturaire, coronales, sagittale	Exorbitisme, hypoplasie de l'étage moyen de la face, nez « crochu », mains et pieds d'aspect normal
FGFR2	AD (n)	Syndrome de Pfeiffer (101600)	Multisuturaire	Pouce et hallux larges, crâne en « trèfle » (cas sévères), anomalies cérébrales, synostose du coude
FGFR2	AD (n)	Bent bone dysplasia (614592)	Coronales	Ostéopénie, incurvation des os longs, défaut de minéralisation de la calvaria, létalité périnatale
FGFR3 (134934)	AD	Syndrome de Muenke (602849)	Coronales	Surdité neurosensorielle, brachydactylie modérée, épiphyses coniques
FGFR3	AD (n)	Crouzon/acanthosis nigricans (612247)	Multisuturaire	Faciès crouzonoide, sténose choanale, hydrocéphalie, acanthosis nigricans
FGFR3	AD (n)	Dysplasie thanatophorique de type II (187601)	Multisuturaire	Dysplasie squelettique léthale, raccourcissement micromélique, fémur droits
IHH (600726)	AD	Craniosynostose de Philadelphia (185900)	Sagittale	Syndactylies cutanées et osseuses

IL11RA (600939)	AR	Craniosynostose et anomalies dentaires (614188)	Multisuturaire	Multisuturaire Hypoplasie maxillaire, éruption dentaire retardée, dents surnuméraires, anomalies digitales, surdité de transmission
MEGF8 (604267)	AR	Syndrome de Carpenter type 2 (614796)	Métopique	Hypertelorisme, arcades sourcillières arquées, brachydactylie, syndactilie, polydactylie
MSX2 (123101)	AD	Craniosynostose de Boston (604757)	Sagittale, coronales, multisuturaire	
POR (124015)	AR	Syndrome d'Antley-Bixler (201750)	Bicoronale, multisuturaire	Sténose choanale, synostoses radiohumérales, fémurs courbés, contractures articulaires, anomalies génitales et de la stéroidogénèse
RAB23 (606144)	AR	Syndrome de Carpenter type 1 (201000)	Multisuturaire	Obésité, défauts cardiaques, polysyndactylie, brachydactylie, genu valgum, hypogonadisme, hernie ombilicale, déficit intellectuel
RUNX2 (600211)	AD (n)		Multisuturaire	
SKI (164780)	AD (n)	Syndrome de Shprintzen-Goldberg (182212)	Sagittale, multisuturaire	Hypertélorisme, micrognathie, palais ogival, arachnodactylie, contractures articulaires, déformations sternales, anévrisme de la racine aortique, prolapsus mitral, déficit intellectuel
TCF12 (600480)	AD	TCF12-related craniosynostosis (615314)	Coronales	Phénotype de type Saethre Chotzen, dans une forme modérée
TWIST1 (601622)	AD	Saethre-Chotzen syndrome (101400)	Coronales	Racine des cheveux basse (frontal), ptosis palpébral, hypertélorisme, fentes palpébrales descendantes, sténoses des canaux lacrymaux, oreilles hypoplasiques avec crus de l'hélix proéminente
WDR35 (613602)	AR	Dysplasie cranioectodermique de type 2 (613610)	Sagittal	Dysmorphisme facial, thorax étroit, raccourcissement des os longs, branchydactylie, cheveux fins et éparses, dents hypoplasiques, reins kystiques, fibrose hépatique
ZIC1 (600470)	AD (n)	Craniosynostose de type ZIC1	Coronal	Déficit intellectuel sévère

Tableau a.1. Liste des gènes mutés retrouvés dans le cadre de phénotype de craniosténose, mode de transmission, noms des syndromes associés, type de suture typiquement fusionnée, et signes phénotypique majeurs et typiques retrouvés (adapté de Twigg and Wilkie, 2015).
AD : autosomique dominant, n, généralement de novo, AR : autosomique récessif.

VI. Références

Abdel-Salam, G. M., Flores-Sarnat, L., El-Ruby, M. O., Parboosingh, J., Bridge, P., Eid, M. M., ... & Temtamy, S. A. (2011). Muenke syndrome with pigmentary disorder and probable hemimegalencephaly: An expansion of the phenotype. *American journal of medical genetics Part A*, *155*(1), 207-214.

Agochukwu, N. B., Solomon, B. D., Benson, L. J., & Muenke, M. (2013). Talocalcaneal coalition in Muenke syndrome: Report of a patient, review of the literature in FGFR-related craniosynostoses, and consideration of mechanism. *American Journal of Medical Genetics Part A*, *161*(3), 453-460.

Al Kaissi A., Ben Chehida F., Kenis V., Ganger R., Radler C., Hofstaetter J. G., et al. (2013). Broad spectrum of skeletal malformation complex in patients with cleidocranial dysplasia syndrome: radiographic and tomographic study. *Clin. Med. Insights Arthritis Musculoskelet. Disord.* 6 45–55. 10.4137/CMAMD.S11933

Alarid, E. T., Rubin, J. S., Young, P., Chedid, M., Ron, D., Aaronson, S. A., & Cunha, G. R. (1994). Keratinocyte growth factor functions in epithelial induction during seminal vesicle development. *Proceedings of the National Academy of Sciences*, *91*(3), 1074-1078.

Alcon, A., Metzler, P., Eswarakumar, J., Wilson, A. T., & Steinbacher, D. M. (2018). Osteogenesis of Crouzon-Mutated Cells in a Murine Model. *The Journal of craniofacial surgery*, *29*(1), 237.

Al-Qattan, M. M., & Phillips, J. H. (1997). Clinical features of Crouzon's syndrome patients with and without a positive family history of Crouzon's syndrome. *The Journal of Craniofacial Surgery*, *8*(1), 11-13.

Amann, R., & Trueb, B. (2013). Evidence that the novel receptor FGFRL1 signals indirectly via FGFR1. *International journal of molecular medicine*, *32*(5), 983-988.

Amano O., Doi T., Yamada T., Sasaki A., Sakiyama K., Kanegae H., et al. (2010). Meckel's cartilage: discovery, embryology and evolution. *J. Oral Biosci.* 52 125–135.

Amano, K., Densmore, M., Nishimura, R., & Lanske, B. (2014). Indian hedgehog signaling regulates transcription and expression of collagen type X via Runx2/Smads interactions. *Journal of Biological Chemistry*, *289*(36), 24898-24910.

Amarasekara, D. S., Kim, S., & Rho, J. (2021). Regulation of osteoblast differentiation by cytokine networks. *International journal of molecular sciences*, 22(6), 2851.

Amin S., Tucker A. S. (2006). Joint formation in the middle ear: lessons from the mouse and guinea pig. *Dev. Dyn.* 235 1326–1333.

Andrew, J. G., Hoyland, J. A., Freemont, A. J., & Marsh, D. R. (1995). Platelet-derived growth factor expression in normally healing human fractures. *Bone*, *16*(4), 455-460.

Anthwal N., Joshi L., Tucker A. S. (2013). Evolution of the mammalian middle ear and jaw: adaptations and novel structures. *J. Anat.* 222 147–160.

Arenas, M. A., Del Pino, M., & Fano, V. (2018). FGFR3-related hypochondroplasia: longitudinal growth in 57 children with the p. Asn540Lys mutation. *Journal of Pediatric Endocrinology and Metabolism*, *31*(11), 1279-1284.

Arnaud-López, L., Fragoso, R., Mantilla-Capacho, J., & Barros-Núñez, P. (2007). Crouzon with acanthosis nigricans. Further delineation of the syndrome. *Clinical genetics*, *72*(5), 405-410.

Arnold M. A., Kim Y., Czubryt M. P., Phan D., McAnally J., Qi X., et al. (2007). transcription factor controls chondrocyte hypertrophy and bone development. *Dev. Cell* 12 377–389.

Asada M, Honda E, Imamura T. Biologically active fibroblast growth factor 1 tagged with various epitopes. *BMC Res Notes*. 2008;1:42. Published 2008 Jul 11.

Bahney, C. S., Hu, D. P., Taylor, A. J., Ferro, F., Britz, H. M., Hallgrimsson, B., ... & Marcucio, R. S. (2014). Stem cell–derived endochondral cartilage stimulates bone healing by tissue transformation. *Journal of Bone and Mineral Research*, *29*(5), 1269-1282.

Bahney, C. S., Zondervan, R. L., Allison, P., Theologis, A., Ashley, J. W., Ahn, J., ... & Hankenson, K. D. (2019). Cellular biology of fracture healing. *Journal of Orthopaedic Research®*, *37*(1), 35-50.

Bankers-Fulbright, J. L., Kalli, K. R., & McKean, D. J. (1996). Interleukin-1 signal transduction. *Life sciences*, *59*(2), 61-83.

Barnes, G. L., Kostenuik, P. J., Gerstenfeld, L. C., & Einhorn, T. A. (1999). Growth factor regulation of fracture repair. *Journal of bone and mineral research*, *14*(11), 1805-1815.

Bartels, C. F., Bükülmez, H., Padayatti, P., Rhee, D. K., van Ravenswaaij-Arts, C., Pauli, R. M., ... & Warman, M. L. (2004). Mutations in the transmembrane natriuretic peptide receptor NPR-B impair skeletal growth and cause acromesomelic dysplasia, type Maroteaux. *The American Journal of Human Genetics*, *75*(1), 27-34.

Baujat, G., Legeai-Mallet, L., Finidori, G., Cormier-Daire, V., & Le Merrer, M. (2008). Achondroplasia. *Best Practice & Research Clinical Rheumatology*, *22*(1), 3-18.

Behonick, D. J., Xing, Z., Lieu, S., Buckley, J. M., Lotz, J. C., Marcucio, R. S., ... & Colnot, C. (2007). Role of matrix metalloproteinase 13 in both endochondral and intramembranous ossification during skeletal regeneration. *PloS one*, *2*(11), e1150.

Bell, D. M., Leung, K. K., Wheatley, S. C., Ng, L. J., Zhou, S., Wing Ling, K., ... & Cheah, K. S. (1997). SOX9 directly regulates the type-ll collagen gene. *Nature genetics*, *16*(2), 174-178.

Bellus GA, Gaudenz K, Zackai EH, Clarke LA, Szabo J, Francomano CA, Muenke M. Identical mutations in three different fibroblast growth factor receptor genes in autosomal dominant craniosynostosis syndromes. *Nat Genet.* 1996 Oct;14(2):174–176.

Bellus, G. A., Bamshad, M. J., Przylepa, K. A., Dorst, J., Lee, R. R., Hurko, O., ... & Francomano, C. A. (1999). Severe achondroplasia with developmental delay and acanthosis nigricans (SADDAN): phenotypic analysis of a new skeletal dysplasia caused by a Lys650Met

mutation in fibroblast growth factor receptor 3. *American journal of medical genetics*, *85*(1), 53-65.

Bellus, G. A., McIntosh, I., Smith, E. A., Aylsworth, A. S., Kaitila, I., Horton, W. A., ... & Francomano, C. A. (1995). A recurrent mutation in the tyrosine kinase domain of fibroblast growth factor receptor 3 causes hypochondroplasia. *Nature genetics*, *10*(3), 357-359.

Bengur, F. B., Ekmekci, C. G., Karaarslan, E., Gunoz, H., & Alanay, Y. (2020). p. Ser348Cys mutation in FGFR3 gene leads to "mild ACH/severe HCH" phenotype. *European Journal of Medical Genetics*, *63*(2), 103659.

Berk, D. R., Del Carmen Boente, M., Montanari, D., Toloza, M. G., Primc, N. B., Prado, M. I., ... & Schrijver, I. (2010). Acanthosis nigricans and hypochondroplasia in a child with a K650Q mutation in FGFR3. *Pediatric dermatology*, *27*(6), 664-666.

Bhaskar S. N., Weinmann J. P., Schour I. (1953). Role of Meckel's cartilage in the development and growth of the rat mandible. *J. Dent. Res.* 32 398–410.

Bilikova P., Svandova E., Vesela B., Doubek J., Poliard A., Matalova E. (2019). Coupling activation of pro-apoptotic caspases with autophagy in the Meckel's cartilage. *Physiol. Res.* 68 135–140.

Biosse Duplan, M., Komla-Ebri, D., Heuzé, Y., Estibals, V., Gaudas, E., Kaci, N., ... & Legeai-Mallet, L. (2016). Meckel's and condylar cartilages anomalies in achondroplasia result in defective development and growth of the mandible. *Human molecular genetics*, *25*(14), 2997-3010.

Blair, H. C., Robinson, L. J., Huang, C. L., Sun, L., Friedman, P. A., Schlesinger, P. H., & Zaidi, M. (2011). Calcium and bone disease. *BioFactors (Oxford, England)*, *37*(3), 159–167.

Blank, C. E. (1959). Apert's syndrome (a type of acrocephalosyndactyly)–observations on a British series of thirty-nine cases. *Annals of Human Genetics*, *24*(2), 151-164.

Blomberg, M., Jeppesen, E. M., Skovby, F., & Benfeldt, E. (2010). FGFR3 mutations and the skin: report of a patient with a FGFR3 gene mutation, acanthosis nigricans, hypochondroplasia and hyperinsulinemia and review of the literature. *Dermatology*, *220*(4), 297-305.

Bober, M. B., Bellus, G. A., Nikkel, S. M., & Tiller, G. E. (2020). Hypochondroplasia. *GeneReviews®[Internet]*.

Bocciardi, R., Giorda, R., Buttgereit, J., Gimelli, S., Divizia, M. T., Beri, S., ... & Gimelli, G. (2007). Overexpression of the C-type natriuretic peptide (CNP) is associated with overgrowth and bone anomalies in an individual with balanced t (2; 7) translocation. *Human mutation*, *28*(7), 724-731.

Bouaoud J, Hennocq Q, Paternoster G, James S, Arnaud E, Khonsari RH. Excessive ossification of the bandeau in Crouzon and Apert syndromes. *J Craniomaxillofac Surg*. 2020;48(4):376-382. doi:10.1016/j.jcms.2020.02.022.

Bouleau, S., Pârvu-Ferecatu, I., Rodriguez-Enfedaque, A., Rincheval, V., Grimal, H., Mignotte, B., ... & Renaud, F. (2007). Fibroblast Growth Factor 1 inhibits p53-dependent apoptosis in PC12 cells. *Apoptosis*, 12(8), 1377-1387.

Breitbart, A. S., Eaton, C., & McCarthy, J. G. (1989). Crouzon's syndrome associated with acanthosis nigricans: ramifications for the craniofacial surgeon. *Annals of plastic surgery*, *22*(4), 310-315.

Brewer, J.R., Mazot, P., Soriano, P., 2016. Genetic insights into the mechanisms of Fgf signaling. *Genes Dev*. 30, 751–771.

Browaeys-Poly, E., Blanquart, C., Perdereau, D., Antoine, A. F., Goenaga, D., Luzy, J. P., ... & Burnol, A. F. (2010). Grb14 inhibits FGF receptor signaling through the regulation of PLCγ recruitment and activation. *FEBS letters*, *584*(21), 4383-4388.

Burgess, W. H., & Maciag, T. (1989). The heparin-binding (fibroblast) growth factor family of proteins. *Annual review of biochemistry*, *58*, 575–606.

Burke, D., Dishowitz, M., Sweetwyne, M., Miedel, E., Hankenson, K. D., & Kelly, D. J. (2013). The role of oxygen as a regulator of stem cell fate during fracture repair in TSP2-null mice. *Journal of Orthopaedic research*, *31*(10), 1585-1596.

Bush, J. R., Berube, N. G., & Beier, F. (2015). A new prescription for growth? Statins, cholesterol and cartilage homeostasis. *Osteoarthritis and cartilage*, *23*(4), 503-506.

Cady, R. J., & Durham, P. L. (2010). Cocoa-enriched diets enhance expression of phosphatases and decrease expression of inflammatory molecules in trigeminal ganglion neurons. *Brain research*, *1323*, 18-32.

Caplan, A. I. (1987). The cellular and molecular embryology of bone formation. *Bone Miner. Res.*, *5*, 117-183.

Catala M. (2019). Développement et croissance de la base du crâne [Development and growth of the skull base]. *Neuro-Chirurgie*, *65*(5), 216–220.

Catala, M., Khonsari, R. H., Paternoster, G., & Arnaud, É. (2019). Development and growth of the vault of the skull. *Neuro-Chirurgie*, *65*(5), 210-215.

Chai, Y., Jiang, X., Ito, Y., Bringas, P., Jr, Han, J., Rowitch, D. H., Soriano, P., McMahon, A. P., & Sucov, H. M. (2000). Fate of the mammalian cranial neural crest during tooth and mandibular morphogenesis. *Development (Cambridge, England)*, *127*(8), 1671–1679.

Chai, Y., Mah, A., Crohin, C., Groff, S., Bringas Jr, P., Le, T., ... & Slavkin, H. C. (1994). Specific transforming growth factor-β subtypes regulate embryonic mouse Meckel's cartilage and tooth development. *Developmental biology*, *162*(1), 85-103.

Chen, F., Degnin, C., Laederich, M., Horton, W. A., & Hristova, K. (2011). The A391E mutation enhances FGFR3 activation in the absence of ligand. *Biochimica et Biophysica Acta (BBA)-Biomembranes*, *1808*(8), 2045-2050.

Chen, F., Sarabipour, S., & Hristova, K. (2013). Multiple consequences of a single amino acid pathogenic RTK mutation: the A391E mutation in FGFR3. *PloS one*, *8*(2), e56521.

Chen, H., Sun, X., Yin, L., Chen, S., Zhu, Y., Huang, J., ... & Deng, Z. (2017). PTH 1-34 ameliorates the osteopenia and delayed healing of stabilized tibia fracture in mice with achondroplasia resulting from gain-of-function mutation of FGFR3. *International Journal of Biological Sciences*, *13*(10), 1254.

Chen, Y., & Struhl, G. (1996). Dual roles for patched in sequestering and transducing Hedgehog. *Cell*, *87*(3), 553–563.

Chen, Y., Whetstone, H. C., Lin, A. C., Nadesan, P., Wei, Q., Poon, R., & Alman, B. A. (2007). Beta-catenin signaling plays a disparate role in different phases of fracture repair: implications for therapy to improve bone healing. *PLoS medicine*, *4*(7), e249.

Chusho, H., Tamura, N., Ogawa, Y., Yasoda, A., Suda, M., Miyazawa, T., ... & Nakao, K. (2001). Dwarfism and early death in mice lacking C-type natriuretic peptide. *Proceedings of the National Academy of Sciences*, *98*(7), 4016-4021.

Ciurea, A. V., & Toader, C. (2009). Genetics of craniosynostosis: review of the literature. *Journal of medicine and life*, *2*(1), 5.

Cohen Jr, M. M. (1993). Pfeiffer syndrome update, clinical subtypes, and guidelines for differential diagnosis. *American journal of medical genetics*, *45*(3), 300-307.

Cohen Jr, M. M. (1999). Let's call it" Crouzonodermoskeletal syndrome" so we won't be prisoners of our own conventional terminology. *American journal of medical genetics*, *84*(1), 74.

Coi, A., Santoro, M., Garne, E., Pierini, A., Addor, M. C., Alessandri, J. L., ... & Barišić, I. (2019). Epidemiology of achondroplasia: A population-based study in Europe. *American journal of medical genetics Part A*, *179*(9), 1791-1798.

Coleman, S.J., Bruce, C., Chioni, A.-M., Kocher, H.M., Grose, R.P., 2014. The ins and outs of fibroblast growth factor receptor signalling. *Clinical Science,* 127, 217–231.

Collins, W. O., & Choi, S. S. (2007). Otolaryngologic manifestations of achondroplasia. *Archives of Otolaryngology–Head & Neck Surgery*, *133*(3), 237-244.

Colnot, C. (2009). Skeletal cell fate decisions within periosteum and bone marrow during bone regeneration. *Journal of Bone and Mineral Research*, *24*(2), 274-282.

Colnot, C., Thompson, Z., Miclau, T., Werb, Z., & Helms, J. A. (2003). Altered fracture repair in the absence of MMP9. *Development (Cambridge, England)*, *130*(17), 4123–4133.

Connerney, J., Andreeva, V., Leshem, Y., Muentener, C., Mercado, M. A., & Spicer, D. B. (2006). Twist1 dimer selection regulates cranial suture patterning and fusion. *Developmental dynamics: an official publication of the American Association of Anatomists*, *235*(5), 1334-1346.

Coquerelle, M., Prados-Frutos, J. C., Benazzi, S., Bookstein, F. L., Senck, S., Mitteroecker, P., & Weber, G. W. (2013). Infant growth patterns of the mandible in modern humans: a closer exploration of the developmental interactions between the symphyseal bone, the teeth, and the suprahyoid and tongue muscle insertion sites. *Journal of anatomy*, *222*(2), 178–192.

Cordero-Herrera, I., Martin, M. A., Fernández-Millán, E., Álvarez, C., Goya, L., & Ramos, S. (2015). Cocoa and cocoa flavanol epicatechin improve hepatic lipid metabolism in in vivo and in vitro models. Role of PKCζ. *Journal of functional foods*, *17*, 761-773.

Cornille, M., Moriceau, S., Khonsari, R. H., Heuzé, Y., Loisay, L., Boitez, V., ... & Legeai-Mallet, L. (2022). FGFR3 overactivation in the brain is responsible for memory impairments in Crouzon syndrome mouse model. *Journal of Experimental Medicine*, *219*(4), e20201879.

Couser, N. L., Pande, C. K., Turcott, C. M., Spector, E. B., Aylsworth, A. S., & Powell, C. M. (2017). Mild achondroplasia/hypochondroplasia with acanthosis nigricans, normal development, and a p. Ser348Cys FGFR3 mutation. *American Journal of Medical Genetics Part A*, *173*(4), 1097-1101.

Crossley, P. H., & Martin, G. R. (1995). The mouse Fgf8 gene encodes a family of polypeptides and is expressed in regions that direct outgrowth and patterning in the developing embryo. *Development*, *121*(2), 439-451.

Czubayko, F., Liaudet-Coopman, E. D., Aigner, A., Tuveson, A. T., Berchem, G. J., & Wellstein, A. (1997). A secreted FGF-binding protein can serve as the angiogenic switch in human cancer. *Nature medicine*, *3*(10), 1137-1140.

De Moerlooze, L., Spencer-Dene, B., Revest, J., Hajihosseini, M., Rosewell, I., & Dickson, C. (2000). An important role for the IIIb isoform of fibroblast growth factor receptor 2 (FGFR2) in mesenchymal-epithelial signalling during mouse organogenesis. *Development*, *127*(3), 483-492.

Deckelbaum, R. A., Holmes, G., Zhao, Z., Tong, C., Basilico, C., & Loomis, C. A. (2012). Regulation of cranial morphogenesis and cell fate at the neural crest-mesoderm boundary by engrailed 1. *Development*, *139*(7), 1346-1358.

Delashaw, J. B., Persing, J. A., Broaddus, W. C., & Jane, J. A. (1989). Cranial vault growth in craniosynostosis. *Journal of neurosurgery*, *70*(2), 159-165.

Delezoide, A. L., Benoist-Lasselin, C., Legeai-Mallet, L., Le Merrer, M., Munnich, A., Vekemans, M., & Bonaventure, J. (1998). Spatio-temporal expression of FGFR 1, 2 and 3 genes during human embryo-fetal ossification. *Mechanisms of development*, *77*(1), 19-30.

DeLise, A. Á., Fischer, L., & Tuan, R. S. (2000). Cellular interactions and signaling in cartilage development. *Osteoarthritis and cartilage*, *8*(5), 309-334.

Di Rocco, F., Biosse Duplan, M., Heuzé, Y., Kaci, N., Komla-Ebri, D., Munnich, A., ... & Legeai-Mallet, L. (2014). FGFR3 mutation causes abnormal membranous ossification in achondroplasia. *Human molecular genetics*, *23*(11), 2914-2925.

Dong, Y., Jesse, A. M., Kohn, A., Gunnell, L. M., Honjo, T., Zuscik, M. J., ... & Hilton, M. J. (2010). RBPjκ-dependent Notch signaling regulates mesenchymal progenitor cell proliferation and differentiation during skeletal development. *Development*, *137*(9), 1461-1471.

Du, X., Xie, Y., Xian, C. J., & Chen, L. (2012). Role of FGFs/FGFRs in skeletal development and bone regeneration. *Journal of cellular physiology*, *227*(12), 3731-3743.

Duan, D. S., Werner, S., & Williams, L. T. (1992). A naturally occurring secreted form of fibroblast growth factor (FGF) receptor 1 binds basic FGF in preference over acidic FGF. *Journal of Biological Chemistry*, *267*(23), 16076-16080.

Dudka, A. A., Sweet, S. M., & Heath, J. K. (2010). Signal Transducers and Activators of Transcription-3 Binding to the Fibroblast Growth Factor Receptor Is Activated by Receptor AmplificationSTAT3 Binds FGFR. *Cancer research*, *70*(8), 3391-3401.

Duvall, C. L., Taylor, W. R., Weiss, D., Wojtowicz, A. M., & Guldberg, R. E. (2007). Impaired angiogenesis, early callus formation, and late stage remodeling in fracture healing of osteopontin-deficient mice. *Journal of Bone and Mineral Research*, *22*(2), 286-297.

Dy, P., Wang, W., Bhattaram, P., Wang, Q., Wang, L., Ballock, R. T., & Lefebvre, V. (2012). Sox9 directs hypertrophic maturation and blocks osteoblast differentiation of growth plate chondrocytes. *Developmental cell*, *22*(3), 597-609.

Eames B. F., Sharpe P. T., Helms J. A. (2004). Hierarchy revealed in the specification of three skeletal fates by Sox9 and Runx2. *Dev. Biol.* 274 188–200.

Eames, B. F., Sharpe, P. T., & Helms, J. A. (2004). Hierarchy revealed in the specification of three skeletal fates by Sox9 and Runx2. *Developmental biology*, *274*(1), 188-200.

Ehrnthaller, C., Huber-Lang, M., Recknagel, S., Bindl, R., Redeker, S., Rapp, A., ... & Ignatius, A. (2013, April). The role of complement in bone healing: Fracture healing in C3 and C5-deficient mice. In *Orthopaedic Proceedings* (Vol. 95, No. SUPP_16, pp. 59-59). The British Editorial Society of Bone & Joint Surgery.

Einhorn, T. A. (1995). Enhancement of fracture-healing. *JBJS*, *77*(6), 940-956.

Elwood ET, Burstein FD, Graham L, Williams JK, Paschal M. Midface distraction to alleviate upper airway obstruction in achondroplastic dwarfs. *Cleft Palate Craniofac J*. 2003;40(1):100-103.

Eswarakumar, V. P., Monsonego-Ornan, E., Pines, M., Antonopoulou, I., Morriss-Kay, G. M., & Lonai, P. (2002). The IIIc alternative of Fgfr2 is a positive regulator of bone formation. *Development (Cambridge, England)*, *129*(16), 3783–3793.

Eswarakumar, V. P., Özcan, F., Lew, E. D., Bae, J. H., Tome, F., Booth, C. J., ... & Schlessinger, J. (2006). Attenuation of signaling pathways stimulated by pathologically activated FGF-receptor 2 mutants prevents craniosynostosis. *Proceedings of the National Academy of Sciences*, *103*(49), 18603-18608.

Fafílek, B., Hampl, M., Ricankova, N., Vesela, I., Bálek, L., Bosakova, M. K., ... & Krejci, P. (2017). Statins do not inhibit the FGFR signaling in chondrocytes. *Osteoarthritis and Cartilage*, *25*(9), 1522-1530.

Feng, X. (2005). RANKing intracellular signaling in osteoclasts. *IUBMB life*, *57*(6), 389-395.

Feng, X. H., & Derynck, R. (2005). Specificity and versatility in TGF-β signaling through Smads. *Annu. Rev. Cell Dev. Biol.*, *21*, 659-693.

Ferguson, H. R., Smith, M. P., & Francavilla, C. (2021). Fibroblast growth factor receptors (FGFRs) and noncanonical partners in cancer signaling. *Cells*, *10*(5), 1201.

Flynn, M. A., & Pauli, R. M. (2003). Double heterozygosity in bone growth disorders: four new observations and review. *American Journal of Medical Genetics Part A*, *121*(3), 193-208.

Frommer, J., & Margolies, M. R. (1971). Contribution of Meckel's cartilage to ossification of the mandible in mice. *Journal of dental research*, *50*(5), 1260–1267.

Fujita, T., Azuma, Y., Fukuyama, R., Hattori, Y., Yoshida, C., Koida, M., ... & Komori, T. (2004). Runx2 induces osteoblast and chondrocyte differentiation and enhances their migration by coupling with PI3K-Akt signaling. *The Journal of cell biology*, *166*(1), 85-95.

Funato, N. (2020). New Insights Into Cranial Synchondrosis Development: A Mini Review. Frontiers in Cell and Developmental Biology, 8.

G Gallagher, E. R., Ratisoontorn, C., & Cunningham, M. L. (2003). Saethre-Chotzen Syndrome. In M. P. Adam (Eds.) et. al., *GeneReviews*®. University of Washington, Seattle.

Galea, G. L., Zein, M. R., Allen, S., & Francis-West, P. (2021). Making and shaping endochondral and intramembranous bones. *Developmental dynamics: an official publication of the American Association of Anatomists*, *250*(3), 414–449.

Gambari, L., Grigolo, B., & Grassi, F. (2019). Hydrogen sulfide in bone tissue regeneration and repair: state of the art and new perspectives. *International Journal of Molecular Sciences*, *20*(20), 5231.

Garcia, S., Dirat, B., Tognacci, T., Rochet, N., Mouska, X., Bonnafous, S., ... & Gouze, E. (2013). Postnatal soluble FGFR3 therapy rescues achondroplasia symptoms and restores bone growth in mice. *Science translational medicine*, *5*(203), 203ra124-203ra124.

Gerber HP, Vu TH, Ryan AM, Kolwalski J, Werb Z, Ferrara N (1999) VEGF couples hypertrophic cartilage remodeling, ossification and angiogenesis during endochondral bone formation. Nat Med 5:623–628

Gerstenfeld, L. C., & Shapiro, F. D. (1996). Expression of bone-specific genes by hypertrophic chondrocytes: Implications of the complex functions of the hypertrophic chondrocyte during endochondral bone development. *Journal of cellular biochemistry*, *62*(1), 1-9.

Gerstenfeld, L. C., Cruceta, J., Shea, C. M., Sampath, K., Barnes, G. L., & Einhorn, T. A. (2002). Chondrocytes provide morphogenic signals that selectively induce osteogenic

differentiation of mesenchymal stem cells. *Journal of Bone and Mineral Research*, *17*(2), 221-230.

Gerstenfeld, L. C., Cullinane, D. M., Barnes, G. L., Graves, D. T., & Einhorn, T. A. (2003). Fracture healing as a post-natal developmental process: molecular, spatial, and temporal aspects of its regulation. *Journal of cellular biochemistry*, *88*(5), 873-884.

Gibbs, L., & Legeai-Mallet, L. (2007). FGFR3 intracellular mutations induce tyrosine phosphorylation in the Golgi and defective glycosylation. *Biochimica et Biophysica Acta (BBA)-Molecular Cell Research*, *1773*(4), 502-512.

Glaser, R. L., Jiang, W., Boyadjiev, S. A., Tran, A. K., Zachary, A. A., Van Maldergem, L., ... & Jabs, E. W. (2000). Paternal origin of FGFR2 mutations in sporadic cases of Crouzon syndrome and Pfeiffer syndrome. *The American Journal of Human Genetics*, *66*(3), 768-777.

Goetz R, Mohammadi M. Exploring mechanisms of FGF signalling through the lens of structural biology. *Nat Rev Mol Cell Biol*. 2013;14(3):166-180. doi:10.1038/nrm3528

Goetz, R., Beenken, A., Ibrahimi, O. A., Kalinina, J., Olsen, S. K., Eliseenkova, A. V., ... & Mohammadi, M. (2007). Molecular insights into the klotho-dependent, endocrine mode of action of fibroblast growth factor 19 subfamily members. *Molecular and cellular biology*, 27(9), 3417-3428.

Goetz, R., Nakada, Y., Hu, M. C., Kurosu, H., Wang, L., Nakatani, T., ... & Mohammadi, M. (2010). Isolated C-terminal tail of FGF23 alleviates hypophosphatemia by inhibiting FGF23-FGFR-Klotho complex formation. *Proceedings of the National Academy of Sciences*, *107*(1), 407-412.

Goldfarb, M., Schoorlemmer, J., Williams, A., Diwakar, S., Wang, Q., Huang, X., ... & D'Angelo, E. (2007). Fibroblast growth factor homologous factors control neuronal excitability through modulation of voltage-gated sodium channels. *Neuron*, *55*(3), 449-463.

Goldstein, J. A., Paliga, J. T., Wink, J. D., Bartlett, S. P., Nah, H. D., & Taylor, J. A. (2014). Earlier evidence of spheno-occipital synchondrosis fusion correlates with severity of midface hypoplasia in patients with syndromic craniosynostosis. *Plastic and reconstructive surgery*, *134*(3), 504–510.

Gómez-Barrena, E., Rosset, P., Lozano, D., Stanovici, J., Ermthaller, C., & Gerbhard, F. (2015). Bone fracture healing: cell therapy in delayed unions and nonunions. *Bone*, *70*, 93-101.

Gordon, S., & Martinez, F. O. (2010). Alternative activation of macrophages: mechanism and functions. *Immunity*, *32*(5), 593-604.

Goriely, A., & Wilkie, A. O. (2012). Paternal age effect mutations and selfish spermatogonial selection: causes and consequences for human disease. *The American Journal of Human Genetics*, *90*(2), 175-200.

Gorlin, R. J. (1997). Fibroblast growth factors, their receptors and receptor disorders. *Journal of Cranio-Maxillofacial Surgery*, *25*(2), 69-79.

Gorry, M. C., Preston, R. A., White, G. J., Zhang, Y., Singhal, V. K., Losken, H. W., ... & Ehrlich, G. D. (1995). Crouzon syndrome: mutations in two spliceoforms of FGFR2 and a common point mutation shared with Jackson—Weiss syndrome. *Human molecular genetics*, *4*(8), 1387-1390.

Hadari, Y., Kouhara, H., Lax, I., & Schlessinger, J. (1998). Binding of Shp2 tyrosine phosphatase to FRS2 is essential for fibroblast growth factor-induced PC12 cell differentiation. *Molecular and cellular biology*, *18*(7), 3966-3973.

Hagiwara, Y., Dyment, N. A., Jiang, X., Jiang Ping, H., Ackert-Bicknell, C., Adams, D. J., & Rowe, D. W. (2015). Fixation stability dictates the differentiation pathway of periosteal progenitor cells in fracture repair. *Journal of orthopaedic research*: official publication of the Orthopaedic Research Society, 33(7), 948–956. https://doi.org/10.1002/jor.22816

Hajihosseini, M. K., Duarte, R., Pegrum, J., Donjacour, A., Lana-Elola, E., Rice, D. P., ... & Dickson, C. (2009). Evidence that Fgf10 contributes to the skeletal and visceral defects of an Apert syndrome mouse model. *Developmental Dynamics*, *238*(2), 376-385.

Hall, B. D., & Spranger, J. (1979). Hypochondroplasia: clinical and radiological aspects in 39 cases. *Radiology*, *133*(1), 95-100.

Hamamoto, J., Yasuda, H., Nonaka, Y., Fujiwara, M., Nakamura, Y., Soejima, K., & Betsuyaku, T. (2018). The FGF2 aptamer inhibits the growth of FGF2-FGFR pathway driven lung cancer cells. *Biochemical and biophysical research communications*, *503*(3), 1330-1334.

Han, Y., & Lefebvre, V. (2008). L-Sox5 and Sox6 drive expression of the aggrecan gene in cartilage by securing binding of Sox9 to a far-upstream enhancer. *Molecular and cellular biology*, *28*(16), 4999–5013.

Hannema, S. E., Van Duyvenvoorde, H. A., Premsler, T., Yang, R. B., Mueller, T. D., Gassner, B., ... & Wit, J. M. (2013). An activating mutation in the kinase homology domain of the natriuretic peptide receptor-2 causes extremely tall stature without skeletal deformities. *The Journal of Clinical Endocrinology & Metabolism*, *98*(12), E1988-E1998.

Haque, T., Amako, M., Nakada, S., Lauzier, D., & Hamdy, R. C. (2007). An immunohistochemical analysis of the temporal and spatial expression of growth factors FGF 1, 2 and 18, IGF 1 and 2, and TGFß1 during distraction osteogenesis. *Histology and histopathology*.

Harada Y., Ishizeki K. (1998). Evidence for transformation of chondrocytes and site-specific resorption during the degradation of Meckel's cartilage. *Anat. Embryol.* 197 439–450.

Harada, M., Murakami, H., Okawa, A., Okimoto, N., Hiraoka, S., Nakahara, T., ... & Koseki, H. (2009). FGF9 monomer–dimer equilibrium regulates extracellular matrix affinity and tissue diffusion. *Nature genetics*, *41*(3), 289-298.

Haseeb, A., Kc, R., Angelozzi, M., de Charleroy, C., Rux, D., Tower, R. J., Yao, L., Pellegrino da Silva, R., Pacifici, M., Qin, L., & Lefebvre, V. (2021). SOX9 keeps growth plates and articular cartilage healthy by inhibiting chondrocyte dedifferentiation/osteoblastic

redifferentiation. *Proceedings of the National Academy of Sciences of the United States of America*, *118*(8), e2019152118.

Hasegawa, K., & Tanaka, H. (2014). Children with short-limbed short stature in pediatric endocrinological services in J apan. *Pediatrics International*, *56*(6), 809-812.

Hattori, T., Müller, C., Gebhard, S., Bauer, E., Pausch, F., Schlund, B., ... & Von Der Mark, K. (2010). SOX9 is a major negative regulator of cartilage vascularization, bone marrow formation and endochondral ossification. *Development*, *137*(6), 901-911.

Havens, B. A., Velonis, D., Kronenberg, M. S., Lichtler, A. C., Oliver, B., & Mina, M. (2008). Roles of FGFR3 during morphogenesis of Meckel's cartilage and mandibular bones. *Developmental biology*, *316*(2), 336-349.

He G., Tavella S., Hanley K. P., Self M., Oliver G., Grifone R., et al. (2010). Inactivation of Six2 in mouse identifies a novel genetic mechanism controlling development and growth of the cranial base. *Dev. Biol.* 344 720–730.

He, L., Shobnam, N., Wimley, W. C., & Hristova, K. (2011). FGFR3 heterodimerization in achondroplasia, the most common form of human dwarfism. *Journal of Biological Chemistry*, *286*(15), 13272-13281.

Heuertz, S., Le Merrer, M., Zabel, B., Wright, M., Legeai-Mallet, L., Cormier-Daire, V., ... & Bonaventure, J. (2006). Novel FGFR3 mutations creating cysteine residues in the extracellular domain of the receptor cause achondroplasia or severe forms of hypochondroplasia. *European Journal of Human Genetics*, *14*(12), 1240-1247.

Hinton, R. J., Jing, Y., Jing, J., & Feng, J. Q. (2017). Roles of chondrocytes in endochondral bone formation and fracture repair. *Journal of dental research*, *96*(1), 23-30.

Hiraki, S. I., Nakamura, I., Okazaki, H., Nakamura, K., & Kurokawa, T. (2006). Skin behavior during leg lengthening in patients with achondroplasia and hypochondroplasia: a short-term observation during leg lengthening. *Journal of Orthopaedic Science*, *11*(3), 267-271.

Hollway, G.E., Suthers, G.K., Battese, K.M., Turner, A.M., David, D.J., Mulley, J.C., 1998. Deafness due to Pro250Arg mutation of FGFR3. The Lancet 351, 877–878. https://doi.org/10.1016/S0140- 6736(98)24012-8.

Holmes, G., Zhang, L., Rivera, J., Murphy, R., Assouline, C., Sullivan, L., ... & Jabs, E. W. (2018). C-type natriuretic peptide analog treatment of craniosynostosis in a Crouzon syndrome mouse model. *Plos one*, *13*(7), e0201492.

Holzman, R. S., Mancuso, T. J., & Polaner, D. M. (2008). A Practical Approach to Pediatric Anesthesia. 1st Edition. Philadelphia, USA: Lippincott Williams and Wilkins.

Hoover-Fong, J. E., Schulze, K. J., Alade, A. Y., Bober, M. B., Gough, E., Hashmi, S. S., ... & McGready, J. (2021). Growth in achondroplasia including stature, weight, weight-for-height and head circumference from CLARITY: achondroplasia natural history study—a multi-center retrospective cohort study of achondroplasia in the US. *Orphanet journal of rare diseases*, *16*(1), 1-19.

Horton, W. A., Hall, J. G., & Hecht, J. T. (2007). Achondroplasia. *The Lancet*, *370*(9582), 162-172.

Hsu, Y. R. et al. Human keratinocyte growth factor recombinantly expressed in Chinese hamster ovary cells: isolation of isoforms and characterization of post-translational modifications. *Protein Expr. Purif.* **12**, 189–200 (1998).

Hu K, Olsen BR. Osteoblast-derived VEGF regulates osteoblast differentiation and bone formation during bone repair. J Clin Invest. 2016 Feb;126(2):509-26.

Hu, D. P., Ferro, F., Yang, F., Taylor, A. J., Chang, W., Miclau, T., ... & Bahney, C. S. (2017). Cartilage to bone transformation during fracture healing is coordinated by the invading vasculature and induction of the core pluripotency genes. *Development*, *144*(2), 221-234.

Huangfu D., Liu A., Rakeman A. S., Murcia N. S., Niswander L., Anderson K. V. (2003). Hedgehog signalling in the mouse requires intraflagellar transport proteins. *Nature* 426 83–87.

Huet, T., Cohen-Solal, M., Laredo, J. D., Collet, C., Baujat, G., Cormier-Daire, V., ... & Beaudreuil, J. (2020). Lumbar spinal stenosis and disc alterations affect the upper lumbar spine in adults with achondroplasia. *Scientific Reports*, *10*(1), 1-7.

Hunt, P., Wilkinson, D., & Krumlauf, R. (1991). Patterning the vertebrate head: murine Hox 2 genes mark distinct subpopulations of premigratory and migrating cranial neural crest. *Development (Cambridge, England)*, *112*(1), 43–50.

Hurley, M. M., Adams, D. J., Wang, L., Jiang, X., Burt, P. M., Du, E., & Xiao, L. (2016). Accelerated fracture healing in transgenic mice overexpressing an anabolic isoform of fibroblast growth factor 2. *Journal of Cellular Biochemistry*, *117*(3), 599-611.

Hyland, V. J., Robertson, S. P., Flanagan, S., Savarirayan, R., Roscioli, T., Masel, J., ... & Glass, I. A. (2003). Somatic and germline mosaicism for a R248C missense mutation in FGFR3, resulting in a skeletal dysplasia distinct from thanatophoric dysplasia. *American Journal of Medical Genetics Part A*, *120*(2), 157-168.

Ibrahimi, O. A., Zhang, F., Eliseenkova, A. V., Linhardt, R. J., & Mohammadi, M. (2004). Proline to arginine mutations in FGF receptors 1 and 3 result in Pfeiffer and Muenke craniosynostosis syndromes through enhancement of FGF binding affinity. *Human molecular genetics*, *13*(1), 69-78.

Ilizarov, G. A. (1969). Some clinical and experimental data concerning lengthening of lower extremities. *Exp Khir Arrestar*, *14*, 27.

Ilizarov, G. A., & Ledyaev, V. I. (1992). The replacement of long tubular bone defects by lengthening distraction osteotomy of one of the fragments. *Clinical Orthopaedics and Related Research (1976-2007)*, *280*, 7-10.

Iseki, S., Wilkie, A. O., & Morriss-Kay, G. M. (1999). Fgfr1 and Fgfr2 have distinct differentiation-and proliferation-related roles in the developing mouse skull vault. *Development*, *126*(24), 5611-5620.

Ishizeki K. (2012). Imaging analysis of osteogenic transformation of Meckel's chondrocytes from green fluorescent protein-transgenic mice during intrasplenic transplantation. *Acta Histochem.* 114 608–619.

Ishizeki K., Kagiya T., Fujiwara N., Otsu K., Harada H. (2009). Expression of osteogenic proteins during the intrasplenic transplantation of Meckel's chondrocytes: a histochemical and immunohistochemical study. *Arch. Histol. Cytol.* 72 1–12.

Ishizeki K., Nawa T., Takigawa M., Suzuki F. (1996). Mouse Meckel's cartilage chondrocytes evoke bone-like matrix and further transform into osteocyte-like cells in culture. *Anat. Rec.* 245 25–35.

Ishizeki K., Saito H., Shinagawa T., Fujiwara N., Nawa T. (1999). Histochemical and immunohistochemical analysis of the mechanism of calcification of Meckel's cartilage during mandible development in rodents. *J. Anat.* 194 265–277.

Ito, Y., Bringas Jr, P., Mogharei, A., Zhao, J., Deng, C., & Chai, Y. (2002). Receptor-regulated and inhibitory Smads are critical in regulating transforming growth factorβ–mediated Meckel's cartilage development. *Developmental dynamics: an official publication of the American Association of Anatomists*, *224*(1), 69-78.

Itoh, K., Pooh, R., Kanemura, Y., Yamasaki, M., & Fushiki, S. (2013). Brain malformation with loss of normal FGFR3 expression in thanatophoric dysplasia type I. *Neuropathology*, *33*(6), 663-666.

Jackson CE, Weiss L, Reynolds WA, Forman TF, Peterson JA. 1976. Craniosynostosis midface hypoplasia, and foot abnormalities: an autosomal dominant phenotype in a large Amish kindred. *J Pediatr* 88: 963–968.

Jang, S., Sun, J., Chen, P., Lakshman, S., Molokin, A., Harnly, J. M., ... & Solano-Aguilar, G. (2015). Flavanol-enriched cocoa powder alters the intestinal microbiota, tissue and fluid metabolite profiles, and intestinal gene expression in pigs. *The Journal of nutrition*, *146*(4), 673-680.

Jaye, M., Schlessinger, J., & Dionne, C. A. (1992). Fibroblast growth factor receptor tyrosine kinases: molecular analysis and signal transduction. *Biochimica et Biophysica Acta (BBA)-Molecular Cell Research*, *1135*(2), 185-199.

Jiang, X., Iseki, S., Maxson, R. E., Sucov, H. M., & Morriss-Kay, G. M. (2002). Tissue origins and interactions in the mammalian skull vault. *Developmental biology*, *241*(1), 106-116.

Jin, L., Nonaka, Y., Miyakawa, S., Fujiwara, M., & Nakamura, Y. (2016). Dual therapeutic action of a neutralizing anti-FGF2 aptamer in bone disease and bone cancer pain. *Molecular Therapy*, *24*(11), 1974-1986.

Johnson, D. E., & Williams, L. T. (1992). Structural and functional diversity in the FGF receptor multigene family. *Advances in cancer research*, *60*, 1-41.

Johnson, D., & Wilkie, A. O. (2011). Craniosynostosis. *European Journal of Human Genetics*, *19*(4), 369-376.

Johnson, D., Iseki, S., Wilkie, A. O. M., & Morriss-Kay, G. M. (2000). Expression patterns of Twist and Fgfr1,-2 and-3 in the developing mouse coronal suture suggest a key role for twist in suture initiation and biogenesis. *Mechanisms of development*, *91*(1-2), 341-345.

Jonquoy, A., Mugniery, E., Benoist-Lasselin, C., Kaci, N., Le Corre, L., Barbault, F., ... & Legeai-Mallet, L. (2012). A novel tyrosine kinase inhibitor restores chondrocyte differentiation and promotes bone growth in a gain-of-function Fgfr3 mouse model. *Human molecular genetics*, *21*(4), 841-851.

Julien, A., Perrin, S., de Lageneste, O. D., Carvalho, C., Bensidhoum, M., Legeai-Mallet, L., & Colnot, C. (2020). FGFR3 in periosteal cells drives cartilage-to-bone transformation in bone repair. *Stem cell reports*, *15*(4), 955-967.

Julliand, S., Boulé, M., Baujat, G., Ramirez, A., Couloigner, V., Beydon, N., ... & Fauroux, B. (2012). Lung function, diagnosis, and treatment of sleep-disordered breathing in children with achondroplasia. *American journal of medical genetics Part A*, *158*(8), 1987-1993.

Kajdic, N., Spazzapan, P., & Velnar, T. (2018). Craniosynostosis-Recognition, clinical characteristics, and treatment. *Bosnian journal of basic medical sciences*, *18*(2), 110.

Kalinina, J., Dutta, K., Ilghari, D., Beenken, A., Goetz, R., Eliseenkova, A.V., Cowburn, D., Mohammadi, M., 2012. The alternatively spliced acid box region plays a key role in FGF receptor autoinhibition. *Structure* 20, 77–88.

Kan, R., Twigg, S. R. F., Berg, J., Wang, L., Jin, F., & Wilkie, A. O. M. (2004). Expression analysis of an FGFR2 IIIc 5′ splice site mutation (1084+ 3A→ G). *Journal of medical genetics*, *41*(8), e108-e108.

Kantomaa, T., Yuominen, M., Pirttiniemi, P., & Rönning, O. (1992). Weaning and the histology of the mandibular condyle in the rat. *Cells Tissues Organs*, *144*(4), 311-315.

Kashanian, A., Stadler, J. A., & Danielpour, M. (2022). Neurosurgical Evaluation and Management of Children with Achondroplasia. *Neurosurgery Clinics*, *33*(1), 17-23.

Kaucka, M., Zikmund, T., Tesarova, M., Gyllborg, D., Hellander, A., Jaros, J., Kaiser, J., Petersen, J., Szarowska, B., Newton, P. T., Dyachuk, V., Li, L., Qian, H., Johansson, A. S., Mishina, Y., Currie, J. D., Tanaka, E. M., Erickson, A., Dudley, A., Brismar, H., … Adameyko, I. (2017). Oriented clonal cell dynamics enables accurate growth and shaping of vertebrate cartilage. *eLife*, *6*, e25902.

Khonsari RH, Haber S, Paternoster G, et al. The influence of fronto-facial monobloc advancement on obstructive sleep apnea: An assessment of 109 syndromic craniosynostoses cases. *J Craniomaxillofac Surg*. 2020;48(6):536-547.

Khonsari, R. H. (2013). *Mechanical forces in craniofacial development and growth* (Doctoral dissertation, King's College London).

Khonsari, R. H., Way, B., Nysjö, J., Odri, G. A., Olszewski, R., Evans, R. D., ... & Britto, J. A. (2016). Fronto-facial advancement and bipartition in Crouzon–Pfeiffer and Apert syndromes:

Impact of fronto-facial surgery upon orbital and airway parameters in FGFR2 syndromes. *Journal of Cranio-Maxillofacial Surgery*, *44*(10), 1567-1575.

Kılıçoğlu, H., Öğütlü, N. Y., & Uludağ, C. A. (2017). Evaluation of skeletal and dental effects of modified jasper jumper appliance and delaire face mask with pancherz analysis. *Turkish Journal of Orthodontics*, *30*(1), 6.

Kim, G. Y., Kim, H. Y., Kim, H. T., Moon, J. M., Kim, C. H., Kang, S., & Rhim, H. (2012). HtrA1 is a novel antagonist controlling fibroblast growth factor (FGF) signaling via cleavage of FGF8. *Molecular and cellular biology*, *32*(21), 4482-4492.

Kitaori, T., Ito, H., Schwarz, E. M., Tsutsumi, R., Yoshitomi, H., Oishi, S., ... & Nakamura, T. (2009). Stromal cell–derived factor 1/CXCR4 signaling is critical for the recruitment of mesenchymal stem cells to the fracture site during skeletal repair in a mouse model. *Arthritis & Rheumatism: Official Journal of the American College of Rheumatology*, *60*(3), 813-823.

Kitoh, H., Kitakoji, T., Tsuchiya, H., Katoh, M., & Ishiguro, N. (2007). Distraction osteogenesis of the lower extremity in patients with achondroplasia/hypochondroplasia treated with transplantation of culture-expanded bone marrow cells and platelet-rich plasma. *Journal of Pediatric Orthopaedics*, *27*(6), 629-634.

Kitoh, H., Matsushita, M., Mishima, K., Nagata, T., Kamiya, Y., Ueda, K., ... & Ishiguro, N. (2020). Pharmacokinetics and safety after once and twice a day doses of meclizine hydrochloride administered to children with achondroplasia. *PloS one*, *15*(4), e0229639.

Kitoh, H., Mishima, K., Matsushita, M., Nishida, Y., & Ishiguro, N. (2014). Early and late fracture following extensive limb lengthening in patients with achondroplasia and hypochondroplasia. *The Bone & Joint Journal*, *96*(9), 1269-1273.

Ko, J. M. (2016). Genetic syndromes associated with craniosynostosis. *Journal of Korean Neurosurgical Society*, *59*(3), 187-191.

Ko, K. R., Shim, J. S., Chung, C. H., & Kim, J. H. (2019). Surgical results of limb lengthening at the femur, tibia, and humerus in patients with achondroplasia. *Clinics in orthopedic surgery*, *11*(2), 226-232.

Komatsu DE, Hadjiargyrou M. Activation of the transcription factor HIF-1 and its target genes, VEGF, HO-1, iNOS, during fracture repair. *Bone*. 2004;34(4):680-688.

Komla-Ebri, D., Dambroise, E., Kramer, I., Benoist-Lasselin, C., Kaci, N., Le Gall, C., ... & Legeai-Mallet, L. (2016). Tyrosine kinase inhibitor NVP-BGJ398 functionally improves FGFR3-related dwarfism in mouse model. *The Journal of clinical investigation*, *126*(5), 1871-1884.

Kouhara, H., Hadari, Y., SpivakKroizman, T., Schilling, J., BarSagi, D., Lax, I., and Schlessinger, J. (1997). A lipid-anchored Grb2-binding protein that links FGFreceptor activation to the Ras/MAPK signaling pathway. *Cell* 89, 693-702.

Kovtun, A., Bergdolt, S., Hägele, Y., Matthes, R., Lambris, J. D., Huber-Lang, M., & Ignatius, A. (2017). Complement receptors C5aR1 and C5aR2 act differentially during the early immune

response after bone fracture but are similarly involved in bone repair. *Scientific reports*, *7*(1), 1-12.

Koyama E., Young B., Nagayama M., Shibukawa Y., Enomoto-iwamoto M., Iwamoto M., et al. (2007). Conditional Kif3a ablation causes abnormal hedgehog signaling topography, growth plate dysfunction, and excessive bone and cartilage formation during mouse skeletogenesis. *Development* 2169 2159–2169.

Kozhemyakina E., Cohen T., Yao T. P., Lassar A. B. (2009). Parathyroid hormone-related peptide represses chondrocyte hypertrophy through a protein phosphatase 2A/histone deacetylase 4/MEF2 Pathway. *Mol. Cell. Biol.* 29 5751–5762.

Kreiborg, S., & Cohen, M. M., Jr (1990). Characteristics of the infant Apert skull and its subsequent development. *Journal of craniofacial genetics and developmental biology*, *10*(4), 399–410.

Kreiborg, S., Barr Jr, M., & Cohen Jr, M. M. (1992). Cervical spine in the Apert syndrome. *American journal of medical genetics*, *43*(4), 704-708.

Krejci, P., Aklian, A., Kaucka, M., Sevcikova, E., Prochazkova, J., Masek, J. K., ... & Balek, L. (2012). Receptor tyrosine kinases activate canonical WNT/β-catenin signaling via MAP kinase/LRP6 pathway and direct β-catenin phosphorylation. *PloS one*, 7(4), e35826.

Krejci, P., Salazar, L., Kashiwada, T. A., Chlebova, K., Salasova, A., Thompson, L. M., ... & Wilcox, W. R. (2008). Analysis of STAT1 activation by six FGFR3 mutants associated with skeletal dysplasia undermines dominant role of STAT1 in FGFR3 signaling in cartilage. *PloS one*, *3*(12), e3961.

Kruszka, P., Addissie, Y. A., Yarnell, C. M., Hadley, D. W., Guillen Sacoto, M. J., Platte, P., ... & Muenke, M. (2016). Muenke syndrome: An international multicenter natural history study. *American Journal of Medical Genetics Part A*, *170*(4), 918-929.

Kruszka, P., Addissie, Y.A., Agochukwu, N.B., Doherty, E.S., Muenke, M., 1993. Muenke Syndrome, in: Adam, M.P., Ardinger, H.H., Pagon, R.A., Wallace, S.E., Bean, L.J., Stephens, K., Amemiya, A. (Eds.), GeneReviews®. University of Washington, Seattle, Seattle (WA).

Kunova Bosakova, M., Varecha, M., Hampl, M., Duran, I., Nita, A., Buchtova, M., ... & Krejci, P. (2018). Regulation of ciliary function by fibroblast growth factor signaling identifies FGFR3-related disorders achondroplasia and thanatophoric dysplasia as ciliopathies. *Human molecular genetics*, *27*(6), 1093-1105.

Kurosu, H., Choi, M., Ogawa, Y., Dickson, A. S., Goetz, R., Eliseenkova, A. V., ... & Kuro-o, M. (2007). Tissue-specific expression of βKlotho and fibroblast growth factor (FGF) receptor isoforms determines metabolic activity of FGF19 and FGF21. *Journal of Biological Chemistry*, *282*(37), 26687-26695.

Kurosu, H., Ogawa, Y., Miyoshi, M., Yamamoto, M., Nandi, A., Rosenblatt, K.P., Baum, M.G., Schiavi, S., Hu, M.-C., Moe, O.W., Kuro-o, M., 2006. Regulation of fibroblast growth factor-23 signaling by klotho. *J. Biol. Chem.* 281, 6120–6123.

Lajeunie, E., Merrer, M. L., Bonaïti-Pellie, C., Marchac, D., & Renier, D. (1995). Genetic study of nonsyndromic coronal craniosynostosis. *American journal of medical genetics*, *55*(4), 500-504.

Lamothe, B., Yamada, M., Schaeper, U., Birchmeier, C., Lax, I., & Schlessinger, J. (2004). The docking protein Gab1 is an essential component of an indirect mechanism for FGF stimulation of the PI 3-kinase/Akt anti-apoptotic pathway. *Mol Cell Biol*, *24*, 5657-5666.

Lana-Elola, E., Rice, R., Grigoriadis, A. E., & Rice, D. P. (2007). Cell fate specification during calvarial bone and suture development. *Developmental biology*, *311*(2), 335-346.

Lanske B., Karaplis A. C., Lee K., Luz A., Vortkamp A., Pirro A., et al. (1996). PTH/PTHrP receptor in early development and indian hedgehog-regulated bone growth. *Science* 273 663–666.

Larsen, W. J., Sherman, L. S., Potter, S. S., & Scott, W. J. (2001). *Human embryology*. Elsevier España.

Lattanzi, W., Barba, M., Di Pietro, L., & Boyadjiev, S. A. (2017). Genetic advances in craniosynostosis. *American journal of medical genetics Part A*, *173*(5), 1406-1429.

Laurita, J., Koyama, E., Chin, B., Taylor, J. A., Lakin, G. E., Hankenson, K. D., ... & Nah, H. D. (2011). The Muenke syndrome mutation (FgfR3P244R) causes cranial base shortening associated with growth plate dysfunction and premature perichondrial ossification in murine basicranial synchondroses. *Developmental Dynamics*, *240*(11), 2584-2596.

Le Douarin, N. M., & Dupin, E. (1993). Cell lineage analysis in neural crest ontogeny. *Journal of neurobiology*, *24*(2), 146–161.

Le, A. X., Miclau, T., Hu, D., & Helms, J. A. (2001). Molecular aspects of healing in stabilized and non-stabilized fractures. *Journal of orthopaedic research : official publication of the Orthopaedic Research Society*, *19*(1), 78–84.

Lee, K., Deeds, J. D., & Segre, G. V. (1995). Expression of parathyroid hormone-related peptide and its receptor messenger ribonucleic acids during fetal development of rats. Endocrinology, 136(2), 453–463.

Legeai-Mallet, L., & Savarirayan, R. (2020). Novel therapeutic approaches for the treatment of achondroplasia. *Bone*, *141*, 115579.

Legeai-Mallet, L., Benoist-Lasselin, C., Munnich, A., Bonaventure, J., 2004. Overexpression of FGFR3, Stat1, Stat5 and p21Cip1 correlates with phenotypic severity and defective chondrocyte differentiation in FGFR3-related chondrodysplasias. *Bone* 34, 26–36.

Lesciotto, K. M., & Richtsmeier, J. T. (2019). Craniofacial skeletal response to encephalization: How do we know what we think we know?. *American journal of physical anthropology*, *168*, 27-46.

Li T. F., Dong Y., Ionescu A. M., Rosier R. N., Zuscik M. J., Schwarz E. M., et al. (2004). Parathyroid hormone-related peptide (PTHrP) inhibits Runx2 expression through the PKA signaling pathway. *Exp. Cell Res.* 299 128–136.

Li, C., Chen, L., Iwata, T., Kitagawa, M., Fu, X.Y., Deng, C.X., 1999. A Lys644Glu substitution in fibroblast growth factor receptor 3 (FGFR3) causes dwarfism in mice by activation of STATs and ink4 cell cycle inhibitors. *Hum. Mol. Genet*. 8, 35–44.

Li, E., You, M., & Hristova, K. (2006). FGFR3 dimer stabilization due to a single amino acid pathogenic mutation. *Journal of molecular biology*, *356*(3), 600-612.

Lian C, Wang X, Qiu X, et al. Collagen type II suppresses articular chondrocyte hypertrophy and osteoarthritis progression by promoting integrin β1-SMAD1 interaction. *Bone Res*. 2019;7:8. Published 2019 Mar 6.

Liu, X., Miramini, S., Patel, M., Liao, J., Shidid, D., & Zhang, L. (2021). Balance Between Mechanical Stability and Mechano-Biology of Fracture Healing Under Volar Locking Plate. *Annals of Biomedical Engineering*, *49*(9), 2533-2553.

Liu, Z., Xu, J., Colvin, J. S., & Ornitz, D. M. (2002). Coordination of chondrogenesis and osteogenesis by fibroblast growth factor 18. *Genes & development*, *16*(7), 859-869.

Long, F., & Ornitz, D. M. (2013). Development of the endochondral skeleton. *Cold Spring Harbor perspectives in biology*, *5*(1), a008334.

Long, F., 2012. Building strong bones: molecular regulation of the osteoblast lineage. *Nat Rev Mol Cell Biol* 13, 27–38.

Lorget, F., Kaci, N., Peng, J., Benoist-Lasselin, C., Mugniery, E., Oppeneer, T., ... & Legeai-Mallet, L. (2012). Evaluation of the therapeutic potential of a CNP analog in a Fgfr3 mouse model recapitulating achondroplasia. *The American Journal of Human Genetics*, *91*(6), 1108-1114.

Lu, X., Forte, A. J., Steinbacher, D. M., Alperovich, M., Alonso, N., & Persing, J. A. (2019). Enlarged anterior cranial fossa and restricted posterior cranial fossa, the disproportionate growth of basicranium in Crouzon syndrome. *Journal of Cranio-Maxillofacial Surgery*, *47*(9), 1426-1435.

Luder, H. U., Leblond, C. P., & Von Der Mark, K. (1988). Cellular stages in cartilage formation as revealed by morphometry, radioautography and type II collagen immunostaining of the mandibular condyle from weanling rats. *American Journal of Anatomy*, *182*(3), 197-214.

Madeline, L. A., & Elster, A. D. (1995). Suture closure in the human chondrocranium: CT assessment. *Radiology*, *196*(3), 747-756.

Maes, C., Coenegrachts, L., Stockmans, I., Daci, E., Luttun, A., Petryk, A., ... & Carmeliet, G. (2006). Placental growth factor mediates mesenchymal cell development, cartilage turnover, and bone remodeling during fracture repair. *The Journal of clinical investigation*, *116*(5), 1230-1242.

Maes, C., Kobayashi, T., Selig, M. K., Torrekens, S., Roth, S. I., Mackem, S., ... & Kronenberg, H. M. (2010). Osteoblast precursors, but not mature osteoblasts, move into developing and fractured bones along with invading blood vessels. *Developmental cell*, *19*(2), 329-344.

Makrythanasis, P., Temtamy, S., Aglan, M. S., Otaify, G. A., Hamamy, H., & Antonarakis, S. E. (2014). A Novel Homozygous Mutation in FGFR 3 Causes Tall Stature, Severe Lateral Tibial Deviation, Scoliosis, Hearing Impairment, Camptodactyly, and Arachnodactyly. *Human mutation*, *35*(8), 959-963.

Mallat J. (2008). The evolution of the vertebrate Jaw: neoclassical ideas verses newer, development-based ideas. *Zool. Sci.* 25 990–998.

Manning, B.D., Cantley, L.C., 2007. AKT/PKB Signaling: Navigating Downstream. *Cell* 129, 1261–1274.

Mantilla-Capacho, J. M., Arnaud, L., Diaz-Rodriguez, M., & Barros-Nunez, P. (2005). Apert syndrome with preaxial polydactyly showing the typical mutation Ser252Trp in the FGFR2 gene. *Genetic Counseling (Geneva, Switzerland)*, *16*(4), 403-406.

Marie P. J. (2008). Transcription factors controlling osteoblastogenesis. *Archives of biochemistry and biophysics*, *473*(2), 98–105.

Maroteaux, P., & Falzon, P. (1988). Hypochondroplasie. Revue de 80 cas [Hypochondroplasia. Review of 80 cases]. *Archives francaises de pediatrie*, *45*(2), 105–109.

Maroteaux, P., Lamy, M., & Robert, J. M. (1967). Le nanisme thanatophore [Thanatophoric dwarfism]. *La Presse medicale*, *75*(49), 2519–2524.

Marsell, R., & Einhorn, T. A. (2009). The role of endogenous bone morphogenetic proteins in normal skeletal repair. *Injury*, *40*, S4-S7.

Martin, L., Kaci, N., Benoist-Lasselin, C., Mondoloni, M., Decaudaveine, S., Estibals, V., ... & Legeai-Mallet, L. (2022). Theobroma cacao improves bone growth by modulating defective ciliogenesis in a mouse model of achondroplasia. *Bone research*, *10*(1), 1-13.

Massagué, J., Seoane, J., & Wotton, D. (2005). Smad transcription factors. *Genes & development*, *19*(23), 2783-2810.

Mathijssen, I., Arnaud, E., Marchac, D., Mireau, E., Morisseau-Durand, M. P., Guérin, P., & Renier, D. (2006). Respiratory outcome of mid-face advancement with distraction: a comparison between Le Fort III and frontofacial monobloc. *Journal of Craniofacial Surgery*, *17*(5), 880-882.

Matsushita T, Wilcox WR, Chan YY, Kawanami A, Bukulmez H, Balmes G, Krejci P, Mekikian PB, Otani K, Yamaura I, et al. 2009. FGFR3 promotes synchondrosis closure and fusion of ossification centers through the MAPK pathway. *Hum Mol Genet*. 18(2):227–240

Matsushita, M., Hasegawa, S., Kitoh, H., Mori, K., Ohkawara, B., Yasoda, A., ... & Ohno, K. (2015). Meclozine promotes longitudinal skeletal growth in transgenic mice with

achondroplasia carrying a gain-of-function mutation in the FGFR3 gene. *Endocrinology*, *156*(2), 548-554.

Matthews, B. G., Novak, S., Sbrana, F. V., Funnell, J. L., Cao, Y., Buckels, E. J., ... & Kalajzic, I. (2021). Heterogeneity of murine periosteum progenitors involved in fracture healing. *Elife*, *10*, e58534.

McBratney-Owen, B., Iseki, S., Bamforth, S. D., Olsen, B. R., & Morriss-Kay, G. M. (2008). Development and tissue origins of the mammalian cranial base. *Developmental biology*, *322*(1), 121–132.

Merrill, A. E., Bochukova, E. G., Brugger, S. M., Ishii, M., Pilz, D. T., Wall, S. A., ... & Maxson Jr, R. E. (2006). Cell mixing at a neural crest-mesoderm boundary and deficient ephrin-Eph signaling in the pathogenesis of craniosynostosis. *Human molecular genetics*, *15*(8), 1319-1328.

Meyers, G. A., Orlow, S. J., Munro, I. R., Przylepa, K. A., & Jabs, E. W. (1995). Fibroblast growth factor receptor 3 (FGFR3) transmembrane mutation in Crouzon syndrome with acanthosis nigricans. *Nature genetics*, *11*(4), 462-464.

Miki, T., Bottaro, D. P., Fleming, T. P., Smith, C. L., Burgess, W. H., Chan, A. M., & Aaronson, S. A. (1992). Determination of ligand-binding specificity by alternative splicing: two distinct growth factor receptors encoded by a single gene. *Proceedings of the National Academy of Sciences*, *89*(1), 246-250.

Miraoui, H., & Marie, P. J. (2010). Fibroblast growth factor receptor signaling crosstalk in skeletogenesis. *Science signaling*, *3*(146), re9-re9.

Mishina, Y., & Snider, T. N. (2014). Neural crest cell signaling pathways critical to cranial bone development and pathology. *Experimental cell research*, *325*(2), 138-147.

Miura, T., Perlyn, C. A., Kinboshi, M., Ogihara, N., Kobayashi-Miura, M., Morriss-Kay, G. M., & Shiota, K. (2009). Mechanism of skull suture maintenance and interdigitation. *Journal of anatomy*, *215*(6), 642-655.

Miyake, M., Ishii, M., Koyama, N., Kawashima, K., Kodama, T., Anai, S., ... & Sugano, K. (2010). 1-tert-butyl-3-[6-(3, 5-dimethoxy-phenyl)-2-(4-diethylamino-butylamino)-pyrido [2, 3-d] pyrimidin-7-yl]-urea (PD173074), a selective tyrosine kinase inhibitor of fibroblast growth factor receptor-3 (FGFR3), inhibits cell proliferation of bladder cancer carrying the FGFR3 gene mutation along with up-regulation of p27/Kip1 and G1/G0 arrest. *Journal of Pharmacology and Experimental Therapeutics*, *332*(3), 795-802.

Mohammadi, M., Dikic, I., Sorokin, A., Burgess, W. H., Jaye, M., & Schlessinger, J. (1996). Identification of six novel autophosphorylation sites on fibroblast growth factor receptor 1 and elucidation of their importance in receptor activation and signal transduction. *Molecular and cellular biology*, *16*(3), 977-989.

Mohammadi, M., Olsen, S. K., & Ibrahimi, O. A. (2005). Structural basis for fibroblast growth factor receptor activation. *Cytokine & growth factor reviews*, *16*(2), 107–137.

Moko, S. B., & de Chalain, T. M. B. (2001). New Zealand Maori family with the pro250arg fibroblast growth factor receptor 3 mutation associated with craniosynostosis. *Journal of Cranio-Maxillofacial Surgery*, *29*(1), 22-24.

Moloney, D. M., Wall, S. A., Ashworth, G. J., Oldridge, M., Glass, I. A., Francomano, C. A., ... & Wilkie, A. O. M. (1997). Prevalence of Pro250Arg mutation of fibroblast growth factor receptor 3 in coronal craniosynostosis. *The Lancet*, *349*(9058), 1059-1062.

Moncla, A., Missirian, C., Cacciagli, P., Balzamo, E., Legeai-Mallet, L., Jouve, J. L., ... & Philip, N. (2007). A cluster of translocation breakpoints in 2q37 is associated with overexpression of NPPC in patients with a similar overgrowth phenotype. *Human mutation*, *28*(12), 1183-1188.

Monsonego-Ornan, E., Adar, R., Feferman, T., Segev, O., & Yayon, A. (2000). The transmembrane mutation G380R in fibroblast growth factor receptor 3 uncouples ligand-mediated receptor activation from down-regulation. *Molecular and cellular biology*, *20*(2), 516-522.

Moon, A.M., Guris, D.L., Seo, J., Li, L., Hammond, J., Talbot, A., Imamoto, A., 2006. Crkl deficiency disrupts Fgf8 signaling in a mouse model of 22q11 deletion syndromes. *Dev. Cell* 10, 71–80.

Mori-Akiyama, Y., Akiyama, H., Rowitch, D. H., & de Crombrugghe, B. (2003). Sox9 is required for determination of the chondrogenic cell lineage in the cranial neural crest. *Proceedings of the National Academy of Sciences*, *100*(16), 9360-9365.

Morice, A., Paternoster, G., Ostertag, A., James, S., Cohen-Solal, M., Khonsari, R. H., & Arnaud, E. (2018). Anterior skull base and pericranial flap ossification after frontofacial monobloc advancement. *Plastic and Reconstructive Surgery*, *141*(2), 437-445.

Morriss-Kay, G. M., & Wilkie, A. O. (2005). Growth of the normal skull vault and its alteration in craniosynostosis: insights from human genetics and experimental studies. *Journal of anatomy*, *207*(5), 637-653.

Motch Perrine, S. M., Wu, M., Stephens, N. B., Kriti, D., Van Bakel, H., Jabs, E. W., & Richtsmeier, J. T. (2019). Mandibular dysmorphology due to abnormal embryonic osteogenesis in FGFR2-related craniosynostosis mice. *Disease models & mechanisms*, *12*(5), dmm038513.

Muenke, M., Gripp, K. W., McDonald-McGinn, D. M., Gaudenz, K., Whitaker, L. A., Bartlett, S. P., ... & Zackai, E. H. (1997). A unique point mutation in the fibroblast growth factor receptor 3 gene (FGFR3) defines a new craniosynostosis syndrome. *American journal of human genetics*, *60*(3), 555.

Nagayama M., Iwamoto M., Hargett A., Kamiya N., Tamamura Y., Young B., et al. (2008). Wnt/β-catenin signaling regulates cranial base development and growth. *J. Dent. Res.* 87 244–249.

Nakajima, A., Shimizu, S., Moriya, H., & Yamazaki, M. (2003). Expression of fibroblast growth factor receptor-3 (FGFR3), signal transducer and activator of transcription-1, and

cyclin-dependent kinase inhibitor p21 during endochondral ossification: differential role of FGFR3 in skeletal development and fracture repair. *Endocrinology*, *144*(10), 4659-4668.

Nakajima, F., Ogasawara, A., Goto, K. I., Moriya, H., Ninomiya, Y., Einhorn, T. A., & Yamazaki, M. (2001). Spatial and temporal gene expression in chondrogenesis during fracture healing and the effects of basic fibroblast growth factor. *Journal of Orthopaedic Research*, *19*(5), 935-944.

Nakashima, K., Zhou, X., Kunkel, G., Zhang, Z., Deng, J. M., Behringer, R. R., & De Crombrugghe, B. (2002). The novel zinc finger-containing transcription factor osterix is required for osteoblast differentiation and bone formation. *Cell*, *108*(1), 17-29.

Naski, M. C., Colvin, J. S., Coffin, J. D., & Ornitz, D. M. (1998). Repression of hedgehog signaling and BMP4 expression in growth plate cartilage by fibroblast growth factor receptor 3. *Development*, *125*(24), 4977-4988.

Naski, M. C., Wang, Q., Xu, J., & Ornitz, D. M. (1996). Graded activation of fibroblast growth factor receptor 3 by mutations causing achondroplasia and thanatophoric dysplasia. *Nature genetics*, *13*(2), 233-237.

Nieman, B. J., Blank, M. C., Roman, B. B., Henkelman, R. M., & Millen, K. J. (2012). If the skull fits: magnetic resonance imaging and microcomputed tomography for combined analysis of brain and skull phenotypes in the mouse. *Physiological Genomics*, *44*(20), 992-1002.

Nieminen, P., Morgan, N. V., Fenwick, A. L., Parmanen, S., Veistinen, L., Mikkola, M. L., van der Spek, P. J., Giraud, A., Judd, L., Arte, S., Brueton, L. A., Wall, S. A., Mathijssen, I. M., Maher, E. R., Wilkie, A. O., Kreiborg, S., & Thesleff, I. (2011). Inactivation of IL11 signaling causes craniosynostosis, delayed tooth eruption, and supernumerary teeth. *American journal of human genetics*, *89*(1), 67–81.

Ochiai T., Nagayama M., Nakamura T., Morrison T., Pilchak D., Kondo N., et al. (2009). Roles of the primary cilium component polaris in synchondrosis development. *J. Dent. Res.* 88 545–550.

Ohbayashi, N., Shibayama, M., Kurotaki, Y., Imanishi, M., Fujimori, T., Itoh, N., & Takada, S. (2002). FGF18 is required for normal cell proliferation and differentiation during osteogenesis and chondrogenesis. *Genes & development*, *16*(7), 870-879.

Oka, K., Oka, S., Sasaki, T., Ito, Y., Bringas Jr, P., Nonaka, K., & Chai, Y. (2007). The role of TGF-β signaling in regulating chondrogenesis and osteogenesis during mandibular development. *Developmental biology*, *303*(1), 391-404.

Olsen SK, Ibrahimi OA, Raucci A, Zhang F, Eliseenkova AV, Yayon A, et al. Insights into the molecular basis for fibroblast growth factor receptor autoinhibition and ligand-binding promiscuity. *Proc Natl Acad Sci* USA 2004;101(4):935–40.

Olsen, S.K., Li, J.Y.H., Bromleigh, C., Eliseenkova, A.V., Ibrahimi, O.A., Lao, Z., Zhang, F., Linhardt, R.J., Joyner, A.L., Mohammadi, M., 2006. Structural basis by which alternative splicing modulates the organizer activity of FGF8 in the brain. *Genes Dev.* 20, 185–198.

Ono, N., Ono, W., Nagasawa, T., Kronenberg, H.M., 2014. A subset of chondrogenic cells provides early mesenchymal progenitors in growing bones. *Nat. Cell Biol.* 16, 1157–1167.

Onodera, K., Niikuni, N., Chigono, T., Nakajima, I., Sakata, H., & Motizuki, H. (2006). Sleep disordered breathing in children with achondroplasia: Part 2. Relationship with craniofacial and airway morphology. *International journal of pediatric otorhinolaryngology*, *70*(3), 453-461.

Ornitz DM, Itoh N. Fibroblast growth factors. *Genome Biol*. 2001;2(3):REVIEWS3005.

Ornitz DM, Itoh N. The Fibroblast Growth Factor signaling pathway. *Wiley Interdiscip Rev Dev Biol*. 2015;4(3):215-266.

Ornitz, D. M., & Marie, P. J. (2002). FGF signaling pathways in endochondral and intramembranous bone development and human genetic disease. *Genes & development*, *16*(12), 1446-1465.

Ornitz, D. M., Yayon, A., Flanagan, J. G., Svahn, C. M., Levi, E., & Leder, P. (1992). Heparin is required for cell-free binding of basic fibroblast growth factor to a soluble receptor and for mitogenesis in whole cells. *Molecular and cellular biology*, *12*(1), 240-247.

Ornitz, D.M., Legeai-Mallet, L., 2017. Achondroplasia: Development, Pathogenesis, and Therapy. *Dev Dyn* 246, 291–309.

Osawa, Y., Matsushita, M., Hasegawa, S., Esaki, R., Fujio, M., Ohkawara, B., ... & Kitoh, H. (2017). Activated FGFR3 promotes bone formation via accelerating endochondral ossification in mouse model of distraction osteogenesis. *Bone*, *105*, 42-49.

Osawa, Y., Matsushita, M., Hasegawa, S., Esaki, R., Fujio, M., Ohkawara, B., ... & Kitoh, H. (2017). Activated FGFR3 promotes bone formation via accelerating endochondral ossification in mouse model of distraction osteogenesis. *Bone*, *105*, 42-49.

Otrock ZK, Mahfouz RA, Makarem JA, Shamseddine AI. Understanding the biology of angiogenesis: review of the most important molecular mechanisms. *Blood Cells Mol Dis*. 2007;39(2):212-220.

Oyama, A., Arnaud, E., Marchac, D., & Renier, D. (2009). Reossification of cranium and zygomatic arch after monobloc frontofacial distraction advancement for syndromic craniosynostosis. *Journal of Craniofacial Surgery*, *20*(8), 1905-1909.

Pacicca, D. M., Patel, N., Lee, C., Salisbury, K., Lehmann, W., Carvalho, R., ... & Einhorn, T. A. (2003). Expression of angiogenic factors during distraction osteogenesis. *Bone*, *33*(6), 889-898.

Paley, D. (2015). PRECICE intramedullary limb lengthening system. *Expert review of medical devices*, *12*(3), 231-249.

Pannier, S., Couloigner, V., Messaddeq, N., Elmaleh-Bergès, M., Munnich, A., Romand, R., & Legeai-Mallet, L. (2009). Activating Fgfr3 Y367C mutation causes hearing loss and inner ear defect in a mouse model of chondrodysplasia. *Biochimica et Biophysica Acta (BBA)-Molecular Basis of Disease*, *1792*(2), 140-147.

Parada, C., & Chai, Y. (2015). Mandible and tongue development. *Current topics in developmental biology*, *115*, 31-58.

Park IK, Cho CS. Stem Cell-assisted Approaches for Cartilage Tissue Engineering. *Int J Stem Cells*. 2010;3(2):96-102.

Passos-Bueno, M. R., Sertié, A. L., Jehee, F. S., Fanganiello, R., & Yeh, E. (2008). Genetics of craniosynostosis: genes, syndromes, mutations and genotype-phenotype correlations. *Frontiers of oral biology*, *12*, 107–143.

Passos-Bueno, M. R., Wilcox, W. R., Jabs, E. W., Sertie, A. L., Alonso, L. G., & Kitoh, H. (1999). Clinical spectrum of fibroblast growth factor receptor mutations. *Human mutation*, *14*(2), 115-125.

Perlyn, C. A., Morriss-Kay, G., Darvann, T., Tenenbaum, M., & Ornitz, D. M. (2006). Model for the Pharmacologic Treatment of Crouzon Syndrome. *Neurosurgery*, *59*(1), 210-215.

Plotnikov AN, Hubbard SR, Schlessinger J, Mohammadi M. Crystal structures of two FGF-FGFR complexes reveal the determinants of ligand-receptor specificity. *Cell* 2000;101(4):413–24.

Plotnikov AN, Schlessinger J, Hubbard SR, Mohammadi M. Structural basis for FGF receptor dimerization and activation. *Cell* 1999;98(5):641–50.

Plotnikov, A. N., Eliseenkova, A. V., Ibrahimi, O. A., Shriver, Z., Sasisekharan, R., Lemmon, M. A., & Mohammadi, M. (2001). Crystal structure of fibroblast growth factor 9 reveals regions implicated in dimerization and autoinhibition. *Journal of Biological Chemistry*, *276*(6), 4322-4329.

Poole, A. R., & Pidoux, I. (1989). Immunoelectron microscopic studies of type X collagen in endochondral ossification. *The Journal of cell biology*, *109*(5), 2547-2554.

Poole, C. A., Matsuoka, A., & Schofield, J. R. (1991). Chondrons from articular cartilage. III. Morphologic changes in the cellular microenvironment of chondrons isolated from osteoarthritic cartilage. *Arthritis and rheumatism*, *34*(1), 22–35.

Priore, R., Dailey, L., & Basilico, C. (2006). Downregulation of Akt activity contributes to the growth arrest induced by FGF in chondrocytes. *Journal of cellular physiology*, *207*(3), 800-808.

Przylepa, K. A., Paznekas, W., Zhang, M., Golabi, M., Bias, W., Bamshad, M. J., ... & Jabs, E. W. (1996). Fibroblast growth factor receptor 2 mutations in Beare–Stevenson cutis gyrata syndrome. *Nature genetics*, *13*(4), 492-494.

Raffioni, S., Zhu, Y. Z., Bradshaw, R. A., & Thompson, L. M. (1998). Effect of Transmembrane and Kinase Domain Mutations on Fibroblast Growth Factor Receptor 3 Chimera Signaling in PC12 Cells: A model for the control of receptor tyrosine kinase activation. *Journal of Biological Chemistry*, *273*(52), 35250-35259.

Ramaesh, T., & Bard, J. B. (2003). The growth and morphogenesis of the early mouse mandible: a quantitative analysis. *Journal of anatomy*, *203*(2), 213–222.

Rauchenberger, R., Borges, E., Thomassen-Wolf, E., Rom, E., Adar, R., Yaniv, Y., ... & Rothe, C. (2003). Human combinatorial Fab library yielding specific and functional antibodies against the human fibroblast growth factor receptor 3. *Journal of Biological Chemistry*, *278*(40), 38194-38205.

Renier, D., Lajeunie, E., Arnaud, E., & Marchac, D. (2000). Management of craniosynostoses. *Child's Nervous System*, *16*(10), 645-658.

Rice, D. P., & Rice, R. (2008). Locate, condense, differentiate, grow and confront: developmental mechanisms controlling intramembranous bone and suture formation and function. *Craniofacial Sutures*, *12*, 22-40.

Rice, D. P., Rice, R., & Thesleff, I. (2003). Fgfr mRNA isoforms in craniofacial bone development. *Bone*, *33*(1), 14–27.

Richtsmeier, J. T., & Flaherty, K. (2013). Hand in glove: brain and skull in development and dysmorphogenesis. *Acta neuropathologica*, *125*(4), 469-489.

Rimoin, D. L., Cohn, D., Krakow, D., Wilcox, W., Lachman, R. S., & Alanay, Y. (2007). The skeletal dysplasias: clinical–molecular correlations. *Annals of the New York Academy of Sciences*, *1117*(1), 302-309.

Roberts, W. E., & Hartsfield Jr, J. K. (2004, June). Bone development and function: genetic and environmental mechanisms. In *Seminars in Orthodontics* (Vol. 10, No. 2, pp. 100-122). WB Saunders.

Robin, N. H., Falk, M. J., & Haldeman-Englert, C. R. (2011). FGFR-related craniosynostosis syndromes.

Rodriguez-Enfedaque, A., Bouleau, S., Laurent, M., Courtois, Y., Mignotte, B., Vayssière, J. L., & Renaud, F. (2009). FGF1 nuclear translocation is required for both its neurotrophic activity and its p53-dependent apoptosis protection. *Biochimica et Biophysica Acta (BBA)-Molecular Cell Research*, *1793*(11), 1719-1727.

Rodriguez-Vazquez J. F., Merida-Velasco J. R., Merida-Velasco J. A., Sanchez-Montesinos I., Espin-Ferra J., Jimenez-Collado J. (1997). Development of Meckel's cartilage in the symphyseal region in man. *Anat. Rec.* 249 249–254.

Rousseau, F., Bonaventure, J., Legeai-Mallet, L., Pelet, A., Rozet, J. M., Maroteaux, P., ... & Munnich, A. (1994). Mutations in the gene encoding fibroblast growth factor receptor-3 in achondroplasia. *Nature*, *371*(6494), 252-254.

Rousseau, F., Bonaventure, J., Legeai-Mallet, L., Schmidt, H., Weissenbach, J., Maroteaux, P., ... & Le Merrer, M. (1996). Clinical and genetic heterogeneity of hypochondroplasia. *Journal of Medical Genetics*, *33*(9), 749-752.

Rubenstein, J. L., Shimamura, K., Martinez, S., & Puelles, L. (1998). Regionalization of the prosencephalic neural plate. *Annual review of neuroscience*, *21*(1), 445-477.

Rundle, C. H., Miyakoshi, N., Ramirez, E., Wergedal, J. E., Lau, K. H. W., & Baylink, D. J. (2002). Expression of the fibroblast growth factor receptor genes in fracture repair. *Clinical Orthopaedics and Related Research®*, *403*, 253-263.

Rutland, P., Pulleyn, L. J., Reardon, W., Baraitser, M., Hayward, R., Jones, B., ... & Wilkie, A. O. (1995). Identical mutations in the FGFR2 gene cause both Pfeiffer and Crouzon syndrome phenotypes. *Nature genetics*, *9*(2), 173-176.

S.V. Guevara Perez, Castolo G. de la Rosa, L. Thollon, M. Behr, A 3D characterization method of geometric variation in edentulous mandibles, Morphologie. 102 (339) (2018 Dec) 255–262.

Sabatino, G., Di Rocco, F., Zampino, G., Tamburrini, G., Caldarelli, M., & Di Rocco, C. (2004). Muenke syndrome. *Child's Nervous System*, *20*(5), 297-301.

Sabir, A. H., Sheikh, J., Singh, A., Morley, E., Cocca, A., Cheung, M. S., & Irving, M. (2021). Earlier detection of hypochondroplasia: A large single-center UK case series and systematic review. *American journal of medical genetics Part A*, *185*(1), 73-82.

Savarirayan, R., Irving, M., Bacino, C. A., Bostwick, B., Charrow, J., Cormier-Daire, V., ... & Hoover-Fong, J. (2019). C-type natriuretic peptide analogue therapy in children with achondroplasia. *New England Journal of Medicine*, *381*(1), 25-35.

Savarirayan, R., Tofts, L., Irving, M., Wilcox, W., Bacino, C. A., Hoover-Fong, J., ... & Day, J. (2020). Once-daily, subcutaneous vosoritide therapy in children with achondroplasia: a randomised, double-blind, phase 3, placebo-controlled, multicentre trial. *The Lancet*, *396*(10252), 684-692.

Saxby, C., Stephenson, K. A., Steele, K., Ifeacho, S., Wyatt, M. E., & Samuels, M. (2018). The effect of midface advancement surgery on obstructive sleep apnoea in syndromic craniosynostosis. *Journal of Craniofacial Surgery*, *29*(1), 92-95.

Svandova, E., Anthwal, N., Tucker, A. S., & Matalova, E. (2020). Diverse Fate of an Enigmatic Structure: 200 Years of Meckel's Cartilage. *Frontiers in cell and developmental biology*, 8, 821.

Scheller, T., Hellerbrand, C., Moser, C., Schmidt, K., Kroemer, A., Brunner, S. M., ... & Lang, S. A. (2015). mTOR inhibition improves fibroblast growth factor receptor targeting in hepatocellular carcinoma. *British journal of cancer*, *112*(5), 841-850.

Schlessinger J, Plotnikov AN, Ibrahimi OA, Eliseenkova AV, Yeh BK, Yayon A, et al. Crystal structure of a ternary FGF-FGFR-heparin complex reveals a dual role for heparin in FGFR binding and dimerization. *Mol Cell* 2000;6(3):743–50.

Schmetz, A., Amiel, J., & Wieczorek, D. (2021, December). Genetics of craniofacial malformations. In *Seminars in Fetal and Neonatal Medicine* (Vol. 26, No. 6, p. 101290). WB Saunders.

Schmid, G. J., Kobayashi, C., Sandell, L. J., & Ornitz, D. M. (2009). Fibroblast growth factor expression during skeletal fracture healing in mice. *Developmental dynamics: an official publication of the American Association of Anatomists*, *238*(3), 766-774.

Secreto, F. J., Hoeppner, L. H., & Westendorf, J. J. (2009). Wnt signaling during fracture repair. *Current osteoporosis reports*, *7*(2), 64-69.

Seo, H. J., & Kim, G. J. (2009). Role of FGF and MEK signaling in formation of the hydrostatic pressure receptor cells during ascidian embryogenesis. *Development and Reproduction*, *13*(4), 291-296.

Shabtai, L., Jauregui, J. J., Herzenberg, J. E., Gesheff, M. G., Standard, S. C., & McClure, P. K. (2021). Simultaneous bilateral femoral and tibial lengthening in achondroplasia. *Children*, *8*(9), 749.

Sharma, V. P., Wall, S. A., Lord, H., Lester, T., & Wilkie, A. O. (2012). Atypical Crouzon syndrome with a novel Cys62Arg mutation in FGFR2 presenting with sagittal synostosis. *The Cleft palate-craniofacial journal*, *49*(3), 373-377.

Shiang, R., Thompson, L. M., Zhu, Y. Z., Church, D. M., Fielder, T. J., Bocian, M., ... & Wasmuth, J. J. (1994). Mutations in the transmembrane domain of FGFR3 cause the most common genetic form of dwarfism, achondroplasia. *Cell*, *78*(2), 335-342.

Shiller, J. G. (1959). Craniofacial dysostosis of Crouzon: a case report and pedigree with emphasis on heredity. *Pediatrics*, *23*(1), 107-112.

Shimo T., Kanyama M., Wu C., Sugito H., Billings P. C., Abrams W. R., et al. (2004). Expression and roles of connective tissue growth factor in Meckel's cartilage development. *Dev. Dyn.* 231 136–147.

Shohat, M., Flaum, E., Cobb, S. R., Lachman, R., Rubin, C., Ash, C., & Rimoin, D. L. (1993). Hearing loss and temporal bone structure in achondroplasia. *American journal of medical genetics*, *45*(5), 548-551.

Shukla, V., Coumoul, X., Wang, R. H., Kim, H. S., & Deng, C. X. (2007). RNA interference and inhibition of MEK-ERK signaling prevent abnormal skeletal phenotypes in a mouse model of craniosynostosis. *Nature genetics*, *39*(9), 1145-1150.

Sisk, E. A., Heatley, D. G., Borowski, B. J., Leverson, G. E., & Pauli, R. M. (1999). Obstructive sleep apnea in children with achondroplasia: surgical and anesthetic considerations. *Otolaryngology—Head and Neck Surgery*, 120(2), 248-254.

Slavotinek, A., Crawford, H., Golabi, M., Tao, C., Perry, H., Oberoi, S., ... & Friez, M. (2009). Novel FGFR2 Deletion in patient with Beare-Stevenson-like syndrome. *American journal of medical genetics. Part A*, *149*(8), 1814.

Sleeman, M., Fraser, J., McDonald, M., Yuan, S., White, D., Grandison, P., Kumble, K., Watson, J. D., & Murison, J. G. (2001). Identification of a new fibroblast growth factor receptor, FGFR5. *Gene*, *271*(2), 171–182.

Song, L. I. N., & Tuan, R. S. (2004). Transdifferentiation potential of human mesenchymal stem cells derived from bone marrow. *The FASEB Journal*, *18*(9), 980-982.

Sørensen, V., Wiedlocha, A., Haugsten, E. M., Khnykin, D., Wesche, J., & Olsnes, S. (2006). Different abilities of the four FGFRs to mediate FGF-1 translocation are linked to differences in the receptor C-terminal tail. *Journal of cell science*, *119*(20), 4332-4341.

Stauber DJ, DiGabriele AD, Hendrickson WA. Structural interactions of fibroblast growth factor receptor with its ligands. *Proc Natl Acad Sci* USA 2000;97(1):49–54.

St-Jacques, B., Hammerschmidt, M., & McMahon, A. P. (1999). Indian hedgehog signaling regulates proliferation and differentiation of chondrocytes and is essential for bone formation. *Genes & development*, *13*(16), 2072–2086.

Su, N., Du, X., & Chen, L. (2008). FGF signaling: its role in bone development and human skeleton diseases. *Frontiers in Bioscience-Landmark*, *13*(8), 2842-2865.

Susarla SM, Mundinger GS, Kapadia H, et al. Subcranial and orthognathic surgery for obstructive sleep apnea in achondroplasia. *J Craniomaxillofac Surg*. 2017;45(12):2028-2034.

Svandova, E., Anthwal, N., Tucker, A. S., & Matalova, E. (2020). Diverse Fate of an Enigmatic Structure: 200 Years of Meckel's Cartilage. *Frontiers in cell and developmental biology*, *8*, 821.

Tahiri Y, Taylor J. An Update on Midface Advancement Using Le Fort II and III Distraction Osteogenesis. *Semin Plast Surg*. 2014;28(4):184-192.

Takeda S., Bonnamy J. P., Owen M. J., Ducy P., Karsenty G. (2001). Continuous Expression of Cbfa1 in nonhypertrophic chondrocytes uncovers its ability to induce hypertrophic chondrocyte differentiation and partially rescues Cbfa1-deficient mice. *Genes Dev.* 15 467–481. 10.1101/gad.845101

Tanimoto, Y., Yokozeki, M., Hiura, K., Matsumoto, K., Nakanishi, H., Matsumoto, T., ... & Moriyama, K. (2004). A soluble form of fibroblast growth factor receptor 2 (FGFR2) with S252W mutation acts as an efficient inhibitor for the enhanced osteoblastic differentiation caused by FGFR2 activation in Apert syndrome. *Journal of Biological Chemistry*, *279*(44), 45926-45934.

Tartaglia, M., Di Rocco, C., Lajeunie, E., Valeri, S., Velardi, F., & Battaglia, P. A. (1997). Jackson-Weiss syndrome: identification of two novel FGFR2 missense mutations shared with Crouzon and Pfeiffer craniosynostotic disorders. *Human genetics*, *101*(1), 47-50.

Tavormina, P. L., Shiang, R., Thompson, L. M., Zhu, Y. Z., Wilkin, D. J., Lachman, R. S., ... & Wasmuth, J. J. (1995). Thanatophoric dysplasia (types I and II) caused by distinct mutations in fibroblast growth factor receptor 3. *Nature genetics*, *9*(3), 321-328.

Taylor, D. K., Meganck, J. A., Terkhorn, S., Rajani, R., Naik, A., O'Keefe, R. J., ... & Hankenson, K. D. (2009). Thrombospondin-2 influences the proportion of cartilage and bone during fracture healing. *Journal of Bone and Mineral Research*, *24*(6), 1043-1054.

Teitelbaum, S. L. (2007). Osteoclasts: what do they do and how do they do it?. *The American journal of pathology*, *170*(2), 427-435.

Tenconi, R., Khirani, S., Amaddeo, A., Michot, C., Baujat, G., Couloigner, V., ... & Fauroux, B. (2017). Sleep-disordered breathing and its management in children with achondroplasia. *American journal of medical genetics Part A*, *173*(4), 868-878.

Teven, C. M., Farina, E. M., Rivas, J., & Reid, R. R. (2014). Fibroblast growth factor (FGF) signaling in development and skeletal diseases. *Genes Dis* 1, 199–213.

Thompson, Z., Miclau, T., Hu, D., & Helms, J. A. (2002). A model for intramembranous ossification during fracture healing. *Journal of Orthopaedic Research*, *20*(5), 1091-1098.

Ting, M. C., Wu, N. L., Roybal, P. G., Sun, J., Liu, L., Yen, Y., & Maxson Jr, R. E. (2009). EphA4 as an effector of Twist1 in the guidance of osteogenic precursor cells during calvarial bone growth and in craniosynostosis.

Toydemir, R. M., Brassington, A. E., Bayrak-Toydemir, P., Krakowiak, P. A., Jorde, L. B., Whitby, F. G., ... & Bamshad, M. J. (2006). A novel mutation in FGFR3 causes camptodactyly, tall stature, and hearing loss (CATSHL) syndrome. *The American Journal of Human Genetics*, *79*(5), 935-941.

Trudel, S., Li, Z. H., Wei, E., Wiesmann, M., Chang, H., Chen, C., ... & Stewart, A. K. (2005). CHIR-258, a novel, multitargeted tyrosine kinase inhibitor for the potential treatment of t (4; 14) multiple myeloma. *Blood*, *105*(7), 2941-2948.

Trudel, S., Stewart, A. K., Rom, E., Wei, E., Li, Z. H., Kotzer, S., ... & Yayon, A. (2006). The inhibitory anti-FGFR3 antibody, PRO-001, is cytotoxic to t (4; 14) multiple myeloma cells. *Blood*, *107*(10), 4039-4046.

Tsang, M., & Dawid, I. B. (2004). Promotion and attenuation of FGF signaling through the Ras-MAPK pathway. *Science's STKE*, *2004*(228), pe17-pe17.

Tsuji, K., Bandyopadhyay, A., Harfe, B. D., Cox, K., Kakar, S., Gerstenfeld, L., ... & Rosen, V. (2006). BMP2 activity, although dispensable for bone formation, is required for the initiation of fracture healing. *Nature genetics*, *38*(12), 1424-1429.

Tsuzurahara F., Soeta S., Kawawa T., Baba K., Nakamura M. (2011). The role of macrophages in the disappearance of Meckel's cartilage during mandibular development in mice. *ActaHistochemica* 113 194–200.

Twigg, S.R.F., Wilkie, A.O.M., 2015. A Genetic-Pathophysiological Framework for Craniosynostosis. *American Journal of Human Genetics* 97, 359.

Vaananen, H. K., Zhao, H., Mulari, M., & Halleen, J. M. (2000). The cell biology of osteoclast function. *Journal of cell science*, *113*(3), 377-381.

Vajo, Z., Francomano, C. A., & Wilkin, D. J. (2000). The molecular and genetic basis of fibroblast growth factor receptor 3 disorders: the achondroplasia family of skeletal dysplasias,

Muenke craniosynostosis, and Crouzon syndrome with acanthosis nigricans. *Endocrine reviews*, *21*(1), 23-39.

Vega R. B., Matsuda K., Oh J., Barbosa A. C., Yang X., Meadows E., et al. (2004). Histone deacetylase 4 controls chondrocyte hypertrophy during skeletogenesis. *Cell* 119 555–566.

Virchow, R. (1857). *Untersuchungen über die Entwickelung des Schädelgrundes im gesunden und krankhaften Zustande: und über den Einfluss derselben auf Schädelform, Gesichtsbildung und Gehirnbau*. De Gruyter, Incorporated.

Vogels, A., & Fryns, J. P. (2006). Pfeiffer syndrome. *Orphanet journal of rare diseases*, *1*(1), 1-3.

Vu, G. H., Xu, W., Go, B. C., Humphries, L. S., Kalmar, C. L., Taylor, J. A., ... & Swanson, J. W. (2021). Physiologic Timeline of Cranial-Base Suture and Synchondrosis Closure. *Plastic and Reconstructive Surgery*, *148*(6), 973e-982e.

W.R. Atchley, B.K. Hall, A model for development and evolution of complex morphological structures, Biol. Rev. Camb. Philos. Soc. 66 (1991) 101–15.

Walker, B. A., Murdoch, J. L., McKusick, V. A., Langer, L. O., & Beals, R. K. (1971). Hypochondroplasia. *American journal of diseases of children*, *122*(2), 95-104.

Wang, T., Zhang, X., & Bikle, D. D. (2017). Osteogenic differentiation of periosteal cells during fracture healing. *Journal of cellular physiology*, *232*(5), 913-921.

Wang, Y., Zheng, Y., Chen, D., & Chen, Y. (2013). Enhanced BMP signaling prevents degeneration and leads to endochondral ossification of Meckel′ s cartilage in mice. *Developmental biology*, *381*(2), 301-311.

Wei X, Hu M, Mishina Y, Liu F. Developmental Regulation of the Growth Plate and Cranial Synchondrosis. *J Dent Res.* 2016 Oct;95(11):1221-9.

Wendt, D. J., Dvorak-Ewell, M., Bullens, S., Lorget, F., Bell, S. M., Peng, J., ... & Bunting, S. (2015). Neutral endopeptidase-resistant C-type natriuretic peptide variant represents a new therapeutic approach for treatment of fibroblast growth factor receptor 3–related dwarfism. *Journal of Pharmacology and Experimental Therapeutics*, 353(1), 132-149.

Wenger, T. L., Hing, A. V., & Evans, K. N. (2019). Apert Syndrome. In M. P. Adam (Eds.) et. al., *GeneReviews®*. University of Washington, Seattle.

Wesche, J., Małecki, J., Więdłocha, A., Skjerpen, C. S., Claus, P., & Olsnes, S. (2006). FGF-1 and FGF-2 require the cytosolic chaperone Hsp90 for translocation into the cytosol and the cell nucleus. *Journal of Biological Chemistry*, *281*(16), 11405-11412.
Wiedemann, M., & Trueb, B. (2000). Characterization of a novel protein (FGFRL1) from human cartilage related to FGF receptors. *Genomics*, *69*(2), 275-279.

Wigg, K., Tofts, L., Benson, S., & Porter, M. (2016). The neuropsychological function of children with achondroplasia. *American Journal of Medical Genetics Part A*, *170*(11), 2882-2888.

Wildemann, B., Schmidmaier, G., Ordel, S., Stange, R., Haas, N. P., & Raschke, M. (2003). Cell proliferation and differentiation during fracture healing are influenced by locally applied IGF-I and TGF-β1: Comparison of two proliferation markers, PCNA and BrdU. *Journal of Biomedical Materials Research Part B: Applied Biomaterials: An Official Journal of The Society for Biomaterials, The Japanese Society for Biomaterials, and The Australian Society for Biomaterials and the Korean Society for Biomaterials*, *65*(1), 150-156.

Wilkes, D., Rutland, P., Pulleyn, L. J., Reardon, W., Moss, C., Ellis, J. P., ... & Malcolm, S. (1996). A recurrent mutation, ala391glu, in the transmembrane region of FGFR3 causes Crouzon syndrome and acanthosis nigricans. *Journal of medical genetics*, *33*(9), 744-748.

Wilkie, A. O. (1997). Craniosynostosis: genes and mechanisms. *Human molecular genetics*, *6*(10), 1647-1656.

Wilkie, A. O., Johnson, D., & Wall, S. A. (2017). Clinical genetics of craniosynostosis. *Current opinion in pediatrics*, *29*(6), 622.

Wilkie, A. O., Slaney, S. F., Oldridge, M., Poole, M. D., Ashworth, G. J., Hockley, A. D., ... & Reardon, W. (1995). Apert syndrome results from localized mutations of FGFR2 and is allelic with Crouzon syndrome. *Nature genetics*, *9*(2), 165-172.

Wilkin, D. J., Szabo, J. K., Cameron, R., Henderson, S., Bellus, G. A., Mack, M. L., ... & Francomano, C. A. (1998). Mutations in fibroblast growth-factor receptor 3 in sporadic cases of achondroplasia occur exclusively on the paternally derived chromosome. *The American Journal of Human Genetics*, *63*(3), 711-716.

Wöhrle, S., Henninger, C., Bonny, O., Thuery, A., Beluch, N., Hynes, N. E., ... & Graus Porta, D. (2013). Pharmacological inhibition of fibroblast growth factor (FGF) receptor signaling ameliorates FGF23-mediated hypophosphatemic rickets. *Journal of Bone and Mineral Research*, *28*(4), 899-911.

Wöhrle, S., Weiss, A., Ito, M., Kauffmann, A., Murakami, M., Jagani, Z., ... & Graus Porta, D. (2013). Fibroblast growth factor receptors as novel therapeutic targets in SNF5-deleted malignant rhabdoid tumors. *PLoS One*, *8*(10), e77652.

Wu, A. C., Raggatt, L. J., Alexander, K. A., & Pettit, A. R. (2013). Unraveling macrophage contributions to bone repair. *BoneKEy reports*, *2*.

Wu, D. Q., Kan, M. K., Sato, G. H., Okamoto, T., & Sato, J. D. (1991). Characterization and molecular cloning of a putative binding protein for heparin-binding growth factors. *Journal of Biological Chemistry*, *266*(25), 16778-16785.

Wyganowska-Swiątkowska M., Przystanska A. (2011). The Meckel's cartilage in human embryonic and early fetal periods. *Anat. Sci. Int.* 86 98–107.

Wynne-Davies, R., & Patton, M. A. (1991). The frequency of mental retardation in hypochondroplasia. *Journal of medical genetics*, *28*(9), 644.

Xie, Y., Luo, F., Xu, W., Wang, Z., Sun, X., Xu, M., ... & Chen, L. (2017). FGFR3 deficient mice have accelerated fracture repair. *International journal of biological sciences*, *13*(8), 1029.

Xing, Z., Lu, C., Hu, D., Yu, Y. Y., Wang, X., Colnot, C., ... & Marcucio, R. S. (2010). Multiple roles for CCR2 during fracture healing. *Disease models & mechanisms*, *3*(7-8), 451-458.

Xu, R. H., Ault, K. T., Kim, J., Park, M. J., Hwang, Y. S., Peng, Y., ... & Kung, H. F. (1999). Opposite effects of FGF and BMP-4 on embryonic blood formation: roles of PV. 1 and GATA-2. *Developmental biology*, *208*(2), 352-361.

Xue, Y., Sun, A., Mekikian, P. B., Martin, J., Rimoin, D. L., Lachman, R. S., & Wilcox, W. R. (2014). FGFR3 mutation frequency in 324 cases from the International Skeletal Dysplasia Registry. *Molecular genetics & genomic medicine*, *2*(6), 497-503.

Yamashita, A., Morioka, M., Kishi, H., Kimura, T., Yahara, Y., Okada, M., ... & Tsumaki, N. (2014). Statin treatment rescues FGFR3 skeletal dysplasia phenotypes. *Nature*, *513*(7519), 507-511.

Yang R.-T., Zhang C., Liu Y., Zhou H.-H., Li Z.-B. (2012). Autophagy prior to chondrocyte cell death during the degeneration of Meckel's cartilage. *Anat. Rec.* 295 734–741.

Yang, X., Ricciardi, B. F., Hernandez-Soria, A., Shi, Y., Camacho, N. P., & Bostrom, M. P. (2007). Callus mineralization and maturation are delayed during fracture healing in interleukin-6 knockout mice. *Bone*, *41*(6), 928-936.

Yang, Y., Topol, L., Lee, H., & Wu, J. (2003). Wnt5a and Wnt5b exhibit distinct activities in coordinating chondrocyte proliferation and differentiation. *Development (Cambridge, England)*, *130*(5), 1003–1015.

Yasoda, A., & Nakao, K. (2010). Translational research of C-type natriuretic peptide (CNP) into skeletal dysplasias. *Endocrine journal*, 1005310427-1005310427.

Yasoda, A., Komatsu, Y., Chusho, H., Miyazawa, T., Ozasa, A., Miura, M., ... & Nakao, K. (2004). Overexpression of CNP in chondrocytes rescues achondroplasia through a MAPK-dependent pathway. *Nature medicine*, *10*(1), 80-86.

Yasui, N., Kawabata, H., Kojimoto, H., Ohno, H., Matsuda, S., Araki, N., ... & Ochi, T. (1997). Lengthening of the lower limbs in patients with achondroplasia and hypochondroplasia. *Clinical orthopaedics and related research*, (344), 298-306.

Yasui, N., Sato, M., Ochi, T., Kimura, T., Kawahata, H., Kitamura, Y., & Nomura, S. (1997). Three modes of ossification during distraction osteogenesis in the rat. *The Journal of bone and joint surgery. British volume*, *79*(5), 824–830.

Yayon, A., Klagsbrun, M., Esko, J.D., Leder, P., Ornitz, D.M., 1991. Cell surface, heparin-like molecules are required for binding of basic fibroblast growth factor to its high affinity receptor. *Cell* 64, 841–848.

Yeh BK, Igarashi M, Eliseenkova AV, Plotnikov AN, Sher I, Ron D, et al. Structural basis by which alternative splicing confers specificity in fibroblast growth factor receptors. *Proc Natl Acad Sci* USA 2003;100(5):2266–71.

Yin, Y., Ren, X., Smith, C., Guo, Q., Malabunga, M., Guernah, I., ... & Ornitz, D. M. (2016). Inhibition of fibroblast growth factor receptor 3-dependent lung adenocarcinoma with a human monoclonal antibody. *Disease models & mechanisms*, *9*(5), 563-571.

Yokota, M., Kobayashi, Y., Morita, J., Suzuki, H., Hashimoto, Y., Sasaki, Y., ... & Moriyama, K. (2014). Therapeutic effect of nanogel-based delivery of soluble FGFR2 with S252W mutation on craniosynostosis. *PloS one*, *9*(7), e101693.

Yoshida, C. A., Yamamoto, H., Fujita, T., Furuichi, T., Ito, K., Inoue, K. I., ... & Komori, T. (2004). Runx2 and Runx3 are essential for chondrocyte maturation, and Runx2 regulates limb growth through induction of Indian hedgehog. *Genes & development*, *18*(8), 952-963.
Yoshida, T., Vivatbutsiri, P., Morriss-Kay, G., Saga, Y., & Iseki, S. (2008). Cell lineage in mammalian craniofacial mesenchyme. *Mechanisms of development*, *125*(9-10), 797-808.

Young B., Minugh-Purvis N., Shimo T., St-Jacques B., Iwamoto M., Enomoto-Iwamoto M., et al. (2006). Indian and sonic hedgehogs regulate synchondrosis growth plate and cranial base development and function. *Dev. Biol.* 299 272–282.

Yu, K., & Ornitz, D. M. (2008). FGF signaling regulates mesenchymal differentiation and skeletal patterning along the limb bud proximodistal axis. *Development (Cambridge, England)*, *135*(3), 483–491.

Yu, K., Karuppaiah, K., & Ornitz, D. M. (2015). Mesenchymal fibroblast growth factor receptor signaling regulates palatal shelf elevation during secondary palate formation. *Developmental Dynamics*, *244*(11), 1427-1438.

Yu, Y. Y., Lieu, S., Lu, C., Miclau, T., Marcucio, R. S., & Colnot, C. (2010). Immunolocalization of BMPs, BMP antagonists, receptors, and effectors during fracture repair. *Bone*, *46*(3), 841-851.

Zhang, X., Ibrahimi, O. A., Olsen, S. K., Umemori, H., Mohammadi, M., & Ornitz, D. M. (2006). Receptor specificity of the fibroblast growth factor family: the complete mammalian FGF family. *Journal of Biological Chemistry*, *281*(23), 15694-15700.

Zhao, H., Feng, J., Ho, T. V., Grimes, W., Urata, M., & Chai, Y. (2015). The suture provides a niche for mesenchymal stem cells of craniofacial bones. *Nature cell biology*, *17*(4), 386-396.

Zhou, X., von der Mark, K., Henry, S., Norton, W., Adams, H., & de Crombrugghe, B. (2014). Chondrocytes transdifferentiate into osteoblasts in endochondral bone during development, postnatal growth and fracture healing in mice. *PLoS genetics*, *10*(12), e1004820.

Zimmerman, L. B., De Jesús-Escobar, J. M., & Harland, R. M. (1996). The Spemann organizer signal noggin binds and inactivates bone morphogenetic protein 4. *Cell*, *86*(4), 599-606.

Résumé

Les patients atteints d'ostéochondrodysplasies, liées à des mutations activatrices dans les gènes *FGFR2* et *FGFR3,* présentent des malformations craniofaciales et mandibulaires. Ce projet de thèse a pour objectif de déchiffrer le rôle précis du gène FGFR3 chez les patients atteints d'ostéochondrodysplasie et dans un modèle murin d'hypochondroplasie *Fgfr3*$^{N534K/+}$ au cours de la formation et de la réparation osseuse mandibulaire. A partir d'un modèle de fracture non stabilisée de la mandibule de souris *Fgfr3*$^{N534K/+}$ et de leurs contrôles, les différentes étapes de la réparation osseuse endochondrale ont été étudiées à l'aide d'approches morphométriques, scanographiques, histologiques et de transcriptomique spatiale. Nous avons tout d'abord montré des anomalies morphologiques mandibulaires majeures chez les patients porteurs de faciocraniosténoses FGFR2 et FGFR3 et dans l'achondroplasie (FGFR3), renforçant l'hypothèse de corrélation génotype phénotype. Notre analyse montre une corrélation entre la sévérité des anomalies morphologiques craniomaxillofaciales des achondroplases et la sévérité des apnées du sommeil, soulignant ici l'importance de la prise en charge des anomalies morphologiques maxillomandibulaires. En parallèle, nous avons étudié l'impact de la mutation *Fgfr3*$^{N534K/+}$ au niveau des cartilages de formation mandibulaire, primaire (Meckel) et secondaires (condylien) en période anté- et postnatale. Des anomalies de formation et de résorption du cartilage de Meckel, et un défaut de différenciation chondrocytaire sont présents au sein du cartilage condylien chez les souris mutantes. L'ensemble de ces anomalies entraînent un défaut de croissance et des modifications morphologiques mandibulaires. Les fractures non stabilisées de la mandibule réalisées chez des souris *Fgfr3*$^{N534K/+}$ont permis d'analyser les cals de réparation. Nous avons observé des anomalies majeures de réparation, caractérisées par un retard sévère de consolidation osseuse, et la présence de pseudarthrose chez les souris *Fgfr3*$^{N534K/+}$. Nos études révèlent un défaut majeur de différenciation chondrocytaire au sein du cartilage de réparation, un retard de mise en place et de résorption du cartilage et des défauts microarchitecturaux de l'os nouvellement formé du cal. Nous avons également conduit des études de transcriptomique spatiale à la fois dans la partie cartilagineuse et osseuse à J14 post fracture. Au niveau du cartilage, les résultats obtenus confirment le défaut de différenciation et de maturation chondrocytaire, comme révélé par la diminution significative de l'expression de gènes exprimés par les chondrocytes matures ou en phase de transdifférenciation en ostéoblastes (*Col11, Col1a, Dmp1, Phospho1, Hmgb2*). L'expression de *Kif17*, un gène exprimé au sein du cil primaire a été retrouvée fortement diminuée chez les mutants, soulignant ici l'impact de la mutation au cours de la formation du cartilage du cal. Au niveau de l'os nouvellement formé du cal, les résultats montrent un défaut d'homéostasie osseuse. Nous avons aussi mis en évidence des différences majeures d'expression de gènes impliqués dans les mécanismes d'autophagie et d'apoptose (*Smad1, Comp, Birc2)* et une diminution de l'expression de *Alkbh2* traduisant un défaut de réparation de l'ADN. Nos analyses montrent la surexpression de gènes impliqués dans la régulation négative de la voie des MAPKinases, suractivée par la mutation *Fgfr3*$^{N534K/+}$, il s'agit de *Dusp9* (cartilage) de *Socs 3* et *Dusp3* (os du cal). Enfin, nous avons étudié l'impact d'antagonistes de FGFR3 (inhibiteur de tyrosine kinase et analogue du CNP) sur la réparation osseuse. Nos études précliniques ont montré que les souris *Fgfr3*$^{N534K/+}$ traitées présentent une consolidation normale, un remodelage osseux du cal de réparation accéléré et une absence de pseudarthrose.

L'ensemble de ces résultats ouvrent des perspectives thérapeutiques majeures chez les patients porteurs d'ostéochondrodysplasies FGFRs au cours de la réparation osseuse.

Mots clés : Ostéochondrodysplasies, FGFR2, FGFR3, mandibule, formation et réparation osseuse, transcriptomique spatiale

Titre : Formation, réparation osseuse mandibulaire et approches thérapeutiques dans les ostéochondrodysplasies liées à des mutations FGFRs

Abstract

Patients with osteochondrodysplasia, linked to activating mutations in the FGFR2 and FGFR3 genes, have craniofacial and mandibular malformations. This thesis project aims to decipher the exact role of FGFR3 gene in patients with osteochondrodysplasia and in a mouse model of hypochondroplasia Fgfr3N534K/+ during mandibular bone formation and repair.

Using a model of non-stabilized mandibular fracture performed in Fgfr3N534K/+ mice and their controls, the different stages of endochondral bone repair were studied using morphometric, microCT, histological and spatial transcriptomics approaches.

We first showed major mandibular morphological abnormalities in patients with FGFR2 and FGFR3 related craniosynostoses and in achondroplasia (FGFR3), reinforcing the hypothesis of genotype phenotype correlation in this context.

In addition, our analysis shows a correlation between the severity of craniomaxillofacial morphological abnormalities and the severity of sleep apnea in achondroplasia patients, highlighting here the importance of managing maxillomandibular morphological abnormalities. In parallel, we studied the impact of the Fgfr3N534K/+ mutation on mandibular, primary (Meckel) and secondary (condylar) cartilage in the ante- and postnatal period. Abnormalities in the formation and resorption of Meckel cartilage and altered chondrocyte differentiation within condylar cartilage were observed in mutant mice. All these abnormalities lead to growth defects and mandibular morphological changes. Following non-stabilized mandibular fractures, we observed major repair abnormalities, characterized by delayed bone consolidation, and the presence of pseudarthrosis in Fgfr3N534K/+ mice. Our studies revealed reduction of chondrocyte differentiation, delayed cartilage formation and formation, and microarchitectural defects in the newly formed bone of the callus. We also conducted spatial transcriptomics studies in both cartilaginous and bone regions at day 14 post fracture. At cartilage level, the results confirm reduction of chondrocyte differentiation and maturation, as revealed by the significant decrease in the expression of genes expressed by mature chondrocytes or in the phase of transdifferentiation into osteoblasts (Col11, Col1a, Dmp1, Phospho1, Hmgb2). The expression of Kif17, a gene expressed within the primary cilia was found greatly diminished in mutants, highlighting here the impact of the mutation during the formation of callus cartilage. At the level of the newly formed bone of the callus, the results show a defect of bone homeostasis. We also highlighted major differences in gene expression involved in autophagy and apoptosis mechanisms (Smad1, Comp, Birc2) and a decrease in Alkbh2 expression reflecting altered DNA repair.

Our analyses show the overexpression of genes involved in the downregulation of the MAPKinase pathway, overactivated by the Fgfr3N534K/+ mutation, these are Dusp9 (cartilage), Socs3 and Dusp3 (bone of callus).

Finally, we investigated the impact of FGFR3 antagonists (tyrosine kinase inhibitor and CNP analog) on bone repair. Our preclinical studies have shown that treated Fgfr3N534K/+ mice present normal consolidation, accelerated bone callus remodeling, and absence of pseudarthrosis. All these results are promising and give major therapeutic perspectives in patients with FGFRs osteochondrodysplasias during bone repair.

Keywords: Osteochondrodysplasia, FGFR2, FGFR3, mandible, bone formation and repair, spatial transcriptomics

Title: Mandibular bone formation and repair and therapeutic approaches in FGFRs osteochondrodysplasia